THE PHYSICAL REVIEW

VOLUME 96 Second Series NUMBER 2

OCTOBER 15, 1954

Published for the

AMERICAN PHYSICAL SOCIETY

by the

AMERICAN INSTITUTE OF PHYSICS

LANCASTER, PA., AND NEW YORK, N. Y.

THE
PHYSICAL REVIEW

A journal of experimental and theoretical physics established by E. L. Nichols in 1893

SECOND SERIES, VOL. 96, NO. 2 OCTOBER 15, 1954

On the Theory of Condensation

A. J. F. SIEGERT*
Institute for Advanced Study, Princeton, New Jersey
(Received June 9, 1954)

In an attempt to understand why approximations of the van der Waals type can yield semiquantitative results in spite of being qualitatively wrong, we have assumed that the partition function for submacroscopic volumes, as a function of the number of particles, is of the van der Waals type. We have considered, as a model of a real fluid, a cubic array of submacroscopic cells with variable numbers of particles and have assumed an interaction energy between adjacent cells only. Since the van der Waals equation predicts two sharp peaks in the probability function for the occupation numbers, one has then essentially a three-dimensional Ising model. Using some of the known properties of the Ising model (and some which can be safely anticipated), we find that with plausible assumptions about the interaction energy between cells this model exhibits condensation, and that its condensation pressure, its isotherm in the stable states, and its critical temperature, are still essentially determined by those of the individual cell.

I

APPROXIMATION formulas for the partition function $Q_N(V)$ of a system of N interacting particles enclosed in a volume V are qualitatively wrong for macroscopic systems if they predict (like the van der Waals equation) a violation of the stability condition. It has been shown by van Hove[1] that, with any realistic assumptions concerning the intermolecular forces, $\partial \ln Q_N(V)/\partial V$ is a nonincreasing function of V/N in the limit $N\to\infty$, $V\to\infty$, N/V finite. In spite of this fact, approximations of this type, when re-interpreted by means of the Maxwell construction, yield a variety of at least semiquantitative results for equilibrium states, and parts of the discarded region of the isotherm can be realized as metastable states. It seems, therefore, reasonable to believe that such expressions of the van der Waals type are approximations to some legitimate physical quantity rather than extrapolations without physical meaning and of merely historical interest. It seems natural to conjecture that they are approximations to the partition function of systems which are very small compared to macroscopic systems. Such a conjecture is not in contradiction with van Hove's theorem. We do not fail to realize that it would probably be very difficult to prove this conjecture directly from assumptions concerning the intermolecular forces, and we have not attempted to do this. The purpose of the calculations presented here is to carry further the investigation of the consequences of this conjecture and to see what other information would be needed to predict the behavior of a macroscopic system built up of submacroscopic systems, if the partition function of the subsystems were given, e.g., by a machine calculation, and if it turned out to be of van der Waals type.

An earlier attempt in this direction was made by Katsura and Fujita.[2] They consider the total volume V of the system as divided into small cubical cells of volume v, and make the conjecture of a van der Waals type partition function for the cells in the form of the assumption that the probability of having n particles in a cell, as function of n, has two sharp maxima, at n_1 and n_2 $(n_1<n_2)$, respectively, over a range of values of the temperature and Gibbs free energy. They studied the behavior of the total system, neglecting interaction between particles in different cells, and found that it is similar to that of a real system. The density of the total system is a single-valued function of the pressure and of the Gibbs free energy and shows a rapid rise over a very small range of pressures, at the pressure and Gibbs free energy which would have been obtained by the

* Guggenheim Fellow, on leave from Northwestern University.
[1] L. van Hove, Physica **15**, 951 (1949).
[2] S. Katsura and H. Fujita, Progr. Theoret. Phys. (Japan) **5**, 997 (1950).

Maxwell construction. Because of the neglect of interaction, however, the density and pressure which Katsura and Fujita obtain are simply those of the single cell in the grand canonical ensemble. They are analytic functions and thus do not satisfy the accepted definition of phase transitions.[3]

We have kept the basic conjecture for the partition function of the single cells, but have introduced, as a next step, an interaction energy between each pair of adjacent cells, which is a function of their occupation numbers, and which we assume to be small of the order of a surface energy as compared with the product of pressure and volume of the individual cells. We thus have a system of objects (cells) capable of two states (n close to n_1 or n_2) with nearest-enighbor interaction, i.e., a "binary alloy" of cells which is known[4] to be mathematically equivalent to the Ising model of a ferromagnet. Since the three-dimensional Ising model has not yet been treated rigorously it is fortunate that we need only the existence of a phase transition, a rough estimate of its Curie temperature, and some estimates of orders of magnitude of its thermodynamic functions which can be obtained from the series expansions (see reference 4, pp. 379–380). The interesting terms in the pressure and density are the free energy and magnetization, respectively, of the Ising model. The quantity which plays the role of the energy μH of a spin in the magnetic field turns out to be $(p_2-p_1)v$ (except for correction terms), where p_1 and p_2 are the pressures formally computed[5] for cells with n_1 and n_2 particles. Except for a small range close to the double point in the graph[6] of the formally computed pressure vs Gibbs free energy, the system therefore corresponds to a magnet in the range $|\mu H| \gg kT$. (The system of Katsura and Fujita corresponds, of course, to the paramagnet, and the steep rise of the density which they considered to be condensation corresponds to the change of magnetization of a paramagnet, when the field passes through zero.) The interaction energy ϵ of a pair of opposite spins is found to correspond to a linear combination of the interaction energies $E_{\sigma\sigma'}$ of a pair of cells with n_σ and $n_{\sigma'}$ particles, and it is plausible that the dominant term in ϵ is $-\frac{1}{2}E_{22}$, so that ϵ is positive (and thus favors parallel spins) if the interaction between "liquid" cells decreases the energy of the pair. The Curie temperature of the model is $T_c \cong 2\epsilon/k \cong |E_{22}|/k$.

The interaction energy required to cause condensation is thus very small compared with values which one would consider plausible. This implies that the critical temperature of the system is the critical temperature determined by the van der Waals type partition function of the cell, not the Curie temperature of the Ising model. We find, furthermore, that already for $\epsilon \geq kT$ quantitative details of the thermodynamic functions of the Ising model become irrelevant, it provides merely the mechanism by which the thermodynamic functions of the total system change from one branch of the thermodynamic functions of the single cell to the other. (There are three branches, but only two correspond to probability maxima.) There are, of course, correction terms to the pressure and density of the individual cell which are of first order in the interaction energies, if pressure and density are written as functions of the Gibbs free energy. In the expression for the pressure as function of the density, however, the first-order correction term appears in the form $(\partial E_{\sigma\sigma}/\partial n_\sigma - E_{\sigma\sigma}/n_\sigma)$ which reduces it appreciably if the interaction energy between cells in the same state is approximately proportional to the number of particles.

In Sec. 3 we have presented some properties of the hypothetical van der Waals type gas, since the statements found in the literature are often not quite correct.

II

The total volume V of the gas is divided into $\mathfrak{N}$ equal cubical cells of volume v. The partition function for the jth cell containing n_j particles is written as

$$Q_{nj}(v) \equiv \frac{1}{n_j!}\int_v e^{-\beta U} \prod_1^{n_j} d\tau_k, \tag{2.1}$$

where U denotes the potential energy of the n_j particles only and $d\tau_k$ is the volume element of the kth particle, and $\beta = 1/kT$. We accept as a *conjecture* the assumption of Katsura and Fujita[7] that the relative probability $y^n Q_n(v)$ of finding n particles in a cell at fugacity y has two sharp maxima, at n_1 and n_2 ($n_2 \gg n_1 \gg 1$), in some region of fugacity values and for some volume v which is large compared to atomic dimensions, but small compared to macroscopic dimensions. The numbers n_1 and n_2 are roots of the equation

$$\ln y + \partial \ln Q_n(v)/\partial n = 0; \tag{2.2}$$

the maxima are furthermore specified by the additional assumption that

$$\sigma^2(n) \equiv -[\partial^2 \ln Q_n(v)/\partial n^2]^{-1} \tag{2.3}$$

is of order n_1 and n_2 at n_1 and n_2, respectively, and changes only negligibly over a region $\sqrt{n_1}$ and $\sqrt{n_2}$ at n_1 and n_2, respectively. The inequality $n_2 \gg n_1$ is to be interpreted as $n_2 - n_1 > \max[\sigma(n_1), \sigma(n_2)]$.

The intent of these assumptions is to describe a gas of van der Waals type at temperatures below its critical temperature.

Neglecting interaction between particles in different

[3] B. Kahn and G. E. Uhlenbeck, Physica **5**, 399 (1938).

[4] G. F. Newell and E. W. Montroll, Revs. Modern Phys. **25**, 353 (1953); p. 382 ff. and literature quoted there.

[5] These are defined by Eq. (2.4) and must not be confused with the ensemble pressure [Eq. (2.5)].

[6] See J. C. Slater, *Introduction to Chemical Physics* (McGraw-Hill Book Company, Inc., New York and London, 1939), p. 188, Fig. XII–4. The third (short) branch corresponds to a probability minimum.

[7] The proof given by Katsura and Fujita (reference 2) is at best a plausibility argument.

cells, Katsura and Fujita then obtain the density ρ^0 and pressure P^0 of the total system, which of course are simply the expectation value of the density in the cells in the grand canonical ensemble and its integral with respect to $\ln y$, respectively. With the notation

$$p_\sigma \equiv (kT/v)(n_\sigma \ln y + \ln Q_{n_\sigma}) \quad (\sigma = 1, 2), \tag{2.4}$$

for the pressure formally computed for cells with n_1 and n_2 particles, these are

$$P^0 = \tfrac{1}{2}(p_1+p_2) + v^{-1}kT \ln \cosh[\tfrac{1}{2}v(p_1-p_2)/kT], \tag{2.5}$$

$$\rho^0 = v^{-1}\{\tfrac{1}{2}(n_1+n_2) + \tfrac{1}{2}(n_1-n_2)\tanh[\tfrac{1}{2}v(p_1-p_2)/kT]\}, \tag{2.6}$$

where, because of the assumed sharpness of the maxima in the sequence of terms in the grand partition function, the summation has been carried only over the numbers n_1 and n_2 in each cell.

The functions P^0 and ρ^0 are indeed similar to those of a condensing system. They are single-valued monotonically increasing functions of $\ln y$ and of each other, and the density increases from n_1 to n_2 over a very small region of pressures at that value of y for which $p_1 = p_2$. However, since the density of the total system is the expectation value of the density for the single cell, the density and, *a fortiori*, the pressure are independent of the number of cells and are analytic functions of y, and thus do not fulfill the specifications of the accepted definition of phase transitions.[3] In terms of the Yang-Lee theory[8] the grand partition function of the $\mathfrak{N}$ cells is simply the $\mathfrak{N}$th power of the grand partition function of the individual cell if interaction is neglected;[9] its roots, therefore, cannot approach the real axis, but remain fixed; only the multiplicity of the roots increases by a factor $\mathfrak{N}$.

In view of the fact that the increase of ρ^0 would be experimentally indistinguishable from a discontinuity, one might consider the insistence on the rigorous definition somewhat dogmatic. However, its physical significance is that the neglected interaction could decrease the steepness of the rise of ρ^0 at the transition point. Even if, therefore, the partition function of the individual subsystem (cell) were known (e.g., from a machine calculation) to be of the type specified by the conjecture, some information concerning the interaction between the subsystem would be required to predict the thermodynamic behavior of the total system.

We will, therefore, try to improve on the ensemble model by taking into account the interaction between adjacent cells (i.e., cells having a surface in common). Instead of the partition function $Q_N^{(0)}(V)$,

$$Q_N^{(0)}(V) = \sum' \prod_j Q_{n_j}(v), \tag{2.7}$$

we then have

$$Q_N(V) = \sum' \prod_j Q_{n_j}(v) \prod_{j\neq k}{}' q(n_j, n_k), \tag{2.8}$$

where the sum extends over the values n_j of all cells and the prime denotes the restriction $N = \sum_j n_j$, and the prime at the product denotes restriction to adjacent cells. The grand partition function then becomes

$$\begin{aligned}\mathcal{Q}_V(y) &= \sum y^{\sum_j n_j} \prod_j Q_{n_j}(v) \prod_{j\neq k}{}' q(n_j, n_k) \\ &= \sum \exp\{\sum_j [n_j \ln y + \ln Q_{n_j}] + \sum_{j\neq k}{}' \ln q(n_j, n_k)\}.\end{aligned} \tag{2.9}$$

Using the conjecture that $y^n Q_n(v)$ has two sharp maxima, at n_1 and n_2, respectively, we obtain for the pressure

$$P = kTV^{-1} \ln \mathcal{Q}_V(y) = kTV^{-1} \ln \sum \exp\beta[\mathfrak{N}_1 p_1 v + \mathfrak{N}_2 p_2 v - \mathfrak{N}_{11}E_{11} - \mathfrak{N}_{12}E_{12} - \mathfrak{N}_{22}E_{22}], \tag{2.10}$$

where the sum now extends only over the two values n_1 and n_2 for the occupation number of each cell,[10] and where $\mathfrak{N}_\sigma$ denotes the number of cells with n_σ particles, $\mathfrak{N}_{\sigma\sigma'}$ the number of adjacent pairs of cells with n_σ and $n_{\sigma'}$ particles, and where $E_{\sigma\sigma'}$ is defined by

$$E_{\sigma\sigma'} = -2kT \ln q(n_\sigma, n_{\sigma'}), \tag{2.11}$$

and p_σ by Eq. (2.4). This is the partition function of a binary alloy, which is known[4] to be mathematically equivalent to the three-dimensional Ising model. Since

$$\mathfrak{N}_{11} = 3\mathfrak{N}_1 - \tfrac{1}{2}\mathfrak{N}_{12} = \tfrac{3}{2}\mathfrak{N} + \tfrac{3}{2}(\mathfrak{N}_1 - \mathfrak{N}_2) - \tfrac{1}{2}\mathfrak{N}_{12}, \tag{2.12}$$

$$\mathfrak{N}_{22} = 3\mathfrak{N}_2 - \tfrac{1}{2}\mathfrak{N}_{12} = \tfrac{3}{2}\mathfrak{N} - \tfrac{3}{2}(\mathfrak{N}_1 - \mathfrak{N}_2) - \tfrac{1}{2}\mathfrak{N}_{12}, \tag{2.13}$$

one can write

$$P = kTV^{-1} \ln\{\exp\mathfrak{N}\alpha\beta \sum \exp(-\beta[H(\mathfrak{N}_1 - \mathfrak{N}_2) + \epsilon\mathfrak{N}_{12}])\}, \tag{2.14}$$

where

$$\alpha = \tfrac{1}{2}\{(p_2 v - 3E_{22}) + (p_1 v - 3E_{11})\}, \tag{2.15}$$

$$H = \tfrac{1}{2}\{(p_2 v - 3E_{22}) - (p_1 v - 3E_{11})\}, \tag{2.16}$$

$$\epsilon = E_{12} - \tfrac{1}{2}(E_{11} + E_{22}), \tag{2.17}$$

and the sum again extends over the two states of each cell. We will denote this sum which is the partition function of the three-dimensional Ising model by Z_I, and write $F(H,\epsilon)$ for the free energy,

$$F(H,\epsilon) \equiv -\mathfrak{N}^{-1}kT \ln Z_I, \tag{2.18}$$

[8] C. N. Yang and T. D. Lee, Phys. Rev. 87, 404 (1952).

[9] Even if the cells are chosen of macroscopic dimensions, as long as they are of fixed and finite volume, interaction between cells is required for a phase transition in the rigorous sense. Since in that case the probability for the occupation numbers must be already almost flat over a finite interval and practically zero outside this interval, the corresponding ferromagnet consists of classical magnetic dipoles.

[10] The error incurred in this step is estimated in Appendix I.

I for the normalized magnetization,

$$I \equiv \mathfrak{N}^{-1}(\mathfrak{N}_2 - \mathfrak{N}_1)_{\mathfrak{N}} = -\partial F/\partial H, \tag{2.19}$$

and define λ by

$$\lambda \equiv \mathfrak{N}^{-1}\langle \mathfrak{N}_{12}\rangle_{\mathfrak{N}} = \partial F/\partial \epsilon. \tag{2.20}$$

We then have

$$P = v^{-1}\{\alpha - F(H,\epsilon)\}. \tag{2.21}$$

The density is then

$$\rho = \beta \partial P/\partial \ln y. \tag{2.22}$$

With dots indicating differentiation with respect to $\ln y$, and using Eqs. (2.2) and (2.4) to obtain

$$\beta \dot{p}_\sigma v = n_\sigma, \tag{2.23}$$

we get

$$\begin{aligned}\rho &= v^{-1}\beta\{\dot{\alpha} + I\dot{H} - \lambda\dot{\epsilon}\} \\ &= v^{-1}\{(n_2 - 3\beta\dot{E}_{22})\tfrac{1}{2}(1+I) \\ &\qquad + (n_1 - 3\beta\dot{E}_{11})\tfrac{1}{2}(1-I) - \beta\lambda\dot{\epsilon}\}.\end{aligned} \tag{2.24}$$

The free energy and magnetization of the paramagnet, ln cosh and tanh in Eqs. (2.5) and (2.6), have thus been replaced by the free energy and the magnetization of the Ising model.

Although the three-dimensional Ising model has not yet been treated exactly it seems safe to anticipate the following properties on the basis of approximative calculations (reference 4, p. 379). The model will have a ferromagnetic phase transition at $H=0$, if $\epsilon>0$, with a Curie temperature $T_c \cong 2\epsilon/k$. At temperatures $T<\epsilon/k$ the spontaneous magnetization will be unity, with an error of $\frac{1}{2}$ percent [$2e^{-6\beta\epsilon}$ according to the low temperature expansion (see reference 4, p. 380)]. This implies that $\lambda \ll 1$ for $T<\epsilon/k$.

If $\epsilon > kT$, we have, therefore,

$$I = \pm 1 \quad \text{for} \quad H \gtrless 0, \quad \text{and} \quad F(H,\epsilon) = -|H| + F(0,\epsilon),$$

and thus

$$\left.\begin{aligned} P &= p_2 - [3E_{22} + F(0,\epsilon)]v^{-1} \\ \rho &= v^{-1}[n_2 - 3\beta\dot{E}_{22} - \beta\lambda\dot{\epsilon}] \end{aligned}\right\} \quad \text{for} \quad p_2 - 3E_{22}v^{-1} > p_1 - 3E_{11}v^{-1}; \tag{2.25, 2.26}$$

$$\left.\begin{aligned} P &= p_1 - [3E_{11} + F(0,\epsilon)]v^{-1} \\ \rho &= v^{-1}[n_1 - 3\beta\dot{E}_{11} - \beta\lambda\dot{\epsilon}] \end{aligned}\right\} \quad \text{for} \quad p_2 - 3E_{22}v^{-1} < p_1 - 3E_{11}v^{-1}. \tag{2.27, 2.28}$$

The interaction energy required to change the continuous increase of the density obtained in the grand ensemble into an actual discontinuity is thus extremely small.[11]

It is plausible that $E_{22} \gg E_{11}$, E_{12} and that $\gtrsim -\frac{1}{2}E_{22}$ is of order $av^{-1}\cdot n_2 u$ (where a is the range of the attractive force and u is an average potential energy of attraction) and thus of order $av^{-1}n_2 kT$.

The Curie temperature of the Ising model is, therefore, so high that it has no bearing on the critical temperature of the gas. The latter is given by the critical temperature of the individual cell, i.e., the temperature at which the two roots n_1 and n_2 coalesce, in distinction to the case of the lattice gas, where it is, of course, the same as the Curie temperature.[12] This agrees well with the fact that the van der Waals equation yields PV/kT at the critical point in rough agreement with experiment.

To estimate the correction terms which are to be applied to the thermodynamic functions of the cell in order to obtain the thermodynamic functions of the total system, we note first that the terms containing $F(0,\epsilon)$ and λ are irrelevant. The leading term in the expansion of $F(0,\epsilon)$ is $-kT\exp[-(9/2)\beta\epsilon]$ [reference 4, p. 380, Eq. (7.5)]. The factor λ can be most readily estimated from the identities

$$\mathfrak{N}_{12} = 6\mathfrak{N}_1 - 2\mathfrak{N}_{11} = 6\mathfrak{N}_2 - 2\mathfrak{N}_{22}, \tag{2.29}$$

which yield

$$\lambda \equiv \mathfrak{N}^{-1}\langle \mathfrak{N}_{12}\rangle_{\mathfrak{N}} \leqslant 6\mathfrak{N}^{-1}\min(\langle \mathfrak{N}_1\rangle_{\mathfrak{N}}, \langle \mathfrak{N}_2\rangle_{\mathfrak{N}}), \tag{2.30}$$

or

$$\lambda \leqq 6\min[\tfrac{1}{2}(1 \pm I)] \cong 6e^{-6\beta\epsilon}. \tag{2.31}$$

The thermodynamic functions of the Ising model thus disappear, as they should, from the pressure and density of the total system above and below the transition pressure.

The surface energy terms E_{22} and E_{11}, of course, remain, since they express the fact that each cell is surrounded by cells which have (except for the fluctuations specified in the basic conjecture) the same number of particles. (The factor 3 instead of 6 comes from the definition of $E_{\sigma\sigma}$ as the interaction energy per *pair* of cells.) The effect of these terms on the isotherm is smaller than would appear on first sight from Eqs. (2.25)–(2.28) because the represent primarily an adjustment of the Gibbs potential for the individual cell. Neglecting terms of second order in the interaction terms one has, in fact, above and below the transition point ($\sigma = 1,2$),

$$\begin{aligned} P(\rho) &= p_\sigma(n_\sigma/v) - 3E_{\sigma\sigma}v^{-1} \\ &= p_\sigma(\rho + 3\beta\dot{E}_{\sigma\sigma}v^{-1}) - 3E_{\sigma\sigma}v^{-1} \\ &= p_\sigma(\rho) + 3\beta\dot{E}_{\sigma\sigma}v^{-1}\dot{p}_\sigma(n_\sigma v^{-1})/\dot{p}_\sigma(n_\sigma v^{-1}) - 3E_{\sigma\sigma}v^{-1} \\ &= p_\sigma(\rho) + 3n_\sigma v^{-1}[\partial E_{\sigma\sigma}/\partial n_\sigma - E_{\sigma\sigma}/n_\sigma]. \end{aligned} \tag{2.32}$$

[11] This fact and the fast convergence of the low-temperature series suggest an attempt to approximate the partition function with cells of very small size, capable of containing only a few particles, provided that there is a possibility of extending the expansions to more complicated Ising models (with more than two states and less restricted interaction).

[12] T. D. Lee and C. N. Yang, Phys. Rev. 87, 410 (1952).

The first-order correction to the isotherm is thus caused only by the deviations from linearity of the interaction energy E_{ss} as a function of n_s.

III

In this section we will state some properties of a hypothetical gas of van der Waals type, which is essentially equivalent to the subsystems defined in the basic conjecture of Sec. 2, simplifying and extending the calculations made in an earlier paper.[13] We have chosen the volume-pressure representation because the properties are easier to visualize in this case than in the density-fugacity representation, which we had to use in Sec. 2 in order to have a fixed cell division.

We shall investigate the consequences of the following assumptions: For a certain *finite* range of the number of particles N, the partition function Q of a substance has qualitatively the form of the partition function of a van der Waals gas. More precisely, it is analytic and, for a certain finite interval of temperatures T and volumes V, $\partial^2 \ln Q/\partial V^2$ is positive. In the regions of V which in the conventional reinterpretation of the van der Waals isotherm are assigned to gas, liquid, undercooled vapor and superheated liquid, we assume $[-V^2\partial^2 \ln Q/\partial V^2]$ to be of order N. Denoting by P_c the condensation pressure and by ΔV the difference between the volumes of liquid and gas which would be obtained from our hypothetical partition function by the conventional construction, we assume $P_c\Delta V$ to be of order NkT.

We shall now consider such a substance, together with a mechanical system whose potential energy is $\Phi(V,V_0)$ (where V_0 is a parameter of the mechanical system) as being in thermodynamic equilibrium with a heat bath.[14] The probability that the substance occupies a volume between V and $V+dV$ is then

$$W(V)dV=C^{-1}\exp\{-\beta\Phi+\ln Q\}dV. \tag{3.1}$$

The function $W(V)$ is stationary at volumes V_s which are the roots of the equation

$$\partial\Phi/\partial V=\beta^{-1}\partial \ln Q/\partial V. \tag{3.2}$$

A stationary value is a maximum if

$$[-\beta\partial^2\Phi/\partial V^2+\partial^2 \ln Q/\partial V^2]_s<0. \tag{3.3}$$

Since Eq. (3.2) yields

$$\left[\frac{\partial}{\partial V_0}\left(\frac{\partial\Phi}{\partial V}\right)\right]_s+\left[\frac{\partial^2\Phi}{\partial V^2}\right]_s\frac{\partial V_s}{\partial V_0}=\beta^{-1}\left[\frac{\partial^2 \ln Q}{\partial V^2}\right]_s\frac{\partial V_s}{\partial V_0}, \tag{3.4}$$

this inequality (3.3) is equivalent to the inequality

$$\left[\frac{\partial}{\partial V_0}\left(\frac{\partial\Phi}{\partial V}\right)\right]_s\Big/\left[\frac{\partial V_s}{\partial V_0}\right]<0. \tag{3.5}$$

[13] A. J. F. Siegert, Phys. Rev. **90**, 97 (1953).

[14] Arbitrarily large positive values of $\partial^2 \ln Q/\partial V^2$ in this region would not essentially affect our conclusions.

The two cases,

$$\Phi=PV \tag{I}$$

and

$$\Phi=\tfrac{1}{2}\alpha(V-V_0)^2, \tag{II}$$

are of interest since case (I) represents a system under a well-determined force per unit area and case (II) a system for which the relative magnitude of the uncertainty of force and volume can be chosen by an appropriate choice of α.

In the first case Eq. (3.2) becomes

$$P=\beta^{-1}\partial \ln Q/\partial V. \tag{3.2 I}$$

While this equation is formally the same as the usual equation for the pressure, its derivation shows its correct interpretation as an equation whose roots are the stationary points of $W(V)$. The inequality (3.3) shows that only those roots V_s correspond to maxima for which

$$[\partial^2 \ln Q/\partial V^2]_s<0, \tag{3.3 I}$$

or—by identification of the parameter V_0 with P according to (3.5)—

$$\partial V_s/\partial P<0. \tag{3.4 I}$$

The magnitude of the maxima is obtained from (3.1) as

$$W(V_s)=C^{-1}e^{-\beta g_s}, \tag{3.6}$$

where g_s is defined by

$$g_s\equiv PV_s-\beta^{-1}\ln[Q]_s, \tag{3.7}$$

and is thus the Gibbs potential, formally computed at V_s. Under the assumptions stated above, there are two maxima of $W(V)$, at V_1 and V_2. If P_c denotes the value of P for which $g_1=g_2$, the ratio of the two maxima of $W(V)$, considered as a function of P, becomes, in the neighborhood of P_c,

$$W(V_1)/W(V_2)=\exp\{-\beta(P-P_c)[V_1(P_c)-V_2(P_c)]\}, \tag{3.8}$$

since

$$g_s(P)\cong g_s(P_c)+(P-P_c)[\partial g_s(P)/\partial P]_{P_c}, \tag{3.9}$$

and

$$\partial g_s/\partial P=V_s+[P-\beta^{-1}\partial \ln Q/\partial V]_s\partial V_s/\partial P=V_s. \tag{3.10}$$

Defining P_l and P_g such that $W(V_1)/W(V_2)$ equals τ for $P=P_l$ and τ^{-1} for $P=P_g$, one gets

$$P_l-P_g=2kT[V_2(P_c)-V_1(P_c)]^{-1}\ln\tau. \tag{3.11}$$

The range of pressures over which the change from one branch to the other occurs is thus of order $N^{-1}P_c$.

The two maxima of $W(V)$ are sharp under the assumptions made, since, in the neighborhood of either V_s, $W(V)$ is of the form

$$\exp[-\tfrac{1}{2}(V-V_s)^2(-\partial^2 \ln Q/\partial V^2)_s]$$

in the region of interest. The expectation value $\bar{V}$ of V can thus be written as

$$\bar{V}=\sum_{s=1,2} V_s e^{-\beta g_s}/\sum_{s=1,2} e^{-\beta g_s}. \tag{3.12}$$

The graph of P *vs* $\bar{V}$ thus follows the curve $\beta^{-1}\partial \ln Q/\partial V$ practically to $V_1(P_c)$, and is practically horizontal between $V_1(P_c)$ and $V_2(P_c)$, where P changes with increasing $\bar{V}$ only by a quantity of order P_1-P_2 given by Eq. (3.11), and follows again $\beta^{-1}\partial \ln Q/\partial V$ for $\bar{V}>V_2(P)$. The almost horizontal isotherm must not be ascribed to the individual van der Waals gas, but to the ensemble only.

Under the conditions of case II, the behavior of the van der Waals gas differs even more from the behavior of a macroscopic system. Equation (3.3) becomes

$$\alpha(V-V_0)=\beta^{-1}\,\partial \ln Q/\partial V. \tag{3.2 II}$$

If α is chosen to be larger than $\max[\beta^{-1}\partial^2 \ln Q/\partial V^2]$ Eq. (3.2 II) has only one root, and, according to (3.3), $W(V_s)$ is a maximum. In this case, there is thus no phenomenon resembling a phase transition. By an appropriate choice of α, the "phase transition" can be made to occur between values V_1 and V_2 other than $V_1(P_c)$ and $V_2(P_c)$ and any pair of points on the descending branches of $\partial \ln Q/\partial V$ can thus be reached. Points on the ascending branch can, however, be reached only if α is chosen large enough so that Eq. (3.2 II) has only one root. The thermodynamic behavior of a van der Waals gas depends thus on the mechanical system with which it is coupled, which means that it is not a thermodynamic system.

By means of a similar argument one can show that the logarithm of the energy level density $\rho(E)$ as function of the energy E cannot, for a macroscopic system, have the shape shown as "Actual Curve" in Fig. 16, p. 486, F. Seitz, *The Modern Theory of Solids* (McGraw-Hill Book Company, Inc., New York and London, 1940). The analog of van Hove's theorem for this case, that is the theorem that $\partial \ln\rho(E)/\partial E$ is a nonincreasing function of E in the usual limit, has not yet been proven directly.

If a macroscopic system is considered as an ensemble of a large number m of systems with van der Waals type partition function, the behavior of the macroscopic system becomes unique, however, and its isotherm—although still analytic—has almost the shape which one attempts to prove for the limit $N\to\infty$, $V\to\infty$, N/V fixed. The probability function $W_{mN}(V_m)$ for the volume of the ensemble of systems under fixed force is

$$W_{mN}(V_m)=C_m(P)e^{-\beta PV_m}Q_{mN}(V_m), \tag{3.13}$$

where mN and V_m are, respectively, the number of particles and the volume of the whole ensemble, and $Q_{mN}(V_m)$ is its partition function. For sufficiently large m, the maximum of $W_{mN}(V_m)$ is located at $V_m=m\bar{V}(P)$ where $\bar{V}(P)$ is the expected value of the volume of the subsystem discussed above [Eq. (3.12)]. We thus have

$$\partial \ln W_{mN}/\partial V_m=-\beta P+\partial \ln Q_{mN}/\partial V_m=0, \tag{3.14}$$

at

$$V_m=m\bar{V}(P).$$

The isotherm of the ensemble is thus the curve of P *vs* $m\bar{V}(P)$.

In the volume-pressure description, the Laplace transform of $Q_N(V)$,

$$C_N(s)=\int_0^\infty e^{-sV}Q_N(V)dV, \tag{3.15}$$

plays a role similar to that of the grand canonical partition function in the paper of Yang and Lee[8] in the density-fugacity representation. The expected value of the volume, $\bar{V}_N(s)$ at a pressure $P=\beta^{-1}s$, is given by

$$\bar{V}_N(s)=-\partial \ln C_N(s)/\partial s. \tag{3.16}$$

We denote the expected volume per mole by $\bar{v}_N=N_0\bar{V}_N/N$, where N_0 is Avogadro's number. Since $C_N(s)$ is regular in the open right half-plane $\mathrm{Re}(s)>0$, the only singularities of $\bar{v}_N(s)$ which can occur in that region are poles of first order. If we think for a moment of $\mathrm{Re}\,\bar{v}_N(s)$ as an electrostatic potential, any poles of $\bar{v}_N(s)$ are to be interpreted as infinite dipole lines perpendicular to the s plane. A steep decrease of the volume over a small range of pressure at P_c corresponds to a steep potential drop on the real axis, which occurs if and only if a grating of dipole lines closes in on the real axis at $s=\beta P_c$.[16] In order to obtain a finite saltus $\Delta\bar{v}$ of $\bar{v}_N$ in the limit $N\to\infty$, the dipole grating must, in this limit, become a dipole layer of dipole strength $\Delta\bar{v}$.

The assumption of a van der Waals type partition function for a finite N yields a dipole grating. We have, writing $s=t+i\vartheta$, with t and ϑ real, and using the fact that $e^{-tV}Q_N(V)$ has one or two sharp peaks as described above,

$$\begin{aligned}C_N(s)&=\int_0^\infty e^{-i\vartheta v}\{p_1(t)\delta(V-V_1(t))\\&\qquad+p_2(t)\delta(V-V_2(t))\}dV\\&=p_1(t)e^{-i\vartheta V_1}+p_2(t)e^{-i\vartheta V_2}.\end{aligned} \tag{3.17}$$

The roots of $C_N(s)$ are thus roots of

$$e^{-i\vartheta(V_2(t)-V_1(t))}=-p_1(t)/p_2(t), \tag{3.18}$$

[16] In order to obtain the theorems of the Yang-Lee theory rigorously one would have to prove the existence of the Gibbs free energy per atom, $\lim_{N\to\infty}[N^{-1}\ln C_N(s)]$, for real values of the pressure only, since the extension into the complex plane is provided by some trivial properties of Laplace transforms and Vitali's theorem [see E. C. Titchmarch, *The Theory of Functions* (Oxford University Press, London, 1939), second edition, p. 168, Sec. 531].

and, since ϑ was to be real, the roots of $C_N(s)$ are simple roots located at the points defined by

$$p_1(l)=p_2(l) \tag{3.19}$$

and

$$\vartheta=\pm\frac{(2l+1)\pi}{V_2(t)-V_1(t)} \quad (l=0, 1, 2\cdots). \tag{3.20}$$

Our assumptions thus yield a grating of dipole lines on the line $t=\mathrm{Re}\ s=\beta P_e$, spaced with separation $2\pi/(V_2-V_1)$. The roots of $C_N(s)$ are of first order and each pole of $\tilde{V}(s)$ is, therefore, of the form $-(s-s_l)^{-1}$, which corresponds to a dipole of moment 2π; the dipole grating has thus a dipole moment per unit length of $[V_2(t)-V_1(t)]$.

In the ensemble the position of the roots remains unchanged. In order to consider interaction we used the density-fugacity representation in Sec. 2 since there is no equivalent to the Ising model available for the irregular array of cells of variable volume which one would have to deal with in the volume-pressure representation.

The author would like to thank Professor L. van Hove for some very interesting discussions, Professor J. R. Oppenheimer for the hospitality of the Institute for Advanced Study, The John Simon Guggenheim Memorial Foundation for a fellowship, and Northwestern University for a leave for research.

APPENDIX I

In order to estimate the effect of fluctuations in the occupation numbers around their most probable values we write the (unnormalized) probability function for the occupation numbers in the form

$$\exp(n_j\ln y+\ln Q_{nj})=\sum_{n_{j\sigma}=n_1,n_2}\exp[n_{j\sigma}\ln y+\ln Q_{n_{j\sigma}} -(n_j-n_{j\sigma})^2/2\sigma^2(n_{j\sigma})], \tag{A1}$$

where $\sigma^2(n)$ is defined by Eq. (2.3), and expand the interaction terms to first order in the fluctuations:

$$\sum_{j\neq k}{}'\ln q(n_j,n_k)=\sum_{j\neq k}{}'\ln q(n_{j\sigma},n_{k\sigma}) +2\sum_j(n_j-n_{j\sigma})\sum_k{}'\frac{\partial\ln q(n_{j\sigma},n_{k\sigma})}{\partial n_{j\sigma}}. \tag{A2}$$

Instead of Eq. (2.10) we then have

$$\mathfrak{Q}_V(y)=\sum\exp\{\sum_j[n_{j\sigma}\ln y+\ln Q_{n_{j\sigma}}] +\sum_{j\neq k}\ln q(n_{j\sigma},n_{k\sigma})+\ln J\}, \tag{A3}$$

where the sum extends again over $n_{j\sigma}=n_1, n_2$ only, for each cell. The correction term J is defined as

$$J=\int\cdots\int\exp\sum_j\{-(n_j-n_{j\sigma})^2/2\sigma^2(n_{j\sigma}) +2(n_j-n_{j\sigma})\sum_k{}'\partial\ln q(n_{j\sigma},n_{k\sigma})/\partial n_{j\sigma}\}\prod_j dn_j, \tag{A4}$$

where the summation over k extends only over nearest neighbors of j. The integration yields

$$\ln J=\tfrac{1}{2}\sum_j\ln(2\pi\sigma^2(n_{j\sigma})) +2\sum_j\sigma^2(n_{j\sigma})[\sum_k{}'\ln q(n_{j\sigma},n_{k\sigma})/\partial n_{j\sigma}]^2. \tag{A5}$$

The logarithmic terms are irrelevant and we thus have

$$\ln J=2\sum_j\sigma^{-2}(n_{j\sigma}) \times[\sum_k{}'\sigma^2(n_{j\sigma})\partial\ln q(n_{j\sigma},n_{k\sigma})/\partial n_{j\sigma}]^2. \tag{A6}$$

Since $\sigma^2(n)$ was assumed to be of order n, the terms $\sigma^2(n)\partial\ln q/\partial n$ are of the order of the surface terms $\ln q$, and the terms of $\sum_j$ become of lower order than the surface terms $\ln q$.

Principle of Minimum Entropy Production*

MARTIN J. KLEIN† AND PAUL H. E. MEIJER‡
Department of Physics, Case Institute of Technology, Cleveland, Ohio

(Received April 1, 1954)

The principle of minimum entropy production says that the steady state of an irreversible process, i.e., the state in which the thermodynamic variables are independent of the time, is characterized by a minimum value of the rate of entropy production. This theorem, due to Prigogine, is proved by the methods of statistical mechanics for a particular process—the flow of matter and energy through a narrow tube connecting two containers of an ideal gas. The two containers are maintained at slightly different temperatures. The resultant form for the entropy production in the steady state, and the method used in the proof, give additional insight into the significance of the principle of minimum entropy production.

I. INTRODUCTION

THE principle of minimum entropy production gives a thermodynamic criterion for determining the steady state of a system in which an irreversible process is taking place. The criterion can be formulated very simply: the steady state is that state in which the rate of entropy production has the minimum value consistent with the external constraints which prevent the system from reaching equilibrium. The equilibrium state takes its natural place in this way of looking at thermodynamic processes as the simplest kind of steady state. When there are no constraints, the system proceeds to that state in which the rate of entropy production is zero, i.e., to the equilibrium state. When constraints, such as an externally maintained temperature difference between parts of the system, prevent the system from reaching equilibrium, the system does the next best thing: it goes to a state in which the thermodynamic variables do not change with time and in which the smallest possible amount of entropy is created per unit time.

This characterization of the steady state as the state of minimum entropy production is due to Prigogine[1] and, in a somewhat generalized form, to de Groot.[2] The proofs given by both authors are based on the Onsager[3] relations, which form the starting point of the recently developed thermodynamic theory of irreversible processes in the steady state.[4]

Because the principle of minimum entropy production has a wide range of applications and because it seems to pick out an essential feature of irreversible processes, we have tried to derive it by the methods of statistical mechanics. The method we have used is a generalization of the method used by Pauli[5] to derive the second law of thermodynamics (or H theorem) from quantum mechanics. This method has recently been discussed by Thomsen,[6] and we have drawn upon Thomsen's paper in our own work.

Using this method we have derived the principle of minimum entropy production for a particular irreversible process—the flow of matter and energy through a small capillary connecting two containers of an ideal gas. The two identical containers are maintained at slightly different temperatures by two heat baths. Starting with a set of equations which gives the time variation of the numbers of molecules in the energy states of the two containers, we have proved that the steady state corresponds to that set of occupation numbers which minimizes the rate of entropy production. Two features of interest in our derivation are the necessity for a small temperature difference between the two containers and the important role played by the two heat baths in the entropy production. Our final form for the rate of entropy production in the steady state has a simple physical interpretation relating the entropy production to the flow of heat from one heat bath to the other.

We conclude this introduction with an outline of the contents of the subsequent sections. Section II contains the detailed specification of the system considered, and includes the basic stochastic equations for rates of change of the relevant probabilities. Section III contains the derivation of the equations for the rate of production of entropy, and includes a discussion of the role played by the heat baths. Section IV contains the proof that the steady state is the state of minimum entropy production, and includes a discussion of the necessary assumptions. The final section contains a brief discussion of the entropy production in the steady state.

II. SPECIFICATION OF THE SYSTEM

Our physical system consists of two identical containers, C_1 and C_2, each of volume V, containing a total

* This research was supported by a grant from The National Science Foundation.

† This work was begun during the tenure of a National Research Fellowship at the Dublin Institute for Advanced Studies.

‡ Travel from the Netherlands was made possible by a Fulbright travel grant.

[1] I. Prigogine, *Etude Thermodynamique des Phénomènes irréversibles* (Editions Desoer, Liège, 1947), Chap. V.

[2] S. R. de Groot, *Thermodynamics of Irreversible Processes* (Interscience Publishers, Inc., New York, 1951), Chap. X.

[3] L. Onsager, Phys. Rev. **37**, 405 (1931); **38**, 2265 (1931).

[4] See references 1 and 2, and also K. G. Denbigh, *The Thermodynamics of the Steady State* (Methuen and Company, Ltd., London, 1951), and L. Onsager and S. Machlup, Phys. Rev. **91**, 1505, 1512 (1953).

[5] W. Pauli in *Probleme der Modernen Physik*, edited by P. Debye (S. Hirzel, Leipzig, 1928), p. 30.

[6] J. S. Thomsen, Phys. Rev. **91**, 1263 (1953).

of N molecules of an ideal gas. The two containers are connected through a narrow capillary tube.[7] We assume that the dimensions of the capillary tube are so chosen that collisions between molecules in the tube can be neglected. We assume also that collisions of the molecules with the walls of the tube do not affect the energies of these molecules. Each container is in good thermal contact with a heat bath, the heat baths having temperatures T_1 and T_2, respectively. We shall eventually have to assume that T_1 and T_2 differ by an amount small compared to either, but we shall not make this assumption until it becomes necessary.

Let us denote the energy levels of a molecule in one of the boxes of volume V by ϵ_i $(i=1, 2, \cdots)$. Since the boxes are identical the energy levels are the same in both containers. We can specify the state of the system at any time by giving the values of the two sets of occupation numbers $n_i^{(1)}$, $n_i^{(2)}$ at that time. The symbol $n_i^{(1)}$ represents the number of molecules in the ith energy state in C_1, and $n_i^{(2)}$ is defined similarly.

For later developments it is slightly more convenient to work in terms of the occupation probabilities rather than the occupation numbers. We, therefore, make the following definitions:

$$p_i=n_i^{(1)}/N, \quad q_i=n_i^{(2)}/N. \tag{1}$$

We notice that p_i is the probability of finding a molecule in the ith energy state of C_1, and q_i is defined similarly. The p_i and q_i are subject to the obvious restriction

$$\sum_i (p_i+q_i)=1, \tag{2}$$

which expresses the constancy of the total number of molecules.

Our first step is to state the equations giving the time variation of the p_i and q_i. Let us define a_{ij} as the probability per unit time that a molecule in C_1, originally in state i makes a transition to state j, remaining in C_1. We define c_{ij} as the corresponding transition probability per unit time for a molecule in C_2. Let b_{ii} be the probability per unit time that a molecule in state i moves from C_1 to C_2 or conversely. By the assumption discussed above we need not consider any but the diagonal b_{ii}.

The equations[8] for the time rates of change dp_i/dt and dq_i/dt are now taken to be

$$dp_i/dt=\sum_j (a_{ji}p_j-a_{ij}p_i)+b_{ii}(q_i-p_i), \tag{3}$$

and

$$dq_i/dt=\sum_j (c_{ji}q_j-c_{ij}q_i)+b_{ii}(p_i-q_i). \tag{4}$$

Equation (3) can readily be interpreted: the time rate of change of p_i is the sum of the probabilities that molecules come into state i (in C_1) from all other states j (in C_1), plus the probability that molecules come into state i from $C_2(b_{ii}q_i)$ minus the corresponding probabilities that molecules leave state i for the other states in C_1 or for C_2.

We must now point out the relations among the a_{ij} and among the c_{ij} which follow from the fact that C_1 and C_2 are in contact with heat baths at temperatures T_1 and T_2, respectively. The relations in question are

$$a_{ij}e^{-\epsilon_i/kT_1}=a_{ji}e^{-\epsilon_j/kT_1}, \tag{5}$$

and

$$c_{ij}e^{-\epsilon_i/kT_2}=c_{ji}e^{-\epsilon_j/kT_2}. \tag{6}$$

These equations are derived in the Appendix. The derivation is based upon the conservation of energy for the system of container and heat bath, and upon the rapid increase of the density of energy states of a macroscopic system with increasing energy.

III. THE ENTROPY PRODUCTION

The rate of entropy production in our problem can now be expressed in the following schematic form:

$$dS/dt=(dS/dt)_{C_1}+(dS/dt)_{C_2}+(dS/dt)_{B_1}+(dS/dt)_{B_2}. \tag{7}$$

The first pair of terms express the rates of entropy production in the gas in the two containers, and the second pair of terms express the entropy production in the two heat baths. The presence of this second pair of terms is worth special mention; we must include them since the heat baths play an important part in the production of entropy. We shall return to a discussion of this point later in the section.

We must now evaluate the four terms of Eq. (7). Consider first the entropy production in the gas, the first pair of terms. The entropy of the gas can be expressed in terms of the molecular occupation numbers as[9]

$$S_{C_1}+S_{C_2}=-k\sum_i [n_i^{(1)}\log n_i^{(1)}+n_i^{(2)}\log n_i^{(2)}], \tag{8}$$

or in terms of the occupation probabilities as

$$S_{C_1}+S_{C_2}=-Nk\sum_i [p_i\log p_i+q_i\log q_i]+Nk\log N. \tag{9}$$

Differentiating with respect to the time and substituting from Eqs. (3)–(4), we obtain

$$(dS/dt)_{C_1}+(dS/dt)_{C_2}=-Nk[\sum_i \log p_i\{\sum_j (a_{ji}p_j-a_{ij}p_i)+b_{ii}(q_i-p_i)\}+\sum_i \log q_i\{\sum_j (c_{ji}q_j-c_{ij}q_i)+b_{ii}(p_i-q_i)\}]. \tag{10}$$

[7] See the discussion in reference 2, and also in H. B. G. Casimir, Revs. Modern Phys. **17**, 343 (1945).

[8] A. J. F. Siegert, Phys. Rev. **76**, 1708 (1949).

[9] R. C. Tolman, *The Principles of Statistical Mechanics* (Oxford University Press, London, 1938), Chap. VI.

Our next task is the evaluation of the entropy production in the two heat baths. Consider the bath B_1 at constant temperature T_1. We can write, for its rate of entropy production,

$$(dS/dt)_{B_1}=(1/T_1)(dU/dt)_{B_1}, \tag{11}$$

where U_{B_1} is the internal energy of the bath, and where the right-hand side expresses the fact that any energy which enters or leaves the bath does so at temperature T_1. Since the bath B_1 exchanges energy only with the gas in C_1, it follows that the rate of change of U_{B_1} is the negative of the rate of change of U_1, the internal energy of the gas in C_1, if we omit from the latter the energy exchanged with container C_2. Thus, we can write the following equation for $(dS/dt)_{B_1}$,

$$(dS/dt)_{B_1}=-(1/T_1)(dU_1/dt)_{\text{internal}}. \tag{12}$$

Since U_1 is just $N\sum_i \epsilon_i p_i$, we can evaluate the right-hand side by omitting the last term in Eq. (3) and obtain

$$(dS/dt)_{B_1}=-(N/T_1)\sum_i \epsilon_i \sum_j (a_{ji}p_j-a_{ij}p_i). \tag{13}$$

Similarly we obtain the equation

$$(dS/dt)_{B_2}=-(N/T_2)\sum_i \epsilon_i \sum_j (c_{ji}q_j-c_{ij}q_i). \tag{14}$$

Combining Eqs. (10), (13), (14), we have the final expression for the total rate of entropy production:

$$\frac{dS}{dt}=-Nk\sum_i\left[\left(\frac{dp_i}{dt}\right)\log p_i+\left(\frac{dq_i}{dt}\right)\log q_i+\frac{\epsilon_i}{kT_1}\left(\frac{dp_i}{dt}\right)_{\text{int.}}+\frac{\epsilon_i}{kT_2}\left(\frac{dq_i}{dt}\right)_{\text{int.}}\right]$$

$$=-Nk\sum_i\left[\left(\log p_i+\frac{\epsilon_i}{kT_1}\right)\sum_j(a_{ji}p_j-a_{ij}p_i)+\left(\log q_i+\frac{\epsilon_i}{kT_2}\right)\sum_j(c_{ji}q_j-c_{ij}q_i)+b_{ii}(\log p_i-\log q_i)(q_i-p_i)\right]. \tag{15}$$

IV. THE STEADY STATE

We must now prove that the set of values of the p_i and q_i which minimize the rate of entropy production, as given by Eq. (15), are constants in time, i.e., constitute a steady state of the system. Before we formulate our theorem, we shall obtain the equations determining the p_i and q_i which minimize dS/dt.[10]

[10] This discussion generalizes that given by Thomsen in reference 6.

Differentiating Eq. (15) with respect to p_r we obtain

$$\frac{\partial}{\partial p_r}\left(\frac{dS}{dt}\right)=-Nk\left[\sum_i\left(\log p_i+\frac{\epsilon_i}{kT_1}\right)(a_{ri}-\delta_{ri}\sum_j a_{rj})+\sum_j\left(a_{jr}\frac{p_j}{p_r}-a_{rj}\right)+b_{rr}\left\{\left(\frac{q_r}{p_r}-1\right)+\log\frac{q_r}{p_r}\right\}\right]. \tag{16}$$

Similarly, by differentiating with respect to q_r, we obtain

$$\frac{\partial}{\partial q_r}\left(\frac{dS}{dt}\right)=-Nk\left[\sum_i\left(\log q_i+\frac{\epsilon_i}{kT_2}\right)(c_{ri}-\delta_{ri}\sum_j c_{rj})+\sum_j\left(c_{jr}\frac{q_j}{q_r}-c_{rj}\right)+b_{rr}\left\{\left(\frac{p_r}{q_r}-1\right)+\log\frac{p_r}{q_r}\right\}\right]. \tag{17}$$

We cannot set these derivatives equal to zero because the p_i and q_i are subject to the constraint expressed by Eq. (2). If we introduce a Lagrange multiplier μ to take care of this constraint, and at the same time make use of Eqs. (5) and (6), we can write the conditions for a minimum of dS/dt as

$$\mu=Nk\left[\sum_i a_{ri}\left\{\log\frac{p_ie^{\epsilon_i/kT_1}}{p_re^{\epsilon_r/kT_1}}+\left(\frac{p_ie^{\epsilon_i/kT_1}}{p_re^{\epsilon_r/kT_1}}-1\right)\right\}+b_{rr}\left\{\log\frac{q_r}{p_r}+\left(\frac{q_r}{p_r}-1\right)\right\}\right],$$

$$\mu=Nk\left[\sum_i c_{ri}\left\{\log\frac{q_ie^{\epsilon_i/kT_2}}{q_re^{\epsilon_r/kT_2}}+\left(\frac{q_ie^{\epsilon_i/kT_2}}{q_re^{\epsilon_r/kT_2}}-1\right)\right\}+b_{rr}\left\{\log\frac{p_r}{q_r}+\left(\frac{p_r}{q_r}-1\right)\right\}\right]. \tag{18}$$

At this point we must introduce the assumption that the system is not far from equilibrium. We may make this more physical by saying that we require that the temperatures T_1 and T_2 be given by $T+\delta T$ and $T-\delta T$, respectively, where only first order terms in $\delta T/T$ need be maintained. Further, we require that the gases in the two containers be nearly in equilibrium at the respective temperatures T_1 and T_2. We may summarize the restrictions by the equations

$$\frac{q_r}{p_r}=1+\delta_r,\qquad \frac{p_je^{\epsilon_j/kT_1}}{p_ie^{\epsilon_i/kT_1}}=1+\rho_{ij},\qquad \frac{q_je^{\epsilon_j/kT_2}}{q_ie^{\epsilon_i/kT_2}}=1+\sigma_{ij}, \tag{19}$$

where δ, ρ, and σ are functions of the time in general but are all small, and second-order terms in any of these quantities may be dropped.[11]

Under these assumptions we shall now prove the basic theorem: the necessary and sufficient condition

[11] Compare with I. Prigogine, Physica 15, 272 (1949).

that the entropy production is a minimum is that all p_i and q_i are independent of the time, i.e, that the system is in a steady state.

A. Sufficiency

Given that $(dp_i/dt)=0$ and $(dq_i/dt)=0$ (all i), we are to prove that for these values of the p_i and q_i, dS/dt is minimum. From Eq. (3) it follows that

$$b_{ii}(q_i-p_i)+\sum_j(a_{ji}p_j-a_{ij}p_i)=0.$$

If we make use of Eq. (5) this can easily be rewritten in the form

$$b_{ii}\left(1-\frac{q_i}{p_i}\right)=\sum_j a_{ij}\left(\frac{p_je^{\epsilon_j/kT_1}}{p_ie^{\epsilon_i/kT_1}}-1\right). \tag{20}$$

Furthermore, if we make use of the assumption expressed in Eq. (19), we can rewrite Eq. (20) as

$$-b_{ii}\log\frac{q_i}{p_i}=\sum_j a_{ij}\log\frac{p_je^{\epsilon_j/kT_1}}{p_ie^{\epsilon_i/kT_1}}. \tag{21}$$

Now, Eq. (20) and (21) tell us that the equations which determine the minimum for dS/dt, Eq. (18), are satisfied for all r with $\mu=0$. This result, with a similar argument for the terms in the q's, proves the sufficiency of our condition.

B. Necessity

Given that dS/dt is a minimum we are to prove that for these values of the p_i and q_i, dp_i/dt, and dq_i/dt vanish. Making use of Eq. (19) we can rewrite the minimum conditions of Eq. (18) in the form

$$\mu=2Nk\left[\sum_i a_{ri}\left(\frac{p_ie^{\epsilon_i/kT_1}}{p_re^{\epsilon_r/kT_1}}-1\right)+b_{rr}\left(\frac{q_r}{p_r}-1\right)\right]. \tag{22}$$

Multiplying by p_r and using Eq. (5) yields

$$\mu p_r=2Nk(dp_r/dt). \tag{23}$$

Similarly, we can obtain the equation

$$\mu q_r=2Nk(dq_r/dt). \tag{24}$$

If we sum Eq. (23) and (24) over all values of r and take note of Eq. (2) it follows that μ must be zero. Hence all dp_r/dt and dq_r/dt must vanish, establishing our theorem.

One point remains for discussion—the proof that the value of dS/dt is actually a minimum, rather than some other stationary value, in the steady state. To show this we shall compute the change $\delta(dS/dt)$ in the entropy production for small changes δp_i, δq_i in the p_i and q_i from their steady-state values which we denote by p_i^0 and q_i^0. A direct calculation from Eq. (15) gives

$$\delta\left(\frac{dS}{dt}\right)=-Nk\left[\sum_{i,j}\left\{\frac{a_{ji}}{p_i^0}\delta p_i\delta p_j-\frac{a_{ij}}{p_i^0}(\delta p_i)^2+\frac{c_{ji}}{q_i^0}\delta q_i\delta q_j-\frac{c_{ij}}{q_i^0}(\delta q_i)^2\right\}+\sum_i b_{ii}\left\{-\frac{(\delta p_i)^2}{p_i^0}-\frac{(\delta q_i)^2}{q_i^0}+\frac{q_i^0+p_i^0}{p_i^0q_i^0}\delta p_i\delta q_i\right\}\right]. \tag{25}$$

There are no first-order terms because we are computing the change from a stationary value. In order to prove that $\delta(dS/dt)$ is positive we show that it can be expressed as a sum of squares. To do this replace $\sum_j a_{ij}$ and $\sum_j c_{ij}$ by their values from the equations

$$\begin{aligned}\sum_j a_{ji}p_j^0-p_i^0\sum_j a_{ij}+b_{ii}(q_i^0-p_i^0)=0,\\ \sum_j c_{ji}q_j^0-q_i^0\sum_j c_{ij}+b_{ii}(p_i^0-q_i^0)=0,\end{aligned} \tag{26}$$

which express the fact that p_i^0, q_i^0 correspond to a steady state. It is also necessary to add to the resulting expression for $\delta(dS/dt)$ the expression obtained from Eq. (25) by interchanging the summation indices i, j in the second and fourth terms of that equation. We obtain finally

$$2\delta\left(\frac{dS}{dt}\right)=Nk\left[\sum_{i,j}a_{ij}\left(\frac{\delta p_i}{(p_i^0)^{\frac{1}{2}}}-\frac{\delta p_j(p_i^0)^{\frac{1}{2}}}{p_j^0}\right)^2+\sum_{i,j}c_{ij}\left(\frac{\delta q_i}{(q_i^0)^{\frac{1}{2}}}-\frac{\delta q_j(q_i^0)^{\frac{1}{2}}}{q_j^0}\right)^2+\sum_i b_{ii}(p_i^0+q_i^0)\left(\frac{\delta p_i}{p_i^0}-\frac{\delta q_i}{q_i^0}\right)^2\right]\geqq 0, \tag{27}$$

which proves that the stationary value of dS/dt is actually a minimum.

This completes our proof that the steady state is the state of minimum entropy production.

V. DISCUSSION

The minimum entropy production in the steady state can be expressed in an interesting form. If we examine the first form of Eq. (15), we notice that in the steady state the first two terms vanish, and we can write

$$\frac{dS}{dt}=-Nk\sum_i\left\{\frac{\epsilon_i}{kT_1}\left(\frac{dp_i}{dt}\right)_{\text{int.}}+\frac{\epsilon_i}{kT_2}\left(\frac{dq_i}{dt}\right)_{\text{int.}}\right\}. \tag{28}$$

In the steady state the rate of change of p_i due to internal transitions is just balanced by its rate of change due to molecules passing to or from the second container. Using this fact as expressed in Eq. (26) we

obtain the equation

$$\frac{dS}{dt}=Nk\sum_i b_{ii}(q_i^0-p_i^0)\left(\frac{\epsilon_i}{kT_1}-\frac{\epsilon_i}{kT_2}\right), \tag{29}$$

or

$$\frac{dS}{dt}=N\sum_i b_{ii}(p_i^0-q_i^0)\epsilon_i\left(\frac{1}{T_2}-\frac{1}{T_1}\right). \tag{30}$$

In this form the entropy production, in the steady state, is expressed as the sum over all states of the product of two factors. The first, $b_{ii}(p_i^0-q_i^0)N$, is the net number of molecules going from the first container to the second per unit time. The second, $(\epsilon_i/T_2)-(\epsilon_i/T_1)$, is the increase in entropy produced when energy ϵ_i is removed from the higher temperature bath (T_1) and delivered to the lower temperature bath (T_2). Hence, the entropy is produced simply by the conduction of heat from the higher to the lower temperature by means of the flow of molecules. The steady state is maintained since the total number of molecules in each container ($N\sum p_i$ and $N\sum q_i$) remain constant in time. [We notice that the expression for dS/dt in Eq. (30) is positive since $p_i^0>q_i^0$ if $T_1>T_2$.]

In conclusion we may say that the theorem of minimum entropy production has been proved, by the methods of statistical mechanics, for a particular type of irreversible process. This proof has helped to clarify the assumptions on which the theorem is based and also its position in the general framework of statistical mechanics.

APPENDIX

This appendix is concerned with the derivation of Eq. (5) of the text which relates the transition probabilities per unit time a_{ij} and a_{ji} for a system in contact with a heat bath at temperature T.

It can be shown by the use of quantum-mechanical perturbation theory that for an isolated system the transition probabilities per unit time are symmetric.[12] More precisely, if we have two nondegenerate states, a and b, each being one of a group of closely spaced states, then the probability per unit time of a transition from a to b is equal to the probability per unit time of a transition from b to a. (The condition of isolation implies that real transitions occur only between states of essentially equal energy.)

We shall use this result to derive Eq. (5) by considering the isolated system consisting of the system of interest plus the heat bath at temperature T with which it is in contact.

We shall denote the states of the system by indices $i, j, \cdots$ and those of the heat bath by indices $\alpha, \beta, \cdots$. If we denote by $W_{i\alpha}$ the probability of finding the combined system in the joint state (i, α), and by $A(i\alpha|j\beta)$ the transition probability per unit time from (i, α) to (j, β), then the equation for $dW_{i\alpha}/dt$ has the form

$$dW_{i\alpha}/dt=\sum_{j,\beta} A(j\beta|i\alpha)W_{j\beta}-W_{i\alpha}\sum_{j,\beta} A(i\alpha|j\beta), \tag{A-1}$$

where

$$A(i\alpha|j\beta)=A(j\beta|i\alpha). \tag{A-2}$$

The probability w_i of finding the system itself in state i is obtained from the $W_{i\alpha}$ by summing over all heat bath states α; thus we have

$$w_i=\sum_\alpha W_{i\alpha}. \tag{A-3}$$

Our problem is to rewrite Eq. (A-1), by summing over α, in such a way as to obtain an equation of the form

$$dw_i/dt=\sum_j a_{ji}w_j-w_i\sum_j a_{ij}, \tag{A-4}$$

and to show that

$$a_{ji}e^{-\epsilon_j/kT}=a_{ij}e^{-\epsilon_i/kT}. \tag{A-5}$$

In our notation ϵ_i is the energy of state i of the system and E_α is the energy of state α of the heat bath.

Summing on α in Eq. (A-1) leads to the equation

$$dw_i/dt=\sum_{j\beta} W_{j\beta}\sum_\alpha A(j\beta|i\alpha)-\sum_{j\beta}\sum_\alpha A(i\alpha|j\beta)W_{i\alpha}. \tag{A-6}$$

We see that Eq. (A-6) is not yet in the desired form of Eq. (A-4). To obtain this form we must assume that

$$W_{i\alpha}=w_i/s_\alpha, \tag{A-7}$$

where s_α is the degeneracy of the level α of the heat bath. It is important that we clarify the assumptions contained in Eq. (A-7). The first assumption is that the probability $W_{i\alpha}$ is the product of the probability w_i that the system is in state i and the probability that the heat bath is in state α. The second assumption is that this latter probability is just the reciprocal of the number of bath states of energy E_α. These assumptions are justified by the fact that a heat bath is a system of arbitrarily large heat capacity. Consequently, the probability of finding the bath in a given state is practically unaffected by the coupling to the system.

Using Eq. (A-7) in Eq. (A-6) we obtain the equation

$$\frac{dw_i}{dt}=\sum_j w_j\sum_{\alpha\beta}\frac{1}{s_\beta}A(j\beta|i\alpha)-w_i\sum_j\sum_{\alpha\beta}\frac{1}{s_\alpha}A(i\alpha|j\beta). \tag{A-8}$$

Equation (A-8) has the form of Eq. (A-4) with

$$a_{ij}=\sum_{\alpha\beta}\frac{1}{s_\alpha}A(i\alpha|j\beta), \quad a_{ji}=\sum_{\alpha\beta}\frac{1}{s_\beta}A(j\beta|i\alpha). \tag{A-9}$$

We must now evaluate s_α and s_β. The density of states in a heat bath varies as the energy raised to an

[12] See reference 9, pp. 424–436, and E. C. Kemble, *The Fundamental Principles of Quantum Mechanics* (McGraw-Hill Book Company, Inc., New York, 1937), Chap. XII.

enormous power M, of the order of the number of molecules in the heat bath.[13] Hence, if $\mathcal{E}$ is the energy of the system plus bath we have

$$s_\alpha = cE_\alpha{}^M = c(\mathcal{E}-\epsilon_i)^M \cong c\mathcal{E}^M[1-(M\epsilon_i/\mathcal{E})]$$
$$\cong c\mathcal{E}^M \exp(-M\epsilon_i/\mathcal{E}), \quad \text{(A-10)}$$

[13] See reference 9, p. 490, and E. Schrödinger, *Statistical Thermodynamics* (Cambridge University Press, Cambridge, 1952), pp. 38 and 89.

where $\mathcal{E}=\epsilon_i+E_\alpha$. Identifying $\mathcal{E}/M$ with kT we have

$$s_\alpha = c\mathcal{E}^M e^{-\epsilon_i/kT}, \quad s_\beta = c\mathcal{E}^M e^{-\epsilon_j/kT}, \quad \text{(A-11)}$$

since $\mathcal{E}$, the total energy, is also equal to ϵ_j+E_β.

Using Eq. (A-2) with Eq. (A-9) and (A-11), we obtain finally

$$a_{ij}e^{-\epsilon_i/kT} = a_{ji}e^{-\epsilon_j/kT},$$

which is Eq. (A-5).

PHYSICAL REVIEW VOLUME 96, NUMBER 2 OCTOBER 15, 1954

Flow of Electrons and Holes through the Surface Barrier Region in Point Contact Rectification*

MELVIN CUTLER
Hughes Research and Development Laboratories, Culver City, California
(Received April 29, 1954; revised manuscript received July 8, 1954)

Equations are derived for the flow of electrons and holes through a surface barrier region by using the emission theory. The solution allows for nonequilibrium concentration of carriers on the semiconductor side of the barrier. It also allows for the possibility that part of the applied potential is between the metal surface and the semiconductor surface, as would occur if the surface states do not remain in equilibrium with the metal. The solution for the rectification characteristic is completed for the special case of small currents by combining the barrier region equations with the solution for current flow beyond the barrier region. The resulting equations are compared with those for p-n junctions, and the implications are discussed with regard to the relative roles of diffusion and emission in the flow of electrons and holes. Finally, the small current equations are compared with experiment, with a discussion of the evidence for the existence of an inter-surface potential.

1. INTRODUCTION

THE early "diode" theory for point contact rectification was based on the flow of a single type of carrier, and did not consider the effects of minority carrier injection.[1,2] After the discovery of the latter phenomenon, the small current theory for p-n junctions was advanced by Shockley.[3] The application of this theory to point contacts was also discussed.[4]

The present theory of point contact rectifiers does not agree with experiment in the current voltage characteristic. The discrepancies have been discussed extensively.[5,6] particularly with reference to the reverse characteristic.[7] In view of this disagreement, it seems desirable to develop the theory in a more systematic and rigorous fashion. In such a manner, one may be able to investigate more carefully the validity of the accepted model for surface rectification.

The behavior of a rectifier may be obtained from the combination of the solutions of two separate problems: The flow of electrons and holes in the barrier region, which is "emission" controlled; and the flow beyond the barrier region, which is diffusion controlled.[8] A solution of the latter kind, which is one dimensional and applicable to p-n junctions or large area surface contacts has been derived by Van Roosbroeck.[9] The purpose of this paper is to present a self-contained solution to the former problem; that is, for the emission of electrons and holes through the barrier region of a semiconductor. In addition the solution will be completed for small currents in point contacts, for which case the diffusion problem has been solved; the results are compared with p-n junction theory. A general solution for the diffusion problem with radial flow, in combination with the emission equations, would permit the discussion of the forward (large current) characteristic of point contact rectifiers. This will be done in a later paper.

The emission equations to be derived are more general than the original diode equations in two ways.

* This work was first presented at the Cambridge American Physical Society Meeting in February, 1953 [Phys. Rev. **90**, 337 (1954)].

[1] R. C. Torrey and C. A. Whitmer, *Crystal Rectifiers* (McGraw-Hill Book Company, Inc., New York, 1948), Chap. 4.

[2] N. F. Mott and R. W. Gurney, *Electronic Processes in Ionic Crystals* (Oxford University Press, London, 1948), Chap. 5.

[3] W. Shockley, *Electrons and Holes in Semiconductors* (D. Van Nostrand Company, Inc., New York, 1950), Chap. 12.

[4] See reference 3, pp. 95–101.

[5] S. Benzer, J. Appl. Phys. **20**, 804 (1949).

[6] J. Bardeen and W. H. Brattain, Phys. Rev. **75**, 1208 (1949).

[7] J. H. Simpson and H. L. Armstrong, J. Appl. Phys. **24**, 25 (1953).

[8] This approach is discussed in a paper which has appeared recently. See P. C. Banbury, Proc. Phys. Soc. (London) **B66**, 833 (1953).

[9] W. Van Roosbroeck, Bell System Tech. J. **29**, 560 (1950).

They allow for nonequilibrium concentrations of electrons and holes near the barrier, and for the possibility that part of the voltage drop in the surface region may occur between the metal and semiconductor surfaces, rather than entirely in the barrier. The former phenomenon, due to injection or depletion of minority carriers, is well established experimentally. The extent to which it takes place will be determined by the associated solution for the diffusion region. The latter phenomenon is hypothetical and is included here mainly to permit its discussion as a possible explanation for the discrepancy between theory and experiment in diode behavior. For the purpose of the derivation, both effects enter in terms of arbitrary parameters, so that the latter hypothesis will not limit the generality of the equations. In order to fix our ideas, we shall consider the particular case of the surface in n-type germanium, which has a barrier for electrons; the extension to other types of barriers will be obvious.

The equations to be obtained are almost self-evident, and the derivation in terms of a kinetic theory would be quite simple. We shall base the solution on the consideration of transitions of electrons between energy levels in the metal and the semiconductor. This has some advantages over considering the flow of particles. One obtains a more rigorous solution, in which the nature of the approximations which are used is made clear. Also, the nature of the flow of holes between metal and semiconductor is clarified. The derivation shows that the unoccupied energy levels of the metal below the Fermi level act as holes as far as electronic transitions with the semiconductor is concerned. In view of the simplicity of the final results, the derivation will be in a condensed form. The reader is referred to a recent paper,[10] in which the theoretical analysis has a similar form.

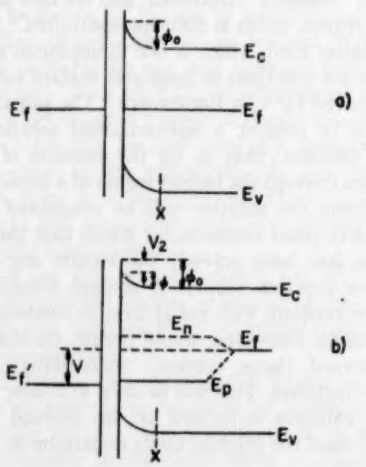

FIG. 1. Energy level diagram for the surface. 1a. Equilibrium, and 1b. forward bias V.

[10] W. Shockley and W. T. Read, Jr., Phys. Rev. **87**, 836 (1952).

2. EMISSION CURRENT THROUGH THE SURFACE BARRIER

a. Model for the Theory

The energy level diagram for the surface region is shown in Fig. 1. At equilibrium, the surface barrier is ϕ_0. On the application of a forward bias V in the surface region, a part of it, V_1, is assumed to lie between the metal surface and the semiconductor surface; the remainder V_2 is in the barrier region between the semiconductor surface and a hypothetical point X, where X is the boundary between the barrier region and the bulk. If E_f' is the Fermi level in the metal when the bias is applied, and E_f the equilibrium Fermi level, then

$$E_f'-E_f=qV. \tag{1}$$

Also, the new barrier height ϕ is lower by the amount qV_2:

$$\phi_0-\phi=qV_2. \tag{2}$$

The holes and electrons at X may not be in equilibrium when a bias exists. They may be regarded as being in quasi-equilibrium, each in their own band, and characterized by quasi-Fermi levels E_p and E_n:[3]

$$p=p_0\exp[(E_f-E_p)/kT], \tag{3}$$

$$n=n_0\exp[(E_n-E_f)/kT], \tag{4}$$

where p and n are hole and electron concentrations, respectively, and the zero subscript denotes equilibrium values. For purposes of the derivation, both E_p and E_n will be referrred to as E_f'', with the understanding that the latter parameter will have different values depending on whether the carriers are in the valence band or in the conduction band.

b. Flow between Single Energy Levels

The rate of flow of electrons j' from states in the metal at an energy level E_1 to states in the semiconductor at an energy level E_2 is

$$j'(E_1,E_2)=g'(E_1)f'(E_1)g''(E_2)\times[1-f''(E_2)]k'(E_1,E_2), \tag{5}$$

where $g'(E_1)$ is the density of energy states in the metal at energy E_1, and $f'(E_1)$ is the Fermi factor

$$\{1+\exp[(E_1-E_f')/kT]\}^{-1}.$$

g'' and f'' are similar functions for the semiconductor; f'' contains E_f'' in place of E_f', and $k'(E_1,E_2)$ is the transfer coefficient from the metal at energy E_1 to the semiconductor at energy E_2. It is noted that $g''(E_2)$ is zero for values of E_2 between the upper valence band edge E_v and the lower conduction band edge E_c.

A similar expression describes the rate of flow of electrons $j''(E_2,E_1)$ in the reverse direction. The net flow of electrons from E_2 and E_1 is the difference

between j'' and j':

$$j(E_2,E_1)=g'(E_1)g''(E_2)\{k''(E_2,E_1)f''(E_2)\times[1-f'(E_1)]-k'(E_1,E_2)f'(E_1)[1-f''(E_2)]\}. \quad (6)$$

The principle of detailed balancing, which requires that $j(E_2,E_1)=0$ at equilibrium (when $E_f'=E_f''=E_f$), leads to the relation:

$$k''(E_2,E_1)=k'(E_1,E_2)\exp[(E_2-E_1)/kT]. \quad (7)$$

On substituting this back into Eq. (6), and simplifying, one obtains

$$j(E_2,E_1)=g'(E_1)g''(E_2)k'(E_1,E_2)f'(E_1)\times[1-f''(E_2)]\{\exp[(E_f''-E_f')/kT]-1\}. \quad (8)$$

c. The Total Current

The total current is obtained from Eq. (8) by integrating over all values of E_1 and E_2. The integration over the semiconductor energy levels E_2 is broken into two parts: the integral from $-\infty$ to E_v gives the net hole current j_p; the integral from E_c to ∞ is the net electron current j_n.

With the assumption that the quasi-Fermi levels are always far from the band edge energies compared to kT, the integrals are simplified by the following considerations: One can expect that $k'(E_1,E_2)$ will be extremely small if $|E_2-E_1|$ is large compared to kT. For all values of E_1 and E_2, then, for which $k'(E_1,E_2)$ is not zero, the Fermi factors can be approximated by the corresponding Boltzmann factors. At this point, E_f'' is replaced by E_p and E_n in the two bands, and the flow equations become:

$$j_p=j_{p0}\{\exp[(E_p-E_f')/kT]-1\}\times\exp[(E_f-E_p)/kT], \quad (9)$$

$$j_n=j_{n0}'\{\exp[(E_n-E_f')/kT]-1\}\times\exp[(E_f'-E_f)/kT], \quad (10)$$

where

$$j_{p0}=\int_{-\infty}^{\infty}dE_1\int_{-\infty}^{E_v}dE_2g'(E_1)g''(E_2)k'(E_1,E_2)\times\exp[(E_2-E_f)/kT], \quad (11)$$

$$j_{n0}'=\int_{-\infty}^{\infty}dE_1\int_{E_c}^{\infty}dE_2g'(E_1)g''(E_2)k'(E_1,E_2)\times\exp[(E_f-E_1)/kT], \quad (12)$$

and j_{p0} is a constant. However, j_{n0}' is not a constant, since $k'(E_1,E_2)$ must be zero for values of E_2 between the conduction band edge E_c and the top of the barrier $(E_c+\phi)$, and ϕ varies with the bias according to Eq. (2). (We are neglecting here the effects of barrier penetration.) A good approximation for Eq. (12) is

$$j_{n0}'=j_{n0}\exp[(\phi_0-\phi)/kT], \quad (13)$$

where j_{n0} is a constant:

$$j_{n0}=\int_{-\infty}^{\infty}dE_1\int_{E_c+\phi_0}^{\infty}dEg'(E_1)g''(E)k''(E,E_1)\times\exp[(E_f-E)/kT]. \quad (14)$$

This is obtained by making the transformation $E_2=E+\phi-\phi_0$, substituting Eq. (7), noting that the integral is zero for $E<E_c+\phi$, and using the assumption that all the other factors in the integral vary slowly compared to the exponential factor.

Equations (9) and (10) are converted into current equations by multiplying by the area A of the contact and by the electron charge magnitude q. On substituting Eqs. (1), (2), (3), (4), and (13), the current equations assume the following form:

$$I_p=I_{pe}[\exp(qV/kT)-p/p_0], \quad (15)$$

where $I_{pe}=j_{p0}Aq$, and

$$I_n=I_{ne}\exp(-qV_1/kT)[(n/n_0)\exp(qV/kT)-1], \quad (16)$$

where $I_{ne}=j_{n0}Aq$. I_p and I_n are the total hole and electron currents, respectively. It is convenient to express the constants I_{pe} and I_{ne} in an alternative form which is in the language of kinetic theory:

$$I_{pe}=qvAp_0t_p, \quad (17)$$

$$I_{ne}=qvAn_0t_n\exp(-\phi_0/kT), \quad (18)$$

where v is the average normal component of thermal velocity of holes and electrons crossing the surface from the semiconductor to the metal. The transmission coefficients for holes and electrons are, respectively, t_p and t_n. They are defined on comparison of the above equations with Eqs. (11), (14), (15), and (16). It is a matter of choice whether the effective masses for holes and electrons are used in determining v, or whether one uses the free electron mass for both and lumps the corrections, which are poorly known, into t_p and t_n; we have chosen the latter course. For most purposes, t_p and t_n may be assumed to be unity; it is expected that such an assumption will generally be correct in order of magnitude.

3. DISCUSSION

a. Comparison of Emission Equations

On comparing Eqs. (15) and (16) with the conventional emission equation,

$$I=I_0[\exp(qV/kT)-1], \quad (19)$$

the effects of the added factors considered here become apparent. The fact that the hole and electron concentrations near the surface barrier are not equilibrium ones leads to the factor p/p_0 in the current equation and n/n_0 in the electron current equation.[11] The exis-

[11] This correction for the electron current equation was used by Swanson in a recent paper, although he did not use the accurate equation for the flow of holes. See J. A. Swanson, J. Appl. Phys. 25, 314 (1954).

tence of an intersurface potential V_1 leads to an additional factor $\exp(-qV_1/kT)$ in the electron current equation. This factor can be combined with I_{ne} and denoted I_{ne}':

$$I_{ne}'=qAvn_0l_n \exp[-(\phi_0+V_1q)/kT]. \quad (20)$$

We see that V_1 is added to the original barrier potential ϕ_0/q, so that it effectively increases the barrier height in the forward direction over what it would be otherwise, and decreases it in the reverse direction.

In order to provide a comparison with p-n junction theory it is desirable to complete the solution for the case of small currents. This will not only illustrate the method of combining the emission and diffusion solutions, but will also provide some further insight into the way in which the emission mechanism can become the determining factor for the point contact saturation current.[4] The total current is assumed to be small compared to the parameter I_{nd}, where

$$I_{nd}=qAn_0D_n/a. \quad (21)$$

D_n is the diffusion constant for electrons and a is the contact radius. The solution of the spreading equations is then[12]

$$p/p_0=1+I_p/I_{pd}, \quad (22)$$

where

$$I_{pd}=qAp_0D_p/a \quad (23)$$

and D_p is the diffusion constant for holes. Equations (22) and (23) imply that $p \ll n_0$ as long as $I \ll I_{nd}$, so that the assumption of electrical neutrality gives $n=n_0$. In addition, the spreading potential is negligibly small, so that the applied voltage can be assumed to equal the barrier voltage V. On combining these results of the diffusion problem with Eqs. (15) and (16), one has

$$I_p=I_{p0}[\exp(qV/kT)-1], \quad (24)$$

$$I_n=I_{ne}'[\exp(qV/kT)-1], \quad (25)$$

where

$$I_{p0}^{-1}=I_{pe}^{-1}+I_{pd}^{-1}. \quad (26)$$

At this point, it is noted that the various I parameters (those with two subscripts) with dimensions of current function as admittances in the sense that the current is proportional to their values for any given voltage.[3] Continuing this analogy, we shall also refer to their reciprocals as impedances. Moreover, they can be described in terms of their origin; thus I_{pe} and I_{ne} are emission admittances, and I_{pd} is a diffusion admittance for holes.

In terms of these concepts, Eqs. (24), (25), and (26) show clearly the difference between surface rectification and p-n junction rectification. The diffusion controlled electron saturation current of p-n junction theory is replaced by an electron emission admittance parameter I_{ne}'. The difference is the result of the fact that the effective diffusion distance of electrons in the surface p region is so small that emission, and not diffusion is the controlling factor. This was implicit in our derivation of the emission equations.

The last point becomes clearer on consideration of the change in the hole current equation. According to Eqs. (25) and (26), the impedance I_{p0}^{-1} for hole flow is the sum of the diffusion impedance I_{pd}^{-1} and emission impedance I_{pe}^{-1}. Thus the hole admittance corresponds to two admittance I_{pd} and I_{pe} in series, and is determined by the smaller one. If, as is usually the case, I_{pd} is small compared to I_{pe}, the diffusion impedance is dominant and determines I_{p0}. But in the opposite situation, the hole current would be emission controlled, as is the electron current. One additional difference is that the saturation hole current $I_{p0}(\cong I_{pd})$ is inversely proportional to the contact radius, rather than the diffusion distance of p-n junction theory.

An interesting result, closely connected with the above discussion, is the fact that the derivation of the rectification equation by the separate consideration of the emission and diffusion provides a quantitative measure of the change in the quasi-Fermi level in the barrier region. Shockley's derivation of the p-n junction equations made use of the approximation that there is no change in the quasi-Fermi level for holes on passing through the barrier. This is equivalent to assuming, in our equations, that $p/p_0=\exp(qV/kT)$. Equations (22), (24), and (26) provide an exact relationship between the two quantities:

$$(p/p_0-1)/[\exp(qV/kT)-1]=I_{pe}/(I_{pe}+I_{pd}). \quad (27)$$

Therefore, Shockley's approximation is correct if the diffusion admittance is small compared to the emission admittance ($I_{pd}/I_{pe} \ll 1$). This requirement is amply fulfilled in large area barriers; it may not be quite true in small area point contacts, which may have values for this ratio of the order of 0.1. Also, as will be shown in a later paper, the approximation is not always valid for large currents.

The introduction of the hypothetical intersurface potential V_1 presents a possible alternative explanation for the deviation of experimental point contact characteristics from the behavior predicted by theory.[13] If one plots $I[\exp(qV/kT)-1]^{-1}$ as a function of V in the range of small V (say, from -100 mv to $+100$ mv), one should obtain a horizontal straight line with an ordinate equal to $I_{p0}+I_{ne}'$, according to Eqs. (24) and (25), if the value of I_{ne}' is constant. In practice, such a plot yields a curve whose ordinate decreases with increasing V. The existence of an intersurface potential, which causes I_{ne}' to be variable, is consistent with this behavior.

[12] This equation is derived by Bardeen, Bell System Tech. J. 29, 469 (1950). In addition, a number of points discussed here are contained either explicitly or implicitly in that paper, or in reference 6.

[13] The hypothesis most commonly accepted involves the multicontact theory; see, for instance, H. J. Yearian, J. Appl. Phys. 21, 214 (1950); Johnson, Smith, and Yearian, J. Appl. Phys. 21, 283 (1950), and reference 4.

One might expect such a potential to occur as the result of a thin oxide layer between the surfaces of the metal and the semiconductor. One could reasonably expect V_1, in such a case, to be a monotonic function of V. The actual relationship would of course depend on the electronic processes which occur in the oxide. It should be noted, however, that extensive scattering of electrons in the oxide might limit the validity of the derivation, in particular the assumption about $k'(E_1,E_2)$ used in obtaining Eqs. (9) and (10). In such a case, our equations would be merely an indication of what to expect.

Finally, we would like to discuss briefly some formal implications of the generalized emission equations for a barrier. In the general case, the equations would have the following form:

$$I_p=qvA\{p_1\exp[-q(V_2-V_1)/kT]-p_2\}, \quad (28)$$

where the subscripts refer to the two sides of the barrier. (The situation for electrons is exactly analogous, and will not be discussed.) It is assumed, without loss of generality, the region 1 is more p type than region 2. On substituting Eqs. (4) and (5), one obtains

$$I_p=qvAp_{20}\exp(E_{f2}/kT)\times[\exp(-E_{p2}/kT)-\exp(-E_{p1}/kT)], \quad (29)$$

where p_{20} is the equilibrium hole concentration in region two. The interesting aspect of this result is that the flow is proportional to the difference in the Boltzmann factors for the quasi-Fermi levels. This is analogous to the expression for the diffustion flow:[3]

$$I_p=qD_pAp\nabla(E_f-E_p)/kT. \quad (30)$$

Indeed, one can derive Eq. (30) in a crude way from Eq. (29) by considering the diffusion process to be the result of emission between successive regions separated by a distance equal to the mean free path for carriers λ. One obtains the above result on assuming that $(E_{p2}-E_{p1})/kT\ll 1$, and identifying the product $v\lambda$ with D_p.

The author would like to gratefully acknowledge the aid of his associates, particularly H. Winston who, through discussions and criticism, have helped to carry out this work.

PHYSICAL REVIEW VOLUME 96, NUMBER 2 OCTOBER 15, 1954

Effect of Oxygen on the Electrical Properties of Lead Telluride Films*

DONALD E. BODE† AND HENRY LEVINSTEIN
Physics Department, Syracuse University, Syracuse, New York

(Received June 7, 1954)

The effect of oxygen on the electrical properties of PbTe films has been investigated. Oxygen, which presumably is adsorbed on the surface of the film, causes an increase in film resistance, followed by a decrease in resistance with increasing exposure to oxygen. The film which is originally "n" type changes to "p" type in the vicinity of the resistance maximum. The magnitude of the photoresistive and photovoltaic effect varies with the amount of oxygen adsorbed by the film. A model has been presented whereby oxygen removes electrons first from the conduction band, then from trapping states, and finally from the valence band, thereby producing the observed effects.

I. INTRODUCTION

IN the study of the electrical properties of thin films adsorbed oxygen is generally undesirable since it obscures the true properties of the film. Sometimes, however, films must be exposed to oxygen to bring out properties which cannot be observed otherwise. PbS, PbSe, and PbTe films exhibit photoconductivity after the films have been treated with oxygen. Sensitization techniques require certain recipes whereby maximum sensitivity is obtained if well-tested empirical rules are followed. Lead telluride cells, as described in the literature,[1-3] have been used in recent years as detectors of infrared radiation. They have a rapid response time (time constants of the order of 10 microseconds), high sensitivity, and a long wavelength threshold at about 5.5 microns with peak sensitivity at about 4.5 microns. PbTe cells show this sensitivity only if they are cooled below 100°K. Figure 1 shows a conventional PbTe cell. The Dewar construction is necessary to permit cooling of the sensitive layer. A sapphire window whose transmission remains satisfactory to 6 microns is sealed to the Pyrex by means of a graded seal.

The cell is prepared by placing powdered PbTe, formed by the fusion of stoichiometric amounts of Pb and Te, into a cell blank and subliming it in a high vacuum. The PbTe vapor is condensed onto the region between previously ruled conducting electrodes by cooling this region with an air jet. Sensitization consists of oxygen treatments until optimum sensitivity is

* This work was supported by the Wright Air Development Center.

† Presently at the International Business Machines Corporation, Endicott, New York.

[1] O. Simpson, Trans. Roy. Soc. (London) **A243**, 547-584 (1951).
[2] R. A. Smith, Advances in Physics **2**, 321-369 (1953).
[3] R. A. Smith, *Semiconducting Materials* edited by H. K. Henisch (Butterworth Publications Ltd., London, 1951), p. 205.

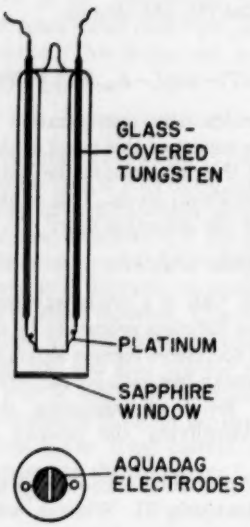

FIG. 1. Conventional cell blank used for the study of spectral sensitivity of films.

obtained. Such a completed cell, however useful, does not provide an insight into the effects of oxygen on the film properties. This study was undertaken to determine the effects of oxygen on various film parameters (such as: resistance, thermoelectric power, and sensitivity to both monochromatic and white radiation) with the aim of correlating these effects and understanding the various phenomena involved. No emphasis has been placed in this study on obtaining films with optimum sensitivity.

II. EXPERIMENTAL ARRANGEMENT

The apparatus used may be placed into four categories: vacuum system, specially constructed PbTe cell blanks for various types of measurements, electrical system, and optical system. The vacuum system consists of a three-stage water-cooled oil diffusion pump backed by a Welch forepump. A high vacuum stopcock and liquid air trap are provided between the diffusion pump and the cell assembly. Pressures lower than 10^{-7} mm of Hg may be obtained with this system. Oxygen can be admitted to the system in the form of pressure pulses from a liter flask containing oxygen. The flask is attached to the vacuum system by means of a capillary tube containing two stopcocks 3 centimeters apart. By opening and then closing the stopcock nearest the flask, oxygen is admitted into the region between the stopcocks. By opening the other stopcock a known amount of oxygen may then be admitted into the cell. Calibrated pulses of oxygen are thus obtained and controlled by varying the pressure in the flask.

Before each cell blank is used, it is evacuated for several hours and the blank, manifold and contents are baked for about 2 hours at about 550°C. Films may then be deposited by either subliming the material from a tungsten basket or by placing the entire cell blank into an oven at about 525°C and cooling the region where the material is to condense.

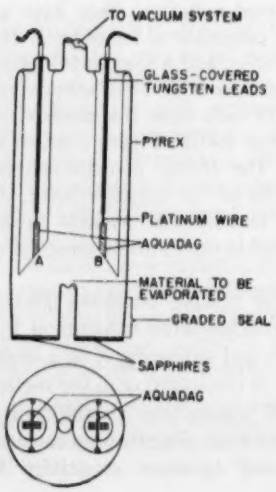

FIG. 2. Dual cell blank used for the determination of the effect of substrate temperature on film properties.

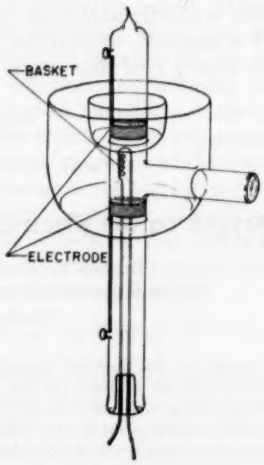

FIG. 3. Cell used for the determination of thermoelectric power and film resistance as a function of oxygen content of the film.

Several experimental cells were used for the measurements. The cell shown in Fig. 1 was used for routine measurements of cell resistance as a function of film temperature. In order to compare films formed under different conditions of substrate temperature, the cell shown in Fig. 2 was constructed. It is similar to that shown in Fig. 1, but since it contains 2 elements controlled experiments were made possible. For the study of thermoelectric power measurements, a tube similar to that used by Hintenberger[4] was constructed. (See Fig. 3.) The material was evaporated from a tungsten basket and condensed between the ring electrodes. The thermoelectric power of the film was then measured while holding liquids in the upper and lower cups at different temperatures. Film resistance at

[4] H. Hintenberger, Z. Physik **119**, 1 (1942).

various temperatures could be measured by filling the lower cup with a liquid at the desired temperature and connecting an ohmmeter to the ring electrodes.

Electrical measurements consisted of resistance measurements most conveniently made with an RCA voltohmyst and of thermoelectric voltage made with a conventional dc amplifier. For measurement of film response to radiation an ac method was used. Radiation from a globar or a galvanometer lamp was interrupted by a chopper before it fell onto the film. The film was connected in series with a resistor and several dry cells. Voltage variations across the resistor were amplified and measured by means of a VTVM or a calibrated oscilloscope.

In order to determine the response to monochromatic radiation, a Perkin-Elmer infrared monochromator was introduced between the globar and the film.

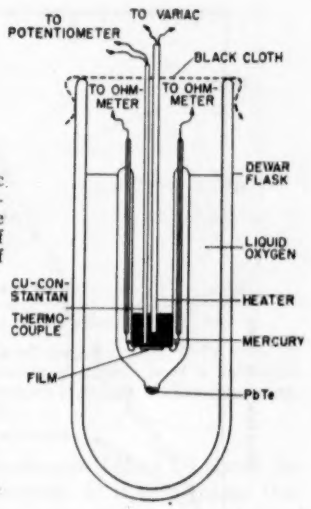

FIG. 4. Cyrostatic arrangement for the determination of the temperature dependence of resistance of PbTe films as a function of oxygen content.

III. PROCEDURE AND RESULTS

A. The Effect of Oxygen on Film Resistance and on the Temperature Coefficient of Resistance

The cell blank shown in Fig. 1 was attached to the vacuum system and evacuated. PbTe was deposited on the glass substrate between graphite electrodes which were 1.0 cm long and 0.1 cm apart. The temperature of the substrate was maintained at 40°C during the deposition by a water-cooled bath. After a deposition time of one hour the film was about 0.5 micron thick and had a resistance of 160 ohms. Mercury was then inserted into the coolant chamber of the cell and a heater element and thermocouple were dipped into this mercury bath. A liquid oxygen bath was then placed around the cell to shield the sensitive area from room temperature radiation. Figure 4 shows a diagram of the experimental setup. The mercury was frozen and cooled to about 80°K by slowly pouring liquid nitrogen into the coolant chamber. The temperature of the mercury slug was then permitted to rise slowly to room temperature by passing a small current through the heater. During this process resistance and temperature measurements were made. As the film temperature approached 295°K a pulse of oxygen was admitted dynamically into the system causing the pressure to increase to about 5 microns. An immediate rise in film resistance was observed. The resistance decreased only slightly to an equilibrium value as the original high vacuum was restored. The film was then cooled and measurements of resistance were again made as it warmed to room temperature. The procedure was repeated until the film had been exposed to 12 oxygen pulses. In order to obtain significant resistance changes the size of the pressure pulses was gradually increased over the last three pulses. Figure 5 shows the results of the entire experiment. Each curve was nearly reversible as long as the film temperature was not raised above about 600°K. When an oxygenated film was heated above about 650°K it was returned to its original condition as shown by curve 0 in Fig. 5. This indicates that oxygen is driven from the film by excessive heating in a high vacuum.

Figure 6 is a plot of resistance isotherms of the PbTe film just described obtained by sectioning Fig. 5. It is to be noted that with the addition of oxygen the resistance of a film rises to a maximum and then falls.

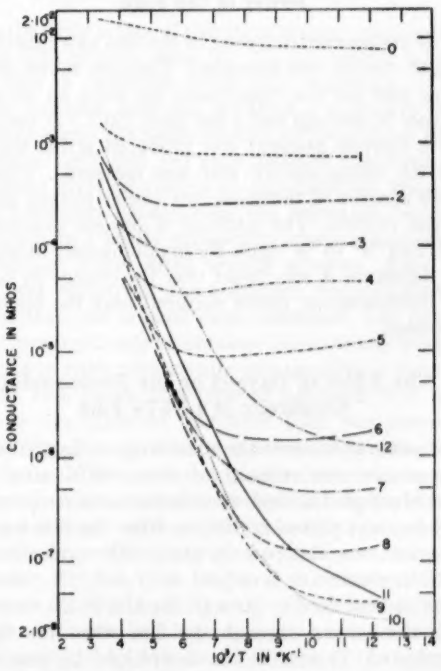

FIG. 5. Conductance of films as a function of film temperature for increasing exposure to oxygen at room temperature.

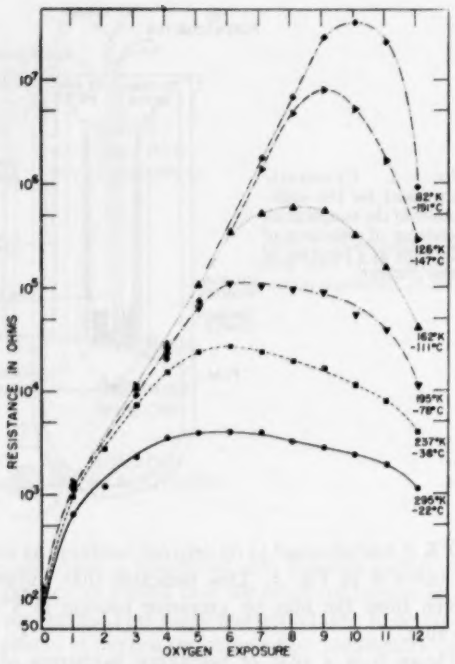

FIG. 6. Conductance of films for various temperatures as a function of oxygen exposures.

B. The Effect of Oxygen on the Thermoelectric Power of the Film

The thermoelectric power of the film as a function of oxygen content was measured. The tube shown in Fig. 3 was used for this experiment. By using an ice water mixture in one cup and a hot bath (50°C) in the other cup a thermal gradient was produced across the film and the thermoelectric emf was measured. Figure 7 shows a curve of thermoelectric power plotted against oxygen content. The addition of oxygen changes the film from "*n*" to "*p*" type. By simultaneously measuring the resistance it was found that the change in sign of the thermoelectric power occurred near the resistance maximum.

C. The Effect of Oxygen on the Photoconductive Sensitivity of a PbTe Film

In order to observe the sensitivity to light, the film temperature was reduced to about 90°K after each pulse of oxygen had been admitted at room temperature. A globar was placed at 100 cm from the film and the radiation was chopped at about 200 cycles/second. The film sensitivity is defined as $(I_1-I_d)/I_d$, where I_d is the current flowing through the film in the dark and I_1 is the current through the film when the film is illuminated. This ratio was determined by measuring the ac voltage across, and the dc current through the load resistor. Figure 8 shows the results of these measurements for a typical case. A peak in sensitivity occurred at a degree of oxygenation somewhat larger than is required to produce the room temperature resistance maximum.

D. The Effect of Oxygen on the Spectral Response of PbTe

In order to determine the effect of oxygen on spectral sensitivity of a PbTe film, chopped radiation from the globar was passed through a Perkin-Elmer infrared monochromator. The spectral sensitivity was then determined with the cell at about 90°K. Oxygen was admitted as in earlier experiments. There seemed to be no variation in the shape of the spectral response until the 90°K-resistance isotherm had passed its maximum. Curve A of Fig. 9 shows a characteristic curve. After the film had been oxygenated beyond its resistance maximum a new sensitivity peak occurred at about 1.5 microns as shown by curve B of Fig. 9. Additional oxygenation lead to the spectral response shown by curve C. The time constant associated with the new peak at about 1.5 microns was generally between 10^{-2} and 10^{-3} second while that associated with the original photoeffect shown in curve A generally varied between 10^{-4} and 10^{-6} second. Continued oxygenation gradually increased the time constant associated with the 4.5 micron effect. In addition, it was observed that if the cell was cooled with dry ice instead of liquid oxygen while the spectral response was measured the peak originally at about 4.5 microns shifted slightly toward the visible (to about 4.0 microns) and the 1.5 micron peak disappeared completely. The over-all signal at 195°K was generally less than 1 percent of the signal at 90°K.

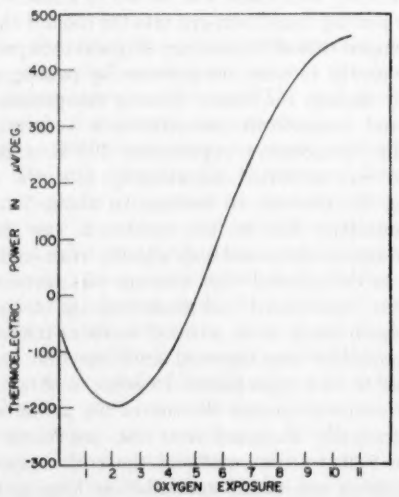

FIG. 7. Variation of thermoelectric power of a film as a function of exposure to oxygen.

E. The Photovoltaic Effect in PbTe Films

All films of PbTe exhibited some degree of photovoltaic sensitivity upon oxygenation. The peak photovoltaic sensitivity at 90°K occurred at the transition from "*n*" to "*p*" type. The upper limit of the photovoltaic effect in films is in approximate agreement with that observed by Gibson[6] for point contact single crystal PbTe photocells.

F. Factors Affecting the Reproducibility of the Experiment

1. Substrate Temperature

During preliminary experiments it was observed that under certain conditions, oxygen had a much greater effect on film properties than has been described. This variation was traced to variations in substrate temperature between different evaporations. An experiment was, therefore, designed to study the effect of substrate temperature during evaporation on the ultimate oxygen susceptibility and properties of the resulting film. The tube shown in Fig. 2 was used for the experiment. Substrate *A* was held at 40°C and substrate *B* at 200°C. The PbTe to be sublimed was pulverized and placed midway between the two substrate surfaces. Thus all parameters except the substrate temperature were the same during film formation. After the films were formed, oxygen was admitted in the conventional fashion with both films at room temperature. The resistance was measured as a function of oxygen content, both at room temperature and liquid oxygen temperature. Figure 10 shows the results of these measurements. It is to be noted that the film deposited on the lower temperature substrate was much more susceptible to oxygen than the one deposited onto the higher temperature surface. Considerably less oxygen was required to transform the film deposited on the 40°C substrate from "*n*" to "*p*" type than that on the 200°C substrate. It is also of interest to note that the magnitudes of the resistance maximum for both film *A* and film *B* were approximately the same.

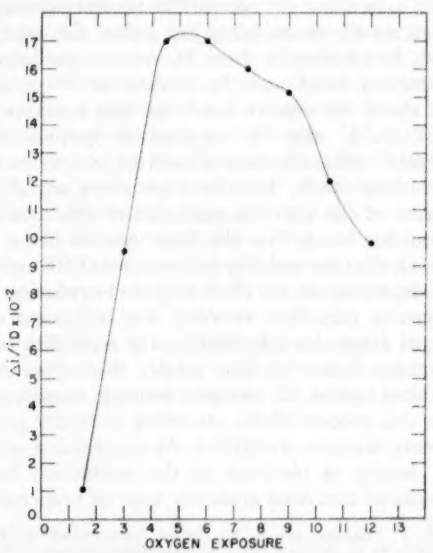

FIG. 8. Variation of film sensitivity as a function of exposure to oxygen.

[6] A. F. Gibson, Proc. Phys. Soc. (London) **B65**, 196 (1952).

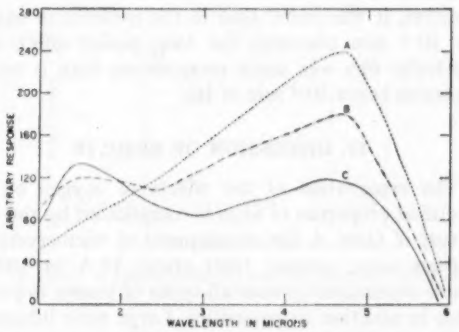

FIG. 9. Spectral response of several typical PbTe films. A: After exposure to small amounts of oxygen (layer is "*n*" type). B: Exposure to moderate amounts of oxygen. C: Heavily oxygenated film (layer is "*p*" type).

2. The Effect of Strong Illumination

In the early stages of this investigation fairly intense white light shining onto the cell for several minutes was used to determine white light sensitivity. It was found, however, that this produced a secondary effect which obscured the measurements on the primary effect. As white light first fell onto some of the films, the resistance dropped sharply as was expected. However, with prolonged illumination, the resistance began to rise again in a nearly exponential manner reaching an equilibrium value after several minutes. After the light was turned off the resistance was considerably higher than the original dark resistance. The original resistance could only be obtained after the cell had been warmed to room temperature and recooled in the dark. Figure 11A shows this type of behavior. For other films it was observed that after light was permitted to fall onto the cell the film resistance dropped at first rapidly, and then more slowly as indicated by curve B in Fig. 11. After removal of the light the dark resistance was lower than before exposure to light, but again it could be returned to its original value by warming and recooling the cell. The long period characteristics of 11A were exhibited by films which did not have sufficient oxygen and were "*n*" type at liquid air temperatures; those exhibited by 11B were "*p*" type at low temperatures. The magnitude shown by curve B increased greatly with the amount of overoxygenation. In

addition, it was found that in the presence of oxygen (at 10^{-4} mm pressure) the long period effect in a particular film was much more severe than it was at pressures below 10^{-7} mm of Hg.

IV. DISCUSSION OF RESULTS

The explanation of the effects of oxygen on the electrical properties of films is complicated by the very nature of films. A film is composed of microcrystals of various sizes, ranging from about 10 A to 1000 A. These crystallites contain all types of known imperfections in addition to impurities. Large scale inhomogeneities may also be produced by differential expansion of substrate and film, by substrate contamination and in general by variations of film growth in different regions of the film. Since the electrical properties are not only dependent on the crystallite structure, but also on contacts between crystallites, additional complications are introduced. At least two models have been proposed to explain photoconductivity in PbTe films. Smith[3] and his collaborators suggest that photoconductivity in PbTe is due to the effects produced by radiation falling on the barriers between crystallites. Simpson,[1] on the other hand, proposes excitation from a modified valence band to the conduction band of PbTe to explain his results. Neither of these models can be used entirely to explain the observed results, although there is considerable merit in each.

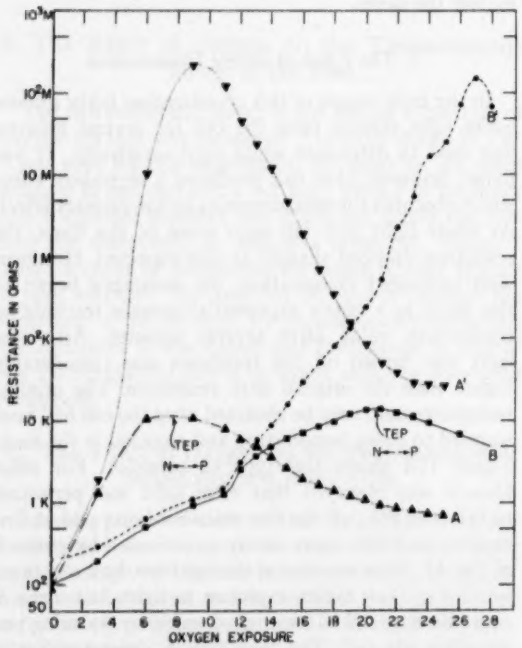

FIG. 10. Variation of film properties as a function of substrate temperature. A. Film deposited on a 40°C substrate—measurements while film is at room temperature. A′. Film deposited on a 40°C substrate—measurements while film is at 90°K. B. Film deposited on 200°C substrate—measurements while film is at room temperature. B′. Film deposited on 200°C substrate—measurements while film is at 90°K.

A model for photoconductivity in PbTe must first of all explain the long wavelength threshold of about 5.5 microns when the film is cooled to 90°K. Measurements of thermal activation energy have yielded a value of 0.62 ev.[6] Such a value would indicate a long wavelength threshold occurring at about 2 microns, if one assumes that photoconductivity is due to excitation of electrons from the valence to the conduction bands. One can perhaps overcome this difficulty by postulating that the long wavelength cutoff be due to excitation of electrons from the valence band to impurity levels. Such a picture could not, however, explain the high absorption coefficient extending to about 5 microns as reported by Gibson.[7] Scanlon[8] in a recent study of thermal activation energy has shown that for PbS crystals the previously measured thermal activation energy of 1.1 ev is reduced to 0.38 ev when purer crystals are used such that the activation energy may be measured in the vicinity of room temperature instead of at 700°K. It is thus entirely probable that when techniques for producing purer PbTe crystals are found, the thermal activation energy will be considerably smaller than first reported by Chasmar and Putley.[6] It seems thus entirely proper to disregard measurements of thermal activation energy in the formulation of a mechanism and assume the forbidden gap width to be about 0.22 ev as determined from absorption and photoeffect data.

The film when freshly deposited is "*n*" type due to an effective excess of Pb atoms. The free electron density in the conduction band of the film has been found to be about 10^{18} per cc.[9] The electrons are supplied by excess Pb atoms lying just below the conduction band. In addition to these Pb centers just below the conduction band and Te centers or Pb vacancies just above the valence band, the film contains many traps which may be represented symbolically as potential wells, somewhere between the valence and conduction bands. Initially these traps are all filled, because of the high concentration of electrons in the conduction band. The film thus behaves like a metal with an electron mobility between 5 and 500 cm^2/volt-sec, depending on the effect of grain boundaries. When oxygen is permitted to enter the cell, some of the oxygen atoms are adsorbed on the crystallite surface. Electrons from the film attach themselves to the adsorbed atoms of oxygen, forming negative ions. It is this process which, according to Smith[3] produces barriers between crystallites. As oxygenation proceeds the density of electrons in the conduction band is diminished and films gradually take on properties of a

[6] R. P. Chasmar and E. H. Putley, *Semiconducting Materials* edited by H. K. Henisch (Butterworth Publications Ltd., London, 1951), p. 208.
[7] A. F. Gibson, Proc. Phys. Soc. (London) **B65**, 378 (1952).
[8] W. W. Scanlon, Phys. Rev. **92**, 573 (1953).
[9] S. J. Silverman and H. Levinstein, Phys. Rev. **94**, 871 (1954).

semiconductor as shown in Fig. 5. Such a model is further substantiated on examination of Fig. 10, the effect of substrate temperature on the resistance-oxygen dependence of films. When the substrate temperature is low, porous films are formed, where the ratio of film surface to crystallite volume is considerably larger than for less porous films formed at higher substrate temperatures. As the films become less porous, the decreased availability of oxygen sites will produce smaller variations in film resistance when the film is exposed to oxygen. If one assumes photoconductivity to be due to excitation of electrons from valence to conduction bands such a model explains the variations of sensitivity with the addition of oxygen as shown in Fig. 8. The relationship $(I_1-I_d)/I_d$ increases as oxygen is added since I_d is at first decreased. Then, as holes are created in the valence band by the continuous addition of oxygen, increasing dark conductivity decreases the sensitivity. Films require cooling for optimum sensitivity to reduce thermal excitation of electrons across the relatively narrow energy gap of 0.22 ev. The change in the sign of the thermoelectric power as shown in Fig. 7, occurs near the point where the conduction band is emptied of electrons. The exact location of the changeover with oxygen depends, of course, on the relative mobility of electrons and holes, and thus varies somewhat from film to film and with film temperature. The lengthening of the time constant with increasing oxygenation may also be understood from this model. As oxygen is added to the film, more and more traps between the conduction and valence bands will be emptied. They will then act as traps for excited electrons and increase the lifetime of holes.

Up to this point, no attention has been paid to the manner in which the entire film changes from "*n*" to "*p*" by the addition of oxygen. It is quite clear that the process is not a slow, uniform change. In all probability the surface layer will become "*p*" type first. This is followed by the diffusion of oxygen along grain boundaries, producing certain "*p*" type regions within the film while the remaining film may still be "*n*" type. These regions may cover areas from one microcrystal to many thousands of microcrystals. Photovoltaic effects, as have been described, are due to *p-n* junctions thus created. These junctions will also account for large deviations from Ohm's law observed in many films. Large "*p*" and "*n*" regions within a film have been observed by scanning the film with a small spot

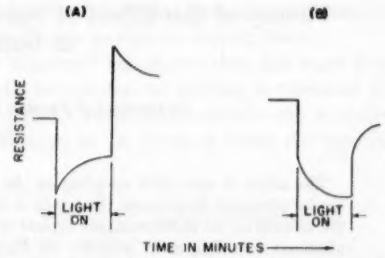

FIG. 11. Effect of strong radiation on film resistance (long period effect). A. "*n*" type film. B. "*p*" type film.

of light. These regions have been altered by the addition of small pulses of oxygen. The peak in spectral response in the vicinity of 1.5 microns and its long time constant could be attributed to the formation of surface layers of energy gaps larger than those of the remaining film as more and more oxygen is permitted to interact with the film.

Long period photoeffects which make dc measurements impossible are evidently caused by deep surface oxygen traps. White light would excite electrons into these traps from the interior of the crystallites. When a film is predominately "*n*" type at low temperature, this trapping will result in a decrease of electrons in the conduction band with an increase in resistance. When the film is predominately "*p*" type any trapping will increase the hole concentration with a resulting decrease in resistance. Warming to room temperature frees the deeply trapped electrons and returns the film to its original condition.

V. CONCLUSIONS

The phenomena described here represent a small phase of rather detailed investigation into the nature of photoconducting layers. The model presented here was adopted only after many other models did not qualitatively stand the test of experiment. While it is desirable to develop a more quantitative picture, the nature of thin films makes this quite impractical. It is hoped that this study will provide an insight into the processes which take place on the surface of crystals, where measurements such as those performed on film would not be possible.

We wish to acknowledge the assistance of Mr. Werner Beyen, Mr. Channing Dichter, and Mr. Dean Mitchell, who have aided in making many of the measurements reported here.

Theory of the Effect of Spin-Orbit Coupling on Magnetic Resonance in Some Semiconductors*

R. J. ELLIOTT†
Department of Physics, University of California, Berkeley, California
(Received May 26, 1954)

The effect of spin-orbit coupling on the usual band theory of electrons in a lattice is considered. Particular attention is given to the bands in impurity semiconductors with diamond-type structure. g-values are calculated for electron states typical of various possible cases and it is found that different values are obtained according as to whether the Fermi level is near or distant from a band degeneracy. The spin-lattice relaxation time is calculated so that the effect of spin-orbit coupling on the wave functions is included, and times in fair agreement with those observed in silicon and alkali metals are obtained.

I. INTRCDUCTION

THERE have recently been reported a number of observations of magnetic resonance in impurity semiconductors,[1] and it is found that the g-values and line-width vary with the material and the impurity concentration. In order to understand these effects a theory is developed here which takes particular account of the effects of spin-orbit coupling. We treat the case in which the electrons can be considered to move through the crystal (and are not trapped at the impurities), and make the usual assumptions of band theory. In another paper (to be referred to as A)[2] we have treated the effect of including spin in band theory from the group theoretical aspect and have shown that one of its main effects is the splitting of otherwise degenerate bands. In this paper it is shown that the properties of the resonance are rather different if the Fermi level is near or far away from a band degeneracy and in this way useful information can be obtained about the bands from the resonances.

The effect of the orbital angular momentum, as measured by the difference of g from the free electron value of 2.0023, is much larger for electrons in states near a degeneracy. This is calculated for particular kinds of states which are of interest in semiconductors but the resulting expressions should give the correct order of magnitude for all similar cases. Other calculations of such a spin-orbit effect have been carried out by Yafet[3] for sodium metal where resonance has also been observed from the conduction electrons.[4] The observed line-width in semiconductors appears to arise from a spin-lattice relaxation time in most cases, and it is the shortness of this time which may account for the absence of resonance in germanium. Because this time is the measure of the interaction between the spins and the lattice, and because the interaction between the lattice and the orbital motion of the electron will be large we expect this effect to be greatly influenced by the spin-orbit interaction. The relaxation times due to the interaction with lattice vibrations and impurity centers will be discussed and it is found that the line widths predicted are usually within an order of magnitude of those observed. Calculations are also made for alkali metals and it is found that the mechanism involving spin-orbit coupling produces shorter times than those calculated by Overhauser[5] on a free-electron model.

II. SPIN-ORBIT COUPLING AND BAND THEORY

The problem of an electron in a solid is usually treated as if it is moving in a perfect rigid lattice under a periodic potential. The Schroedinger equation is

$$[(\mathbf{p}^2/2m)+V]\Psi=E\Psi, \tag{1}$$

where V has both the point and translational symmetry of the lattice. The resulting wave functions are of course the well-known Bloch functions

$$u_k e^{i\mathbf{k}\cdot\mathbf{r}}, \tag{2}$$

where u_k has the translational symmetry of the lattice. In order to introduce the appropriate spin-orbit interaction into (1) we start with the four-component Dirac equation and reduce it to two components in the usual way.[6] The resulting power series in $(mc)^{-2}$ is to first order

$$\left[\frac{\mathbf{p}^2}{2m}+V-\frac{\mathbf{p}^4}{8m^3c^2}+\frac{\hbar}{4m^2c^2}(\nabla V\cdot\mathbf{p})+\frac{\hbar}{4m^2c^2}(\nabla V\times\mathbf{p})\cdot\boldsymbol{\sigma}\right]\Psi=E\Psi. \tag{3}$$

The third term gives the first-order relativistic correction, and will be neglected. The fourth term gives a

* This work has been supported in part by the U. S. Office of Naval Research and the U. S. Signal Corps.
† Now at Atomic Energy Research Establishment, Harwell, England.
[1] Honig, Portis, Kip, Kittel, and Morin (to be published). Portis, Kip, Kittel, and Brattain, Phys. Rev. 90, 988 (1953). N. Bloembergen and F. K. Willenbrock, Phys. Rev. 91, 1281 (1953).
[2] R. J. Elliott, following paper, Phys. Rev. 95, 280 (1954).
[3] Y. Yafet, Phys. Rev. 85, 478 (1952).
[4] G. Feher (to be published); Griswold, Kip, and Kittel, Phys. Rev. 88, 951 (1951).
[5] A. W. Overhauser, Phys. Rev. 89, 689 (1953).
[6] E. U. Condon and G. H. Shortley, *Theory of Atomic Spectra* (Cambridge University Press, Cambridge, 1935), p. 129.

small contribution to the energy of states whose eigenfunctions are nonzero at singularities of V. It has the same symmetry properties as V and does not change the form of the Hamiltonian in (1) and can therefore be neglected. The last term is the spin-orbit coupling. (It reduces to the well-known form $\zeta(r)\mathbf{l}\cdot\mathbf{s}$ when V is spherically symmetric.) For the moment we simply note that this term has the same symmetry properties as V. Because there is a term in the spin operator in our Hamiltonian, the resulting eigenfunctions will now be linear combinations of different spin functions and will in general be written

$$[a_k|+\rangle+b_k|-\rangle]e^{i\mathbf{k}\cdot\mathbf{r}}, \tag{4}$$

where $|+\rangle$, $|-\rangle$ are the two spin states with component of angular momentum $\pm\frac{1}{2}$ along some chosen direction. Considering the components of the matrix equation (3), it is clear that a_k and b_k have the symmetry of the lattice, like u_k in (2).

The symmetry properties of these wave functions are discussed in A, for some interesting lattices. In particular, it is shown that as a consequence of time-reversal symmetry, there is always a twofold degeneracy provided there is inversion in the symmetry group (as there is in the cases of interest here). By operating with the inversion operation on (4) we get a function

$$[a_{-k}|+\rangle+b_{-k}|-\rangle]e^{-i\mathbf{k}\cdot\mathbf{r}}, \tag{5}$$

where a_{-k}, b_{-k} are suitably defined. Inversion has no effect on the spin functions. This has the same energy as (4); and so has the function obtained by reversing the time axis of (5) which is by Kramers' theorem[7]

$$[a_{-k}^*|-\rangle-b_{-k}^*|+\rangle]e^{i\mathbf{k}\cdot\mathbf{r}}. \tag{6}$$

Thus we obtain two functions with the same $\mathbf{k}$ [(4) and (6)] and the same energy. At some points of high symmetry in the Brillouin zone we see in A that time reversal does not give any extra degeneracy. In this case there is still a function like (6) degenerate with (4), but it can be obtained from (4) by an operation with a symmetry group element.

III. APPROXIMATIONS

In order to be able to find the energy level splittings and the actual admixtures of the wave functions caused by the spin-orbit coupling we must find the matrix elements of the term in (3). In general these can only be obtained by complicated calculations of V and the wave functions. Approximate forms can be obtained by using a cellular method like that of Wigner-Seitz[8] (see Yafet's calculation[3]). If the tight-binding approximation[9] is valid it can be shown that the spin-orbit coupling effect is rather similar to that in atomic theory.

Now Wannier[10] has shown that the wave function in a periodic lattice can be written in terms of functions centered about each lattice point—the so-called Wannier functions, w. In terms of these the eigenfunctions are

$$\Psi=\frac{1}{\sqrt{N}}\sum_{\mathbf{d}} w_k^s(\mathbf{r}-d)\exp(i\mathbf{k}\cdot\mathbf{d}), \tag{7}$$

where $\mathbf{d}$ denotes the vector coordinate of a lattice point. The w centered about different points are orthogonal, but they do overlap by a considerable amount. If we reduce all $\mathbf{k}$ into the first zone, each band must be designated by a number s.

If we draw polyhedra around each lattice point made up of the planes perpendicularly bisecting the lines to nearby lattice points, the potential V will be the same in each cell and have a center of symmetry at the lattice point. That is,

$$V=\sum_{\mathbf{d}} V(\mathbf{r}-\mathbf{d}), \tag{8}$$

where $V(\mathbf{r}-\mathbf{d})$ is defined in the polyhedron about $\mathbf{d}$ and is zero elsewhere. Then the spin-orbit coupling can be written

$$\frac{\hbar}{4m^2c^2}\sum_{\mathbf{d}}(\nabla V(\mathbf{r}-\mathbf{d})\times\mathbf{p})\cdot\boldsymbol{\sigma}=C. \tag{9}$$

Within the cell about $\mathbf{d}$, the expression can be written in the usual form,

$$\frac{\hbar^2}{4m^2c^2}\frac{1}{r}\frac{\partial V}{\partial r}\mathbf{l}\cdot\mathbf{s},$$

if $\mathbf{d}$ is the center of the coordinates and V has spherical symmetry. Because of the surrounding atoms, however, V will in fact have a symmetry lower than spherical and this expression must be modified.[11] Nevertheless since almost all the spin-orbit interaction arises when the electron is close to the nucleus and since the external field then has little effect, this expression remains a reasonable approximation.

We approximate by putting

$$\begin{aligned}&\langle\Psi_s(\mathbf{k})|C|\Psi_t(\mathbf{k}')\rangle\\&=\frac{1}{N}\sum_{\mathbf{d}}\exp[i(\mathbf{k}'-\mathbf{k})\cdot\mathbf{d}]\langle w_k^s(\mathbf{r}-\mathbf{d})|C|w_{k'}^t(\mathbf{r}-\mathbf{d})\rangle\\&=\delta_{kk'}\langle w_k^s(\mathbf{r})|\zeta(\mathbf{r})\mathbf{l}\cdot\mathbf{s}|w_{k'}^t(\mathbf{r})\rangle\\&=\delta_{kk'}\lambda\langle w_k^s(\mathbf{r})|\mathbf{l}\cdot\mathbf{s}|w_{k'}^t(\mathbf{r})\rangle.\end{aligned} \tag{10}$$

[7] H. A. Kramers, Proc. Acad. Sci. Amsterdam **33**, 959 (1930).
[8] E. Wigner and F. Seitz, Phys. Rev. **43**, 804 (1933); **46**, 509 (1934).
[9] See for example F. Seitz, *Modern Theory of Solids* (McGraw-Hill Book Company, Inc., New York, 1940).
[10] G. H. Wannier, Phys. Rev. **53**, 671 (1938).
[11] K. W. H. Stevens (private communication). I am indebted to Dr. Stevens for instructive discussions on the effect of symmetry and the magnitude of λ.

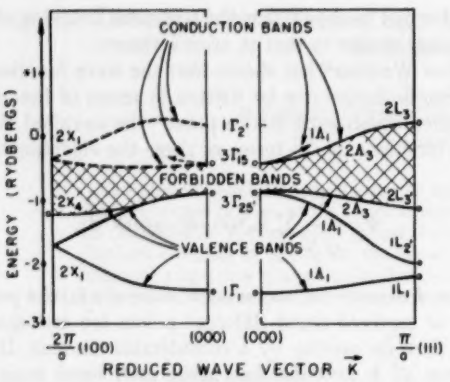

FIG. 1. Energy bands of diamond (after Herman, see reference 12). Slope of energy contour is zero at points marked "0."

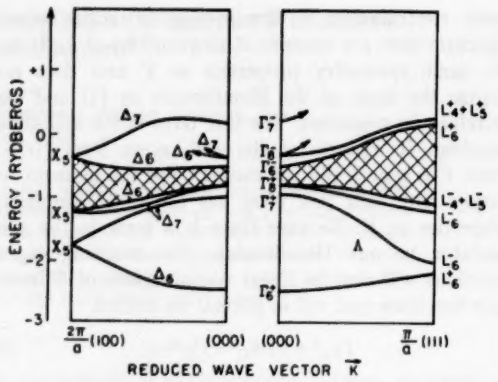

FIG. 2. Schematic representation of the energy bands of diamond including spin-orbit coupling effects. (Based on Herman's calculation, see Fig. 1).

That is to say, we neglect that part of w which spills over into other cells, and all overlap effects. Similarly for the matrix elements of the orbital angular momentum, $-i(\mathbf{r}\times\mathbf{p})=\mathbf{l}$, we make the same approximation and write

$$\langle\Psi_s(\mathbf{k})|\mathbf{l}|\Psi_{s'}(\mathbf{k}')\rangle$$
$$=\frac{1}{N}\sum_{\mathbf{d}}\exp[i(\mathbf{k}'-\mathbf{k})\cdot\mathbf{d}]\langle w_k{}^s(\mathbf{r}-\mathbf{d})|\mathbf{l}|w_{k'}{}^{s'}(\mathbf{r}-\mathbf{d})\rangle$$
$$=\delta_{kk'}\langle w_k{}^s(\mathbf{r})|\mathbf{l}|w_{k'}{}^{s'}(\mathbf{r})\rangle. \tag{11}$$

Various effects can now be calculated if it is further assumed that the angular dependence of the w is just that of the atomic functions used in the tight-binding method. The radial integration over ζ will remain an arbitrary parameter λ in our theory although if the tight-binding method gives a reasonable approximation we expect it to be somewhat like the spin-orbit coupling parameter for the appropriate atomic electrons.

IV. ENERGY BANDS IN DIAMOND TYPE CRYSTALS

A very extensive investigation of the energy bands in these crystals is being conducted by Herman. The calculated bands for diamond[12] are shown in Fig. 1, and preliminary results show that germanium has a somewhat similar band structure[13] from a symmetry point of view. In Fig. 2 we show schematically what the band structure is like when we include spin-orbit effects.

From the character tables 1, 2, 5, 7, 9 of A, we have found the degeneracies of the new irreducible representations and the way in which the old representations are split by adding spin (multiplying by $D_{\frac{1}{2}}$). There is further splitting of Γ_{15}, Γ_{25}', Δ_5, Δ_5', Λ_3, L_3, L_3', but not of X_1 and X_4. Because of time reversal each of the bands is doubly degenerate in Fig. 2 as it was in Fig. 1 because of the spin orientations. In the figure we have not attempted to draw the new bands accurately or the splittings to scale. Away from the places where there are extra splittings the energies have been left unchanged. In fact there will be a slight admixture of wave functions from other bands which now have the same transformation properties, and a second-order change in energy.

The details of the band structure are greatly affected near these degeneracies which are now split; like Γ_{15}, Γ_{25}'. Herman investigated these points in some detail by means of a perturbation procedure, and it is therefore convenient to take them as a detailed example of the effects we are considering. For small values of $\mathbf{k}$ the original triplet is split and Herman obtains the energies from a secular determinant of the form:

$$\begin{vmatrix} Ak^2+(B-A)k_x^2-E & Dk_xk_y & Dk_xk_z \\ Dk_xk_y & Ak^2+(B-A)k_y^2-E & Dk_yk_z \\ Dk_xk_z & Dk_yk_z & Ak^2+(B-A)k_z^2-E \end{vmatrix}=0 \tag{12}$$

(where A, B, and D are constants obtained by numerical computation). An effective mass can be defined for the three bands in the usual way,

$$E=\hbar^2k^2/2m^*, \tag{13}$$

although m^* varies in a complicated way with angle. With the inclusion of spin-orbit coupling, however, the energy E may not be proportional to k^2 over a sufficient range of k to make the concept of effective mass useful. Possible results have been sketched diagrammatically in Figs. 3 to 6. In Fig. 3 we have drawn typical curves of energy *versus* $\mathbf{k}$ for an arbitrary direction in $\mathbf{k}$ space and for small values of $\mathbf{k}$ in Herman's picture. The

[12] F. Herman, Phys. Rev. **88**, 1210 (1952); thesis, Columbia University, 1953 (unpublished).

[13] F. Herman and J. Calloway, Phys. Rev. **89**, 518 (1953). Dr. Herman has informed me that more accurate calculations are now being made.

curves are the parabolic solutions (13) of the secular determinant (12). Figure 4 shows a possible effect of the introduction of spin-orbit coupling; for large $\mathbf{k}$ the curves are similar to those in Fig. 3, but for smaller $\mathbf{k}$ the splitting makes the picture very different. Thus if we have an electron system in which the Fermi level is F_2 in the figures, the effective mass and general properties of the electrons at the top of the distribution would not be greatly altered by the spin-orbit effects. This would also be true at high temperatures where the electrons have thermal energies and obey Boltzmann statistics rather than Fermi-Dirac. On the other hand, if we have an electron system with a Fermi level F_1, it is clear that Herman's calculations will not be applicable. Figures 5 and 6 show a different kind of splitting and display how complicated the addition of the spin-orbit coupling may make the band forms.

We can make more explicit calculations of these effects by making the approximations discussed in Sec. III. That is, we calculate the matrix elements of the spin-orbit coupling by assuming that the tight-binding wave functions give a representation of the actual wave functions with the correct symmetry properties. The tight-binding approximation for the diamond crystal has been solved by Morita.[14] His band structure did not agree with Herman's in that his bands occurred in a different order but he did have bands with the same symmetry properties which he built up from $2s$ and $2p$ atomic wave functions. We label the atomic wave functions of the s-type ϕ_s and the three p-types ϕ_x, ϕ_y, and ϕ_z. The symmetry properties of the tight-binding functions will be the same whatever the principal quantum number n, and the results will apply to diamond $n=2$, silicon $n=3$, germanium $n=4$, and grey tin, $n=5$. To obtain the wave functions, we note that the diamond lattice is built up from two interpenetrating face-centered cubic lattices, with principal vectors $\frac{1}{2}a(0,1,1)$; $\frac{1}{2}a(1,0,1)$; $\frac{1}{2}a(1,1,0)$; and so we define functions

$$\chi_j(\mathbf{r})=\frac{1}{\sqrt{N}}\sum_{\mathbf{d}}\exp(i\mathbf{k}\cdot\mathbf{d})\phi_j(\mathbf{r}-\mathbf{d}), \qquad (14)$$

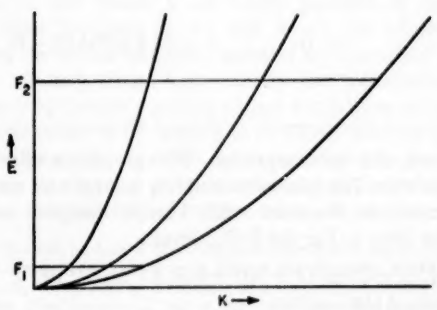

FIG. 3. Typical curves of energy *vs* k near a band degeneracy without spin-orbit coupling. F_1 and F_2 are Fermi levels (see text).

[14] A. Morita, Science Repts. Tôhoku Univ. **33**, 92 (1949).

where $\mathbf{d}$ are the lattice points of such an f.c.c. structure and j can be s, x, y, or z. Now one of the lattices is obtained from the other by a translation $\mathbf{t}=\frac{1}{4}a(1,1,1)$, and the general tight-binding wave function built from these functions can be written

$$\Psi=\sum_j[a_j\chi_j(\mathbf{r})+\alpha_j\exp(i\mathbf{k}\cdot\mathbf{t})\chi_j(\mathbf{r}+\mathbf{t})], \qquad (15)$$

where, since the two lattices are equivalent, $|a_j|^2=|\alpha_j|^2$. In particular Morita finds that at $\mathbf{k}=(0,0,0)$ the eight eigenfunctions are

$$\Psi_j=\frac{1}{(2N)^{\frac{1}{2}}}\sum_{\mathbf{d}}[\phi_j(\mathbf{r}-\mathbf{d})\pm\phi_j(\mathbf{r}-\mathbf{d}+\mathbf{t})]. \qquad (16)$$

For the irreducible representations in which we are interested, the appropriate forms of (16) are,

for Γ_1,
$$\frac{1}{(2N)^{\frac{1}{2}}}\sum_{\mathbf{d}}[\phi_s(\mathbf{r}+\mathbf{d})+\phi_s(\mathbf{r}+\mathbf{d}-\mathbf{t})],$$
for Γ_2',
$$\frac{1}{(2N)^{\frac{1}{2}}}\sum_{\mathbf{d}}[\phi_s(\mathbf{r}+\mathbf{d})-\phi_s(\mathbf{r}+\mathbf{d}-\mathbf{t})],$$
for Γ_{25}',
$$\frac{1}{(2N)^{\frac{1}{2}}}\sum_{\mathbf{d}}[\phi_j(\mathbf{r}+\mathbf{d})-\phi_j(\mathbf{r}+\mathbf{d}-\mathbf{t})] \qquad (17)$$
where $j=x, y, z$,
for Γ_{15},
$$\frac{1}{(2N)^{\frac{1}{2}}}\sum_{\mathbf{d}}[\phi_j(\mathbf{r}+\mathbf{d})+\phi_j(\mathbf{r}+\mathbf{d}-\mathbf{t})].$$

Since we are assuming that spin-orbit coupling is small, the wave functions of the representations formed from these when we include the spin will just be linear combinations of (17). By inspection we see that just as in an atom when spin and spin-orbit effects are included, the component ϕ's are the same in the s-states but in the p-states they are those corresponding to a total

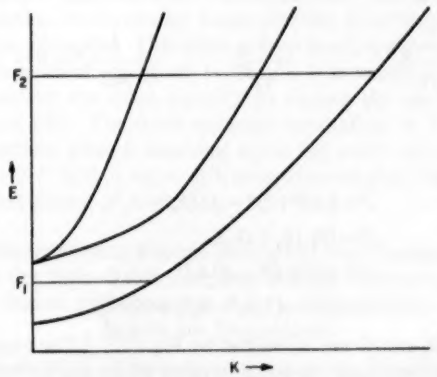

FIG. 4. Effect of inclusion of spin-orbit coupling on the curves shown in Fig. 3.

angular momentum J of $\frac{1}{2}$ in the twofold representation and $\frac{3}{2}$ in the fourfold. Then we have,

for Γ_6^+,

$$\frac{1}{(2N)^{\frac{1}{2}}}\sum_{\mathbf{d}}[\phi_s(\mathbf{r}-\mathbf{d})+\phi_s(\mathbf{r}-\mathbf{d}+t)]|\pm\rangle,$$

for Γ_7^-,

$$\frac{1}{(2N)^{\frac{1}{2}}}\sum_{\mathbf{d}}[\phi_s(\mathbf{r}-\mathbf{d})-\phi_s(\mathbf{r}-\mathbf{d}+t)]|\pm\rangle,$$

for Γ_7^+,

$$\frac{1}{(2N)^{\frac{1}{2}}}\sum_{\mathbf{d}}[\phi_{\frac{3}{2}}(\mathbf{r}-\mathbf{d})-\phi_{\frac{3}{2}}(\mathbf{r}-\mathbf{d}+\mathbf{t})],$$

for Γ_6^-, (18)

$$\frac{1}{(2N)^{\frac{1}{2}}}\sum_{\mathbf{d}}[\phi_{\frac{3}{2}}(\mathbf{r}-\mathbf{d})+\phi_{\frac{3}{2}}(\mathbf{r}-\mathbf{d}+\mathbf{t})],$$

for Γ_8^+,

$$\frac{1}{(2N)^{\frac{1}{2}}}\sum_{\mathbf{d}}[\phi_{\frac{3}{2}}(\mathbf{r}-\mathbf{d})-\phi_{\frac{3}{2}}(\mathbf{r}-\mathbf{d}+\mathbf{t})],$$

for Γ_8^-,

$$\frac{1}{(2N)^{\frac{1}{2}}}\sum_{\mathbf{d}}[\phi_{\frac{3}{2}}(\mathbf{r}-\mathbf{d})+\phi_{\frac{3}{2}}(\mathbf{r}-\mathbf{d}+\mathbf{t})],$$

where $\phi_{\frac{1}{2}}$ are the functions:

$$\frac{1}{\sqrt{2}}(\phi_x+i\phi_y)|+\rangle,\ \frac{1}{\sqrt{6}}[(\phi_x+i\phi_y)|-\rangle-2\phi_z|+\rangle],$$

$$\frac{1}{\sqrt{6}}[(\phi_x-i\phi_y)|+\rangle+2\phi_z|-\rangle],\ \frac{1}{\sqrt{2}}(\phi_x-i\phi_y)|-\rangle;$$

and $\phi_{\frac{3}{2}}$ are the functions: (19)

$$\frac{1}{\sqrt{3}}[(\phi_x+i\phi_y)|-\rangle+\phi_z|+\rangle],$$

$$\frac{1}{\sqrt{3}}[(\phi_x-i\phi_y)|+\rangle-\phi_z|-\rangle].$$

Using the functions (19) as basic functions and calculating the spin-orbit matrix elements by means of (10), we can now construct the secular determinant which gives the energies of the bands near $\mathbf{k}=(0,0,0)$ analogous to (12). Since we know the matrix elements of the potential more accurately from Herman's calculation than from a tight-binding approximation like the above, we have used his calculation and written these elements in terms of the constants A, B, and D. The determinant is:

$$\begin{vmatrix}
\frac{1}{2}\lambda+\frac{1}{2}P-E & \frac{1}{\sqrt{3}}R & \frac{1}{2\sqrt{3}}S & 0 & \frac{1}{\sqrt{6}}R & -\frac{1}{\sqrt{6}}S \\
\frac{1}{\sqrt{3}}\bar{R} & \frac{1}{2}\lambda+\frac{1}{6}(P+4Q)-E & 0 & -\frac{1}{2\sqrt{3}}S & -\frac{1}{3\sqrt{2}}(P-2Q) & -\frac{1}{\sqrt{2}}R \\
\frac{1}{2\sqrt{3}}\bar{S} & 0 & \frac{1}{2}\lambda+\frac{1}{6}(P+4Q)-E & \frac{1}{\sqrt{3}}R & \frac{1}{\sqrt{2}}\bar{R} & -\frac{1}{3\sqrt{2}}(P-2Q) \\
0 & -\frac{1}{2\sqrt{3}}\bar{S} & \frac{1}{\sqrt{3}}\bar{R} & \frac{1}{2}\lambda+\frac{1}{2}P-E & \frac{1}{\sqrt{6}}\bar{S} & \frac{1}{\sqrt{6}}\bar{R} \\
\frac{1}{\sqrt{6}}\bar{R} & -\frac{1}{3\sqrt{2}}(P-2Q) & \frac{1}{\sqrt{2}}R & \frac{1}{\sqrt{6}}S & -\frac{1}{4}\lambda+\frac{1}{3}(P+Q)-E & 0 \\
-\frac{1}{\sqrt{6}}\bar{S} & -\frac{1}{\sqrt{2}}\bar{R} & -\frac{1}{3\sqrt{2}}(P-2Q) & \frac{1}{\sqrt{6}}R & 0 & -\frac{1}{4}\lambda+\frac{1}{3}(P+Q)-E
\end{vmatrix}=0, \tag{20}$$

where

$$P=2Ak^2+(B-A)(k_x^2+k_y^2),$$
$$R=Dk_z(k_x+ik_y),$$
$$Q=Ak^2+(B-A)k_z^2,$$
$$S=(B-A)(k_x^2-k_y^2)+2iDk_xk_y.$$

[A, B, and D are as defined by Eq. (12).] The roots of this determinant are equal in pairs, which can be readily checked since it can be transformed into a skew-symmetric form. The roots are, however, complicated solutions of a cubic equation. We can obtain effective masses when the spin-orbit coupling is large and we are interested in electrons with kinetic energies much smaller than λ. For the $\frac{3}{2}$ (Γ_8) levels,

$$E=\tfrac{1}{6}\{2(P+Q)\pm[(P-2Q)^2+3(4|R|^2+|S|^2]^{\frac{1}{2}}\}$$
$$=Bk^2\pm\tfrac{1}{3}\{(B-A)^2k^4$$
$$[D^2-3(B-A)^2](k_x^2k_y^2+k_y^2k_z^2+k_z^2k_x^2)\}^{\frac{1}{2}}. \tag{21}$$

For the $\frac{1}{2}$ (Γ_7) levels,

$$E=\tfrac{1}{3}(P+Q)=Bk^2. \tag{22}$$

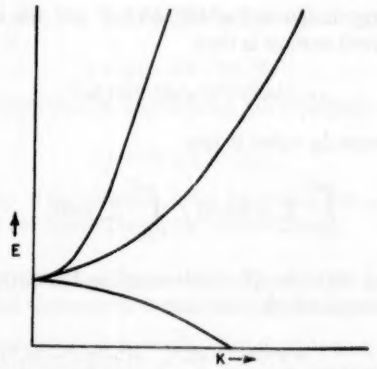

FIG. 5. Another possible form of band degeneracy. The curves shown are parabolas, so the curves can be described in terms of an effective mass.

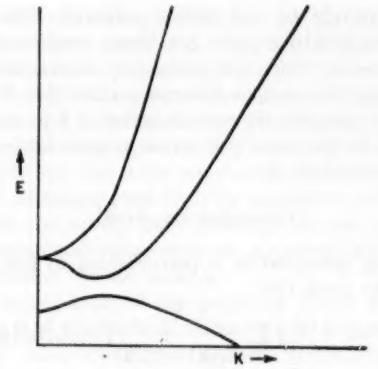

FIG. 6. Possible effect of spin-orbit coupling on the curves shown in Fig. 5. The curves are now more complicated in form and cannot be described in terms of an effective mass.

In fact spin-orbit coupling has such a profound effect on bands near a degeneracy that any attempt to explain observations of the effective mass, magnetoresistance, etc. of electrons occupying such bands should be made with the above methods.

V. g-VALUES

The Hamiltonian of the interaction between a magnetic field and an electron is $\beta\mathbf{H}\cdot(\mathbf{l}+2\mathbf{s})$. This lifts the remaining twofold degeneracy of the electron states and causes a splitting which we call $g\beta H$, thus defining g as the matrix element of $2(\mathbf{l}+2\mathbf{s})$ in the direction of the field. In general g will depend on the direction of H and on $\mathbf{k}$. However, in a metal, collisions of the electron with lattice waves and impurity centers take place so often (every 10^{-13} second or less) that the measurement sees only an average effect. We shall compute the average value of g in three cases which seem to cover the possible band forms which can occur in these substances.

A. Electrons in a Nondegenerate Band

In the absence of spin-orbit coupling the wave functions for any vector $\mathbf{k}$ are simply products of orbital and spin functions $\Psi|+\rangle$ and $\Psi|-\rangle$. In all singlet states the orbital magnetic moment is "quenched" and thus all such states have exactly the free-electron g value.[15] Spin-orbit coupling causes admixtures of states corresponding to the same $\mathbf{k}$ in all bands with the same transformation properties. In the general case, we saw in Sec. IV that the wave functions of all bands belong to the same irreducible representation; this means that wave functions from all bands will be admixed. Since the matrix elements of spin-orbit coupling are small compared to the separation between bands, we can write the wave functions by perturbation theory in the form (15); and if χ_0, χ_1, $\cdots\chi_n$, were the original localized functions, the new localized function will be

$$\chi_0|+\rangle+\tfrac{1}{2}\sum_n \frac{1}{E_0(\mathbf{k})-E_n(\mathbf{k})}[\langle\chi_n|\zeta l_z|\chi_0\rangle\chi_n|+\rangle + \langle\chi_n|\zeta(l_x+il_y)|\chi_0\rangle\chi_n|-\rangle]. \quad (23)$$

The matrix element of l_z is, to first order (using 11),

$$\sum_n \frac{\langle\chi_0|\zeta l_z|\chi_n\rangle\langle\chi_n|l_z|\chi_0\rangle}{E_0(\mathbf{k})-E_n(\mathbf{k})}. \quad (24)$$

The average value of the matrix element of l for any direction will be of the same order of magnitude and so we expect that in this case the change in g from the free-electron value to be of the order

$$\Delta g\sim\lambda/\Delta E, \quad (25)$$

where λ is the spin-orbit coupling constant and ΔE the separation to the nearest band with the same transformation properties. This effect is very small, and because of the uncertainty in the value of λ it is hardly worth calculating the exact equality to replace the approximation (25). The more accurate calculation of Yafet for sodium gives a resulting Δg of the order expected from (25), with a value of λ somewhat smaller than in the free atom.

B. Electrons with Kinetic Energies Large Compared to the Spin-Orbit Coupling Energy Occupying States with Energies Near a Point Where Bands are Degenerate

An example of this would be that of the electron system with Fermi energy F_2 in Fig. 4. The electrons at the Fermi surface are in states which are determined

[15] This will be true if the component of angular momentum in an arbitrary direction z is zero. This is the quantity $\int\Psi^* L_z\Psi d\tau$, where $L_z=-i(\mathbf{r}\times\nabla)_z$. Writing Ψ as a Bloch function $u_k e^{i\mathbf{k}\cdot\mathbf{r}}$ we require $\int u_k^* L_z u_k d\tau$. If (as is the case here) the crystal has inversion symmetry $u_k^*=au_{-k}$, where $aa^*=1$, then

$$\int u_k^* L_z u_k=\int u_{-k} L_z u_{-k}^*=\int u_k L_z u_k^*=-\left(\int u_k^* L_z u_k\right)^*=0,$$

since it must be real.

almost entirely by the lattice potential. The states around each lattice point are linear combinations of ϕ_x, ϕ_y, and ϕ_z which are completely determined as is their energy by a secular determinant like (12). Without spin-orbit coupling the wave function at $\mathbf{k}$ in one band r, say, is in the form (15) where at each lattice point the wave function is

$$|r_0\rangle = a_r\phi_x + b_r\phi_y + c_r\phi_z. \tag{26}$$

Regarding spin-orbit as a perturbation to first order, we get, by using (10),

$$|r,+\rangle = |r_0,+\rangle + \tfrac{1}{2}\sum_{s\neq r}\frac{\lambda}{E_r(\mathbf{k})-E_s(\mathbf{k})}\{\langle s_0|l_z|r_0\rangle|s_0,+\rangle + \langle s_0|l_x+il_y|r_0\rangle|s_0,-\rangle\}. \tag{27}$$

From (11),

$$\Delta g_s = 2\sum_{s\neq r}\frac{\lambda}{E_r(\mathbf{k})-E_s(\mathbf{k})}|\langle r_0|l_z|s_0\rangle|^2. \tag{28}$$

Using the functions (26) and noting that

$$l_x\phi_x = i\phi_y, \quad l_x\phi_y = -i\phi_x, \quad l_x\phi_z = 0,$$

we find

$$\langle r_0|l_z|s_0\rangle = a_r^*b_s - a_sb_r^*. \tag{29}$$

Now we need the average value, which we will define for simplicity as

$$\Delta g = \tfrac{1}{3}(\Delta g_x + \Delta g_y + \Delta g_z). \tag{30}$$

By symmetry, from (29),

$$\Delta g = \tfrac{2}{3}\sum_{s\neq r}\frac{\lambda}{E_r(\mathbf{k})-E_s(\mathbf{k})}[\sum_{abc}(a_r^*b_s - a_sb_r^*)(a_rb_s^* - a_s^*b_r)]$$

$$= \tfrac{2}{3}\sum_{s\neq r}\frac{\lambda}{E_r(\mathbf{k})-E_s(\mathbf{k})}[(\sum_a a_ra_r^*)(\sum_a a_sa_s^*) - (\sum_a a_r^*a_s)(\sum_a a_ra_s^*)],$$

and since the wave functions (26) are normalized and orthogonal this is just

$$\Delta g = \tfrac{2}{3}\sum_{s\neq r}\frac{\lambda}{E_r(\mathbf{k})-E_s(\mathbf{k})}. \tag{31}$$

Besides averaging over the direction of $\mathbf{H}$ we require the average over all directions and all those values of $\mathbf{k}$ in all three bands which have energies equal to the Fermi energy; $E(\mathbf{k}) = W_F$. Now in a given direction in space we define an effective mass for each surface by means of (13). The number of electron states within a solid angle $d\Omega$ of $\mathbf{k}$ and with wave vectors of magnitude between $\mathbf{k}$ and $\mathbf{k}+\Delta\mathbf{k}$ are

$$Vk^2\Delta k d\Omega/(2\pi)^3.$$

The energy spread of such states is, from (13), $\hbar^2k\Delta k/2m^*$ so that the number of energy states per unit energy range is $Vm^*kd\Omega/\hbar^2(2\pi)^3$ and the density at the Fermi surface is then

$$\rho = (2m^*)^{\frac{1}{2}}VW_F^{\frac{1}{2}}d\Omega/2\hbar^3(2\pi)^3. \tag{32}$$

The average Δg value is just

$$\int_0^{4\pi}\sum_r \rho_r\Delta g_r d\Omega \Big/ \int_0^{4\pi}\sum_r \rho_r d\Omega. \tag{33}$$

Assuming that the spin-orbit coupling has little effect on the energies $E_r(\mathbf{k})$, we have

$$E_r(\mathbf{k}) - E_s(\mathbf{k}) = \frac{\hbar^2k^2(m_s^* - m_r^*)}{2m_r^*m_s^*} = \frac{W_F(m_s^* - m_r^*)}{m_s^*}, \tag{34}$$

when $\mathbf{k}$ is such that the electron in the rth band is at the Fermi surface. After some manipulation from (34), (32), and (30), Eq. (33) becomes:[16]

$$\Delta g = \frac{2\lambda}{3W_F}\int\sum_{r\neq s}\frac{m_r^*m_s^*}{\sqrt{m_r^*}+\sqrt{m_s^*}}d\Omega \Big/ \int\sum_r (m_r^*)^{\frac{1}{2}}d\Omega. \tag{35}$$

The Fermi temperature depends on the number n of conduction electrons,

$$n = \sum_r\int_0^{k_0}\int_0^{4\pi}\frac{V}{(2\pi)^3}k^2dkd\Omega = \frac{2\sqrt{2}VW_F^{\frac{3}{2}}}{3(2\pi)^3\hbar^3}\int_0^{4\pi}\sum_r(m_r^*)^{\frac{3}{2}}d\Omega, \tag{36}$$

so

$$\Delta g = \frac{\lambda V^{\frac{1}{3}}}{\pi^3(3n)^{\frac{1}{3}}\hbar^2}\int_0^{4\pi}\sum_{r\neq s}\frac{m_r^*m_s^*}{\sqrt{m_r^*}+\sqrt{m_s^*}}d\Omega \Big/ \left[\sum_r\int_0^{4\pi}(m_r^*)^{\frac{1}{2}}d\Omega\right]^{\frac{1}{3}}. \tag{37}$$

In our approximation the m^* are determined completely by the secular determinant (12), but the averages in (35) and (37) are found to depend in a very complicated way on the constants A, B, and D.

Another useful result which can be calculated on this approximation is the expression for Δg at high temperatures when the electrons obey Boltzmann statistics. Then

$$\Delta g = \int\int\sum_r n_r(\mathbf{k})\Delta g_r(k)k^2dkd\Omega \Big/ \int\int\sum_r n_r(\mathbf{k})k^2dkd\Omega, \tag{38}$$

[16] I am indebted to Professor C. Kittel for first pointing out that one might expect $\Delta g \sim \lambda/W_F$ in this case.

where $n_r(\mathbf{k})$, the number of electrons in the rth band with $\mathbf{k}$, is

$$A \exp(-\hbar^2 k^2/2m_r^* \mathbf{k}T). \tag{39}$$

After manipulation, and writing the expression (35) as $(\Delta g)_F$,

$$\Delta g = (W_F/\mathbf{k}T)(\Delta g)_F. \tag{40}$$

Thus Δg will decrease with increasing temperature once we get above the Fermi temperature.

C. Electrons in a Degenerate Band with Energies Small Compared to the Spin-Orbit Coupling

An example of this would be the electron system in Fig. 4 with Fermi level F_1. In this case the electrons at the Fermi surface would have wave functions given in first order by (18). Thus they would have the Landé g factor for these J states which is $\frac{2}{3}$ for the single $J=\frac{1}{2}$ band, and 4/3 for the double $J=\frac{3}{2}$ band. In any practical case the states will be considerably perturbed and g can be expected to have a wide range of possible values. Explicit calculations unfortunately require the solution of the determinant (20) and hence must be numerical. Some idea of the possibilities can be obtained by considering a simple model where the energy depends only on $|\mathbf{k}|$ and the interaction is independent of direction. For a general value of $\mathbf{k}$ the three p bands will have wave functions around each nucleus like

$$\begin{aligned} &\frac{1}{\sqrt{2}}(\phi_x + i\phi_y)|+\rangle, \\ &\sin\theta\frac{1}{\sqrt{2}}(\phi_x + i\phi_y)|-\rangle + \cos\theta\phi_z|+\rangle, \\ &\cos\theta\frac{1}{\sqrt{2}}(\phi_x + i\phi_y)|-\rangle - \sin\theta\phi_z|+\rangle, \end{aligned} \tag{41}$$

and their Kramers' conjugates. The first two, which have $g_\parallel = 4$, $g_\perp = 0$, and $g_\parallel = 2\cos^2\theta$, $g_\perp = 2\cos^2\theta + 2\sqrt{2}\sin\theta\cos\theta$, respectively, are degenerate when $k=0$. The other has $g_\parallel = 2\sin^2\theta$, $g_\perp = 2\sin^2\theta - 2\sqrt{2}\sin\theta\cos\theta$ and arises from the $J=\frac{1}{2}$ band. In the case of large λ, when only one or two of these bands are occupied, it is clear that g may have a wide range of values, and the actual result will depend in a complicated way on the electron-lattice interaction.

Δg will have the same order of magnitude as that calculated in case B for any degeneracy which is lifted by the spin-orbit coupling. For any such degeneracy and case C the g will in general differ widely from 2 but its actual value will depend on the actual wave functions. If there is a degeneracy which is not affected by the introduction of spin-orbit coupling, case A will apply.

VI. REVIEW OF EXPERIMENTAL DATA

In an impurity semiconductor the extra electrons (or holes) have two kinds of energy states. There are those which represent the electron trapped around the impurity centers, and others in which the electrons move freely (and occupy states in the bands). At high enough impurity concentrations there are no trapped states and the electrons are in the conduction band even at very low temperatures. The experiments[1] seem to indicate that this is the case in some of the specimens studied. Assuming then that the impurities have little effect on the actual band structure we can compare the experimental values with the g's calculated for the band states in the last section.

The actual form of the bands in silicon and germanium is of considerable interest at the present time. Herring[17] and others have deduced something about their form from magnetoresistance, and measurements of cyclotron resonance[18] also throw some light on the problem. Since in n silicon the g-values are very close to 2, we can conclude that case A holds, and that the lowest point of the conduction band is not near a band degeneracy. Herman's calculation for diamond gave the minima in the conduction bands at six points along the (1,0,0), (0,1,0), and (0,0,1) directions. This is also likely to be true in Si and would certainly fit the observed g values. Δg seems to be about 3×10^{-3}, which, if λ is about 100 cm^{-1} as discussed below, gives $\Delta E \sim 4$ ev, which is quite reasonable for the separation to the nearest Δ_7 band.

It is of some interest to consider briefly what values one might expect for λ in general. Now λ for $3p$ electrons on a Si atom[19] with configuration $3s^2 3p^3\ ^3P$ is 150 cm^{-1} and on Si$^+$ with $3s^2 p\ ^2P$ is 190 cm^{-1}, i.e., somewhat larger. In silicon metal the ground state with completely filled valence bands is roughly equivalent to a $3s3p^3$ configuration for each atom so that the extra electrons in n Si make a $3p^4$ configuration and the holes in p Si a $3p^2$. There are no measurements of λ on atomic Si with these configurations but atomic S has $\lambda = 175$ cm^{-1} and 300 cm^{-1} in similar configurations. Thus if the electron wave functions in the metal are just linear combinations of the atomic wave functions around each lattice point we might expect λ to be very roughly about 100 cm^{-1} for electrons in n-type Si and 200 cm^{-1} for holes in p-type. The overlap of the atomic wave functions with those of neighboring atoms has a profound effect, however. The largest contribution to λ is made when the electron is very near the nucleus, so that the overlap region is not important from this point of view, but this overlap gives a contribution to the normalizing factor so that in effect the electron spends less of its time near a nucleus than it would do in an atom. Even in the general case when the tight-binding approximation is bad, one might expect the electron to behave rather like an atomic electron near the nucleus

[17] C. Herring (private communication).
[18] Dresselhaus, Kip, and Kittel, Phys. Rev. **92**, 827 (1953).
[19] This and other numerical values quoted here are calculated from spectral measurements given by C. E. Moore, National Bureau of Standards Circular No. 467, 1949 (unpublished).

(where the field comes overwhelmingly from the nuclear charge)[7] and hence λ to be still that of a free atom reduced by the fact that it spends less time there.

In the case of germanium λ will be very much larger, and only for high concentrations can we expect W_F to be larger than the splitting. In atomic Ge, with configuration $4s^24p^2\,{}^3P$, λ is about 1150 cm^{-1}. Se has $\lambda=1090$ cm^{-1} for $4p^4$ and 5400 for $4p^2$ so that, following our argument for Si, we might expect λ to be, say, 500 cm^{-1} for electrons and 1500 cm^{-1} for holes in Ge. Even though the actual λ for the solid may be several times smaller as we have seen, the splitting will still be considerable. A similar situation will arise in grey tin.

VII. SPIN LATTICE RELAXATION AND RESONANCE LINE WIDTHS

The widths of the resonance lines observed from conduction electrons vary a great deal from substance to substance and with frequency and temperature in a given case. This width arises from a variety of causes. Because of the motion of the electrons there is a "diffusive broadening"[20] which, however, becomes very small for particles much smaller than a skin depth. A width remains which increases rapidly with increasing temperature[1,4] and is therefore probably due to a spin lattice relaxation time. The width which occurs in paramagnetic resonance of salts and arises because electrons in different states have different g values and see differing magnetic fields from the other electrons and nuclei is negligible in this case because of motional narrowing. It has been shown for similar problems[21] that, if the expected energy spread is $\hbar\omega$ but the electrons change states in a time τ_e because of interactions with the lattice, the actual spread is $\hbar\omega^2\tau_e$. Since τ_e is very short (10^{-12} sec or less) this line width is never appreciable except possibly in case C.

Overhauser[5] has studied spin-lattice relaxation on a free-electron picture, but he finds that the times obtained from various mechanisms are somewhat longer than those observed in alkali metals.[4] If his formulas are naively extended to the semiconductor results, the agreement is much worse. We shall discuss below an effect involving the spin-orbit coupling which gives fair agreement with experiment, and some of the discrepancies are possibly due to the crudity of the approximations involved.

The relaxation time τ can be conveniently defined[5,22] in terms of the number N_+ of electrons with spins parallel to the applied magnetic field and the number N_- antiparallel. If the population difference $D=N_+-N_-$ is denoted by D_0 at equilibrium, we have

$$D_0-D/\tau_S=dD/dt=W_{+\to-}-W_{-\to+}, \tag{42}$$

where $W_{+\to-}$ is the rate of transitions of electrons from the (+) to the (−) states. These W are proportional to the square of the matrix elements of an interaction between the electron and the lattice which causes a spin flip.

It was shown in Sec. II that when spin-orbit interaction is considered, the two classes of electrons which make up each band no longer differ just by the spin orientation but are described by wave functions of mixed character like Eqs. (4) and (6). Except when we are near a degeneracy point, the wave function can usually be written in a form where the function is overwhelmingly one of spin type with just a small admixture of the other orientation. In other words $a\gg b$. For convenience we shall continue to refer to these states simply as the (+) and (−) types. Now let us suppose that there is some interaction which scatters an electron from $\mathbf{k}$ to $\mathbf{k}'$ without changing the spin. The matrix element in the process will contain in first order the integral

$$\int a_{k'}{}^*\mathcal{H}_{\rm int}a_k e^{i(\mathbf{k}-\mathbf{k}')\cdot\mathbf{r}}d\tau. \tag{43}$$

Then the same interaction will cause transitions from one kind of spin state to the other but the matrix element (43) must be replaced by

$$\int (a_{-k'}\mathcal{H}_{\rm int}b_k-b_{-k'}\mathcal{H}_{\rm int}a_k)e^{i(\mathbf{k}-\mathbf{k}')\cdot\mathbf{r}}d\tau. \tag{44}$$

In a number of cases we shall show in detail below that the matrix elements (43) and (44) are in the ratio b_k/a_k ($=c$, say). Then the probability of an electron making a transition from $|\mathbf{k},+\rangle$ to $|\mathbf{k}',-\rangle$ is c^2 times the probability of it making the transition $|\mathbf{k},+\rangle$ to $|\mathbf{k}',+\rangle$. Now, except for an angular factor which discriminates against forward scattering, the matrix element $\langle\mathbf{k},+|\mathcal{H}_{\rm int}|\mathbf{k}',+\rangle$ enters into the expression for the relaxation time τ_R characteristic of electrical resistivity,[23] in exactly the same way in which $\langle k,+|\mathcal{H}_{\rm int}|k',-\rangle$ enters into τ_S as obtained by (42). Thus we expect $c^2\tau_S=\tau_R$. Further in Secs. V (A) and (B) we showed that $c\sim\lambda/\Delta E$ which is also of the same order as Δg. Thus we have

$$\tau_S\sim\tau_R(g-2)^2. \tag{45}$$

In order to completely satisfy ourselves of the applicability of this relation, we shall consider in detail below the expressions pertaining to lattice scattering in alkali metals, and to lattice and impurity scattering in semiconductors. The formula is not expected to apply to the case when the spin-orbit coupling is large and g is not nearly 2 as in Sec. V (C), but this must be considered separately.

[20] E. Abrahams and C. Kittel, Phys. Rev. **92**, 544 (1953). F. Dyson (unpublished). See also reference 4.
[21] P. W. Anderson and P. R. Weiss, Revs. Modern Phys. **25**, 269 (1953).
[22] Bloembergen, Purcell, and Pound, Phys. Rev. **73**, 679 (1948).
[23] See for example A. H. Wilson, *Theory of Metals* (Cambridge University Press, Cambridge, 1936) or F. Bloch's original paper, Z. Physik **52**, 555 (1928).

VIII. RELAXATION BY LATTICE SCATTERING IN ALKALI METALS

In an alkali metal the wave functions of the partially occupied band can be written to a good approximation by Bardeen's method[24] in the form

$$\frac{1}{\sqrt{N}}[\sum_{\mathbf{d}} u_0(\mathbf{r}-\mathbf{d})+i(\mathbf{k}\cdot\mathbf{r}-\mathbf{d})u_1(\mathbf{r}-\mathbf{d})]e^{i\mathbf{k}\cdot\mathbf{r}}, \quad (46)$$

where u_0 and u_1 are spherically symmetric. Yafet incorporated spin-orbit coupling into Bardeen's method and obtained wave functions of the same form except around each lattice point the expression in square brackets had the form

$$[u_0(r)+i(\mathbf{k}\cdot\mathbf{r})u_1(r)+c(\mathbf{k}\times\mathbf{r})_Z u_2(r)]|+\rangle + c'(\mathbf{k}\times\mathbf{r})_{X+iY}u_3(r)|-\rangle. \quad (47)$$

The subscripts X, Y, Z refer to the components of these vectors along axes chosen so that the Z axis is the axis of the applied magnetic field $\mathbf{H}$, which is also chosen as the axis of quantization for the spin. u_2 and u_3 are spherically symmetric wave functions, and c and c' are constants, which Yafet obtains by numerical computation. If first-order perturbation theory had been used, the same form would have resulted with

$$c=c'\sim\lambda/\Delta E=(g-2), \quad (48)$$

and

$$u_1(r)=u_2(r)=u_3(r).$$

We write the interaction Hamiltonian arising from the distortion of the lattice by the phonons as

$$\mathcal{H}_{\text{int}}=\frac{1}{\sqrt{M}}\sum_{q} a(\mathbf{q})\mathbf{t}_q\cdot\mathbf{A}e^{i\mathbf{q}\cdot\mathbf{r}}, \quad (49)$$

where M is the mass of the crystal, $\mathbf{q}$ the wave vector, $a(\mathbf{q})$ the amplitude and $\mathbf{t}_q$ the polarization vector of a phonon and the summation is carried over all allowed phonons. In calculations of resistivity an explicit expression has to be taken for $\mathbf{A}$, but we need only assume its transformation properties since we wish only to compare our τ_S with τ_R (for which we can take the experimental value). We assume that $\mathbf{A}$ transforms as a vector, in common with some other resistivity calculations.[23,25] This simplifies the algebra considerably but gives the same order of magnitude as a more general interaction. We first outline the simple perturbation method of calculating τ_R using the Hamiltonian (49). Bloch[23] finds that, assuming the effective mass concept is adequate [i.e., $E(\mathbf{k})=\hbar^2\mathbf{k}^2/2m^*$],

$$\frac{1}{\tau_R}=\left(\frac{m^*KV}{\hbar^3\pi}\right)\int \Pi(k,k')(1-\cos\theta)d(\cos\theta), \quad (50)$$

where $\Pi(\mathbf{k},\mathbf{k}')$ is the probability that an electron in state $\mathbf{k}$ is scattered into state $\mathbf{k}'$ and θ is the angle between $\mathbf{k}$ and $\mathbf{k}'$. By using perturbation theory, Π is proportional to the square of the matrix element,

$$\langle P,\mathbf{k},+|\mathcal{H}_{\text{int}}|Q,\mathbf{k}',+\rangle = \langle P|\sum_q \frac{1}{N\sqrt{M}}\sum_d \exp[i(\mathbf{k}'-\mathbf{k}+\mathbf{q})\cdot\mathbf{d}] \times\int_{\text{cell}} u_0(r)(\mathbf{t}_q\cdot\mathbf{A})[(\mathbf{k}'-\mathbf{k})\cdot\mathbf{r}]u_1(r)a(\mathbf{q}) \times\exp[i(\mathbf{k}'-\mathbf{k}+\mathbf{q})\cdot\mathbf{r}]d\tau|Q\rangle \quad (51)$$

[using state (47)]. Here P and Q are states of the lattice, and Π is an average over all such possible states. Now

$$\sum_d \exp[i(\mathbf{k}'-\mathbf{k}+\mathbf{d})\cdot\mathbf{r}]=N\delta(\mathbf{k}'-\mathbf{k}+\mathbf{d}-\mathbf{K}_n),$$

where $\mathbf{K}_n$ is a vector in the reciprocal lattice. If we make the further simplifying assumption that $K_n=0$ (i.e., if we neglect the "Umklappprozesse"), Eq. (51) can be written

$$\frac{B}{\sqrt{M}}\langle P|\sum_q(\mathbf{t}_q\cdot(\mathbf{k}'-\mathbf{k})a(\mathbf{q})\delta(\mathbf{k}'-\mathbf{k}+\mathbf{q})|Q\rangle,$$

where

$$B=\int_{\text{cell}} u_0(r)(\mathbf{A}\cdot\mathbf{r})u_1(r)d\tau. \quad (52)$$

Then, following the usual calculation, one gets at high temperatures, where $T\gg\theta_D$ (the Debye temperature),

$$\frac{1}{\tau_R}=\left(\frac{2mk_0V\mathbf{k}T}{\pi\hbar^3MS^2}\right)B^2\int(1-\cos\theta)\sin\theta d\theta, \quad (53)$$

where k_0 is the value of k at the top of the Fermi distribution and S is the velocity of sound. If we assume the simple Debye theory, the maximum possible value of q

$$q_{\max}=2^{\frac{1}{2}}k_0. \quad (54)$$

Thus, with $\mathbf{K}_n=0$, the limits of the integral in (53) are 0 and $\theta=2\sin^{-1}(2^{-\frac{1}{2}})$ and the value of the integral becomes $2^{-8/3}$. With these approximations then

$$1/\tau_R=m^*k_0V\mathbf{k}TB^2/2^{\frac{1}{2}}\hbar^3MS^2\pi. \quad (55)$$

τ_S, the spin-relaxation time, can be readily calculated using Overhauser's method.[5] It is simply necessary to substitute the matrix element of (44) into his formula for $W_{+\to-}$ and carry out the appropriate averages. In

[24] J. Bardeen, J. Chem. Phys. **6**, 367 (1938).
[25] The best calculation for alkali metals is that of J. Bardeen, Phys. Rev. **52**, 688 (1937).

this case the element required is

$$\langle P, \mathbf{k}, +|\mathcal{H}_{\rm int}|Q, \mathbf{k}', -\rangle$$
$$=\langle P|\sum_{\mathbf{q}} \frac{1}{N\sqrt{M}} \sum_{\mathbf{d}} \exp[i(\mathbf{k}'-\mathbf{k}+\mathbf{q})\cdot\mathbf{d}]$$
$$\times \int_{\rm cell} u_0(\mathbf{r})(\mathbf{t}_q\cdot\mathbf{\Lambda})[(\mathbf{k}+\mathbf{k}')\times\mathbf{r})]_{X+iY}$$
$$\times u_0(\mathbf{r})a(\mathbf{q}) \exp[i(\mathbf{k}'-\mathbf{k}+\mathbf{q})\cdot\mathbf{r}]d\tau|Q\rangle$$
$$=\langle P|\sum_{q}[(\mathbf{t}_q\times(\mathbf{k}'+\mathbf{k})]_{X+iY}$$
$$\times a(\mathbf{q})\delta(\mathbf{k}'-\mathbf{k}+\mathbf{q})|Q\rangle B(g-2), \quad (56)$$

if we use (48), and put $\mathbf{K}_n=0$ as before. We can follow the argument in Sec. II of Overhauser's paper. The square of the matrix element (56) when averaged over all polarizations of $\mathbf{q}$ is

$$B^2(g-2)^2(n_q+1)\hbar|\mathbf{k}+\mathbf{k}'|^2/MSq$$

(where q is written for his k). With this we obtain, instead of his expression, on p. 692

$$\frac{dD}{dt}=\frac{VB^2(g-2)^2}{\pi MSkT}\int[ff_q'(n_q+1)+ff_{-q}'n_q]$$
$$\times|\mathbf{k}+\mathbf{k}'|^2kdkdq. \quad (D-D_0). \quad (57)$$

At high temperature $T\gg\Theta_D$, this gives

$$\frac{1}{\tau_S}=\frac{mk_0V\mathbf{k}TB^2(g-2)^2}{2\pi\hbar^3MS^2}\left(2\log\frac{q_{\max}}{q_{\min}}-2^{-1}\right), \quad (58)$$

where $q_{\max}$ is given by (54) and $q_{\min}$ depends on the particle size (see Overhauser). In fact $q_{\max}/q_{\min}$ is approximately equal to the particle diameter divided by the atomic diameter. For the small particles used in resonance the log may be expected to be of the order of 10.

With the above approximations we have

$$\tau_S=\frac{\tau_R}{2^{5/3}(g-2)^2\log(q_{\max}/q_{\min})}=\frac{\tau_R}{30(g-2)^2}. \quad (59)$$

The numerical factor arises partly from the different values for the averages of $(\mathbf{t}_q\cdot\mathbf{q})^2$ and $|[\mathbf{t}_q\times(\mathbf{k}+\mathbf{k}')]_{X+iY}|^2$ over the directions of polarization of the phonons. Another numerical factor arises from the $(1-\cos\theta)$ term which is present in resistivity calculations to discriminate against forward scattering but does not appear in the relaxation calculation. Because our treatment used a B independent of θ, neglected the "Umklappprozesse," and assumed the simple Debye theory for the lattice waves, the above calculation cannot be very accurate. Nevertheless we can expect $\tau_S=\alpha\tau_R/(g-2)^2$, where α is a numerical factor somewhat smaller than unity, at high temperatures. At low temperatures however the $(1-\cos\theta)$ term has a much more profound effect. Since only long wavelength phonons are present only small angle collisions can occur (the maximum value of θ is $\mathbf{k}T/\hbar Sk_0$ if $T\ll\Theta_D$). The angular integral therefore varies as T^2 and since the number of phonons varies as T^3, $1/\tau_R\propto T^5$. On the other hand, in the absence of the angular factor $1/\tau_R\propto T^3$. Bloch[26] showed that the ratio of τ_R at T_1 and T_2 if $T_1\ll\Theta_D\ll T_2$ is

$$\tau_R(2)/\tau_R(1)=497.6(T_1/\Theta_D)^4(T_1/T_2).$$

If we make the simple assumption that $1/\tau_S$ is proportional to the number of phonons we obtain from the Debye function a similar expression

$$\tau_S(2)/\tau_S(1)=13.3(T_1/\Theta_D)^2(T_1/T_2).$$

Therefore, if $T\ll\Theta_D$,

$$\tau_S\sim(\tau_R/(g-2)^2)(T/\Theta_D)^2. \quad (60)$$

A more correct calculation would no doubt change the numerical factor, but if the conductivity obeys the usual T^{-5} law at low temperature as is the case in the alkali metals, we can expect τ_S to vary as T^{-3} and to be given roughly by (60) in the same region.

It may be pointed out that because of the factor $(\mathbf{t}_q\cdot\mathbf{q})$ occurring in (52), only longitudinal phonons contribute to the resistivity (as is well known), while the $[\mathbf{t}_q\times(\mathbf{k}+\mathbf{k}')]$ in (56) means both transverse and longitudinal phonons contribute to the spin relaxation.

In the alkali metals the relaxation time for resistivity is at room temperature approximately 1×10^{-14}, 3×10^{-14}, and 2×10^{-14} sec in Li, Na, and K, respectively. Unfortunately, the g values are so close to the free-electron value that there is as yet no reliable experimental value of Δg except that in Li and Na it is $\sim10^{-3}$ or less. In view of the usual increase of spin-orbit coupling with increasing atomic number we might expect Δg to increase as we pass along the series. Yafet[3] calculated Δg in Na to be 3×10^{-4}, which by our formula (45) leads to a spin-lattice time of about 3×10^{-8} sec, whereas the observed[4] line width at room temperature corresponds to about 1×10^{-8} sec. The agreement is surprisingly good—in fact much better than our crude assumptions justify. The experimental value of Δg may of course make some difference. Overhauser[5] obtained relaxation times of about this order, but somewhat longer, by his process, and it is not possible to rule this out because of the above agreement. It is, however, possible that more detailed experiments could decide between the two processes since Overhauser's shortest time varies slightly with H.

We expect that our mechanism will hold for most metals and it is of interest to consider briefly the order of relaxation time we may expect. In the noble metals

[26] F. Bloch, Z. Physik **59**, 208 (1930).

the resistivities are low and τ_R is again 10^{-14} sec, but it is believed from measurements on the transition metals that the band overlaps with bands made up largely from the atomic d electrons. Thus we would expect this band to have some d character and because of the nearness of the other band we expect $\lambda/\Delta E$ and hence Δg to be somewhat larger than in the alkalis. If Δg were $\sim 10^{-2}$, this would lead to $\tau_S \sim 10^{-10}$ sec and a very broad line at room temperature, which may prevent the observation of the resonance. However, it should be easier to see at helium temperatures where τ_R is 100 times longer. In other metals it is known that the bands overlap and here again this may lead to small ΔE and larger Δg with similar effects. In these metals the resistance is often larger than in the alkalis and τ_R may be less than 10^{-14} sec at room temperature.

IX. RELAXATION BY LATTICE SCATTERING IN SEMICONDUCTORS

In this case it is not as easy as it is in the alkali metals to write down wave functions which are a good approximation for calculating resistivity, and hence the argument for proving that (45) is a good approximation cannot be as precise. However, Bardeen and Shockley[27] have been able to relate the scattering of electrons by lattice waves to the elastic constants and so account for the resistivity observed at high temperatures in n and p-type silicon and germanium.

The interaction is very similar to the one discussed in the last section, although the details of the calculation are modified by the fact that the electrons involved have small $\mathbf{k}$ vectors and can only interact with phonons with small $\mathbf{q}$ (i.e., long wavelength); and the statistics are different. These modifications can be readily taken over into a calculation of τ_S which will go through in exactly the same way as in the last section with both kinds of phonons taking part. For a single band where the wave functions have the form (4) and the component of the wave function with reversed spin is of order $\lambda/\Delta E \sim (g-2)$ the matrix elements for a spin flip process are $(g-2)$ times those for resistivity as before, and $\tau_S \sim \tau_R/(g-2)^2$. If case (B) of Sec. V holds and the electrons occupy states near a band degeneracy the calculation is complicated by the fact that electrons can be scattered from states in one band to states in another. However a rough calculation shows that for every scattering there is an equivalent process which causes a spin flip and again the matrix elements are in the ratio $(g-2):1$ except for some angular factors which will on the average be of order unity. So the expression for τ_S still holds. In the other case (C) the situation is more complicated still. For example at sufficiently high temperatures there will be phonons present which could give electrons sufficient energy to jump from one band to another, but this will not be true at low temperatures. We shall not consider this case in detail here, but rough calculations show that for electrons with kinetic energies comparable with the splitting of the degeneracy τ_S is of the same order as τ_R.

For n-type silicon[28] the resistivity at high temperatures appears to be independent of impurity content and

$$\tau_R \sim 10^{-9} T^{-\frac{1}{2}} \text{ sec},$$

where T is the temperature in °K. The experiments indicate that $\Delta g \sim 3 \times 10^{-3}$ which gives

$$\tau_S \sim 10^{-9} \text{ sec at } 300°\text{K},$$

and a line width of 50 gauss compared to an observed 30 gauss which can be considered good agreement in view of the uncertainties in the formulas and in Δg. In germanium the τ_R are some 5 times longer,[29] and the over-all absence of resonance can be accounted for only if Δg is large in both types. Certainly if we have the nearly degenerate bands this can be expected. Even if the bands were like those in silicon and case A could be applied, we would expect $\Delta g = \lambda/\Delta E$ to be greater since λ is greater by what could well be a factor of 20. Allowing for the longer τ_R would increase the line width by a factor of 10^2 and account for the failure to observe resonance at high temperatures.

X. RELAXATION BY IMPURITY SCATTERING IN SEMICONDUCTORS

In germanium and silicon semiconductors[29,28] of relatively low impurity content it is found that τ_R, which we noted in the last section varies as $T^{-\frac{1}{2}}$ at high temperatures, passes through a maximum as the temperature is decreased and then decreases with decreasing temperature. This is caused by the interaction between the electrons and the impurity centers, an interaction which increases with decrease in velocity (and hence in temperature as long as we remain above the Fermi distribution). We expect that this mechanism will also give rise to a spin-lattice relaxation time, since the argument of Sec. VII would still seem to apply. However, if there is a similar proportionality factor we would expect the curve of line width against temperature to have exactly the form as the inverse of the mobility curves (see Fig. 9 of reference 28), but the resonance experiments do not show this.[1]

Unfortunately it has not so far been possible to give an account of resistivity from this mechanism in terms of reasonably correct wave functions. Conwell and Weisskopf[30] calculated the effect by use of a free electron model and obtained curves which give quite good agreement with the form of the experimental results. We have calculated the relaxation time due to the spin-orbit effects caused by the impurity itself on a similar

[27] J. Bardeen and W. Shockley, Phys. Rev. **80**, 72 (1950).

[28] G. L. Pearson and J. Bardeen, Phys. Rev. **75**, 865 (1949).

[29] J. R. Hayes and W. Shockley, Phys. Rev. **81**, 835 (1951). The experimental data have recently been reviewed by E. M. Conwell, Proc. Inst. Radio Engrs. **40**, 1327 (1952).

[30] E. M. Conwell and V. F. Weisskopf, Phys. Rev. **71**, 388 (1950).

model but find that the times are far too long to give an observable effect. (See Appendix.)

We consider that the impurities cause an interaction which in a medium of dielectric constant κ is

$$\sum_{\mathbf{D}} \frac{e^2 \exp(-r/\rho)}{\kappa|\mathbf{r}-\mathbf{D}|},$$

where $\mathbf{D}$ are a random selection of η of the lattice points and ρ is a screening radius which will be taken as the Debye length.

Fourier-analyzing this potential[31]

$$V=\int V_k \exp(i\mathbf{k}\cdot\mathbf{r})d\mathbf{k}$$

we find

$$V_k=(\sum_{\mathbf{D}} \exp(i\mathbf{k}\cdot\mathbf{D}))\frac{e^2}{\kappa}\frac{\rho^2}{k^2\rho^2+1}. \quad (61)$$

The matrix element

$$\langle k'+|\mathcal{H}|k+\rangle=\frac{e^2\rho^2}{\kappa(q^2\rho^2+1)}(\sum_{\mathbf{D}} \exp(i\mathbf{k}\cdot\mathbf{d})) \times\int (a_{k'}{}^*a_k+b_{k'}{}^*b_k)d\tau, \quad (62)$$

where $\mathbf{k}-\mathbf{k}'+\mathbf{q}=0$. The matrix element required for τ_S is

$$\langle k'-|\mathcal{H}|k+\rangle=\frac{e^2\rho^2}{\kappa(q^2\rho^2+1)}(\sum_{D} \exp(i\mathbf{k}\cdot\mathbf{D})) \times\int (a_{-k'}b_k-b_{-k'}a_k)d\tau. \quad (63)$$

Thus, except for some small numerical factors arising from the angular dependences, τ_S/τ_R is proportional to the ratio of the squares of the integrals in (62) and (63).

Now in case (A) we saw by perturbation theory that $b_k\sim(\lambda/\Delta E)v_k$, where $v_k e^{i\mathbf{k}\cdot\mathbf{r}}$ is the wave function of another band in the absence of spin-orbit coupling. In a semiconductor where we are concerned with just a few electrons in a band, $\mathbf{k}$ will not be very different from $\mathbf{k}'$, and all the wave vectors will be clustered around some value $\mathbf{k}_1$ which is not necessarily at the center of the zone (e.g., in the 6-valley model for n-Si). We may therefore use a perturbation procedure.[32] To first order $a_k=a_{k'}=a_{k_1}$ and $v_k=v_{k'}=v_{k_1}$, so the integral in (63) is zero. To second order, each wave function contains terms linear in $(k-k_1)$ and then (63) is seen to be of order of magnitude $\lambda k_{kv}R/\Delta E$ where k_{kv} is the average value of k measured relative to an origin at k_1 and R is a quantity of the dimension of length which represents the magnitude of these second-order terms. If the electron wave functions are tightly bound about the nuclei, R can be very roughly taken as the atomic radius. (It may be noted that the alkali metal wave functions (47) lead to an order of magnitude $ck_{kv}{}^2R^2$ since b is zero to first order.) If we neglect the small numerical factor arising from the angular dependence, we obtain

$$\tau_S\sim\tau_R/(g-2)^2R^2k_{kv}{}^2. \quad (64)$$

Below the Fermi temperature the average value of k is k_0, the value at the top of the Fermi distribution. If each impurity donates one electron, $k_0=(3\pi^2n/V)^{\frac{1}{3}}$, so that $Rk_0=(3\pi n/4N)^{\frac{1}{3}}$. So if c is the concentration of impurities,

$$\tau_S\sim\tau_R/(g-2)^2c^{\frac{1}{3}}. \quad (65)$$

Above the Fermi temperature $k_{kv}{}^2\sim 2mkT/\hbar^2$, so

$$\tau_S\sim\tau_R[\hbar^2/2mkT(g-2)^2a_0{}^2], \quad (66)$$

where a_0 is the atomic radius.

For case (B) of Sec. V, however, (63) is no longer small since the difference between a_k and $a_{k'}$ is a first-order effect in their angular dependence. And so, since $b\sim(g-2)a$ we again have $\tau_S\sim\tau_R/(g-2)^2$. If case (C) holds in the general case where the electrons have kinetic energies comparable with the band splitting b and a will be of the same order of magnitude and our crude argument gives $\tau_S\sim\tau_R$.

In n-type silicon, (65) is satisfactory in that the extra term $c^{-\frac{1}{3}}$ not present in τ_S given by the phonon scattering ensures that τ_S is determined by the phonons to a much lower temperature and there is no maximum as there is in τ_R. The actual magnitude of τ_S given by (65) is a factor 10^2 too small to account for the line width at 4°K′. This may partly be accounted for if the picture of six energy minima is correct. In this case the nearest excited band is relatively close and admixture of it may be somewhat larger than ka_0. Further the scattering process in which the electrons change from states in one minimum to those in another gives a relaxation time related to the τ_R for this process given by (46) rather than (67). This τ_R is, however, much smaller than that observed.

ACKNOWLEDGMENTS

The author is very much indebted to Professor Charles Kittel for much help and encouragement, and to Professor A. F. Kip, Dr. A. M. Portis, and Mr. George Feher, who kindly communicated and discussed their results. Some criticisms by Dr. C. Herring of an earlier draft of the paper have been most useful.

[31] In accordance with a suggestion of C. Herring. See also H. Brooks, Phys. Rev. 83, 879 (1951).

[32] An appropriate perturbation theory has been discussed by W. Shockley, Phys. Rev. 78, 173 (1950) and was used by Herman to obtain our Eq. (12). It is similar to Bardeen's method (see reference 24) which gave the wave function (46).

APPENDIX

If the spin-orbit effect is included, the equation describing the scattering of a free electron by a point charge $+|e|$ representing an impurity center in a medium of dielectric constant k is

$$\left(-\frac{\hbar^2}{2m}\nabla^2-\frac{e^2}{kr}+\frac{\hbar^2e^2}{2km^2c^2}\frac{1}{r^3}\mathbf{l}\cdot\mathbf{S}\right)\Psi=E\Psi. \quad \text{(A1)}$$

The last term gives a probability that the electron will flip its spin in the process of scattering. We consider the electron as free so that its wave function is $(1/\sqrt{V})e^{i\mathbf{k}\cdot\mathbf{r}}$ when in a state $|\mathbf{k}\rangle$. From the Born approximation, the probability that an electron is scattered from $\mathbf{k}$ to $\mathbf{k}'$ and flips its spin is proportional to the square of the matrix element,

$$\langle\mathbf{k},+|\lambda\frac{1}{r^3}(\mathbf{l}\cdot\mathbf{S})|\mathbf{k}',-\rangle$$
$$=\frac{\lambda}{2V}\int e^{-i\mathbf{k}\cdot\mathbf{r}}\frac{1}{r^3}(l_X+il_Y)e^{i\mathbf{k}'\cdot\mathbf{r}}r^2dr\,d(\cos\theta)d\phi, \quad \text{(A2)}$$

where $\lambda=\hbar^2e^2/2km^2c^2$, and X, Y, are two axes chosen perpendicular to the axis of quantization Z of the spin. If there are n such impurity centers in the volume V, the total scattering probability will be n times the probability of scattering by a single center. It is convenient to assume that at any time the electron sees only the nearest center and that on the average it sees each center when it is within a distance R of it; where $4\pi R^3/3=V/n$. The integral in (A2) is therefore taken over a sphere of radius R. If we put $\mathbf{k}-\mathbf{k}'=\mathbf{K}$, elementary integration gives the matrix element equal to

$$\frac{2i\pi\lambda}{VK^2}\left(\frac{\sin KR}{KR}-1\right)[(\mathbf{k}\times\mathbf{k}')_X+i(\mathbf{k}\times\mathbf{k}')_Y].$$

Because of energy conservation $|\mathbf{k}|=|\mathbf{k}'|$, so that if the angle between $\mathbf{k}$ and $\mathbf{k}'$ is α $|\mathbf{K}|=2k\sin(\alpha/2)=2ks$. If we further call the angle between $(\mathbf{k}\times\mathbf{k})$ and Z, β (A2) becomes

$$I=i\pi\frac{\lambda}{V}\left(\frac{\sin 2kRS}{2kRS}-1\right)\cot\frac{\alpha}{2}\sin\beta. \quad \text{(A3)}$$

Following Overhauser[6] we let the electrons with spin parallel to Z form a Fermi distribution with Fermi energy ϵ_+ and those with spin antiparallel have Fermi energy ϵ_-. By writing the Fermi distribution function $f(k,\epsilon)$ and substituting in (42),

$$\frac{dD}{dt}=\mu\frac{2\pi}{\hbar}\int\int\{f(k,\epsilon_+)[1-f(k',\epsilon_-)]$$
$$-f(k',\epsilon_-)[1-f(k,\epsilon_+)]\}\delta[E(k)-E(k')$$
$$+2\beta H]|I|^2\frac{4V^2}{(2\pi)^6}d\mathbf{k}d\mathbf{k}'. \quad \text{(A4)}$$

But

$$f(k,\epsilon_+)-f(k',\epsilon_-)=(\epsilon_+-\epsilon_-)[\partial f(k,\epsilon)/\partial\epsilon]_{\epsilon=\epsilon_0}$$
$$=(\epsilon_+-\epsilon_-)\delta[(\hbar^2k^2/2m)-\epsilon_0],$$

where ϵ_0 is the Fermi energy. After some manipulation we obtain

$$\frac{1}{\tau}=\frac{32\pi\mu mk_0}{3V\hbar^3}\lambda^2\int_0^1\left(\frac{\sin 2k_0SR}{2k_0SR}\right)^2\frac{(1-S^2)}{S}dS. \quad \text{(A5)}$$

The integral in (A5) can be reduced by tedious but elementary manipulation to

$$\frac{1}{2}+\sin 2k_0R-\frac{\cos 2k_0R}{2k_0^2R^2}-\frac{\sin 4k_0R}{4k_0R}$$
$$-\frac{1}{16k_0^2R^2}(1-\cos 4k_0R)+\left(1-\frac{1}{8k_0^2R^2}\right)\log 2\gamma k_0R$$
$$-\left(1+\frac{1}{8k_0^2R^2}\right)[\log 2-Ci(4k_0R)]-2Ci(2k_0R), \quad \text{(A6)}$$

where

$$Ci(x)=\log\gamma x-\int_0^x\frac{1-\cos t}{t}dt,$$

and is given in Jahnke and Emde[33] (γ is Euler's constant). If we apply a simple one band model and if each impurity has donated one electron to the semiconductor,

$$k_0=(3\pi^2\mu/V)^{\frac{1}{3}}=(1/R)(9\pi/4)^{\frac{1}{3}}. \quad \text{(A7)}$$

Putting $kR=2$ then, we find (A6) has the value 1.81. In a typical observation[1] n-Si was used where $\mu/V\sim10^{18}/\text{cm}^3$ and $k\sim10$. If we put these values in (A5) and (A7) we get $\sim10^2$ sec. This is very much too long to give any observable line width. It is possible that the effect has been somewhat underestimated because (a) the fact that the electron will spend relatively more time near an impurity than the free model allows; and (b) the effective charge seen by the electron when near the impurity center will be greater than one and hence λ will be greater. Nevertheless it does not seem feasible to introduce the factor 10^{10} which would be required to make this mechanism effective, and we conclude that it can make no contribution to the line width.

[33] E. Jahnke and F. Emde, *Tables of Functions* (Dover Publications, New York, 1945).

Spin-Orbit Coupling in Band Theory—Character Tables for Some "Double" Space Groups

R. J. ELLIOTT*
Department of Physics, University of California, Berkeley, California
(Received May 26, 1954)

To take account of the electron spin in band theory, a method is outlined which allows us to construct character tables for the double space groups of the simple, face-centered, and body-centered cubic, diamond, and hexagonal close packed lattices. The effects of time reversal are also considered. Particular attention is given to the splitting of otherwise degenerate bands by the spin-orbit coupling.

THE symmetry of crystal lattices has important effects on the band theory of electron energy states. Bouckaert, Smoluchowski, and Wigner[1] have considered the group theoretical properties of these symmetries and constructed character tables of the irreducible representations for some simple lattices while Herring[2] has extended this to more complicated lattices.

It has recently become evident from measurements of magnetic properties like paramagnetic resonance,[3,4] that the coupling of the electron spin to the orbital motion has important effects. Moreover this spin-orbit coupling can introduce changes in energy of the order of the atomic spin-orbit coupling constant (0.1 ev or more in crystals of heavy atoms) and may therefore greatly change the details of the band form. This may be very important when we are considering properties of electrons with a kinetic energy which is only of the order of this spin-orbit coupling energy, such as occurs for example in impurity semiconductors.[5]

It therefore seemed of some interest to consider the effect of spin-orbit coupling on the symmetry properties of the bands. In this paper we outline a method and use it to construct character tables for a number of interesting space groups which are applicable when the spin is included. Bethe[6] and Opechowski[7] have shown in the case of point groups that this may be achieved by constructing the "double" group and their methods may be readily extended to space groups. Extra degeneracies are also caused by time-reversal symmetry and it is found that the general considerations of Wigner,[8] which were used for ordinary space groups by Herring,[9] can be readily applied to the dosuble group. The most significant effects of spin-orbit coupling arise when it removes degeneracies in the bands, and this effect can be readily seen by inspection of the character tables.

GENERAL THEORY

The Schrödinger equation of an electron in a crystal when spin-orbit coupling is included is

$$\left[-\frac{\hbar^2\nabla^2}{2m}+V+\frac{\hbar}{4m^2c^2}(\boldsymbol{\nabla} V\times\mathbf{p}\cdot\boldsymbol{\sigma})\right]\psi=\epsilon\psi.$$

The Hamiltonian operator and therefore the state function still have the translation and point symmetry of the lattice. We can therefore still obtain the symmetry properties of ψ by considering the space group of the crystal. This consists of an invariant subgroup of translations and a set of operations which leave the unit cell invariant. In simple lattices like simple cubic (s.c.), face-centered cubic (f.c.c.), and body-centered cubic (b.c.c.), this latter set is an invariant subgroup of the space group and is a point group (a subgroup of the full rotation group) but in more complicated lattices like diamond and hexagonal close packed (h.c.p.), it contains elements which consist of a rotation about a point together with a translation. We shall therefore employ in these cases the notation introduced by Seitz[10] and used by Herring.[2] The operation $[\alpha|a]$ represents a rotation α about the origin followed by a vector translation $\mathbf{a}$. The product of two such elements is given by

$$[\alpha|a][\beta|b]=[\alpha\beta|a+\alpha b].$$

Seitz showed that any irreducible representation can be based on a set of functions of the type $u_{\mathbf{k}}e^{i\mathbf{k}\cdot\mathbf{r}}$ (i.e., on the usual Bloch electron wave functions) each of which represents an element $[\epsilon|l]$ of the translation group by $\exp(-i\mathbf{k}\cdot\mathbf{t})$ (ϵ is used for the unit element of the rotation group throughout the paper). Operating on this basis function with some elements of the unit cell group we shall transform it into a function with wave vector different from $\mathbf{k}$. All wave vectors which can be reached from $\mathbf{k}$ in this way are called the "star" of $\mathbf{k}$.[1] We are interested in energy degeneracies for wave functions with a fixed $\mathbf{k}$. We therefore consider that subgroup G^k of the space group which

* Now at Atomic Energy Research Establishment, Harwell, Berkshire, England.
[1] Bouckaert, Smoluchowski, and Wigner, Phys. Rev. **50**, 58 (1936).
[2] C. Herring, J. Franklin Inst. **233**, 525 (1942).
[3] Portis, Kip, Kittel, and Brittain, Phys. Rev. **90**, 988 (1953).
[4] R. J. Elliott, preceding paper, Phys. Rev. **95**, 266 (1954). (See this paper for further references.)
[5] Discussion of the relation of the band forms to measurements of properties like magnetoresistance has been given by C. Herring (private communication).
[6] H. A. Bethe, Ann. Physik **3**, 133 (1929).
[7] W. Opechowski, Physica **7**, 552 (1940).
[8] E. Wigner, Göttingen Nachr. p. 546 (1932).
[9] C. Herring, Phys. Rev. **52**, 361 (1937).
[10] F. Seitz, Ann. Math. **37**, 17 (1936).

contains only those elements which transform a basis into one with the same $\mathbf{k}$. At a general point in the Brillouin zone this will consist only of the translation group, but at a place of high symmetry a subgroup of the unit cell group will also be included. That subgroup T^k of the translation group $(\epsilon|l)$ such that $\exp(i\mathbf{k}\cdot\mathbf{t})=1$ can also be removed since each element is equivalent to the unit element. We are left with a factor group G^k/T^k which can be greatly simplified because it is usually a direct product of an abelian subgroup which consists of most of the translations together with the subgroup which consists of the unit cell element in G^k with possibly a few translations. In simple lattices, s.c., f.c.c., b.c.c., the unit cell elements are rotations and this product is simply that of a subgroup of translations T/T^k and one of rotations G^k/T, but the more complicated conditions apply if there are screw axes or glide planes in the group.

All these considerations hold in exactly the same way when we consider spin except that we now consider double groups. Opechowski shows how to construct these for any group of rotations. He points out that the rotation group δ_3 is isomorphous with the group of 2×2 unitary matrices with determinant $+1$. For any rotation a matrix can be written

$$\begin{pmatrix}\alpha & -\beta^* \\ \beta & \alpha^*\end{pmatrix} \qquad |\alpha|^2+|\beta|^2=1,$$

and if we specify the rotation by Euler angles (θ,ϕ,ψ), $\beta=\sin\frac{1}{2}\theta e^{i(\phi-\psi)/2}$ and $\alpha=\cos\frac{1}{2}\theta e^{-i(\phi+\psi)/2}$.[11] This representation of the rotation group is however two valued since the matrix with all the elements changed in sign is also isomorphous with the rotation. This two valuedness is just what is required to include spin, and we therefore work with a group in which each rotation corresponds to two elements which can be represented by these two matrices. The improper rotations $i\times\delta$ where i is the inversion cannot be so represented but we may simply treat δ in the way outlined above and consider the products $i\times\delta$ using the facts that i commutes with all rotations and that $i^2=\epsilon$ even when spin is included.[11] Each of the two forms of the rotation u, which we can conveniently call u and $\bar{u}$, correspond to an ordinary rotation in Cartesian space and therefore have the same effect when operating on a vector; i.e.,

$$u\mathbf{t}=\bar{u}\mathbf{t}.$$

By using these facts the classes and the characters of the irreducible representations can be readily obtained from the well-known product, orthogonality, and normalization conditions.[12] Opechowski[7] obtained a number of simple rules which help considerably in constructing a double group from a known single point group. The most important are:

(1). If δ_n form a class of rotations through $2\pi/n$ in the single group δ_n, $\bar{\delta}_n$ form two separate classes in the double group.

(2). There is one exception to (1). If the rotations are through π $(n=2)$, then δ_2, $\bar{\delta}_2$ form one class in the double group if, and only if, there is also in the group another rotation through π about an axis perpendicular to the axis of δ_2.

(3). For the extra irreducible representations in the double group

$$\chi^d(\delta_n)=-\chi^d(\bar{\delta}_n),$$

and in the exceptional case (2), $\chi(\delta_2)=0$.

Similar rules can be constructed when the group elements are of the more general form $(\alpha|a)$.

(1). The condition above is a negative one: δ_n, $\bar{\delta}_n$ form separate classes because there is no rotation ξ in the group such that $\delta_n\xi=\xi\bar{\delta}_n$. With the addition of translations therefore rule (1) above still holds.

(2). In the exceptional case the translations impose a further condition. If there is another rotation $(\delta_2'|\tau')$ about a perpendicular axis $(\delta_2|\tau)$, $(\bar{\delta}_2|\tau)$ are only in the same class if

$$(\delta_2|\tau)(\delta_2'|\tau')=(\delta_2'|\tau')(\bar{\delta}_2|\tau),$$

i.e., if

$$(\epsilon-\delta_2')\tau=(\epsilon-\delta_2)\tau'.$$

In fact it is $(\bar{\delta}_2|l)$ which is in the same class as $(\delta_2|\tau)$ where $l=(\epsilon-\delta_2)\tau'-\delta_2'\tau$. Each class of δ_2 elements must therefore be tested carefully in this way when the double group is formed.

(3). As before when two classes are formed from one, whether in (1) or (2) the extra irreducible representations have characters which are of opposite sign. If there is only one class, the character is zero.

TIME REVERSAL

Wigner[8] has demonstrated that extra degeneracies often occur because of time-reversal symmetry. The effects of time reversal can be seen for three different cases, depending on the nature of the complex matrices D which form an irreducible representation of the group. They are:

(a) D is real.

(b) D, D^* belong to inequivalent irreducible representations.

(c) D, D^* belong to equivalent representations but are distinct.

For electrons with spin Wigner shows that for the

[11] See for example B. L. van der Waerden, *Die Gruppentheoretische Methode in der Quantenmechanik* (Verlag Julius Springer, Berlin, 1932).

[12] These are outlined in references 2 and 7. See also A. Speiser, *Theorie der Gruppen von endlicher Ordnung* (Verlag Julius Springer, Berlin, 1927).

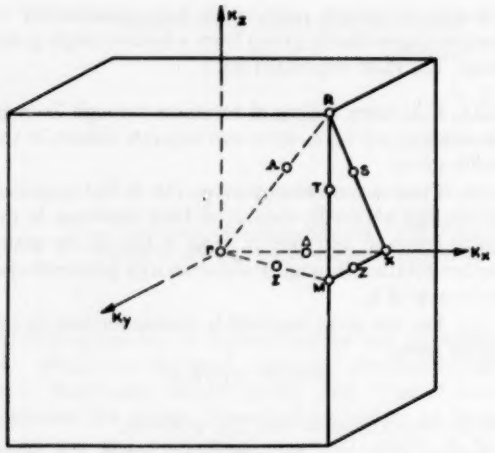

FIG. 1. First Brillouin zone for a s.c. lattice.

various cases,

(a) There is an extra degeneracy and the representation D always occurs doubled.

(b) There is extra degeneracy and the two representations D and D^* always occur together.

(c) There is no extra degeneracy.

This is different from the case when there is no spin—then the roles (a) and (c) are reversed. Herring[1] has considered the effects of this in space groups, by modification of a general theorem of Frobenius and Schur.[13] They show that in a group of N elements T for the three cases listed,

(a) $$\sum_T \chi(T^2)=N,$$

(b) $$=0,$$

(c) $$=-N.$$

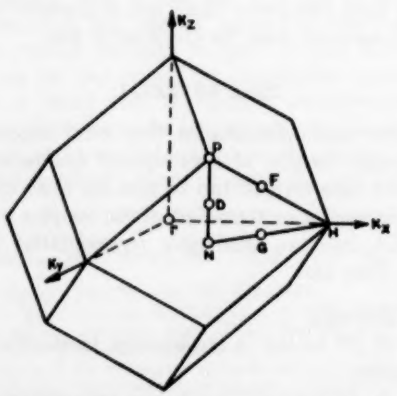

FIG. 2. First Brillouin zone for a b.c.c. lattice.

[13] G. Frobenius and I. Schur, S. B. Pruss. Akad. Wiss. 186 (1906).

For space groups this test reduces to

$$\sum_{Q_0} \chi(Q_0^2)=n,\ 0,\ \text{or}\ -n,$$

where Q_0 are those elements of G which turn $\mathbf{k}$ into $-\mathbf{k}$.

For $\mathbf{k}$s where the inversion operation I is not in G^k the Q_0 are $I\times G^k$. If I is in G^k the Q_0 are just the elements of G^k. Q_0^2 is an element of G^k so the above χ can be taken in an irreducible representation of the group of $\mathbf{k}$ which has n elements.

At a general point in the Brillouin zone G^k/T^k contains the translation group and the identity which now corresponds to two elements ϵ and $\tilde{\epsilon}$. The only Q_0 which take $\mathbf{k}$ into $-\mathbf{k}$ are the inversions $(i|\tau)$ and $(\tilde{i}|\tau)$ and therefore if the group G contains the inversion,

$$\sum_{Q_0} \chi(Q_0^2)=2\chi(\epsilon)=2,$$

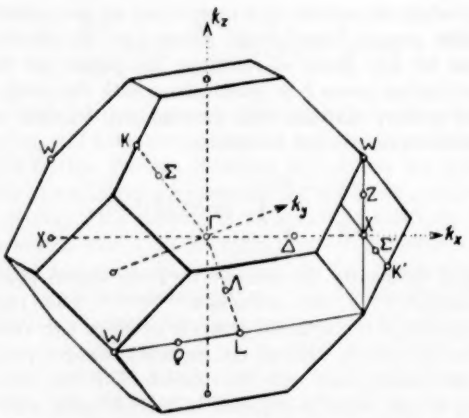

FIG. 3 First Brillouin zone for f.c.c. and diamond lattices.

which means case (a) holds and there is always a double degeneracy at the general point because of time reversal. There must always be at least a double degeneracy therefore at all points of the zone if the crystal has inversion symmetry. Any singly degenerate representations occurring at points of higher symmetry must therefore belong to cases (a) or (b). Such representations have been tested and the extra degeneracies are listed in the Tables.

When case (b) applies it is often useful to discover which are the representations of the group of $\mathbf{k}$ which correspond to the conjugate representations D, D^* of the whole group G. Let $\psi_{\mathbf{k}}{}^i$, $\psi_{\mathbf{k}'}{}^j$ form a basis for a representation of G. Then the set $\mathbf{k}'$ will include all wave vectors in the star of $\mathbf{k}$, and if as in the crystals we are discussing the group contains the inversion I, it will include $-\mathbf{k}$. The appropriate $\psi_{-\mathbf{k}}{}^i$ can be obtained from $\psi_{\mathbf{k}}{}^i$ by operating with I. The basis representing the time-reversed wave functions can be obtained by operating with Wigner's K, which consists of a unitary

TABLE I. Character table of the extra representations in the "double" group of Γ.

96		$\Gamma_6^{\pm}$	$\Gamma_7^{\pm}$	$\Gamma_8^{\pm}$		
1	E	2	2	4	Γ_i	$\Gamma_i\times D_{\frac{1}{2}}$
1	$\bar{E}$	−2	−2	−4	Γ_1	Γ_6^+
6	$C_4^2, \bar{C}_4^2$	0	0	0	Γ_2	Γ_7^+
6	C_4	$\sqrt{2}$	$-\sqrt{2}$	0	Γ_{12}	Γ_8^+
6	$\bar{C}_4$	$-\sqrt{2}$	$\sqrt{2}$	0	Γ_{15}'	$\Gamma_6^+ + \Gamma_8^+$
12	$C_2, \bar{C}_2$	0	0	0	Γ_{25}'	$\Gamma_7^+ + \Gamma_8^+$
8	C_3	1	1	−1	Γ_1'	Γ_6^-
8	$\bar{C}_3$	−1	−1	1	Γ_2'	Γ_7^-
48	$I\times Z$	$\pm\chi(Z)$	$\pm\chi(Z)$	$\pm\chi(Z)$	etc.	etc.

TABLE II. Character table of the extra representations in the "double" group of Δ.

16		Δ_6	Δ_7		
1	E	2	2		
1	$\bar{E}$	−2	−2	Δ_i	$\Delta_i\times D_{\frac{1}{2}}$
2	$C_4^2, \bar{C}_4^2$	0	0	Δ_1	Δ_6
2	C_4	$\sqrt{2}$	$-\sqrt{2}$	Δ_2	Δ_7
2	$\bar{C}_4$	$-\sqrt{2}$	$\sqrt{2}$	Δ_2'	Δ_7
4	$I\times C_4^2, I\times\bar{C}_4^2$	0	0	Δ_1'	Δ_6
4	$I\times C_2, I\times\bar{C}_2$	0	0	Δ_5	$\Delta_6+\Delta_7$

TABLE III. Character table of the extra representations in the "double" group of P.

48		P_6	P_7	P_8		
1	E	2	2	4	P_i	$P_i\times D^{\frac{1}{2}}$
1	$\bar{E}$	−2	−2	−4	P_1	P_6
6	$C_4^2, \bar{C}_4^2$	0	0	0	P_2	P_7
8	C_3	1	1	−1	P_3	P_8
8	$\bar{C}_3$	−1	−1	1	P_4	P_7+P_8
6	$I\times C_4$	$\sqrt{2}$	$-\sqrt{2}$	0	P_5	P_6+P_8
6	$I\times\bar{C}_4$	$-\sqrt{2}$	$\sqrt{2}$	0		
12	$I\times C_2, I\times\bar{C}_2$	0	0	0		

TABLE IV. Character table of the extra representation in the "double" group of M.

32		$M_6^{\pm}$	$M_7^{\pm}$		
1	E	2	2	M_i	$M_i\times D_{\frac{1}{2}}$
1	$\bar{E}$	−2	−2	M_1	M_6^+
4	$C_4^2, \bar{C}_4^2$	0	0	M_2	M_7^+
2	$C_4^2, \bar{C}_4^2, \perp$	0	0	M_3	M_7^+
2	$C_4, \perp$	$\sqrt{2}$	$-\sqrt{2}$	M_4	M_6^+
2	$\bar{C}_4, \perp$	$-\sqrt{2}$	$\sqrt{2}$	M_5	$M_6^+ + M_7^+$
4	$C_2, \bar{C}_2$	0	0	M_1'	M_6^-
16	$I\times Z$	$\pm\chi(Z)$	$\pm\chi(Z)$	etc.	etc.

operation U, and the operation of taking complex conjugates, i.e., it becomes $U\psi_{\mathbf{k}}{}^{i*}$, $U\psi_{\mathbf{k}'}{}^{j*}$, etc. Since we are considering character properties we may omit the U. The time-reversed functions which form a basis for the irreducible representation of the group of $\mathbf{k}$ are therefore $\psi_{-k}{}^*$ or $(I\psi_k)^*$.

Now if R is any element of the group of k,

$$R\psi_{\mathbf{k}}{}^i = r_{ij}\psi_{\mathbf{k}}{}^j.$$

Operating with I and defining a translation $\mathbf{t}$ by the expression $IR=(\epsilon|t)RI$, we find

$$R\psi_{-\mathbf{k}}{}^i = \exp(-i\mathbf{k}\cdot\mathbf{t})r_{ij}\psi_{-\mathbf{k}}{}^j$$

since R is real

$$R\psi_{-\mathbf{k}}{}^{i*} = \exp(i\mathbf{k}\cdot\mathbf{t})r_{ij}\psi_{-\mathbf{k}}{}^{j*}.$$

So the character of the representation corresponding to D^* is given in terms of that corresponding to D by

$$\chi(D^*) = \exp(i\mathbf{k}\cdot\mathbf{t})\chi^*(D).$$

TABLE V. Character table of the extra representations in the "double" group of L.

24		$L_4^{\pm}$	$L_5^{\pm}$	L_6		
1	E	1	1	2	L_i	$L_i\times D_{\frac{1}{2}}$
1	$\bar{E}$	−1	−1	−2	L_1	L_6^+
2	C_3	−1	−1	1	L_2	L_6^+
2	$\bar{C}_3$	1	1	−1	L_3	$L_4^+ + L_5^+ + L_6^+$
3	C_2	i	$-i$	0	L_1'	L_6^-
3	$\bar{C}_2$	$-i$	i	0	etc.	etc.
12	$I\times Z$	$\pm\chi(Z)$	$\pm\chi(Z)$	$\pm\chi(Z)$		

L_4^+, L_5^+ and L_4^-, L_5^- are degenerate by time reversal.

TABLE VI. Character table of the extra representations in the "double" group of W.

16		W_6	W_7		
1	E	2	2	W_i	$W_i\times D_{\frac{1}{2}}$
1	$\bar{E}$	−2	−2	W_1	W_6
2	$C_4^2, \bar{C}_4^2$	0	0	W_2	W_6
4	$C_2, \bar{C}_2$	0	0	W_1'	W_7
2	$I\times C_4$	$\sqrt{2}$	$-\sqrt{2}$	W_2'	W_7
2	$I\times\bar{C}_4$	$-\sqrt{2}$	$\sqrt{2}$	W_3	W_6+W_7
4	$I\times C_4^2$	0	0		

THE SPLITTING OF DEGENERACIES BY SPIN-ORBIT COUPLING

At a general point of the zone the representation is singly degenerate in the absence of spin, but because of time reversal, becomes doubly degenerate when we introduce the two possible spin components. The only effect then will be an energy change in the band, but this will in general be small because the spin-orbit coupling energy is small compared to the band separations. At points of high symmetry in the zone the addition of spin may cause some splitting. To find out when this occurs we consider a state which transforms like a representation Γ_i of the group of $\mathbf{k}$. The spin

TABLE VII. Character table of the extra representations in the "double" group of X.

64		X_5	
1	$(\epsilon\|0)$	4	For all the single group representations
1	$(\epsilon\|0)$	−4	X_i $(i=1, 2, 3, 4)$, $X_i\times D_{\frac{1}{2}}=X_5$.
1	$(\epsilon\|t_{xy})$	−4	
1	$(\epsilon\|t_{xy})$	4	
60	$(\alpha\|a)$	0	

(for all other classes of the group)

TABLE VIII. Character table of the representations of W.[a]

64		W_1	W_2	W_3	W_4	W_5	W_6	W_7
1	$(\epsilon\|0)$	2	2	1	1	1	1	2
1	$(\bar{\epsilon}\|0)$	2	2	-1	-1	-1	-1	-2
2	$(\delta_{2x}\|0)$, $(\bar{\delta}_{2x}\|t_{xy})$	0	0	$-i$	$-i$	$-i$	$-i$	$+2i$
4	$\{(\delta_{2xy}\|\tau)$, $(\bar{\delta}_{2xy}\|\tau+t_{xy})$ $(\delta_{2\bar{x}y}\|\tau+t_{yz})$, $(\bar{\delta}_{2\bar{x}y}\|\tau+t_{xz})\}$	0	0	1	1	-1	-1	0
2	$(\sigma_{4x}\|0)$, $(\sigma_{4x}^{-1}\|t_{yz})$	$(1-i)$	$-(1-i)$	$\frac{1}{\sqrt{2}}(1-i)$	$-\frac{1}{\sqrt{2}}(1-i)$	$\frac{1}{\sqrt{2}}(1-i)$	$-\frac{1}{\sqrt{2}}(1-i)$	0
2	$(\bar{\sigma}_{4x}\|0)$, $(\bar{\sigma}_{4x}^{-1}\|t_{yz})$	$(1-i)$	$-(1-i)$	$-\frac{1}{\sqrt{2}}(1-i)$	$\frac{1}{\sqrt{2}}(1-i)$	$-\frac{1}{\sqrt{2}}(1-i)$	$\frac{1}{\sqrt{2}}(1-i)$	0
4	$\{(\rho_x\|\tau)$, $(\bar{\rho}_x\|\tau+t_{xy})$ $(\rho_y\|\tau+t_{xz})$, $(\bar{\rho}_y\|\tau+t_{yz})\}$	0	0	$\frac{1}{\sqrt{2}}(1+i)$	$-\frac{1}{\sqrt{2}}(1+i)$	$-\frac{1}{\sqrt{2}}(1+i)$	$\frac{1}{\sqrt{2}}(1+i)$	0
16	$(\alpha\|a)\times(\epsilon\|t_{yz})$			$-i\chi[(\alpha\|a)]$				
16	$(\alpha\|a)\times(\epsilon\|t_{xy})$			$-\chi[(\alpha\|a)]$				
16	$(\alpha\|a)\times(\epsilon\|t_{xz})$			$i\chi[(\alpha\|a)]$				

$W_1\times D_{\frac{1}{2}}=W_2+W_5+W_7$; $W_2\times D_{\frac{1}{2}}=W_4+W_6+W_7$.

W_3, W_5 and W_4, W_6 are degenerate by time reversal.

[a] Dr. Herring has pointed out that there is an error in his single group W. In order to define its representations properly, we give the characters for the single group as well.

functions transform like $D_{\frac{1}{2}}$ of the rotation group and since the spin and coordinate spaces are quite distinct we form the direct product,

$$\Gamma_i\times D_{\frac{1}{2}}=\sum a_{ij}\Gamma_j.$$

Γ_i is a representation which occurred in the single group and so it occurs in the double group also with $\chi(E)=\chi(\bar{E})$. On the other hand in $D_{\frac{1}{2}}$, $\chi(E)=-\chi(\bar{E})=2$. Therefore only those representations with $\chi(E)=-\chi(\bar{E})$ occur in the sum on the right of expression, i.e., only the new representations introduced by forming the double group. The constants a_{ij} can be readily obtained by finding the product of the characters. The character of a rotation through an angle $2\pi/n$ in $D_{\frac{1}{2}}$ is $2\cos(\pi/n)$.

It is also of interest to find out how the representation changes as we move from one point in the zone to another with different symmetry properties. To do this we construct compatability relations as defined by Bouckaert, Smoluchowski, and Wigner.[1] Various interesting sequences of these are given in the Tables. These are much fewer in number than in the single group, because most of the symmetry lines do not now have more than one available irreducible representation, and the effect of moving away from a symmetry point can be seen simply by examining the dimensions of the representation.

TABLE IX. Character table of the extra representations in the "double" group of $\Delta(X)$.

32		$\Delta_6(X)$	$\Delta_7(X)$		
1	$(\epsilon\|0)$	2	2	Δ_1	$\Delta_1\times D_{\frac{1}{2}}$
1	$(\bar{\epsilon}\|0)$	-2	-2	Δ_1	Δ_6
2	$(\delta_{2x},\bar{\delta}_{2x}\|0)$	0	0	Δ_1'	Δ_6
2	$(\delta_{4x},\delta_{4x}^{-1}\|\tau)$	$-\sqrt{2}i$	$\sqrt{2}i$	Δ_2	Δ_7
2	$(\bar{\delta}_{4x},\bar{\delta}_{4x}^{-1}\|\tau)$	$\sqrt{2}i$	$-\sqrt{2}i$	Δ_2'	Δ_7
4	$(\rho_x,\bar{\rho}_x,\rho_y,\bar{\rho}_y\|\tau)$	0	0	Δ_5	$\Delta_6+\Delta_7$
4	$(\rho_{yz},\bar{\rho}_{yz},\rho_{\bar{y}z},\bar{\rho}_{\bar{y}z}\|0)$	0	0		
16	$(\alpha\|a)\times(\epsilon\|t_{xy})$	$-\chi[(\alpha\|a)]$			

TABLES OF CHARACTERS

Only the extra representations which arise in the double group are given in these Tables. To avoid confusion the same notation is used as in the papers where the single group character Tables are given. When the group is a direct product, the Tables have been shortened by writing the products $(\alpha|a)\times(\gamma|c)$ where $(\alpha|a)$ are all the elements already listed. To

TABLE X. Character table of the extra representations in the "double" group of $Z(X)$.

16		Z_2	Z_3	Z_4	Z_5
1	$(\epsilon\|0)$	1	1	1	1
1	$(\epsilon\|t_{xy})$	-1	-1	-1	-1
2	$(\delta_{2z}\|0)$, $(\bar{\delta}_{2z}\|t_{xy})$	i	i	$-i$	$-i$
2	$(\rho_x\|\tau)$, $(\bar{\rho}_x\|\tau+t_{xy})$	i	$-i$	i	$-i$
2	$(\rho_y\|\tau)$, $(\bar{\rho}_y\|\tau+t_{xy})$	-1	1	1	-1
8	$(\alpha\|a)\times(\bar{\epsilon}\|0)$		$-\chi[(\alpha\|a)]$		

$Z_1\times D_{\frac{1}{2}}=Z_2+Z_3+Z_4+Z_5$

Z_2, Z_3 and Z_4, Z_5 are degenerate by time reversal.

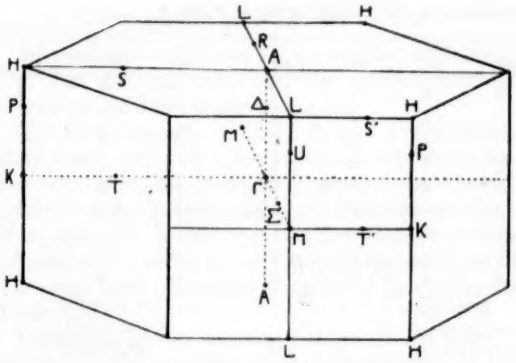

FIG. 4. First Brillouin zone for h.c.p. lattice.

every class listed there will be a further class in this product. The character of the product is given in terms of the character of $(\alpha|a)$ already listed.

Simple, Face-Centered, and Body-Centered Cubic Lattices

For the s.c., f.c.c., and b.c.c. lattices[1] we need only consider point groups and we give Tables I–VI for the positions Γ, Δ, P, M, L, and W and others which are isomorphous with them. The double groups of Λ, F, Σ, S, Z, G, K, U, D, Q, are trivial since the only extra representation is one where $\chi(E)=2$, $\chi(\bar{E})=-2$, $\chi(C)=0$, where C is any rotation, and the wave functions of all bands transform in the same way. This representation is the same as the one for the general $\mathbf{k}$ which we have seen is double by time reversal. For N there are two extra representations one of which is even and the other odd with respect to the inversion, so the results are again trivial. The positions of the symmetry points can be seen by reference to the Figs. 1–3 which are the first Brillouin zones of the s.c., b.c.c., and f.c.c. lattices, respectively.

Δ is the only symmetry line where the representations are nontrivial, and we need therefore only consider

TABLE XI. Character table of the extra representations in the "double" group of A and Γ.

96		A_4	A_5	A_6	Γ_7^+	Γ_8^+	Γ_9^+
1	$(\epsilon\|0)$	2	2	4	2	2	2
1	$(\bar{\epsilon}\|0)$	−2	−2	−4	−2	−2	−2
1	$(\epsilon\|t_{xy})$	−2	−2	−4			
1	$(\bar{\epsilon}\|t_{xy})$	2	2	4			
4	$(\delta_3,\delta_3^{-1}\|\tau,\tau+t_1)$	0	0	0	$\sqrt{3}$	$-\sqrt{3}$	0
4	$(\bar{\delta}_3,\bar{\delta}_3^{-1}\|\tau,\tau+t_1)$	0	0	0	$-\sqrt{3}$	$\sqrt{3}$	0
2	$(\delta_3,\delta_3^{-1}\|0)$	−2	−2	2	1	1	−2
2	$(\bar{\delta}_3,\bar{\delta}_3^{-1}\|0)$	2	2	−2	−1	−1	2
2	$(\delta_3,\delta_3^{-1}\|t_1)$	2	2	−2			
2	$(\bar{\delta}_3,\bar{\delta}_3^{-1}\|t_1)$	−2	−2	2			
4	$(\delta_3,\bar{\delta}_2\|\tau,\tau+t_1)$	0	0	0	0	0	0
6	$(\delta_{2i}'\|\tau)$, $(\bar{\delta}_{2i}'\|\tau+t_1)$	$2i$	$-2i$	0	0	0	0
6	$(\bar{\delta}_{2i}'\|\tau)$, $(\delta_{2i}'\|\tau+t_1)$	$-2i$	$2i$	0			
12	$(\delta_{2i}'',\bar{\delta}_{2i}''\|\tau,\tau+t_1)$	0	0	0	0	0	0
2	$(i\|\tau,\tau+t_1)$	0	0	0	± 2	± 2	± 2
2	$(\bar{i}\|\tau,\tau+t_1)$	0	0	0	∓ 2	∓ 2	∓ 2
4	$(\sigma_3,\sigma_3^{-1}\|0,t_1)$	0	0	0	$\pm\sqrt{3}$	$\mp\sqrt{3}$	0
4	$(\bar{\sigma}_3,\bar{\sigma}_3^{-1}\|0,t_1)$	0	0	0	$\mp\sqrt{3}$	$\pm\sqrt{3}$	0
4	$(\sigma_6,\sigma_6^{-1}\|\tau,\tau+t_1)$	0	0	0	± 1	± 1	∓ 2
4	$(\bar{\sigma}_6,\bar{\sigma}_6^{-1}\|\tau,\tau+t_1)$	0	0	0	∓ 1	∓ 1	± 2
4	$(\rho,\bar{\rho}\|0,t_1)$	0	0	0	0	0	0
6	$(\rho_i',\bar{\rho}_i'\|0)$	0	0	0	0	0	0
6	$(\rho_i',\bar{\rho}_i'\|t_1)$	0	0	0			
12	$(\rho_i'',\bar{\rho}_i''\|\tau,\tau+t_1)$	0	0	0	0	0	0

A_4, A_5 are degenerate by time reversal.

Γ_i	Γ_1^+	Γ_2^+	Γ_3^+	Γ_4^+	Γ_5^+	Γ_6^+	A_1	A_2	A_3
$\Gamma_i\times D_1$	Γ_7^+	Γ_7^+	Γ_8^+	Γ_8^+	$\Gamma_7^+ + \Gamma_9^+$	$\Gamma_7^+ + \Gamma_9^+$	A_6	A_6	$A_4 + A_5 + A_6$

TABLE XII. Character table of the extra representations in the "double" group of L and M.

64		L_3	L_4	M_5^+	
1	$(\epsilon\|0)$	2	2	2	
1	$(\bar{\epsilon}\|0)$	−2	−2	−2	$L_1\times D_1 = L_2\times D_1$
1	$(\epsilon\|t_1)$	−2	−2		$= L_3 + L_4$
1	$(\bar{\epsilon}\|t_1)$	2	2		For all M_i^+ $(i=1, 2, 3, 4)$
2	$(\delta_{2z}'\|\tau_2)$, $(\bar{\delta}_{2z}'\|\tau_2+t_1)$	$2i$	$-2i$	0	$M_i^+\times D_1 = M_5^+$
2	$(\bar{\delta}_{2z}'\|\tau_2)$, $(\delta_{2z}'\|\tau_2+t_1)$	$-2i$	$2i$		
4	$(\delta_{2z}'',\bar{\delta}_{2z}''\|0,t_1)$	0	0	0	L_3, L_4 are degenerate by time reversal.
4	$(\delta_2, \bar{\delta}_2\|\tau_2, \tau_2+t_1)$	0	0	0	
2	$(i\|\tau_2, \tau_2+t_1)$	0	0	± 2	
2	$(\bar{i}\|\tau_2, \tau_2+t_1)$	0	0	∓ 2	
2	$(\rho_2',\bar{\rho}_2'\|0)$	0	0	0	
2	$(\rho_2',\bar{\rho}_2'\|t_1)$	0	0		
4	$(\rho_2'', \bar{\rho}_2''\|\tau_2, \tau_2+t_1)$	0	0	0	
4	$(\rho,\bar{\rho}\|0,t_1)$	0	0	0	
32	$(\alpha\|a)\times(\epsilon\|t_3)$	$-\chi[(\alpha\|a)]$		$-\chi[(\alpha\|a)]$	

TABLE XIII. Character table of the extra representations in the "double" group of H and K.

144		H_4	H_5	H_6	H_7	H_8	H_9	K_7	K_8	K_9
1	$(\epsilon\|0)$	1	1	1	1	2	2	2	2	2
1	$(\epsilon\|t_1)$	−1	−1	−1	−1	−2	−2			
2	$(\delta_2\|t_2)$, $(\delta_2^{-1}\|-t_2)$	−1	−1	−1	−1	1	1	1	1	−2
2	$(\delta_2\|t_1+t_2)$, $(\delta_2^{-1}\|-t_1-t_2)$	1	1	1	1	−1	−1			
6	$(\delta_{2i}'\|\tau_i)$, $(\bar{\delta}_{2i}'\|\tau_1+t_1)$	i	i	$-i$	$-i$	0	0	0	0	0
2	$(\sigma_3\|-t_2)$, $(\sigma_3^{-1}\|t_1+t_2)$	i	$-i$	i	$-i$	i	$-i$	$\sqrt{3}$	$-\sqrt{3}$	0
2	$(\sigma_3\|-t_1-t_2)$, $(\sigma_3^{-1}\|t_2)$	$-i$	i	$-i$	i	$-i$	i			
2	$(\rho\|0)$, $(\bar{\rho}\|t_1)$	$-i$	i	$-i$	i	$2i$	$-2i$	0	0	0
6	$(\rho_i''\|\tau_i)$, $(\bar{\rho}_i''\|\tau_i+t_1)$	1	−1	−1	1	0	0	0	0	0
24	$(\alpha\|a)\times(\bar{\epsilon}\|0)$			$-\chi[(\alpha\|a)]$					$-\chi[(\alpha\|a)]$	
48	$(\gamma\|c)\times(\epsilon\|t_2)$			$\omega\chi[(\gamma\|c)]$					$\omega\chi[(\gamma\|c)]$	
48	$(\gamma\|c)\times(\epsilon\|-t_2)$			$\omega^2\chi[(\gamma\|c)]$					$\omega^2\chi[(\gamma\|c)]$	

H_i	H_1	H_2	H_3	K_1	K_2	K_3	K_4	K_5	K_6
$H_i\times D_{\frac{1}{2}}$	H_8+H_9	$H_4+H_6+H_8$	$H_5+H_7+H_9$	K_7	K_8	K_7	K_8	K_8+K_9	K_7+K_9

H_4, H_6 and H_5, H_7 are degenerate by time reversal.

TABLE XIV. Character table of the extra representations in the "double" group of Δ.

48		$\Delta_7(A)$	$\Delta_8(A)$	$\Delta_9(A)$	$\Delta_7(\Gamma)$	$\Delta_8(\Gamma)$	$\Delta_9(\Gamma)$		
1	$(\epsilon\|0)$	2	2	2	2	2	2	Δ_i	$\Delta_i\times D_{\frac{1}{2}}$
1	$(\bar{\epsilon}\|0)$	−2	−2	−2	−2	−2	−2	Δ_1	Δ_7
2	$(\delta_6,\delta_6^{-1}\|\tau)$	$-\sqrt{3}i$	$+\sqrt{3}i$	0	$\sqrt{3}$	$-\sqrt{3}$	0	Δ_2	Δ_8
2	$(\bar{\delta}_6,\bar{\delta}_6^{-1}\|\tau)$	$+\sqrt{3}i$	$-\sqrt{3}i$	0	$-\sqrt{3}$	$\sqrt{3}$	0	Δ_3	Δ_7
2	$(\delta_3,\delta_3^{-1}\|0)$	1	1	−2	1	1	−2	Δ_4	Δ_8
2	$(\bar{\delta}_3,\bar{\delta}_3^{-1}\|0)$	−1	−1	2	−1	−1	2	Δ_5	$\Delta_7+\Delta_9$
2	$(\delta_3,\bar{\delta}_3\|0)$	0	0	0	0	0	0	Δ_6	$\Delta_8+\Delta_9$
6	$(\rho_i',\bar{\rho}_i'\|0)$	0	0	0	0	0	0		
6	$(\rho_i'',\bar{\rho}_i''\|\tau)$	0	0	0	0	0	0		
24	$(\alpha\|a)\times(\epsilon\|t_1)$		$-\chi[(\alpha\|a)]$						

its compatibility relations: $\Gamma_6^{\pm}\to\Delta_6$, $\Gamma_7^{\pm}\to\Delta_7$, and $\Gamma_8^{\pm}\to\Delta_6+\Delta_7$; $M_6\to\Delta_6$. $M_7\to\Delta_7$.

Diamond Lattice

We shall use throughout the notation adopted by Herring.[2] The lattice has the same translational symmetry as the face-centered cubic, but its unit cell is more complicated since it contains two atoms and therefore the cell group contains screw elements. Even so some of the groups are isomorphous with those of the f.c.c. lattice, and we need not consider them again. The exact correspondence of the elements is discussed by Herring. The groups for the points X and W, and the lines Δ and Z are however different. We evaluate the double groups of these in the limit as they approach X. The first Brillouin zone is equivalent to that for f.c.c. (Fig. 2).

The lines of symmetry Δ and Z in this lattice have nontrivial compatibility relations: $\Gamma_6^{\pm}\to\Delta_6(\Gamma)$, $\Gamma_7^{\pm}\to\Delta_7(\Gamma)$, $\Gamma_8^{\pm}\to\Delta_6(\Gamma)+\Delta_7(\Gamma)$, and $X_5\to\Delta_6(X)+\Delta_7(X)$. $X_5\to Z_2+Z_3+Z_4+Z_5$, $W_3+W_5\to Z_4+Z_5$, $W_4+W_6\to Z_4+Z_5$, $W_7\to Z_2+Z_3$.

TABLE XV. Character table of the extra representations in the "double" group of P.

72		$P_4(H)$	$P_5(H)$	$P_6(H)$	$P_4(K)$	$P_5(K)$	$P_6(K)$
1	$(\epsilon\|0)$	1	1	2	1	1	2
2	$(\delta_2\|t_2)$, $(\delta_2^{-1}\|-t_2)$	−1	−1	1	−1	−1	1
3	$(\rho_i''\|\tau_i)$	1	−1	0	$-i$	i	0
6	$(\alpha\|a)\times(\bar{\epsilon}\|0)$	$-\chi[(\alpha\|a)]$			$-\chi[(\alpha\|a)]$		
12	$(\gamma\|c)\times(\epsilon\|t_2)$	$\omega\chi[(\gamma\|c)]$			$\omega\chi[(\gamma\|c)]$		
12	$(\gamma\|c)\times(\epsilon\|-t_2)$	$\omega^2\chi[(\gamma\|c)]$			$\omega^2\chi[(\gamma\|c)]$		
36	$(\beta\|b)\times(\epsilon\|t_1)$	$-\chi[(\beta\|b)]$					

P_4, P_5 are degenerate by time reversal,

$P_1\times D_{\frac{1}{2}}=P_2\times D_{\frac{1}{2}}=P_6$ $P_3\times D_{\frac{1}{2}}=P_4+P_5+P_6$

TABLE XVI. Character table of the extra representations in the "double" group of S.

16		S_2	S_3	S_4	S_5
1	$(\epsilon\|0)$	1	1	1	1
1	$(\epsilon\|t_1)$	−1	−1	−1	−1
2	$(\delta_{2i}'\|\tau_2)$, $(-\bar{\delta}_{2i}'\|\tau_2+t_1)$	i	i	$-i$	$-i$
2	$(\rho\|0)$, $(\bar{\rho}\|t_1)$	$-i$	i	i	$-i$
2	$(\rho_2''\|\tau_2)$, $(\bar{\rho}_2''\|\tau_2+t_1)$	1	−1	1	−1
8	$(\alpha\|a)\times(\bar{\epsilon}\|0)$		$-\chi[(\alpha\|a)]$		

$S_1\times D_{\frac{1}{2}}=S_2+S_3+S_4+S_5$

S_2, S_4 and S_2, S_5 are degenerate by time reversal.

Hexagonal Close-Packed Lattice

We shall again follow exactly the notation of Herring.[2] The first Brillouin zone and the various kinds of symmetry point are shown in Fig. 4.

The double groups of U, Σ, R, and T are trivial; there being only one extra representation which has zero character for everything except the identity ($\chi(\epsilon)=-\chi(\bar{\epsilon})=2$) and translations. This representation of R, however, always occurs twice because of time reversal so the states are all fourfold degenerate on R. The only other symmetry position S has character Table XVI.

Depending on the limiting position of the point S we should also consider primary translations in the group of S. This would give the same results as in Herring's single tables and they are omitted here.

The compatibility relations for the lines Δ, P and S are nontrivial: $\Gamma_i^{\pm}\rightarrow\Delta_i(\Gamma)$ $(i=7, 8, 9)$. $A_4\rightarrow\Delta_9(A)$, $A_5\rightarrow\Delta_9(A)$, $A_6\rightarrow\Delta_7(A)+\Delta_8(A)$. H_4+H_6, $H_5+H_7\rightarrow P_4(H)+P_5(H)$; H_8, $H_9\rightarrow P_6(H)$. K_7, $K_8\rightarrow P_6(K)$; $K_9\rightarrow P_4(K)+P_5(K)$. A_4+A_5, $A_6\rightarrow S_2(A)+S_3(A)+S_4(A)+S_5(A)$. $H_4\rightarrow S_2(H)$, $H_5\rightarrow S_3(H)$, $H_6\rightarrow S_5(H)$. $H_7\rightarrow S_4(H)$, $H_8\rightarrow S_3(H)+S_4(H)$, $H_9\rightarrow S_2(H)+S_5(H)$.

ACKNOWLEDGMENTS

The author is greatly indebted to Dr. W. M. Lomer of Atomic Energy Research Establishment, Harwell for many useful discussions, and to Dr. Conyers Herring and Professor C. Kittel for a number of helpful suggestions. This work was extended and completed during the tenure of a Harwell Fellowship at the Atomic Energy Research Establishment.

PHYSICAL REVIEW VOLUME 96, NUMBER 2 OCTOBER 15, 1954

Magnetization of Tin at the Superconducting Transition

J. C. THOMPSON* AND C. F. SQUIRE
The Rice Institute, Houston, Texas

(Received June 22, 1954)

Measurements have been made of the steady-state magnetization of a tin cylinder in the presence of an external magnetic field and with an externally supplied current at the transition to superconduction. In accord with earlier work in Germany, a longitudinal flux in excess of that caused by the external field is observed for certain combinations of external field and current. The dependence of the effect on the external parameters is given and it is shown that the metal is not in the pure superconducting state. No satisfactory theory for the effect has been found, but some numerical relationships have been computed.

INTRODUCTION

SUPERCONDUCTION in metals is an electronic state characterized by zero electrical field and by zero magnetic induction. The independent variables which may determine whether a metal is in the superconducting state, if it becomes one at all, are the temperature T, the magnetic field B, and finally because a current in the specimen may produce its own field, we must consider the current I, as a variable. At sufficiently low values of each of these variables, the metal may be in the superconducting state; just how low is a characteristic of each superconductor.[1] In this research we dealt with very pure monocrystalline tin made in the form of a cylinder and we were concerned with some unusual properties just at the transition into and out of the superconducting state. At a temperature just below the zero field transition temperature for ordinary tin, 3.735°K, and in a small externally created magnetic field of 1 to 4×10^{-4} weber/sq meter applied along the long axis of the cylinder, a steady current of from 1 to 13 amperes was allowed to flow along the cylinder and we measured the magnetic flux content of the tin specimen. The work of Steiner[2] and of Meissner, Schmeissner, and Meissner[3] has shown that under these conditions the longitudinal flux through a conductor, instead of decreasing monotonically to zero at the transition to superconduction, first shows an *increase* provided one uses certain conditions of a large current, a small external magnetic field, and a temperature such that with the currents and fields used the super to normal transition may be effected. The results which we now report are in accord with the above authors and represent a continuation of the preliminary studies by Mendelssohn, Squire, and Teasdale[4] and by Teasdale and Rorschach.[5] Dr. Mendelssohn suggested these studies and indicated the method of measurement which we have continued to use since his work with us here in this laboratory. The present apparatus has

* Shell Company Fellow in Physics.

[1] D. Shoenberg, *Superconductivity* (Cambridge University Press, Cambridge, 1952); also F. London, *Superfluids* (John Wiley and Sons, Inc., New York, 1950), Vol. I.

[2] K. Steiner and H. Schoeneck, Physik. Z. **44**, 346 (1943); also K. Steiner, Z. Naturforsch. **4a**, 271 (1949).

[3] Meissner, Schmeissner, and Meissner, Z. Physik **130**, 521, 529 (1951); **132**, 529 (1952).

[4] Mendelssohn, Squire, and Teasdale, Phys. Rev. **87**, 589 (1952).

[5] T. Teasdale and H. E. Rorschach, Jr., Phys. Rev. **90**, 709 (1953).

allowed us to obtain quantitative results and to overcome many, if not all, difficulties which might interfere with the interpretation of the experimental results.

EXPERIMENTAL

The apparatus used in the present studies is shown schematically in Fig. 1. The method used to study the flux content of the tin cylinder specimen was to move a coil C from its position around the tin upward to a position around a copper cylinder. The difference in magnetic flux induced a current in a ballistic-type galvanometer. The copper, being a normal metal, was used as a reference flux standard and the superconducting Sn gave the characteristic zero flux behavior. Silk threads W were used to link the test coil with the iron slug I which could be moved with a strong solenoid (not shown) placed outside the gas-tight glass envelope housing the iron slug. The detecting coil C, made of 1900 turns of No. 40 copper wire wound upon a Lucite form, was fitted about the tin-copper specimen with just enough clearance to move easily. The exact position of the coil was controlled by the stops L which were made of Lucite.

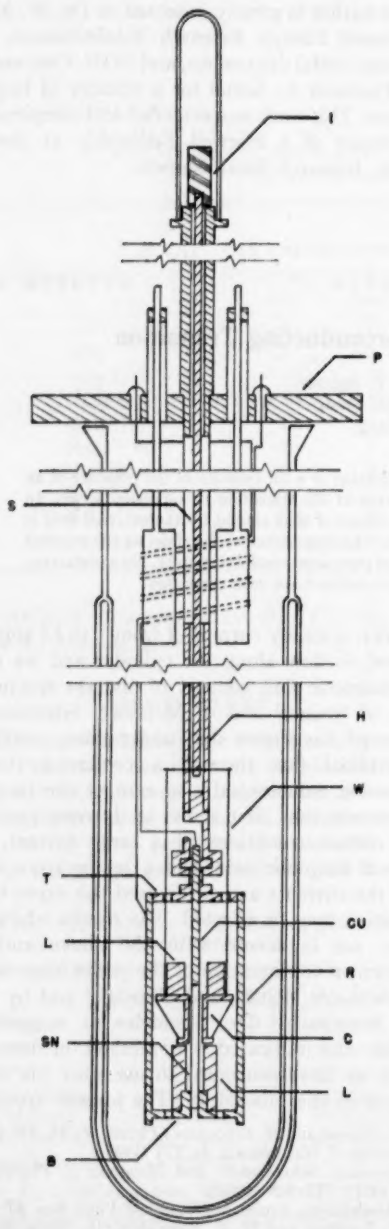

FIG. 1. Schematic diagram of experimental apparatus.

The direct current leads to the specimen are shown in Fig. 1 entering the top of the cryostat through gas-tight seals and then spiraling around a vessel which contained liquid nitrogen. Below that point and extending on down into the liquid helium vessel the current-carrying wires were of smaller diameter, such that neither heat leaks nor Joule heating effects were excessive. The current could be sent through the specimen in either direction by a reversing switch in the power supply (large Edison cells). It will be noted in Fig. 1 that the return lead is by the concentric copper shell R, and we must add that this shell was slotted so that liquid helium was always in direct contact with the specimen cylinder. Not shown in Fig. 1 are the external liquid nitrogen Dewar and the external wire-wound solenoid for producing small homogeneous fields (1 to 5×10^{-4} weber/m^2—i.e., 1 to 5 gauss) whose direction was along the specimen cylinder. The external magnetic field could also be reversed in direction. The arrangement in Fig. 1 allows one to measure the flux in the tin compared to that in the copper at any desired combination of values of current, external field, and temperature.

The tin specimen was from Baker Chemical Company 99.99-percent pure laboratory stock. The molten metal was drawn up into a glass tube by vacuum and then an electric furnace was slowly (6 cm/hr) removed in the well-known manner for growing single crystals. The glass tube was gently removed and the tin specimen was electrolytically polished with perchloric acid so that one could observe directly the crystal faces. The final cut shape was a cylinder 7.2 cm long and 0.615 cm in diameter, composed of a large single crystal in the central portion with a few small crystals at each cut end. The tin cylinder was butted to a copper cylinder of the same cross section and the two welded together.

RESULTS

A given cycle of measurements was taken as follows: the external parameters, T, B, and I were adjusted to the desired starting values (say 3.694°K, 1.0×10^{-4} weber/m^2, and 2.5 amp) and the detecting coil was

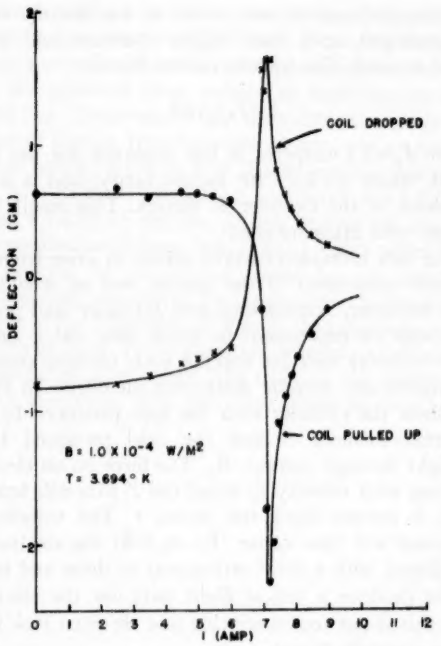

FIG. 2. Transition at constant temperature and field showing effect of direction of coil motion.

then raised quickly from its position about the tin to its position about the copper. The galvanometer deflection was noted and plotted as on Fig. 2. The detecting coil was then dropped and an opposite deflection noted. One external parameter, such as the current I, was slightly changed to a new steady-state value (say 3.0 amp) and the next point taken. In this way the current in the tin-copper cylinder was increased in small steps until the tin entered the normal state. Figure 2 clearly shows that the deflections for current values in the region of 7 amperes are such as to denote a greater flux in the tin than in the copper. The current in the cylinder was lowered, stepwise, and points taken as the tin was put back into the completely superconducting state. The plot of Fig. 2 is completely reversible. The existence of the increased magnetic flux content in the tin does not depend on whether the directions of I and B are parallel or antiparallel. Alternatively, the current could be set at a constant value (less then critical) and the transition made by changing the external longitudinal field. Likewise the temperature can be used[5] as the parameter moved across the phase transition. The effect is always observed with proper values of current and field.

The magnetic field at the surface of the cylinder caused by the current I is only 0.651×10^{-4} weber/m^2 per ampere. Thus, if there were enough heating to cause the temperature in the tin to be 0.01°K higher than the vapor pressure over the helium indicated, we would expect the critical current actually to be reached for a value 2.3 amperes lower than anticipated. This is illustrated in Fig. 3 showing another set of values of galvanometer deflection *vs* current with the expected critical current I_c marked at about 11 amperes for $T=3.680$°K and $B=3.0\times10^{-4}$ weber/m^2. The destruction of the Meissner effect, $B=0$, is observed at 9 amperes, and by 10 amperes we have the additional magnetic field produced by the circular motion of the current so that surely the tin is in the normal state at that point. The two curves in Fig. 3 are for field and current parallel and then antiparallel and their slight difference is considered insignificant. The curves are reversible going in and out of the superconducting state.

DISCUSSION

The detecting coil certainly informs us that the magnetic flux within the tin specimen is greater than that of the copper for certain values of I, B, and T. In the pure superconducting state the tin contains no flux. At temperatures of 4.2°K, well above the superconducting transition, the tin and copper are identical in flux content so far as the detecting coil can observe. The deflection of the galvanometer tells us directly and quantitatively the flux change. The increased flux contant in the tin over the copper is a maximum for a certain current I, and for fixed values of external field B, and of temperature T. Suppose at this maximum flux content we were to assume the induction

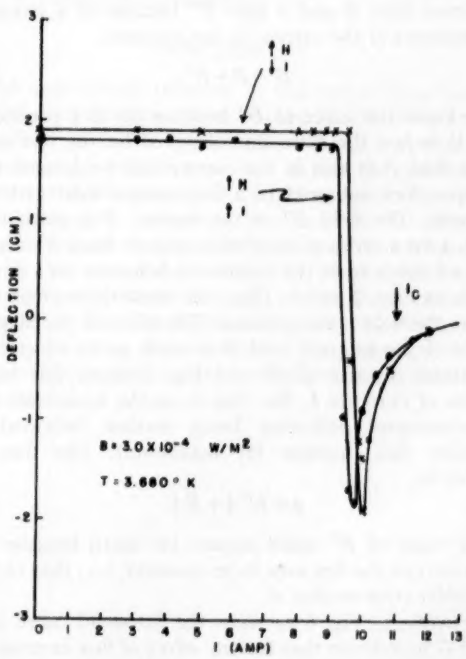

FIG. 3. Transition at constant temperature and field showing effect of current-field parallelism.

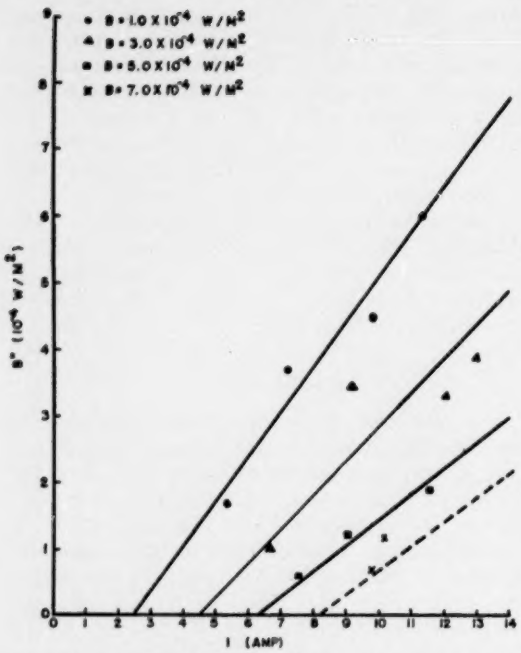

FIG. 4. Field produced in tin at maximum of "paramagnetic effect" as a function of current in specimen and for several fields.

vector B' to be constant over the area of cross section of the tin and assert that B' was the resultant of the external field B and a field B'' because of a circular component of the current in the specimen

$$B'=B+B''. \tag{1}$$

We know the value of B'' because the flux produced by it is just the extra flux observed by the test coil. The field B is also in the copper and we assume the copper does not produce a longitudinal field with its current. The field B'' *vs* the current I is plotted in Fig. 4 for a series of externally applied fields B. These are all taken from the maximum deflection on a curve such as Figs. 2 and 3. Thus, the more the current the more the field it can produce. The effect of the magnitude of the external field B is such as to effectively diminish the size of B'' and Fig. 5 shows this for a series of currents I. But this is on the basis that the galvanometer deflection being smaller indicated a smaller flux increase (at maximum). The flux is given by

$$\phi=B''A+BA. \tag{2}$$

The value of B'' could appear too small because we have taken the flux area to be constant, i.e., that of the cylinder cross section A.

Finally, in Fig. 6 we show the threshold curve in I and B to indicate that for any effect of flux increase to be observed at all, we must have currents and external fields in the so-called "paramagnetic" region. The experimental points were taken at successively lower temperatures such that higher currents and fields could be used. The equation of the line is

$$I=I_0+\gamma dB, \tag{3}$$

where $I_0=1.2$ amperes is the intercept for the field $B=0$, where $\gamma=1.7\times10^6$ meters/henry, and d is the diameter of the cylinder in meters. This result is in accord with Meissner *et al.*[3]

The flux increase observed seems to arise from the circular component of the current and we would say that Meissner, Schmeissner, and Meissner[3] had proved this with an experiment in which they cut a slot in their cylinder thereby making such circular currents impossible and thereby destroying the effect. In Fig. 7 we show the cylinder with the field produced by the external solenoid B and the field produced by a straight through current, B_φ. The force on an electron moving with velocity v_f along the Z axis will tend to push it inward along the radius r. The velocity so acquired will then cause ($\mathbf{F}=ev_r\times\mathbf{B}$) the electron to be pushed with a force orthogonal to these and hence might produce a helical flight path for the electron. But this is not too convincing and we must look for a more complete theory.

How many turns must a certain current make per unit length in order to produce the observed maximum flux? In our work (Fig. 2) a current of 7.2 amperes

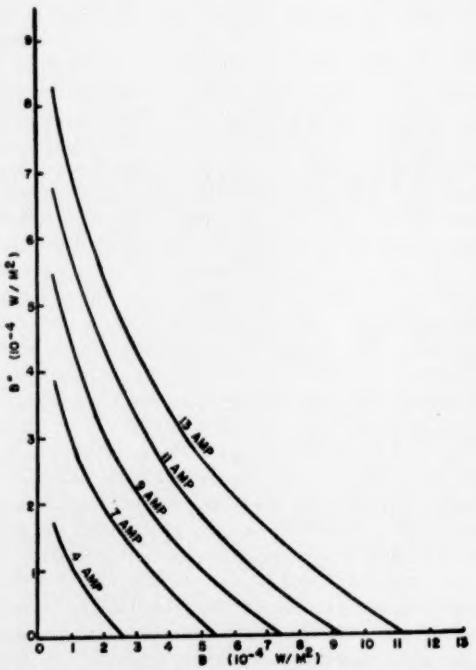

FIG. 5. Field produced in tin at maximum of "paramagnetic effect" *vs* external field and for several currents.

produced a $B''=3.7\times10^{-4}$ weber/m^2 by making 0.363 turns/cm, i.e., a total of 2.43 turns in passing through the tin specimen. The value of B'' is assumed constant over the specimen cross section to make up the observed flux. Likewise, we say the current is all on the surface of the tin. Now for a free electron the cyclotron angular velocity is $\omega=(e/m)B'$. So in the above example, with $B'=4.7\times10^{-4}$ weber/m^2, we have $\omega=8.3\times10^7$ rad/sec$=1.32\times10^7$ rev/sec. It will be recalled that in this example the external field B was 1×10^{-4} weber/m^2. The number of revolutions made by an electron traveling from one end of the tin specimen to the other (6.7 cm in the apparatus of Fig. 1) then depends upon the time of flight. If the electrons suffered no collisions, corresponding to a mean free path of the length of the tin specimen, then this time could be $t=6.7/v_f$,

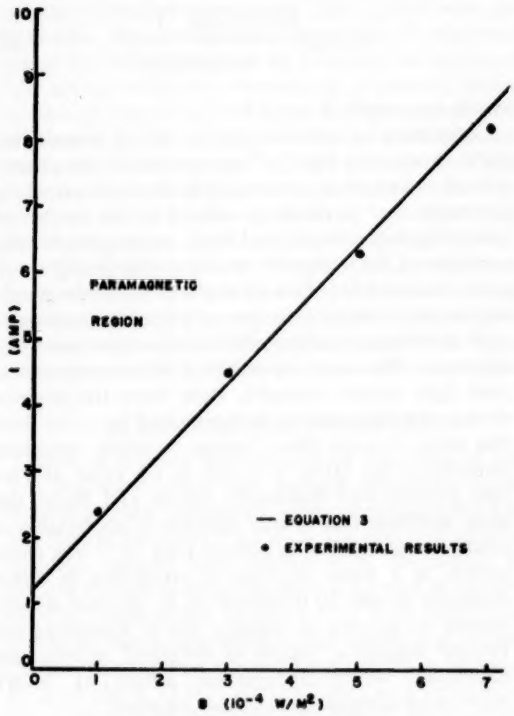

FIG. 6. Threshold for "paramagnetic effect."

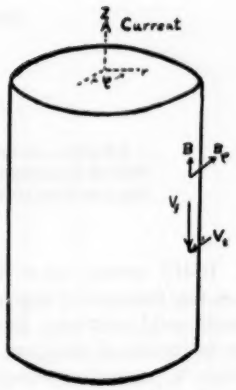

FIG. 7. The cylinder of tin showing possible velocity components of the electron in steady flight.

where v_f is the velocity of the electrons at the top of the Fermi distribution. This velocity is of the order of 10^8 cm/sec so that the electrons would make about 0.9 turn. This would agree exactly with our experimental value (2.4) if we choose a slightly slower velocity for v_f. Such a mean free path is acceptable for a superconductor, but it is too large by a factor of 10^5 for tin in the normal state at 4.2°K. The orbit of the electron has a radius given by: $R=v_t/\omega$, where v_t is the tangential velocity to the circular motion. If this is 2×10^7 cm/sec, a reasonable value, then the electron flight path easily fits inside the specimen used in our work. The above crude numerical relationships are in sore need of theoretical justification.

CONCLUSION

The experiments reported in this paper have been carried out in such a way as to remove difficulties and objections to earlier experiments. There is certainly an interesting flux increase just as the tin specimen passes out of the pure superconducting state. There is need for a clear theoretical treatment of the effect.

The authors are indebted to Professor W. Meissner, Dr. H. Meissner, and to Dr. K. Mendelssohn for stimulating discussions. We wish also to thank several colleagues at The Rice Institute, in particular Professor W. V. Houston, for assistance. The research was supported in part by a grant from the National Science Foundation.

Light Output of Luminescent Plastics

W. A. THORNTON
General Electric Research Laboratory, Schenectady, New York
(Received May 7, 1954)

Efficiency of transfer of excitation energy from solvent to solute in a luminescent plastic solid solution is derived and compared to a previously published expression. Capture cross-section ratios and the nature of the quenching parameter are discussed.

LIGHT output, as a function of concentration of the fluorescent organic molecule in luminescent plastic solid solutions, involves energy transfer from the molecules of the base material to those of solute which is present, generally, in small concentrations. Swank and Buck[1] have shown that polystyrene, for instance, has a considerable probability of emission in the ultraviolet when excited by the passage of a charged particle, and that this radiation is quite completely absorbed by small concentrations of the solute molecule. They have shown also that nonradiative transfer is important.

Initially, a particle-induced excitation of a solvent molecule to a state from which transfer of the excitation energy can take place occurs; the efficiency of this initial excitation is low. Given such an excitation, the efficiency of energy transfer from solvent to solute in these materials, both by reabsorption of ultraviolet emission by the solvent and by some nonradiative process, is therefore given by

$$\eta_t=(p_{t(em)}+p_{t(nr)})/(p_{t(em)}+p_{t(nr)}+p_q),$$

where the p's are relative probabilities of (a) transfer by emission of the solvent, (b) nonradiative transfer, and (c) quenching in the solvent, respectively. Capture of a migrating quantum of excitation energy occurs with a relative probability $\sigma_0(1-c)$, where σ_0 is the cross section for capture by the solvent molecule and c is the concentration of solute. Probability of emission by the solvent, to which the probability for radiative transfer to the solute is equal in the presence of complete absorption by the solute, is then $q_0\sigma_0(1-c)$, where q_0 is the quantum efficiency of emission by the solvent. That is,

$$p_{t(em)}=p_{em}=q_0\sigma_0(1-c).$$

Nonradiative transfer probability (capture by the solute) is given by $p_{t(nr)}=\sigma c$, where σ is the capture cross section of the solute molecule. Therefore,

$$\eta_t=\frac{q_0\sigma_0(1-c)+\sigma c}{q_0\sigma_0(1-c)+\sigma c+(1-q_0)\sigma_0(1-c)}. \tag{1}$$

The fraction of "nonadjacent" solute molecules capable of emission, assuming solute self-quenching takes place over a certain radius, is given by Johnson and Williams[2] as $(1-c)^z$, where z is the number of neighboring quenching sites. The transfer efficiency to effective solute molecules is then $\eta_t(1-c)^z$. If the approximations $(1-c)^z\approx(1+zc)^{-1}$ and $(1-c)\approx 1$ are made, the effective transfer efficiency, to which the light output will be proportional, is given by

$$\eta_{t(eff)}\cong\frac{q_0+(\sigma/\sigma_0)c}{1+(\sigma/\sigma_0)c}\,\frac{1}{1+zc} \tag{2}$$

within ten percent if $zc\leq 0.5$.

Comparison of this relation to (9) of Swank and Buck[1] shows that their "σ" corresponds to the present ratio of capture cross sections, while their self-quenching parameter "m" is evidently related to the number of quenching sites z. Swank and Buck report good fit with a relation of the form of (2) above to data on light output *vs* concentration of a number of solutes. Their quenching parameter varies from zero to 100, corresponding to radii of strong quenching effects up to three molecular diameters. The mean separation of solute molecules at peak light output is roughly three times the range of strong quenching effects, as determined by z; therefore this range is more like a radius at which quenching probability has fallen to $1/e$th of its value at $r=0$ (see Johnson and Williams[3]). Swank and Buck[1] also show evidence that energy transfer is appreciable at solute concentrations no greater than 10^{-6}; this corresponds to a mean distance of separation of solute molecules of near 50 diameters or, in the case of polystyrene as solvent, of roughly 300 A. Ehrenberg and Franks[4] suggest a "length of diffusion" of some undetermined energy-transporting agents as several microns for a luminescent plastic material.

Finally, although Johnson and Williams[5] suggest that in the case of certain luminescent liquid solutions (where q_0 is approximately zero) the ratio σ/σ_0 is roughly a constant of the solvent, the data of Swank and Buck[1] on plastics show a range of σ/σ_0 from zero to 700 for a number of solid solutions with polystyrene the base material and indicate strong dependence upon the solute.

[1] R. K. Swank and W. L. Buck, Phys. Rev. **91**, 927 (1953).
[2] P. D. Johnson and F. E. Williams, J. Chem. Phys. **18**, 323 (1950).
[3] P. D. Johnson and F. E. Williams, J. Chem. Phys. **18**, 1477 (1950).
[4] W. Ehrenberg and J. Franks, Proc. Phys. Soc. (London) **B66**, 1057 (1953).
[5] P. D. Johnson and F. E. Williams, Phys. Rev. **81**, 146 (1951).

Afterglow of Magnesium Oxide Single Crystals

EISO YAMAKA
Electrical Communication Laboratory, Tokyo, Japan
(Received December 28, 1953; revised manuscript received June 8, 1954)

Magnesium oxide single crystals have been irradiated with ultraviolet light at room temperature and the glow curves and accompanying electric current recorded simultaneously from room temperature to 300°C. The measurements of optical absorption show the disappearance of absorption bands in visible region. Trap depths of the luminescent centers are given.

I. INTRODUCTION

MAGNESIUM oxide is a useful material for studying electronic processes in divalent ionic crystals, since it has the advantages of being available in large single crystals, of being very inert, and, moreover, of having a simple body-centered cubic lattice with good cleavage. The fundamental properties of magnesium oxide are well known,[1] but its photoconducting properties are not sufficiently understood at present, because of its high resistivity. In recent years the measurements of its optical absorptions, produced by irradiation with ultraviolet light,[2] x-rays,[3] and by coloring with magnesium and oxygen,[4] have been performed. Also measurements of the photoconductivity associated with optical absorption have been recently carried out.[5]

In the present work the afterglow and accompanying electric current of single uncolored and colored crystals are measured in order to study the electronic processes in magnesium oxide. The disappearance of absorption bands associated with luminescence will be mentioned briefly.

II. EXPERIMENTAL PROCEDURE

Most of samples were cleaved on the order of one-half millimeter thick and one-half centimeter square from large clear (uncolored) single crystals supplied by the Norton Company.[6] To study the effects of additive coloring, samples were colored with magnesium by heating them in magnesium vapor in a vessel of stainless steel at temperatures of about 1250°C to 1300°C for one hour (magnesium colored) and colored with oxygen by heating them in a stream of dry oxygen at temperatures of about 1300°C for two hours at a pressure of about one atmosphere (oxygen colored). Spectroscopic analysis revealed no impurities other than calcium (smaller than 0.1 percent). Conducting coatings of gold were sputtered on both sides of the plates.

The light emitted was received by a 1P21 R.C.A. photomultiplier tube followed by two Horton type dc amplifiers[7] and a recorder. A cesium-silver oxide photocell, with a 10^{11} ohm resistor, a UX-54 electrometer tube, and a dc amplifier, was also used because of its high sensitivity for the bitter orange luminescent light. In order analyze the wavelength distribution of the light emitted, a Corning 3–68 filter which transmits light above 5600A was interposed. The electrical current associated with luminescence was measured simultaneously with a 10^{11} ohm resistor and electrometer tube followed by a dc amplifier and recorder. Space-charge effects might be negligible because of the small current. The samples were warmed up at a constant rate of 5°C per minute which was so slow that a good resolution was obtained, except for temperatures below 35°C. The luminescent light entered a electrically shielded box containing the photomultiplier through a window of fused quartz on the top of the box. The temperatures were measured with chromel-alumel thermocouple which was in contact with the sample. The block diagram of the apparatus is shown in Fig. 1.

The plates were colored by irradiation with x-rays (50-kv, 10-ma, tungsten target) and unmonochromized mercury discharge light at room temperature. Both sources, however, gave the same glow and conduction curves in the temperature range studied, so that the latter was used mainly because of convenience. Saturation of coloration was obtained in about half an hour. Both glow and conduction curves obtained were reproducible.

III. RESULTS

(a) Afterglow and Accompanying Charge Conduction

The data for uncolored crystal are shown in Fig. 2. The solid curves of lower and higher intensity are the

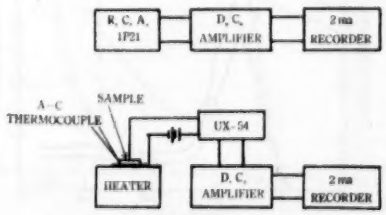

FIG. 1. Block diagram of the apparatus.

[1] See for example, F. Seitz, *The Modern Theory of Solids* (McGraw-Hill Book Company, Inc., New York, 1940).
[2] J. H. Hibben, Phys. Rev. **51**, 530 (1937).
[3] J. P. Molnar and C. D. Hartman, Phys. Rev. **91**, 1015 (1950).
[4] H. Weber, Z. Physik **130**, 392 (1951).
[5] H. R. Day, Phys. Rev. **91**, 822 (1953).
[6] The Norton Company, Niagera Falls, New York. Appreciation is expressed to the Norton Company for making this work possible.
[7] J. W. Horton, J. Franklin Inst. **216**, 749 (1933).

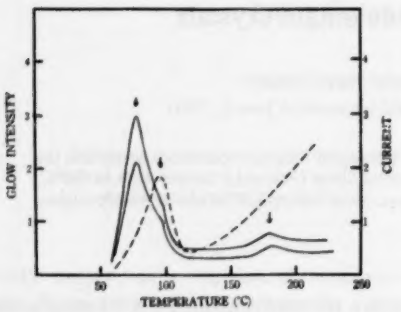

FIG. 2. Glow curves and conduction curve for uncolored crystal. The solid curve of lower and higher intensity are the glow curves obtained with and without a Corning 3–68 filter, which transmits light above 5600 A, interposed between the crystal and phototube. The dotted curve shows the conduction current recorded simultaneously.

glow curves obtained with and without the Corning filter interposed. The shape of the curves is not altered by transmission through the filter, but the intensity is decreased about one-quarter. The dotted curve shows the conduction current. It is seen that the second peak of the glow curve (95°C) is accompanied by a peak in the electric current, but the first (77°C) and third (180°C) peaks are not. The gradual rise in the conduction curve might be caused by the current from an impurity level, as described later.

The glow and conduction curves for magnesium colored crystals, shown in Fig. 3, are almost the same of those for uncolored crystals below 150°C, except a small hump (65°C) in the glow curve of magnesium-colored crystals. However, there is no peak at 180°C in the glow curve, but a peak at 20°C, accompanied with large conduction current.

Finally the glow and conduction curves of oxygen colored crystals, shown in Fig. 4, are different from those of uncolored ones, since the peak at 95°C disappears in the glow and conduction curves, and the peak at 180°C in the glow curve becomes large. The various peaks in the glow and conduction curves are summarized in Table I.

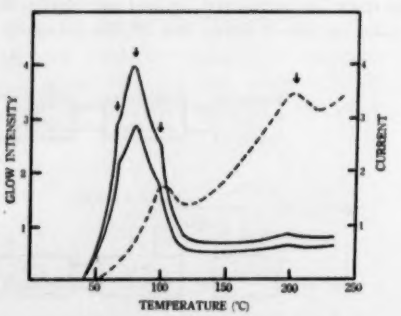

FIG. 3. Glow and conduction curves for the magnesium-colored crystal.

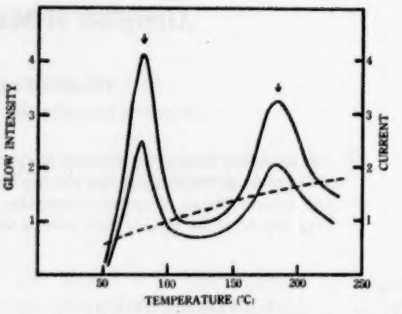

FIG. 4. Glow and conduction curves for the oxygen-colored crystal.

(b) Conductivity of Uncolored Crystals

The gradually increasing background in the conduction curve in Figs. 2, 3, and 4 was also found without irradiation with ultraviolet light. Measurements of conductivity against temperature were carried out in order to study its origin. A plot of current *vs* $1000/T$(°K) for the uncolored crystal, measured with a UX-54 electrometer tube, has a slope of 2.1 ev in the higher-temperature range and of 0.58 ev in the lower-temperature range as shown in Fig. 5. The background in the conduction curve may be attributed to carriers originating from an impurity level which has the value 1.16 ev for the activation energy.

(c) Disappearance of Absorption Bands

Disappearance of the absorption bands associated with luminescence was measured by the following manner. The absorption of the irradiated crystal was measured, first at room temperature, and again at

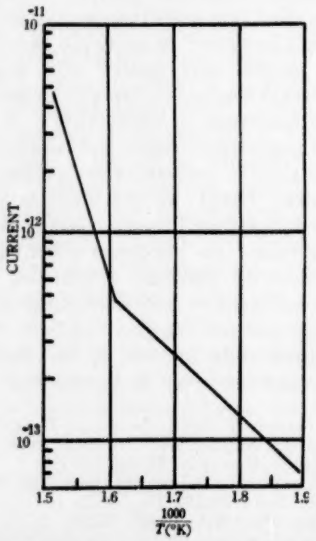

FIG. 5. Current *vs* $1000/T$ for the uncolored crystal.

room temperature after the crystal had been warmed momentarily to some higher temperature which corresponded with a peak in the glow curve. A succession of such measurements was made at temperatures corresponding to the various peaks after a definite duration of irradiation. The absorption curves of uncolored and colored samples without irradiation are shown in Fig. 6. It is seen that the uncolored clear samples show appreciable absorption in the ultraviolet range before coloring with oxygen and also that the magnesium-colored samples show slight absorption in that range. The additional absorption produced by irradiation with ultraviolet light in all samples occurred in the visible region without remarkable peaks. Momentary warming to about 100°C mainly decreased the band at 5200 A which was produced by additive coloring with magnesium, as shown in Fig. 7, but the differences of variation of absorption bands between the samples of three types and the correspondence with various peaks in the glow and conduction curves could not be deduced because of the broad absorption band in the visible region.

TABLE I. Summary of various peaks in the glow and condition curves.

temp. °C of peaks ν		65	77	95	180	200
trap depth (ev)	$s=10^{6}$	0.56	0.59	0.62	0.77	0.88
	$s=10^{10}$	0.82	0.85	0.90	1.12	1.17
	$s=10^{12}$	0.95	0.99	1.04	1.29	1.35
uncolored	glow		○	○	○	
	cond.			○		
magnesium-colored	glow	○	○	○		○
	cond.			○		○
oxygen-colored	glow		○		○	
	cond.					

IV. DISCUSSION OF RESULTS

The energies required for electrons or holes to move from their traps to luminescent centers are related to the temperatures at which the peaks of the glow curves occur. Trap depths E for the peaks are computed by the following formula from Randall and Wilkins:[8]

$$E=kT\log S\{1+\log(kT^2/\beta E)/\log S\},$$

where β is the constant warming rate. Unfortunately the frequency S, the "attempt-to-escape" frequency, is not known accurately and, moreover, we could not estimate it from an experiment like that of Randall and Wilkins, because various curves were superimposed and could not be separated by the filter. If we assume that S is 10^{6}, 10^{10} and 10^{12} sec^{-1}, the values in Table I are obtained.

[8] J. T. Randall and M. H. F. Wilkins, Proc. Roy. Soc. (London) **A184**, 366 (1945).

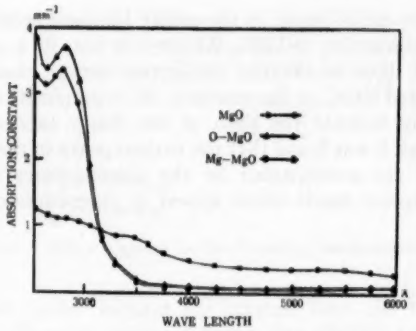

FIG. 6. Absorption curves for the uncolored, magnesium-, and oxygen-colored crystal. No correction for surface reflection is made.

Trap depths of the peaks in the glow curves that corresponded to peaks in the conduction curves represent the energy of a level below the conduction band that yields an electron to the conduction band, or a level above the filled band that yields a hole to the filled band. However, the derivation of the electronic model of the luminescent processes from this simple assumption seems to be hasty. Day[5] has concluded from his measurements of photoconductivity that the photocurrent associated with the absorption bands which appear in magnesium-colored crystal was carried by holes. Furthermore he concluded that these optical transitions measure the energy of the localized levels above the filled band. This view seems to be different from that usually accepted. On the other hand, it is possible that the localized level in a divalent crystal which contains excess positive ions is so far below the conduction band that electrons in the filled band

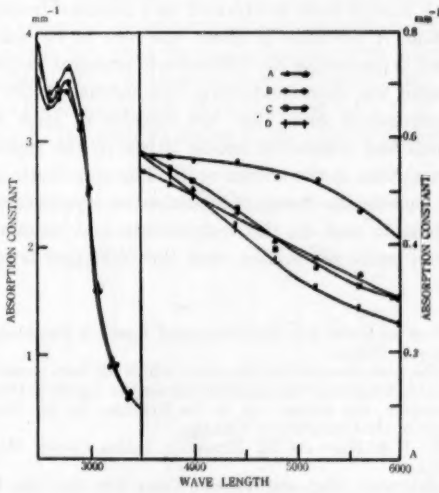

FIG. 7. (A) Absorption curve before irradiation with ultraviolet light; (B) after irradiation for 90 minutes; (C) after warming at 107°C for 3 minutes; (D) after warming at 210°C for 3 minutes.

can be easily raised to the empty localized levels with the absorption of light. Whether or not, in a case of MgO, hole or electron conduction occurs cannot be deduced since, at the moment, the experiments do not clearly indicate the signs of the charge carriers. Although it was found that the various peaks in the afterglow are accompanied by the disappearance of the absorption bands which appear in magnesium-colored crystals, the determination of the electronic model of the luminescent processes requires more experiments.

Acknowledgment should be given to Mr. T. Ichimiya and Mr. T. Shindo for their encouragement during these investigations. We wish to thank Mr. O. Mikami and Mr. K. Sawamoto and Mr. I. Mitsufuji for the measurements of optical absorption and spectroscopic analysis.

PHYSICAL REVIEW VOLUME 96, NUMBER 2 OCTOBER 15, 1954

Elastic Moduli of Tin at the Superconducting Transition

JOSEPH K. LANDAUER*
Physics Department,† The University of Chicago, Chicago 37, Illinois
(Received April 15, 1954)

A composite oscillator technique was used to measure the elastic moduli of tin in the normal and superconducting states. The experiments were performed on single crystals at about 50 kc/sec. A difference in moduli was observed, indicating that the velocity of sound is less in the superconducting than in the normal state. At 3.7°K the relative change at the superconducting transition is about 4 parts in 10^6 for the longitudinal modulus S_{11} and about 6 parts in 10^6 for the torsional modulus, $2(S_{44}+S_{66})$. These relative changes increase with decreasing temperature. At room temperature, the adiabatic modulus S_{11} was found to be 1.55×10^{-12} cm²/dyne, and $2(S_{44}+S_{66})$ was 9.4×10^{-12} cm²/dyne.

I. INTRODUCTION

MANY experiments have been carried out that indicate no change in elastic properties of tin at its superconducting transition.[1–3] Nevertheless, a change of approximately one part in 10^5 is predicted by thermodynamics.[4] An experimental determination was undertaken with sufficient accuracy to verify this change. Tin was used as the superconducting material, and the elastic moduli were determined by a resonant frequency method. A precision of about one part in 10^6 was obtained in measuring the difference in resonant frequency between the superconducting and normal states. The measurements show that the velocity of both longitudinal and transverse sound is less in the superconducting than in the normal state. The magnitude of the relative velocity change is dependent on crystallographic orientation and on the temperature and amounts to several parts per million near the transition temperature.

II. EXPERIMENTAL TECHNIQUES

The elastic moduli were determined by a composite oscillator technique using a single-crystal cylinder of tin glued coaxially to a piezoelectric quartz crystal.[5] The resonant frequency of the composite was compared with the frequency of a second quartz crystal which served as a standard. By using similar quartz crystals and by carefully adjusting the length of the tin crystal, a small difference in frequency was obtained between the standard and the composite. This difference in frequency was measured in both the normal and superconducting states. The change in the difference frequency was used to calculate the change in the elastic moduli of the tin. This method eliminated the need for an accurate determination of the absolute frequency.

A schematic diagram for the frequency measurement is shown in Fig. 1. Both the composite and standard quartz crystals were in a vacuum enclosure in the helium cryostat. Each was connected to a separate amplifier immediately at the top of the cryostat. The crystals served as filter elements[6] in the positive feedback loops of the amplifiers. The oscillators, thus formed, operated at approximately the resonant frequencies of the crystals. The two oscillator frequencies were mixed and filtered to give the difference frequency,

* Now at Snow, Ice, and Permafrost Research Establishment, Wilmette, Illinois.

† The work described in this paper, which has been presented in partial fulfillment of the requirements for the degree of Doctor of Philosophy, was carried out in the Institute for the Study of Metals of the University of Chicago.

[1] W. J. de Haas and M. Kinoshita, Leiden Comm. No. 187b (1927).

[2] McLennan, Allen, and Wilhelm, Trans. Roy. Soc. Can. III 25, 13 (1931).

[3] H. Bommel and J. L. Olsen, Phys. Rev. 91, 1017 (1953).

[4] D. Shoenberg, *Superconductivity* (Cambridge University Press, Cambridge, 1952), p. 76.

[5] S. Quimby, Phys. Rev. 25, 558 (1925).

[6] W. G. Cady, *Piezoelectricity* (McGraw-Hill Book Company, Inc., New York, 1946), p. 491.

TABLE I. Orientation of the tin crystals. The angles are given between the casting axis and the X, Y, and Z directions of the unit cell.

Crystal	Orientation (degrees) X	Y	Z
1	(a axis about 1 degree from casting axis)		
2	8.0	4.5+90	6.0+90
G1	3.8	0.8+90	3.4+90
G5a	28.2	28.0+90	3.5+90

which was measured by counting the number of cycles in a given time with a scaler and clock.

Figure 2 is the circuit diagram for the oscillators. The amount of positive feedback was controlled by a potentiometer and during operation was adjusted to as low a value as possible, still allowing oscillation. The mixer was conventional, using a 6L7 pentagrid mixer tube. The output was fed to a scaling circuit. The frequency was measured by gating the scaler with an integer minute signal. This signal was obtained by an appropriate relay system from an accurate pendulum clock.

Single crystals of tin were used for all experiments. The tin was degassed in high vacuum and cast in 0.187-in. i.d. precision bore Pyrex tubing and had a measured purity of better than 99.99 percent. The crystals were grown by lowering through a gradient furnace. Orientation was determined by x-ray analysis, using the back reflection Laue technique. Data on the crystals used are compiled in Table I. Crystals *G1* and *G5a* were from the same batch of tin but were grown individually. *G1a'*, *G1b*, and *G1c* were cut from *G1* and therefore have the same orientation.

Two sets of piezoelectric quartz crystals were used (see Table II). Each set was made up of two crystals of approximately equal frequency, one used as frequency standard and the other as driver of the composite oscillator. One set consisted of x-cut crystals vibrating longitudinally at about 58.7 kc/sec, and the other set consisted of y-cut crystals vibrating torsionally at about 41.1 kc/sec. (These were relapped later to 42.45 kc/sec.) The crystals were circular cylinders of 0.472-cm diameter.

The cryostat was of standard design, consisting of coaxial helium and nitrogen Dewars (see Fig. 3). A

TABLE II. The quartz crystals. The approximate frequency of the crystal set and the frequency difference between the two crystals in the set are indicated.

Crystal set	Mode	Length cm	Approximate frequency kc/sec	Frequency difference cps
1	Longitudinal	4.643 4.699	58.7	10
2	Torsional	4.77 4.80	41.22	80
2'	Torsional	4.595 4.654	42.45	25

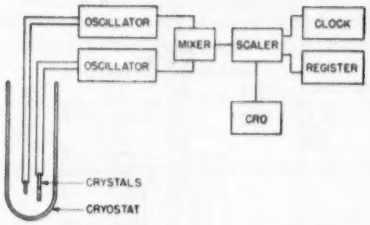

FIG. 1. Block diagram for the frequency measurement.

crystal holder isolated the crystals from the helium bath. Thermal contact between the crystals and the bath was obtained by use of about 0.1 mm Hg helium exchange gas. A pair of Helmholtz coils in the nitrogen Dewar provided a magnetic field coaxial with the crystals.

The Q, defined as usual as the ratio of inductive reactance to resistance, is a measure of the reciprocal of the damping of a crystal. The Q's of the composite and standard quartz crystals were determined by decay time experiments and measurements of the crystal currents at series and parallel resonance.[7] The high Q necessary for good frequency stability was produced by careful lapping, plating, cleaning of the crystals, and operation at low temperatures and pressures. The Q's obtained were about 2×10^6.

The error in measurement of the change in elastic modulus was composed of errors in the frequency and temperature measurements and fluctuations in the operating frequencies of the oscillators due to finite Q. The error in the frequency measurement was due to errors in timing and counting and with typical values amounted to about 4 parts in 10^7. The temperature was determined by the vapor pressure of the helium bath using the Shoenberg and van Dijk conversion scale.[8] The error due to temperature measurement is less than 2 parts in 10^7. Thus the total calculable error is less than 5 parts in 10^7. The observed errors of about 1 part in 10^6 are of the magnitude to be expected for a Q of about 2×10^6. The limiting factor in the accuracy, therefore,

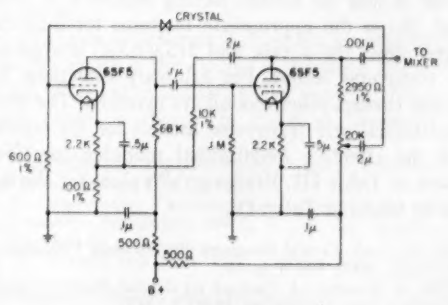

FIG. 2. Oscillator circuit.

[7] A. W. Lawson, Phys. Rev. **60**, 330 (1941).
[8] D. Shoenberg and H. van Dijk, Nature **164**, 151 (1949).

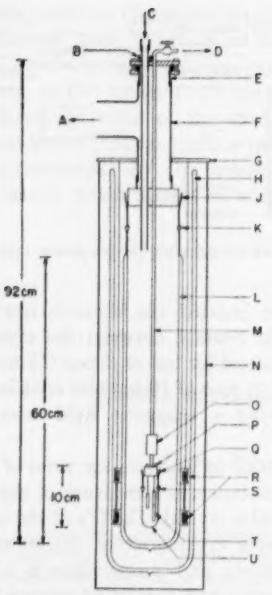

FIG. 3. The cryostat. (*A*) To Kinney pump and helium return line. (*B*) Kovar-glass terminals. (*C*) Helium transfer tube inlet. (*D*) High vacuum. (*E*) 2-in. i.d. Cu–Ni. (*F*) 2-in. i.d. Cu. (*G*) ¾-in. brass plate. (*H*) Nitrogen dewar. (*J*) Rose's Metal joint. (*K*) Cu-glass seal. (*L*) Helium Dewar. (*M*) ½-in. Cu–Ni pumping tube. (*N*) Brass can. (*O*) Radiation trap. (*P*) Kovar-glass terminals. (*Q*) Rose's Metal seal. (*R*) Helmholtz coils. (*S*) Cu-glass seal. (*T*) Crystals. (*U*) Crystal holder.

is assumed to be due to the finite Q, and the indicated errors were calculated from the observed deviations.

The error in the absolute elastic moduli was introduced by uncertainty in the orientation of the tin crystals and amounted to about one percent.

III. THEORETICAL CALCULATIONS

(a) The Elastic Moduli of Tin

Tin has a tetragonal structure, and its elastic properties can be specified by six elastic moduli Sij.[9,10] If Wooster's notation[11] which differs from Voigt's[12] by a factor of four for moduli having indices 4, 5, and 6 is used, S_{11} is the appropriate modulus for longitudinal sound along the a axis, and $2(S_{44}+S_{66})$ is appropriate for transverse sound. For arbitrary directions in the crystal various other moduli are involved. The effective longitudinal and transverse moduli for tin crystal *G*1 and the effective longitudinal modulus for *G5a* are shown in Table III. Bridgman's[13] values for the moduli can be found in Table IV.

[9] R. Wyckoff, *Crystal Structures* (Interscience Publishers, Inc., New York, 1948), Vol. 1, p. 13.
[10] W. A. Wooster, *A Textbook on Crystal Physics* (Cambridge University Press, Cambridge, 1938), p. 243.
[11] See reference 10, Chapter III.
[12] W. Voigt, *Lehrbuch Der Kristallphysik* (B. G. Teubner, Leipzig, 1928).
[13] P. W. Bridgman, Proc. Nat. Acad. Sci. U. S. **10**, 411 (1924).

(b) The Change in the Elastic Moduli

The relationship between the resonant frequency of the composite and that of the tin can be specified and becomes quite simple under the experimental conditions used. The resonant frequency of the tin crystal is related to the resonant frequency of the composite oscillator and the quartz driver frequency by the equation:[14]

$$M_t f_t \tan(\pi f_c/f_t)+M_q f_q \tan(\pi f_c/f_q)=0, \qquad (1)$$

where M is the mass, f the resonant frequency, and t, q, and c refer to the tin, quartz, and composite, respectively.

The resonant frequency of the tin crystal is related to its length L, its density ρ, and the appropriate elastic modulus S by

$$f_t=[2L(\rho S)^{\frac{1}{2}}]^{-1}. \qquad (2)$$

A change in the frequency of the tin could be attributed to a change in either modulus or length. It can be seen from Eq. (8) (using the values in Table IV) that the change in volume at the transition is less than one part in 10^7. Since the observed change in resonant frequency is greater than several parts in 10^6, the size effect can be neglected, and the cause of the change can be attributed to a change in the modulus.

Under the conditions of the experiment, the composite, tin, and quartz frequencies are approximately equal, and all changes are small. Combining Eqs. (1) and (2) and neglecting small terms, we find the relative change in modulus to be related to the change in composite frequency by

$$\Delta S/S=-2(1+M_q/M_t)\Delta f_c/f_c. \qquad (3)$$

(c) The Thermodynamics of the Transition

An estimate of the change in compressibility at the superconducting transition can be made using thermodynamics and some previously measured quantities. Along the transition curve, the Gibbs free energy per mole G^s in the superconducting state is equal to the free energy G^n in the normal state. The difference in free energy for $H=0$ is[15]

$$G^n-G^s=\Delta G=(1/8\pi)V_m H_c^2, \qquad (4)$$

TABLE III. Effective moduli for the tin crystals.

Crystal	Modulus	Effective modulus
*G*1	S_{11}	$0.991S_{11}+0.001(S_{44}+S_{66})$ $+0.007S_{13}+0.013S_{44}$
*G*1	$2(S_{44}+S_{66})$	$0.996\times2(S_{44}+S_{66})-0.014S_{44}$ $+0.007(S_{11}+S_{33}-2S_{31})$
G5a	S_{11}	$0.652S_{11}+0.016(S_{44}+S_{66})$ $+0.668S_{66}+0.342S_{12}+0.008S_{13}$

[14] L. Balmuth, Phys. Rev. **45**, 715 (1937), p. 716, Eq. (**14**).
[15] See reference 4, p. 73.

where H_c is the critical magnetic field and V_m is the molar volume. The critical field is related to the temperature, to good approximation, by $H_c=H_0(1-t^2)$, where H_0 is the critical field at absolute zero and $t=T/T_c$ is the reduced temperature. Equation (4) becomes

$$\Delta G=(1/8\pi)V_mH_0^2(1-t^2)^2. \quad (5)$$

The difference in the specific heats per mole, calculated from Eq. (5), is equal to

$$\Delta C_p=(1/2\pi T_c^2)V_mH_0^2(T-3T^3/T_c^2), \quad (6)$$

where some very small terms have been neglected.

It can be shown from the electron theory of metals that the specific heat in the normal state contains a term linear with the temperature.[16] Its coefficient γ is proportional to $V_m^{\frac{1}{3}}$.[17] Identification between γ and the linear term in Eq. (6) is made. In what follows this assumption amounts to neglect to the pressure dependence of the effective mass of the electrons. Equation (5) can be rewritten

$$\Delta G=(1/4)\gamma T_c^2(1-t^2)^2. \quad (7)$$

The difference in volume, expansion coefficient α, and the isothermal compressibility χ_T, can be calculated from Eq. (7). Near $t=1$, the following hold approximately:

$$\Delta V=(1/2)\gamma T_c\beta(1-t^4); \quad (8)$$

$$\Delta\alpha=-2\gamma t^3\beta/V_m; \quad (9)$$

and

$$\Delta\chi_T=-(1/2V_m)\gamma[\beta^2(1+3t^4)+T_c(1-t^4)(d^2T_c/dP^2)_T]; \quad (10)$$

TABLE IV. Thermodynamic values for tin.

Quantity	Value	Remarks	Reference
C_p	0.0053 cal/mole/deg	Normal state at T_c	a
C_p	0.0078 cal/mole/deg	Superconducting state at T_c	a
χ_S	10^{-13} cm²/dyne	Estimated at T_c	b
S_{11}	1.85×10^{-13} cm²/dyne	Bridgman's isothermal	b
S_{33}	1.18×10^{-13} cm²/dyne	Values for room	b
S_{44}	1.42×10^{-13} cm²/dyne	Temperature using reference 13	b
S_{12}	-0.99×10^{-13} cm²/dyne	Wooster's notation	b
S_{13}	-0.25×10^{-13} cm²/dyne		b
S_{66}	3.38×10^{-13} cm²/dyne		b
V_m	16.3 cc/mole		c
T_c	3.72 deg K	From this experiment	
α	5.6×10^{-5} deg^{-1}	Calculated from Grueisen's law. α and C_p from reference 21	c
$\Delta\alpha$	5.7×10^{-5} deg^{-1}	Calculated from Eq. (9′)	
dH_c/dT	−147 gauss/deg	At T_c	d
dT_c/dP	-3.3×10^{-11} deg/(dyne/cm²)	Revaluated to 95 kg/cm²	e
γ	1.4×10^4 erg deg^{-2} mole^{-1}		f

[a] See reference 20.
[b] See reference 13.
[c] See reference 21.
[d] See reference 22.
[e] See reference 23.
[f] See reference 17.

[16] F. Seitz, *The Modern Theory of Solids* (McGraw-Hill Book Company, Inc., New York, 1940), p. 152.
[17] F. London, *Superfluids* (John Wiley and Sons Inc., New York, 1950), Vol. 1, p. 24.

TABLE V. The adiabatic elastic moduli. The units are 10^{-12} cm²/dyne. The Bridgman values are for room temperature.

Modulus	Absolute temperature 3.7	78	194	295	Bridgman
S_{11}	1.34	1.37	1.45	1.55	1.73
$2(S_{44}+S_{66})$	5.79	6.0		9.4	9.6

where

$$\beta=(dT_c/dP)_T.$$

At $t=1$, these reduce to

$$\Delta V=0, \quad (8')$$

$$\Delta\alpha=-2\gamma\beta/V_m \quad (9')$$

and

$$\Delta\chi_T=-2\gamma\beta^2/V_m. \quad (10')$$

Similar results could have been obtained directly from Eq. (5) by neglecting certain of the derivatives. Using the values from Table IV we find the change in isothermal compressibility at $t=1$ to be $\Delta\chi_T=-1.9\times10^{-13}$ cm²/dyne.

A calculation based on a formula of Zener's[18] shows that the moduli of tin are essentially adiabatic at the frequency and temperature used. The change in adiabatic compressibility should therefore be calculated and compared with the experimental results. The relationship between the two compressibilities is[19]

$$\chi_S=\chi_T-\alpha^2TV_m/C_p. \quad (11)$$

By making use of the above equations and values in Table IV,[13,17,20–23] it is found that the adiabatic compressibility at $t=1$ is less in the normal than in the superconducting state by $\Delta\chi_S=-4.1\times10^{-13}$ cm²/dyne.

(d) The Effect of Damping on the Resonant Frequency of the Tin

The resonant frequency of a circuit is dependent on the degree of damping. It is necessary to show that the observed change in frequency of several parts in 10^6 is larger than that to be expected from any possible change in damping, which could amount to, at the most, several percent.

Two effects due to change in damping are considered. The smaller effect is the change in resonant frequency of the tin. For a Q of 2×10^5, a five percent change in damping causes a change in resonant frequency of

[18] C. Zener, *Elasticity and Anelasticity of Metals* (University of Chicago Press, Chicago, 1948), p. 90.
[19] E. A. Guggenheim, *Thermodynamics* (North Holland Publishing Company, Amsterdam, 1949), p. 100, Eq. (4.24.6) and p. 102, Eq. (4.26.6).
[20] W. H. Keesom and J. A. Kok, Leiden Comm. No. 221e (1932).
[21] *International Critical Tables* (McGraw-Hill Book Company, Inc., New York, 1933), Vol. 1, p. 104.
[22] E. Maxwell, Phys. Rev. **86**, 235 (1952).
[23] G. J. Sizoo and H. Kamerlingh Onnes, Leiden Comm. No. 180b (1925).

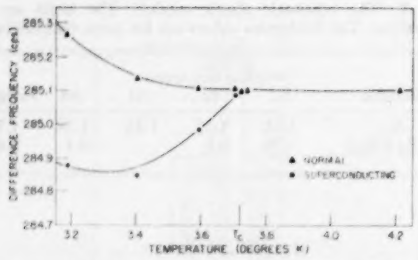

FIG. 4. Isothermal experiments, I. The difference in frequency between the composite oscillator and the standard longitudinal quartz crystal is shown for tin *G5a*. Below T_c values for the normal state were obtained by use of a sufficiently strong magnetic field.

about one part in 10^{10}. The second effect is in connection with change in operating point of the oscillator. Because the amplifier and crystal leads introduce a phase shift, the crystal oscillates sufficiently off resonance to make a total phase shift of zero. The further the crystal is off resonance, the more the frequency changes for a given change in damping. A calculation of this effect shows that a five percent change in Q leads to a relative frequency change of 2×10^{-8}. One would not, therefore, expect damping effects to contribute appreciably to the observed change in frequency.

IV. EXPERIMENTAL RESULTS

(a) The Absolute Moduli

The absolute values of the elastic moduli were calculated from the resonant frequency of the composite oscillator, using Eqs. (1) and (2). In Table V, the experimental values of S_{11} and $2(S_{44}+S_{66})$ are given and compared with the results of Bridgman. The moduli measured in these experiments are adiabatic while those of Bridgman are isothermal. A correction of 6.6 percent was subtracted from Bridgman's S_{11} to make the results comparable at room temperature [see Eq. (11)]. For the torsional modulus the correction is zero.

(b) The Change in Moduli at the Transition

Most of the experimental results were derived from isothermal measurements where the difference in frequency between the composite oscillator and the standard quartz crystal was measured as a function of

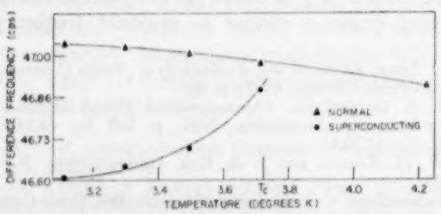

FIG. 5. Isothermal experiments, II. The difference in frequency between the composite oscillator and the standard torsional quartz crystal is shown for tin *G1a'*.

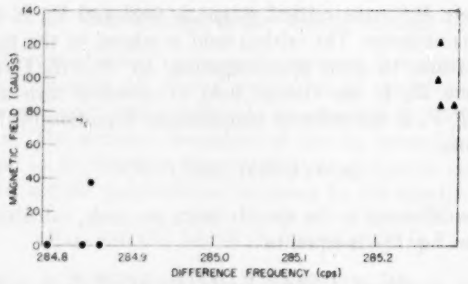

FIG. 6. Isothermal experiment. The difference in frequency between the composite oscillator and the standard longitudinal quartz crystal is given as a function of magnetic field at 3.190 deg K for tin *G5a*.

magnetic field at constant temperature. At temperatures below the superconducting transition, the difference frequency had two values, depending on the state of the tin. Therefore in an isothermal experiment below the transition temperature a change in difference frequency was produced by magnetic fields of sufficient strength to change the state of the tin. Above the transition temperature, of course, no change was observed. Figures 4 and 5 show the experimental values of the difference frequency for two of the tin crystals. Each point is the average of the number of measurements indicated in Table VI.

At a given temperature, changes in the magnetic field did not alter the difference frequency except in the neighborhood of the critical field. A typical example of the difference frequency as a function of field strength is shown in Fig. 6. Above the transition temperature, the frequency was not affected by fields as high as 150 gauss.

The frequency difference between the longitudinal quartz crystals was compared from 4.2 degrees to 3.0 degrees. No change was observed to within the experimental error of 3 parts in 10^6 per degree.

Isothermal experiments were performed for five tin crystals. At each temperature, a number of measurements were made in both states. The difference in fre-

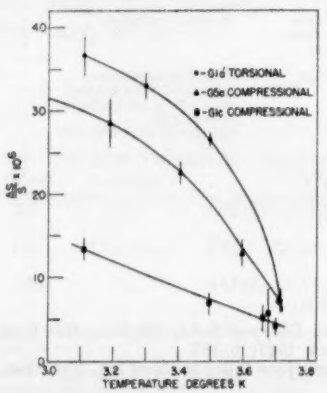

FIG. 7. The change in elastic moduli at the superconducting transition.

quency was converted into change in elastic modulus by use of Eq. (3) and the results are given in Table VI and Fig. 7. The indicated error is the square root of the sum of the squares of the average deviations in the two states.

Several measurements were made on the change in moduli in a zero-field transition, and the results agree roughly with those obtained isothermally. Because of the time delay necessary to establish temperature equilibrium, these results are probably not as reliable as those obtained isothermally.

In all cases the moduli were greater in the superconducting than in the normal state.

For longitudinal vibrations the oscillator voltage increased by about thirty percent as the composite was brought into the superconducting state. This effect was characteristic of the tin only and indicates a decrease in damping in the superconducting state. Absolute determinations indicated no change in Q within the experimental error of about five percent. Calibration showed that the oscillator voltage increased about ten times as fast as the Q under typical feedback conditions. The voltage change of thirty percent could be accounted for by a change in Q of about three percent in the longitudinal mode.

TABLE VI. The change in moduli at the transition. n refers to the normal state and s to the superconducting state.

Date	Tin crystal	Quartz crystals	Temp.	$(\Delta S/S)\times 10^6$	Measurements n	Measurements s
10–25–52	1	Long.	(H=O)	7.4±6	10	10
11– 1–52	1	Long.	(H=O)	6.4±4	5	5
12–16–52	2	Long.	3.685	6.8±2.2	6	10
			3.556	10 ±4	2	7
4– 4–53	*G1b*	Tor.	3.668	16 ±6	8	6
4–11–53	*G1c*	Long.	3.676	5.6±3.0	7	17
4–26–53	*G1c*	Long.	3.660	5.2±1.6	23	26
5– 9–53	*G5a*	Long.	3.708	7.2±0.3	3	3
			3.596	12.9±1.6	4	6
			3.407	22.6±1.2	3	4
			3.190	28.6±3.0	4	4
5–19–53	*G1c*	Long.	3.669	4.2±1.0	3	3
			3.495	6.9±1.4	3	5
			3.110	13.4±1.4	3	4
6–29–53	*G1a'*	Tor.	3.714	7.2±1.4	6	6
			3.497	26.6±0.8	6	6
			3.300	33.0±1.6	6	6
			3.112	36.6±2.4	6	6

V. CONCLUSIONS

(a) Comparison with Thermodynamics

The observed changes in moduli at the superconducting transition cannot be compared directly with the thermodynamic predictions since an insufficient number of moduli were investigated to obtain an experimental value for the compressibility.

For the longitudinal modulus in tin crystal *G1c*, the observed relative change at $t=1$ is $\Delta S_{11}/S_{11}\simeq 4\times 10^{-6}$. This is close to the predicted change in compressibility of $\Delta\chi_S/\chi_S\simeq 4.1\times 10^{-6}$. For the torsional case, the adiabatic and isothermal moduli are equal. However, since the compressibility does not involve the torsional modulus, the derived results do not apply to the observed results for tin *G1a'*.

It should be noted that tin *G5a*, although excited longitudinally, has a relatively large change in modulus (see Fig. 7). This can be accounted for by the high percentage of S_{66} present in its effective modulus, thus making its behavior more nearly like *G1a'*.

(b) General

A number of arguments and experiments have been introduced to show that the observed change in difference frequency is indeed due to a change in the elastic modulus of tin at the superconducting transition. To recapitulate, it was found that, without the tin crystal, no change in difference frequency was observed, and with the tin a change at a given temperature was produced only by a critical magnetic field. It was shown that changes in damping and physical size did not cause the effect. Added credibility is given by the agreement of the change in modulus in zero field and that obtained isothermally near the transition temperature. The magnitude of the change is in good agreement with the thermodynamic prediction. The results were consistent for several crystals with similar orientation and were reproducible over long periods.

That there is a change in the velocity of sound at the superconducting transition is in accord with the electron-lattice theories.[24,25] The lowering of the velocity in the superconducting state is in agreement with Wentzel's prediction.[26] However, due to the relatively large observed change in the torsional modulus, it appears that a complete theory of superconductivity must include the interaction of the electrons with transverse as well as longitudinal lattice vibrations.

The author wishes to express his gratitude to A. W. Lawson for his constant guidance, to L. Meyer and E. A. Long for advice pertaining to the cryogenics, and to J. K. Hulm and M. Cohen for helpful discussions.

[24] H. Frohlich, Phys. Rev. **79**, 845 (1950).
[25] J. Bardeen, Phys. Rev. **80**, 567 (1950).
[26] G. Wentzel, Phys. Rev. **83**, 168 (1951).

Derivation of Magnetostriction and Anisotropic Energies for Hexagonal, Tetragonal, and Orthorhombic Crystals

W. P. MASON
Bell Telephone Laboratories, Murray Hill, New Jersey
(Received June 8, 1954)

In order to determine the measurements necessary to characterize the anisotropic energy and the saturation magnetostriction in hexagonal cobalt, a phenomenological derivation has been given for the equations which characterize the effects. Out to fourth rank tensors, the results are the same as those for circular symmetry and it requires two constants to specify the anisotropic energy and four to specify the magnetostriction. When sixth rank tensors are evaluated, a characteristic hexagonal symmetry appears. It requires four constants to characterize the anisotropic energy and nine to characterize the magnetostriction. These constants can be measured by using two oriented slabs. Four of the constants can be determined by measurements parallel to the saturation magnetization, four when the magnetostriction is perpendicular to the magnetization and one when they are 45° apart.

In the Appendix the first approximations for the magnetostrictive and anisotropy energies are derived for tetragonal and orthorhombic crystals.

I. INTRODUCTION

IN order to determine what measurements have to be taken to characterize the saturation magnetostriction and the magnetic anisotropic energy of a hexagonal cobalt crystal (class $6/m$, $2/m$, $2/m$), which are discussed in an accompanying paper by R. M. Bozorth, a phenomenological derivation has been given for the equations which describe these effects. These equations can be derived from a general thermodynamic function of which there are several depending on which variables are considered the fundamental ones. In order to give directly the measured magnetostriction constants and the magnetic anisotropic energy at constant stress (the ordinarily measured values), it is better to use the stresses, intensities of magnetization, and entropy as the fundamental variables. Furthermore, since we are not interested in temperature effects, we can assume the entropy constant and introduce only the stresses and intensity of magnetization as the fundamental variables.

A general expression has been derived in a previous paper[1] for a crystal with a center of symmetry. Since cobalt belongs to the crystal class $6/m$, $2/m$, $2/m$ (Herman-Mauguin) or D_{6h} (Schönflies), it has a center of symmetry and hence the expression derived previously is valid. In tensor notation, this expression can be written in the form

$$2H_1=-[s_{ijkl}{}^I T_{ij}T_{kl}+R_{ijklno}I_iI_jT_{kl}T_{no}+M_{ijmn}I_iI_jT_{mn}+N_{ijklmn}I_iI_jI_kI_lT_{mn}]+K_{mn}{}^TI_mI_n+K_{mnop}{}^TI_mI_nI_oI_p+K_{mnopqr}{}^TI_mI_nI_oI_pI_qI_r. \quad (1)$$

In this equation T_{ij} are the stresses expressed as a second rank tensor with i interchangeable with j, I_i are the three magnetic intensities along the three rectangular coordinates, $s_{ijkl}{}^I$ are the elastic compliances, R_{ijklno} are the terms added to the elastic compliances when the crystal is magnetized in various directions (neglected in the present paper), M_{ijmn} are the first-order magnetostriction terms, N_{ijklmn} the second-order magnetostriction terms, and the three K terms are the first-, second-, and third-order anisotropic energy terms, all measured for constant stress.

All that is required to evaluate these terms is a knowledge of the components of the tensors in the sym-

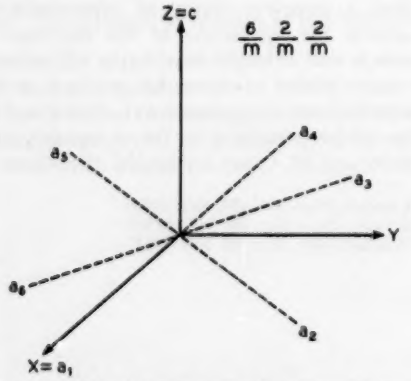

FIG. 1. Relation between x, y, and z rectangular axes and the crystallographic axes.

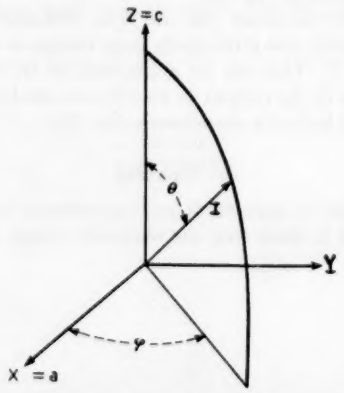

FIG. 2. Relation between spherical coordinate angles and rectangular x, y, and z axes.

[1] W. P. Mason, Phys. Rev. 82, 715 (1951).

metry system $6/m$, $2/m$, $2/m$. Up to fourth rank tensors, the number and kinds of terms are well known and are given in Sec. II.

The components of sixth rank tensors for this symmetry have been derived only recently.[2] As discussed in Sec. III, these components can be used to evaluate the morphic R constants, the second-order (N) magnetostriction terms and the third-order anisotropic energy terms. In all the sixth rank tensors, the characteristic hexagonal symmetry appears and the results are different from those derived on the basis of circular symmetry.

II. ELASTIC COMPLIANCES, FIRST-ORDER MAGNETOSTRICTION, AND FIRST- AND SECOND-ORDER ANISOTROPIC ENERGY TERMS IN COBALT

The matrices of the second and fourth rank tensors using the engineering shearing strains, i.e., $(S_{ij}=\partial u_i/\partial x_j+\partial u/\partial x_i)$ rather than the tensor strains, can be written in the form[3]

$$K_{mn}=\begin{vmatrix} K_{11} & 0 & 0 \\ 0 & K_{11} & 0 \\ 0 & 0 & K_{33} \end{vmatrix};\quad s_{ijkl}=\begin{vmatrix} s_{1111} & s_{1122} & s_{1133} & 0 & 0 & 0 \\ s_{1122} & s_{1111} & s_{1133} & 0 & 0 & 0 \\ s_{1133} & s_{1133} & s_{3333} & 0 & 0 & 0 \\ 0 & 0 & 0 & s_{2323} & 0 & 0 \\ 0 & 0 & 0 & 0 & s_{2323} & 0 \\ 0 & 0 & 0 & 0 & 0 & 2(s_{1111}-s_{1122}) \end{vmatrix};$$

$$K_{mnop}=\begin{vmatrix} K_{1111} & K_{1122} & K_{1133} & 0 & 0 & 0 \\ K_{1122} & K_{1111} & K_{1133} & 0 & 0 & 0 \\ K_{1133} & K_{1133} & K_{3333} & 0 & 0 & 0 \\ 0 & 0 & 0 & K_{1133} & 0 & 0 \\ 0 & 0 & 0 & 0 & K_{1133} & 0 \\ 0 & 0 & 0 & 0 & 0 & K_{1111}-K_{1122} \end{vmatrix}; \qquad (2)$$

$$M_{ijmn}=\begin{vmatrix} M_{1111} & M_{1122} & M_{1133} & 0 & 0 & 0 \\ M_{1122} & M_{1111} & M_{1133} & 0 & 0 & 0 \\ M_{3311} & M_{3311} & M_{3333} & 0 & 0 & 0 \\ 0 & 0 & 0 & M_{2323} & 0 & 0 \\ 0 & 0 & 0 & 0 & M_{2323} & 0 \\ 0 & 0 & 0 & 0 & 0 & M_{1111}-M_{1122} \end{vmatrix}.$$

Since the first two and last two numbers of the subscripts can be interchanged with each other, it has become customary to replace two interchangeable indices by single indices according to the convention

$$1=11;\quad 2=22;\quad 3=33;\quad 4=23;\quad 5=13;\quad 6=12.$$

With this substitution we can write the expression for H_1 as

$$\begin{aligned} 2H_1=&-[s_{11}{}^I(T_1{}^2+T_2{}^2)+2s_{12}{}^IT_1T_2+2s_{13}{}^I(T_1+T_2)T_3 \\ &+s_{33}{}^IT_3{}^2+s_{44}{}^I(T_4{}^2+T_5{}^2)+2(s_{11}{}^I-s_{12}{}^I)T_6{}^2 \\ &+2M_{11}(I_1{}^2T_1+I_2{}^2T_2)+2M_{12}(I_1{}^2T_2+I_2{}^2T_1) \\ &+2M_{13}(I_1{}^2T_3+I_2{}^2T_3)+2M_{31}[I_3{}^2(T_1+T_2)] \\ &+2M_{33}I_3{}^2T_3+4M_{44}(I_2I_3T_4+I_1I_3T_5) \\ &+4(M_{11}-M_{12})I_1I_2T_6]+K_1{}^T(I_1{}^2+I_2{}^2)+K_3{}^TI_3{}^2 \\ &+K_{11}{}^T(I_1{}^4+2I_1{}^2I_2{}^2+I_2{}^4)+6K_{13}{}^T(I_1{}^2+I_2{}^2)I_3{}^2 \\ &+K_{33}{}^TI_3{}^4, \qquad (3) \end{aligned}$$

where the z or 3 axis coincides with the c hexagonal axis as shown by Fig. 1, and the x axis coincides with one of the 6 hexagonal a axes.

These equations hold for a crystal with a large number of domains when the directions of the domains are uncorrelated, for then the components of magnetization are independent. For a single domain or for a saturated crystal, the intensity of magnetization has a fixed value I_s, and only the direction of magnetism can be changed. If α_1, α_2, α_3 are the direction cosines of the intensity of magnetization with respect to the crystal axes, one has

$$I_1=\alpha_1I_s;\quad I_2=\alpha_2I_s;\quad I_3=\alpha_3I_s, \qquad (4)$$

where $\alpha_1{}^2+\alpha_2{}^2+\alpha_3{}^2=1$.

Furthermore, the energy H_1 is usually expressed as a change from the energy of the demagnetized crystal. For cobalt the direction of easy magnetization is along the hexagonal axis with $\alpha_3=\pm1$. Hence, on the average,

$$\sum_1^n \alpha_3=0;\quad \frac{1}{n}\sum_1^n \alpha_3{}^2=1.$$

With these substitutions the expression for $2H_1$ becomes

$$\begin{aligned} 2H_1=&-[s_{11}{}^I(T_1{}^2+T_2{}^2)+2s_{12}{}^IT_1T_2+2s_{13}{}^I(T_1+T_2)T_3 \\ &+s_{33}{}^IT_3{}^2+s_{44}{}^I(T_4{}^2+T_5{}^2)+2(s_{11}{}^I-s_{12}{}^I)T_6{}^2] \\ &-[2(M_{11}-M_{12})I_s{}^2(\alpha_1{}^2T_1+\alpha_2{}^2T_2+2\alpha_1\alpha_2T_6) \\ &+2(M_{33}-M_{13})I_s{}^2(\alpha_3{}^2-1)T_3+2(M_{31}-M_{12}) \\ &\times I_s{}^2(\alpha_3{}^2-1)(T_1+T_2)+4M_{44}I_s{}^2(\alpha_2\alpha_3T_4+\alpha_1\alpha_3T_5)] \\ &+[(K_1-K_3)I_s{}^2+(2K_{11}-6K_{13})I_s{}^4][1-\alpha_3{}^2] \\ &+[4K_{13}-K_{11}-K_{33}]I_s{}^4[1-\alpha_3{}^4]. \qquad (5) \end{aligned}$$

[2] R. Fieschi and F. G. Fumi, Nuovo cimento **10**, 865 (1953). Hexagonal and trigonal systems were also considered by Dr. H. Wondratschek and are in course of publication.

[3] The K_{mn} tensor is similar to the dielectric tensor and the s_{ijkl} tensor is given in W. P. Mason, *Piezoelectric Crystals and Their Application to Ultrasonics* (D. Van Nostrand Company, Inc., New York, 1950). The K_{mnop} tensor can be obtained from the s_{ijkl} tensor by interchanging all the subscripts. The M_{ijkl} tensor is similar to the photoelastic tensor of Pockels as corrected by Bhagavantum.

Since

$$(1-\alpha_3^2)=1-\cos^2\theta=\sin^2\theta, \quad (1-\alpha_3^4)=(1-\cos^4\theta) =2\sin^2\theta-\sin^4\theta, \quad (6)$$

where θ is the angle of the saturation magnetization from the hexagonal axis, as shown by Fig. 2, the anisotropic energy can be written in the form

$$A\sin^2\theta+B\sin^4\theta, \quad (7)$$

where

$$A=\tfrac{1}{2}(K_1-K_3)I_s^2+(K_{13}-K_{33})I_s^4,$$
$$B=\tfrac{1}{2}(K_{11}+K_{33}-4K_{13})I_s^4.$$

This is a well-known result for cobalt.[4]

The form of the saturation magnetostriction, which has not previously been derived, can be obtained from the equation for the magnetostrictive strain in any direction which is given by the formula

$$\lambda=-\beta_1^2\frac{\partial H_1}{\partial T_1}-\beta_2^2\frac{\partial H_1}{\partial T_2}-\beta_3^2\frac{\partial H_1}{\partial T_3} -\beta_2\beta_3\frac{\partial H_1}{\partial T_4}-\beta_1\beta_3\frac{\partial H_1}{\partial T_5}-\beta_1\beta_2\frac{\partial H_1}{\partial T_6}, \quad (8)$$

where β_1, β_2, β_3 are the direction cosines of the direction for magnetostrictive strain with respect to the x, y, and z axes defined above and λ is the saturation magnetostriction. Performing the above differentiation and collecting terms,

$$\lambda=(M_{11}-M_{12})I_s^2(\alpha_1\beta_1+\alpha_2\beta_2)^2+(M_{12}-M_{31}) \times I_s^2(1-\alpha_3^2)(1-\beta_3^2)+(M_{13}-M_{33})I_s^2(1-\alpha_3^2)\beta_3^2 +2M_{44}I_s^2(\alpha_1\beta_1+\alpha_2\beta_2)\alpha_3\beta_3. \quad (9)$$

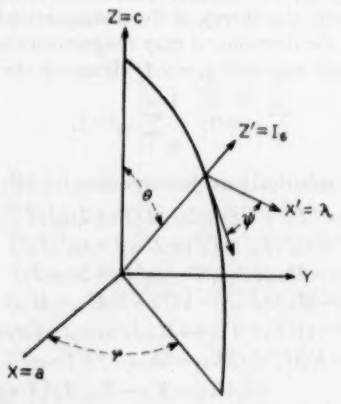

FIG. 3. Relation between rotated coordinate system x', y', and z' and original rectangular coordinate system x, y, and z.

[4] R. M. Bozorth, *Ferromagnetism* (D. Van Nostrand Company, Inc., New York, 1951), p. 564.

To evaluate the M constants in terms of the measured values of magnetostriction, we first put the field in the same direction as the magnetostriction. Then $\alpha_1=\beta_1$, $\alpha_2=\beta_2$, $\alpha_3=\beta_3$, and

$$\lambda=(M_{11}-M_{31})I_s^2(1-\beta_3^2)^2 +(-M_{33}+M_{13}+2M_{44})I_s^2(1-\beta_3^2)\beta_3^2. \quad (10)$$

Hence, only two constants can be obtained under these conditions. These are obtained by setting $\alpha_1=\beta_1=1$, giving λ_A and $\alpha_1=\beta_1=1/\sqrt{2}$, $\alpha_3=\beta_3=1/\sqrt{2}$, giving λ_D. From Eq. (10),

$$\lambda_A=(M_{11}-M_{31})I_s^2; \quad \lambda_D=[\tfrac{1}{4}(M_{11}-M_{31}) +\tfrac{1}{4}(-M_{33}+M_{13}+2M_{44})]I_s^2. \quad (11)$$

To determine the other two constants, we have to determine the expansion in a different direction from the field. The two simplest directions are when the field is perpendicular to the hexagonal axis and the saturation magnetostriction is measured at right angles to the field in the basal plane, and perpendicular to the basal plane. Calling $\lambda_B(\alpha_1=1, \beta_2=1)$ and $\lambda_C(\alpha_1=1, \beta_3=1)$ the two values, we find for these

$$\lambda_B=(M_{12}-M_{31})I_s^2; \quad \lambda_C=(M_{13}-M_{33})I_s^2. \quad (12)$$

With these values, the four constants become

$$(M_{11}-M_{12})I_s^2=\lambda_A-\lambda_B,$$
$$(M_{12}-M_{31})I_s^2=\lambda_B, \quad (M_{13}-M_{33})I_s^2=\lambda_C,$$
$$2M_{44}I_s^2=(-\lambda_A+4\lambda_D-\lambda_C). \quad (13)$$

Inserting these values in the magnetostrictive equation, we find

$$\lambda=\lambda_A[(\alpha_1\beta_1+\alpha_2\beta_2)^2-(\alpha_1\beta_1+\alpha_2\beta_2)\alpha_3\beta_3] +\lambda_B[(1-\alpha_3^2)(1-\beta_3^2)-(\alpha_1\beta_1+\alpha_2\beta_2)^2] +\lambda_C[(1-\alpha_3^2)\beta_3^2-(\alpha_1\beta_1+\alpha_2\beta_2)\alpha_3\beta_3] +4\lambda_D(\alpha_1\beta_1+\alpha_2\beta_2)\alpha_3\beta_3. \quad (14)$$

These four constants have been evaluated for cobalt in the following paper by Bozorth, who finds the following values:

$$\lambda_A=-45\times10^{-6}, \quad \lambda_B=-95\times10^{-6},$$
$$\lambda_C=+110\times10^{-6}, \quad \lambda_D=-100\times10^{-6}. \quad (15)$$

The properties of polycrystalline materials can be calculated to this order of approximation by assuming that all orientations of the crystal grains are equally probable. The two quantities of interest are the magnetostriction $\lambda_{\parallel}$ along a rod in the direction of the applied field and the change in dimension, $\lambda_{\perp}$, perpendicular to the applied field. The volume magnetostriction ω is then equal to

$$\omega=\lambda_{\parallel}+2\lambda_{\perp}. \quad (16)$$

If we saturate along a given direction, the increase in length along this direction for any orientation in the crystal is given by

$$\lambda=\lambda_A[(1-\alpha_3^2)^2-(1-\alpha_3^2)\alpha_3^2]+4\lambda_D(1-\alpha_3^2)\alpha_3^2, \quad (17)$$

where α_3 is the direction cosine between the direction of the magnetic field and the Z axis of the crystal. If we call this angle θ, the expression for λ is

$$\lambda=\lambda_A[\sin^4\theta-\sin^2\theta\cos^2\theta]+4\lambda_D\sin^2\theta\cos^2\theta. \quad (18)$$

To obtain λ_{II}, we have to average this expression over all possible orientations. The average values of $\sin^4\theta$ and $\sin^2\theta\cos^2\theta$ over a unit sphere are given by the integrals

$$\int_0^{\pi/2}\sin^5\theta d\theta=\frac{8}{15}, \quad \int_0^{\pi/2}\sin^3\theta\cos^2\theta d\theta=\frac{2}{15}. \quad (19)$$

Hence

$$\lambda_{II}=\tfrac{2}{5}\lambda_A+(8/15)\lambda_D. \quad (20)$$

The volume magnetostriction of a single crystal material can be calculated by taking a three-axis system x', y', z' located in any orientation and adding the magnetostrictive strains in all three systems. If we take the axes of the three-axis system with respect to the axes for which the direction of magnetization has the direction cosines $\alpha_1, \alpha_2, \alpha_3$ as shown by Fig. 3, the direction cosines for the x', y' and z' axes are given by

$$\begin{aligned} &x': \beta_1=\cos\theta\cos\varphi;\ \beta_2=\cos\theta\sin\varphi;\ \beta_3=-\sin\theta;\\ &y': \beta_1=-\sin\varphi;\ \beta_2=\cos\varphi;\ \beta_3=0;\\ &z': \beta_1=\sin\theta\cos\varphi;\ \beta_2=\sin\theta\sin\varphi;\ \beta_3=\cos\theta. \end{aligned} \quad (21)$$

Using these values in Eq. (14), leaving $\alpha_1, \alpha_2, \alpha_3$ arbitrary, and adding all these values of λ, we find

$$\begin{aligned}(\lambda_{x'}+\lambda_{y'}+\lambda_{z'})=\omega&=(\lambda_A+\lambda_B+\lambda_C)(1-\alpha_3^2)\\&=(\lambda_A+\lambda_B+\lambda_C)\sin^2\theta, \end{aligned} \quad (22)$$

where θ is the angle of magnetization with respect to the hexagonal axis. Hence, irrespective of the orientation of the crystallite considered, the volume magnetostriction depends only on the direction of the intensity of magnetization with respect to the hexagonal axis.

For a polycrystalline material, this angle is averaged over all directions and hence, since

$$\int_0^{\pi/2}\sin^3\theta d\theta=\tfrac{2}{3}, \quad (23)$$

we find that the volume magnetostriction for a polycrystalline material is

$$\tilde{\omega}=\tfrac{2}{3}(\lambda_A+\lambda_B+\lambda_C). \quad (24)$$

From Eqs. (16) and (20) we find

$$\lambda_\perp=(2/15)\lambda_A+\tfrac{1}{3}(\lambda_B+\lambda_C)-(4/15)\lambda_D. \quad (25)$$

III. ANISOTROPIC ENERGY AND SATURATION MAGNETOSTRICTION TAKING ACCOUNT OF SIXTH RANK TENSORS

When one takes account of the sixth rank tensors of Eq. (1), additional terms are added to the anisotropic energy terms and the saturation magnetostriction, and these reveal the hexagonal properties of the crystal. The simplest term to consider is the anisotropy energy term

$$K_{mnopqr}I_mI_nI_oI_pI_qI_r. \quad (26)$$

According to Fieschi and Fumi,[2] the energy product has the form

$$\begin{aligned}&K_{111}I_1^6+15K_{112}I_1^4I_2^2+15K_{122}I_1^2I_2^4+15K_{113}I_1^4I_3^2\\&\quad+15K_{223}I_2^4I_3^2+90K_{123}I_1^2I_2^2I_3^2+15K_{133}I_1^2I_3^4\\&\quad+15K_{233}I_2^2I_3^4+K_{333}I_3^6. \end{aligned} \quad (27)$$

In the hexagonal system $6/m$, $2/m$, $2/m(D_{6h})$, there are a number of relations between the constants. For the case where all six indices can be interchanged, in three-index symbols, these relations take the form

$$\begin{aligned}&5K_{112}=-2K_{111}+3K_{222};\quad 5K_{122}=3K_{111}-2K_{222};\\&K_{113}=3K_{123};\quad K_{113}=K_{223};\quad K_{133}=K_{233}. \end{aligned} \quad (28)$$

Introducing these values, the expression for the anisotropic energy becomes

$$\begin{aligned}&K_{111}[I_1^6-6I_1^4I_2^2+9I_1^2I_2^4]\\&\quad+K_{222}[I_2^6-6I_2^4I_1^2+9I_2^2I_1^4]+15K_{113}[I_1^2+I_2^2]^2I_3^2\\&\quad+15K_{133}(I_1^2+I_2^2)I_3^4+K_{333}I_3^6. \end{aligned} \quad (29)$$

Introducing the values

$$I_1=\alpha_1I_s,\quad I_2=\alpha_2I_s,\quad I_3=\alpha_3I_s, \quad (30)$$

and subtracting out the demagnetization energy, the sixth rank term becomes

$$\begin{aligned}&K_{111}I_s^6(\alpha_1^6-6\alpha_1^4\alpha_2^2+9\alpha_1^2\alpha_2^4)\\&\quad+K_{222}I_s^6(\alpha_2^6-6\alpha_2^4\alpha_1^2+9\alpha_2^2\alpha_1^4)\\&\quad+15K_{113}I_s^6(\alpha_1^2+\alpha_2^2)^2\alpha_3^2+15K_{133}I_s^6(\alpha_1^2+\alpha_2^2)\alpha_3^4\\&\quad+K_{333}I_s^6(\alpha_3^6-1). \end{aligned} \quad (31)$$

If we go to spherical coordinates as shown by Fig. 2,

$$\alpha_1=\sin\theta\cos\varphi;\quad \alpha_2=\sin\theta\sin\varphi;\quad \alpha_3=\cos\theta. \quad (32)$$

Introducing these values and combining and reducing terms, and adding the lower order terms of (7), the total anisotropic energy can be written in the form

$$A\sin^2\theta+B\sin^4\theta+\sin^6\theta(C+D\cos6\varphi), \quad (33)$$

where

$$\begin{aligned}A&=\tfrac{1}{2}(K_1-K_3)I_s^2+(K_{13}-K_{33})I_s^4-\tfrac{3}{2}K_{333}I_s^6;\\B&=\tfrac{1}{2}(K_{11}+K_{33}-4K_{13})I_s^4\\&\quad+\tfrac{1}{2}(15K_{113}-30K_{133}+3K_{333})I_s^6;\\C&=[\tfrac{1}{2}(-15K_{113}+15K_{133}-K_{333})+\tfrac{1}{4}(K_{111}+K_{222})]I_s^6;\\D&=\tfrac{1}{4}(K_{111}-K_{222})I_s^6. \end{aligned} \quad (34)$$

The sixth rank magnetostriction tensor containing the second-order magnetostrictive terms can be evaluated in a similar manner. The energy products become

$$N_{111}I_1^4T_1+(N_{112}I_1^4T_2+6N_{121}I_1^2I_2^2T_1+8N_{166}I_1^3I_2T_6)$$
$$+(N_{221}I_2^4T_1+6N_{122}I_1^2I_2^2T_2+8N_{266}I_1I_2^3T_6)$$
$$+(N_{113}I_1^4T_3+6N_{131}I_1^2I_3^2T_1+8N_{155}I_1^3I_3T_5)$$
$$+(N_{331}I_3^4T_1+6N_{133}I_1^2I_3^2T_3+8N_{355}I_1I_3^3T_5)$$
$$+(N_{223}I_2^4T_3+6N_{232}I_2^2I_3^2T_2+8N_{244}I_2^3I_3T_4)$$
$$+(N_{332}I_3^4T_2+6N_{233}I_2^2I_3^2T_3+8N_{344}I_3^3I_2T_4)$$
$$+(6N_{123}I_1^2I_2^2T_3+6N_{132}I_1^2I_3^2T_2+6N_{231}I_2^2I_3^2T_1$$
$$+24N_{144}I_1^2I_2I_3T_4+24N_{255}I_1I_2^2I_3T_5$$
$$+24N_{366}I_1I_2I_3^2T_6)+N_{222}I_2^4T_2+N_{333}I_3^4T_3. \quad (35)$$

For a hexagonal symmetry $6/m$, $2/m$, $2/m$ there are a number of relations between these constants. On account of the form of Eq. (1), we can interchange the first four indices or, in terms of three-index terms,

$$N_{abc}=N_{bac}. \quad (36)$$

From this relationship, the equivalences given by Fieschi and Fumi[2] take the form

$$N_{112}=-2N_{111}+3N_{222}-4N_{166}; \qquad 3N_{121}=-2N_{111}+3N_{222}-2N_{166};$$
$$N_{122}=-N_{111}+2N_{222}-2N_{166}-2N_{121}; \qquad N_{266}=N_{111}-N_{222}+N_{166};$$
$$N_{221}=2N_{222}-N_{111}-4N_{166};$$
$$N_{113}=3N_{123}=N_{223}; \quad N_{131}=N_{132}+2N_{366}=N_{232}; \qquad N_{133}=N_{233}; \quad N_{213}=N_{123};$$
$$N_{331}=N_{332}; \quad N_{355}=N_{344}; \quad N_{132}=N_{231}; \qquad N_{155}=3N_{144}=N_{244}. \quad (37)$$

These 16 relations reduce the number of constants appearing in the equation to 11. Introducing these values, the sixth rank tensor, after subtracting the demagnetized value $N_{331}I_s^4(1-\beta_3^2)+N_{333}I_s^4\beta_3^2$, becomes

$$N_{111}I_s^4[\alpha_1^4\beta_1^2+2\alpha_1^4\beta_2^2-8\alpha_1^3\alpha_2\beta_1\beta_2+3\alpha_2^4\beta_1^2+6\alpha_1^2\alpha_2^2\beta_2^2]$$
$$+N_{222}I_s^4[\alpha_2^4\beta_2^2-3\alpha_1^4\beta_2^2+12\alpha_1^3\alpha_2\beta_1\beta_2-4\alpha_2^4\beta_1^2$$
$$-6\alpha_1^2\alpha_2^2\beta_2^2+4\alpha_1\alpha_2^3\beta_1\beta_2]+6N_{121}I_s^4(\alpha_1\beta_2-\alpha_2\beta_1)^2(1-\alpha_3^2)$$
$$+3N_{123}I_s^4\beta_3^2(1-\alpha_3^2)^2+6N_{131}I_s^4\alpha_3^2(\alpha_1\beta_1+\alpha_2\beta_2)^2$$
$$+6N_{132}I_s^4\alpha_3^2(\alpha_1\beta_2-\alpha_2\beta_1)^2+8N_{155}I_s^4\alpha_3\beta_3(1-\alpha_3^2)$$
$$\times(\alpha_1\beta_1+\alpha_2\beta_2)+N_{331}I_s^4(\alpha_3^4-1)(1-\beta_3^2)$$
$$+6N_{133}I_s^4\alpha_3^2\beta_3^2(1-\alpha_3^2)+8N_{344}I_s^4\alpha_3^3\beta_3(\alpha_1\beta_1+\alpha_2\beta_2)$$
$$+N_{333}I_s^4(\alpha_3^4-1)\beta_3^2. \quad (38)$$

By combining these terms with the first-order terms of Eq. (19), and combining and reducing terms, the sum can be written in the form of a nine-constant equation:

$$\lambda=A[2\alpha_1\alpha_2\beta_1+(\alpha_1^2-\alpha_2^2)\beta_2]^2+B\alpha_3^2[(\alpha_1\beta_1+\alpha_2\beta_2)^2$$
$$-(\alpha_1\beta_2-\alpha_2\beta_1)^2]+C[(\alpha_1\beta_1+\alpha_2\beta_2)^2-(\alpha_1\beta_2-\alpha_2\beta_1)^2]$$
$$+D(1-\alpha_3^2)(1-\beta_3^2)+E\alpha_3^2\beta_3^2(1-\alpha_3^2)+F\alpha_3^2(1-\alpha_3^2)$$
$$+G\beta_3^2(1-\alpha_3^2)+H\alpha_3\beta_3(\alpha_1\beta_1+\alpha_2\beta_2)$$
$$+I\alpha_3^3\beta_3(\alpha_1\beta_1+\alpha_2\beta_2), \quad (39)$$

where

$$A=(N_{222}-N_{111})I_s^4;$$
$$B=[3(N_{131}-N_{132}+N_{121})+N_{111}-2N_{222}]I_s^4;$$
$$C=[(2N_{222}-N_{111}-3N_{121})I_s^4+\tfrac{1}{2}(M_{11}-M_{12})I_s^2];$$
$$D=[(2N_{111}-2N_{222}+3N_{121}-N_{331})I_s^4+\tfrac{1}{2}(M_{11}+M_{12}-2M_{31})I_s^2];$$
$$E=[2(N_{111}-N_{222})+3(N_{121}-N_{131}-N_{132}-N_{123})+6N_{133}+N_{331}-N_{333}]I_s^4;$$
$$F=[2(N_{222}-N_{111})-N_{331}+3(N_{131}+N_{132}-N_{121})]I_s^4;$$
$$G=[(3N_{123}-N_{333})I_s^4+(M_{13}-M_{33})I_s^2];$$
$$H=[8N_{155}I_s^4+2M_{44}I_s^2];$$
$$I=8(N_{344}-N_{155})I_s^4.$$

To evaluate the 9 constants requires the measurement of 9 independent orientations. The simplest measurements are those for which the magnetization is parallel or perpendicular to the saturation magnetostriction. Eight independent constants can be determined from these measurements. The remaining constant has to be determined when the magnetization and magnetostriction are in directions not 0° or 90° with respect to each other. For the parallel case,

$$\alpha_1=\beta_1; \quad \alpha_2=\beta_2; \quad \alpha_3=\beta_3, \quad (40)$$

and the equation becomes

$$\lambda_{11}=A[3\alpha_1^2\alpha_2-\alpha_2^3]^2+B\alpha_3^2(1-\alpha_3^2)^2$$
$$+(C+D)(1-\alpha_3^2)^2+(E+I)\alpha_3^4(1-\alpha_3^2)$$
$$+(F+G+H)\alpha_3^2(1-\alpha_3^2). \quad (41)$$

Introducing spherical coordinates as shown by Fig. 2, we find that

$$\alpha_1=\sin\theta\cos\varphi; \quad \alpha_2=\sin\theta\sin\varphi; \quad \alpha_3=\cos\theta. \quad (42)$$

If these values are introduced in (41) and all the values are expressed in even powers of $\sin\theta$, Eq. (41) reduces to

$$\lambda_{11}=A'\sin^2\theta+B'\sin^4\theta+C'\sin^6\theta+D'\sin^6\theta\cos6\varphi, \quad (43)$$

where

$$A'=E+F+G+H+I;$$
$$B'=B+C+D-2E-2I-F-G-H;$$
$$C'=\tfrac{1}{2}A-B+E+I; \quad D'=-\tfrac{1}{2}A.$$

The first three constants can be determined by measuring the magnetostriction when the values are measured in the x-z plane with λ_1 90° from z, λ_2 60° from z and λ_3 30° from z, while the fourth value is determined by measuring the saturation magnetostriction when $\theta=90°$, $\varphi=90°$, i.e., for measurements in the y-z plane with the direction of measurement 90° from the z axis as shown by Fig. 4(a). These four values are determined from the equations

$$\begin{aligned}
\lambda_1&=A'+B'+C'+D';\\
\lambda_2&=\tfrac{3}{4}A'+(9/16)B'+(27/64)(C'+D');\\
\lambda_3&=\tfrac{1}{4}A'+(1/16)B'+(1/64)(C'+D');\\
\lambda_4&=A'+B'+C'-D'.
\end{aligned}\tag{44}$$

Solving for these values, we get

$$\begin{aligned}
A'&=8\lambda_3-(8/3)\lambda_2+\lambda_1;\\
B'&=-(56/3)\lambda_3+(40/3)\lambda_2-(16/3)\lambda_1;\\
(C'+D')&=(32/3)\lambda_3-(32/3)\lambda_2+(16/3)\lambda_1;\\
D'&=\tfrac{1}{2}(\lambda_1-\lambda_4).
\end{aligned}\tag{45}$$

Hence 4 of the 9 constants can be evaluated by measurements for which the magnetostriction is in the same direction as the saturation magnetization.

These constants also determine the value of the saturation magnetostriction for a polycrystalline material, since as shown by Eq. (17), all the contributions to the polycrystalline material are in the direction of the saturation magnetization. Since the average values of $\sin^2\theta$, $\sin^4\theta$, and $\sin^6\theta$ over the sphere are given by the integrals

$$\int_0^{\pi/2}\sin^3\theta d\theta=\tfrac{2}{3};\quad \int_0^{\pi/2}\sin^5\theta d\theta=\frac{8}{15};\quad \int_0^{\pi/2}\sin^7\theta d\theta=\frac{48}{105},\tag{46}$$

the average value for a magnetostrictive cobalt rod is

$$\begin{aligned}
\lambda_{11}&=\frac{2}{3}A'+\frac{8}{15}B'+\frac{48}{105}C'=\frac{2}{3}\left(8\lambda_3-\frac{8}{3}\lambda_2+\lambda_1\right)\\
&+\frac{8}{15}\left(-\frac{56}{3}\lambda_3+\frac{40}{3}\lambda_2-\frac{16}{3}\lambda_1\right)\\
&+\frac{48}{105}\left(\frac{32}{3}\lambda_3-\frac{32}{3}\lambda_2+\frac{16}{3}\lambda_1\right)-\frac{48}{105}(\lambda_1-\lambda_4)\\
&=\frac{16}{63}\lambda_3+\frac{16}{35}\lambda_2+\frac{2}{63}\lambda_1+\frac{8}{35}\lambda_4.
\end{aligned}\tag{47}$$

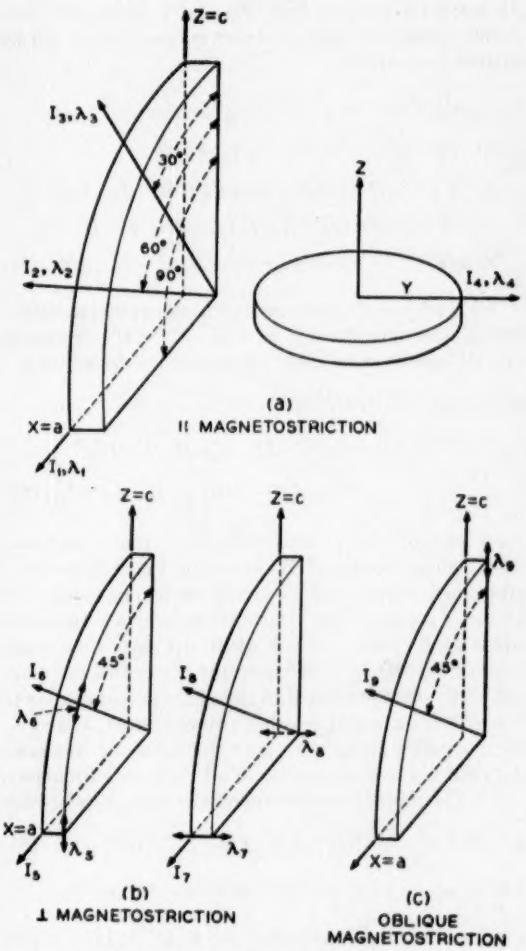

FIG. 4. Crystal cuts for measuring nine independent constants in magnetostriction equations for hexagonal crystal.

When the field is perpendicular to the direction of measurement,

$$\alpha_1\beta_1+\alpha_2\beta_2+\alpha_3\beta_3=0.\tag{48}$$

With this simplification,

$$\begin{aligned}
\lambda_\perp&=A[(\alpha_1^2-3\alpha_2^2)\beta_2-2\alpha_2\alpha_3\beta_3]^2+(B-I)\alpha_3^4\beta_3^2\\
&-B\alpha_3^2(\alpha_1\beta_2-\alpha_2\beta_1)^2+(C-H)\alpha_3^2\beta_3^2-C(\alpha_1\beta_2-\alpha_2\beta_1)^2\\
&+D(1-\alpha_3^2)(1-\beta_3^2)+E\alpha_3^2\beta_3^2(1-\alpha_3^2)\\
&+F\alpha_3^2(1-\alpha_3^2)+G\beta_3^2(1-\alpha_2^2).
\end{aligned}\tag{49}$$

If we introduce spherical coordinates as shown by Fig. 3, with the magnetization directed along the z' axis and the magnetostriction measured along x', the direction cosines become

$$\alpha_1=\sin\theta\cos\varphi;\quad \alpha_2=\sin\theta\sin\varphi;\quad \alpha_3=\cos\theta;\tag{50}$$

$$\beta_1=\cos\theta\cos\varphi\cos\psi-\sin\varphi\sin\psi;\quad \beta_2=\cos\theta\sin\varphi\cos\psi+\cos\varphi\sin\psi;\quad \beta_3=-\sin\theta\cos\psi.$$

By inserting these in Eq. (49) and reducing and collecting terms, the perpendicular magnetization can be written in the form

$$\lambda_\perp = A\sin^4\theta[\cos\theta\sin\varphi\cos\psi(3\cos^2\varphi-\sin^2\varphi)$$
$$+\sin^2\psi\cos\varphi(\cos^2\varphi-3\sin^2\varphi)]^2+\sin^2\theta$$
$$\times[(B+C+D+F-H-I)\cos^2\psi+(D+F-B-C)$$
$$\times\sin^2\psi]+\sin^4\theta[(2I+H+E+G-2B-C-D-F)$$
$$\times\cos^2\psi+(B-F)\sin^2\psi]+\sin^6\theta[B-E-I]\cos^2\psi. \quad (51)$$

A has previously been derived from parallel measurements, and since the last term is $-(C'+D')$ this equation determines four more constants. By designating

$$B+C+D+F-H-I=E',$$
$$2I+H+E+G-2B-C-D-F=F',$$
$$D+F-B-C=G', \quad B-F=H', \quad (52)$$

these four constants can be related to four new magnetostrictive measurements. As shown by Fig. 4(b) and (c), all of these measurements can be made on a single slab in the x-z plane. The constants λ_5 and λ_6, measured when $\psi=0$, are measured when the saturation magnetization is 90° and 45° from the z axis and the magnetostriction is measured in the plane perpendicular to the magnetization. The other two constants, λ_7 and λ_8, are measured along the plane thickness for the same directions of magnetization. In all these measurements, $\varphi=0$. For the first set, $\psi=0$ and the equations become

$$\lambda_5=E'+F'-(C'+D'); \lambda_6=\tfrac{1}{2}E'+\tfrac{1}{4}F'-\tfrac{1}{8}(C'+D'). \quad (53)$$

The second set are obtained when $\psi=90°$, so that

$$\lambda_7=G'+H'+A; \quad \lambda_8=\tfrac{1}{2}G'+\tfrac{1}{4}(H'+A). \quad (54)$$

Since $A=\lambda_4-\lambda_1$, we can solve these equations simultaneously for E', F', G', and H', obtaining

$$E'=4\lambda_6-\lambda_5-\tfrac{1}{2}(C'+D'); \; F'=2\lambda_5-4\lambda_6+\tfrac{3}{2}(C'+D');$$
$$G'=4\lambda_8-\lambda_7; \quad H'=2\lambda_7-4\lambda_8-A. \quad (55)$$

Since $C'+D'=(32/3)\lambda_3-(32/3)\lambda_2+(16/3)\lambda_1$ and $A=\lambda_4-\lambda_1$, these values are related to the measured magnetostriction values by the equations

$$E'=4\lambda_6-\lambda_5-(16/3)\lambda_3+(16/3)\lambda_2-(8/3)\lambda_1;$$
$$F'=2\lambda_5-4\lambda_6+(48/3)\lambda_3-(48/3)\lambda_2+(24/3)\lambda_1;$$
$$G'=4\lambda_8-\lambda_7; \quad H'=2\lambda_7-4\lambda_8+\lambda_1-\lambda_4. \quad (56)$$

If we introduce the A to I values in the expression for A' to H' of Eqs. (43) and (56) and solve simultaneously for the unprimed values, we determine A, C, D, and G uniquely and have four more relations between the other five constants.

To determine the other constant requires a measurement for which the magnetization and magnetostriction are not parallel or perpendicular. The simplest method for determining the measurement to make is to introduce a vector for the saturation magnetization having the direction cosines

$$\alpha_1=\sin\theta_1\cos\varphi_1; \quad \alpha_2=\sin\theta_1\sin\varphi_1; \quad \alpha_3=\cos\theta_1, \quad (57)$$

and another vector for the magnetostriction having the direction cosines

$$\beta_1=\sin\theta_2\cos\varphi_2; \quad \beta_2=\sin\theta_2\cos\varphi_2; \quad \beta_3=\cos\theta_2. \quad (58)$$

If these values are introduced into the general expression, Eq. (39), the equation becomes

$$\lambda=A\sin^4\theta_1\sin^2\theta_2\sin^2(2\varphi_1+\varphi_2)$$
$$+\tfrac{1}{4}B\sin^2 2\theta_1\sin^2\theta_2[\cos(\varphi_2-\varphi_1)+\sin(\varphi_2-\varphi_1)]^2$$
$$+C\sin^2\theta_1\sin^2\theta_2[\cos(\varphi_2-\varphi_1)+\sin(\varphi_2-\varphi_1)]^2$$
$$+D\sin^2\theta_1\sin^2\theta_2+\tfrac{1}{4}E\sin^2 2\theta_1\cos^2\theta_2+\tfrac{1}{4}F\sin^2 2\theta_1$$
$$+G\sin^2\theta_1\cos^2\theta_2+\tfrac{1}{4}H\sin 2\theta_1\sin 2\theta_2\cos(\varphi_2-\varphi_1)$$
$$+\tfrac{1}{4}I\cos^2\theta_1\sin 2\theta_1\sin 2\theta_2\cos(\varphi_2-\varphi_1). \quad (59)$$

An examination of this equation shows that if

$$\theta_1=45°; \quad \theta_2=0°; \quad \varphi_1=\varphi_2=0; \quad \text{i.e.,} \quad \alpha_1=\alpha_3=1/\sqrt{2};$$
$$\alpha_2=0; \quad \beta_1=\beta_2=0; \quad \beta_3=1, \quad (60)$$

the measured magnetostriction λ_9 will equal

$$\lambda_9=\tfrac{1}{4}(E+F)+\tfrac{1}{2}G, \quad \text{or} \quad E+F=4\lambda_9-2\lambda_5. \quad (61)$$

This orientation is shown by Fig. 4(c). This gives enough relations to solve for all the constants in terms of the measured values, and we find

$$A=\lambda_4-\lambda_1; \quad B=-2\lambda_9-2\lambda_5+\lambda_7+2\lambda_6-\tfrac{1}{2}\lambda_4$$
$$+(4/3)\lambda_3+(4/3)\lambda_2-(5/6)\lambda_1; \quad C=\tfrac{1}{2}(\lambda_4-\lambda_7);$$
$$D=\lambda_1+\tfrac{1}{2}(\lambda_7-\lambda_4); \quad E=6\lambda_9-2\lambda_8+\lambda_7-2\lambda_6-2\lambda_5$$
$$-\tfrac{1}{2}\lambda_4-(4/3)\lambda_3-(4/3)\lambda_2+(11/6)\lambda_1;$$
$$F=-2\lambda_9+2\lambda_8-\lambda_7+2\lambda_6+\tfrac{1}{2}\lambda_4+(4/3)\lambda_3$$
$$+(4/3)\lambda_2-(11/6)\lambda_1; \quad G=\lambda_5;$$
$$H=4\lambda_9-4\lambda_6-\lambda_5-(16/3)\lambda_3+(16/3)\lambda_2-(5/3)\lambda_1;$$
$$I=-8\lambda_9+4\lambda_6+2\lambda_5+(40/3)\lambda_3$$
$$-(24/3)\lambda_2+(8/3)\lambda_1. \quad (62)$$

These values can be checked by direct substitution. As shown by Fig. 4(a), (b), (c), all of these nine constants can be measured from two oriented slabs, one in the x-z plane and the other in the basal x-y plane.

Another relation of interest is the value of the volume magnetostriction in terms of these constants and the direction of the saturation magnetization. This can be calculated by introducing the direction cosines of Eq. (21) into the more general expression, Eq. (39), and carrying out the summation. This results in the equation

$$\tilde{\omega}=(2D+E+3F+G)\sin^2\theta+(A-E-3F)\sin^4\theta. \quad (63)$$

Introducing the value of these constants in terms of the λ's, we find

$$\omega=\{4[\lambda_8+\lambda_6+\tfrac{2}{3}(\lambda_2+\lambda_3)-\tfrac{1}{6}\lambda_1]-[\lambda_1+\lambda_5+\lambda_7]\}\sin^2\theta +\{-4[\lambda_8+\lambda_6+\tfrac{2}{3}(\lambda_2+\lambda_3)-\tfrac{1}{6}\lambda_1] +2(\lambda_1+\lambda_5+\lambda_7)\}\sin^4\theta. \quad (64)$$

Since $\frac{2}{3}(\lambda_2+\lambda_3)-\frac{1}{6}\lambda_1=\lambda_D$ of Sec. II, this equation reduces to

$$\omega=[4(\lambda_8+\lambda_6+\lambda_D)-(\lambda_1+\lambda_5+\lambda_7)]\sin^2\theta +[-4(\lambda_8+\lambda_6+\lambda_D)+2(\lambda_1+\lambda_5+\lambda_7)]\sin^4\theta. \quad (65)$$

The average value for a polycrystalline material is

$$\tilde{\omega}=\tfrac{2}{3}(2D+E+3F+G)+(8/15)(A-E-3F) =(8/15)(\lambda_8+\lambda_6+\lambda_D)+\tfrac{2}{3}(\lambda_1+\lambda_5+\lambda_7). \quad (66)$$

The perpendicular component then is

$$\lambda_\perp=\tfrac{1}{2}(\tilde{\omega}-\lambda_{11})=(4/15)(\lambda_6+\lambda_8)+(1/5)(\lambda_5+\lambda_7) +(16/315)\lambda_3-(16/315)\lambda_2 +(51/315)\lambda_1-(4/35)\lambda_4. \quad (67)$$

The morphic R constants, which determine the change in elastic constants due to the change in symmetry resulting from magnetization can be determined in a similar manner, but since no measurements have been made for cobalt, they will not be derived here.

IV. ANISOTROPY ENERGY DUE TO MAGNETOSTRICTION

The measurements of the anisotropic energy are carried out at constant stress so that the lattice is allowed to deform under the action of the magnetostriction forces. Hence, part of the anisotropic energy is due to magnetostrictive strains. Since it is desirable to determine how much anisotropic energy is inherent in the lattice and how much occurs due to magnetostriction, a calculation is given for the first-order magnetostrictive terms of Sec. II.

This value can be determined by evaluating the magnetostrictive energy that is required to go from a condition of constant stress to constant strain and subtract this from the anisotropic energy at constant stress. From Eq. (5), we find that the six components of strain are given by the equations

$$\begin{aligned}
S_1&=s_{11}{}^IT_1+s_{12}{}^IT_2+s_{13}{}^IT_3+\lambda_A\alpha_1{}^2+\lambda_B\alpha_2{}^2,\\
S_2&=s_{12}{}^IT_1+s_{11}{}^IT_2+s_{13}{}^IT_3+\lambda_A\alpha_2{}^2+\lambda_B\alpha_1{}^2,\\
S_3&=s_{13}{}^I(T_1+T_2)+s_{33}{}^IT_3+\lambda_C(1-\alpha_3{}^2),\\
S_4&=s_{44}{}^IT_4+(-\lambda_A-\lambda_C+4\lambda_D)\alpha_2\alpha_3,\\
S_5&=s_{44}{}^IT_5+(-\lambda_A-\lambda_C+4\lambda_D)\alpha_1\alpha_3,\\
S_6&=2(s_{11}{}^I-s_{12}{}^I)T_6+2(\lambda_A-\lambda_B)\alpha_1\alpha_2.
\end{aligned} \quad (68)$$

Hence, in the absence of any applied stresses T_1 to T_6, the crystal will be strained by the values on the right-hand side of each equation. To determine the anisotropic energy due to magnetostriction, we have to calculate the energy required to distort the crystal so that the resultant strains are all zero. To perform this calculation, it is desirable to express the stresses in terms of the strains, which can be done by solving Eq. (68) for the T's when all the magnetostrictive strains are zero. This results in the equations

$$T_1=c_{11}{}^IS_1+c_{12}{}^IS_2+c_{13}{}^IS_3;\quad T_2=c_{12}{}^IS_1+c_{11}{}^IS_2+c_{13}{}^IS_3;$$

$$T_3=c_{13}{}^I(S_1+S_2)+c_{33}{}^IS_3;\quad T_4=c_{44}{}^IS_4;$$

$$T_5=c_{44}{}^IS_5;\quad T_6=\tfrac{1}{2}(c_{11}{}^I-c_{12}{}^I)S_6; \quad (69)$$

where

$$2c_{11}{}^I=\frac{s_{33}{}^I}{\alpha}+\frac{1}{s_{11}{}^I-s_{12}{}^I};\quad 2c_{12}{}^I=\frac{s_{33}}{\alpha}-\frac{1}{s_{11}{}^I-s_{12}{}^I};$$

$$c_{13}{}^I=\frac{-s_{13}{}^I}{\alpha};\quad c_{33}{}^I=\frac{s_{11}{}^I+s_{12}{}^I}{\alpha};\quad c_{44}{}^I=\frac{1}{s_{44}{}^I};$$

$$\frac{c_{11}{}^I-c_{12}{}^I}{2}=\frac{1}{2(s_{11}{}^I-s_{12}{}^I)};\quad \alpha=s_{33}{}^I(s_{11}{}^I+s_{12}{}^I)-2s_{13}{}^{I2}.$$

The total energy required is calculated from the formula

$$E_A{}^T-E_A{}^S=\tfrac{1}{2}[T_1S_1+T_2S_2+T_3S_3 +T_4S_4+T_5S_5+T_6S_6], \quad (70)$$

since the strain changes from the value given in Eq. (68) to zero during the motion. Introducing the negative of the values of S_1 to S_6 of Eq. (68), when the T's are zero, into Eq. (69) to determine the values of T and inserting both the S and T values in Eq. (70), the energy required to erase the magnetostrictive strains is

$$E_A{}^T-E_A{}^S=\tfrac{1}{2}\{(1-\alpha_3{}^2)^2[c_{11}{}^I(\lambda_A{}^2+\lambda_B{}^2) +2c_{12}{}^I\lambda_A\lambda_B+2c_{13}{}^I(\lambda_A+\lambda_B)\lambda_C+c_{33}{}^I\lambda_C{}^2] +c_{44}{}^I(1-\alpha_3{}^2)\alpha_3{}^2(-\lambda_A-\lambda_C+4\lambda_D)^2\}. \quad (71)$$

Hence, since $(1-\alpha_3{}^2)^2=\sin^4\theta$, $(1-\alpha_3{}^2)\alpha_3{}^2=\sin^2\theta\cos^2\theta =\sin^2\theta-\sin^4\theta$, the anisotropic energy at constant strain

can be written in the form

$$E_A{}^S=[\tfrac{1}{2}(K_1{}^T-K_3{}^T)+K_{13}{}^T-K_{33}{}^T$$
$$-\tfrac{1}{2}c_{44}{}^I(-\lambda_A-\lambda_C+4\lambda_D)^2]\sin^2\theta$$
$$+\{\tfrac{1}{2}(K_{11}{}^T+K_{33}{}^T-4K_{13}{}^T)-\tfrac{1}{2}[c_{11}{}^I(\lambda_A{}^2+\lambda_B{}^2)$$
$$+2c_{12}{}^I\lambda_A\lambda_B+2c_{13}{}^I(\lambda_A+\lambda_B)\lambda_C+c_{33}{}^I\lambda_C{}^2$$
$$-c_{44}{}^I(-\lambda_A-\lambda_C+4\lambda_D)^2]\}\sin^4\theta. \quad (72)$$

ACKNOWLEDGMENTS

The writer is indebted to Dr. R. M. Bozorth for suggesting this problem. Dr. P. W. Anderson has independently derived the expression for the magnetostriction in a tetragonal crystal as discussed in the appendix. Dr. J. A. Lewis has independently derived the first-order constants for a crystal with circular symmetry.

APPENDIX A. CALCULATIONS FOR TEGRAGONAL AND ORTHORHOMBIC CRYSTALS

The first-order approximations discussed in Sec. II have been extended to tetragonal and orthorhombic crystals, since cobalt ferrite, heat-treated in a magnetic field, probably crystallizes in one of these two systems. Since the procedures necessary to calculate these constants have already been discussed in Sec. II, only the final results are given. In agreement with experiment, it is assumed that the easy direction of magnetization lies along the z axis, and all the formulas given are for the difference between the saturated conditions for any direction and the demagnetized condition with equal numbers of domains directed along $\pm z$.

For tetragonal crystals,[5] the anisotropy energy E_A, magnetostriction λ_S, and difference between anisotropy energy at constant stress and constant strain, $E_A{}^T-E_A{}^S$, are:

$$E_A{}^T=K_1\sin^2\theta+K_2\sin^4\theta+K_3\sin^4\theta\sin^2\varphi\cos^2\varphi, \quad (73)$$

$$\lambda=\tfrac{1}{2}\lambda_1[(\alpha_1\beta_1-\alpha_2\beta_2)^2-(\alpha_1\beta_2+\alpha_2\beta_1)^2+(1-\beta_3{}^2)(1-\alpha_3{}^2)$$
$$-2\alpha_3\beta_3(\alpha_1\beta_1+\alpha_2\beta_2)]+4\lambda_2\alpha_3\beta_3(\alpha_1\beta_1+\alpha_2\beta_2)$$
$$+4\lambda_3\alpha_1\alpha_2\beta_1\beta_2+\lambda_4[\beta_3{}^2(1-\alpha_3{}^2)-\alpha_3\beta_3(\alpha_1\beta_1+\alpha_2\beta_2)]$$
$$+\tfrac{1}{2}\lambda_5[(\alpha_1\beta_2-\alpha_2\beta_1)^2-(\alpha_1\beta_1+\alpha_2\beta_2)^2$$
$$+(1-\beta_3{}^2)(1-\alpha_3{}^2)], \quad (74)$$

[5] For tetragonal crystals the magnetostriction formula was first calculated by P. W. Anderson with results similar to those given here.

where

$$\lambda_1=\lambda(\alpha_1=1,\beta_1=1);\quad \lambda_2=\lambda(\alpha_1=\beta_1=\alpha_3=\beta_3=1/\sqrt{2});$$
$$\lambda_3=\lambda(\alpha_1=\alpha_2=\beta_1=\beta_2=1/\sqrt{2});$$
$$\lambda_4=\lambda(\alpha_1=1,\beta_3=1);\quad \lambda_5=\lambda(\alpha_1=1,\beta_2=1);$$

$$E_A{}^T-E_A{}^S=\{\tfrac{1}{2}c_{44}(4\lambda_2-\lambda_1-\lambda_4)^2\sin^2\theta+[c_{11}(\lambda_1{}^2+\lambda_5{}^2)$$
$$+c_{33}\lambda_4{}^2+2c_{12}\lambda_1\lambda_5+2c_{13}(\lambda_1+\lambda_5)\lambda_4$$
$$-c_{44}(4\lambda_2-\lambda_1-\lambda_4)^2]\sin^4\theta+[-2(c_{11}-c_{12})(\lambda_1-\lambda_5)^2$$
$$+c_{66}(4\lambda_3-2(\lambda_1+\lambda_5))^2]\sin^4\theta\sin^2\varphi\cos^2\varphi\}. \quad (75)$$

For orthorhombic crystals,

$$E_A{}^T=\sin^2\theta[K_1\cos^2\varphi+K_2\sin^2\varphi]$$
$$+\sin^4\theta[K_3\cos^4\varphi+K_4\sin^2\varphi\cos^2\varphi+K_5\sin^4\varphi]$$
$$+\sin^2\theta\cos^2\theta[K_6\cos^2\varphi+K_7\sin^2\varphi], \quad (76)$$

$$\lambda=\lambda_1[\alpha_1{}^2\beta_1{}^2-\alpha_1\alpha_2\beta_1\beta_2-\alpha_1\alpha_3\beta_1\beta_3]$$
$$+\lambda_2[\alpha_2{}^2\beta_1{}^2-\alpha_1\alpha_2\beta_1\beta_2]+\lambda_3[\alpha_1{}^2\beta_2{}^2-\alpha_1\alpha_2\beta_1\beta_2]$$
$$+\lambda_4[\alpha_2{}^2\beta_2{}^2-\alpha_1\alpha_2\beta_1\beta_2-\alpha_2\alpha_3\beta_2\beta_3]+\lambda_5[\alpha_1{}^2\beta_3{}^2$$
$$-\alpha_1\alpha_3\beta_1\beta_3]+\lambda_6[\alpha_2{}^2\beta_3{}^2-\alpha_2\alpha_3\beta_2\beta_3]+4\lambda_7(\alpha_1\alpha_2\beta_1\beta_2)$$
$$+4\lambda_8\alpha_1\alpha_3\beta_1\beta_3+4\lambda_9\alpha_2\alpha_3\beta_2\beta_3, \quad (77)$$

where

$$\lambda_1=\lambda(\alpha_1=1,\beta_1=1);\quad \lambda_2=\lambda(\alpha_2=1,\beta_1=1);$$
$$\lambda_3=\lambda(\alpha_1=1,\beta_2=1);\quad \lambda_4=\lambda(\alpha_2=1,\beta_2=1);$$
$$\lambda_5=\lambda(\alpha_1=1,\beta_3=1);\quad \lambda_6=\lambda(\alpha_2=1,\beta_3=1);$$
$$\lambda_7=\lambda(\alpha_1=\beta_1=\alpha_2=\beta_2=1/\sqrt{2});$$
$$\lambda_8=\lambda(\alpha_1=\alpha_3=\beta_1=\beta_3=1/\sqrt{2});$$
$$\lambda_9=\lambda(\alpha_2=\alpha_3=\beta_2=\beta_3=1/\sqrt{2});$$

$$E^T-E^S=\tfrac{1}{2}(\sin^2\theta-\sin^4\theta)[c_{55}(4\lambda_8-(\lambda_1+\lambda_5))^2\cos^2\varphi$$
$$+c_{44}(4\lambda_9-(\lambda_4+\lambda_6))^2\sin^2\varphi]+\tfrac{1}{2}\sin^4\theta\{(c_{11}\lambda_1{}^2$$
$$+2c_{12}\lambda_1\lambda_2+2c_{13}\lambda_1\lambda_5+c_{22}\lambda_2{}^2+2c_{23}\lambda_2\lambda_5+c_{33}\lambda_5{}^2)\cos^4\varphi$$
$$+2[c_{11}\lambda_1\lambda_2+c_{12}(\lambda_1\lambda_4+\lambda_2\lambda_3)+c_{13}(\lambda_1\lambda_6+\lambda_2\lambda_5)$$
$$+c_{22}\lambda_3\lambda_4+c_{23}(\lambda_3\lambda_6+\lambda_4\lambda_5)+c_{33}\lambda_5\lambda_6$$
$$+\tfrac{1}{2}c_{66}(4\lambda_7-(\lambda_1+\lambda_2+\lambda_3+\lambda_4))^2]\sin^2\varphi\cos^2\varphi$$
$$+(c_{11}\lambda_2{}^2+2c_{12}\lambda_2\lambda_4+2c_{13}\lambda_2\lambda_6+c_{22}\lambda_4{}^2$$
$$+2c_{23}\lambda_4\lambda_6+c_{33}\lambda_6{}^2)\sin^4\varphi\}. \quad (78)$$

Magnetostriction and Crystal Anisotropy of Single Crystals of Hexagonal Cobalt

R. M. Bozorth
Bell Telephone Laboratories, Murray Hill, New Jersey
(Received June 8, 1954)

Magnetostriction at saturation has been measured in various crystallographic directions in a single crystal of cobalt. Results are described by Mason's formula [see Eq. (1)] with 4 constants, which are now evaluated. Magnetization causes contractions as large as 100×10^{-6}, and expansions up to 150×10^{-6}, depending on crystallographic direction. A fractional decrease in volume, associated with domain orientation, is observed to be as large as 26×10^{-6}. Superposed on this contraction is a small isotropic increase in volume of 0.6×10^{-9} per oersted. Magnetic crystal anisotropy constants are determined and used in a calculation of the magnetostriction as dependent on the magnitude of the field applied to a disk with given demagnetizing factor. Calculation and observation agree, and show that the direction and magnitude of magnetization and of true field can be calculated in any applied field as long as it is considerably above the coercive force.

INTRODUCTION

THE magnetostriction of cubic crystals of iron, nickel, and various alloys of these metals has been investigated and the constants determined.[1,2] As a result, one can calculate the expansion or contraction that occurs in any crystallographic direction when a magnetic field is applied in sufficient strength to saturate the crystal in the same or any other crystallographic direction. The dimensional changes are usually described adequately by two constants.

Mason[3] has derived the expression for the saturation magnetostriction of a hexagonal crystal in terms of the direction cosines of the magnetization and the change in length. In the approximation used, which contains the direction cosines to the fourth power, there are four constants, which are determined by the measurements described below. To this approximation the magnetostriction has cylindrical symmetry.

The expression for the magnetic crystal anisotropy has also been derived by Mason,[3] and in accordance with the 2-constant expression generally used there is cylindrical symmetry when fourth-order terms are the highest used. Hexagonal symmetry appears only when sixth-power terms are used. In cobalt these terms are negligibly small.

The magnetostriction of a single crystal of cobalt was studied in 1929 by Nishiyama,[4] who used a maximum field of 7000 oersteds and observed a maximum contraction of about 30×10^{-6}. His results indicate cylindrical symmetry, with a maximum contraction at about 70° to the hexagonal axis; these observations are confirmed in the present study, and are extended to 25 000 oersteds.

[1] R. Becker and W. Döring, *Ferromagnetismus* (Verlag Julius Springer, Berlin, 1939).
[2] R. M. Bozorth, *Ferromagnetism* (D. Van Nostrand Company, Inc., New York, 1951).
[3] W. P. Mason, Phys. Rev. **96**, 302 (1954).
[4] Z. Nishiyama, Science Repts. Tôhoku Imp. Univ. **18**, 341 (1929).

EXPRESSIONS FOR K AND λ

The expression for magnetostriction at saturation in a hexagonal crystal is:

$$\begin{aligned}\lambda=&\lambda_A[(\alpha_1\beta_1+\alpha_2\beta_2)^2-(\alpha_1\beta_1+\alpha_2\beta_2)\alpha_3\beta_3]\\&+\lambda_B[(1-\alpha_3^2)(1-\beta_3^2)-(\alpha_1\beta_1+\alpha_2\beta_2)^2]\\&+\lambda_C[(1-\alpha_3^2)\beta_3^2-(\alpha_1\beta_1+\alpha_2\beta_2)\alpha_3\beta_3]\\&+4\lambda_D(\alpha_1\beta_1+\alpha_2\beta_2)\alpha_3\beta_3. \quad (1)\end{aligned}$$

Here λ is the fractional change in length in the direction defined by the direction cosines β_1, β_2, and β_3, when the crystal is magnetized to saturation in the direction defined by α_1,α_2, α_3. The z or 3 axis is chosen parallel to the hexagonal c axis, the x axis parallel to the crystallographic a axis and the y axis at right angles to x and z. It is assumed in accordance with the data for cobalt at room temperature that the direction of easy magnetization lies along the c axis so that $\lambda=0$ when the magnetization is in this direction ($\alpha_3=1$). The change in length is then measured from this initial state.

When I_s is parallel to the direction of measurement of λ (i.e., $\alpha_i=\beta_i$), Eq. (1) reduces to

$$\lambda_{\parallel}=\lambda_A[(1-\alpha_3^2)^2-(1-\alpha_3^2)\alpha_3^2]+4\lambda_D(1-\alpha_3^2)\alpha_3^2. \quad (2)$$

If θ is the angle between I_s and the z axis, Eq. (2) reduces to

$$\lambda_{\parallel}=(\tfrac{1}{4}\lambda_A+\tfrac{1}{2}\lambda_D)-\tfrac{1}{2}\lambda_A\cos2\theta+(\tfrac{1}{4}\lambda_A-\tfrac{1}{2}\lambda_D)\cos4\theta, \quad (3)$$

containing two constants. The cylindrical symmetry is here apparent.

In any plane parallel to the hexagonal axis (e.g., y, z plane), the magnetostriction measured at right angles to the magnetization is

$$\begin{aligned}\lambda_{\perp}=&(\tfrac{1}{4}\lambda_A+\tfrac{1}{2}\lambda_C-\tfrac{1}{2}\lambda_D)+\tfrac{1}{2}\lambda_C\cos2\theta\\&-(\tfrac{1}{4}\lambda_A-\tfrac{1}{2}\lambda_D)\cos4\theta. \quad (4)\end{aligned}$$

In all directions in the hexagonal (x,y) plane $\lambda_{\parallel}=\lambda_A$, and λ measured perpendicular to I_s is $\lambda_{\perp}'=\lambda_B$. In the y, z plane $\lambda_{\perp}=\lambda_C$ for $\theta=0$ and $\lambda_{\parallel}=\lambda_D$ for $\theta=45°$. The constants are evaluated from the measurements made in this way, as described below.

According to Mason,[3] the magnetic anisotropy energy density is

$$E=K_1\sin^2\theta+K_2\sin^4\theta+K_3\sin^6\theta+K_4\sin^6\theta\cos6\varphi, \quad (5)$$

where θ is the polar and φ the azimuthal angle. The first two terms comprise the well-known expression, and were the only ones used in the present study.

SPECIMENS

A single crystal of cobalt was obtained from Horizons, Inc., where it was prepared by Mr. Straughan by slow cooling of the melt.[5] The material from which it was grown contained as principal impurities Ni(0.3 percent), Mn(0.08 percent), and Fe(<0.1 percent).

Specimens were cut for magnetostriction and anisotropy measurements as described in Table I. Surfaces were checked to an estimated 10′ by using an x-ray spectrometer, and directions to about 0.5° by using Laue photographs. All surfaces were carefully ground and electrolytically polished until no strain was evident from observation of Laue spots.

Specimens were cut from the same lot for measurement of the elastic constants by McSkimin.[6]

MEASUREMENTS

Magnetostriction was measured using strain gauges as described by Goldman.[7] The crystal, to which was fixed a single gauge, was placed in a 2-in. gap between the 11-in. diameter poles of an electromagnet in which a field strength of over 20 000 oersteds could be produced.

For control a second gauge from the same lot was fixed to brass, and a third was stuck to wood with Scotch tape. The apparent changes in length observed when the second and third gauges were separately subjected to a field were in agreement with each other and were used as corrections to the readings for the gauge on the cobalt crystal.

The difference between the magnetostriction of the disk used and that of an infinite sheet was calculated[8] from the dimensional ratio and the elastic constants and found to be about 1×10^{-6}, and was neglected.

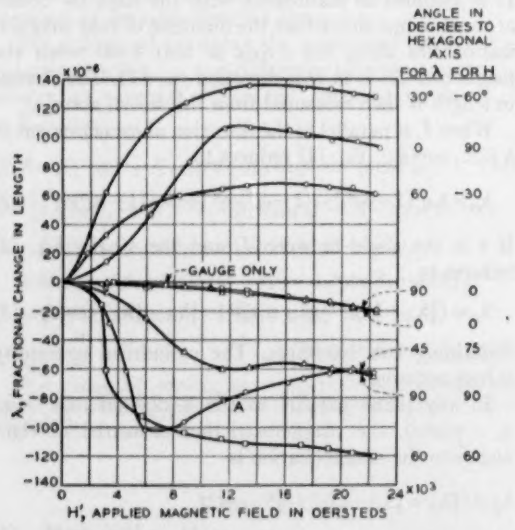

FIG. 1. Magnetostriction in (10·0) plane as dependent on applied field for various orientations of field and gauge with respect to z axis, as noted.

RESULTS

Some of the curves of λ *vs* H', the applied field, are shown in Fig. 1 for various directions of H' and gauge. These measurements are uncorrected for the effect of the field on the gauge alone. After such correction the saturation λ's for the $\lambda\|H$ and $\lambda\perp H$ curves were determined and are given in Fig. 2. The constants are derived from these data for Specimen 1 and from other data for Specimen 2 plotted in the same figure.

TABLE I. Description of specimens cut for magnetostriction and anistropy measurements.

No.	Shape	Dimensions (in.)	Orientation
1	disk	0.592×0.080	(10·0)
2	plate	0.472×0.295×0.078	(00·1),[10·0],[12̄·0]
3	plate	0.408×0.250×0.021	(11·0),[11̄·0],[00·1]
4	disk	0.116×0.017	(11·0)
5	disk	0.134×0.032	(10·0)
6	disk	0.136×0.050	(00·1)

Measurements were also made of λ at 45° to the hexagonal axis in the (10·0) plane (Specimen 1) when the field was applied in various directions in the plane. Saturation magnetostriction is shown by the crosses in Fig. 3.

The constants derived from the data are:

$$\lambda_A=-45\times10^{-6}, \qquad \lambda_B=-95\times10^{-6},$$
$$\lambda_C=+110\times10^{-6}, \qquad \lambda_D=-100\times10^{-6}.$$

With these values, the saturation magnetostriction in the (10·0) plane, measured parallel and perpendicular to the applied field, are:

$$\lambda_{\|}=\tfrac{1}{2}\lambda_A(1-\cos2\theta)-(\tfrac{1}{4}\lambda_A-\tfrac{1}{2}\lambda_D)(1-\cos4\theta)$$
$$=(-61+22\cos2\theta+39\cos4\theta)\times10^{-6}, \quad (6)$$

$$\lambda_{\perp}=\tfrac{1}{2}\lambda_C(1+\cos2\theta)+(\tfrac{1}{4}\lambda_A-\tfrac{1}{2}\lambda_D)(1-\cos4\theta)$$
$$=(94+55\cos2\theta-39\cos4\theta)\times10^{-6}, \quad (7)$$

as shown by the dotted lines of Fig. 2.

The saturation magnetostriction in the (10·0) plane at 45° to the hexagonal axis, when H is applied at

[3] A similar specimen was grown some years ago by Cioffi, Williams, and Bozorth, Phys. Rev. **51**, 1009 (1937).
[6] McSkimin, Williams, and Bozorth, Phys. Rev. **95**, 616 (1954).
[7] J. E. Goldman, Phys. Rev. **72**, 529 (1947).
[8] W. J. Carr and R. Smoluchowski, Phys. Rev. **83**, 1236 (1951). Note omission of a minus sign in the middle of their Eq. (A-7).

angle θ, is

$$\lambda_{45}=(\tfrac{1}{4}\lambda_A+\tfrac{1}{4}\lambda_C)(1-\cos 2\theta)-(\tfrac{1}{4}\lambda_A+\tfrac{1}{4}\lambda_C-\lambda_D)\sin 2\theta$$
$$=(16-16\cos 2\theta-116\sin 2\theta)\times 10^{-6}. \quad (8)$$

This is the equation for an ellipse, and when plotted on a polar diagram has the form shown by the solid line on the right-hand half of Fig. 3. The major axis of the ellipse is rotated a few degrees from $\theta=45°$.

Calculated curves for λ_0 and $\lambda_{90}(\theta=0°$ or $90°)$ are also shown there in quadrants 2 and 3.

It is evident from Figs. 2 and 3 that the largest contraction occurs when H is applied at about 50° to the hexagonal axis, and that it then diminishes as the direction of H approaches 90°, as was also observed by Nishiyama.[4] It is at first surprising that the maximum magnetostriction is not at $\theta=90°$, as it would be in the simplest possible model in which the strain is represented by an ellipsoid of revolution with its axis

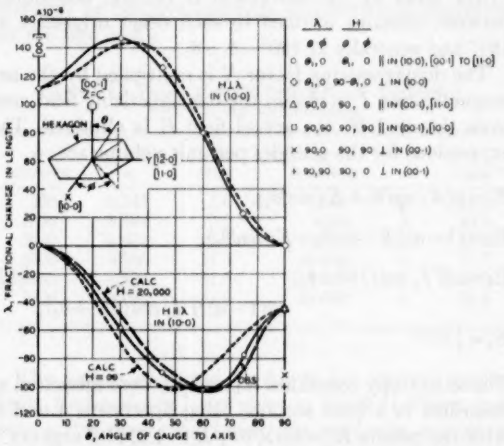

FIG. 2. Magnetostriction when applied field is $H'=20\,000$ oersteds, measured $\parallel$ and $\perp$ H', in (10·0) plane.

parallel to the magnetization. This is a true model, however, only when $\lambda_D=\frac{1}{2}\lambda_A$.

The maximum contraction now observed at about 50° to the hexagonal axis may be connected with the fact that in the close-packed hexagonal structure of cobalt this is the direction of *next*-nearest neighbors, the direction in which there are no nearest neighbors.

A noticeable feature of the curves of Fig. 1 is the initial large contraction and subsequent expansion of the specimen as shown in curve marked A. The explanation of this, and a calculation that shows good agreement with experiment, are given in the second section following.

VOLUME EFFECTS

The fractional change in volume associated with domain rotation is

$$\omega=\lambda_{\parallel}+\lambda_{\perp}+\lambda_{\perp}', \quad (9)$$

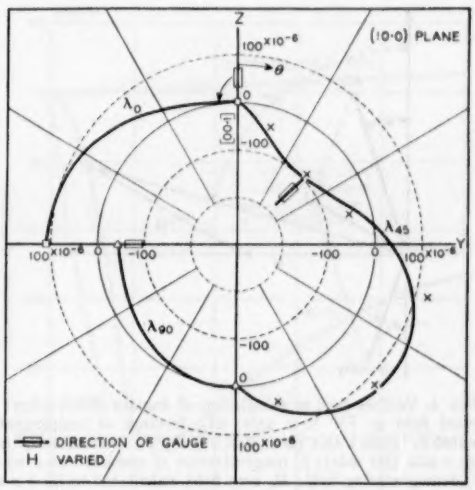

FIG. 3. Quadrants 1 and 4: λ measured at 45° to z-axis as dependent on strength of field applied at various angles to z-axis in (10·0) plane. Quadrant 2: Magnetostriction measured $\parallel z$ axis with H at various angles to z axis. Quadrant 3: Same with gauge $\perp z$ axis.

where $\lambda_{\perp}$ and $\lambda_{\perp}'$ are measured in the two directions at right angles to the direction of magnetization and to each other. Direct measurement of this change is obtained by combining the data for Specimens 1 and 2. Results are: $\lambda_{\parallel}=-45\times10^{-6}$, $\lambda_{\perp}=-93\times10^{-6}$ in the (00·1) plane, $\lambda_{\perp}'=+112\times10^{-6}$ in the (10·0) plane, so $\omega=-26\times10^{-6}$. This compares with ω calculated[3] from the chosen constants:

$$\omega=(\lambda_A+\lambda_B+\lambda_C)\sin^2\theta=-30\times10^{-6}. \quad (10)$$

This is the first unambiguous determination of a volume change associated with rotation, although a possible change of this kind has been reported[9] in an iron-nickel alloy containing 78 percent nickel.

The calculated volume magnetostriction of polycrystalline cobalt with crystals oriented at random is[3]

$$\bar{\omega}=\tfrac{2}{3}(\lambda_A+\lambda_B+\lambda_C)=-20\times10^{-6}. \quad (11)$$

The isotropic volume change associated with the change of spontaneous magnetization with field can readily be observed in principle by measuring the magnetostriction along the [00·1] axis of easy magnetization, parallel to which the domains lie, because the change in the sense of the magnetization results in zero magnetostriction [Eq. (1) with $\theta=0$]. Measured changes in this direction, with corrections applied for the effect of the field on the gauge alone, yield the data plotted in the upper part of Fig. 6 (see below). The slope of this line is approximately 0.2×10^{-9}/oersted, so that $\omega/H=0.6\times10^{-9}$/oersted. This is consistent with the data of Kornetzki[10] who measured the total

[9] R. M. Bozorth and R. W. Hamming, Phys. Rev. **89**, 865 (1953).

[10] M. Kornetzki, Z. Physik **87**, 560 (1934).

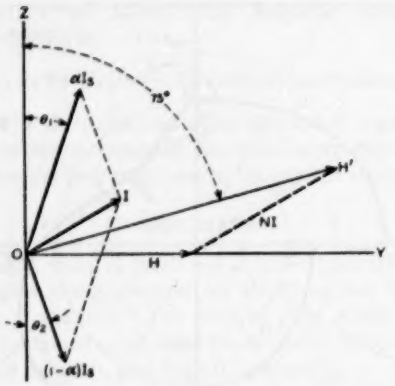

FIG. 4. Vectors used in calculation of domain distribution: H', applied field at 75° to z axis; αI_s, fraction of magnetization oriented $\theta_1°$ from z axis (near side); $(1-\alpha)I_s$, fraction at $\theta_2°$ from from z axis (far side); I, magnetization of specimen as a whole; NI, demagnetizing field; H, true field, calculated to lie $\parallel z$ axis when $\alpha<1$.

volume change, including that attributable to domain rotation, in fields up to 10 500 oersteds. After an initial contraction, presumably caused by domain rotation, he observed a net volume expansion of 0.5×10^{-9}/oersted when $H>9500$.

The magnitude of the isotropic volume change is not here determined with high accuracy. The sign of the change is such that any error in aligning the gauge parallel to the z axis would cause the observed change to be too small.

FIELD DEPENDENCE OF MAGNETOSTRICTION

The general form of Curve A of Fig. 1 can be understood in terms of the curve of λ_{45} of Fig. 3. A field is applied at 75° to the hexagonal axis, and the gauge measures change in length at 45° to this axis. Then as the field is increased in strength the angle of the magnetization vector varies from $\theta=0°$ to 75°. The maximum contraction takes place, in accordance with Curve λ_{45} of Fig. 3 and Eq. (8), when $\theta\approx45°$. After that the contraction diminishes and λ approaches a limit of -28×10^{-6}.

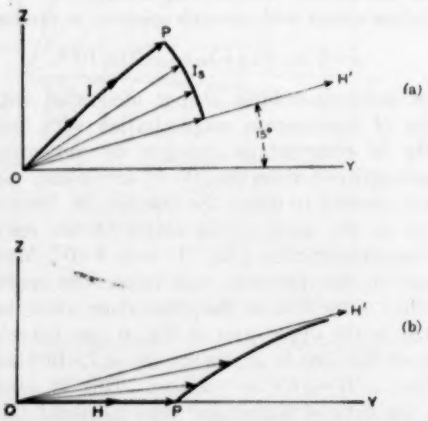

FIG. 5. (a) Increase of magnitude and direction of I with increase in H' applied 75° to z axis. (b) Change of (true) field H with applied field H'.

A quantitative consideration of the magnitudes involved was then carried out. In order to do this it is necessary to evaluate the various energies involved and then to determine the variables corresponding to minimum total energy.

The energies are (1) the magnetic crystal anisotropy, (2) the mutual energy between field and magnetization, and (3) the energy of demagnetization, which is originally derived from (2). In accordance with Fig. 4 the applied field is H', a fraction α of the domains of magnetization I_s is oriented at the angle θ_1 from the "near" hexagonal axis, $(1-\alpha)$ is at θ_2 from the "far" axis. It is assumed that $\alpha=\frac{1}{2}$ at $H'=0$ and that as H' increases some of the domains change from one direction to the other by the movement of domain boundaries between domains inclined to each other originally at 180° and generally at $180°-\theta_1-\theta_2$.

The demagnetizing factor N is multiplied by the net magnetization I to obtain the demagnetizing field, and from this and H' the actual field H is obtained. The expressions for the energies per unit volume are:

$$\begin{aligned}
&E_1=\alpha(K_1\sin^2\theta_1+K_2\sin^4\theta_1),\\
&E_2=(1-\alpha)(K_1\sin^2\theta_2+K_2\sin^4\theta_2),\\
&E_3=\alpha H'I_s\cos(75°-\theta_1)\\
&\qquad\qquad+(1-\alpha)H'I_s\cos(75°+\theta_2),\\
&E_4=\tfrac{1}{2}NI^2.
\end{aligned}\tag{12}$$

The anisotropy constants K_1 and K_2 were measured as described in a later section, using Specimens 4 and 5, with the results $K_1=4.3\times10^6$, $K_2=1.2\times10^6$ ergs cm^{-3}. These are close to the values derived[2] from the magnetization curves of Honda and Masumoto.[11] The demagnetizing factor is calculated to be $N=1.1$, assuming it is the same as that for an ellipsoid of the same major and minor axes as the disk.

The values of the parameters α, θ_1, and θ_2 for given values of H' up to $H'=20\,000$ oersteds were obtained by Miss M. C. Gray with the help of the analog computer and numerical calculations. By calculation and by analysis she also showed that $\theta_1=\theta_2$.

Calculation of H from H' and NI showed that H is parallel to the y axis when $\alpha<1$, and that when $\alpha=1$ it approaches the direction of H' as H' increases. This is also a consequence of the identity of θ_1 and θ_2 because these angles will be equal only when H makes the same angle with αI_s and $(1-\alpha)I_s$. A similar situation exists in a disk cut from a cubic crystal: the actual field H tends to be nearer the direction of hard magnetization

[11] K. Honda and H. Masumoto, Science Repts. Tôhoku Imp. Univ. **20**, 323 (1931).

than does the applied field H', as was shown qualitatively previously.[12]

As a consequence of these results, the direction of magnetization in weak fields can be calculated for a disk with given N. If the z axis makes the angle θ_0 with H', and Φ with I, then analysis shows that in weak fields ($\alpha \approx \frac{1}{2}$),

$$\tan\theta_0 = \frac{\frac{1}{2}NI_s^2 + K_1}{\frac{1}{2}NI_s^2} \cdot \tan\Phi. \qquad (13)$$

When α just becomes equal to 1 (point P in Fig. 5), analysis gives

$$\tan\theta_0 = \frac{(K_1 + K_2 + \frac{1}{2}NI_s^2)\sin 2\Phi - \frac{1}{2}K_2 \sin 4\Phi}{\frac{1}{2}NI_s^2(1+\cos 2\Phi)}, \qquad (14)$$

which reduces to Eq. (13) when $K_2 = 0$. The calculated course of the I vector in Fig. 5(a), is then a straight or slightly curved line over the length OP. In general the line may be concave upwards or downwards depending on the sign of K_2.

TABLE II. Values of α and $\theta = \theta_1 = \theta_2$, for specimen 1 with various applied fields.

H' (oersteds)	α	θ (deg)	H' (oersteds)	α	θ (deg)
500	0.542	3.6	6000	1	38.4
1000	0.584	7.2	7000	1	42.3
2000	0.671	14.3	8000	1	45.9
3000	0.766	21.1	10 000	1	51.7
4000	0.874	27.6	15 000	1	60.8
5000	0.999	33.9	20 000	1	65.4

The values of α and $\theta = \theta_1 = \theta_2$ for various applied fields, for Specimen 1, are given in Table II. From these values the magnetostriction can easily be calculated from Eq. (8). The resulting λ_{45} *vs* H' curve is shown in Fig. 6. The data were taken in a special run made with more care than for Curve A of Fig. 1.

The agreement between calculation and experiment indicates strongly that the assumed mechanism of magnetization is correct. The distribution of the domains among the two directions, which themselves are calculated from the crystal anisotropy and applied field and demagnetizing factor, is thus generally calculable from known expressions for the various energies involved.

CRYSTAL ANISOTROPY

The crystal anisotropy constants K_1 and K_2 of Eq. (5) were determined by measuring the torque on a disk subjected to a high field in its plane. The most careful measurements were made on the (10·0) disk, Specimen 5, using an applied field of 25 000 oersteds. Data are given as solid circles in Fig. 7.

[12] R. M. Bozorth and H. J. Williams, Phys. Rev. **59**, 827 (1941).

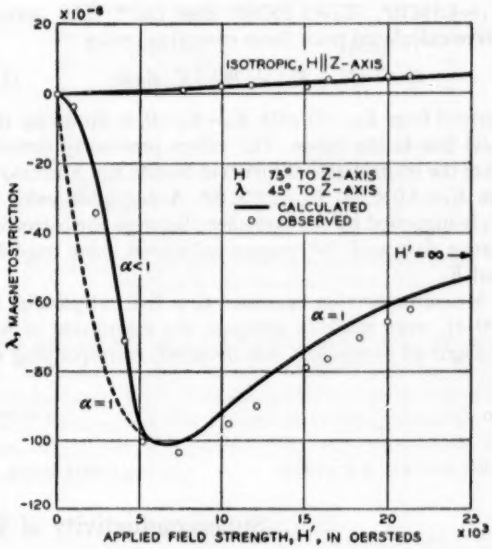

FIG. 6. Magnetostriction measured at 45° to z axis when field is applied at 75° to z axis. Points, observed, after correction for effect of gauge alone; solid line, calculated as described in text; broken line, calculated for zero demagnetizing factor. Upper line, isotropic magnetostriction measured with H and $\lambda \parallel z$ axis; $\omega/H = 3\lambda/H = 0.6\times10^{-6}$/oersted.

The sum $K_1 + K_2$ was put equal to the area under the torque curve from $\theta = 0$ to $\theta = 90$. Correction was then applied to the torque curve for lack of saturation, in accordance with a suggestion of H. J. Williams. Since in reasonably high fields the torque is

$$L = -HI_s \sin\alpha,$$

the angle α between H and I_s can be calculated and the observed L *vs* θ curve can be corrected by displacing each point along the θ axis by the appropriate amount α. Data so corrected are shown in Fig. 7 by crosses. The maximum value of α was found to be 9°.

Separate values of K_1 and K_2 were determined by a least-squares fit with the corrected curve. Results are

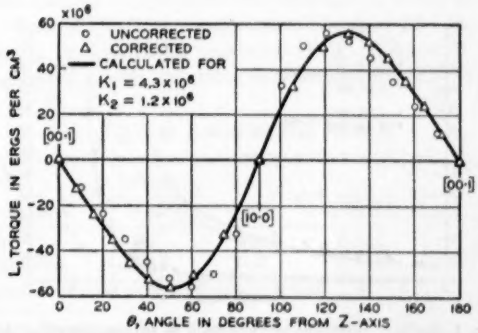

FIG. 7. Torque *vs* angle with z axis, in (10·0) plane. Circles, observed; triangles, corrected; line, theoretical with $K_1 = 4.3\times10^6$, $K_2 = 1.2\times10^6$ ergs cm^{-3}.

$K_1=4.3\times10^6$, $K_2=1.2\times10^6$ ergs cm^{-3}. The torque curve calculated from these constants, using

$$L=-(K_1+K_2)\sin2\theta+\tfrac{1}{2}K_2\sin4\theta, \qquad (15)$$

derived from Eq. (5) with $K_3=K_4=0$, is shown by the solid line in the figure. The values previously derived from the magnetization curves of Honda and Masumoto are $K_1=4.0\times10^6$, $K_2=2.0\times10^6$. A negligible value of K_3 is suggested by the agreement between the corrected torque data and the torques calculated using only K_1 and K_2.

Measurements on Specimen 6, a disk cut parallel to (00·1), were made to estimate the magnitude of K_4. A slight 6θ component was detected, corresponding to $K_4=+3000$ ergs cm^{-3}. This is about $10^{-3}K_1$ and is considered negligible and uncertain.

The field necessary to saturate cobalt at right angles to the hexagonal axis is calculated to be

$$H_s=(2K_1+4K_2)/I_s=9500.$$

I am indebted to Mr. R. C. Sherwood for preparation of the specimens from the crystals, and to Mrs. E. F. Tilden and Mr. A. J. Williams for assistance with the measurements. My appreciation is also due to Miss M. C. Gray for evaluating the constants used in calculating magnetostriction as dependent on field strength, and to Mrs. G. J. Rowe for setting up and operating the analog computer used in this evaluation.

PHYSICAL REVIEW VOLUME 96, NUMBER 2 OCTOBER 15, 1954

Superconductivity of Vanadium at 24 000 Mc/sec

C. J. GREBENKEMPER
Naval Research Laboratory, Washington, D. C.

(Received June 4, 1954)

The high-frequency resistance of vanadium was measured at frequencies in the vicinity of 24 000 Mc/sec in both the normal and superconducting states using resonant cavity techniques.

The normal conductivity was not affected by the "anomalous skin effect" as much as the "soft superconductors." The inner surfaces of the cavities were mechanically polished to a good surface finish. The normalized surface resistance extrapolated to absolute zero yields a value of 0.007 times its initial resistance.

INTRODUCTION

SUPERCONDUCTIVITY of vanadium is of interest because this metal belongs to the class of "hard superconductors." Most of the metals in this class do not exhibit a sharp transition between the normal and superconducting state. The "soft superconductors" almost always exhibit an extremely sharp transition. The behavior of vanadium at high frequencies is of interest since very little work has been done on the "hard superconductors" at high frequencies. McLennan[1] and co-workers investigated tantalum at 10 Mc/sec many years ago and found an abnormally high resistance.

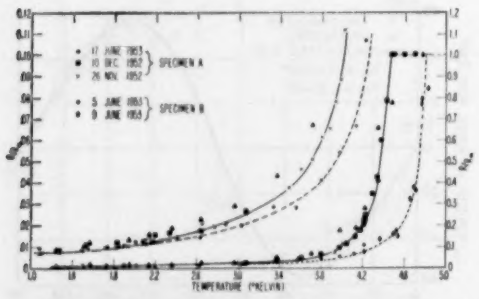

FIG. 1. Surface resistance of vanadium in superconducting state.

APPARATUS AND TECHNIQUES

The present work was done at frequencies near 24 000 Mc/sec. The method used was to measure the electric Q factor of a resonant cavity and from these measurements calculate the surface resistance. The method of Q measurements and techniques[2] are described in an earlier paper and will not be discussed here. In the earlier paper the cavities operated in the TE_{111} mode, in this particular case the TE_{114} mode is used. The ratio of diameter to length is 1.0. The cavity was formed from two pieces that were machined from a vanadium ingot. The junction of the two parts was along a plane which has no transverse currents flowing. The interior surface of the cavity was polished mechanically to a good finish. The polishing compounds used were: first, No. 275 carborundum, then No. 400 corborundum and the final polishing was done with Linde "b" polishing compound using distilled water and aerosol as a wetting agent. Because of the difficulty of attaching vanadium to standard wave guides a special holder was constructed of brass. A gold O ring was used to seal the two parts of the holder. This arrangement was satisfactory in the normal helium region.

[1] McLennan, Burton, Pitt, and Wilhelm, Proc. Roy. Soc. (London) **136**, 52 (1931).

[2] C. J. Grebenkemper and J. P. Hagen, Phys. Rev. **86**, 673 (1952).

In the helium II region "superleaks" were troublesome.

The vanadium used in the present experiments was obtained from the Electro Metallurgical Division of the Union Carbide and Carbon Company and was of high purity. Table I gives the purity analysis of the metal. The ingot was not perfect since a number of blowholes were present. These were probably due to gases trapped in the melt. Hardness tests were conducted on a sample of the metal and yielded a Vickers hardness number of 164. After the sample was annealed at 1000°C for several hours at a residual vacuum of 4×10^{-6} mm Hg the hardness number rose to 172. From this it would appear that annealing can be detrimental unless carried out under an extremely high vacuum.

SUPERCONDUCTING STATE

A plot of R/R_n *vs* temperature is shown in Fig. 1. It can be seen from the curves that the two specimens do not have the same transition temperature even though the specimens were formed from adjoining

TABLE I. Purity analysis of the metal.

Elements	Amount of impurities in percent (by weight)
O_2	0.063–0.068
N_2	0.030
H_2	0.0016–0.0024
Cr	0.05
Spectro chemical analysis	
Si	0.01–0.1 percent
Mn	0.01–0.1 percent
Fe	0.01–0.1 percent
Al	0.01–0.1 percent
Ti	0.001–0.01 percent
Cu	0.001–0.01 percent

sections of the ingot. The specimen was immersed in liquid helium at the bottom of the flask as described previously.[2] The temperature of the bath was controlled by adjusting the pressure of the helium vapor in the flask. Care was used in raising the bath temperature so that equilibrium conditions would prevail. To obtain temperatures above 4.2°K, current is passed through a resistor, which was installed underneath the cavity to raise the vapor pressure above atmospheric pressure. The temperatures were determined from vapor pressure measurements using the 1948 temperature scale.

The consistency of measurements for a given specimen was quite good. The possibility of the lack of equilibrium conditions was investigated. The bath temperatures were raised and lowered in the usual way and there were no marked discrepancies for a given specimen. In the final analysis it appears that the difference in the transition temperature for the two specimens is real and must be ascribed to the difference in internal strains in the ingot. After the measurements were completed the cavities were disassembled and hardness tests were conducted on each specimen. It was found

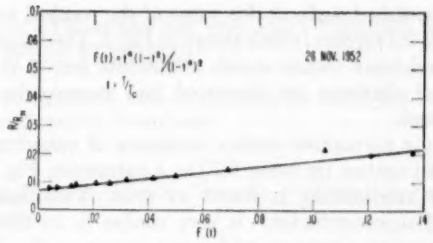

FIG. 2. Linear plot of the low-temperature resistance of vanadium in the superconducting state.

that specimen *B* was considerably softer than specimen *A*. Specimen *A* had a Vickers hardness number of 192 and specimen *B* the Vickers hardness number was 170. This difference in the transition temperatures due to the differences in hardness is in agreement with the work of Wexler *et al.*[3]

NORMAL STATE

Q measurements in the normal region were determined by band width measurements in addition to decrement measurements. The decrement method is not too precise for the low values of *Q* encountered here. The two methods did not disagree by more than 10 percent however. The normal conductivity, which is given in Table II, was not affected as much by the anomalous skin effect as the "soft superconductors." The calculated *Q* value for this particular cavity was 13 900 if one used the results of Wexler for the low-temperature conductivity of vanadium. The measured value was quite close to this figure. For the "soft superconductors" the anomaly is much greater, the measured *Q* value for "soft superconductors" being about one-fifth the calculated *Q*, using classical theory. A possible explanation of the smaller anomalous skin effect in vanadium is that the electron has a shorter mean-free path in vanadium than in tin. This would appear plausible, since, in transition metals with incomplete "*d*" shells, a much larger scattering probability exists, hence a shorter mean-free path is expected with this material as compared with metals with closed cores.[4]

When R/R_n is extrapolated to absolute zero, shown in Fig. 2, a residual resistance of 0.7 percent of the resistance at the transition is obtained. For tin with a

TABLE II. EXPERIMENTAL RESULTS

Metal	Surface conductivity ohm^{-1}	$A(\omega)$	R/R_n extrapolated to absolute zero	Frequency Mc/sec
Tin	80	0.25	0.002	24 080
Vanadium	13.8	0.11	0.007	23 970

[3] A. Wexler and W. S. Corak, Phys. Rev. **85**, 85 (1952).

[4] See N. F. Mott and H. Jones *The Theory of the Properties of Metals and Alloys* (Oxford University Press, London, 1936), pp. 247 and 266.

good polished surface[5] this value of the residual resistance is 0.2 percent; this is shown in Fig. 3. Theoretically, the resistance should vanish at absolute zero if all the normal electrons are converted into superconducting electrons.

If the normalized surface resistance of vanadium is plotted against tin using $f(T)$ as a parameter, Fig. 4, a linear relationship is found to exist. Vanadium, a "hard superconductor," is very similar in its manner of changing resistance with temperature to the "soft superconductors" in the superconducting state. It is quite possible that with a high purity strain free specimen that had a good surface finish the residual resistance at absolute zero would approach zero. This work appears to support Wexler's suggestion that the internal stresses due to atoms located in interstitial positions in the lattice markedly affect the superconducting properties. The transition temperature for the softer specimen compares more favorably with Wexler's value of 5.13°K than the earlier value of Meissner and Westerhoff[6] of 4.3°K.

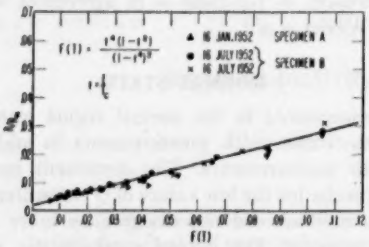

FIG. 3. Linear plot of the low-temperature resistance of tin in the superconducting state.

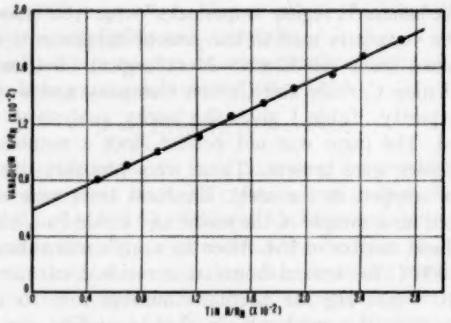

FIG. 4. Linear plot of the normalized surface resistance of vanadium *vs* tin with $f(T)$ as a parameter.

ACKNOWLEDGMENTS

The author is indebted to Dr. J. P. Hagen for his frequent advice and discussions. Special thanks are due to A. R. Donaldson, of the Metallurgy Division, for his advice on polishing techniques and the hardness measurements and to D. I. Walter of the Metallurgy Division for the analysis of the impurities in the vanadium.

[5] C. J. Grebenkemper and J. P. Hagen, Proceedings of the Schenectady Cryogenics Conference, 1952 (unpublished).

[6] W. Meissner and H. Westerhoff, Z. Physik **87**, 206 (1934).

Analysis of the Three Parameter Wave Function of Hylleraas for the He I Ground State in Terms of Central Field Wave Functions*

LOUIS C. GREEN, MARJORIE M. MULDER,† PAUL C. MILNER,‡ MARGARET N. LEWIS,§ AND JOHN W. WOLL, JR.‡
Strawbridge Observatory, Haverford College, Haverford, Pennsylvania

AND

ELEANOR K. KOLCHIN AND DAVID MACE, *Watson Scientific Computing Laboratory, Columbia University, New York, New York*

(Received June 8, 1954)

A study of configuration interaction in the ground state of He I has been carried through by expanding the various angular components of the three parameter wave function of Hylleraas in orthonormal sets of functions. The different sets have been constructed from symmetrized products of hydrogenic wave functions with different values of the parameter Z. The importance of the various configurations for $Z=2$ is commented upon at some length. Configurations involving a free electron are shown to make surprisingly large contributions. The changing importance of the various components with changing Z is illustrated. In particular, the minimum with respect to Z of the contribution of configurations containing a free electron is pointed out. The implications of the results of these expansions for attempts to obtain wave functions for both normal and excited states of two-electron systems by the minimum principle from linear combinations of products of hydrogenic functions of the proper symmetry are discussed.

EXCELLENT approximate solutions of the Schrödinger equation can be obtained variationally for two-electron systems by using as one coordinate r_{12}, the interelectron distance. It has been pointed out[1–3] that a study of configuration interaction in these simple structures can be carried out by expanding such excellent solutions in central field wave functions.[4] In earlier work[1] an expansion of this type in symmetrized numerical self-consistent field functions was undertaken for the three- and the six-parameter wave functions given by Hylleraas[5] for the ground state of He I. For the three-parameter function a second expansion was also obtained using analytic variationally determined wave functions for the $1s^2$ and $1s2s$ configurations. However, the coefficient of the $1s2s$ configuration was distinctly different in the numerical and the analytic expansions. It seemed probable that the same would be true of other configurations as well. This would mean that, unless one made relatively complete expansions in sets of orthonormal functions, one would find differing importance for the various angular components of the ground-state wave function depending on which type of radial functions was employed in the expansion. Furthermore, the size of the various expansion coefficients suggested that for the purpose in hand one would not obtain a satisfactory approximation to a complete set unless one considered a large number of configurations. The effort required to find the necessary numerical radial functions appeared to be prohibitive.

To avoid these difficulties, an expansion of the form[6]

$$\Psi_H{}^N(r_1,r_2,r_{12})=\sum_i c_i\Phi_i{}^N(r_1,r_2)P_i{}^N(\cos\theta) \qquad (1)$$

was employed.[2] Here $\Psi_H{}^N$ is the normalized Hylleraas wave function of r_1 and r_2, the nuclear distances of the two electrons, and r_{12}, the interelectron distance. The $\Phi_i{}^N$'s are normalized functions of r_1 and r_2 whose form is determined by Eq. (1).[2] The $P_i{}^N$'s are the normalized Legendre polynomials of order i of the cosine of the angle between the two radius vectors. $\Psi_H{}^N$ was normalized with respect to integration over r_1, θ_1, and φ_1, the coordinates of the first electron, r_2 for the second electron, r_{12}, and φ, the Euler angle, which together with r_{12} specifies the direction of $\mathbf{r}_2$ with respect to $\mathbf{r}_1$. The $\Phi_i{}^N$'s were normalized with respect to integration over r_1, θ_1, φ_1, r_2, and φ. The expressions for the $\Phi_i{}^N$'s and the values of the c_i's have been presented in an earlier paper for both the three- and the six-parameter Hylleraas functions.[2] This earlier work also gives the values of the E_{ij}'s, the interaction energies between the ith and jth angular components, that is,

$$E=\sum_{ij}E_{ij}=\int\sum_i(c_i\Phi_i{}^NP_i{}^N)^*H\sum_j(c_j\Phi_j{}^NP_j{}^N)d\tau. \qquad (2)$$

The results obtained in this way, as to the importance of the various angular components of $\Psi_H{}^N$, are, of course, not dependent on the choice of the radial

* This research was supported in part by The United States Air Force under a contract monitored by the Office of Scientific Research, Air Research and Development Command, in part by a U. S. Office of Naval Research contract, and in part by a grant from the Research Corporation. The two contracts were administered by the University of Pennsylvania.

† Now with Remington Rand Inc., Philadelphia, Pennsylvania.

‡ Now at Princeton University, Princeton, New Jersey.

§ Now at Brown University, Providence, Rhode Island.

[1] Green, Mulder, Ufford, Slaymaker, Krawitz, and Mertz, Phys. Rev. **85**, 65 (1952).

[2] Green, Mulder, and Milner, Phys. Rev. **91**, 35 (1953).

[3] Green, Lewis, Mulder, Wyeth, and Woll, Phys. Rev. **93**, 273 (1954).

[4] The possibility of investigating configuration interaction in He I in this manner was suggested to one of us (L. C. G.) by Dr. G. Breit.

[5] E. A. Hylleraas, Z. Physik **54**, 347 (1929).

[6] The value of an expansion in terms of Legendre functions was pointed out to two of us (L. C. G. and M. M. M.) by Dr. E. U. Condon.

eigenfunctions of any particular central-field problem. One of the most interesting results of this work was the large size found for the nonspherically symmetric components of the ground state wave function.

In the present paper we extend this earlier work by expanding the Φ_i^N's for the three-parameter Hylleraas function in terms of symmetrized products of the eigenfunctions of hydrogenic central fields for several different Z's.

The expansion has the form

$$2\sqrt{2}\pi\Phi_i^N=\sum_{nm}c_{nlml}[2+2\delta(n,m)]^{-\frac{1}{2}}$$
$$\times\{R^N(nl|1)R^N(ml|2)+R^N(ml|1)R^N(nl|2)\}$$
$$+\sum_n\int c_{nl\epsilon l}\frac{1}{\sqrt{2}}\{R^N(nl|1)R^N(\epsilon l|2)$$
$$+R^N(\epsilon l|1)R^N(nl|2)\}d\epsilon+\int c_{\epsilon l\eta l}[2+2\delta(\epsilon,\eta)]^{-\frac{1}{2}}$$
$$\times\{R^N(\epsilon l|1)R^N(\eta l|2)+R^N(\eta l|1)R^N(\epsilon l|2)\}d\epsilon d\eta. \quad (3)$$

Here Φ_i^N is the particular normalized angular component of the ground-state wave function that is to be expanded. The c's are the various expansion coefficients. The δ's are Kronecker deltas. $R^N(nl)$ and $R^N(ml)$ are normalized radial eigenfunctions for discrete states of the central field, and $R^N(\epsilon l)$ and $R^N(\eta l)$ are normalized radial eigenfunctions for states lying in the continuum. These continuum eigenfunctions are normalized, so that for sufficiently large ρ the amplitude will approach[7]

$$\frac{1}{\sqrt{\pi}}\left[\epsilon+\frac{2Z}{\rho}-\frac{l(l+1)}{\rho^2}\right]^{-\frac{1}{4}}.$$

Here ϵ is the energy measured in units of $R_{\mathrm{He}}hc$, where R_{He} is the Rydberg constant for He expressed in cm^{-1}, and ρ is the nuclear distance expressed in atomic units. The factor $2\sqrt{2}\pi$ on the left side of Eq. (3) arises from the difference in the normalization of the Φ_i^N's and the R^N's. The complexity which might accompany an expansion in central field wave functions has been greatly reduced in Eq. (3) by several considerations. In the first place, superposition of configurations can only occur between configurations of the same parity.[8] Thus, among the configurations of even parity which involve electrons with smaller l values, we need only consider *ss*, *pp*, *sd*, and *dd*. Second, the intervals in the $1s2p\ ^3P$ term of He I are roughly two thousand times smaller than the separation of the ^3P and ^1P. The coupling is therefore closely Russell-Saunders. If the assumption is made that it is precisely so, it is only necessary to include on the right-hand side of Eq. (3) terms with the same L and S as the He I ground state since these are the only ones which interact in pure Russell-Saunders coupling.[8] The *sd* configurations can therefore be dropped since they do not yield a ^1S term, and in the *ss*, *pp*, and *dd* configurations, only those combinations of single electron wave functions which yield ^1S terms need to be considered. In the third place, the only configurations which can contribute to the spherically symmetric component of the ground state are the *ss* configurations, since these are the only ones for which the spherical harmonics in θ_1, φ_1, and θ_2, φ_2 can combine to yield $P_0^N(\cos\theta)$. Similarly the only ones which can contribute to the expansion of Φ_1^N are *pp* configurations. The justification for the notation in Eq. (3) is now clear: the only nonvanishing coefficients in the expansion of Φ_i^N are those of the symmetrized products of the radial components of the ll configuration.

The choice still remains as to what type of radial wave functions to employ in the expansions. Earlier work[1] suggested that to obtain a relatively complete expansion, it would be necessary to employ a large number of configurations. Although a rapid convergence in the first few terms could be had by using numerical Hartree functions, it was not clear that the convergence would be more rapid in the later terms than with other simpler orthogonal sets. Among the possible sets of analytic functions, the hydrogenic functions offered the advantages of relative simplicity and of reasonably rapid convergence. It was decided to use two different sets of hydrogenic functions. In the first set, the emphasis in the expansion was to be on ease of determining the coefficients. It was expected that this expansion would require a large number of configurations to obtain a satisfactory approximation to completeness. In the second set, the emphasis was to be on the rapidity of the convergence. It was thought that the physical interpretation of the results would be about equally easy in the two cases. For the first set, hydrogenic functions with $Z=2$ were employed, that is, the solutions of the radial part of the Schrödinger equation for He^+. For the second set, certain expansion coefficients were evaluated for hydrogenic functions for a series of values of Z, and then that Z was chosen which made the sum of the squares of those coefficients a maximum.

EXPANSION COEFFICIENTS FOR $Z=2$

The results of the expansion of Φ_0^N, the spherically symmetric component of the ground-state wave function, in terms of hydrogenic functions with $Z=2$ are given in Table I. In the first section the values of the expansion coefficients and their squares are given for each of the configurations listed in the first column. The integrals necessary to determine these quantities were first computed directly and were then checked by the factorization method.[9] In the second section is given

[7] E. C. Kemble, *Fundamental Principles of Quantum Mechanics* (McGraw-Hill Book Company, Inc., New York, 1937), p. 178.

[8] E. U. Condon and G. H. Shortley, *The Theory of Atomic Spectra* (Cambridge University Press, London, 1935), p. 366.

[9] L. Infeld and T. E. Hull, Revs. Modern Phys. **23**, 21 (1951).

the value for the sum of the squares of the coefficients for all the configurations from $1s6s$ to $1s\infty s$, estimated as described below, and the integral from $\epsilon=0$ to $\epsilon=\infty$ of the square of the coefficient for configurations involving a $1s$ function and an s continuum function. The final line of Table I gives the sum of the squares of the coefficients for all configurations which were considered. If the expansion represented $\Phi_0{}^N$ exactly, this sum would be one since both the wave functions for the different configurations and $\Phi_0{}^N$ are normalized.

The estimated value, which appears in Table I, for the sum of the squares of the coefficients for the configurations from $1s6s$ to $1s\infty s$ was arrived at in the following manner. The series of discrete states from $6s$ to ∞s was replaced by a continuum of states. The wave functions for these states were taken to be the series expansion for the hydrogenic continuum function in terms of powers of the energy, ϵ, and Bessel functions of the nuclear distance, r.[10] This expansion converges rapidly for small ϵ. Symmetrized products of this wave function and a $1s$ wave function were constructed in the usual manner. The accuracy with which this symmetrized function gives the square of the expansion coefficients for the discrete states was determined by computing the integral of the square of the expansion coefficient between negative values of ϵ corresponding to the quantum numbers $n=3.5$ and $n=4.5$ and between values corresponding to $n=4.5$ and $n=5.5$. The values of these integrals were then compared with the values found for $(c_{1s4s})^2$ and $(c_{1s5s})^2$ by the usual methods. The differences proved to be 4.8 percent and 2.6 percent, respectively. It therefore seemed probable, that if the sum of the squares of the expansion coefficients for the configurations from $1s6s$ to $1s\infty s$ was taken to be the value of the above integral from an ϵ corresponding to $n=5.5$ to $\epsilon=0$, the resulting error would be less than 2.0 percent.

The values of the expansion coefficients for configurations involving a free electron were computed using the hydrogenic s continuum function. For small values of ϵ the results were checked by the use of the Bessel function expansion for the continuum function.[10] The results were further checked over a wider range of ϵ by using numerical hydrogenic wave functions computed at the Watson Scientific Computing Laboratory of IBM at Columbia University. Among other values of ϵ, the values of $c_{1s\epsilon s}$ were found at $\epsilon=0.0$, 2.0, 4.0, 10.4, and 21.6 to be -0.1043, -0.0407, -0.0215, -0.0059, and -0.0017, respectively. When the values of $c_{1s\epsilon s}$ had been determined, the integral of the square of these coefficients from $\epsilon=0$ to $\epsilon=21.6$ was computed numerically. Beyond $\epsilon=21.6$ the integrand was estimated to be too small to contribute in the fifth decimal place to the value of the integral. The integral is therefore listed in the next to last line of Table I as extending from $\epsilon=0$ to $\epsilon=\infty$.

The last line of Table I shows that the expansion of $\Phi_0{}^N$ is relatively complete in spite of the fact that only one configuration not involving a $1s$ electron has been considered. This is true even though Z has been set equal to 2, a value which must be rather far from that which best describes the average field acting on each electron. With $Z=2$ one might expect that configurations including two excited electrons would play an important role. In fact, configurations involving $1s$ electrons account for at least 99.82 percent of the sum of the squares of the expansion coefficients. Perhaps the most interesting result in Table I is the large contribution of those configurations in which one electron is in a continuum state. In fact the $1s\epsilon s$ configurations taken together account for more than any other configuration except $1s^2$ and $1s2s$. The continuum configurations which are considered here account for 49 percent of what remains after the contribution of the $1s^2$ and $1s2s$ configurations have been removed from the sum of the squares of expansion coefficients. Without a complete expansion of $\Phi_0{}^N$, it is, of course, impossible to say what the absolute importance of the higher configurations is in the wave function, but it is clear that the relative importance of $1s2s$ and the continuum configurations to the $1s^2$ is large.

The results of the expansion of $\Phi_1{}^N$ in terms of hydrogenic functions with $Z=2$ are given in Table II. The arrangement of Table II is the same as that of Table I. The computations for the various quantities were carried out in the same way as described above, except that in the case of $c_{2p\epsilon p}$, only numerical con-

TABLE I. Coefficients for the expansion of $\Phi_0{}^N$ in the form of Eq. (3) where the R^N's are hydrogenic functions with $Z=2$.

Configuration	c_{1snsn}	$(c_{1snsn})^2$
$1s^2$	0.96430	0.92988
$1s2s$	−0.21637	0.04682
$1s3s$	−0.07586	0.00576
$1s4s$	−0.04316	0.00186
$1s5s$	−0.02913	0.00085
$2s^2$	−0.01437	0.00021
$\sum_{n=6}^{n=\infty}(c_{1snsn})^2$		0.00156
$\int_{\epsilon=0}^{\epsilon=\infty}(c_{1s\epsilon s})^2 d\epsilon$		0.01199
Sum		0.99893

[10] Yost, Wheeler, and Breit, Phys. Rev. 49, 174 (1936).

TABLE II. Coefficients for the expansion of $\Phi_1{}^N$ in the form of Eq. (3) where the R^N's are hydrogenic functions with $Z=2$.

Configuration	c_{2pnp}	$(c_{2pnp})^2$
$2p^2$	−0.47010	0.22100
$2p3p$	−0.27863	0.07763
$2p4p$	−0.16661	0.02776
$3p^2$	−0.08401	0.00706
$\sum_{n=5}^{n=\infty}(c_{2pnp})^2$		0.0387
$\int_{\epsilon=0}^{\epsilon=\infty}(c_{2p\epsilon p})^2 d\epsilon$		0.290
Sum		0.662

TABLE III. Coefficients for the expansion of Φ_1^N using symmetrized products of hydrogenic s wave functions with $Z=2$.

Wave functions	c_{nsns}	$(c_{nsns})^2$
$1s^2$	−0.84620	0.71605
$1s2s$	0.24799	0.06150
$1s3s$	0.12162	0.01479
$1s4s$	0.07130	0.00508
$2s^2$	−0.09154	0.00838
$3s^2$	−0.04515	0.00204
$4s^2$	−0.02696	0.00073
$\sum_{n=5}^{n=\infty}(c_{1sns})^2$		0.0075
$\int_{\epsilon=0}^{\epsilon=\infty}(c_{1s\epsilon s})^2 d\epsilon$		0.113
Sum		0.929

tinuum functions and the Bessel function expansion for the continuum function were employed. The values of $c_{2p\epsilon p}$ were estimated for ϵ greater than 4.0.

The most interesting result which appears in Table II is the small size of the contribution to Φ_1^N of $2p^2$, the lowest configuration considered. The higher discrete configurations contribute more to the expansion relative to the lower than in the case of Φ_0^N. This is clearly shown by the importance of the continuum configurations, which contribute more to the expansion than any one of the discrete configurations considered. The sum of the squares of the c's in the final line of Table II is rather far from 1.0, that is, the expansion is rather far from complete. This result is somewhat surprising in view of the considerable number of configurations which are included in the expansion. One notes that $(c_{1s^2})^2$ for the expansion of Φ_0^N is 0.92988 but that $(c_{2p^2})^2$ for the expansion of Φ_1^N is only 0.22100. Furthermore $(c_{3d^2})^2$ for the expansion of Φ_2^N is still smaller, 0.00140. It is therefore clear that any relatively complete expansion of the Φ_i^N's for $i>0$ in terms of hydrogenic functions with $Z=2$ will be a laborious undertaking. One reason for this situation is that the exponential factor is the same in all Φ_i^N's, but increasingly different from the exponential factors in the $(nl)^2$ wave functions as l increases. It therefore seemed worthwhile to attempt the expansion of the higher Φ_i^N's in terms of s electron wave functions even though s wave functions used in this way cannot be considered as belonging strictly to the class of central field wave functions. The results of this expansion are given in Table III. The arrangement of Table III is similar to that of Table II and the computations for the various quantities have been carried out in the same way. It is clear that for low n,s wave functions are much more effective in representing Φ_1^N than are the p wave functions. Similarly the expansions of Φ_2^N and Φ_3^N in terms of $1s^2$ yield 0.60635 and 0.50747 for $(c_{1s^2})^2$. The former value is more than 400 times as large as $(c_{3d^2})^2$ found for the expansion of Φ_2^N in $3d^2$. These results, and those given in Table III, suggest the desirability of using values of Z other than 2 in the expansions.

The same suggestion also follows from the work of Taylor and Parr on He I.[11] These authors constructed various linear combinations of $1s^2$, $2p^2$, $3d^2$, and $4f^2$ hydrogenic wave functions. The $1s^2$ configuration was assigned one or two values of the parameter Z. To each of the other configurations, a single value of Z was assigned. The particular combination which gave the lowest energy was then chosen. They obtained a wave function giving the ground-state energy correct to 0.2 percent by the choice of $Z=4.95$ for the $2p$ function, $Z=11.3$ for the $3d$, and $Z=19.0$ for the $4f$. The exponents in the exponential factors in these wave functions were therefore 2.5, 3.8, and 4.8 whereas for the choice of $Z=2$ they would have been 1.0, 0.67, and 0.50, respectively.

TABLE IV. Squares of the coefficients in the expansion of Φ_0^N in hydrogenic s wave functions for different values of Z.

	Z 1.5	1.6	1.7	1.8	1.9	2.0
$(c_{1s^2})^2$	0.98338	0.99247	0.98967	0.97704	0.95653	0.92988
$(c_{1s2s})^2$	0.00145	0.00015	0.00406	0.01332	0.02772	0.04682
$(c_{2s^2})^2$	0.00026	0.00043	0.00053	0.00051	0.00039	0.00021
$\int(c_{1s\epsilon s})^2 d\epsilon$	0.010	0.0030	0.0012	0.00303	0.00722	0.01199
Sum	0.995	0.9961	0.9955	0.99390	0.99186	0.98890

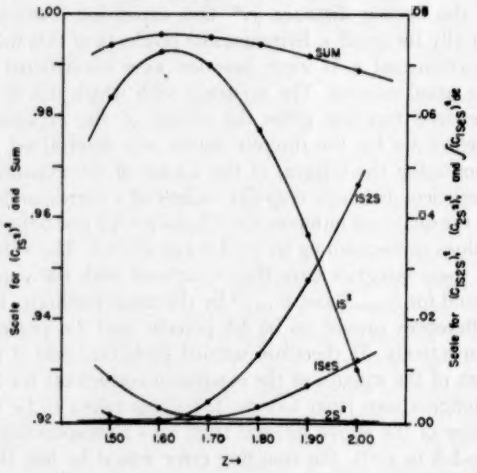

FIG. 1. Squares of the coefficients for the expansion of Φ_0^N in symmetrized products of hydrogenic s wave functions for different values of Z.

EXPANSION COEFFICIENTS FOR Z VARIABLE

In view of the above results, the Φ_i^N's were also expanded in hydrogenic functions with variable Z with the purpose of choosing that Z which would give the best representation of the Φ_i^N's in a few terms.

The results of the expansion of Φ_0^N in terms of various configurations of s electrons for different Z's are presented in Table IV and Fig. 1. Values of $c_{1s\epsilon s}$

[11] G. R. Taylor and R. G. Parr, Proc. Nat. Acad. Sci. U. S. 38, 154 (1952).

were found using the analytic hydrogenic ϵs continuum function in all cases except for $Z=2$, which has been discussed previously. The computations were made for a series of values of ϵ up to at least $\epsilon=16.8$. Beyond this point the values of $c_{1s\epsilon s}$ were estimated. It is thought that any error resulting from these estimates will not be large enough to change the values of the integrals of $(c_{1s\epsilon s})^2$ in Table IV by more than 1 in the last decimal place given.

By summing the squares of the coefficients for various groups of the configurations given in Table IV, and interpolating for the value of Z which makes the sum a maximum, one finds the results in Table V.

The corresponding information on the expansion of $\Phi_1{}^N$ in terms of configurations of p electrons is given in Tables VI and VII and Fig. 2. Values of $c_{2p\epsilon p}$ were found using the hydrogenic $2p$ continuum function for

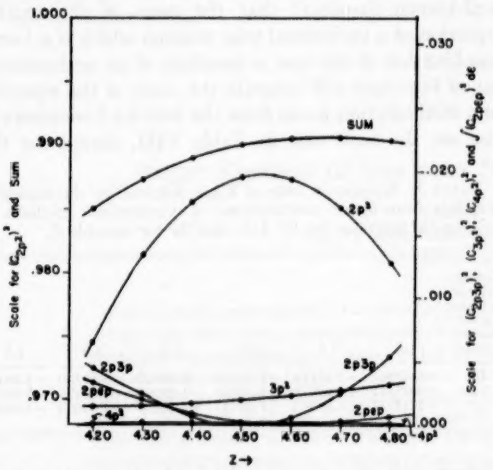

FIG. 2. Squares of the coefficients for the expansion of $\Phi_1{}^N$ in symmetrized products of hydrogenic p wave functions for different values of Z.

$Z=4.3$, 4.5, and 4.7. The computations for each Z were carried out to at least $\epsilon=100$. Beyond this point the values of $c_{2p\epsilon p}$ were estimated. In no case did the estimated values contribute to the integral of $(c_{2p\epsilon p})^2$ as much as one in the last decimal place in the figures given in Table VI.

The improvement of the representation which can result from allowing Z to vary is at once obvious from an examination of Tables IV and VI. Whereas, the value of $(c_{1s^2})^2$ for $Z=2$ is 0.92988, its value for $Z=1.62$ is 0.99279. For the value of $(c_{1s^2})^2+(c_{1s2s})^2$ one obtains 0.97670 when $Z=2$, but 0.99396 when $Z=1.67$. The results for $(c_{2p^2})^2$ are even more improved. For $Z=2$ one finds $(c_{2p^2})^2=0.22100$ but for $Z=4.54$ one obtains 0.98777. This latter value is also considerably better than the 0.71605 found for $(c_{1s^2})^2$ when $\Phi_1{}^N$ was expanded in radial s wave functions. Indeed the $2p^2$ configuration for $Z=4.54$ represents $\Phi_1{}^N$ more effectively than the entire list of either p configurations or

TABLE V. Expansion of $\Phi_0{}^N$ in hydrogenic s wave functions with Z chosen to give the maximum sum for the squares of the coefficients.

Configurations	Z	Sum of squares of coefficients
$1s^2$	1.62	0.99279
$1s^2$, $1s2s$	1.67	0.99396
$1s^2$, $1s2s$, $2s^2$	1.67	0.99438
$1s^2$, $1s2s$, $2s^2$, $1s\epsilon s$	1.60	0.996

s configurations for $Z=2$ which are given in Tables II and III, respectively. Over the ranges of values of Z shown in Figs. 1 and 2, the contributions of the higher p configurations to $\Phi_1{}^N$ are considerably less than that of the higher s configurations to $\Phi_0{}^N$.

It is extremely interesting to see in Tables IV and VI or Figs. 1 and 2 how the importance of the various configurations changes with changing Z. For example, the rapid falling off of $(c_{1s^2})^2$ and the accompanying increase in $(c_{1s2s})^2$ and in the integrated value of $(c_{1s\epsilon s})^2$ for larger Z is very obvious from Fig. 1. One also notes that in both Figs. 1 and 2, the plots of the

TABLE VI. Squares of the coefficients in the expansion of $\Phi_1{}^N$ in hydrogenic p wave functions for different values of Z.

	Z 4.2	4.3	4.4	4.5	4.6	4.7	4.8
$(c_{2p^2})^2$	0.97453	0.98131	0.98562	0.98760	0.98740	0.98517	0.98100
$(c_{2p3p})^2$	0.00550	0.00248	0.00063	0.00000	0.00059	0.00240	0.00540
$(c_{3p^2})^2$	0.00151	0.00161	0.00177	0.00199	0.00230	0.00269	0.00319
$(c_{4p^2})^2$	0.00012	0.00012	0.00012	0.00012	0.00013	0.00013	0.00014
$\int(c_{2p\epsilon p})^2 d\epsilon$	0.00337[a]	0.00197	0.00096[a]	0.00033	0.00009[a]	0.00023	0.00076[a]
Sum	0.98503	0.98749	0.98910	0.99004	0.99051	0.99062	0.99049

[a] Interpolated or extrapolated from the values of $\int(c_{2p\epsilon p})^2 d\epsilon$ computed for $Z=4.3$, 4.5, and 4.7.

c^2's for configurations of the nonequivalent electrons are distinctly concave upward in the neighborhood of the maximum of $(c_{1s^2})^2$ and $(c_{2p^2})^2$, respectively. This is not true for the plots of the c^2's for the remaining equivalent electrons.

One aspect of particular importance in the changing size of the contribution of the different configurations with changing Z, is the low minimum found for the integrated $(c_{1s\epsilon s})^2$ and $(c_{2p\epsilon p})^2$. The importance of this point arises in connection with any attempt to obtain a good ground-state wave function by the minimum principle, using linear combinations of symmetrized products of hydrogenic wave functions as trial functions. By far the most difficult configurations to include

TABLE VII. Expansion of $\Phi_1{}^N$ in hydrogenic p wave functions with Z chosen to give the maximum sum for the squares of the coefficients.

Configurations	Z	Sum of squares of coefficients
$2p^2$	4.54	0.98777
$2p^2$, $2p3p$	4.60	0.98799
$2p^2$, $2p3p$, $3p^2$	4.65	0.99036
$2p^2$, $2p3p$, $3p^2$, $4p^2$, $2p\epsilon p$	4.69	0.99062

TABLE VIII. Energies in units of $R_{He}hc$ octained by the minimum principle from linear combinations of symmetrized products of hydrogenic s wave functions with $Z=2$.

Superposed configurations	Conventional configuration assignments $1s^2$	$1s2s$	$1s3s$	$1s4s$
$1s^2$	−5.50000			
$1s^2$, $2s^2$	−5.50189			
$1s^2$, $1s2s$	−5.66088	−3.91183		
$1s^2$, $1s2s$, $1s3s$	−5.67730	−4.27238	−3.64645	
$1s^2$, $1s2s$, $1s3s$, $1s4s$	−5.68278	−4.27380	−4.11489	−3.53477
Experimental	−5.80752	−4.29213	−4.12273	−4.06736

in such treatments are those involving continuum functions. The necessity for their inclusion in the case of hydrogenic functions with $Z=2$ is indicated in Table VIII, where the best linear combination of the configurations on the left have been chosen by the minimum principle to yield the energies for the conventional configuration assignments along the top. The last line of Table VIII gives the experimental values of the energies of the $^1S_0$ terms in the configurations at the heads of the columns.[12] The successive values of the energy of the ground state, which appear in the second column, make it unlikely that the addition of more configurations of bound s electrons with $Z=2$ would give an energy as low as -5.76, the energy which spherically symmetric functions may be expected to yield.[8] The only remaining spherically symmetric configurations are those involving a free electron. In the expansions above of $\Phi_0{}^N$ in hydrogenic functions with $Z=2$, configurations involving a free electron have, of course, been shown to be important. On the other hand, both Table IV and Fig. 1 suggest that if in the attempt to obtain a ground-state function one uses a linear combination of symmetrized products of hydrogenic s functions with $Z=1.70$, one may hope to find a very good spherically symmetric component, even though no continuum wave functions are employed.

In comparing the results of expanding $\Phi_0{}^N$ with the results of an attempt to obtain the spherically symmetric component of the ground-state wave function by the minimum principle, it is also of interest to compare the values of the squares of the expansion coefficients with the squares of the weighting constants for the various configurations in the linear combination.

TABLE IX. Values of the squares of the weighting constants obtained by the minimum principle in linear combinations of symmetrized products of hydrogenic s functions with $Z=2$.

Superposed configurations	$(c_{1s^2})^2$	$(c_{1s2s})^2$	$(c_{1s3s})^2$	$(c_{1s4s})^2$
$1s^2$	1.00000			
$1s^2$, $2s^2$	0.99954			
$1s^2$, $1s2s$	0.90802	0.09198		
$1s^2$, $1s2s$, $1s3s$	0.90874	0.08110	0.01016	
$1s^2$, $1s2s$, $1s3s$, $1s4s$	0.90926	0.07805	0.00937	0.00332

[12] The experimental values of the energies were taken from Charlotte E. Moore, *Atomic Energy Levels*, National Bureau of Standards Circular 467 (U. S. Government Printing Office, Washington, D. C., 1949), p. 5.

The latter quantities are presented in Table IX, where all the functions which are concerned have been normalized. A comparison of Tables I and IX shows that for the configurations considered $(c_{1s^2})^2$ is somewhat larger and $(c_{1s2s})^2$, $(c_{1s3s})^2$, and $(c_{1s4s})^2$ are considerably smaller for the expansion. However, as more configurations are included in the application of the minimum principle, there is a tendency for a slow increase in $(c_{1s^2})^2$ and corresponding decrease in the other c^2's.

An attractive aspect of the application of the minimum principle to a linear combination of configurations is the fact that by using the different roots of the secular equation to determine the c's, one obtains not only a ground-state wave function, but also wave functions for the excited configurations as well. Table VIII lists the various energies found from wave functions obtained in this way. These results illustrate the well-known theorem[13] that the roots of the secular equation of a variational trial solution which is a linear combination of the first n members of an orthonormal set of functions will separate the roots of the equation of a trial solution made from the first $n+1$ members of the set. In each case in Table VIII, except for the highest root, the energies obtained are at once recognizable as corresponding to certain experimental values. It seemed possible that if, following the suggestion above for avoiding the inclusion of continuum wave functions, one made up trial solutions using hydrogenic functions with $Z=2$, one might obtain a better spherically symmetric component for the ground state but poorer components for the excited states. To investigate this point the energies yielded by the superposition of $1s^2$, $1s2s$, and $2s^2$ were computed for six values of Z. The results appear in Table X. The values in Table X suggest that a choice of Z in the neighborhood of 1.7 would yield a good spherically symmetrical component, not only for the ground state, but also for at least some of the excited states as well. Therefore, the possibility is strengthened of obtaining moderately good wave functions for both ground and excited states from linear combinations which do not include continuum functions.

TABLE X. Energies in units of $R_{He}hc$ obtained by the minimum principle from linear combinations of symmetrized products of hydrogenic functions for $1s^2$, $1s2s$, and $2s^2$ for variable Z.

Conventional configuration assignment	Z 1.5	1.6	1.7	1.8	1.9	2.0
$1s^2$	−5.62821	−5.68175	−5.70725	−5.70920	−5.69250	−5.66199
$1s2s$	−4.05341	−4.10078	−4.11335	−4.08790	−4.02205	−3.91394
$2s^2$	−1.35924	−1.38313	−1.41737	−1.42693	−1.42054	−1.39521

On the other hand, there is considerable doubt that

[13] L. Pauling and E. B. Wilson, *Introduction to Quantum Mechanics* (McGraw-Hill Book Company, Inc., New York, 1935), p. 188.

wave functions of high accuracy for the two-electron systems can be found in the form of variationally chosen linear combinations of hydrogenic wave functions of the proper symmetry unless continuum functions are included. This statement follows from the fact that a relatively poor wave function may yield a relatively good energy, or stated in other words, the minor components of a wave function as measured by their contribution to the energy may make up proportionately a much larger part of the wave functions. This result is well-known, and specific examples have been given in earlier papers in the present series.[2,3] As a further illustration, one sees from Table IX that in the superposition of $1s^2$ and $1s2s$ the ratio c_{1s2s} to c_{1s^2} is 0.32 but the ratio of the contributions to the ground state energy of the $1s2s$ configuration and the interaction term between the $1s^2$ and the $1s2s$ to the contribution of the $1s^2$ configuration is 0.13.

In summary, the present work has presented expansions of the various angular components of the three-parameter wave function of Hylleraas for the He I ground state in terms of symmetrized products of hydrogenic wave functions for different values of the parameter, Z. The results of these expansions are interpreted in terms of configuration interaction. The changing importance of the different configurations with changing Z is illustrated. In particular, the minimum with respect to Z of the integral over all positive ϵ of $(c_{1s\epsilon s})^2$ is pointed out. The implications of these results are discussed for attempts to obtain wave functions for both ground and excited states of two-electron systems by the minimum principle from linear combinations of products of hydrogen functions of the proper symmetry.

The authors wish to thank Anita Y. Schwab for help in the computations leading to Tables IV and VI.

PHYSICAL REVIEW VOLUME 96, NUMBER 2 OCTOBER 15, 1954

Auger Ejection of Electrons from Tungsten by Noble Gas Ions

HOMER D. HAGSTRUM
Bell Telephone Laboratories, Murray Hill, New Jersey

(Received June 16, 1954)

Experimental investigation of electron ejection from atomically clean tungsten by singly and multiply charged ions of the noble gases is reported. Total electron yield, γ_i, and distribution in kinetic energy of the secondary electrons have been measured. Ion energies range from 10 to 1000 ev for singly charged ions. γ_i is found in each case to be roughly constant over this interval although the variations observed are significant and can be accounted for by theory. γ_i values of 0.293, 0.213, 0.094, 0.047, and 0.018 were obtained for 10 ev He^+, Ne^+, Ar^+, Kr^+, and Xe^+ ions, respectively. Comparison with theory makes it quite clear that for 10-ev ions essentially all electrons observed are ejected by a process of Auger neutralization in which the interaction of two conduction electrons causes one electron to neutralize the ion in the ground state and the other to be excited into the continuum above the filled band. The observed γ_i is determined by the probability that these excited electrons escape from the metal. In the case of Ne^+, indications are that as ion energy increases toward 100 ev a two-stage electronic transition process occurs in a small fraction of the encounters. In this process the ion is first resonance neutralized to an excited state and the resulting excited atom is subsequently de-excited in an Auger ejection process. Variation of the electron energy distribution with ion energy has been investigated. Careful measurement for Ne^{20} and Ne^{22} at 200 ev shows γ_i to be independent of nuclear mass. Results of γ_i and energy distribution measurements for electrons from multiply charged ions up to Xe^{5+} are also reported. A value of *ca* 6.3 ev for the energy of the Fermi level above the ground state in the conduction band in tungsten comes out of this work.

I. INTRODUCTION

A SERIES of studies of electron ejection from atomically clean metals by ions of the noble gases is extended in this work to tungsten. The singly charged ions of He, Ne, Ar, Kr, and Xe, as well as a number of the multiply charged ions ranging up to Xe^{5+}, have been used. Evidence presented indicates the tungsten surface to be atomically clean.

The use of singly charged ions of all the noble gases has proved to be particularly fruitful. Comparison with theory shows that for very slow ions (<10 ev) essentially all the electrons are ejected from tungsten by the process of direct Auger neutralization. Here the role of the incoming ion is to provide a low-lying vacant electronic level (its ground state) for the Auger process. Since the position of this level is determined by the ionization energy of the atom, it is clearly advantageous to study the process for a series of ions.

Of interest is the somewhat anomalous case of Ne^+ on tungsten. Here it appears that for ions of energies near 100 ev a fraction ($\sim$10 percent) of the ions are resonance neutralized, the excited atoms so formed being subsequently de-excited in an Auger process in which a secondary electron may be ejected. The explanation of the restriction of this possibility to Ne^+ and the means of its detection in that case are thought to be particularly convincing of the essential correctness of the theoretical picture.

The detailed interpretation of the results for tungsten is used as illustrative material in the companion paper on theory.[1] Identification of experimental results with theoretical ideas is made here, however. A summary of the basic experimental results which theory is called upon to explain is included in Sec. IX. Experimental apparatus and procedure are dealt with only briefly (Sec. II) inasmuch as these have already been treated in a separate publication.[2] Vacuum conditions, particularly those obtaining with CO_2 and acetone on the traps, and the evidence concerning the state of the target surface are discussed in Sec. III. Measurements of total electron yield for singly charged ions and for a pair of isotopic ions are presented in Secs. IV and V, respectively. Energy distribution measurements for slow ions including the dependence on kinetic energy of the incident ion are discussed in Secs. VII and VIII. Results for multiply charged ions are given in Sec. VIII.

No attempt has been made to explain theoretical ideas referred to in this paper. For this reason much of the discussion here presupposes familiarity with the content of the accompanying paper on theory.[1] Notation used is defined as introduced in the text (see also Table I of the accompanying paper on theory[1]).

II. EXPERIMENTAL APPARATUS AND PROCEDURE

The apparatus used in this investigation is a form of mass spectrometer in which ions produced by electron impact in a gas are mass analyzed and then focussed on the target by electrostatic lenses. The target is a ribbon which can be flashed to high temperature for cleaning. The geometry of the target and surrounding spherical electron collector is such as to make possible quite acceptable retarding potential measurements on electrons leaving the target. This instrument has been discussed extensively as Instrument II in the paper on experimental apparatus and procedure.[2]

Liquid nitrogen (77.4°K) was used on the traps in the studies involving He and Ne. For Ar, Kr, and Xe the traps were cooled with a CO_2 and acetone mixture (194.7°K). In the latter case it was found convenient to use gas reservoirs containing mixtures of the noble gases as follows. One reservoir contained He, Ne, and Kr, a second, Ar and Xe. The mixed gases from either of these reservoirs could be independently leaked into the system. These combinations were chosen so as to avoid serious overlapping of singly and multiply charged ions in the mass spectrum. By properly adjusting the electron beam energy it was always possible to find isotopic peaks of a given m/e with no contaminating admixture of an ion from another gas.

Pressure was measured with a Bayard-Alpert type ionization manometer and adsorption rate measurements were used to investigate the state of the target surface. Contact potential between target and electron collector and work function of the target were measured as described elsewhere (see Figs. 20 and 21, respectively, of reference 2).

The use of the heavier noble gas ions in this work necessitated the use of higher magnetic fields in the mass analysis. This brought with it the problem of a higher fringing magnetic field in the neighborhood of the target. The effect of this field on the measured electron energy distributions and the steps taken to reduce the magnetic field intensity inside the electron collector are discussed in Sec. VI.

III. VACUUM CONDITIONS AND THE STATE OF THE TUNGSTEN SURFACE

Background pressure in the apparatus with liquid nitrogen on the traps was in the range of $2\text{–}4\times10^{-10}$ mm Hg as measured with the ionization manometer (N_2 calibration).[3] These conditions were achieved by the "more drastic" evacuation procedure described in the paper on instrumentation and procedure.[2] As is discussed in Sec. VII of the instrumentation paper the actual background pressure must have been in the 10^{-11} mm Hg range. The monolayer adsorption time Δt_m is seen from Fig. 1 to be of the order of 14 hours. Assuming the same sticking probability and monolayer surface density as for N_2 on tungsten one calculates a partial pressure of the adsorbable component in the background gas of about 2×10^{-11} mm Hg.[4]

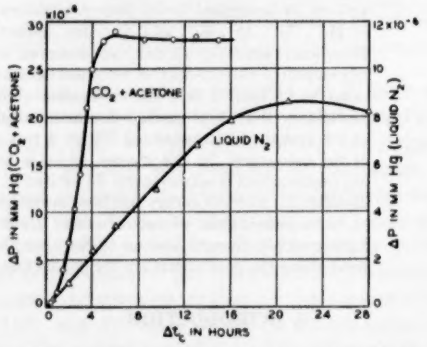

FIG. 1. Curves of pressure rise on target flash Δp *vs* cold interval Δt_c for background gas (or vapor) in the instrument taken with liquid N_2 and with CO_2 and acetone cooling on the traps. Pressure readings are those obtained with the ionization gauge calibrated for nitrogen. The monolayer adsorption time, Δt_m, is the value of Δt_c at which the curve departs from the initial linear rise. Some evidence of a maximum in the curve for liquid N_2 cooling is to be seen (see reference 9).

[1] H. D. Hagstrum, following paper [Phys. Rev. **96**, 336 (1954)].
[2] H. D. Hagstrum, Rev. Sci. Instr. **24**, 1122 (1953).

[3] The ionization manometer used in the present work had a plate wire of 0.010-in. diameter. Thus a somewhat higher x-ray limit is to be expected with it than with a gauge having a plate wire of smaller diameter.

[4] Use is made of the observation of Becker and Hartman, J. Phys. Chem. **57**, 153 (1953) that a monolayer of N_2 forms on tungsten in about one second at 10^{-6} mm Hg ($p\Delta t_m \cong 10^{-6}$ mm Hg×sec). Those authors give 0.6 as the mean sticking probability

The tungsten target was flashed to 2200°K. This is a temperature sufficiently high to remove oxygen very rapidly[5] and is assumed in this work to be sufficiently high to remove any other adsorbed atoms which may be present. The monolayer adsorption time was found to rise somewhat when He or Ne were admitted indicating admission of adsorbable impurities with these gases. However, the Δt_m remained well above 5 hours with liquid N_2 on the traps and with the pressure of these noble gases in the target chamber in the range $1\text{–}4\times10^{-7}$ mm Hg.

When the refrigerant on the traps was changed from liquid N_2 to the CO_2 and acetone mixture, the background pressure reading, with the gauge calibration for N_2, rose from the neighborhood of 2×10^{-10} to about 1×10^{-8} mm Hg. Over a period of time the pressure reading was found to vary between 8×10^{-9} and 1.4×10^{-8} mm Hg. Some correlation was found between the observed pressure reading and the amount of CO_2 solid in the refrigerant and how well it was mixed. If the observed pressure rise is caused solely by the rise in Hg vapor pressure admitted to the system, the true pressure is obtained from the above readings by multiplying by 0.29.[6]

It seems quite clear that the residual pressure in the system with CO_2 and acetone on the traps is to be attributed to mercury vapor. Using the vapor pressure formula for Hg given by Kelley,[7] one calculates the vapor pressure at the sublimation temperature of CO_2 to be 2.66×10^{-9} mm Hg. This is in good agreement with the observed pressure range of $2.3\text{–}4.0\times10^{-9}$ mm Hg (gauge reading corrected by the factor 0.29 to the Hg calibration). The variability in the residual pressure reading seems not unreasonable when it is noted that the observed pressure range could be spanned by less than a 4°K temperature change of the bath. Perhaps the only other possible vapor which could be responsible for the residual pressure is that of water. That there must have been very little water vapor present is indicated by the fact that the vapor pressure of H_2O at 194.7°K is *ca* 4×10^{-4} mm Hg.

Attributing the residual pressure with CO_2 and acetone on the traps to Hg makes the Δp *vs* Δt_c curve of Fig. 1 look reasonable. The value of Δp at $\Delta t_c > \Delta t_m$ is *ca* 28×10^{-6} mm Hg on the N_2 calibration. If this is multiplied by 0.29 one obtains 8.1×10^{-6} mm Hg as the true pressure in agreement with the observed Δp for $\Delta t_c > \Delta t_m$ with liquid N_2 on the traps. A consistent picture is then obtained if the monolayer surface density of adsorbed atoms or molecules is about the same in the two cases. The vapor pressure of Hg at 77.4°K, calculated from Kelley's formula,[7] comes out to be *ca* 4×10^{-35} mm Hg.

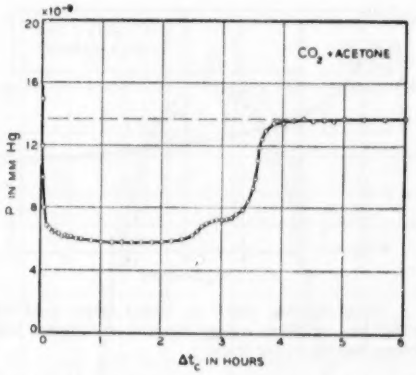

FIG. 2. Curve of pressure, p, *vs* cold interval, Δt_c, with CO_2 and acetone cooling on the traps. The background pressure is 13.8×10^{-9} mm Hg if the calibration for N_2 gas is used or 4×10^{-9} mm Hg if the calibration for mercury vapor is used. The kink in the curve between 2.6 and 2.9 hours is perhaps not significant. Refrigerant on the traps was renewed at 2.9 hours. Note that the monolayer is formed in about 3.5 hours.

The data of Fig. 1 show a monolayer adsorption time of about 4 hours with CO_2 and acetone on the traps. From this an estimate of the sticking probability of Hg on tungsten may be obtained. Since the pressure was about 3×10^{-9} mm Hg (using the Hg calibration) $p\Delta t_m \simeq 4.3\times10^{-5}$ mm Hg×sec. This is about 50 times the $p\Delta t_m$ value of N_2 on tungsten.[4] Hence the sticking probability of Hg on tungsten is about 0.02 times that of N_2 on tungsten or about 0.01. From this it is also clear that the partial pressure of adsorbable impurity having a sticking probability near that of nitrogen could certainly be no more than 0.02 times the observed pressure. This is perhaps another evidence that the pressure observed is to be attributed predominantly to Hg. Finally, baking of the apparatus and the traps followed by cooling directly with the CO_2 and acetone mixture produced no change in the observed background pressure.

A p *vs* Δt_c curve with CO_2 and acetone on the traps is shown in Fig. 2. It indicates general agreement with the Δp *vs* Δt_c curve of Fig. 1.

Admission of either the He-Ne-Kr or the Ar-Xe mixture produced an increase in the initial slope of the Δp *vs* Δt_c curve (Fig. 1) of about two. This would indicate a corresponding decrease in Δt_m due to admission of adsorbable impurities or some small adsorption of the heavier noble gases themselves. Under the least favorable conditions Δt_m is still of the order of two hours or more. One may thus have confidence that the tungsten surface is atomically clean to within a

---

of N_2 on tungsten. Other work (private communication) shows the observed sticking probability to vary in the range 0.2 to 0.6 from sample to sample presumably depending on crystal orientation on the surface. Figure 16 of reference 2 indicates that for N_2 on molybdenum $p\Delta t_m \sim 1.8\times10^{-6}$ mm Hg×sec.

[5] I. Langmuir and D. S. Villars, J. Am. Chem. Soc. **53**, 495 (1931), report on oxygen film to be removed from tungsten at 2070°K at a rate such that half disappeared in 20 seconds. I. Langmuir, J. Am. Chem. Soc. **35**, 105 (1913), found O_2 to affect the thermionic emission from tungsten at $T<2200$°K.

[6] S. Dushman and A. H. Young, Phys. Rev. **68**, 278 (1945).

[7] K. K. Kelley, Bulletin 383, U. S. Bureau of Mines, Washington, 1935 (unpublished), p. 69 gives $\Delta F^\circ = -RT\ln p = 15\,455 + 0.92T\log T + 0.0037T^2 - 30.06T$ for the vapor pressure of Hg in bars above solid Hg at the temperature T°K.

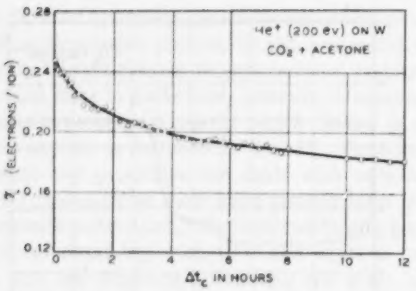

FIG. 3. Total electron yield, γ_i, *versus* target cold interval, Δt_c, for He^+ ions of 200-ev energy incident on tungsten with CO_2 and acetone cooling on the traps.

few percent for measurements made within minutes of a target flash. All data reported here meet this requirement.

A further evidence of the cleanliness of the tungsten surface comes from the observation of total secondary yield with time after a target flash. Such data for He^+ ions of 200 ev, obtained from the He-Ne-Kr mixture with CO_2 and acetone on the traps, are plotted in Fig. 3. The rate of change of γ_i with time as a gas layer forms on the target surface is clearly slow enough to permit measurements under clean conditions.

The target is made of tungsten ribbon 0.015 in. thick and 7 mm wide. On removal from the experimental tube it appeared to be thermally etched. Back reflection Laue patterns showed the surface to consist of crystals of 0.05 to 0.3 mm in size. The x-ray goniometer showed no high degree of crystal orientation, the 100 plane making angles up to $\pm 30°$ with the plane of the surface.

IV. γ_i FOR SINGLY CHARGED IONS

The data for γ_i of singly charged ions in the kinetic energy range 10 to 1000 ev are plotted in Fig. 4. These data were taken with the electron collector five volts positive relative to the target to insure collection of all ejected electrons. Collector voltages considerably higher than five volts were found to increase noticeably the loss of slow electrons through the entrance aperture.

The data on γ_i indicate a number of features relating to the magnitude of γ_i and its variation with incident ion energy. Perhaps the most striking feature is the small dependence of γ_i on ion kinetic energy. This is a basic evidence that the ejection process is an Auger process in which ion kinetic energy plays only a very secondary role.

A second interesting feature is the magnitude of γ_i. For no ion is it greater than 0.3, and for 10-ev ions it is seen to decrease steadily as one passes through the sequence from the lighter to the heavier ions. It is now clear that the Auger processes are so probable that the magnitude of γ_i is determined by the probability of the excited electron escaping from the metal rather than by the probability that the process occur while the ion is near the surface. The decrease in γ_i from He^+ to Xe^+ is, of course, the result of decreasing ionization energy. The depth in the metal from which an electron can be ejected by Auger neutralization is approximately $E_i/2$. The ground state of the conduction band in tungsten lies some 10.9 ev below the zero vacuum level. Thus, whereas for He and Ne all, or essentially all, electrons excited in the Auger process have enough energy to leave the metal if properly directed, in Ar, Kr, and Xe only electrons raised from the top approximately 50, 40, and 25 percent of the filled portion of the band, respectively, have any chance of leaving the metal.

Although essentially independent of ion energy the γ_i data of Fig. 4 show some energy dependences which are thought to be significant and for which reasons can be given. These are largely the results of broadening of the electron energy distribution as the ion is neutralized closer to the metal at higher incident energy. This can be shown to account both for the initial drop in γ_i of He^+ and the rise in γ_i of Ar^+, Kr^+, and Xe^+. The rise in $\gamma_i(He^+)$ at higher energies (above 400 ev) is probably the result of electron ejection by a process other than Auger ejection, perhaps of the type discussed by Ploch[8] in which bound electrons are released from surface atoms. One should expect the probability of such ejection to increase with the ion's incident velocity. It should appear at lowest energy in the case of the lightest and hence fastest ion (He^+ and He^{++}). Further evidence on this point is obtained from the

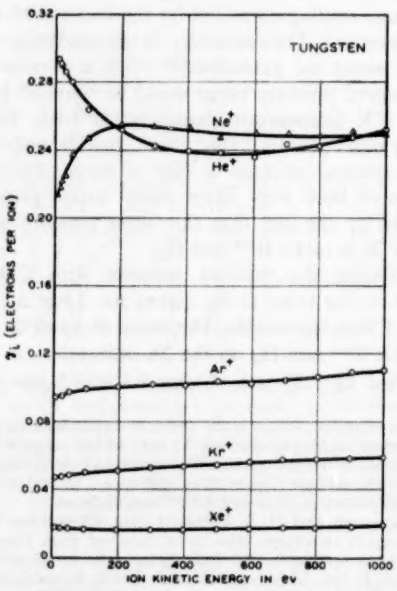

FIG. 4. Total electron yield, γ_i, *vs* ion kinetic energy for singly charged ions of the noble gases on atomically clean tungsten.

[8] W. Ploch, Z. Physik **130**, 174 (1951); see also M. E. Gurtovoy, J. Exptl. Theoret. Phys. (U.S.S.R.) **10**, 483 (1940).

electron energy distributions (Sec. VI). The anomalous behavior of $\gamma_i(Ne^+)$ is to be attributed to the increase in the proportion of the two-stage ejection process with increasing ion velocity. It is interesting to note that $\gamma_i(He^+)$ on molybdenum exhibited the same dependence on $E_k(He^+)$ as is reported here.[9]

The variation of $\gamma_i(He^+)$ with ion energy below 200 ev is very sensitive to surface contamination. γ_i at low ion energy is larger the cleaner the surface. It was found that during the course of the measurements γ_i values thought to be characteristic of an atomically clean surface slowly rose. At 10 ev, for example, this rise in $\gamma_i(He^+)$ was from 0.26 to 0.29. As indicated in the instrumentation paper[2] it is difficult even under the best conditions to reduce the residual adsorbed gas to less than about 1 percent of a monolayer.

The value of γ_i at ion energies a few times thermal energy is of interest in gaseous electronics. It has been possible to estimate γ_i at energies below those actually used in the experiment from the theory of the variation of γ_i with incident ion energy (Sec. XV of the accompanying paper).[1]

V. γ_i FOR ISOTOPIC IONS

γ_i has been measured carefully for Ne^+ ions of $m/e=20$ and 22 at 200-ev ion energy. 35 readings of γ_i for each ion were made alternately. The current from the source was adjusted to give amplifier readings for each ion on the same shunt and the same meter deflection to within 5 percent. The target was flashed every third reading so as to treat measurements for the two ions alike. The average γ_i for both sets of 35 readings came out to be 0.2561 with a standard deviation in each case very close to 0.0014.

Thus γ_i is found not to depend on the isotope used. This is clearly what one would expect for these Auger processes. The result is of some interest, however, in view of the results of Ploch[8] on the mass dependence of the electron yield for isotopic ions, in particular Ne^+ on beryllium and platinum. The present results do not necessarily contradict Ploch's since he used faster ions and surfaces which were most likely not atomically clean. Both of these conditions favor kinetic ejection. The slope of his γ_i *vs* ion energy curves even at 1 kev do not agree with the present work but look much like results the author has obtained with contaminated surfaces.

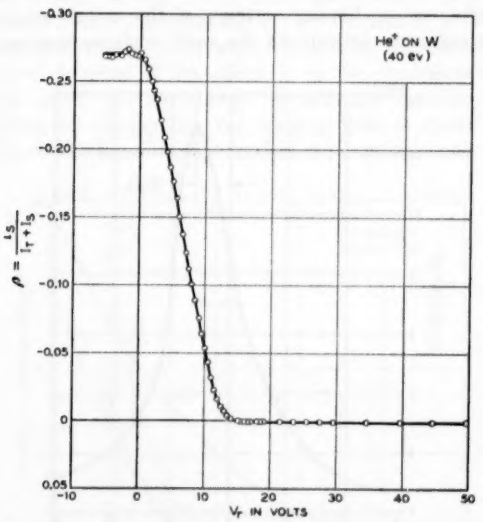

FIG. 5. Typical retarding potential data from which an electron energy distribution is obtained by the method described in the text. V_r is the voltage between target and electron collector corrected for contact potential.

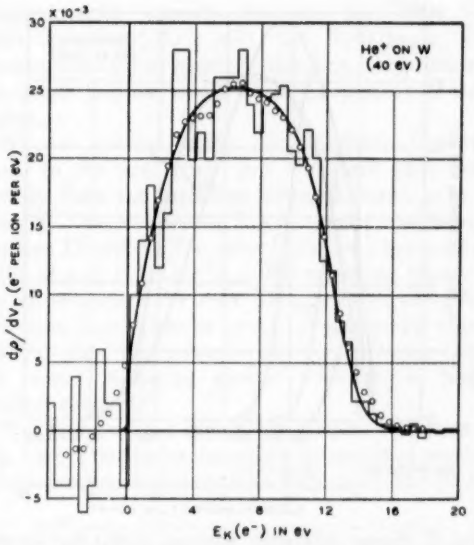

FIG. 6. Plots of $\Delta\rho/\Delta V_r$ and a smoothed $d\rho/dV_r$ curve from the data of Fig. 5. The points are $d\rho/dV_r$ values obtained from the smoothing formula given in the text.

VI. ELECTRON ENERGY DISTRIBUTIONS FOR SLOW IONS

Electron energy distributions are measured in this work by means of retarding potentials. Currents to the electron collector I_S and to the target I_T are measured as functions of V_{ST}, the voltage between target and collector. The ratio of currents $\rho=I_S/(I_T+I_S)$ is obtained as a function of retarding potential V_r which is V_{ST} corrected for contact potential (see Fig. 5). Contact potential between target and collector was measured several times during the course of the experiment and found to lie in the range 0.3 to 0.4 v (target positive). This did not change on replacing liquid N_2 with CO_2 and acetone on the traps. These measurements and the characteristics of the ρ *vs* V_r curve are discussed in the paper on instrumentation and procedure.[2]

[9] H. D. Hagstrum, Phys. Rev. **89**, 244 (1953).

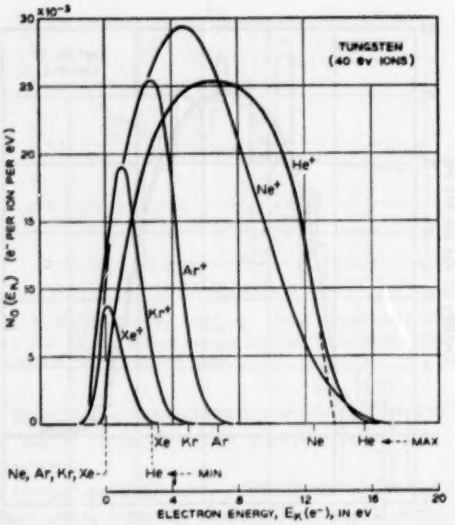

FIG. 7. Energy distribution functions $N_0(E_k)$ for electrons ejected from atomically clean tungsten by singly charged noble gas ions of 40-ev incident kinetic energy. The maximum and minimum energies indicated on the abscissa scale are the values $E_i-2\varphi$ and $E_i-2\epsilon_0$ or zero, respectively. These are the maxima and minima to be expected on the simple theory in which energy level shifts in the atom near the metal surface and broadening of the distributions are not taken into account.

In the present work the energy distribution $N_0(E_k) = d\rho/dV_r$ has been obtained from the retarding potential data in the following way. First $\Delta\rho/\Delta V_r$ is plotted from the ρ *vs* V_r data of Fig. 5 as shown by the stepped curve in Fig. 6. Smoothed values of the slope $d\rho/dV_r$ are also calculated from a smoothing formula, suggested to the author by Kaplan[10] which we shall discuss presently. The points plotted in Fig. 6 are those obtained from this formula. The $N_0(E_k)$ distribution is obtained by drawing a smooth curve through the stepped function being guided by the points obtained from the smoothing formula. The smoothing formula departs quite radically from the true curve wherever $d^2\rho/dV_r^2$ is large as is seen near the low- and high-energy limits of the curve in Fig. 6. In other regions, however, the smoothed points are helpful in drawing the final curve.

Kaplan suggested a smoothing formula based on the following considerations. If the data were precise the slope at a point, designated $(n+\frac{1}{2})$, which lies halfway between the points at $(V_r)_n$ and $(V_r)_{n+1}$ is $(d\rho/dV_r)_{n+\frac{1}{2}} = (\rho_{n+1}-\rho_n)/\Delta V_r$, where $\Delta V_r=(V_r)_{n+1}-(V_r)_n$. If the data are not precise, the slope at $(n+\frac{1}{2})$ of a straight line fitted to the data by least squares is $(d\rho/dV_r)_{n+\frac{1}{2}} = 2(\cdots-3\rho_{n-1}-\rho_n+\rho_{n+1}+3\rho_{n+2}+\cdots)/\Delta V_r(\cdots 3^2+1^2+1^2+3^2+\cdots)$. Whereas the first formula puts all the weight on the data points adjacent to the point $(n+\frac{1}{2})$, the second formula weights most heavily data points which are most distant from the point $(n+\frac{1}{2})$. The compromise suggested by Kaplan weights equally all data points used. Eight data points are smoothed by the formula:

$$\left(\frac{d\rho}{dV_r}\right)_{4\frac{1}{2}}=\frac{\rho_1+\rho_2+\rho_3+\rho_4-\rho_5-\rho_6-\rho_7-\rho_8}{16\Delta V_r}.$$

The procedure followed here is thought to be more accurate than that of measuring the slope of a smoothed ρ *vs* V_r plot as was done in earlier work.[9]

Energy distributions, $N_0(E_k)=d\rho/dV_r$, obtained in the manner just described for electrons ejected by He^+, Ne^+, Ar^+, Kr^+, and Xe^+, are plotted in Fig. 7. Note that the curves extend more or less to the left of the zero axis. This is an experimental effect resulting from the presence in the target-collector region of a small, uncompensated magnetic field fringing from the magnet of the m/e analyzer. For He^+ this fringing field is negligible. For the heavier ions, on the other hand, it becomes appreciable. Most of the fringing field has been balanced out by a field applied by a magnet which straddles the tube in the region of the target.[2] This bucking field is adjusted to optimum by observing a value of ρ on the steep side of the ρ *vs* V_r characteristic (Fig. 5) as a function of auxiliary magnet current. One finds the field which maximizes this ρ value. Such data for Xe^+ are plotted in Fig. 8. The optimum current for Xe is seen to be 3 ma corresponding to a target magnetic field of some 12 gauss. Since the fringing field at the target is *ca* 45 gauss at the field used for Xe^+, it is evident that the presence of the target magnet itself shunts the fringing field in the target region. Similar settings of the target magnet current were determined for each analyzer magnetic

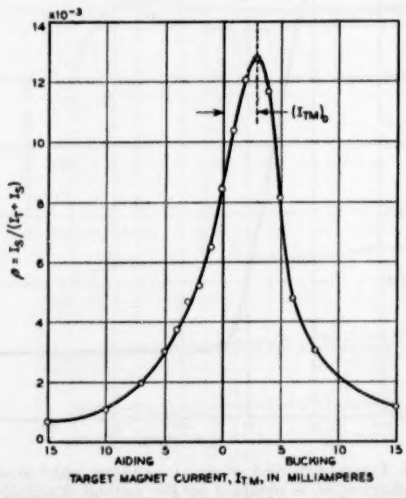

FIG. 8. The value of $\rho[=I_S/(I_T+I_S)]$ at a point on the steep slope of the ρ *vs* V_r characteristic plotted as a function of current through the coils of a magnet which straddles the tube in the region of the target.

[10] The author is also indebted to R. W. Hamming for a helpful discussion on data smoothing.

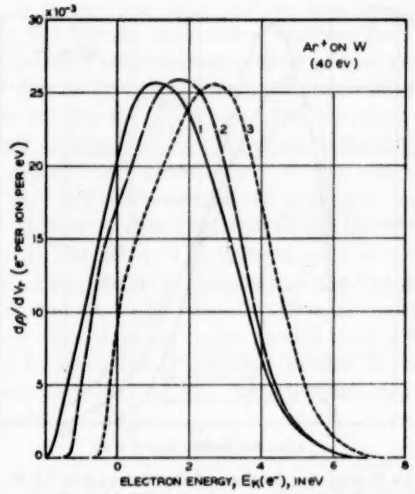

FIG. 9. Illustration of the effect of fringing magnetic field on the determination of the electron energy distribution function for electrons ejected by Ar^+. Curve 1: fringe field uncompensated, analyzer magnetic field of 1840 gauss; curve 2: fringe field uncompensated, analyzer field 1350 gauss; curve 3: fringe field compensated, analyzer field 1840 gauss. Note that in the compensated case (curve 3) some extension of the curve to negative $E_k(e^-)$ indicates incomplete compensation over the entire volume of the electron collector.

field used. All data presented in this paper were taken with the fringing field compensated for in this manner. The fact that the $N_0(E_k)$ curves of Fig. 7 do extend to negative $E_k(e^-)$ in spite of this procedure indicates that the fringe field is not balanced out uniformly over the volume of the 4 cm diameter collector sphere. Since $rB=3.4$ cm-gauss for a 1 ev electron it is clear that the residual field must be reduced considerably below 1 gauss if its effect is to be unobservable. The effect on an energy distribution function of failure to compensate for fringing field is shown in Fig. 9. The figure is explained in the caption. Analyzer

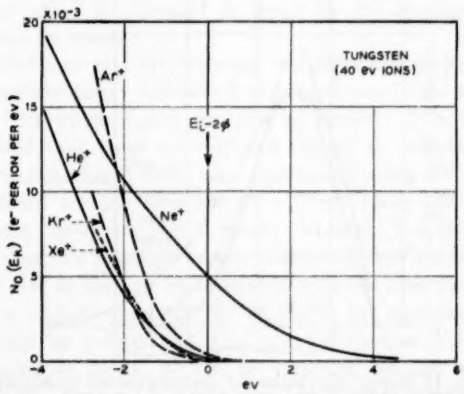

FIG. 10. A plot of the high energy tails of the distributions of Fig. 7 in which the curves have been shifted along the abscissa axis, so that the values $E_i-2\varphi$ for all distributions coincide.

magnetic fields normally used are: He^+, 580; Ne^+, 1300; Ar^+, 1840; Kr^+, 2670; Xe^+, 3200 gauss. With no compensation or magnetic shielding, fringe fields at the target position would be *ca* 1.5 percent of these values.

We now discuss briefly the distribution function data. In the first place two important data come directly from the retarding potential curve, ρ *vs* V_r (Fig. 5). One is $\gamma_i=\rho$ at $V_r<0$, already discussed in Sections IV and V. The other is the very low positive value of ρ at $V_r>E_k(e^-)_{max}$, the maximum energy of ejected secondary electrons. This indicates very small reflection of slow ions as ions or as metastable atoms. ρ at $V_r>E_k(e^-)_{max}$ is found to increase with increasing ion energy indicating greater reflection at higher incident energies.[11]

The forms of the energy distribution functions of Fig. 7 are of particular theoretical interest in as much as theory predicts such functions with which the experi-

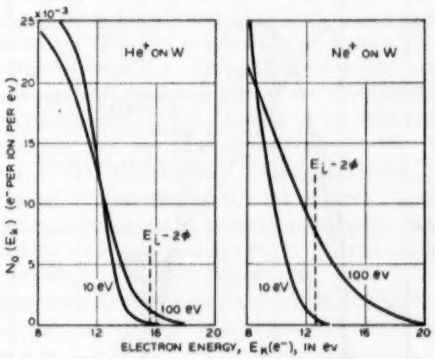

FIG. 11. Plots of tails of $N_0(E_k)$ distributions for He^+ and Ne^+ ions at 10- and 100-ev incident kinetic energies. Note agreement with the limit $E_i-2\varphi$ in each case at 10 ev. Note also that Ne^+ displays a much greater violation of the $E_i-2\varphi$ limit than does He^+ as ion energy is increased.

mentally determined ones may be compared. Furthermore, the form is found to be sensitive to the state of the target surface.[12] Of more specific interest, however, is the form of the distribution function near the minimum and maximum energy. Evidence is to be seen in Fig. 7 of a marked depletion of slow electrons in the distribution for He^+ compared to the Ne^+ and Ar^+ distributions. Investigation of the reasons behind this observation leads to a value (*ca* 6.3 ev) for the width ϵ_F of the filled portion of the conduction band in tungsten.[1]

The experimental data concerning the forms of the distributions near their energy maxima are perhaps more clearly shown in Fig. 10 than in Fig. 7. In Fig.

[11] These evidences of reflection of ions as ions and as metastable atoms have been studied further and will be reported in a separate publication now in preparation.

[12] Work is in progress on the effect on Auger ejection of adsorption of common gases on the target surface. A preliminary report is in print: H. D. Hagstrum, Phys. Rev. **89**, 338 (1953).

10 the high-energy tails of the distributions for 40-ev ions are plotted to an energy scale on which $E_i-2\varphi$ for all ions coincide. This makes it clearly evident that for He^+, Ar^+, Kr^+, and Xe^+ the maximum energy is quite close to the $E_i-2\varphi$ limit but that for Ne^+ it is not. This state of affairs can be shown to result from the fact that for He^+, Ar^+, Kr^+, and Xe^+ only Auger neutralization occurs, whereas at 40 ev in some 10 percent of the Ne^+ encounters the two-stage process of resonance neutralization and Auger de-excitation results. To demonstrate the validity of this conclusion it is necessary to show (1) that for Auger neutralization an energy limit at or below $E_i-2\varphi$ is expected, (2) that for Auger de-excitation this limit may be exceeded, and (3) that resonance neutralization can occur at an atomically clean tungsten surface only for Ne^+. This

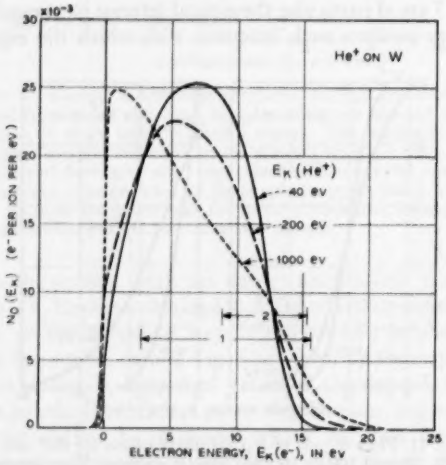

FIG. 12. Energy distributions of electrons ejected by He^+ ions of 40-, 200-, and 1200-ev incident kinetic energy. The energy intervals labeled 1 and 2 here and in Fig. 13 are those predicted for Auger neutralization and de-excitation, respectively, if energy level shifts near the metal and broadening of the distribution are neglected.

demonstration is undertaken in the paper on theory.[1] The theory indicates further that the rise in $\gamma_i(Ne^+)$ at low energies (see Fig. 4 and Sec VII) results from an increase in the fraction of two-stage processes with increasing ion energy and that for 10-ev ions the fraction of two-stage processes is essentially zero. If this is the case we expect no violation of the $E_i-2\varphi$ limit even in the case of Ne^+ at 10 ev. That this is indeed found to be the case is seen in Fig. 11. Here the high-energy tails of the $N_0(E_k)$ distributions for He^+ and Ne^+ are plotted for 10- and 100-ev ions. For 10-ev ions in each case the distribution limit agrees well with the $E_i-2\varphi$ limit. For He^+ at 100 ev this limit is exceeded by an amount which is readily attributable to the broadening of the distribution due to the causes discussed in Sec. XII of the theory paper.[1] For Ne^+ at 100 ev, on the other hand, a very much larger tail is evident which

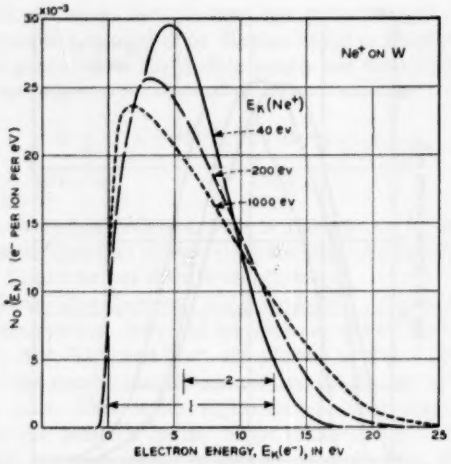

FIG. 13. Energy distributions of electrons ejected by 40-, 200-, and 1000-ev Ne^+ ions. See caption of Fig. 12 for explanation of the intervals labeled 1 and 2.

can only result from electrons ejected in the Auger de-excitation process.

VII. VARIATION OF ELECTRON ENERGY DISTRIBUTION WITH ION KINETIC ENERGY

Electron energy distributions have been determined for each of the singly charged ions at incident ion energies of 40, 200, and 1000 ev. Results for He^+, Ne^+, and Kr^+ are plotted in Figs. 12, 13, and 14, respectively. These three cases are representative of distinguishable variations with initial energy to be expected theoretically.

For all cases we expect and observe an extension of the distribution to higher electron energies at higher ion energies. This is the result of the greater broadening of the distribution for processes occurring closer to the

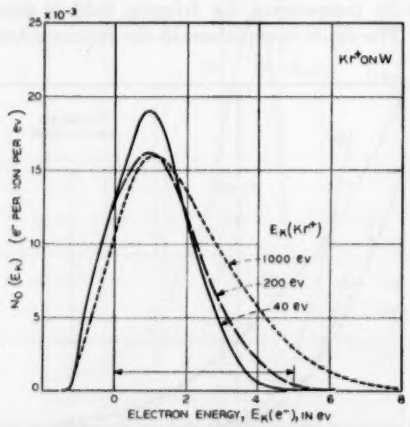

FIG. 14. Energy distributions of electrons ejected by 40-, 200-, and 1000-ev Kr^+ ions. The changes observed for Kr^+ are representative of those observed for Ar^+ and Xe^+. The energy interval indicated corresponds to that labeled 1 in Figs. 12 and 13 (see caption of Fig. 12).

metal as is the case when the ion approaches more rapidly. For Ne^+ the admixture of electrons from Auger de-excitation is seen to cause a much greater violation of the $E_i-2\varphi$ limit at ion energies above 10 ev than is observed for the other ions. The agreement with the limit at 10 ev and its explanation is thought to be good experimental confirmation of the theory. For both He^+ and Ne^+ we observe a relative increase in the number of slow electrons, as the ion energy is increased. The effect of broadening only is observed for Kr^+. This difference is traceable to the fact that for He^+ and Ne^+ all, for Kr^+ only a fraction, of the internal electrons excited in the Auger process have sufficient energy to surmount the surface barrier if properly directed. How each of the characteristics mentioned

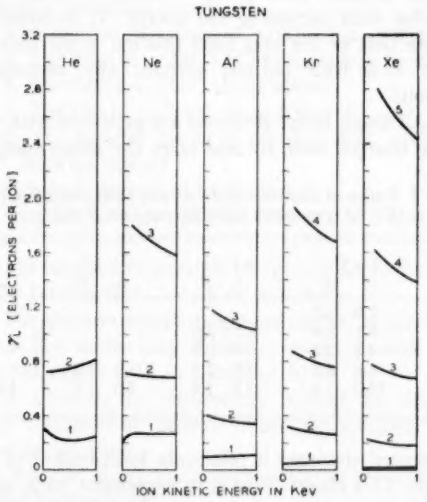

FIG. 15. Total yield *vs* ion kinetic energy for singly and multiply charged ions of the noble gases incident upon atomically clean tungsten. The charge of the ion is indicated at each curve.

here arises is discussed in detail in the companion paper on theory.[1]

He^+ ions of 1000-ev energy are observed to eject a relatively larger number of slow electrons $[E_k(e^-)<5$ ev$]$ for which theory can give no account. It is suggested that these are electrons ejected in non-Auger processes. Such have been postulated (Sec. IV) to account for the slow rise in $\gamma_i(He^+)$ above 400 ev where theory predicts a steady decrease. The failure to observe a disproportionate number of slow electrons for Ne^+ is then to be correlated with the observation that $\gamma_i(Ne^+)$ does not rise at higher ion energies. It should be pointed out that the distribution $N_0(E_k)$ plotted as $d\rho/dV_r$ should be corrected for the term dR/dV_r [see Eq. (6) of reference 2] which is appreciable at 1000 ev. Removal of this term would in no way affect the conclusions stated above.

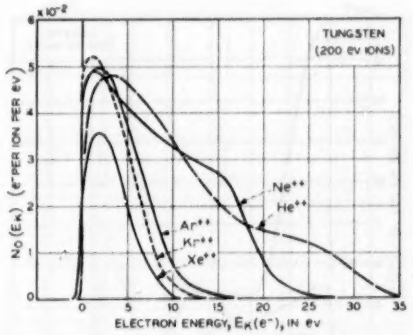

FIG. 16. Energy distributions of electrons ejected from tungsten by doubly charged ions of the noble gases. In this case $N_0(E_k)=2d\rho/dV_r$. Ion energy in each case is 200 ev.

VIII. RESULTS FOR MULTIPLY CHARGED IONS

The results obtained in this work for multiply charged ions are to be found in Figs. 15 through 20. They include measurements of total yield as a function of ion energy (Fig. 15) and of electron energy distribution. Distribution for all doubly and triply charged ions are plotted together in Figs. 16 and 17, respectively. Although included in Figs. 16 and 17 the distributions for the Ne ions are plotted together in Fig. 18 to illustrate the particularly interesting evidence of "inclusion" of the distribution for a given ion in the distribution of the ion of next higher charge. Data for Kr and Xe ions not plotted in Figs. 16 and 17 are to be found in Figs. 19 and 20, respectively.

There are some five experimental conclusions having theoretical implications which come out of this work. These are:

1. γ_i is found to increase with ionic charge and hence total ionization energy. This is thought to be the result of the neutralization of multiply charged ions near the metal surface in a series of stages at each one of which an electron is excited inside the metal. Subject to some qualification this means more electrons but not faster ones as the charge of the ion increases (see item 3 below). A more detailed look at this situation is obtained if the ratios of electron yield and total ioniza-

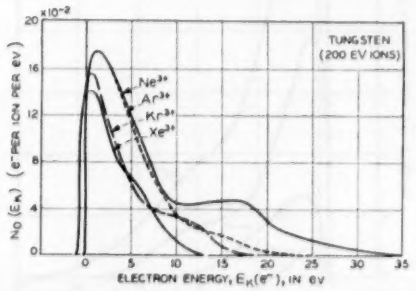

FIG. 17. Energy distributions of electrons ejected from tungsten by triply charged ions of the noble gases of 200-ev energy $[N_0(E_k)=3d\rho/dV_r]$.

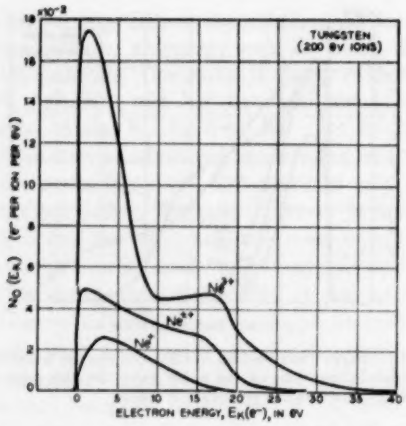

FIG. 18. Energy distributions of electrons ejected from tungsten by 200-ev neon ions [$N_0(E_k)=zd\rho/dV_r$ where z=ionic charge].

tion energy for ions which differ by one unit of charge are compared (Table I). Here it is seen that for He and Ne and for the more highly charged ions of Ar, Kr, and Xe reasonable agreement between these ratios prevails. This is not true for the less highly charged ions of the heavier gases (lower left-hand corner of Table I). If one assumes that multiply charged ions are neutralized in a series of approximately isoenergetic steps one can understand the main features of Table I as follows. For the lighter atoms and the more highly charged heavier ions the energy released per step in the neutralization process is sufficient to excite all or nearly all electrons above the surface barrier. The escape probability then cancels out of the ratio of electron yields which should then be approximately equal to the ratio of total energies available. For the ions Ar^+, Kr^+, and Xe^+, on the other hand only a fraction of the excited electrons have enough energy to escape. Since this fraction can increase markedly for the doubly charged ion it is reasonable that the ratio of γ_i values exceed the ratio of E_i values. This effect is greatest for Xe which has the lowest ionization energy.

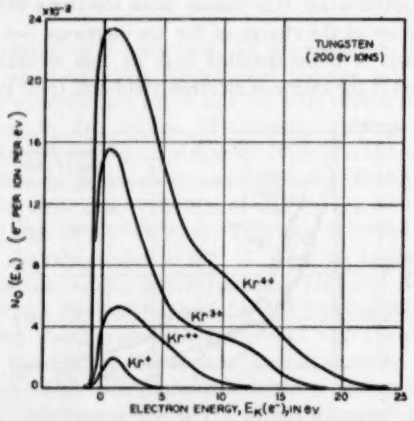

FIG. 19. Energy distributions of electrons ejected from tungsten by 200-ev krypton ions.

2. γ_i for each of the multiply charged ions except He^{++} is found to drop with increasing ion energy. This is taken to result from the broadening of the component energy distributions as the steps of neutralization occur closer to the metal. The explanation is thus the same as that of the drop in $\gamma_i(He^+)$ with increasing ion energy. Each step in the cascade neutralization process thus produces a distribution in energy of excited electrons inside the metal which lies above the zero vacuum level and for which broadening can be shown to reduce the chance of escape. The exception of He^{++} remains unexplained. It is probable that for He^{++} as for He^+ some electrons are released from surface atoms. This process should become more probable with increasing ion energy. It is interesting to note that of the ions used this ion is the only one which is a bare nucleus without any surrounding electrons.

3. Although faster electrons are produced with more highly charged ions, by and large the mean energy of the ejected electrons is relatively independent of ionic charge. This observation is in agreement with, and is indeed good evidence for, the conclusion that neutralization occurs predominantly in a series of steps.

TABLE I. Ratios of electron yield (γ_i) and total ionization energy (E_i) for ions which differ by one unit of charge.

Atom	2+/1+ γ_i	2+/1+ E_i	3+/2+ γ_i	3+/2+ E_i	4+/3+ γ_i	4+/3+ E_i	5+/4+ γ_i	5+/4+ E_i
He	2.6	3.2						
Ne	3.1	2.9	2.5	2.0				
Ar	4.3	2.8	3.0	2.0				
Kr	6.8	2.8	2.9	2.0	2.2	1.7		
Xe	12.0	2.8	3.5	1.9	2.0	1.8	1.8	1.5

4. The maximum in the $N_0(E_k)$ curve appears to be a function of ionic charge but is essentially independent of mass (ionization energy) of the ion. Thus the maxima of the $N_0(E_k)$ curves for doubly charged ions (Fig. 16) are near 5×10^{-2} electron per ion per ev and for triply charged ions (Fig. 17) near 16×10^{-2} electron per ion per ev. These figures may be compared with the approximately 2.5×10^{-2} electron per ion per ev value for singly charged ions (Fig. 7). The falling off toward the heavier ions is thought to be the result of the lower ionization energy and the consequent inability of all excited electrons to escape if properly directed. This effect is less apparent the higher the ionic charge, as is reasonable. The increase in the maximum values of $N_0(E_k)$ noted here is really only another manifestation of the step-by-step neutralization process. It may perhaps be taken as evidence of greater similarity in the neutralization schemes than the ratios of total yield alone would require.

5. There is evidence in the data of the "inclusion"

of the energy distribution for a given ion in that for the ion of next higher charge (see Fig. 18). This is further evidence pointing to the stepwise neutralization through ions of lower charge to the ground state of the neutral atom.

IX. SUMMARY OF EXPERIMENTAL RESULTS FOR SINGLY CHARGED IONS

In conclusion a listing is given of the experimental results for singly charged ions. The list is restricted to the results for singly charged ions inasmuch as a similar listing of results for multiply charged ions has already been given in Sec. VIII.

1. The total electron yield, γ_i, depends in a relatively minor way on ion kinetic energy.
2. γ_i is uniformly less than 0.3.
3. γ_i for the slowest ions decreases steadily with decreasing ionization energy.
4. The smaller variations of γ_i with ion energy are:
   a. The drop in $\gamma_i(He^+)$ at ion energy up to 400 ev
   b. The rise in $\gamma_i(He^+)$ above 400 ev,
   c. The rise in $\gamma_i(Ne^+)$ up to 100 ev,
   d. The general rise in γ_i for Ar^+, Kr^+, and Xe^+ with ion energy.
5. γ_i is independent of ionic mass.
6. Very few ions are reflected as ions or as metastable atoms.
7. The maxima in electron energy are approximately $E_i-2\varphi$ for the He^+, Ar^+, Kr^+, and Xe^+.
8. The electron energy maximum for Ne^+ appreciably exceeds $E_i-2\varphi$ for ions of kinetic energy greater than 10 ev but agrees with this limit at 10 ev.
9. In all cases the high-energy tails of the electron energy distribution become more pronounced with increasing ion energy.
10. For He^+ fewer low-energy electrons are observed than for Ne^+ and Ar^+.
11. For He^+ and Ne^+ increase in ion energy results in a relative increase in the number of slow electrons.

It is interesting to note that all of these observations with two exceptions can be accounted for in terms of the processes of Auger neutralization, resonance neutralization, and Auger de-excitation. The rise in $\gamma_i(He^+)$ above 400 ev and the increase in the number of slow electrons with increasing He^+ energy appear to be anomalous. As has been suggested it is reasonable that these effects arise from a small amount of ejection (non-Auger) by the ion when it is very close to the metal or has penetrated into the lattice.*

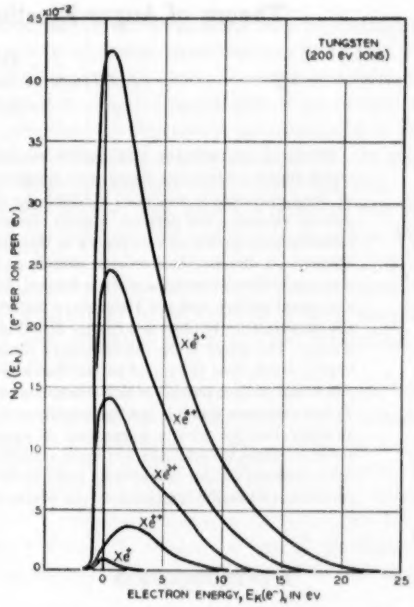

FIG. 20. Energy distributions of electrons ejected from tungsten by 200-ev xenon ions.

The author wishes to acknowledge with thanks the work of C. D'Amico, who took the data which are published here.

* *Note added in proof.*—Very recently it has been found that metastably excited singly charged ions are produced in Ar, Kr, and Xe if the bombarding electrons are fast enough. Such ions are detectable only by the fact that their ability to eject electrons from a metal is greater than that of unexcited singly charged ions. Work to be published later shows that the values of γ_i reported here for Ar^+, Kr^+, and Xe^+ are approximately 5 percent, 10 percent, and 30 percent larger, respectively, than they should be for ions all of which are unexcited.

Theory of Auger Ejection of Electrons from Metals by Ions

HOMER D. HAGSTRUM
Bell Telephone Laboratories, Murray Hill, New Jersey
(Received June 16, 1954)

Electrons ejected from atomically clean metals by slow ions of the noble gases arise in Auger transitions which involve either the direct neutralization of the ion or the de-excitation of an excited atom. A theory of these processes is presented in which the form of the distribution in energy and relative total yield, γ_i, of ejected electrons are derived. Matrix elements are not evaluated from first principles, but specific use of experimental results at two points in the theory leads to a determination of the dependence of the matrix element on distance between the atomic particle and the metal surface and the angle between the excited electron's velocity and the surface normal. Inclusion of the effects of variation of atomic energy levels near the metal surface and the Heisenberg uncertainty principle makes it possible to account in some detail for the experimentally observed energy distributions as well as the variation of these and of γ_i with ion kinetic energy. The effect upon the resonance ionization and neutralization processes of the variation of atomic energy levels near the metal surface has also been investigated. The theory predicts a critical distance from the metal surface outside which resonance neutralization and inside which resonance ionization are possible. It has also been possible for the specific case of noble gas ions on tungsten, used as an illustrative example, to determine the relative proportion of electrons ejected by each of the possible Auger processes, to estimate γ_i values for ions incident upon a metal with thermal energies, and to fix limits on the width of the filled portion of the conduction band in the metal. The role of the state density function in the metal and the effect of possible variation of the matrix element with electron energy in the band are also investigated.

I. INTRODUCTION

IT has been recognized for some time that electrons can be ejected from metals by slow ions of sufficiently large ionization energy. The Auger transitions in which these electrons are released do not involve directly the translational energy of the incoming particle. Two possible processes have been proposed and treated theoretically. After Oliphant and Moon[1] suggested the *resonance neutralization* of an ion at a metal surface by tunneling of an electron to populate an excited level, Massey,[2] Shekhter,[3] and Cobas and Lamb[4] have treated the two-stage process of *resonance neutralization* followed by electron ejection in *Auger de-excitation* of the excited atom. Shekhter[3] has also proposed and investigated theoretically the single process of electron ejection by *Auger neutralization* in which the ion is neutralized directly to the ground state. In each of these treatments the primary emphasis has been placed upon the calculation of the matrix elements and the determination of transition probability per unit time as a function of distance from the metal surface for such cases as H^+ or He^+ incident upon molybdenum.

Recent experimental work[5-7] involving noble gas ions incident on atomically clean metals has produced a number of results for which existing theory provides no explanation. The present work attempts to take account of the following effects not treated in the early theories:

1. the distribution of the participating electrons over the initial states in the metal (Secs. III and IV),
2. the dependence of the matrix element on angle which the excited electron's velocity makes with the surface normal (Secs. III and IV),
3. the probability that an excited electron will escape from the metal (Sec. VI),
4. the variation of atomic energy levels when the particle is near the metal surface (Secs. VIII, IX, and X),
5. the finite lifetime of the initial state of the system of metal and ion (Sec. XII), and
6. the role of the resonance processes in determining partition between Auger neutralization and de-excitation processes (Secs. XI and XIV).

No attempt is made in this work to evaluate matrix elements from first principles. However, two fits to the experimental data make it possible to evaluate the magnitude of the matrix element as a function of distance of the atomic particle from the surface and its dependence upon the angle between the excited electron's velocity and the surface normal (Sec. XIII).

For the case of noble gas ions on tungsten,[7] used as an illustrative example, it is possible to show that the Auger neutralization process accounts for all electrons ejected by very slow ions (<10 ev). At somewhat higher energies it is shown that only in the case of Ne^+ does the two-stage ejection process play any role. Even in this case a relatively small percentage of encounters (~ 10 percent) result finally in the Auger de-excitation process. With reasonable assumptions concerning the state density function in the conduction band of the metal and concerning the dependence of

[1] M. L. E. Oliphant and P. B. Moon, Proc. Roy. Soc. (London) **A127**, 388 (1930).
[2] H. S. W. Massey, Proc. Cambridge Phil. Soc. **26**, 386 (1930); **27**, 469 (1931).
[3] S. S. Shekhter, J. Exptl. Theoret. Phys. (U.S.S.R.) **7**, 750 (1937).
[4] A. Cobas and W. E. Lamb, Jr., Phys. Rev. **65**, 327 (1944).
[5] H. D. Hagstrum, Phys. Rev. **89**, 244 (1953).
[6] H. D. Hagstrum, Phys. Rev. **91**, 543 (1953).
[7] H. D. Hagstrum, preceding paper, Phys. Rev. **96**, 325 (1954).

the matrix element on initial energies of the participating electrons it has been possible to derive theoretical electron energy distributions and total yields which account for all the major features of the experimental results (Sec. XIV) and their dependences upon ion kinetic energy (Sec. XV). A reasonable extrapolation of the experimental results to the energy range of interest in gas discharges is now possible.

The theory of the resonance processes predicts that the distance between atomic particle and the metal surface must exceed a critical value for resonance neutralization to occur and must be less than this critical value for resonance ionization to occur (Sec. X). This situation further restricts the possibility of two-stage ejection but makes possible a three-stage process in the case of incident ions.

As might be expected the Auger processes considered here depend in an important way upon the electronic band structure of the metal involved. It appears possible to derive some information concerning the band structure from this work, in particular, concerning the energy levels of the top and bottom of the filled portion of the conduction band (Sec. XVI).

Notation used in this paper is defined in Table I. Energy values used are given in Table II. A general discussion of the processes which may occur as an ion or excited atom strikes a metal surface is included in the next section.

II. ELECTRONIC TRANSITIONS INVOLVING AN ION OR EXCITED ATOM NEAR A METAL SURFACE

In considering what can happen to an ion or excited atom as it approaches and strikes a metal surface it is convenient to distinguish electronic transitions which occur farther from the surface and involve principally the potential energy of the particle from processes which require much closer approach or actual penetration of the lattice and involve much more directly the kinetic energy of the particle. All evidence points to the conclusion that the electrons ejected from metals by slow ions of the noble gases arise in processes falling into the first of these categories. It is the purpose in this section to identify the basic electronic transitions and to discuss briefly the other possible interactions with the metal.

Electronic transitions in which an excited atom or ion near a metal surface could conceivably become involved are of the *resonance*, *Auger*, and *radiative* types. However, Shekhter[3] has shown that the probability of neutralization of an ion near a metal accompanied by radiation is very low ($\sim 5\times 10^{-7}$). The probability of any radiative process is expected to be low because the lifetime for radiation ($\sim 10^{-8}$ sec) is very long compared to the time which even a thermal particle spends within a few angstrom units of the surface ($\sim 10^{-12}$ sec). Ions and excited atoms near but not in intimate contact with a metal surface must thus undergo electronic changes in resonance- or Auger-type processes. Four basic electronic transitions may be distinguished. These are: 1. *resonance neutralization* of an ion, 2. *resonance ionization* of an atom, 3. *Auger neutralization* of an ion, and 4. *Auger de-excitation* of an excited atom. These processes are illustrated schematically in Figs. 1, 2, and 3, in which the energy levels shown are approximately those appropriate to He and tungsten.

It would appear that kinetic energy of the atomic particle can play no role in the transitions of Figs. 1, 2, and 3. When account is taken of energy level shifts near the metal surface, however, it becomes possible for some kinetic energy to be involved by first being transformed into potential energy in the interaction field near the surface.

Of the processes which require more intimate contact with the metal those in which electrons are released are of primary interest here. There appear to be three possible means of kinetic ejection of electrons.[8] These are: 1. acceleration of nearly free electrons inside the metal,[9,10] 2. thermal emission of electrons by local heating,[11–13] and 3. release of bound electrons from atoms at the surface or in the interior of the metal.[8,14]

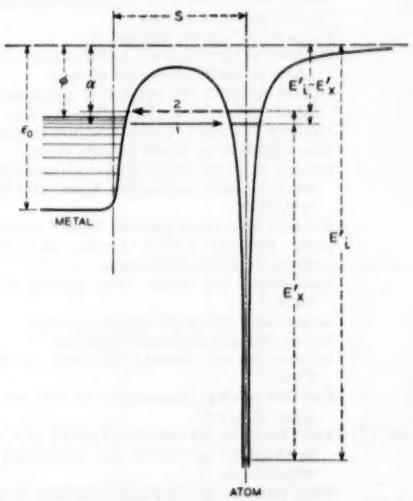

FIG. 1. Schematic diagram illustrating resonance neutralization of an ion (transition 1) or resonance ionization of an excited atom (transition 2) at a metal surface. Transition 1 can occur only at energy levels which are filled inside the metal, transition 2 at levels which are empty. It is evident that for the noble gases resonance ionization of an atom can occur only if the atom is excited. The possibility of shift of a given excited level with distance s such that $(E_i'-E_x')>\varphi$ for $s>s_c$ and $(E_i'-E_x')<\varphi$ for $s>s_c$ is discussed in Sec. X of the text. Notation used is defined in Table I.

[8] W. Ploch, Z. Physik **130**, 174 (1951).
[9] A. Becker, Ann. Physik **75**, 217 (1924).
[10] G. Schneider, Ann. Physik **11**, 357 (1931).
[11] P. L. Kapitza, Phil. Mag. **45**, 989 (1923).
[12] N. D. Morgulis, J. Exptl. Theoret. Phys. (U.S.S.R.) **4**, 449 (1934); **9**, 1484 (1939); **11**, 300 (1941).
[13] S. V. Izmailov, J. Exptl. Theoret. Phys. (U.S.S.R.) **9**, 1473 (1939).
[14] M. E. Gurtovoy, J. Exptl. Theoret. Phys. (U.S.S.R) **10**, 483 (1940).

TABLE I. Definitions of notation.[a]

e^-	electron (subscript M indicates electron is inside metal; energy of electron may be given in parentheses behind the symbol)
X	normal atom
X^m	metastable atom (in some cases any excited atom)
X^+	ion
α, β	energy below the vacuum level of an electron in the metal
$\epsilon, \epsilon', \epsilon''$	energy of an electron in the conduction band measured from the bottom of the band
ϵ_k	energy above bottom of conduction band of excited electron inside metal
$\epsilon_0, \epsilon_0(M)$	energy of vacuum level above bottom of conduction band in metal M
$\epsilon_F, \epsilon_F(M)$	energy of Fermi level of metal M above bottom of conduction band
$\varphi, \varphi(M)$	work function of metal M
E_k	kinetic energy of a particle (ion, atom, electron) outside metal
E_i	ionization energy
E_x	excitation energy
E_i', E_x'	effective ionization and excitation energies near a metal surface, respectively
$E(n-M)$	energy of interaction of normal atom and metal surface
$E(m-M)$	energy of interaction of metastable (sometimes excited) atom and metal surface
$E(i-M)$	energy of interaction of ion and metal surface
E_t	total energy in a system
$\delta(\epsilon)$	Dirac δ function on energy
s	distance of particle from metal surface ($s=0$ at plane of nuclei of surface atoms)
s_c	critical distance for resonance processes: neutralization at $s>s_c$, ionization at $s<s_c$
s_m	distance at which $P_t(s,v_0)$ function is maximum
$\bar{s}$	mean distance at which process occurs
d	particle diameter (subscripts n, m, and i indicate normal atom, metastable atom, and ion, respectively)
v_0	incident velocity of particle toward metal
θ	angle between surface normal and velocity vector of excited electron
θ_c	maximum θ for escape over surface potential barrier
φ	azimuthal angle about surface normal
H_{fi}	matrix element of Auger transition[b]
f	ratio of matrix element for $\theta<\theta_c$ to that for $\theta>\theta_c$[b]
$F(\epsilon',\epsilon'')$	function giving dependence of H_{fi} on initial state energies[b]
$u_M'(1), u_M''(2)$	wave functions of electrons 1 and 2 at ϵ' and ϵ'' in the filled portion of the conduction band, respectively
u_F	wave function of the excited electron at ϵ_k
u_G	wave function of electron in the ground state of the neutralized atom
u_E	wave function of the excited (metastable) electron in the atom
γ_N	electron yield from pure Auger neutralization in electrons per incident particle
γ_D	electron yield from pure Auger de-excitation in electrons per incident particle
γ_i	electron yield per incident particle which is an ion at $s=\infty$
γ_m	electron yield per incident particle which is a metastable atom at $s=\infty$
f_N	fraction of incident ions which decay finally by Auger neutralization
α	atomic polarizability (subscripts n and m indicate normal and metastable atom, respectively)
k_m	wave number of fastest electron in conduction band of metal
A, a	parameters in transition rate function $A\exp(-as)$[b,c]
B, b	parameters in repulsive interaction term $B\exp(-bs)$ (subscripts i, m, n denote ion, metastable atom, and normal atom, respectively)
n	number of electrons inside metal
$W(P_t), W(\Phi_\sigma)$	widths at half-maximum of P_t and Φ_σ functions, respectively
$R_t(s)$	total transition rate[b,c]
$P_\Omega(\theta,\epsilon_k)d\Omega$	probability that an excited electron of energy ϵ_k has its velocity vector lying in $d\Omega=\sin\theta d\theta d\varphi$ at θ, φ[b]
$P_k(\epsilon_k,s)d\epsilon_k$	probability that a process occurring with incident particle at s will produce an excited electron having energy in $d\epsilon_k$ at ϵ_k[b]
$P_t(s,v_0)ds$	probability that a particle starting from $s=\infty$ toward the metal with velocity v_0 will undergo an electronic transition in ds at s[b,c]
$P_0(s,v_0)$	probability that a particle approaching a metal surface with velocity v_0 will reach the distance s without undergoing a specific electronic transition
$P_e(\epsilon_k), P_e(E_k)$	probability that an excited electron of energy $\epsilon_k=E_k+\epsilon_0$ will escape from the metal[b]
$\rho(E_t)$	density of final states in Auger process at total energy E_t
$N_c(\epsilon)$	density of states in conduction band
$N(\epsilon_k)$	density of final states available to excited electrons
$N_i(\epsilon_k)$	distribution in energy of excited electrons inside metal[b]
$N_0(E_k)$	distribution in energy of external secondary electrons[b]
$T(\epsilon)$	Auger transform of $N_c(\epsilon)$ [Eq. (15)][b]
$T_\sigma(\epsilon)$	Auger transform broadened by variation of energy levels and Heisenberg uncertainty principle [Eq. (76)][b]
$I(\delta,s)$	distribution in energy difference δ from the nominal ϵ_k for the elemental Auger process ["line profile," Eq. (74)]
$\Phi_\sigma(y)$	Gaussian distribution [Eq. (80)]
σ	parameter determining spread of Gaussian distribution[b] [$\sigma=\langle\sigma_1^2+\sigma_2^2\rangle^{\frac{1}{2}}$]
σ_1	σ factor from variation of energy levels[b]
σ_2	σ factor from Heisenberg uncertainty principle[b]

[a] Notation used at only one point in the paper is not included in this table.
[b] No superscript indicates that the quantity refers to Auger neutralization or all processes generally; the superscript prime (') indicates that the quantity refers to Auger de-excitation.
[c] The double-prime superscript (") indicates that the quantity refers to a resonance process.

For slow ions only a negligible amount of kinetic energy can be transferred to an essentially free electron. Furthermore, the theory of thermal emission does not account for the observed dependence of kinetic ejection on work function[15] nor the dependence on ion mass of kinetic ejection by isotopic ions.[8] It appears that the release of bound electrons from surface atoms is the most probable kinetic ejection process for an ion of kinetic energy less than 1000 ev. In the experimental work[7] there is evidence of electrons from kinetic ejection only in the case of He^+ at energies above 400 ev.

[15] H. Paetow and W. Walcher, Z. Physik **110**, 69 (1938).

Kinetic energy may be lost at the metal surface to elastic vibrations in the solid and to sputtered atoms, and in producing disorder in the lattice.[16] It is clear that appreciable kinetic energy loss can occur only at distances from the surface where the repulsive forces are large. Evidence presented in this paper indicates that for slow ions (<100 ev) incident upon atomically clean metal surfaces the Auger processes occur with high probability on the inward trip of the particle toward the surface before processes involving the kinetic energy become important. Consistent with this is the observation of very few reflected ions or metastable atoms (~ 0.1 percent) for ions of energy less than 100 ev.[7]

Before proceeding with the theory the assumptions made as to the nature of the metal surface will be stated. It is assumed that the surface is smooth and structureless. Thus a one-dimensional theory is given in which no distinction is made between approach directly above a surface atom or between surface atoms. The properties attributed to this surface are those of the polycrystalline surfaces with which the experimental work has been performed.

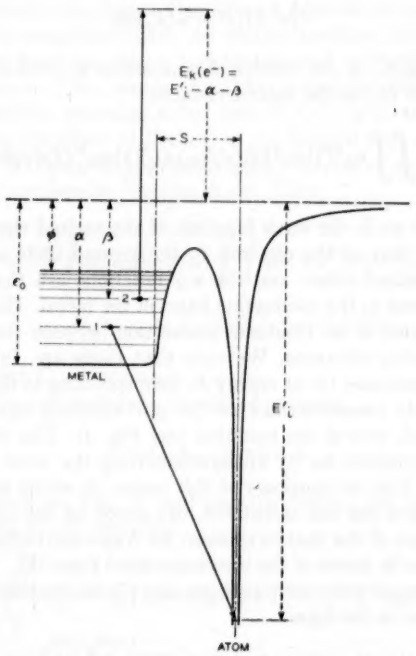

FIG. 2. Schematic diagram illustrating Auger neutralization of an ion at a metal surface. If the excited electron escapes, $E_k(e^-)$ is its kinetic energy observed outside the metal. The limits of $E_k(e^-)$ are seen to be $E_k(e^-)_{max} = E_i' - 2\varphi$; $E_k(e^-)_{min} = E_i' - 2\epsilon_0$ (zero if $E_i' < 2\epsilon_0$). Note that $E_i' > 2\varphi$ is necessary for production of an *external* secondary electron. Neutralization by this process can always occur if $E_i' > \varphi$ although resonance neutralization (Fig. 1) is more probable at a given s if $\varphi < E_i' < \epsilon_0$.

[16] See the review of experiment and theory concerning these topics in H. S. W. Massey and E. H. S. Burhop, *Electronic and Ionic Impact Phenomena* (Oxford University Press, London, 1952), pp. 610 ff. and 578 ff. G. K. Wehner, Phys. Rev. **93**, 633 (1954), has recently reported work in which the kinetic energy threshold of sputtering for Hg^+ on tungsten is found to be 80–100 ev.

III. THEORY OF AUGER NEUTRALIZATION

We discuss first the process of Auger neutralization depicted in Fig. 2. For convenience we redraw the energy level diagram (Fig. 4) and measure internal energy, ϵ, from the ground state in the conduction band. Thus

$$\epsilon' = \epsilon_0 - \alpha, \tag{1}$$

$$\epsilon'' = \epsilon_0 - \beta, \tag{2}$$

$$\epsilon_k = \epsilon_0 + E_k. \tag{3}$$

The elemental process of Auger neutralization, with the interacting electrons initially at ϵ' and ϵ'' in the conduction band, consists of the system $X^+ + e_M^-(\epsilon') + e_M^-(\epsilon'')$ transforming itself at constant total energy E_t, into the isoelectronic system $X + e^-(\epsilon_k)$. This transition, which takes place with the atomic particle a

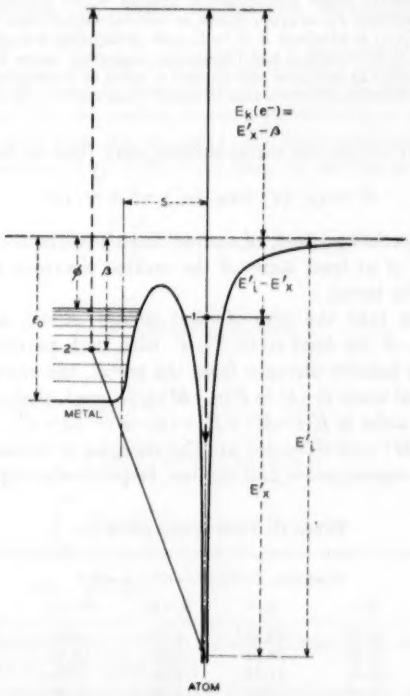

FIG. 3. Schematic diagram illustrating Auger de-excitation of an excited atom at a metal surface. The exchange transition is indicated by the full lines, the process not involving electron exchange between metal and atom by the dashed lines. Note here that the process can occur whenever $E_i' > \varphi$, but that resonance ionization (Fig. 1) followed by Auger neutralization (Fig. 2) is more probable at a given s if $(E_i' - E_x') < \varphi$. External secondary electrons are produced if $E_x' > \varphi$. The kinetic energy extrema are $E_k(e^-)_{max} = E_x' - \varphi$; $E_k(e^-)_{min} = E_x' - \epsilon_0$ (zero if $E_x' < \epsilon_0$)

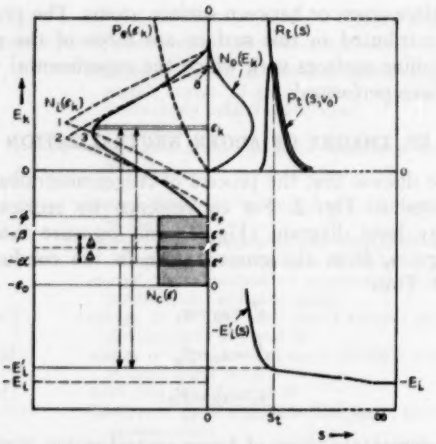

FIG. 4. A composite plot of energy levels, energy distribution functions, and other functional dependences related to the process of Auger neutralization of an ion at a metal surface. The horizontal line labeled 0–0 is the zero energy level in the vacuum. The vertical line labeled 0–0 represents the metal surface. The interior of the metal is at the left, the vacuum outside the metal at the right. The filled portion of the conduction band is indicated between $\epsilon=0$ and $\epsilon=\epsilon_F$ by stippling. The electronic transitions of an elemental Auger neutralization process which populate the energy element $d\epsilon_k$ at ϵ_k are shown as vertical dashed lines. Curve 1 for $N_i(\epsilon_k)$ is obtained if $E_i'=E_i$ and broadening is neglected, curve 2 if $E_i'=E_i'(s_m)$ and broadening neglected, curve 3 if E_i' varies with s as indicated and account is taken of broadening. The $N_0(E_k)$ function shown is that obtained from curve 3 for $N_i(\epsilon_k)$.

distance s from the metal surface, may thus be written

$$X^+ + e_M^-(\epsilon') + e_M^-(\epsilon'') \rightarrow X + e^-(\epsilon_k). \quad (4)$$

The ejection process, of course, must involve the final escape of at least some of the excited electrons $e^-(\epsilon_k)$ from the metal.

If we take the zero of total energy, $E_t=0$, as the energy of the final state $X+e^-$ with both particles at rest an infinite distance from the metal, the energy of the final state in (4) is $E(n-M)+(\epsilon_k-\epsilon_0)$, that of the initial state is $E(i-M)+E_i-(\epsilon_0-\epsilon')-(\epsilon_0-\epsilon'')$. Here $E(n-M)$ and $E(i-M)$ are the energies of interaction of the normal atom and the ion, respectively, with the metal at the distance s from the surface. Equating the energies of the initial and final states, which are each equal to E_t, leads to the relations

$$\epsilon'+\epsilon''=2\epsilon=\epsilon_k+\epsilon_0-E_i'(s), \quad (5)$$

$$E_i'(s)=E_i+E(i-M)-E(n-M). \quad (6)$$

$E'(s)$ defines an effective ionization energy for the atom at a distance s from the metal surface. It should be noted that evaluation of the initial and final energies at the same value of s is the tantamount to assuming that the Franck-Condon principle holds for these electronic transitions. (See Secs. IX and X.)

The transition rate for the process which occurs when the ion is at s, which involves electrons initially at ϵ' and ϵ'' in the metal, and which results in an excited electron of energy ϵ_k with velocity vector lying in the element of solid angle $d\Omega$, is given by the method of variation of constants as

$$(2\pi/\hbar)|H_{fi}|^2\rho(E_t)d\Omega. \quad (7)$$

Here $\rho(E_t)$ is the density of final states at total energy E_t and H_{fi} is the matrix element,[17]

$$H_{fi}=\int\int u_F^*(1)u_G^*(2)(e^2/r_{12})u_M'(1)u_M''(2)d\tau_1 d\tau_2. \quad (8)$$

In (8) u_F is the wave function of the excited electron, u_G is that of the electron in the ground state of the neutralized atom, and the u_M functions are those of electrons in the conduction band in the metal. The perturbation is the Coulomb interaction between the participating electrons. We note that there are, in fact, two processes (4) at energy E_t corresponding to the two possible identifications of the participating electrons on each side of the equation (see Fig. 4). This should be accounted for by antisymmetrizing the wave functions. For the purposes of this paper, in which matrix elements are not calculated, discussion of the characteristics of the matrix element for Auger neutralization is done in terms of the unsymmetrized form (8).

We now write the transition rate (7) for the elemental process in the form

$$(2\pi/\hbar)|H_{fi}|^2N(\epsilon_k)d\Omega=F(\epsilon',\epsilon'')N(\epsilon_k)P_\Omega(\theta,\epsilon_k)d\Omega. \quad (9)$$

In this expression $\rho(E_t)$ has been replaced by the density of final states, $N(\epsilon_k)$, available to the excited electron at ϵ_k inside the metal. $P_\Omega(\theta,\epsilon_k)d\Omega$ is the probability that the excited electron of energy ϵ_k has its velocity vector lying in $d\Omega=\sin\theta d\theta d\varphi$ at the polar angles θ, φ. $F(\epsilon',\epsilon'')$ is a function of initial state energies only. The matrix element is thus assumed to depend only on the angle θ

TABLE II. Table of energies in ev.

Atom	E_i [a]	E_a [a]	E_i-E_a	$E_i-2\varphi$	$E_a-\varphi$
	Tungsten: $\varphi=4.5$;[a] $\epsilon_F=6.4$;[b] $\epsilon_0=10.9$				
He	24.58	19.81	4.77	15.58	15.31
Ne	21.56	16.61	4.95	12.56	12.11
Ar	15.76	11.55	4.21	6.76	7.05
Kr	14.00	9.91	4.09	5.00	5.41
Xe	12.13	8.31	3.82	3.13	3.81

[a] See compilation of work function data by H. B. Michaelson, J. Appl. Phys. 21, 536 (1950).
[b] This is Manning and Chodorow's value (reference 24). See discussion in Sec. XVI.
[a] He, Ne, Ar: C. E. Moore, *Atomic Energy Levels*, National Bureau of Standards Circular No. 467 (U. S. Government Printing Office, Washington, D. C., 1949), Vol. I; Kr: National Bureau of Standards Circular No. 467, Vol. II (1952); Xe: Landol-Börnstein, *Tables* (Julius Springer, Berlin, 1950), Vol. I, Part 1.

[17] Matrix elements for the Auger effect are discussed in E. H. S. Burhop, *The Auger Effect and Other Radiationless Transitions* (Cambridge University Press, London, 1952), Chap. II, Secs. 2.1 and 2.4. See also reference 3.

with the surface normal and to be independent of aximuthal angle φ.

The total transition rate for all processes occurring when the ion is at a distance s from the surface is

$$R_i(s)=\int\int\int\int(2\pi/\hbar)|H_{fi}|^2N(\epsilon_k)d\Omega d\epsilon_k \times\delta(\epsilon'+\epsilon''+E_i'-\epsilon_0-\epsilon_k)N_c(\epsilon')N_c(\epsilon'')d\epsilon'd\epsilon'', \quad (10)$$

which, by use of (9), may be written

$$R_i(s)=\int\int N(\epsilon_k)P_\Omega(\theta,\epsilon_k)\int\int F(\epsilon',\epsilon'') \times\delta(\epsilon'+\epsilon''+E_i'-\epsilon_0-\epsilon_k)N_c(\epsilon') \times N_c(\epsilon'')d\epsilon'd\epsilon''d\Omega d\epsilon_k. \quad (11)$$

In (10) and (11) $N_c(\epsilon)$ is the state density function in the conduction band. The Dirac δ function on energy assures compliance with the energy condition (5).

The function $F(\epsilon',\epsilon'')$ expresses the unknown dependence of H_{fi} on the initial state energies. We may proceed by assuming either that $F(\epsilon',\epsilon'')$ is a constant or that the effect of $F(\epsilon',\epsilon'')$ in the integral over ϵ' and ϵ'' in (11) may be approximated by the use of an effective state density function $N_c(\epsilon)$. Then

$$R_i(s)=C\int\int N(\epsilon_k)P_\Omega(\theta,\epsilon_k)\int\int\delta(\epsilon'+\epsilon''+E_i'-\epsilon_0-\epsilon_k) \times N_c(\epsilon')N_c(\epsilon'')d\epsilon'd\epsilon''d\Omega d\epsilon_k, \quad (12)$$

in which C is a constant.

If we now make the change of variable,

$$\epsilon'=\epsilon-\Delta, \quad \epsilon''=\epsilon+\Delta, \quad (13)$$

indicated in Fig. 4, and specify limits, the double integral in (12) becomes

$$\int_0^{\epsilon_F/2}\int_0^{\epsilon}N_c(\epsilon-\Delta)N_c(\epsilon+\Delta)\delta(2\epsilon+E_i'-\epsilon_0-\epsilon_k)d\Delta d\epsilon + \int_{\epsilon_F/2}^{\epsilon_F}\int_0^{\epsilon_F-\epsilon}N_c(\epsilon-\Delta)N_c(\epsilon+\Delta) \times\delta(2\epsilon+E_i'-\epsilon_0-\epsilon_k)d\Delta d\epsilon = \int_0^{\epsilon_F}T(\epsilon)\delta(2\epsilon+E_i'-\epsilon_0-\epsilon_k)d\epsilon = T[(\epsilon_k+\epsilon_0-E_i')/2]. \quad (14)$$

Here $T(\epsilon)$ is the so-called Auger transform[18] defined thus:

$$T(\epsilon)=\int_0^{\epsilon}N_c(\epsilon-\Delta)N_c(\epsilon+\Delta)d\Delta, \quad 0<\epsilon<\epsilon_F/2$$

$$=\int_0^{\epsilon_F-\epsilon}N_c(\epsilon-\Delta)N_c(\epsilon+\Delta)d\Delta, \quad \epsilon_F/2<\epsilon<\epsilon_F$$

$$=0; \quad \epsilon<0, \quad \epsilon>\epsilon_F. \quad (15)$$

The total transition rate, from (12) and (14), is thus:

$$R_i(s)=C\int\int N(\epsilon_k)T[(\epsilon_k+\epsilon_0-E_i')/2]P_\Omega(\theta,\epsilon_k)d\Omega d\epsilon_k$$

$$=C\int_{\epsilon_F}^{\infty}N(\epsilon_k)T[(\epsilon_k+\epsilon_0-E_i')/2]d\epsilon_k, \quad (16)$$

since $\int_0^{2\pi}\int_0^{\pi}P_\Omega(\theta,\epsilon_k)\sin\theta d\theta d\varphi=1$ at all ϵ_k. In (16) account is taken of the fact that only states for which $\epsilon_k>\epsilon_F$ are available as final states inside the metal. We neglect the small population of states above ϵ_F demanded by the Fermi distribution at temperatures above absoiute zero.

We now define a second probability distribution function $P_k(\epsilon_k,s)$ such that $P_k(\epsilon_k,s)d\epsilon_k$ is the probability that the excited electron produced in a process occurring with the ion at s will have energy in the interval $d\epsilon_k$ at ϵ_k. Then $R_i(s)$ may be written as

$$R_i(s)=\int\int R_i(s)P_k(\epsilon_k,s)P_\Omega(\theta,\epsilon_k)d\Omega d\epsilon_k$$

$$=\int_{\epsilon_F}^{\infty}R_i(s)P_k(\epsilon_k,s)d\epsilon_k, \quad (17)$$

from which, with (16),

$$P_k(\epsilon_k,s)=\frac{N(\epsilon_k)T[(\epsilon_k+\epsilon_0-E_i')/2]}{\int_{\epsilon_F}^{\infty}N(\epsilon_k)T[(\epsilon_k+\epsilon_0-E_i')/2]d\epsilon_k}, \quad \epsilon_k>\epsilon_F$$

$$=0, \quad \epsilon_k<\epsilon_F. \quad (18)$$

The dependence of P_k on s comes through the dependence of E_i' on s [Eq. (6)].

We wish now to determine the distribution in energy, $N_i(\epsilon_k)$, of electrons excited in the Auger neutralization process. To do this we need the probability $P_i(s,v_0)ds$ that an incoming ion of velocity v_0, assumed constant, undergoes Auger neutralization in the distance interval ds at s. $P_i(s,v_0)$ is determined from $R_i(s)$ in Sec. V. Illustrative R_i and P_i functions are plotted in Fig. 4. Using the probability distributions P_k and P_Ω defined

[18] The author first encountered this Auger transform in the work of J. J. Lander, (private communication) Phys. Rev. 91, 1382 (1953), to whom he is much indebted.

previously, we may write

$$N_i(\epsilon_k)=\int_0^\infty\int_0^{2\pi}\int_0^{\pi} P_i(s,v_0)P_k(\epsilon_k,s) \times P_\Omega(\theta,\epsilon_k)\sin\theta d\theta d\varphi ds$$
$$=\int_0^\infty P_i(s,v_0)P_k(\epsilon_k,s)ds. \quad (19)$$

In writing this expression it has been assumed that all significant contributions to $N_i(\epsilon_k)$ occur on the inward trip of the ion toward the metal surface. The justification for this in the light of the experimental evidence is discussed in Sec. XIII. The integral of $N_i(\epsilon_k)$ over all ϵ_k is thus

$$\int_0^\infty N_i(\epsilon_k)d\epsilon_k=\int_0^\infty P_i(s,v_0)ds\simeq 1, \quad (20)$$

since $\int_0^\infty P_k(\epsilon_k,s)d\epsilon_k=1$ at all s. $N_i(\epsilon_k)$ is thus normalized to a total area of one electron per incident ion when Auger neutralization is the only possible Auger process.

Even with $\int_0^\infty P_i(s,v_0)ds=1$ one cannot determine $N_i(\epsilon_k)$ without integration over s because $P_k(\epsilon_k,s)$ depends on s. A method of approximating the integration over s in Eq. (19) is suggested by the fact that $P_i(s,v_0)$ is large over only a relatively small range of s. The effect of $P_i(s,v_0)$ in (19) is thus to broaden somewhat the function $P_k(\epsilon_k,s)$ evaluated at the distance $s=s_m$ at which $P_i(s,v_0)$ is a maximum. The results of this procedure are discussed in Secs. XII and XIV. If the interaction energies $E(n-M)$ and $E(i-M)$ in (6) are neglected, $E_i'(s)=E_i$, a constant, P_k becomes independent of s and $N_i(\epsilon_k)=P_k(\epsilon_k)$ if $\int_0^\infty P_i(s,v_0)ds$ is taken to be unity. The consequences of these assumptions are discussed in Sec. VII.

The distribution in energy, $N_0(\epsilon_k)$, of electrons which escape from the metal is

$$N_0(\epsilon_k)=\int_0^\infty\int_0^{2\pi}\int_0^{\theta_c} P_i(s,v_0)P_k(\epsilon_k,s) \times P_\Omega(\theta,\epsilon_k)\sin\theta d\theta d\varphi ds$$
$$=\int_0^\infty P_i(s,v_0)P_k(\epsilon_k,s)ds \times\int_0^{2\pi}\int_0^{\theta_c} P_\Omega(\theta,\epsilon_k)\sin\theta d\theta d\varphi$$
$$=N_i(\epsilon_k)P_e(\epsilon_k). \quad (21)$$

Here $\theta_c(\epsilon_k)$ is the maximum value of θ for which escape of the excited electron over the surface barrier is possible. The quantity $P_e(\epsilon_k)$, defined by the equation

$$P_e(\epsilon_k)=\int_0^{2\pi}\int_0^{\theta_c} P_\Omega(\theta,\epsilon_k)\sin\theta d\theta d\varphi, \quad (22)$$

is the probability that an excited electron of energy ϵ_k will escape over the surface barrier. It is discussed further in Sec. VI. Since $P_e(\epsilon_k)>0$ only if $\epsilon_k>\epsilon_0$ (or $E_k>0$) we shall usually write N_0 as a function of $E_k=\epsilon_k-\epsilon_0$. Illustrative $N_i(\epsilon_k)$, $P_e(\epsilon_k)$, and $N_0(E_k)$ functions are shown in Fig. 4.

Finally we obtain the total electron yield, γ_N, in electrons per incident particle for the process of Auger neutralization by integrating $N_0(E_k)$ over E_k. Thus,

$$\gamma_N=\int_0^\infty N_0(E_k)dE_k. \quad (23)$$

This is one of four secondary electron yield parameters which are introduced in this paper. γ_N defined above and γ_D to be defined similarly in the next section are the yields for the so-called pure Auger neutralization and de-excitation processes, respectively, that is, for processes in which all incident particles decay by the process in question. These yields are clearly to be distinguished from γ_i and γ_m which are the experimentally observed yields for incident ions and metastable atoms, respectively. Thus, for example, we cannot identify γ_i with γ_N until it has been demonstrated that each incident ion finally decays to the ground state of the atom via Auger neutralization. The possibility exists that in some cases a fraction of the ions will be resonance neutralized and that the excited atoms so formed will undergo Auger de-excitation. The total observed yield per incident ion, γ_i, must then be compounded by γ_N and γ_D as described in Sec. XIV.

IV. THEORY OF AUGER DE-EXCITATION

We turn now to a discussion of Auger de-excitation of a metastable atom at a metal surface (Fig. 3).[19] The process which proceeds at constant total energy E_t may be written

$$X^m+e_M^-(\epsilon'')\rightarrow X+e^-(\epsilon_k), \quad (24)$$

where $\epsilon''=\epsilon_0-\beta$, it being understood that only a fraction of the excited electrons $e^-(\epsilon_k)$ leave the metal. Again taking E' to be zero for X and e^- at rest an infinite distance from the metal we find that $E_t=E_x+E(m-M)-(\epsilon_0-\epsilon'')=(\epsilon_k-\epsilon_0)+E(n-M)$, from which

$$\epsilon''=\epsilon_k-E_x'(s), \quad (25)$$

$$E_x'(s)=E_x+E(m-M)-E(n-M). \quad (26)$$

Here $E(m-M)$ and $E(n-M)$ are the interaction energies of the metastable atom and the normal atom with the metal surface, respectively. $E_x'(s)$ defines an effective excitation energy for the atom at a distance s from the metal surface. Again the Franck-Condon principle is assumed in evaluating the energies which depend on s.

The formalism developed above for Auger neutralization may be taken over for Auger de-excitation if it

[19] Even though the discussion and notation refer here to metastable atoms it is clear that any excited atom near the metal may undergo Auger de-excitation.

is assumed that ϵ' is a constant at the value demanded by resonance capture of the first electron into the isoenergetic excited level in the atom. Thus,

$$\epsilon' = \epsilon_0 - \alpha = \epsilon_0 - (E_i' - E_x'), \tag{27}$$

$$E_i' - E_x' = (E_i - E_x) + E(i-M) - E(m-M), \tag{28}$$

from Eqs. (1), (6), and (26).

The transition rate for the process at constant E_t again has the form of relation (7) above with $\rho(E_t)$ again equal to $N(\epsilon_k)$. The matrix element, H_{fi}', for Auger de-excitation may be written as follows for processes in which an electron is or is not exchanged between metal and atom, respectively:

$$(H_{fi}')_{\text{exch}} = \int\int u_F^*(1) u_G^*(2) (e^2/r_{12}) \times u_E(1) u_M''(2) d\tau_1 d\tau_2, \tag{29}$$

$$(H_{fi}')_{\text{nonexch}} = \int\int u_F^*(2) u_G^*(1) (e^2/r_{12}) \times u_E(1) u_M''(2) d\tau_1 d2_2. \tag{30}$$

Here the u_E function, not previously defined, is the wave function of the electron in the excited (metastable) state in the atom. Both matrix elements are written out here for use in subsequent discussion.

The transition rate for the elemental Auger de-excitation process, in analogy to (9), is written in the form $F'(\epsilon'')N(\epsilon_k)P_\Omega'(\theta,\epsilon_k)d\Omega$, and the total transition rate for all processes occurring at s as

$$R_t'(s) = \int\int N(\epsilon_k) P_\Omega'(\theta,\epsilon_k) \int F'(\epsilon'') \times \delta(\epsilon'' + E_x' - \epsilon_k) N_c(\epsilon'') d\epsilon'' d\Omega d\epsilon_k. \tag{31}$$

The primed functions F', P_Ω', R_t' and the functions T', P_k', N_i', N_0', and P_e' to be introduced presently have the same definitions with respect to Auger de-excitation as do the unprimed functions for Auger neutralization. If F' is assumed constant (C') or its dependence on ϵ'' included in an effective $N_c(\epsilon'')$ function, the transition rate is

$$R_t'(s) = C' \int_{\epsilon_F}^{\infty} N(\epsilon_k) N_c(\epsilon_k - E_x') d\epsilon_k = C' \int_{\epsilon_F}^{\infty} N(\epsilon_k) T'(\epsilon_k - E_x') d\epsilon_k. \tag{32}$$

Thus the Auger transform for the de-excitation process is the state density function (or an effective one including the possible dependence of the matrix element on ϵ''). Thus,

$$T'(\epsilon) = N_c(\epsilon). \tag{33}$$

It follows that other functions describing Auger de-excitation are

$$P_k'(\epsilon_k, s) = \frac{N(\epsilon_k) N_c(\epsilon_k - E_x')}{\int_{\epsilon_F}^{\infty} N(\epsilon_k) N_c(\epsilon_k - E_x') d\epsilon_k}, \quad \epsilon_k > \epsilon_F = 0, \quad \epsilon_k < \epsilon_F \tag{34}$$

and $N_{ii}(\epsilon_k)$, $N_{0i}(\epsilon_k)$, and $P_{ei}(\epsilon_k)$, which are identical in form with the corresponding functions for Auger neutralization defined in Eqs. (19), (21), and (22), respectively. If Auger de-excitation is the only process possible the total yield of secondary electrons per incident particle, which we call γ_D, is the integral of $N_0'(E_k)$ over E_k in analogy to the definition of γ_N in Eq. (23).

V. TRANSITION RATE AND RELATED PROBABILITY FUNCTIONS

The characteristics of the matrix elements for the Auger processes are specified by the functions R_t, P_Ω, and F. The total transition rate, $R_t(s)$, specifies the dependence of the matrix element on s; $P_\Omega(\theta,\epsilon_k)$ gives the dependence on angle which the excited electron's velocity vector makes with the surface normal; $F(\epsilon',\epsilon'')$ accounts for the dependence on initial state energies. F has been assumed a constant or its effect considered to be accounted for by use of an effective state density function, $N_c(\epsilon)$. The functions R_t and P_Ω are discussed in this section and the next, respectively.

Upon specific evaluation of matrix elements both Shekhter[3] [his Eq. (3.11)] and Cobas and Lamb[4] [their Eq. (5)] find $R_t(s)$ to be expressed as an exponential in s multiplied by a polynomial in s. In view of the fact that each of the processes being considered occurs over a limited range of s only it is sufficient to assume

$$R_t(s) = A \exp(-as). \tag{35}$$

The form (35) is taken to be appropriate for Auger neutralization (A,a), exchange de-excitation (A',a'), and the resonance processes (A'',a'').

The matrix element for the nonexchange Auger de-excitation [Eq. (30)] is zero if the states u_E and u_G have different spins and is small if u_E and u_G are both S states. In other cases the matrix element may be expected to vary algebraically with s. Since we shall assume the rate functions for Auger neutralization and de-excitation to be equal ($A = A'$, $a = a'$) we are in effect neglecting the nonexchange de-excitation process. Note the similarities between the matrix elements for Auger neutralization and exchange de-excitation [Eqs. (8) and (29), respectively]. It is possible to estimate a value for a with reasonable accuracy. The parameter A is determined by fitting the theory to the experimental results as discussed in Sec. XIII.

In the matrix elements (8) and (29) exponential terms involving s arise in the $u_G^*(2)$ and $u_M''(2)$

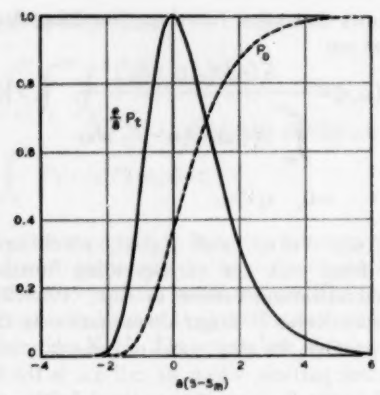

FIG. 5. Plots of the P_0 and P_t functions given in Eqs. (43) and (44) in the text. P_0 is the probability that an incident particle subject to a single electronic transition process, will reach s without the process occurring. P_t is the probability distribution governing transition in ds at s. s_m is defined by Eq. (40) and the transition rate function $R_t(s)$ by Eq. (35).

functions. These terms are of the form $\exp(-\lambda s)$ with $\lambda=(2m\eta/\hbar^2)^{\frac{1}{2}}$. For the atomic function $\eta=E_i$; for the metal function η lies in range $\varphi<\eta<\epsilon_0$. We thus expect that at large distances the exponential from the metal function will predominate. A value of $a=2\lambda$ of the order of 3×10^8 cm^{-1} is estimated in this way. Values of a which arise in the matrix element calculation are listed in Table X. Cobas and Lamb's value for a' may perhaps be expected to be somewhat large because the wave functions for the metallic electrons were taken to be zero outside the metal. Calculations have been carried out in the present work with the values $a=2\times10^8$ cm^{-1} and 5×10^8 cm^{-1}. It will be seen that these values represent limits between which the value of a for Auger neutralization most likely lies (see Sec. XIII). Very little of a quantitative nature comes out of the present work concerning the parameters A'' and a'' for the resonance process.

If we start with the transition rate, $R_t(s)$, it is convenient to derive two related probability functions. From the definition of $R_t(s)$ it follows that $R_t(s)ds/v_0$ is the probability that a particle in moving with speed v_0 through the element ds at s will undergo transition. Then the probability $P_0(s,v_0)$ that the incident particle starting from an infinite distance toward the metal will reach the distance s *without* undergoing transition is

$$P_0(s,v_0)=\exp\left[-\int_s^\infty R_t(s)ds/v_0\right]. \tag{36}$$

The probability that the particle, having started from infinity, will undergo transition in ds at s is then

$$P_t(s,v_0)ds=[R_t(s)ds/v_0]\exp\left[-\int_s^\infty R_t(s)ds/v_0\right]. \tag{37}$$

Evidently P_0 and P_t functions may be defined for each of the resonance and Auger processes. Putting the exponential form (35) for $R_t(s)$ into Eqs. (36) and (37) and assuming v_0 to be constant, we obtain

$$P_0(s,v_0)=\exp[-(A/av_0)\exp(-as)] \tag{38}$$

and

$$P_t(s,v_0)=(A/v_0)\exp[-(A/av_0)\exp(-as)-as]. \tag{39}$$

Cobas and Lamb[4] have derived the expressions (37) and (39) for the probability distribution $P_t(s,v_0)$.

The $P_t(s,v_0)$ function may be shown to pass through a maximum value at $s=s_m$ with

$$s_m=(1/a)\ln(A/av_0). \tag{40}$$

The value of $P_t(s,v_0)$ at $s=s_m$ is

$$P_t(s_m)=a/e=0.368a, \tag{41}$$

independent of v_0. A graphical solution gives for the width on the s scale of the P_t function at half-maximum,

$$W(P_t)=2.48/a. \tag{42}$$

Written in terms of s_m expressions (38) and (39) become

$$P_0(s,v_0)=\exp\{-\exp[-a(s-s_m)]\}, \tag{43}$$

and

$$P_t(s,v_0)=a\exp\{-\exp[-a(s-s_m)]-a(s-s_m)\}. \tag{44}$$

These expressions depend upon v_0 only through s_m. Thus the form of each is independent of v_0 but the placement relative to the metal surface is determined by v_0 through Eq. (40). The P_0 and P_t functions of (43) and (44) are plotted in Fig. 5.

It is of interest to calculate the mean distance $\bar{s}$ at which a process occurs where $\bar{s}$ is defined by the integral

$$\bar{s}=\int_0^\infty sP_t(s,v_0)ds. \tag{45}$$

By means of (39) $\bar{s}$ can be shown to be[20]

$$\bar{s}=(1/a)[C+\ln(A/av_0)+E_i(A/av_0)], \tag{46}$$

in which C is Euler's constant $(0.5772\cdots)$ and $E_i(y)$ is the exponential integral $\int_y^\infty \exp(-z)dz/z$. As A/av_0 will turn out to be of the order 10^2 or more, the E_i term is completely negligible. Thus,

$$\bar{s}-s_m=C/a=0.58/a. \tag{47}$$

For $a=2\times10^8$ cm^{-1}, $\bar{s}-s_m$ is of the order of 0.3 A so that without a great deal of error we may use s_m and $\bar{s}$ interchangeably.

If it is assumed that the exponential transition rate of Eq. (35) holds to $s=0$ it can be shown that

$$\int_0^\infty P_t(s,v_0)ds=1-P_0(0,v_0)=1-\exp(-A/av_0)$$
$$=1-\exp[-\exp(as_m)]. \tag{48}$$

[20] The author is much indebted to Miss M. C. Gray for performing this integration.

This integral is of interest because it specifies the probability that the process occurs on the inward trip toward the metal surface. From (48) it follows that

$$\lim_{v_0 \to 0} \int_0^\infty P_i(s,v_0)ds = 1. \tag{49}$$

For the lower ion velocities used in the experimental work s_m is large enough to make the probability of Auger neutralization on the inward trip very nearly unity (Sec. XIII).

VI. THE PROBABILITY OF ESCAPE OF AN EXCITED ELECTRON FROM THE METAL

The probability that an excited electron of energy ϵ_k will leave the metal is defined by Eq. (22). The critical angle θ_c, which is the maximum value of θ for escape over the surface barrier, is readily calculable. Refraction at the surface is such that

$$\epsilon_k \cos^2\theta = \epsilon_0 + (\epsilon_k - \epsilon_0)\cos^2\theta', \tag{50}$$

where θ and θ' are the angles of the electron's velocity vector with the surface normal inside and outside the metal, respectively (Fig. 6). If the electron is to leave the metal it is necessary that $\theta' > 0$. If $\theta' = 0$, then $\theta = \theta_c$, where

$$\theta_c = \cos^{-1}(\epsilon_0/\epsilon_k)^{\frac{1}{2}}. \tag{51}$$

The probability distribution $P_\Omega(\theta,\epsilon_k)$ can be obtained from first principles only by evaluating H_{fi}. In lieu of this the simplest *a priori* assumption one can make about the angular distribution is that it is isotropic. Then P_Ω is a constant and equal to $1/4\pi$, and

$$\begin{aligned} P_e(\epsilon_k) &= \tfrac{1}{2}[1-(\epsilon_0/\epsilon_k)^{\frac{1}{2}}], \quad \epsilon_k > \epsilon_0 \\ &= 0, \quad \epsilon_k < \epsilon_0 \end{aligned} \tag{52}$$

by Eq. (22).

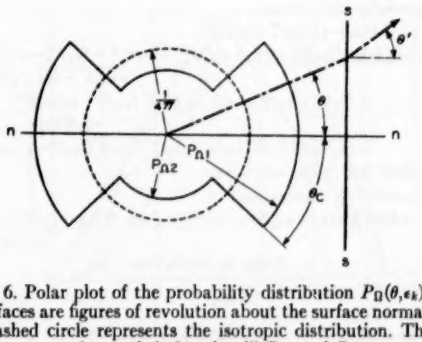

FIG. 6. Polar plot of the probability distribution $P_\Omega(\theta,\epsilon_k)$. The P_Ω surfaces are figures of revolution about the surface normal n–n. The dashed circle represents the isotropic distribution. The full line contour, made up of circles of radii $P_{\Omega 1}$ and $P_{\Omega 2}$, corresponds to a constant matrix element for $\theta < \theta_c$ f times larger than the constant matrix element for $\theta > \theta_c$. This P_Ω surface is symmetrical about the plane through its center parallel to the surface s–s. The specific values of $P_{\Omega 1}$ and $P_{\Omega 2}$ used in this plot are calculated from Eqs. (53) and (54) for $f = 2.2$, $\epsilon_0 = 10.9$ ev, $\epsilon_k = 18.9$ ev. Shown also on the figure is the refraction of the path of an electron which approaches the surface s–s at an angle θ and escapes at the angle θ'. $\theta = \theta_c$ is the critical angle for escape at which $\theta' = 0$.

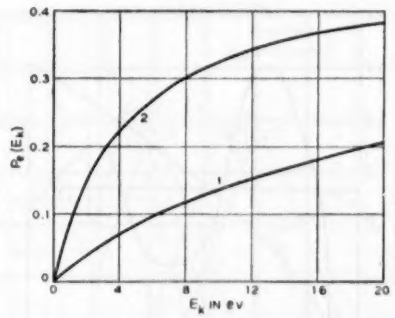

FIG. 7. Plots of two electron escape probability functions $P_e(E_k)$ Curve 1 is that appropriate to an isotropic distribution of electron velocities inside the metal [Eq. (52) in the text]. Curve 2 is a plot of Eq. (55) with $f = 2.2$. The parameter f for curve 2 has been chosen so that the theoretical $\gamma_i(He^+)$ at $E_k(He^+) = 40$ ev equals the experimental value.

Expression (52) for $P_e(\epsilon_k)$ is plotted as curve 1 in Fig. 7. γ_N values calculated with it are found uniformly to be much too small (Table IV). As is pointed out in Sec. VII this can only mean that P_Ω is not isotropic but is of such form as to favor the production of electrons which escape from the metal. Inspection of the matrix elements (8) and (29) shows that this result is in fact to be expected. H_{fi} in (8) may be regarded as the electrostatic interaction energy of two charge clouds of the form $eu_F^*(1)u_M'(1)$ and $eu_G^*(2)u_M''(2)$. Clearly the value of H_{fi} will depend strongly on the value of the first of these clouds near the atomic particle since the second cloud is in some degree localized there by $u_G^*(2)$. It is evident that $eu_F^*(1)u_M'(1)$ will be larger near the atom if u_F represents an electron which can leave the metal than if it represents an electron internally reflected at the surface barrier. C. Herring has suggested to the author that it is reasonable to assume the matrix element constant for $\theta < \theta_c$ and of value (H_1) greater than the value (H_2), also assumed constant, which it has for $\theta > \theta_c$. If $P_{\Omega 1}$ and $P_{\Omega 2}$ are the constant values of $P_\Omega(\theta,\epsilon_k)$ for $\theta < \theta_c$ and $\theta > \theta_c$, respectively, and if $H_1/H_2 = f$, it follows that

$$P_{\Omega 1}/P_{\Omega 2} = |H_1/H_2|^2 = f^2. \tag{53}$$

The $P_\Omega(\theta,\epsilon_k)$ function, furthermore, should be symmetrical about the origin because $H_{fi}(\theta) = iH_{fi}(\pi+\theta)$. This latter fact follows from the circumstance that in (8) u_M', u_M'', and u_G may be taken as real functions and u_F is of the form $\exp(i\mathbf{k}\cdot\mathbf{r})$.

The $P_\Omega(\theta,\epsilon_k)$ function which we assume is thus of the form shown by the solid curve of Fig. 6. Normalization ($\iint P_\Omega d\Omega = 1$) yields

$$P_{\Omega 1} = (1/4\pi)[1-(1-1/f^2)(\epsilon_0/\epsilon_k)^{\frac{1}{2}}]^{-1}. \tag{54}$$

The resulting $P_e(\epsilon_k)$ function from (22) is

$$\begin{aligned} P_e(\epsilon_k) &= \tfrac{1}{2}\left[\frac{1-(\epsilon_0/\epsilon_k)^{\frac{1}{2}}}{1-(1-1/f^2)(\epsilon_0/\epsilon_k)^{\frac{1}{2}}}\right], \quad \epsilon_k > \epsilon_0 \\ &= 0, \quad \epsilon_k < \epsilon_0. \end{aligned} \tag{55}$$

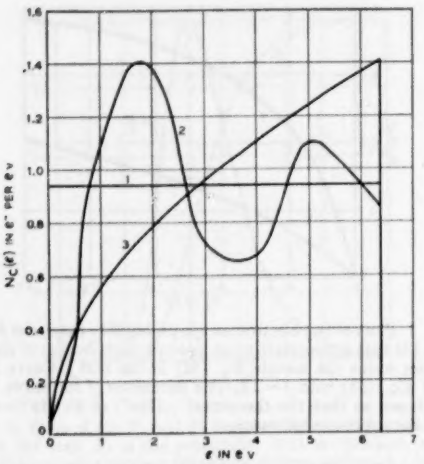

FIG. 8. Plots of three possible state density functions for the conduction band of tungsten. Curve 1. $N_e(\epsilon)=k_1$ (a constant) $=0.94$ electron per ev; 2. The $N_e(\epsilon)$ functions derived by Manning and Chodorow (reference 24); 3. $N_e(\epsilon)=k_2\epsilon^{\frac{1}{2}}=0.555\epsilon^{\frac{1}{2}}$. Each function is normalized to give six valence electrons in the band from $\epsilon=0$ to $\epsilon=\epsilon_F=6.4$ ev.

Expression (55) has been used in the present work.[21] The parameter f has been determined by fitting to the γ_i data for He^+ at 40-ev ions. As discussed in Sec. XIII this gives $f=2.2$, a reasonable value for the ratio of the matrix elements H_1 and H_2. $P_e(\epsilon_k)$ from expression (55) with $f=2.2$, $(1-1/f^2)=0.987$, is plotted as curve 2 in Fig. 7.

In this paper we use the same $P_e(\epsilon_k)$ function for Auger neutralization and de-excitation. That $P_{\Omega 1}/P_{\Omega 2}$ is the same in the two cases appears reasonable because the u_F function appears in the matrix elements (8) and (29) in the same way. Inasmuch as the image barrier extends well beyond the position of the atomic particle we may use the same value of θ_c in either case.

It should be pointed out that in obtaining an expression for $P_e(\epsilon_k)$, we have taken no account of possible changes in direction caused by electron-electron collisions inside the metal. The justification for this neglect lies in the calculations of Wolff[22] which show that an excited electron loses about one-half of its energy per collision and thus quickly sinks back into the Fermi sea.

Finally, it should also be noted that the reflection coefficient at the metal surface for electrons of normal components of energy greater than the barrier height has been assumed zero. That it is small for tungsten in general has been pointed out by Herring and Nichols.[23]

VII. ENERGY DISTRIBUTION AND YIELD NEGLECTING LEVEL SHIFTS AND BROADENING

In this section we shall obtain the form of the electron energy distributions and relative electron yields for the cases of pure Auger neutralization and pure Auger de-excitation neglecting the variation of atomic energy levels near the metal and the effect of the Heisenberg uncertainty principle. Although admittedly crude, these determinations illustrate the basic procedures of the theory and indicate in what ways the theory should be refined. The calculations have been carried out for the singly charged ions and the metastable atoms of lowest energy of each of the noble gasses He, Ne, Ar, Kr, and Xe.

Assumption of no atomic energy level shifts near the metal means that $E_i'=E_i$ and $E_z'=E_z$. The P_k function of Eq. (18) is thus independent of s, and the distribution in energy, $N_i(\epsilon_k)$, of electrons excited in the Auger processes has the form of P_k by (19) and (20). The P_k and P_k' functions in turn are obtained from the assumed initial and final state density functions by Eqs. (18) and (15), and (34), respectively.

TABLE III. Expressions for Auger transforms.[a]

Auger neutralization

$N_e(\epsilon)=k_1,\ 0<\epsilon<\epsilon_F;\ =0,\ \epsilon>\epsilon_F$

$T(\epsilon)=k_1^2\epsilon,\quad 0<\epsilon<\epsilon_F/2$

$\quad=k_1^2(\epsilon_F-\epsilon),\ \epsilon_F/2<\epsilon<\epsilon_F$

$T_\sigma(\epsilon)=[k_1^2\sigma/(2\pi)^{\frac{1}{2}}]\{\exp[-\epsilon^2/2\sigma^2]-2\exp[-(\epsilon_F/2-\epsilon)^2/2\sigma^2]+\exp[-(\epsilon_F-\epsilon)^2/2\sigma^2]\}$

$\quad+(k_1^2\epsilon/2)\{\mathrm{erf}[\epsilon/\sigma\sqrt{2}]+2\,\mathrm{erf}[(\epsilon_F/2-\epsilon)/\sigma\sqrt{2}]-\mathrm{erf}[(\epsilon_F-\epsilon)/\sigma\sqrt{2}]\}$

$\quad+(k_1^2\epsilon_F/2)\{\mathrm{erf}[(\epsilon_F-\epsilon)/\sigma\sqrt{2}]-\mathrm{erf}[(\epsilon_F/2-\epsilon)/\sigma\sqrt{2}]\},$

$N_e(\epsilon)=k_2\epsilon^{\frac{1}{2}},\ 0<\epsilon<\epsilon_F;\ =0,\ \epsilon>\epsilon_F$

$T(\epsilon)=\pi k_2^2\epsilon^2/4,\quad 0<\epsilon<\epsilon_F/2$

$\quad=(k_2^2/2)\{(\epsilon_F-\epsilon)[2\epsilon\epsilon_F-\epsilon_F^2]^{\frac{1}{2}}+\epsilon^2\sin^{-1}[(\epsilon_F-\epsilon)/2]\},\quad \epsilon_F/2<\epsilon<\epsilon_F.$

Auger de-excitation

$N_e(\epsilon)=k_1,\ 0<\epsilon<\epsilon_F;\ =0,\ \epsilon>\epsilon_F$

$T'(\epsilon)=k_1,$

$T_{\sigma'}'(\epsilon)=(k_1/2)\{\mathrm{erf}[(\epsilon_F-\epsilon)/\sigma'\sqrt{2}]+\mathrm{erf}[\epsilon/\sigma'\sqrt{2}]\}.$

[a] These functions are plotted in Figs. 9 and 26 for the specific case of tungsten ($\epsilon_F=6.4$ev; $\int_0^{\epsilon_F}N_e(\epsilon)d\epsilon=6$ electrons).

[21] It is interesting to note that one can derive other one-parameter $P_e(\epsilon_k)$ functions which at one end of the range of the parameter give expression (52) for isotropic P_Ω and at the other end give $P_e(\epsilon_k)=\frac{1}{2}$ independent of ϵ_k. Two such may be obtained by assuming P_Ω to be independent of ϵ_k and proportional to: 1, the area within $d\Omega$ on the surface of an oblate spheroid of eccentricity e, and 2, the volume of the spheroid within $d\Omega$. The first of these assumptions leads to

$$P_e(\epsilon_k)=\tfrac{1}{2}\left[1-\frac{\tanh^{-1}e(\epsilon_0/\epsilon_k)^{\frac{1}{2}}}{\tanh^{-1}e}\right].$$

The second assumption gives

$$P_e(\epsilon_k)=\tfrac{1}{2}\left[1-\left(\frac{(1-e^2)(\epsilon_0/\epsilon_k)}{1-e^2(\epsilon_0/\epsilon_k)}\right)^{\frac{1}{2}}\right].$$

When fitted to $\gamma_i(He^+)$ at 40 ev we get $e=0.984$ for the first expression, $e=0.928$ for the second. Although the $P_e(\epsilon_k)$ functions thus obtained agree quite closely with expression (55) with $f=2.2$, the ratio of P_Ω values at $\theta=0$ and $\theta=\pi/2$ obtained from (53) is more reasonable than the ratio of 30 to 1 calculated in either case from the spheroid assumption.

[22] P. A. Wolff, Phys. Rev. **95**, 56 (1954).

[23] C. Herring and M. H. Nichols, Revs. Modern Phys. **21**, 185 (1949); see also L. A. MacColl, Phys. Rev. **56**, 699 (1939), and Bell System Tech. J. **30**, 888 (1951).

We have assumed throughout that the final state density $N(\epsilon_k)$ is proportional to $\epsilon^{\frac{1}{2}}$. For the initial state density $N_c(\epsilon)$ more than one assumption has been made. In Fig. 8 are plotted three possible $N_c(\epsilon)$ functions for tungsten. The corresponding Auger transforms $T(\epsilon)$ are plotted in Fig. 9. Analytic expressions are given in Table III for $T(\epsilon)$ with $N_c(\epsilon)=k_1$ and $k_2\epsilon^{\frac{1}{2}}$. $T(\epsilon)$ for the Manning and Chodorow $N_c(\epsilon)$ function[24] was calculated on the analog computer. It differs so little from that for $N_c(\epsilon)=k_1$ that further calculation with it appeared unprofitable.

For pure Auger neutralization $N_i(\epsilon_k)$ functions have been determined in this way for $N_c(\epsilon)=k_1$ (Fig. 10 and $N_c(\epsilon)=k_2\epsilon^{\frac{1}{2}}$ (Fig. 11). $N_0(E_k)$ functions [$N_0=N_iP_e$ by (21)] have been obtained from these $N_i(\epsilon_k)$ functions using the probability of escape, P_e, of Eq. (52) corresponding to isotropic P_Ω. These are plotted in Figs. 12 and 13. The total electron yield, γ_N, which by (23) is the area under the $N_0(E_k)$ curve, has been calculated for each case and is given in Table IV where comparison is made with experimentally determined values for the slowest ions used.[7] The broadening effects and level shifts neglected here are least important at the lowest ion energies.

For pure Auger de-excitation $N_i'(E_k)$ functions for $N_c(\epsilon)=k_1$ have been determined and are shown in Fig. 14. $N_0'(E_k)$ functions obtained from these by use of the $P_e(\epsilon_k)$ function for isotropic P_Ω' [Eq. (52)] are plotted in Fig. 15. γ_D values (the areas under these curves) have been computed and are included in Table IV.

The energy extremes which the excited electrons may possess under the assumptions of this section may be seen in Figs. 10 through 15 or may be calculated directly from the energy relations (5) and (6) or (25) and (26) with $E(m-M)=E(m-M)=E(i-M)=0$. The metastable states involved here and throughout this paper are the lowest lying such states, $2s^3S$ for He, $ns[1\frac{1}{2}]^\circ$

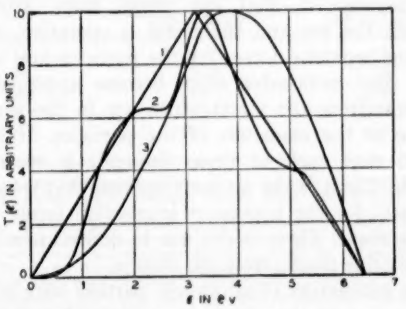

FIG. 9. Auger transforms obtained from Eq. (15) in the text from the $N_c(\epsilon)$ functions of Fig. 8. Curves 1, 2, and 3 here correspond to curves 1, 2, and 3 of Fig. 8, respectively. $T(\epsilon)$ is plotted in the figure to an arbitrary scale which makes $T(\epsilon)=10$ at its maximum in each case. Analytic expressions for curves 1 and 3 are to be found in Table III ($\epsilon_F=6.4$ ev). Curve 2 was obtained by numerical calculation on an analog computer.

[24] M. F. Manning and M. I. Chodorow, Phys. Rev. **56**, 787 (1939).

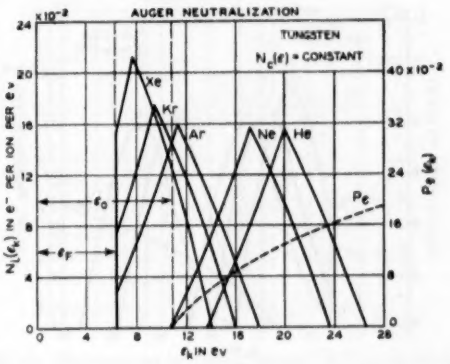

FIG. 10. Distributions in kinetic energy inside the metal, $N_i(\epsilon_k)$, of electrons excited by the Auger neutralization of the singly charged noble gas ions at a tungsten surface. $\epsilon_F=6.4$; $\varphi=4.5$; $\epsilon_0=10.9$ ev. Here $N_c(\epsilon)$ is assumed constant and no account is taken of atomic energy level shifts near the metal nor of the Heisenberg uncertainty principle. Areas under the $N_i(\epsilon_k)$ curves are normalized to one electron per incident ion. The escape probability function, $P_e(\epsilon_k)$, corresponding to isotropic distribution of electron velocities inside the metal [Eq. (52) in the text], is also plotted in this figure.

with $n=3$, 4, 5, and 6 for Ne, Ar, Kr, and Xe, respectively.

The above results exhibit a number of interesting features which we now discuss.

1. The forms of $N_0(E_k)$ and $N_0'(E_k)$ for Auger neutralization and de-excitation are seen to be quite different. The experimental energy distributions (Fig. 7 of reference 7, for example) certainly look more like the calculated curves for the neutralization process (Fig. 12) than those for the de-excitation process (Fig. 15) indicating the relative infrequency of resonance neutralization followed by Auger de-excitation. The details of form of the experimental distributions are not reproduced by the theory, it is true. The theoretical curves approach zero at the maximum energy much more abruptly than do the experimental curves.

2. The energy maxima in Figs. 12, 13, and 15 agree reasonably well with the experimental results for He^+, Ar^+, Kr^+, and Xe^+ (Fig. 7 of reference 7), but there appears to be no way to account for the anomalously high energy maximum observed experimentally for Ne^+ (Fig. 10 of reference 7).

3. The γ_N and γ_D values of Table IV show the experimentally observed decrease in passing through the sequence from He to Xe but the calculated values are all much too small. In the case of He the $N_i(\epsilon_k)$ distribution lies entirely at energies $\epsilon_k>\epsilon_0$. Variation of the form of $N_i(\epsilon_k)$ by variation of the $N_c(\epsilon)$ function (compare Figs. 10 and 11) cannot change γ_N much, as long as the area under the $N_i(\epsilon_k)$ curve is normalized to unity. The low theoretical γ_N for He is thus attributable only to the $P_e(\epsilon_k)$ function used. For Ar, Kr, and Xe where the $N_i(\epsilon_k)$ distribution lies partly above and partly below $\epsilon_k=\epsilon_0$, the form of $N_i(\epsilon_k)$ as determined by

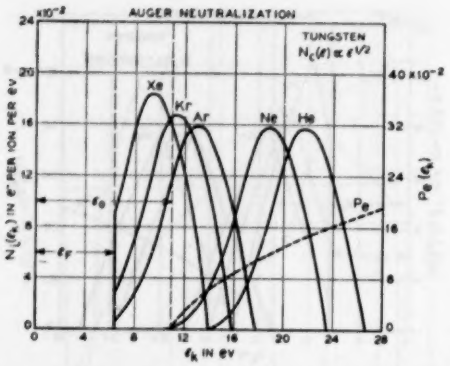

FIG. 11. $N_i(\epsilon_k)$ functions for $N_c(\epsilon) \propto \epsilon^{\frac{1}{2}}$, other conditions and assumptions the same as those for Fig. 10. The same $P_e(\epsilon_k)$ function is plotted here as in Fig. 10.

$N_c(\epsilon)$ has greater effect on γ_N as is to be seen in Table IV.

4. Table IV indicates that γ_D is larger than γ_N. Thus we expect the two-stage process of resonance neutralization followed by Auger de-excitation to be more productive of secondary electrons per incident ion than direct Auger neutralization of the incident ion.

5. The $N_0(E_k)$ functions and γ values derived above are independent of kinetic energy of the incident particle since this energy enters in no way into the theory. Although this state of affairs is in general agreement with the experiment we are as yet unable to account for the finer details of the observed energy dependence.

VIII. ATOMIC ENERGY LEVEL SHIFTS NEAR THE METAL

The variation of atomic energy levels near the metal surface is accounted for in the theory of Secs. III and IV by inclusion of the interaction energy terms, $E(n-M)$, $E(i-M)$, and $E(m-M)$. These terms appear in the effective ionization energy [Eq. (6)] and effective excitation energy [Eq. (26)]. In the treatment of Sec. VII these terms were neglected. We wish now to discuss these terms and to estimate their values for inclusion in the theory.

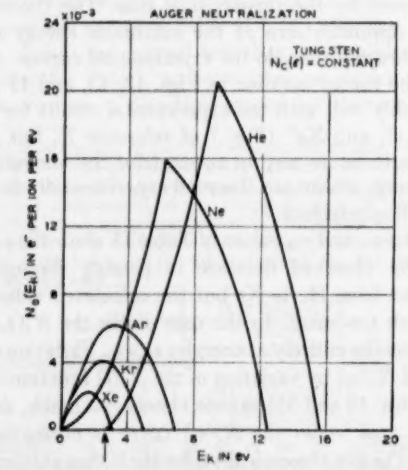

FIG. 12. $N_0(E_k)$ functions derived from the $N_i(\epsilon_k)$ and $P_e(\epsilon_k)$ functions of Fig. 10. The minimum energy in the He distribution is indicated by the arrow on the E_k axis. γ_N values (areas) derived from these curves are given in Table IV.

Since the interaction between an atomic particle and a metal surface certainly cannot be said to be well known it is perhaps to the point to begin this discussion by pointing out that the basic results which follow from inclusion of the interaction terms are insensitive to the specific estimates of their values. There are two basic experimental results which we wish to explain by including the interactions with the metal as well as the effects of the Heisenberg uncertainty principle. These are: 1. the observed departures in form of the observed $N_0(E_k)$ functions from those determined in the preceding section, in particular the observation of appreciable numbers of electrons beyond the energy limit $E_x - \varphi \simeq E_i - 2\varphi$ for Ne^+ on tungsten, and 2. the relative infrequency of the two-stage process of resonance neutralization followed by Auger de-excitation. It will be seen that these results can be explained if we may assume: 1. that the image force attraction between the ion and the metal is operative, and 2. that the repulsive forces for the particles ion, normal atom, and metastable atom become appreciable at distances from the metal which are in the same sequence as the diameters of the particles. It is submitted that each of these demands is reasonable. Beyond this it is the author's opinion that reasonable estimates for the important interaction terms can in fact be made. These enable one to derive approximate quantitative results from the theory.

TABLE IV. γ_N and γ_D values obtained from the calculated energy distributions assuming no atomic energy level shifts, isotropic P_0, and neglecting the Heisenberg principle (Figs. 12, 13, and 15).

Atom	γ_N $N_c(\epsilon)$ = const (Fig. 12)	γ_N $N_c(\epsilon) \propto \epsilon^{\frac{1}{2}}$ (Fig. 13)	γ_D $N_c(\epsilon)$ = const (Fig. 15)	Measured γ_i for 10-ev ions
He	0.136	0.142	0.155	0.293
Ne	0.103	0.114	0.129	0.213
Ar	0.028	0.040	0.063	0.094
Kr	0.013	0.021	0.038	0.047
Xe	0.0044	0.0065	0.017	0.018

The interaction of an atomic particle with a metal surface may be thought to be compounded of the following possible components:

1. the Coulombic image force attraction for ions,
2. the van der Waals attraction resulting from the particle's polarizability,
3. a possible exchange force of the type responsible for the covalent bond, and

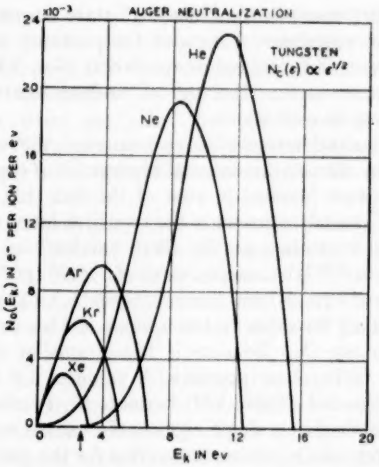

FIG. 13. $N_0(E_k)$ functions derived from the $N_i(\epsilon_k)$ and $P_e(\epsilon_k)$ functions of Fig. 11. The minimum energy in the He distribution is indicated by the arrow on the E_k axis. γ_N values derived from these curves are given in Table IV.

4. the repulsion resulting from interpenetration of the electron clouds and the Pauli principle.

We proceed to discuss these forces in turn.

The *image potential* is

$$-e^2/4s = -3.6/s \text{ ev}, \tag{56}$$

where s is in A.[25]

For the *van der Waals interaction* between an atomic particle and a metal we use the expression derived by Prosen and Sachs,[26]

$$-(2\pi)^{-3}\alpha e^2 \pi k_m{}^2 s^{-2} \ln(2k_m s). \tag{57}$$

TABLE V. Polarizabilities for normal atoms (α_n) and metastable atoms (α_m) of the noble gases.

	$10^{23}\,\alpha_n$ (cm³)[a]	$10^{23}\,\alpha_m$ (cm³)[b]
He	2.16	57
Ne	3.98	76
Ar	16.3	230
Kr	24.3	280
Xe	40.1	410

[a] Determined from measurements of the dielectric constant. Landolt-Börnstein, *Tables* (Julius Springer, Berlin, 1950), sixth edition, Vol. I, Part I, p. 401.

[b] These estimates are obtained as $\alpha_m \sim [E_i/(E_i - E_x)]^3$, which expression is derived from Margenau's formula (reference 27) for the static polarizability by assuming equal oscillator strengths, $\Delta = E_i$ for the normal atom, and $\Delta = E_i - E_x$ for the metastable atom. It is interesting to note that the assumption that α is proportional to volume gives α_m values of 40, 59, 261, 332, 436 for He^m, Ne^m, Ar^m, Kr^m, and Xe^m, respectively, by using the diameters given in Table VI.

[25] R. G. Sachs and D. L. Dexter, J. Appl. Phys. **21**, 1304 (1950), have discussed the quantum limits on the electrostatic image force and conclude that this classical expression is accurate if the distance from the surface is larger than the lattice constant. Although the classical expression is used here, the magnitude of the image potential very close to the surface is not involved in any conclusions of the theory.

[26] E. J. R. Prosen and R. G. Sachs, Phys. Rev. **61**, 65 (1942).

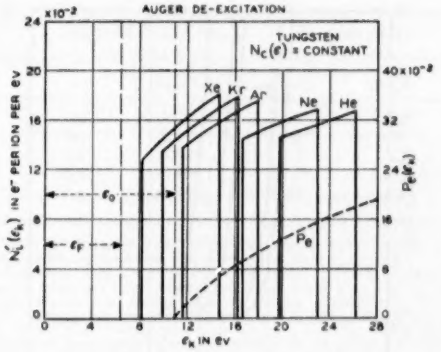

FIG. 14. Distributions in kinetic energy, $N_i'(\epsilon_k)$, of electrons excited by the Auger de-excitation at a tungsten surface of the least energetic metastable atoms of the noble gases. $N_c(\epsilon)$ is taken as constant and the effects of atomic energy level shifts near the metal and the Heisenberg uncertainty principle are neglected. The $N_i'(\epsilon_k)$ functions are normalized to an area of one electron per incident metastable atom. The probability of escape function, P_e, plotted here is the same as that used for Auger neutralization in Figs. 10 and 11.

Here α and k_m are the polarizability of the atom and the wave number of the fastest electron in the metal, respectively.

For free electrons $k_{max} = (2m\epsilon_F)^{\frac{1}{2}}/\hbar$. Using Manning and Chodorow's value[24] for $\epsilon_F = 0.47$ ry $= 6.4$ ev, we calculate $k_m = 1.3\times10^8$ cm^{-1}. Manning and Chodorow plot curves of ϵ *vs* k from which it appears that at $\epsilon = 0.47$ ry, $\theta \sim 45°$ or $k_m \sim 1\times10^8$ cm^{-1}. This latter value is used in expression (57), which on evaluation of other constants becomes

$$-1.83\times10^{23}\alpha s^{-2} \ln(2s) \text{ ev}, \tag{58}$$

with s in A and α in cm³. Values for the polarizabilities used in this expression are given in Table V. The

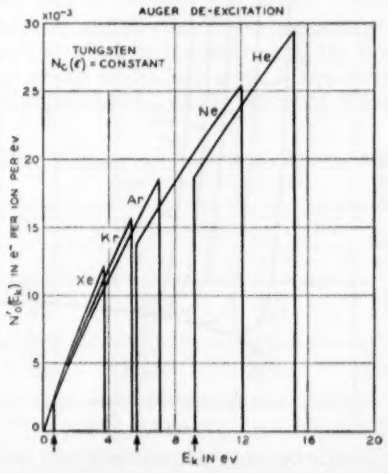

FIG. 15. $N_0'(E_k)$ functions derived from the $N_i'(\epsilon_k)$ and $P_e(\epsilon_k)$ functions of Fig. 14. The minimum energies in the distributions for He^m, Ne^m, and Ar^m are indicated on the E_k axis. γ_D values derived from these curves are given in Table IV.

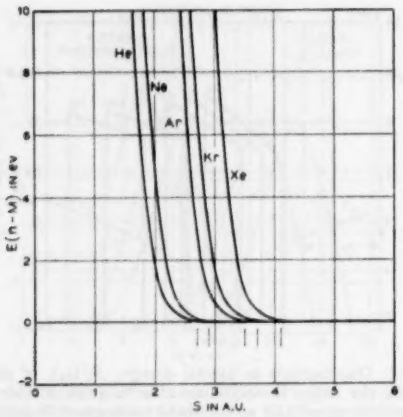

FIG. 16. Plots of the energy of interaction of normal noble gas atoms with a tungsten surface estimated by the methods described in the text [Eq. (60)].

polarizability of the ion is so small that its van der Waals force is neglected in this work. A means of estimating polarizabilities for the metastable atoms based on a formula of Margenau[27] is indicated in footnote b to Table V.

The exchange force listed as the third possible interaction component need be considered only for the metastable atom and the ion. The fact is that we know nothing about it for these cases. We shall proceed as though it does not exist on the grounds that even if it does the interaction need not occur in a bonding state on every encounter. One may point to the analogy of the possible bonding and antibonding states on approach of two atoms to form a diatomic molecule. If some

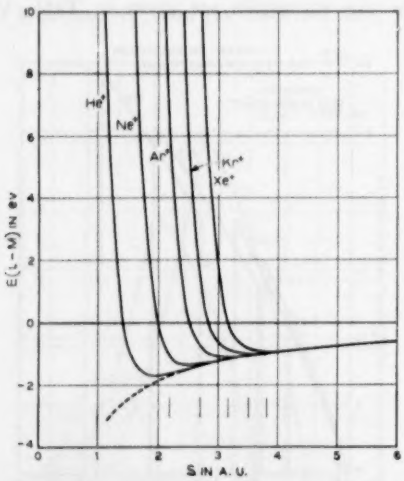

FIG. 17. Plots of the energy of interaction of noble gas ions with a tungsten surface estimated by the procedures discussed in the text [Eq. (61)]. The dashed line indicates the extension of the image potential term only.

[27] H. Margenau, Revs. Modern Phys. **11**, 1 (1939), formula (C9).

encounters result in the "bonding" state our estimates from the experimental data of the partition between Auger neutralization and de-excitation (Sec. XIV) will be in error in the direction of underestimating the fraction of de-excitations.

For ions and normal atoms we represent the repulsive energy by the one-dimensional exponential $B\exp(-bs)$. This appears justified in view of the fact that such a form adequately represents the repulsive interaction of atoms in crystals, e.g., the alkali halides,[28] as well as free atoms.[29,30] We assume a value of 5×10^8 cm$^{-1}=5$ A^{-1} for b for all ions (b_i) and normal atoms (b_n). (Table VII, footnote a.) We expect a lower value of b for the metastable atom (b_m) because it has a smaller electron density in its outer portions. A value of 1.5 A^{-1} has been estimated (Table VII, footnote b). Furthermore, it is evident that a single exponential cannot represent adequately the repulsive interaction for the metastable atom. On sufficiently close approach the interaction of

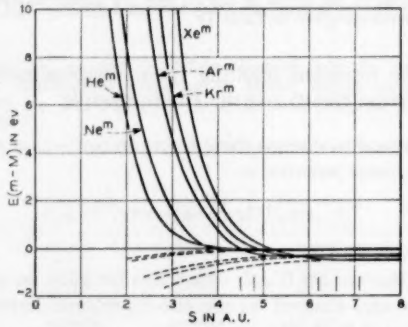

FIG. 18. Plots of the energy of interaction of metastable atoms with a tungsten surface estimated by the methods given in the text [Eq. (62)]. The dashed lines indicate the extensions of the van der Waals terms only.

ion, normal atom, and metastable atom should all approach the same interaction, namely that of the atomic core. Thus a low value of b_m can characterize the metastable interaction only at larger values of s. For these reasons the metastable repulsion is compounded of two exponentials as indicated below.

For given b the value of B in the term $B\exp(-bs)$ determines the distance from the metal at which the repulsive interaction becomes large. Absolute values cannot be determined with accuracy, but one should be able to estimate relative values which are reasonably good. Any method adopted for estimating B may be taken to define a distance scale. The procedure used here is the following. A distance s_0 at which the atomic particle "touches" the metal surface is defined as

$$s_0=d/2+a_l/2, \tag{59}$$

[28] M. Born and J. E. Mayer, Z. Physik **75**, 1 (1932).

[29] J. C. Slater, Phys. Rev. **32**, 339 (1928).

[30] W. E. Bleick and J. E. Mayer, J. Chem. Phys. **2**, 252 (1934).

the sum of the particle's radius and half the lattice constant of the metal. One makes the energy of repulsive interaction at this distance equal to that calculated by Bleick and Mayer[30] for the interaction of two free Ne atoms when separated by the viscosity diameter (Table VI) of the Ne atom. The procedure is admittedly arbitrary but should define a reasonable relative distance scale.

The theoretical Ne−Ne interaction $[1.18\times10^4 \times\exp(-4.8r)$ ev, r in A$]$ amounts to 0.044 ev at $r=2.59$ A. Here we have assumed the repulsive interaction to be 0.05 ev at $s=s_0$. With the values of b and d estimated above, the B values listed in Table VII have been obtained.

For the value of a_l to be used in Eq. (59), the edge length of the fundamental cube in the metal lattice, we have takent he value of 3.16 A for tungsten.[31] The values of s_0 obtained from Eq. (59) with the diameters of Table VI are indicated in Figs. 16, 17, and 18 by the short vertical lines. In each case they are to be identified from left to right with He, Ne, Ar, Kr, and Xe, in that order.

The interactions with the metal used in the present work may now be summarized. For the normal atom the van der Waals attraction turns out to be negligible [0.014 ev for He at 2 A, 0.095 ev for Xe at 4 A]. Thus we take

$$E(n-M)=B_n\exp(-b_ns), \tag{60}$$

with B_n and b_n given in Table VII. These interaction energies for He, Ne, Ar, Kr, and Xe are plotted in Fig. 16.

For the ion, $E(i-M)$ comprises the image force and repulsive interactions. Thus,

$$E(i-M)=B_i\exp(-b_is)-3.6/s. \tag{61}$$

These interaction energies are plotted in Fig. 17.

The metastable atom-metal interaction, $E(m-M)$, comprises three terms: (1) the repulsive term operating at larger distances, (2) the repulsive term representing the effect of the atomic core as discussed above, and (3) the van der Waals interaction which is appreciable. Thus, from Eq. (58), using the polarizability of the metastable atom we obtain

$$E(m-M)=B_m\exp(-b_ms)+B_i\exp(-b_is) -1.83\times10^{23}\alpha_ms^{-2}\ln(2s). \tag{62}$$

These interactions are plotted in Fig. 18.

The interaction energies of Eqs. (60), (61), and (62) have been used in determining the effects of energy level shifts on the resonance and Auger transitions which occur when an atomic particle is near a metal surface. The fact that a better understanding of the phenomena results lends credibility to the interaction energies derived here.

[31] R. W. G. Wyckoff, *Crystal Structures* (Interscience Publishers, Inc., New York, 1951), Table II, 4.

TABLE VI. Particle diameters for normal atoms (d_n), metastable atoms (d_m), and ions (d_i) of the noble gases.

	$d_n(A)$	$d_m(A)$	$d_i(A)$
He	2.19[a]	5.8[b]	1.3[e]
Ne	2.57[a]	6.4[c]	2.3[f]
Ar	3.66[a]	9.2[c]	3.3[f]
Kr	4.18[a]	10.0[d]	3.8[f]
Xe	4.93[a]	10.9[c]	4.4[f]

[a] Viscosity diameter from Landolt-Börnstein, *Tables* (Julius Springer, Berlin, 1950), sixth edition, Vol. 1, Part I, p. 325.
[b] Estimated from the extension of the calculated electron density functions for unexcited H(1s) and excited H(2s). From Fig. 20 of G. Herzberg, *Atomic Spectra and Atomic Structure* (Dover Publications, New York, 1944), second edition, we conclude $d_n[H(2s)]\simeq2.6d_n[H(1s)]$. Since $r\propto1/Z$, $d_n[H(2s)]\simeq5.2d_i[He^+]$. If we take account of the incomplete shielding of the nucleus in the case of He^m by assuming $d\propto(E_i)^{-\frac{1}{4}}$, then $d_m[He^m]=(3.4/4.77)^{\frac{1}{4}}d_n[H(2s)]$ and $d_m[He^m]\simeq4.5d_i[He^+]$.
[c] From the ratio of d_m/d_n given by J. P. Molnar, Phys. Rev. **83**, 940 (1951) using the viscosity d_n.
[d] Interpolated between the values for Ar and Xe.
[e] Obtained from the viscosity diameter of H (reference a) taking $r\propto1/Z$. Thus $d[He^+]=d[H]/2=1.26$ A.
[f] Taken as $0.9d_n$.

IX. EFFECT OF LEVEL SHIFTS ON THE AUGER TRANSITIONS

Having in our possession what are at least plausible potential curves representing the interactions of noble gas atoms and ions with a metal surface, we may proceed to discuss the Auger transitions in terms analogous to those used in the discussion of electronic transitions in diatomic molecules. The procedure is to place the potential curves properly on an energy-distance plot and to discuss the Auger transitions as jumps between these curves which obey the Franck-Condon principle.

Consider first the process of Auger neutralization. In Eq. (4) the process was written for the system of the incoming ion and two interacting electrons in the metal transforming itself to the isoelectronic system of the normal atom and a free electron. We find it more convenient here to consider the system comprising the incoming ion and all electrons in the metal (taken as n in number) which is transformed to the isoelectronic system of the neutralized atom, a free electron, and $(n-2)$ electrons remaining in the metal. Thus we write

TABLE VII. Values of parameters B and b in the repulsive interaction term: $B\exp(-bs)$.

	$b_n=5A^{-1}$,[a] $b_m=1.5A^{-1}$,[b] $b_i=5A^{-1}$,[a]		
	$10^{-5}B_n$ (ev)	$10^{-5}B_m$ (ev)	$10^{-5}B_i$ (ev)
He	0.36	0.43	0.03
Ne	0.99	0.67	0.36
Ar	19.8	5.5	4.45
Kr	54.8	10.0	19.8
Xe	398.0	20.0	88.5

[a] Theoretical attempts to explain the data of J. K. Roberts, Proc. Roy. Soc. (London) **A129**, 146 (1930); **A135**, 192 (1932), on the temperature variation of the accomodation coefficient for interaction of an atom and a metal have yielded $b=4A^{-1}$ [J. M. Jackson and A. Howard, Proc. Roy. Soc. (London) **A142**, 447 (1933)] and $2A^{-1}$ [A. F. Devonshire, Proc. Roy. Soc. (London) **A158**, 269 (1937)]. The interaction in solids (alkali halides) gives $b=2.9A^{-1}$ (reference 28), between free He atoms, $4.6A^{-1}$ (reference 29), and free Ne atoms, $4.8A^{-1}$ (reference 30).
[b] Estimated on the basis that equal repulsive forces arise when there is equal overlap of charge between the metal and the atomic particle.

the Auger neutralization process as

$$X^+ + ne_M^- \rightarrow X + e^- + (n-2)e_M^-. \qquad (63)$$

The energy of the system $X^+ + ne_M^-$ with X^+ at rest at $s=\infty$ is a discrete value, taken to be zero. The system $X + e^- + (n-2)e_M^-$ with $X + e^-$ at rest at $s=\infty$ may assume a band of energies corresponding to the n^2 possible choices of energy levels in the metal from which the two electrons are drawn. This band extends from $-(E_i - 2\epsilon_0)$ to $-(E_i - 2\varphi)$ below the zero level as just defined. These energy limits may be derived by considering the energy transformations in carrying out the process of Eq. (63) at $s=\infty$. As s decreases toward zero the energy of the system $X^+ + ne_M^-$ varies as $E(i-M)$ [see Fig. 17], that of $X + e^- + (n-2)e_M^-$ as $E(n-M) - (E_i - \alpha - \beta)$ [see Fig. 16]. The potential curves relevant to the Auger neutralization of He^+ on tungsten are shown in Fig. 19.

The curves of Fig. 19 are potential energy curves which are independent of the kinetic energy of the particles in the system. The total energy of the system including kinetic energy would be represented by a horizontal line at $E_i = E_{k\infty}(He^+)$ on the ordinate scale of Fig. 19. At any value of s, $E_k(He^+)$ is the energy distance from this total energy line to curve 1. The energy interval between a point on a curve in the band between curves 2 and 3 and the total energy line is $E_k(He) + E_k(e^-)$. We assume that the Franck-Condon principle holds. Thus transitions occur vertically at constant $s = s_t$ on a plot such as Fig. 19, and $E_k(He^+)$ immediately before the transition equals $E_k(He)$ just after the transition. Thus $E_k(e^-)$, the kinetic energy which the escaping electron assumes outside the metal, is the energy interval at the distance s_t between curve 1 and some curve lying between 2 and 3 in Fig. 19. This

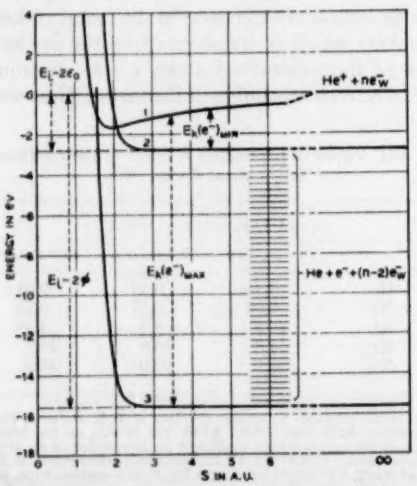

FIG. 19. Potential curve diagram appropriate to the Auger neutralization of He^+ at a tungsten surface. The process is that given in Eq. (63) in the text.

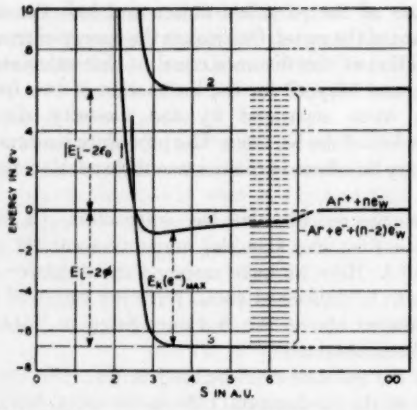

FIG. 20. Potential curve diagram appropriate to the Auger neutralization of Ar^+ at a tungsten surface.

conclusion leads, of course, to the same energy condition as relation (5) when E_k is transformed to ϵ_k by Eq. (3).

The potential curve diagram appropriate to Auger neutralization of Ar^+ is shown in Fig. 20. This is an example of the situation which prevails when $E_i - 2\epsilon_0 < 0$. Curve 1 lies imbedded in the continuum of levels between curves 2 and 3. Only those final states which lie below curve 1 are available for the transition. $E_k(e^-)$ is seen to have a minimum value of zero at all s.

Potential curve diagrams for Auger de-excitation of a metastable atom may be drawn and interpreted in a similar fashion; that appropriate to the de-excitation of Ne^m is shown in Fig. 21. Here the process is written in the form,

$$X^m + ne_M^- \rightarrow X + e^- + (n-1)e_M^-. \qquad (64)$$

The energy conditions (25) and (26) fix the relative positions of the potential curves in this case and the kinetic energy of the ejected electron is again the vertical distance from curve 1 to a curve in the band between curves 2 and 3, at the distance at which the transition occurs.

It is now clear what the effect of inclusion of energy level shifts near the metal has upon the Auger processes, in particular on the energy limits of ejected electrons. From Figs. 19 and 20 it is evident that for a given Auger neutralization process both $(E_k)_{min}$ and $(E_k)_{max}$ decrease as the distance s_t at which the process occurs decreases and are at no distance larger than the limits at $s=\infty$. This amounts to shifting the $N_i(\epsilon_k)$ functions like those of Figs. 10 and 11 lower on the ϵ_k scale. In the case of Auger de-excitation, on the other hand, Fig. 21 indicates that the energy extrema increase if the transition takes place close to the metal. This results from the fact that the potential curve for the metastable atom rises above its asymptote at larger values of s than does that for the normal atom. If one takes no account of effects which broaden the energy

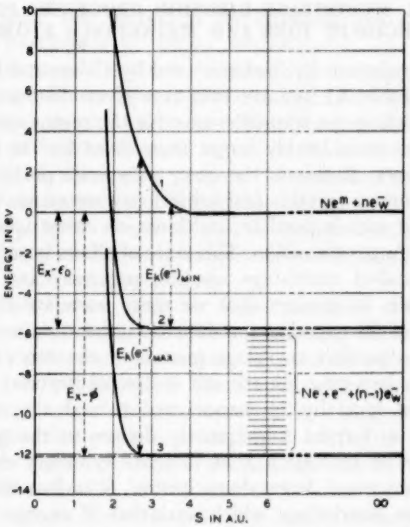

FIG. 21. Potential curve diagram appropriate to the Auger de-excitation of He^m at a tungsten surface. The process is that of Eq. (64) in the text.

distributions one determines from the potential curve diagrams the kinetic energy maxima shown in Fig. 22 for Auger neutralization of Ne^+ (curve 1) and Auger de-excitation of Ne^m (curve 2). It is evident that a means of accounting for the observed violation of the energy limit $E_i-2\varphi\simeq E_z-\varphi$ in the case of Ne^+ is provided by the process of Auger de-excitation.

The energy level shifts depicted by the potential curves of Figs. 19, 20, and 21 are incorporated into the theory of Secs. III and IV in the effective ionization and excitation energies defined in Eqs. (6) and (26). These energies may be evaluated from the interaction energies of Eqs. (60), (61), and (62) or from Figs. 16, 17, and 18. This has been done for the effective ionization energy. The results, plotted as (E_i-E_i') *vs* s are shown in Fig. 23. From the equations referred to we derive

$$(E_i-E_i')=E(n-M)-E(i-M)$$
$$=B_n\exp(-b_ns)-B_i\exp(-b_is)+3.6/s. \quad (65)$$

E_z' functions have not been plotted. E_z' has been used, however, to fix the effective metastable energy level as is discussed in the next section.

X. EFFECT OF LEVEL SHIFTS ON THE RESONANCE TRANSITIONS

We discuss in this section the effect of energy level shifts on the resonance neutralization of ions and the resonance ionization of atoms near a metal surface. For noble gases these processes must involve excited atoms. In what follows the excited level is designated by the metastable atom notation even though resonance processes near a metal surface are not restricted to metastable states. Resonance neutralization is written as

$$X^++e_M^-(-\alpha)\rightarrow X^m, \quad \varphi<\alpha<\epsilon_0, \quad (66)$$

resonance ionization as

$$X^m\rightarrow X^++e_M^-(-\alpha), \quad \alpha<\varphi. \quad (67)$$

Here we consider the system of the ion and one electron in the metal and the isoelectronic system of the neutralized metastable atom.

If we balance energies on the two sides of either of these equations we obtain for α,

$$\alpha=E_i'-E_z'$$
$$=E_i-E_z+E(i-M)-E(m-M). \quad (68)$$

Equation (68) expresses the resonance nature of the transition.

If energy level shifts near the surface are neglected (68) reduces to $\alpha=E_i-E_z$ and one expects resonance neutralization to be possible only if $\varphi<E_i-E_z<\epsilon_0$. Resonance ionization of the metastable atom, X^m, is then possible only if $E_i-E_z<\varphi$. Under this assumption we expect only He^+ and Ne^+ of the singly charged ions of the noble gases to be neutralized at a tungsten surface by the process (66) and only Ar^m, Kr^m, and Xe^m to be ionized at a tungsten surface by the process (67) (see Table II).

If we include the interaction terms $E(i-M)$ and $E(m-M)$ and assume that the Franck-Condon principle holds, α becomes a function of s. Thus, from expressions (61) and (62) in (68),

$$\alpha=E_i-E_z-3.6/s+1.83\times10^{23}\alpha_m s^{-2}\ln(2s)$$
$$-B_m\exp(-b_ms). \quad (69)$$

The Franck-Condon principle is implied in writing Eq. (69) since we evaluate $E(i-M)$ and $E(m-M)$ at the same value of s and neglect translational energy of the atom. This amounts to assuming that the electronic transition affects neither position nor momentum of the atomic particle.

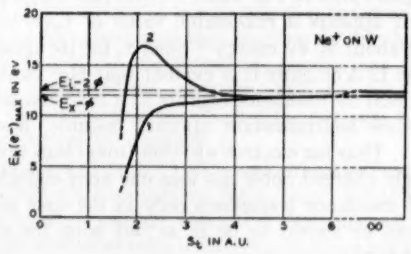

FIG. 22. Kinetic energy maxima as a function of distance s_i at which the transition occurs for Auger neutralization of Ne^+ (curve 1) and Auger de-excitation of Ne^m (curve 2) at a tungsten surface, no account being taken of effects which broaden the distributions. Note the fact that Auger de-excitation can yield electrons whose external energies may exceed the limit $E_z-\varphi$ calculated on the basis of no atomic energy level shifts.

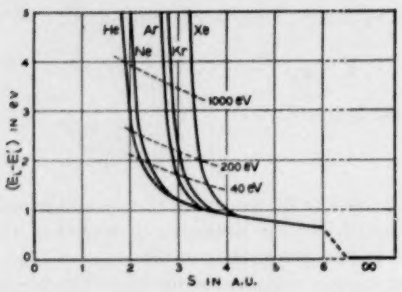

FIG. 23. Plot of (E_i-E_i'), the change in effective ionization energy near the metal surface, as a function of distance from the surface. The lower part of each curve which is common to all curves represents the effect of the image potential of the ion outside the metal. The dashed lines are the loci of $E_i-E_i'(s_m)$ for ions of the incident kinetic energies indicated.

As s decreases from large values toward zero α decreases, since the image potential term, $-3.6/s$, at larger s and the exponential term at closer approach predominate over the van der Waals term. The distance at which $\alpha=\varphi$ is a critical distance, s_c, since resonance neutralization is possible only for $\alpha>\varphi$, $s>s_c$, whereas resonance ionization is possible only if $\alpha<\varphi$, or $s<s_c$.[32] We neglect the small population of states in the metal above the Fermi level at temperatures above absolute zero.

It is possible to plot potential curve diagrams descriptive of the resonance processes which are the analogs of those plotted in Figs. 19, 20, and 21 for the Auger processes.[6,33] A more convenient plot perhaps is that of Fig. 24 in which $-(E_i'-E_s')=-\alpha$ [from Eqs. (68) and (69)] is plotted as a function of s. The energy band structure in tungsten in indicated to the left of the $s=0$ axis in Fig. 24. The critical distances (s_c) for He^m and Ne^m are indicated by the arrows labeled 1 and 2, respectively.

It is clear that the variation of energy levels near a metal surface further restricts the possibility of resonance neutralization of noble gas ions. The process is possible only if the probability distribution function for the process, $P_i''(s,v_0)$, has become appreciable in the region $s>s_c$. In Fig. 24 a $P_i''(s,v_0)$ function is placed at what appears a reasonable value of $s_m(\sim 5A)$ for ions of about 40 ev energy.[33] Since s_c for He appears to be some 12 A or more it is evident that He^+ cannot be neutralized by resonance capture at a tungsten surface. Resonance neutralization appears possible, however, for Ne^+. Thus for electron ejection from clean tungsten by singly charged noble gas ions one need consider the role of resonance transitions only in the case of Ne^+. This can be shown to be in accord with the experimental facts.

[32] The basic ideas concerning the critical distance, s_c, and some of its implications have already been published (reference 6). L. J. Varnerin, Jr., Phys. Rev. **91**, 859 (1953), has recognized independently that inclusion of the image potential yields the critical distance, s_c.

[33] D. Sternberg (private communication).

XI. MULTISTAGE EJECTION PROCESSES FOR INCIDENT IONS AND METASTABLE ATOMS

Calculations by Shekhter[3] and by Cobas and Lamb[4] (see Table X) indicate that at a given distance from the surface the transition rate for the resonance processes is considerably larger than those for the Auger processes. If this is the case, an atomic particle approaching a metal is first subject to a resonance transition, if such is possible, and later, on closer approach, to an Auger transition. This state of affairs is necessary if so-called multistage ejection processes are to be possible. It appears that we must postulate these if some of the experimental data are to be explained.

In a possible two-stage process of electron ejection by an incoming ion the ion is first neutralized to an excited level by resonance capture and the excited atom so formed subsequently decays to the ground state with excitation of an internal secondary electron in a process of Auger de-excitation. It is clear that the further restrictions which variation of energy levels near the metal impose upon the resonance process make the two-stage ejection process less likely. The interpretation of the experimental results for noble gas ions on clean tungsten bear this out.

A two-stage electron ejection process for incident metastable atoms is also possible. In it the metastable atom is first resonance ionized and the ion so formed subsequently neutralized in an Auger process. The conditions which make resonance neutralization less probable make resonance ionization more probable and it is evident that metastable atoms of the noble gases incident on metals will, for the most part, eject electrons by the two-stage process. Thus ejection by incident ions or metastable atoms should be essentially indistinguishable. This conclusion is in accord with the experimental facts but seems not to have been recognized by previous investigators using incident metastable atoms. Thus the energy distributions measured by Greene[34] for incident metastable atoms look much like those characteristic of Auger neutralization (Figs. 12, 13, and 28) and not like those characteristic of Auger de-excitation (Fig. 15). The observation of a minimum electron energy at or near zero which Greene had difficulty in explaining in terms of Auger de-excitation then becomes reasonable. For a clean surface of tungsten it is evident (see below) that even for neon most slow incident metastable atoms will be resonance ionized before the Auger processes become very probable.

When atomic energy level shifts with s are taken into account and when the critical distance s_c, defined in Sec. X, lies in the range in which the resonance processes are possible there arises the interesting possibility of a three-stage ejection process for incident ions in which an incoming ion is first resonance neutralized at $s>s_c$ then resonance ionized at $s<s_c$, and finally Auger

[34] D. Greene, Proc. Phys. Soc. (London) **B63**, 876 (1950).

neutralized. The fraction of the incoming ions which finally participate in Auger neutralization and the complementary fraction involved finally in Auger de-excitation will now depend quite critically on the specific value of s_e, the transition rate functions for the resonance and Auger processes, as well as the incident velocity, v_0, of the atomic particle. The solution of the problem is somewhat involved but can be done with only minor restrictive assumptions. One can obtain an adequate picture of what happens from the simplified version which is included here.

We shall assume that the Auger processes of neutralization and de-excitation occur instantly when the particle reaches a given distance, s_A, assumed to be the same for the two processes. The fraction of Auger neutralization processes is then the probability $P_0(s_A,v_0)$ that an incoming ion reach s_A as an ion. $1-P_0(s_A,v_0)$ then gives the fraction of Auger de-excitations. The P_0 function follows directly from a consideration of the resonance processes. For $s>s_c$ ions may turn to metastable atoms by resonance neutralization and the population of ions in the incoming beam decays according to the P_0 function of Eq. (43) with parameters characterizing the resonance processes. For $s<s_c$ resonance neutralization is no longer possible but metastable atoms formed from ions in the region $s>s_c$ may now turn back to ions by resonance ionization. The population of ions then increases again with decreasing distance. The probability, P_0, that the incident particle is an ion at the distance s can be shown to be

$$\begin{aligned} P_0(s,v_0) &= \exp\{-\exp[-a''(s-s_m'')]\}, \quad s>s_c, \\ &= 1+\{1-\exp[-a''(s_c-s_m'')]\} \\ &\quad \times\exp\{-\exp[-a''(s-s_m'')]\}, \quad s<s_c. \end{aligned} \tag{70}$$

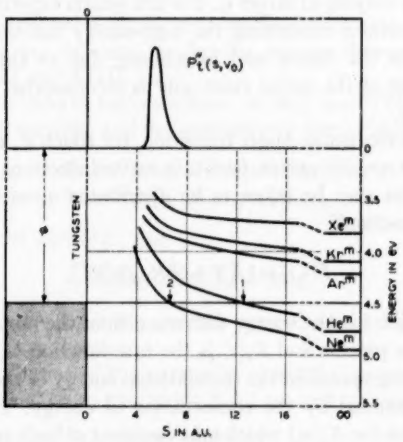

FIG. 24. Plot of the variation of the metastable levels (lowest lying) of He, Ne, Ar, Kr, and Xe with distance outside a tungsten surface. The filled portion of the conduction band in tungsten is indicated by stippling. The critical distances (s_c) for He^m and Ne^m are indicated at 1 and 2, respectively. A representative $P_i''(s,v_0)$ function for resonance ionization is shown at the top of the figure.

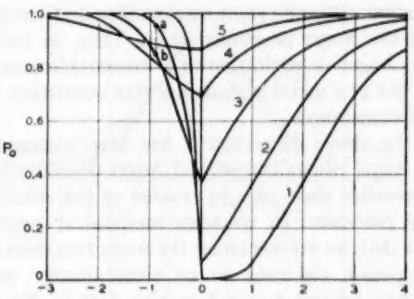

FIG. 25. Plots of the probability, $P_0(s,v_0)$, that an incident ion remains an ion for the case in which the critical distance s_c lies in the range of s where the resonance processes are probable. The Auger processes are neglected in these plots. Curves 1 through 5 are for increasing incident velocity v_0 in that order, the velocity ratio between adjacent curves being e. For curve 3 the incident velocity is such that $s_m=s_c$.

The P_0 function from (70) is plotted in Fig. 25 for various incident velocities. Two conclusions may be drawn from the figure: 1. Inasmuch as the rise in P_0 at $s<s_c$ is rapid we expect a relatively low percentage of incident particles to remain metastable atoms long enough to become de-excited by Auger de-excitation. This result is in accord with the experiment which indicates that a high percentage of incident Ne^+ ions do finally reach the atomic ground state via the Auger neutralization process (Sec. XIV). 2. Increase in velocity of the incoming particle should *increase* the fraction of incident ions which participate in the two-stage ejection process. Thus if the Auger processes occur at a distance $s_A<s_c$ such that, as an example, $a''(s_A-s_c)=-0.9$ in Fig. 25, an increase in velocity of a factor of e from curve 2 to curve 3 will decrease the fraction of ions at s_A from 0.95 (point a) to 0.85 (point b). This is the result of the interesting cross-over of the curves of Fig. 25 at $s<s_c$. This is a manifestation of the fact that slower particles are transformed in larger proportion from ions to metastable atoms for $s>s_c$ but revert more rapidly to ions at $s<s_c$ than do faster particles. This effect makes it possible to account for the observed variation of γ_i for Ne^+ on tungsten as is explained in Sec. XV. A calculation of the P_0 function based on the inclusion of an exponential rate function for the Auger processes as well as the resonance process has been shown to preserve this variation with velocity for suitably chosen parameters defining the two rate functions and the critical distance, s_c.

The variation of energy levels does not make possible a three-stage ejection process for incident metastable atoms because resonance ionization can succeed but not precede resonance neutralization as distance between atom and metal decreases. Thus incident metastable atoms remain such till the distance s_c is reached after which they may turn to ions. If s_c lies in the range of s in which the resonance processes occur but the Auger processes have not yet become probable, this transformation, as Fig. 25 indicates, is so rapid that a large

proportion of the incident metastables do become ions before the Auger processes set in. Thus, as indicated above, Auger de-excitation of a metastable atom of a noble gas at a metal surface is a rare occurrence under any circumstances.

In the above discussion it has been assumed that when Auger neutralization and Auger de-excitation are both possible they may be treated as individual competing processes. In quantum-mechanical terms this means that we are assuming the wave functions of the participating electrons to be either purely metallic (electrons labeled 1 and 2 in Fig. 2, 2 in Fig. 3) or purely atomic (electron labeled 1 in Fig. 3). We are thus neglecting the cross product terms which arise when the true wave functions of electrons participating in a sort of combined process are used. An electron whose energy is near that of the metastable level outside the metal should be represented by a wave function which is partly inside the metal and partly in the atom. The integrated ratio of the probability of finding the electron in the metastable level to that of finding it inside the metal is taken here to be the ratio of the probability of Auger de-excitation to the probability of Auger neutralization.

XII. EFFECTS WHICH BROADEN THE ELECTRON ENERGY DISTRIBUTION

We proceed now to include specifically in the theory those effects which broaden the energy distribution function, $N_i(\epsilon_k)$. We expect the true $N_i(\epsilon_k)$ functions to be broader than those shown in Figs. 10, 11, and 14 by virtue of the following:

1. E_i' is a function of s and $P_i(s,v_0)$ has finite width on the s scale, and,
2. the initial and final states of the process have finite lifetimes.

For the case of Auger neutralization the energy distribution $N_i(\epsilon_k)$ is obtained from expression (19) by use of $P_k(\epsilon_k,s)$ from (18). This gives

$$N_i(\epsilon_k)=N(\epsilon_k)\int_0^\infty \frac{P_i(s,v_0)T[(\epsilon_k+\epsilon_0-E_i')/2]ds}{\int_{\epsilon_F}^\infty N(\epsilon_k)T[(\epsilon_k+\epsilon_0-E_i')/2]d\epsilon_k}, \quad \epsilon_k>\epsilon_F$$
$$=0, \quad \epsilon_k<\epsilon_F. \tag{71}$$

If one puts into this expression $E_i'(s)$ from Eq. (65), for example, the first cause of broadening listed above is then included in the theory although the calculation indicated is prohibitively tedious. We simplify expression (71) by assuming the integral over ϵ_k in the denominator to be independent of s and by writing

$$E_i'(s)=E_i'(s_m)+k(s-s_m), \tag{72}$$

where k is $[dE_i'/ds]_{s=s_m}$. Then we may write

$$N_i(\epsilon_k)\propto N(\epsilon_k)\int_0^\infty P_i(s,v_0)T[(\epsilon_k+\epsilon_0-E_i'(s_m)-k(s-s_m))/2]ds. \tag{73}$$

The second cause of broadening listed above, namely that due to finite lifetimes, is included as follows. The lifetime in the initial state is determined by the transition rate $R_i(s)$ if we assume only one process to be of importance in the range of s over which the $P_i(s,v_0)$ function has value. The final state has a finite lifetime because the electrons participating in the Auger ejection process leave holes in the filled portion of the conduction band which are filled by secondary Auger processes involving electrons lying higher in the band. These secondary processes are the same as those proposed by Skinner[35] to account for the observed tailing at the long wavelength limit in the soft X-ray spectra of metals. Landsberg[36] has calculated the broadening by these secondary Auger processes and has shown it to be zero when the holes lie at the top of the filled band [$\epsilon'=\epsilon''=\epsilon_F$ in the present case; see Fig. 4] and maximum when the holes lie at the bottom of the band [$\epsilon'=\epsilon''=0$]. Thus tailing at the low-energy limit of the $N_i(\epsilon_k)$ distribution is caused by the finite lifetimes in both initial and final states whereas that at the high-energy limit results from initial state lifetime only. Broadening of the $N_i(\epsilon_k)$ function at lower ϵ_k is difficult to observe in the experimental $N_0(E_k)$ curves because it is largely obscured by the effects of the probability of escape and target-collector geometry. The high-energy tail of the $N_0(E_k)$ function, on the other hand, resembles closely that of the $N_i(\epsilon_k)$ function because $P_e(\epsilon_k)$ is relatively slowly varying at larger ϵ_k. For this reason experimental observations concerning the high-energy tail only are used in the theory and broadening due to the finite lifetime of the initial state only is incorporated in the theory.

The elemental Auger transition, for which ϵ', ϵ'', and s have specific values, results in excited electrons whose energies may be taken to be distributed according to the function[37]

$$I(\delta,s)=1/[\delta^2+(\hbar R_i(s)/2)^2], \tag{74}$$

in which δ is the energy difference from the nominal ϵ_k for the process and $R_i(s)$ is the rate function. A corresponding spread in the translational energy of the atom is demanded by the conservation of energy. The expression for $N_i(\epsilon_k)$ which takes account of both types of

[35] H. W. B. Skinner, Phil. Trans. Roy. Soc. (London) **A239**, 95 (1940).
[36] P. T. Landsberg, Proc. Phys. Soc. (London) **A62**, 806 (1949).
[37] This is the natural line profile discussed, for example, in Sec. 18 of W. Heitler, *The Quantum Theory of Radiation* (Oxford University Press, London, 1954), third edition.

broadening is thus

$$N_i(\epsilon_k) \propto N(\epsilon_k) \int_{-\infty}^{\infty} \int_{0}^{\infty} P_t(s,v_0) I(\delta,s) \times T[(\epsilon_k+\delta+\epsilon_0-E_i'(s_m)-k(s-s_m))/2] ds d\delta. \quad (75)$$

We further simplify expression (75) by evaluating $I(\delta,s)$ at $s=s_m$ and by approximating P_t and I by Gaussian distributions $\Phi_{\sigma 1}$ and $\Phi_{\sigma 2}$ having widths at half-maximum equal to those of P_t and I, respectively. Thus we replace the double integral in (75) by

$$T_\sigma(\epsilon_m) = \int_{-\infty}^{\infty} \int_{-\infty}^{\infty} \Phi_{\sigma 1}(y) \Phi_{\sigma 2}(z) T(\epsilon_m+y+z) dy dz = \int_{-\infty}^{\infty} \Phi_\sigma(x) T(\epsilon_m+x) dx, \quad (76)$$

in which

$$\epsilon_m = [\epsilon_k+\epsilon_0-E_i'(s_m)]/2, \quad (77)$$

$$y = \delta/2, \quad (78)$$

$$z = -k(s-s_m)/2 = -(1/2)(s-s_m)[dE_i'/ds]_{s=s_m}, \quad (79)$$

$$\Phi_\sigma(x) = [1/\sigma(2\pi)^{\frac{1}{2}}] \exp(-x^2/2\sigma^2), \quad (80)$$

and

$$\sigma = (\sigma_1^2+\sigma_2^2)^{\frac{1}{2}}. \quad (81)$$

The limits of integration over z in (76) are taken as $-\infty$ to ∞ in place of $-\infty$ to $ks_m/2$ because $P_t(s,v_0)$ is essentially zero in the range $ks_m/2 < z < \infty$. The T function in (76) is given in (15). Thus, finally,

$$N_i(\epsilon_k) = \frac{N(\epsilon_k) T_\sigma[(\epsilon_k+\epsilon_0-E_i'(s_m))/2]}{\int_{\epsilon_F}^{\infty} N(\epsilon_k) T_\sigma[(\epsilon_k+\epsilon_0-E_i'(s_m))/2] d\epsilon_k}. \quad (82)$$

In this expression $N_i(\epsilon_k)$ is normalized to an area of one electron per incident ion for the reasons discussed in Secs. III and XIII.

The widths at half-maximum, $W(\Phi_{\sigma 1})$ and $W(\Phi_{\sigma 2})$, of the functions $\Phi_{\sigma 1}$ and $\Phi_{\sigma 2}$, respectively, are evidently

$$W(\Phi_{\sigma 1}) = (1/2) W(P_t) [dE_i'/ds]_{s=s_m} = (1.25/a)[dE_i'/ds]_{s=s_m}, \quad (83)$$

from (79) and (42), and

$$W(\Phi_{\sigma 2}) = \hbar R_t(s_m) = \hbar a v_0, \quad (84)$$

from (74), (35), (40), and the simplification of evaluating $I(\delta,s)$ at $s=s_m$.

The relation of the parameter σ in the Gaussian distribution (80) to the width $W\Phi_\sigma$ at half-maximum is

$$\sigma = W(\Phi_\sigma)/2.37, \quad (85)$$

from which it follows that

$$\sigma_1 = (0.53/a)[dE_i'/ds]_{s=s_m}, \quad (86)$$

and

$$\sigma_2 = 0.42 \hbar a v_0. \quad (87)$$

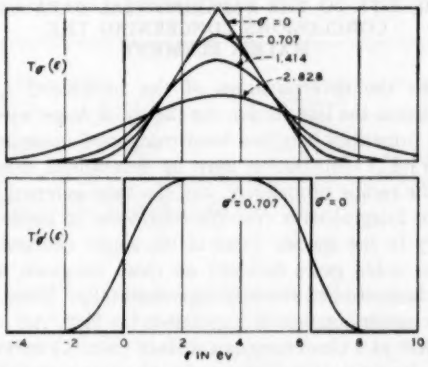

FIG. 26. Plots of $T_\sigma(\epsilon)$ and $T_{\sigma'}'(\epsilon)$ functions for $N_e(\epsilon)$ = constant (k_1) and for several choices of the parameters σ and σ'. Analytic expressions for these functions are to be found in Table III.

The procedure to be followed to determine a broadened $N_i(\epsilon_k)$ function for Auger neutralization is then the following:

1. Calculate the Auger transform $T(\epsilon)$ from Eq. (15) assuming a state density function $N_e(\epsilon)$.

2. Calculate the broadened Auger transform $T_\sigma(\epsilon_m)$ from (76) using (77), (80), (81), and σ_1 and σ_2 parameters from (86) and (87). This involves a fit to the experimental data to get σ_1 as discussed in the next section.

3. Shift $T_\sigma(\epsilon_m)$ on the energy axis as indicated in (82), multiply by $N(\epsilon_k)$, and normalize to unity area. In this step a final state density function $N(\epsilon_k)$ proportional to $\epsilon_k^{\frac{1}{2}}$ has been assumed.

The broadening of the $N_i'(\epsilon_k)$ distribution for Auger de-excitation may be treated in a manner entirely analogous to that just discussed for Auger neutralization. By carrying through the argument using the results of Sec. IV it can be shown that

$$N_i'(\epsilon_k) = \frac{N(\epsilon_k) T_{\sigma'}'[\epsilon_k - E_x'(s_m')]}{\int_{\epsilon_F}^{\infty} N(\epsilon_k) T_{\sigma'}'[\epsilon_k - E_x'(s_m')] d\epsilon_k}, \quad \epsilon_k > \epsilon_F = 0, \quad \epsilon_k < \epsilon_F, \quad (88)$$

where

$$T_{\sigma'}'(\epsilon_m') = \int_{-\infty}^{\infty} \Phi_{\sigma'}(x) N_e(\epsilon+x) dx \quad (89)$$

and

$$\epsilon_m' = \epsilon_k - E_x'(s_m').$$

σ' is again $(\sigma_1'^2+\sigma_2'^2)^{\frac{1}{2}}$, where now

$$\sigma_1' = (1.06/a)[dE_x'/ds]_{s=s_m'}, \quad (90)$$

and

$$\sigma_2' = 0.42 \hbar a' v_0. \quad (91)$$

Analytic expressions for the $T(\epsilon)$, $T'(\epsilon)$, $T\sigma(\epsilon)$ and $T_{\sigma'}'(\epsilon)$ functions are listed in Table III for some choices of $N_e(\epsilon)$. $T_\sigma(\epsilon)$ and $T_{\sigma'}'(\epsilon)$ for $N_e(\epsilon) = k_1$ are plotted in Fig. 26 for several choices of σ and σ'.

XIII. FITS TO THE EXPERIMENTAL DATA AND CONCLUSIONS CONCERNING THE MATRIX ELEMENT

With the determination of the broadened $N_i(\epsilon_k)$ function in the last section the theory of Auger ejection to be presented here has been completed inasmuch as the $N_0(E_k)$ distribution may be determined from N_i and the escape probability, and the total external yield as the integral over N_0. We wish now to apply this theory to the specific cases of the singly charged ions of the noble gases incident on clean tungsten which have been studied recently experimentally.[7] Since resonance neutralization is impossible for He^+, Ar^+, Kr^+, and Xe^+ at a clean tungsten surface (Sec. X) we expect these ions to eject electrons by the process of Auger neutralization only. In this section we estimate or determine by fits to the experimental data the unknown parameters in the theory of Auger neutralization. The role played by Auger de-excitation in the case of Ne^+ on clean tungsten and what is learned about the process from fitting the theory to the experimental data are discussed in the next section.

We now discuss the basic functions which we need before the theory of Auger neutralization can be applied.

1. The state density function, $N_e(\epsilon)$, is needed to determine the Auger transform, $T(\epsilon)$, by Eq. (15). We have taken $N_e(\epsilon)$ = constant as the best approximation to the function calculated by Manning and Chodorow[24] (see Figs. 8 and 9 and Sec. VII).

2. We also need the transition probability per unit time, $R_i(s)=A\exp(-as)$, which specifies the dependence of the matrix element on s. As indicated in Sec. V values of $a=2\times10^{8}$ cm^{-1} and 5×10^{8} cm^{-1} have been used. A is determined from the experimental data by fitting to the high-energy tail of the experimental $N_0(E_k)$ curves in the following way. The tangent line through the point of inflection on the high-energy side of experimental $N_0(E_k)$ distribution is extrapolated to the $E_k(\epsilon^-)$ axis (see He^+ curve in Fig. 7 of the accompanying paper).[7] This intercept is taken to give a reasonable value for $E_i'(s_m)-2\varphi$. That this should be so is to be seen by comparing the $N_i(\epsilon_k)$ distributions labeled 2 and 3 in Fig. 4. Here curve 2 is the unbroadened distribution resulting from transitions all of which occur at $s=s_m$. Curve 3 is the broadened $N_i(\epsilon_k)$ distribution. It is evident that curve 2 approximates a tangent through the point of inflection of curve 3 on the high energy side. Point a, which is the maximum energy in the distribution 2 and thus approximately the position of the intercept of the line tangent to 3, lies at $E_i'(s_m)-2\varphi$. The value $E_i'(s_m)$ determined in this way may be used with the appropriate curve of Fig. 23 to give a value of s_m (Table VIII). This, by Eq. (40), specifies the parameter A, when a and v_0 are known. The values of A found in this way are listed in Table IX. Transition rate parameters to be found in the literature are listed in Table X. For convenience, velocities of noble gas ions for various incident kinetic energies of interest are listed in Table XI.

3. Finally, we need the probability distribution $P_Q(\theta,\epsilon_k)$ which gives the θ dependence of the matrix element. On the basis of the assumptions discussed in Sec. VI, $P_Q(\theta,\epsilon_k)$ is determined by the parameter f which specifies the ratio of matrix elements for processes yielding escaping and internally reflected excited electrons. f is determined by fitting the theoretical γ_N for He^+ ions of 40 ev incident energy to the experimental value of 0.282. This procedure yields $f=2.2$ and the escape probability function plotted as curve 2 in Fig. 7. Whereas we determine a value of the parameter A for each noble gas ion we use the same value of f for all.

In addition to the above functions we need values of the σ_1 and σ_2 parameters which determine the broadening of the $N_i(\epsilon_k)$ distribution. By Eq. (86) σ_1 depends on the parameter a and $[dE_i'/ds]_{s=s_m}$, which may be determined from Fig. 23 or Eq. (65) using the s_m value determined above. By Eq. (87), σ_2 is calculable directly from a and v_0. σ_1, σ_2, and the resulting σ are listed in Table VIII for each choice of the parameter a.

By virtue of the two fits to the experimental results which yield values of the parameters A and f we have in effect determined the two basic characteristics of the matrix element, namely its dependence on s and θ, which an evaluation of the matrix element from first principles would be expected to supply. Although there is nothing in previous calculations with which to compare the value $f=2.2$, it appears to be reasonable. On the other hand, the values for A determined in this work are much larger than those calculated by Shekhter[3] and Cobas and Lamb.[4] In the light of the present work these earlier values look much too low. For 40-ev

TABLE VIII. Parameters which characterize Auger neutralization by 40-ev ions.

Ion	$E_i'(s_m)$ (ev)	s_m (A)	$a=2\times10^8$ cm^{-1} σ_1 (ev)	σ_2 (ev)	σ (ev)	$a=5\times10^8$ cm^{-1} σ_1 (ev)	σ_2 (ev)	σ (ev)
He^+	22.6	2.2	0.63	0.244	0.69	0.25	0.61	0.66
Ne^+	19.6[a]	2.4	0.63	0.108	0.64	0.25	0.27	0.37
Ar^+	14.0	3.0	0.63	0.080	0.64	0.25	0.20	0.32
Kr^+	12.3	3.2	0.63	0.056	0.63	0.25	0.14	0.29
Xe^+	10.6	3.6	0.63	0.044	0.63	0.25	0.11	0.27

[a] Since $E_i'(s_m)-2\varphi$ cannot be obtained from the experimental curve for Ne^+ at 40 ev because of the tail due to Auger de-excitation, this value has been determined from the intersection with the Ne curve of the locus of $E_i-E_i'(s_m)$ values for 40-ev ions in Fig. 23.

TABLE IX. Transition rate parameters for Auger neutralization from the present work.

	A (sec^{-1}) $a=2\times10^8$ cm^{-1}	$a=5\times10^8$ cm^{-1}
He^+	7.1×10^{16}	1.5×10^{20}
Ne^+	4.8×10^{16}	1.6×10^{20}
Ar^+	1.1×10^{17}	2.3×10^{21}
Kr^+	1.2×10^{17}	4.6×10^{21}
Xe^+	2.1×10^{17}	2.5×10^{22}

TABLE X. Summary of published transition rate parameters.

	Auger processes					
	Neutralization		De-excitation		Resonance processes	
	A (sec^{-1})	a(cm^{-1})	A'(sec^{-1})	a'(cm^{-1})	A''(sec^{-1})	a''(cm^{-1})
Shekhter[c]	6.35×10^{14} [a]	3.9×10^{8} [a]			5.74×10^{19}	3.2×10^{8}
Cobas and Lamb[d]			9.6×10^{16}	7.3×10^{8}	9.1×10^{18} [b]	1.9×10^{8} [b]

[a] Evaluated by expanding in Taylor's series the polynomial in Shekhter's expression for $R_1(s)$ [his Eq. (3.11)] about the point $s=2.2$ A.
[b] Evaluated by expanding in Taylor's series the polynomial in Cobas and Lamb's expression for $R_1''(s)$ about the point $s=5.0$ A.
[c] See S. S. Shekhter (see reference 3).
[d] See A. Cobas and W. E. Lamb (see reference 4).

He^+ ions Shekhter's parameters A and a give $s_m<0$. Cobas and Lamb's values for A' and a' give $s_m'=0.47$ A for 40-ev He^m. It is clear that if the variation of atomic energy levels near the metal is anything like that derived in this paper one cannot produce with the theory the form of $N_0(E_k)$ observed in the experiment for such low values of A. The observed $N_0(E_k)$ distributions are so nearly like those calculated for no variation of energy levels (e.g., Fig. 12) that the $P_t(s,v_0)$ function must lie at distances from the surface where only relatively small displacements of the energy levels have occurred. This is thought to be a fairly important and direct conclusion. The specific range of A values which this indicates does depend upon the details of the potential curves used in Sec. IX and upon the distance scale prescribed by the procedures of Sec. VIII. But it is evident that the rate functions calculated thus far from first principles make it necessary that the process occur very close to the surface and this seems difficult to reconcile with the experimental observations.

It is difficult to put a finger on the reason for the low values of A calculated from direct evaluation of the matrix element. Cobas and Lamb's A' value should be low inasmuch as they took the wave functions of metal electrons to be zero outside the metal. However, Shekhter, who retained the tails outside the metal, calculated a smaller transition rate than did Cobas and Lamb. In this connection it is interesting to note that the parameters for resonance neutralization calculated by Shekhter and by Cobas and Lamb (Table X) give $s_m''=3.3$ A and 4.9 A, respectively. These are not far from what one would think reasonable in the light of the Ne^+ results. Finally, it should be noted in Table IX how profoundly the choice of a affects the value of A.

Fixing A at the values given in Table IX may now be seen to justify the assumption made earlier that $\int_0^\infty P_t(s,v_0)ds\cong1$ or the equivalent statement that $\int_0^\infty N_i(\epsilon_k)d\epsilon_k\cong1$ electron per incident ion. For the least favorable case in Table IX (He^+: $a=2\times10^{-8}$ cm^{-1}, $A=7.1\times10^{16}$ sec^{-1}) we find $\int_0^\infty P_t(s,v_0)ds\cong1-\exp(-81)$ by Eq. (48). Another way of stating the high probability of the Auger transition occurring on the inward trip of the ion is that $\int_s^\infty P_t(s,v_0)ds>0.999$ at $s=s_m-1$A for $a=2\times10^{8}$ cm^{-1} or $s=s_m-0.4$ A for $a=5\times10^{-8}$ cm^{-1}. With the relatively large values of s_m given in Table VIII it follows that at 40 ev essentially all ions will have participated in an Auger transition before the ion gets close enough for other means of its neutralization to become operative. These conclusions are in agreement with the observation of very low reflection of ions as ions or as metastable atoms at low incident kinetic energy.

XIV. THEORETICAL ELECTRON ENERGY DISTRIBUTIONS AND ELECTRON YIELDS

We are now in a position to construct theoretical electron energy distributions which include the effects of atomic energy level variation near the metal and the Heisenberg prinçiple. For He^+, Ar^+, Kr^+, and Xe^+, since Auger neutralization only is possible, $N_i(\epsilon_k)$ distributions are obtained from Eq. (82) using Manning and Chodorow's calculated value of $\epsilon_F=6.4$ ev, $\epsilon_0=\epsilon_F+\varphi=10.9$ ev, and the values of $E_i'(s_m)$ given in Table VIII. To avoid lengthy computation a single value of σ equal to 0.707 has been used for all ions. The $N_i(\epsilon_k)$ functions obtained in this way are plotted in Fig. 27. The distribution in energy of external secondary electrons, $N_0(E_k)$, is obtained from the $N_i(\epsilon_k)$ function in each case by multiplying by the escape probability, $P_e(\epsilon_k)$, of Eq. (55) with $f=2.2$ (curve 2 of Fig. 7). These curves are plotted in Fig. 28. Total electron yields determined as areas under these $N_0(E_k)$ distributions are listed in Table XII where are also listed the experimental values for comparison.

It is evident that the high-energy tail of the experimental $N_0(E_k)$ curve for Ne^+ cannot be simulated if electrons are ejected only in the process of Auger neutralization (dashed curve in Fig. 28). It has been seen, however, that resonance neutralization is possible for Ne^+ at a clean tungsten surface (Sec. X) and that Auger de-excitation of Ne^m can produce electrons of energies outside the metal greater than can arise in Auger neutralization (Sec. IX). By virtue of these facts it has been possible to construct a distribution for electrons from Ne^+ on tungsten which resembles the experimentally observed one. It is compounded of $N_i(\epsilon_k)$ and $N_i'(\epsilon_k)$ functions in the manner $f_NN_i(\epsilon_k)+(1-f_N)N_i'(\epsilon_k)$, where f_N is the fraction of incident ions which finally decay by Auger neutralization and N_i and N_i' are the distributions for Auger neutralization and de-excitation, respectively, each normalized to an area of one electron per incident ion.

In order to calculate a broadened $N_i'(\epsilon_k)$ function it is evident that we need to know σ_1', σ_2', $E_x'(s_m')$, s_m'.

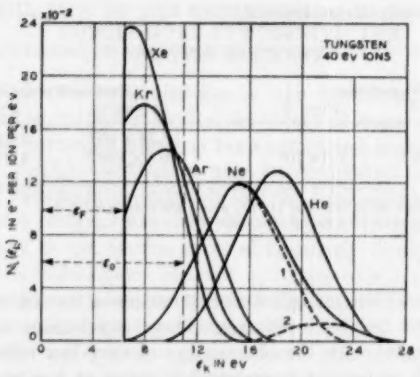

FIG. 27. Theoretical $N_i(\epsilon_k)$ distributions for 40-ev ions incident on clean tungsten determined from the theory which includes effects of the variation of energy levels near the metal and the Heisenberg uncertainty principle. For He^+, Ar^+, Kr^+, and Xe^+ the electrons come from the process of Auger neutralization. For Ne^+ *ca* 90 percent of the electrons arise in Auger neutralization (curve 1), 10 percent in Auger de-excitation (curve 2) as explained in the text.

Assuming the rate functions $R_t(s)$ and $R_t'(s)$ to be equal (Sec. V) means that $s_m'=s_m$, $a'=a$, and thus $\sigma_2'=\sigma_2$. Evaluation of σ_1' by Eq. (90) involves more detailed knowledge of $E_z'(s)$ than we possess, and no attempt to evaluate σ_1' has been made. In finding $T_{\sigma'}'(\epsilon)$ it is perhaps reasonable to use $\sigma'=0.707$, the same value as that used for σ in finding $T_\sigma(\epsilon)$. The $T_{\sigma'}'(\epsilon)$ functions for $\sigma'=0$ and 0.707 are plotted in Fig. 26. We have used the same escape probability function for the de-excitation process as for the neutralization process, i.e., $P_e'=P_e$. This means that we assume the same ratio f of matrix elements in the two cases, a not unreasonable assumption for the exchange de-excitation process.

After some trial and error it has been found that the experimentally observed tail on the $N_0(E_k)$ curve for Ne^+ at 40 ev can be closely approximated with $E_z'(s_m')-E_z=2.5$ ev and $f_N=0.9$. This value of $E_z'(s_m')$ is a little less than that indicated in Fig. 22 for $s_m'=2.4$ A ($s_m'=s_m$ taken from Table VIII). Another method of determining f_N is based on the fact that the total yield for the combined process may be written as

$$\gamma_i=f_N\gamma_N+(1-f_N)\gamma_D. \tag{92}$$

Values for γ_N and γ_D values equal to 0.208 and 0.340, respectively, have been calculated by using $E_i'(s_m)=19.6$ ev, $E_z'(s_m')-E_z=2.5$ ev, and $P_e'=P_e$. A value of f_N may now be determined which makes the γ_i of (92) equal the experimentally observed value of 0.232 at $E_k(Ne^+)=40$ ev. The value $f_N=0.82$ found in this way is in reasonable agreement with the value 0.9.

It is evident that a high value of f_N is indicated by the experiment. This requires that the critical distance s_c lie in the range of s in which the $P_i''(s,v_0)$ function for the resonance process in Ne has value for ion energies near 100 ev. The two-stage process of electron ejection is thus much less important for ions of the noble gases incident on clean metals than has formerly been supposed.

We may now compare the theoretical and experimental results for γ_i and $N_0(E_k)$. Table XII indicates that the trend of γ_i is predicted and, in fact, with reasonable accuracy, the magnitudes themselves, once the fit for He^+ has been made. Comparison of Fig. 28 with Fig. 7 of the accompanying paper[7] shows the general forms of the $N_0(E_k)$ distributions, in particular the high-energy tails, to be reproduced quite well also. The deficiency of slow electrons observed for He^+ is evidently to be understood as resulting from the fact that $E_i'-2\epsilon_0>0$ for this ion at the values of s where the process occurs. Even though the relative maxima of the $N_0(E_k)$ distributions observed for He^+ and Ne^+ are not reproduced by the theory, the relative γ_i values are quite good in spite of the complication with Auger de-excitation for Ne^+. For Ar^+, Kr^+, and Xe^+, on the other hand, the theory gives γ_i values which are clearly too low. This is not too surprising inasmuch as we espect the results for these ions to be much more sensitive to the specific choices made for $N_c(\epsilon)$, $F(\epsilon',\epsilon'')$ and P_Ω, and thus to the form of the $N_i(\epsilon_k)$ distribution, than are the results for He^+ and Ne^+. This arises from the fact that only those electrons lying in the high-energy tail of the $N_i(\epsilon_k)$ distribution for Ar^+, Kr^+, and Xe^+ have any chance of leaving the metal whereas for He^+ and Ne^+ essentially the whole of the $N_i(\epsilon_k)$ distribution lies at $\epsilon_k>\epsilon_0$. Furthermore, the use of the same f parameter in determining $P_\Omega(\theta,\epsilon_k)$ and $P_e(\epsilon_k)$ for all ions may introduce some error.

It is interesting to note the effect of the choice of the parameter a in the rate function $R_t(s)$. Table VIII indicates that for $a<2\times10^8$ cm^{-1} $\sigma\simeq\sigma_1$ and the broadening of $N_i(\epsilon_k)$ is determined entirely by the variation in E_i' over the values of s at which the process occurs [Eq. (86)]. For $a>5\times10^8$ cm^{-1} $\sigma\simeq\sigma_2$ and broadening is governed only by the Heisenberg principle [Eq. (87)]. In the latter case σ depends upon v_0 and thus varies from ion to ion at a given energy. That this is perhaps more in agreement with experiment than is a constant σ is indicated in the next section. Values of σ obtained for values of a much outside the range 2 to 5×10^8 cm^{-1} appear to be so large as to make difficult a good prediction of the forms of the high-energy tails of the $N_0(E_k)$ distributions.

TABLE XI. Velocities of noble gas ions.

Ion	$10^{-6}\times$velocity in cm/sec. $E_k=1$ ev	$E_k=40$ ev	$E_k=200$ ev	$E_k=1000$ ev
He^+	0.70	4.38	9.8	21.9
Ne^+	0.32	1.96	4.38	9.8
Ar^+	0.22	1.39	3.11	6.95
Kr^+	0.16	0.96	2.15	4.8
Xe^+	0.13	0.77	1.72	3.85

XV. VARIATIONS WITH ION KINETIC ENERGY

To a first, rather crude approximation Auger ejection of electrons from metals is independent of incident ion energy in both experiment and theory. The smaller variations observed in the study of tungsten,[7] however, present something of a challenge to any theory of the phenomenon. The observed variations of γ_i with incident ion energy are: 1. the drop in $\gamma_i(He^+)$ at ion energies up to 400 ev, 2. the rise in $\gamma_i(He^+)$ above 400 ev, 3. the rise in $\gamma_i(Ne^+)$ in the range of 10 to 100 ev and the levelling off at higher energies, 4. the slow rise in γ_i of Ar^+, Kr^+, and Xe^+ with increasing ion energy. The main effect of increasing ion energy on the electron energy distributions, $N_0(E_k)$ is to lengthen the high-energy tail. The increase in the relative proportion of slow electrons observed in the case of He^+ is also of interest.

In considering variations with ion kinetic energy from the point of view of theory we shall discuss first the cases of pure Auger neutralization, namely, those for He^+, Ar^+, Kr^+, and Xe^+. The theory predicts variation of γ_i and form of $N_0(E_k)$ through the effects of variation of energy levels near the metal surface and the Heisenberg uncertainty principle. As the incident velocity of the ion is increased, s_m decreases by Eq. (40), but the form of the $P_i(s,v_0)$ function remains invariant. This means that for higher incident velocities the Auger transitions take place closer to the metal. There are two results of faster ion approach and the consequent neutralization closer to the metal which then determine the variation of γ_i and $N_0(E_k)$. These are:

1. The effective ionization energy is smaller for transitions occurring closer to the metal (see Figs. 4 and 23).

2. The broadening of the $N_i(\epsilon_k)$ distribution is greater both because of the increase of dE_i'/ds, which increases σ_1 [Eq. (86)], and because of the increase of σ_2 with incident velocity [Eq. (87)].

Reduction of $E_i'(s_m)$ can be seen by Eq. (82) to shift the $N_i(\epsilon_k)$ distribution to lower values of ϵ_k, the final effect of which is to reduce γ_i. We may look upon the effect of greater broadening of the $N_i(\epsilon_k)$ distribution, somewhat crudely, as removing electrons from the middle of the distribution and placing half of these in the high-energy and half in the low-energy tails. The effect of this upon γ_i depends upon where, with respect to the level $\epsilon_k=\epsilon_0$, the $N_i(\epsilon_k)$ distribution lies. For He^+ the $N_i(\epsilon_k)$ distribution lies essentially entirely at $\epsilon_k>\epsilon_0$ (Fig. 27). Here broadening of the distribution results in reducing γ_i because electrons in the enlarged low-energy tail never leave the metal. On the other hand, for a distribution $N_i(\epsilon_k)$ of which only a portion near the high-energy end lies at $\epsilon_k>\epsilon_0$, broadening of the distribution increases γ_i because there are more electrons in the high-energy tail which can leave the metal. The observed variation in γ_i is thus a combination of effects due to energy level variation and distribution broadening, both of which decrease γ_i for He^+ but have opposite effects on γ_i for the heavier ions.

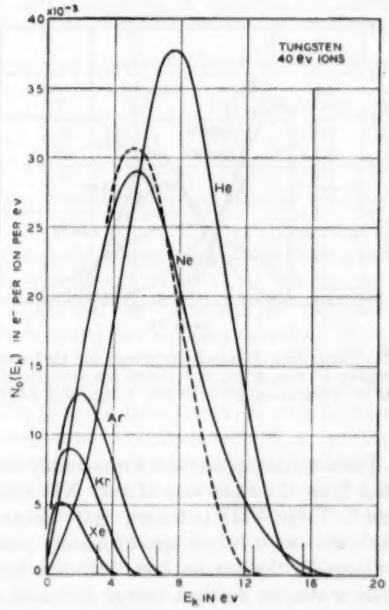

FIG. 28. Theoretical $N_0(E_k)$ distributions for 40 ev ions determined from the theory which includes effects of the variation of energy levels near the metal and the Heisenberg uncertainty principle. These curves have been obtained from the $N_i(\epsilon_k)$ distributions of Fig. 27 using the $P_s(\epsilon_k)$ function of Eq. (55) with $f=2.2$. The energy limits $E_i-2\varphi$ are indicated by the vertical lines above the E_k axis. The dashed curve for Ne indicates what $N_0(E_k)$ for this ion would be if all Ne^+ ions decayed finally via Auger neutralization. Thus it is obtained from an $N_i(\epsilon_k)$ distribution like curve 1 of Fig. 27 which is normalized to unity area.

In Fig. 29 are shown $N_i(\epsilon_k)$ distributions calculated for He^+ and Kr^+ ions of 40-, 200-, and 1000-ev incident energy. The values of $E_i'(s_m)$ at 40 ev are those given in Table VIII. $E_i'(s_m)$ values at 200 and 1000 ev are determined from Fig. 23 using values of s_m calculated by Eq. (40) with $a=5\times10^8$ cm^{-1} and the corresponding values of A given in Table IX.

For simplicity of calculation, the values 0.707, 1.414, and 2.828 have been used for σ at 40, 200, and 1000 ev, respectively, in determining the $N_i(\epsilon_k)$ functions of

TABLE XII. Theoretical and experimental electron yields for 40 ev ions.

Ion	Calculated yield[a]	Measured yield
He^+	0.279	0.282
Ne^+	0.220[b]	0.232
Ar^+	0.050	0.097
Kr^+	0.027	0.048
Xe^+	0.012	0.017

[a] The calculation of these γ_i values involves a fit to the data for He^+ only from which fit the parameter $f=2.2$ has been determined.
[b] This is the value calculated assuming $f_N=0.9$, that is, using the composite $N_i(\epsilon_k)$ distribution of Fig. 27.

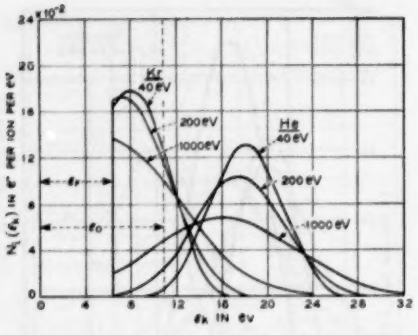

FIG. 29. Theoretical $N_i(\epsilon_k)$ distributions for He^+ and Kr^+ on clean tungsten corresponding to incident ion energies of 40, 200, and 1000 ev using σ values of 0.707, 1.414, and 2.828, respectively.

Fig. 29. These values approximate reasonably well those calculated from the equations of Sec. XII using $a=5\times10^8$ cm^{-1}. Table VIII indicates that for $a=5\times10^8$ cm^{-1} the value $\sigma=0.707$ is approximately correct for He^+ but large for the heavier ions. The distributions of Fig. 29 show that as incident energy increases the distribution broadens and its peak shifts to lower ϵ_k by virtue of the decrease in E_i'.

The $N_0(E_k)$ distributions which result from multiplication of the $N_i(\epsilon_k)$ functions of Fig. 29 by P_e from Eq. (55) with $f=2.2$ are shown in Fig. 30. The γ_i values calculated from these curves and other parameters characterizing the calculations are listed in Tables XIII and XIV for He^+ and Kr^+, respectively. Note

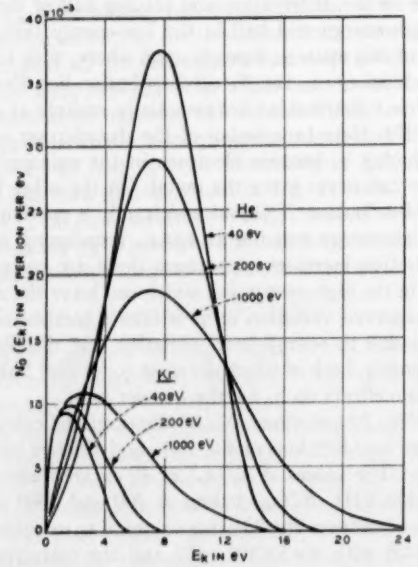

FIG. 30. Theoretical $N_0(E_k)$ distributions for He^+ and Kr^+ of 40, 200, and 1000 ev energy incident on tungsten, obtained from the $N_i(\epsilon_k)$ curves of Fig. 29 by use of the $P_e(\epsilon_k)$ escape probability of Eq. (55) in the text with $f=2.2$. γ_N values derived from these curves are listed in Tables XIII and XIV.

again that the theory is fitted to the experiment only for $\gamma_i(He^+)$ at 40 ev. Since both the effect of reduction in E_i' and increase in broadening is to reduce γ_i for He^+ we find the calculated γ_i in Table XIII reduces steadily with increasing $E_k(He^+)$. For Kr^+, on the other hand, reduction in E_i' reduces γ_i, but broadening increases γ_i. The net result, as the calculated γ_i values of Table XIV show, is to increase γ_i.

Because the σ values used here are perhaps large for Kr^+, a second series of calculations, also listed in Table XIV, were carried out for $\sigma=0$, 0.707, and 1.414 for 40-, 200-, and 1000-ev Kr^+ ions, respectively. The $N_i(\epsilon_k)$ and $N_0(E_k)$ functions for these cases are shown in Fig. 31. The calculated γ_i values first drop and then rise with increasing energy. Comparison with experiment shows that the correct values of σ must lie somewhere between the two sets of values used. This is perhaps evidence that a lies nearer 5×10^8 cm^{-1}, which

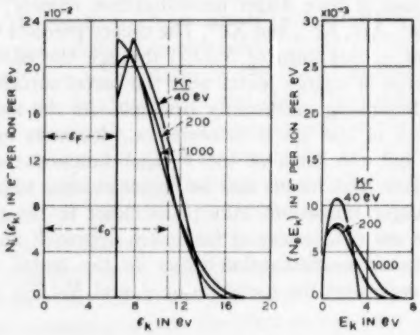

FIG. 31. Theoretical $N_i(\epsilon_k)$ and $N_0(E_k)$ distributions for Kr^+ of 40, 200, and 1000 ev energy incident on tungsten determined using σ values of 0, 0.707, and 1.414, respectively. γ_N values derived from the $N_0(E_k)$ curves are listed in Table XIV.

choice gives σ values which decrease in going from He^+ to Xe^+, than 2×10^8 cm^{-1}, for which choice σ is approximately constant (Table VIII).

For the cases of pure Auger neutralization it is evident that the theory can account for the initial drop in γ_i for He^+ and the slow rise in γ_i for Ar^+, Kr^+, and Xe^+ but cannot account for the rise at higher energies observed for He^+. This latter is thought to be the result of electron ejection by a process other than an Auger process setting in at higher energies. The reasons for this assignment are the following.

1. Other processes are known to set in at greater incident velocities. According to Ploch[8] the most probable of these is the release of bound electrons from surface atoms.

2. The deviation of experiment from what can be explained by the theory of Auger processes is observed first for He^+, the ion having the greatest velocity at a given ion kinetic energy. Ploch believes release of bound electrons from surface atoms to be purely velocity-

dependent for isotopic ions. It is thus not unreasonable to find such electrons first for He^+.

3. The extra electrons released at higher velocities of the ion are predominantly slow electrons which are not to be expected from the Auger process.

The principal effect of increasing ion energy on the form of the $N_0(E_k)$ distribution is to increase the high-energy tail. This is the direct result of the $N_i(\epsilon_k)$ distribution broadening and is to be observed in Figs. 30 and 31. Comparison of the theoretical curves with the experimental results (Figs. 12 and 14 of the accompanying paper)[7] again shows quite good agreement for He^+ and evidence that the true state of affairs for Kr^+ lies between those calculated for the two sets of σ values.

We turn now to discuss the variation of γ_i and $N_0(E_k)$ for the case of Ne^+ on clean tungsten. The evidence already presented makes it appear that the electrons ejected by Ne^+ arise predominantly in Auger neutralization with a small admixture from the two-stage process of resonance neutralization followed by Auger de-excitation. We expect the velocity dependence of the pure Auger neutralization of Ne^+ to lie between the He^+ and Ar^+ cases since a large portion but not all of the $N_i(\epsilon_k)$ distribution lies at $\epsilon_k > \epsilon_0$. γ_N for Ne is thus expected to drop with increasing ion velocity but not as drastically as is observed for He^+. We expect little if any ejection by non-Auger processes below 1000-ev ion energy for Ne^+. This conclusion is borne out by the relatively minor increase in slow electrons with increasing ion energy (see Fig. 13 and discussion in the accompanying experimental paper).[7] The yield γ_D of electrons which arise from pure Auger de-excitation in the case of Ne^+, although larger than γ_N, is also expected to drop with increasing ion velocity for reasons like those given to explain the He^+ case.

By far the largest factor in determining the variation of $\gamma_i(Ne^+)$ with ion energy is the variation of the factor f_N which determines the partition between Auger neutralization and Auger de-excitation. It has been shown in Sec. XI that as ion velocity increases we expect a decrease in f_N, thus an increase in the relative proportion of two-stage electron ejection. Since Auger de-excitation, on the average, produces faster electrons inside the metal than does Auger neutralization a decrease in f_N results in an increase in γ_i. This is proposed as the explanation for the rise in $\gamma_i(Ne^+)$ with velocity observed in the low-velocity range (Fig. 4 of accompanying paper).[7] A more detailed analysis of the variation of f_N with ion velocity, not given in this paper, shows that the required variation can be achieved with reasonable choices of the parameters determining the rate functions for resonance and Auger processes and the critical distance s_c. The final variation of $\gamma_i(Ne^+)$ with ion energy is, of course, a rather complicated averaging of the variations for pure Auger neutralization, pure Auger de-excitation, as well as the factor f_N which determines the relative proportion of the two.

TABLE XIII. Comparison of calculated and experimentally observed variation of γ_i with incident ion energy for He^+ on tungsten.

$E_k(He^+)$ (ev)	s_m (A)	$E_i'(s_m)$ (ev)	σ (ev)	γ_N calculated	γ_i measured
40	2.20	22.6	0.707	0.279	0.282
200	2.02	22.0	1.414	0.254	0.252
1000	1.84	20.6	2.828	0.231	0.253

We expect f_N to be nearly unity for 10-ev ions and, in fact, the experiment (Fig. 11 of the accompanying paper)[7] shows that the tail on the Ne^+ distribution due to Auger de-excitation has disappeared at 10 ev.

The success achieved in accounting for all the observed variations with ion energy makes it appear reasonable that the theory may be used to extrapolate the experimental measurements of γ_i to the near-thermal ion energies of interest in gas discharges. There has long existed a question as to the validity of using γ_i values measured for ions of 10 ev or greater energy in the quantitative consideration of electrical discharges through gases where the ion energies are more nearly 0.1 ev. It is felt that this point may now largely be settled inasmuch as the causes of the variations of γ_i with ion velocity appear to be known.

A first point which should be made concerns the acceleration of the ion toward the surface by the image force. One may calculate the value of s_m for ions which start toward the surface with negligible velocity by eliminating v_0 between the equations $A/av_0 = \exp(as_m)$ [from Eq. (40)] and $mv_0^2/2 = e^2/4s_m$ [from Eq. (56)] and solving graphically for s_m. This yields the values 2.6, 2.8, 3.4, 3.6, 4.0 A for He^+, Ne^+, Ar^+, Kr^+, and Xe^+, respectively. Equation (56) shows that the ions at these distances are moving with energies of 1.4, 1.3, 1.1, 1.0, and 0.9 ev, respectively. Thus ions which start toward the surface with negligible velocity are moving at the distances from the surface at which Auger neutralization takes place with velocities of the order of one-third those which ions of 10-ev incident energy possess. For this reason we expect the γ_i values of very slow ions to differ little from those measured for 10-ev ions. Theoretical estimates made by the methods of Sec. XIV indicate that for He^+ and Ne^+ γ_i values for very slow

TABLE XIV. Comparison of calculated and experimentally observed variation of γ_i with incident ion energy for Kr^+ on tungsten.

$E_k(Kr^+)$ (ev)	s_m (A)	$E_i'(s_m)$ (ev)	σ (ev)	γ_N calculated	γ_i measured
40	3.20	12.3	0.707	0.027	0.048
			0	0.023	
200	3.02	11.8	1.414	0.038	0.051
			0.707	0.021	
1000	2.84	10.5	2.828	0.072	0.059
			1.414	0.026	

ions should be very little (<5 percent) greater than those measured for 10-ev ions. The reason for this is the fact that the $N_i(\epsilon_k)$ distributions for these ions lie almost entirely at $\epsilon_k > \epsilon_0$ and the increase in $E_i'(s_m)$ and decrease in broadening which a decrease in v_0 entails have a small effect. For Ar^+, Kr^+, and Xe^+ the effect upon γ_i is perhaps larger because of the fact that $N_0(E_k)$, being composed of electrons in the high-energy tail of $N_i(\epsilon_k)$, is more sensitive to changes in $E_i'(s_m)$ and broadening. The indications are that γ_i for these ions at very low incident energies are greater than those measured at 10 ev by a factor which is no greater than 1.2. This rise in γ_i must be attributed almost entirely to the increase in $E_i'(s_m)$ with decrease in v_0.

XVI. CONCLUSIONS CONCERNING THE ELECTRONIC BAND STRUCTURE OF THE METAL

It is evident from the discussions of this paper that the characteristics of the Auger ejection processes are intimately bound up with the electronic band structure of the metal. Thus it is of interest to explore the possibilities of using these processes to provide information concerning the band structure of metals. The method has a number of distinct advantages. In the first place, the low-lying vacant energy level, which is provided for the Auger process by the incoming ion, may be varied in energy relative to the conduction band by the use of different ions. This possibility of observing the same process for a series of low-lying levels has turned out to be particularly fruitful. Also, the position of the vacant level in space is known to be just outside the metal surface. Thus these processes are bona fide surface effects which probe, in particular, the energy band structure near the surface. There are, to be sure, disadvantages inherent in the Auger processes which will become evident in the subsequent discussion.

We may look to the study of Auger ejection processes for information concerning the following items: 1. the form of the state density function $N_e(\epsilon)$, 2. the energy levels of the top and bottom of the filled portion of the conduction band, and 3. possible variation of the band near the metal surface.

Although the form of the $N_e(\epsilon)$ function plays a role in determining the form of the electron energy distribution $N_0(E_k)$, it is difficult to work back to $N_e(\epsilon)$ from an experimental $N_0(E_k)$. There are two reasons for this for the case of Auger neutralization. Here the form of $N_0(E_k)$ is determined principally by the Auger transform of $N_e(\epsilon)$ [Eq. (15)] rather than $N_e(\epsilon)$ itself. Figures 8 and 9 show how the transform distorts the state density function. Secondly, it is impossible to disentangle $N_e(\epsilon)$ from the possible variation of the matrix element with energy of the interacting electrons specified by the function $F(\epsilon',\epsilon'')$. However, some information concerning $F(\epsilon',\epsilon'')$ might be gained from the study of metals for which $N_e(\epsilon)$ is known. In the case of tungsten the reasonable agreement obtained between the calculated and observed forms for the $N_0(E_k)$ function for He^+ indicates that the assumptions that $N_e(\epsilon)$ and $F(\epsilon',\epsilon'')$ are constant cannot be seriously in error. It is evident that the form of $N_e(\epsilon)$ is to be judged from the $N_0(E_k)$ distributions for cases, like He^+ on tungsten, in which the $N_i(\epsilon_k)$ function lies entirely at $\epsilon_k > \epsilon_0$ and for which there is no admixture of Auger de-excitation. In such cases the effect of the escape probability on the form of the $N_0(E_k)$ function is minimized.

In the Auger de-excitation process the form of the final $N_0(E_k)$ function depends more directly on the $N_e(\epsilon)$ function, since $T'(\epsilon) = N_e(\epsilon)$. To use this process to study $N_e(\epsilon)$ it is necessary to find a situation in which it occurs without an admixture of Auger neutralization. It may not be impossible to find a metal-ion combination for which an excited level in the atom remains opposite the filled portion of the conduction band to a distance from the metal sufficiently small to allow the Auger de-excitation process to occur before reionization of the neutralized particle becomes possible.

Determination of the energy limits of the filled portion of the conduction band from Auger ejection processes appears to be more promising than determination of the form of $N_e(\epsilon)$. The energy of the top of the filled portion, φ ev below the vacuum level for metals, may be obtained roughly from the maximum energy observable in the $N_0(E_k)$ distribution. This is admittedly crude because of variation of energy levels and broadening of the distribution. A perhaps more sensitive indication of φ is to be obtained from the observations of the occurrence or nonoccurrence of the two-stage ejection process. Here again one must estimate the variation of energy levels to obtain a value of φ. In the case of Ne^+ on tungsten the high value of f_N which is still definitely less than unity indicates that s_e is most probably of the order of the value actually obtained using $\varphi = 4.5$ ev for tungsten. Whereas it is true that much better methods exist for finding the energy level of the top of the filled band in clean metals, it is not unreasonable to suppose that for metals covered with foreign atoms or for semiconductors the method described here may prove useful.

The energy level of the bottom of the filled part of conduction band, lying ϵ_0 ev below the vacuum level, may also be estimated on the basis of the Auger ejection data. If we consider all Auger neutralization processes to proceed at $s = s_m$, the maximum of the $P_t(s,v_0)$ function, a minimum electron energy greater than zero and equal to $E_i'(s_m) - 2\epsilon_0$ should result if $E_i'(s_m) > 2\epsilon_0$. It is difficult to observe this minimum directly because of the broadening of the distribution at its low energy end and because of the effect of target-collector geometry. For cases in which $E_i'(s_m) > 2\epsilon_0$ one should observe a depletion of low-energy electrons in the $N_0(E_k)$ distribution, however. This was observed to be the case for He^+ on tungsten for which the $N_0(E_k)$ curve (Fig. 7 of the accompanying paper)[7] at low energy is seen to lie definitely below those for Ne^+, Ar^+, Kr^+, and Xe^+.

The coincidence of the $N_0(E_k)$ curves for these other ions at low electron energy is what is expected if for these ions $E_i'(s_m) \leq 2\epsilon_0$. These observations are taken as experimental evidence that

$$\tfrac{1}{2}E_i'(s_m)_{\mathrm{Ne}} < \epsilon_0(W) < \tfrac{1}{2}E_i'(s_m)_{\mathrm{He}}. \tag{93}$$

The width of the filled portion of the conduction band, ϵ_F, is then obtained as $\epsilon_0 - \varphi$.

From Fig. 23 it appears that $E_i'(s_m)$ for both He^+ and Ne^+ of 40-ev energy is some two volts less than the corresponding E_i. Using $E_i'(s_m)_{\mathrm{He}} = 22.6$, $E_i'(s_m)_{\mathrm{Ne}} = 19.6$, and $\varphi(W) = 4.5$ ev we find

$$5.3 < \epsilon_F(W) < 6.8 \text{ ev}. \tag{94}$$

The observation of an appreciable depletion of slow electrons for He^+ must mean that $\epsilon_F(W)$ does not lie at or very near the upper bound. It appears unlikely also that $\epsilon_F(W)$ is as low as 5.3 ev, for then the minimum electron energy for He^+ would be 3.0 ev. A value somewhere near the middle of the above range, perhaps within 0.5 ev of the 6.4 value calculated by Manning and Chodorow[24] for tungsten, is indicated. Bearden and Snyder[38] estimate $\epsilon_F(W)$ to be 7.0 ± 0.5 and 6.5 ± 0.5 ev from the widths of the soft x-ray levels resulting from transitions from the conduction band to the L_{II} and L_{III} levels, respectively.

Finally, we discuss the information to be gained from the Auger ejection processes concerning the variation of energy levels inside the metal near the surface. Here admittedly one must compare the experimental results with data from other sources. In the case of tungsten, for example, it has been shown that the Auger processes indicate a φ of 4.5 ev and ϵ_F near 6.4 ev in agreement with other work. From this we must conclude that these values characterize the conduction band in tungsten right up to the surface. In the case of a solid for which the properties of the filled band deep in the lattice are known it is not inconceivable that the results of Auger ejection studies might indicate variations in the band near the surface of the solid.

The author wishes to acknowledge with thanks many helpful discussions with C. Herring, J. J. Lander, K. G. McKay, D. Sternberg, G. H. Wannier, and P. A. Wolff. C. Herring and D. Sternberg have kindly read and criticized the manuscript. Thanks are also due Miss B. B. Cetlin, who carried out the numerical calculations, and Miss M. C. Gray and R. W. Hamming for advice concerning the calculations.

Note added in proof.—The experimental values of γ_i quoted in this paper for Ar^+, Kr^+, and Xe^+ are somewhat too large for the reason given in the note added in proof to the preceding paper, in which note the magnitude of the effect is also given.

[38] J. A. Bearden and T. M. Snyder, Phys. Rev. **59**, 162 (1941)

Statistical Atom with Angular Momentum*

A. M. SESSLER† AND H. M. FOLEY
Columbia University, New York, New York

(Received July 12, 1954)

By means of a variational principle, the method of Thomas and Fermi is extended, in a semiclassical manner, to atoms with a net total angular momentum. The resulting equation for the potential, which is valid for large angular momentum, is solved for small angular momentum, yielding approximate charge and current distributions for atoms in P and D states. Orbital magnetic hyperfine structure, and electric quadrupole hfs are calculated as a function of atomic number, and it is shown that the first is in approximate agreement with experiment.

I. INTRODUCTION

THE method of Thomas[1] and Fermi[2] yields an approximate charge distribution for atoms with no net angular momentum. This method, because of statistical approximations and inexact treatment of quantization rules, is valid in the limit of large atomic number (implying a large number of electrons and high quantum numbers). In this limit, however, it is more accurate than the single-particle Hartree[3] method, for the statistical model is completely self-consistent, whereas the Hartree method assumes separability of the angular coordinates.

Certain atomic properties are particularly sensitive to the amount of correlation between electrons. In particular, the quadrupole coupling constant q can be related to the magnetic hfs coupling constant, if it is assumed that the last electron moves in a spherically symmetric potential caused by the nucleus and core of electrons.[4] Corrections to this, due to electron correlation, have been calculated by Sternheimer[5] starting from the Hartree single-particle model.

It was suggested by Rabi[6] that a completely self-consistent statistical model for an atom with angular momentum might, in the appropriate limit, be more accurate than the Hartree model, since it would include angular correlations and thus give immediately a result corresponding to the quadrupole shielding effect found by Sternheimer by a perturbation calculation. This paper is devoted to the treatment of the statistical model with a net total angular momentum.

In Sec. II, starting from a variational principle for the total energy of the atom, while keeping the total number of electrons and total angular momentum constant, we obtain a differential equation for the potential. It is then shown that this equation corresponds to uniform rotation of the atom as a whole.

In Sec. III we solve the previously mentioned equation approximately, and use the resulting solution to compute the magnetic field at the nucleus due to electron motion. This is in fair agreement with experiment. A corresponding calculation of q is in disagreement with Sternheimer's results. We will show that the statistical model is invalid for calculating phenomena of this type. The reason for this is that the statistical model (with its inexact treatment of quantization rules) leads to an atom model in which an excessive degree of configuration interaction has taken place. As a result the charge symmetric characteristics of actual atomic states have been lost, although the magnetic properties are affected to a much smaller degree.

Atomic units ($\hbar=m=e=1$) are employed throughout the paper.

II. DERIVATION OF THE BASIC EQUATION

As a starting point, we must determine the distribution of electrons in momentum space at some arbitrary point in configuration space. If these electrons are to have some net angular momentum about the origin, then they must have some net linear momentum. Clearly this can be best accomplished by displacing the usual spherical distribution of a totally degenerate electron gas ($T=0$) by an amount $\mathbf{D}$, as indicated in Fig. 1. This obvious result may easily be obtained formally, by the proceedures well known in statistical mechanics for maximizing the probability of the configuration in phase space.[7] One must simply add the constraint of a nonvanishing total angular momentum, to the usual constraints of total number and total energy.

The procedure now consists of evaluating the total energy of the atom, assuming that the atom consists of

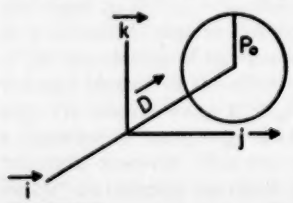

FIG. 1. Distribution of electrons in momentum space at some arbitrary point of configuration space.

* Supported in part by a grant from the National Science Foundation.

† National Science Foundation Postdoctoral Fellow now at Cornell University, Ithaca, New York.

[1] L. H. Thomas, Proc. Cambridge Phil. Soc. **23**, 542 (1927).
[2] E. Fermi, Z. Physik **48**, 73 (1928).
[3] D. Hartree, Proc. Cambridge Phil. Soc. **24**, 89 (1928).
[4] Davis, Feld, Zabel, and Zacharias, Phys. Rev. **76**, 1076 (1949).
[5] R. Sternheimer, Phys. Rev. **84**, 244 (1951).
[6] I. I. Rabi (private communication).
[7] R. W. Gurney, *Introduction to Statistical Mechanics* (McGraw-Hill Book Company, Inc., New York, 1949), p. 35.

completely degenerate electrons whose configuration is specified by $\mathbf{D}(\mathbf{r})$ and $P_0(\mathbf{r})$. The total energy is then minimized subject to two constraints, namely that the total number of electrons is N, and the total angular momentum is J. The angular momentum is treated classically, and J_z is taken equal to J.

$$\mathcal{E}_k=\frac{2}{(2\pi\hbar)^3}\int d\mathbf{r}\int_{\text{sphere}} d\mathbf{p}\frac{p^2}{2m}=\int d\mathbf{r}\left[\frac{P_0{}^5}{10\pi^2}+\frac{P_0{}^3D^2}{6\pi^2}\right], \quad (1)$$

$$\mathcal{E}_P=\tfrac{1}{2}\int d\mathbf{r}\int d\mathbf{r}'\frac{n(\mathbf{r})n(\mathbf{r}')}{|\mathbf{r}-\mathbf{r}'|}-\int d\mathbf{r}n(\mathbf{r})V_N(\mathbf{r}), \quad (2)$$

where

$$n(\mathbf{r})=\frac{2}{(2\pi\hbar)^3}\int_{\text{sphere}} d\mathbf{p}=\frac{1}{3\pi^2}P_0{}^3, \quad (3)$$

V_N = potential of the nucleus,

$$N=\int d\mathbf{r}n(\mathbf{r}), \quad (4)$$

and

$$\mathbf{J}=\int d\mathbf{r}\mathbf{r}\times\mathbf{D}(\mathbf{r})n(\mathbf{r})=\int d\mathbf{r}D(\mathbf{r})r\sin\theta n(\mathbf{r}) \quad (5)$$

[where (r,θ,φ) are spherical polar coordinates]. We have anticipated the result and set $\mathbf{D}(\mathbf{r})$ in the $\boldsymbol{\theta}_0$ direction. We now eliminate the variable $P_0(\mathbf{r})$ in favor of $n(\mathbf{r})$, and introducing the Lagrangian multipliers λ and μ, we have for the quantity to be minimized

$$\mathcal{E}=\int d\mathbf{r}\left\{\frac{(3\pi^2)^{5/3}}{10\pi^2}n^{5/3}+\frac{D^2n}{2}\right\}+\frac{1}{2}\int\int\frac{n(\mathbf{r})n(\mathbf{r}')d\mathbf{r}d\mathbf{r}'}{|\mathbf{r}-\mathbf{r}'|}$$
$$-\int d\mathbf{r}n(\mathbf{r})V_N+\lambda\int d\mathbf{r}rD\sin\theta n(\mathbf{r})+\mu\int d\mathbf{r}n(\mathbf{r}). \quad (6)$$

A straightforward variation with respect to D yields

$$D(\mathbf{r})=\lambda r\sin\theta. \quad (7)$$

Variation with respect to $n(\mathbf{r})$, with the double integral in the potential energy taken into account, yields

$$-\frac{\lambda^2r^2\sin^2\theta}{2}+\frac{5}{3}\frac{(3\pi^2)^{5/3}n^{\frac{1}{3}}}{10\pi^2}-\varphi+\mu=0, \quad (8)$$

where

$$\varphi(\mathbf{r}')=V_N-\int d\mathbf{r}\frac{n(\mathbf{r})}{|\mathbf{r}-\mathbf{r}'|}=\text{potential at }\mathbf{r}'. \quad (9)$$

We eliminate $D(\mathbf{r})$ and solve for $n(\mathbf{r})$. Invoking Laplace's equation, we obtain

$$\nabla^2\varphi=\frac{4}{3\pi}\{2(\varphi-\mu)+\lambda^2r^2\sin^2\theta\}^{\frac{1}{2}}, \quad (10)$$

with the boundary conditions that

$$\text{and}\qquad \begin{aligned} r\varphi&\to z \quad \text{as} \quad r\to 0,\\ r\varphi&\to 0 \quad \text{as} \quad r\to\infty. \end{aligned} \quad (11)$$

The parameters λ and μ are determined through Eqs. (4) and (5).

Examination of $D(\mathbf{r})=\lambda r\sin\theta$ shows that the model corresponds to a rigid sphere rotating uniformly with angular velocity λ. The associated centrifugal potential is $\frac{1}{2}\lambda^2r^2\sin^2\theta$, which makes the effective potential at a point $\mathbf{r}$:

$$\varphi_{\text{electric}}+\tfrac{1}{2}\lambda^2r^2\sin^2\theta. \quad (12)$$

Thus we see that Eq. (10) can be obtained immediately from the usual Thomas-Fermi equation with the insertion of this effective potential. We have established the interesting fact that a statistical atom with angular momentum rotates as a whole.

III. APPROXIMATE SOLUTION AND APPLICATIONS

We are interested in atoms in P states ($J=1$), and hence λ small. Thus we may solve Eq. (10) by a perturbation method. Expanding the right-hand side in powers of λ^2 and μ, we obtain

$$n(\mathbf{r})=\frac{1}{3\pi^2}(2\varphi)^{\frac{1}{2}}+\frac{1}{2\pi^2}(2\varphi)^{\frac{1}{2}}(\lambda^2r^2\sin^2\theta-2\mu). \quad (13)$$

Let

$$\text{and}\qquad \begin{aligned} n(\mathbf{r})&=n_0(r)+\lambda^2n_1(\mathbf{r})\\ \varphi(\mathbf{r})&=\varphi_0(r)+\lambda^2\varphi_1(\mathbf{r}), \end{aligned} \quad (14)$$

where φ_0 satisfies

$$\nabla^2\varphi_0(r)=\frac{4}{3\pi}(2\varphi_0)^{\frac{1}{2}}=4\pi n_0, \quad (15)$$

and is the well-known[8] solution to the Thomas-Fermi equation. From Eqs. (4) and (7),

$$J=\lambda\int r^2\sin^2\theta n(\mathbf{r})d\mathbf{r}. \quad (16)$$

Thus we may set $n(\mathbf{r})=n_0(r)$ in Eq. (16), and obtain λ directly with a relative error of only λ^2 (typically $\lambda=0.03$). By the well-known change of variables this may be put in universal form, i.e., the atomic number Z may be eliminated.

Inserting Eq. (14) into Eq. (10) we obtain

$$\nabla^2\varphi_1-\frac{4}{\pi}(2\varphi_0)^{\frac{1}{2}}\varphi_1=\frac{2}{\pi}(2\varphi_0)^{\frac{1}{2}}(\lambda^2r^2\sin^2\theta-2\mu), \quad (17)$$

which is an eigenvalue equation for μ. We thus have

$$n_1(\mathbf{r})=\frac{1}{\pi^2}(2\varphi_0)^{\frac{1}{2}}\varphi_1+\frac{1}{2\pi^2}(2\varphi_0)^{\frac{1}{2}}(\lambda^2r^2\sin^2\theta-2\mu). \quad (18)$$

[8] V. Bush and S. H. Caldwell, Phys. Rev. **38**, 1898 (1931).

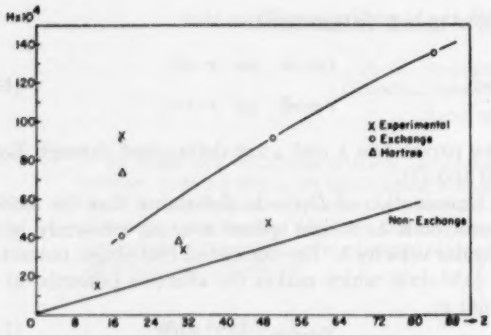

FIG. 2. Magnetic field at the nucleus, due to electron orbital motion, as a function of atomic number.

In order to get a more accurate result, the theory and calculations were repeated including exchange.[9] φ_0 now has the property of being zero outside of a cut-off radius r_0. In the perturbation analysis we assumed that r_0 did not change with the introduction of angular momentum. Allowing for a change in r_0 is possible,[10] but rather complicated. Including this effect would not affect the magnetic hyperfine coupling, nor would it change the results for the quadrupole coupling in an essential way. For the theory with exchange the equation cannot be put in to universal form, and numerical calculations were carried through for $Z=18$, $Z=50$, and $Z=84$.[11]

In order to compare with experiment, we calculated the magnetic field at the nucleus due to the orbital motion of the electrons.

$$H=\frac{e}{2mc}\int\frac{\mathbf{j}(\mathbf{r})\times\mathbf{r}}{r^3}d\mathbf{r}. \tag{19}$$

Thus, with negligible error

$$H=\frac{8}{9\pi}\left(\frac{\lambda}{137}\right)\int_0^\infty(2\varphi_0)^{\frac{1}{2}}rdr. \tag{20}$$

This gives, in the nonexchange approximation,

$$H=ZJ(0.73\times10^4)\text{ gauss}. \tag{21}$$

This, as well as values including exchange, and values obtained from the Hartree method, are compared with experimental values (obtained from $\Delta\nu$ and known nuclear magnetic moments) in Fig. 2. Note how the statistical method averages the effect of shell structure.

The quadrupole coupling constant q is given by

$$q=\int P_2(\cos\theta)n(\mathbf{r})d\mathbf{r}/r^3. \tag{22}$$

For $Z=18$, φ_1 was evaluated and shown to contribute to q an amount of the same order of magnitude as the contribution of the second term in Eq. (18). Using only this second term, we obtain in the nonexchange approximation

$$q=-\frac{27\pi J^2}{80}\frac{\int(2\varphi_0)^{\frac{1}{2}}rdr}{\left[\int(2\varphi_0)^{\frac{1}{2}}r^4dr\right]^2}. \tag{23}$$

The integral is weakly divergent at large r, and must be cut off at a reasonable value, yielding

$$q=-(J^2/Z^{\frac{1}{3}})(0.002). \tag{24}$$

For the model with exchange, in the same approximation

$$q_{18}=-2.2\times10^{-3},\quad q_{50}=-9.0\times10^{-4},\quad\text{and}\quad q_{84}=-4.5\times10^{-4}. \tag{25}$$

It will be observed that these values are two orders of magnitude smaller than Sternheimer's results.

That this is reasonable may be seen by noting that the statistical model does not take into account properly the spatial charge distribution associated with quantum-mechanical angular momentum. The statistical atom model can not hope to yield properties which vary in the characteristic way of the Periodic Table, even though one has explicitly inserted the proper angular momentum. In particular, q changes sign in actual atoms according as one considers atoms with one more or one less electron than corresponds to a closed shell. The magnetic properties do not behave in this manner, since the connection with angular momentum is more direct. (We may note how the atomic magnetic moment is given directly by the angular momentum, whereas the atomic quadrupole moment is only indirectly related to the angular momentum.)

[9] P. A. M. Dirac, Proc. Cambridge Phil. Soc. **26**, 376 (1930).

[10] P. Gombás, *Die Statistische Theorie des Atoms und ihre Anwendungen* (Springer Verlag, Berlin, 1949), p. 79.

[11] We are indebted to Dr. L. H. Thomas who kindly supplied us with solutions to the statistical atom with exchange.

Gamma Radiation from Deuterons on Several Light Nuclei*

L. C. THOMPSON†
The Rice Institute, Houston, Texas
(Received July 13, 1954)

A single crystal NaI scintillation spectrometer has been used to measure the energy of gamma rays from $B^{10}+d$, $B^{11}+d$, $N^{14}+d$, $C^{13}+d$, $F^{19}+d$, and $Si^{28}+d$. Several gamma rays were found and their energy and relative intensity are given. It is also deduced what transitions these gamma rays represent.

INTRODUCTION

ONE of the ways to study the energy levels of nuclei is to measure the energy and relative intensity of the gamma rays produced under charged particle bombardment. This has not been done completely for low-energy gamma rays from deuteron bombardment of several light elements. Pair spectrometers have been used to study the high-energy gamma rays from most deuteron reactions among the light elements.[1–4] The low-energy gamma rays have been studied in the case of Li^7+d, Be^9+d, $C^{12}+d$, and $C^{13}+d$.[5] This investigation concerns low-energy gamma rays from $B^{10}+d$, $B^{11}+d$, $N^{14}+d$, $F^{19}+d$, $C^{12}+d$, and $Si^{28}+d$.

APPARATUS AND EXPERIMENTAL PROCEDURE

A NaI scintillation spectrometer was used to measure the energy of the gamma rays produced. A NaI crystal 1½ inches in diameter by 1 inch in length, commercially prepared by The Harshaw Chemical Company, was mounted on a Du Mont 6292 photomultiplier tube in the standard manner. The pulses from the photomultiplier tube went through a standard cathode follower preamplifier, an A-1 linear amplifier, a single channel pulse-height analyzer, and scaler. The photoelectric peak of the 661-kev gamma ray from Cs^{137} had a full width at half-maximum of not more than 10 percent and a peak to valley ratio not less than 18 to 1.

The deuterons were accelerated by the 2-Mev Rice Institute Van de Graaff accelerator. The magnetic analyzer and regulator were used to hold the beam at constant energy. The NaI crystal was placed directly behind the target that was to be bombarded by deuterons. The axis of the NaI photomultiplier tube combination coincided with the extension of the line of flight of the deuteron beam. The distance of the front face of the crystal from the target varied from 1 inch to 10 inches depending on the intensity of the gamma rays from the reaction.

Differential pulse-height curves were run from 10 volts to 60 or more volts. The window of the pulse-height analyzer was set at 1.00 volt, and points were taken every volt. The number of gamma rays from the target were monitored by the current integrator. Statistics on the points shown are between 2 and 3 percent.

The energy of an unknown gamma ray was measured by first changing the gain of the amplifier until the peak to be measured was between 40 and 50 volts. Several alternating runs were made over the peak to be measured and over a calibration peak chosen to be as close as possible to the unknown peak. A rotating target holder was used, and the beam was allowed to bombard a silver blank while running on the calibration peak.

Background was almost negligible above a γ-ray energy of 600 kev. Below 600 kev, however, difficulties were experienced because of low-energy gamma radiation produced in the NaI crystal by neutrons and also because of the annihilation radiation from some of the reaction products.

$B^{10}+d$

The B^{10} target was made of 96 percent B^{10} and 4 percent B^{11}. Targets were made both by evaporating elemental boron off a tungsten filament upon a silver blank in a vacuum and by pressing elemental boron upon a silver blank.

No gamma rays from $B^{10}+d$ could be resolved below the well-known 4.46-Mev gamma ray from $B^{10}(d,p)B^{11}$.[1–4] There seemed to be several unresolved peaks between 1.5 and 2.5 Mev. Many attempts were made to resolve these gamma rays but without success. Annihilation radiation and neutron background made it difficult to see weak low-energy lines. However, no strong low-energy lines were present.

$B^{11}+d$

The B^{11} target was composed of 81 percent B^{11} and 19 percent B^{10}. It was made by evaporating natural boron off a tungsten filament upon a silver blank.

The pulse-height distribution of B^{11} bombarded by 1.05-Mev deuterons is shown in Fig. 1. The upper curve was taken at a higher amplifier gain than the lower curve. The peaks marked 940 kev and 1.64 Mev are the photoelectric peaks of gamma rays of these

* Supported in part by the U. S. Atomic Energy Commission.
† Now at the Naval Research Laboratory, Washington D. C.
[1] J. Terrell and G. C. Phillips, Phys. Rev. **83**, 703 (1951).
[2] J. Bame, Jr., and L. M. Baggett, Phys. Rev. **84**, 891 (1951).
[3] Rutherglen, Rae, and Smith, Proc. Phys. Soc. (London) **A64**, 906 (1951).
[4] Bent, Bonner, and Sippel, Phys. Rev. **91**, 472 (1953); and private communication.
[5] R. G. Thomas and T. Lauritsen, Phys. Rev. **88**, 969 (1952).

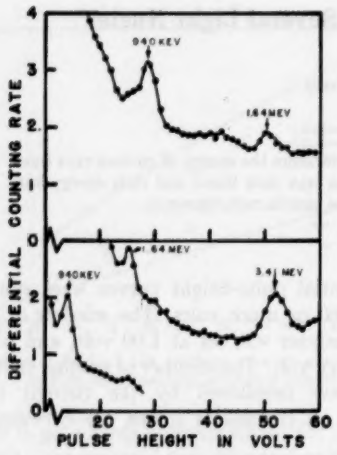

FIG. 1. Pulse-height distribution obtained from $B^{11}+d$.

energies. They probably represent the decay to the ground state of the 0.947- and 1.65-Mev levels[6] in B^{12} made by the $B^{11}(d,p)B^{12}$ reactions. The peak marked 3.41 Mev is the pair peak with the escape of both annihilation photons of the well-known 4.43-Mev gamma ray from the $B^{11}(d,n)C^{12}$ reaction.[1-3] The relative intensities of the 940-kev, 1.64-Mev, and 4.43-Mev gamma rays are approximately 2, 1, and 2.

$N^{14}+d$

The N^{14} target was made by pressing CrN upon a silver blank. The pulse height distribution of this target bombarded by 1.05-Mev deuterons is shown in Fig. 2. The upper curve was taken at a higher amplifier gain than the lower curve.

The peak marked 1.88 Mev is the photoelectric peak of a 1.88-Mev gamma ray. It probably represents a cascade decay of the 7.16-Mev level in N^{15} (made by the $N^{14}(d,p)N^{15}$ reaction) to the 5.28- or 5.31-Mev levels[7] in N^{15}. This may be deduced for the following reasons: (1) the 1.88-Mev gamma ray is almost exactly the correct energy for this transition, (2) work with a pair spectrometer on the $N^{14}+d$ reaction indicates that all levels in N^{15} below 10-Mev decay directly to the ground state except the 7.16-Mev level,[4] (3) the ratio of the intensity of the 1.88-Mev gamma ray to the intensity of the 5.3-Mev gamma ray is equal within the large experimental errors to the ratio of the proton yield from the 7.16-Mev level to the total proton yield from the 5.28-, 5.31-, and 7.16-Mev levels reported elsewhere.[8]

From a study of the angular distribution of protons from the $N^{14}(d,p)N^{15}$ reaction, Gibson and Thomas report that either the 7.32- or 7.16-Mev levels in N^{15} or both have a spin of $\frac{1}{2}+$ or $\frac{3}{2}+$ and that the 5.31- and 5.28-Mev levels have a large spin.[9] It may be concluded, therefore, that the 7.32-Mev level has the spin $\frac{1}{2}+$ on $\frac{3}{2}+$ since it does decay directly to the ground state[4] and that the 7.16-Mev level has spin $\frac{5}{2}$ or more.

The peak marked 0.84 Mev may be a combination of three effects. (1) The pair peak with the escape of both annihilation photons of the 1.88-Mev gamma ray would be expected to give a small peak. However, this peak is probably too large to be attributed to this effect alone. (2) It may be that the 7.16-Mev level does decay to the 6.33-Mev level as well as the doublet at 5.3 Mev. This is still in keeping with our earlier conclusion since Gibson and Thomas conclude that the 6.33-Mev level may have a spin as large as $\frac{5}{2}-$. If this cascade to the 6.33-Mev level does occur, the cascade to the 5.3-Mev doublet occurs at least 20 times as often. (3) There is always some oxygen impurity in the target and the 875-kev gamma ray from $O^{16}(d,p)O^{17}$ would be expected.

The peak marked 3.40 Mev is probably the pair peak with the escape of both annihilation photons of the 4.43-Mev gamma ray from the $N^{14}(d,\alpha)C^{12}$ reaction. The relative intensities of the 1.88-Mev, 4.43-Mev, and 5.3-Mev gamma rays are approximately as 2.5, 1, and 7.

$C^{12}+d$

A C^{12} target was made by cracking methyl iodide on a heated tungsten filament. Besides the well-known 3.08-Mev gamma ray from $C^{12}(d,p)C^{13}$, a higher energy component of 3.68 Mev has been reported at 3-Mev deuteron bombarding energy.[10] This gamma ray

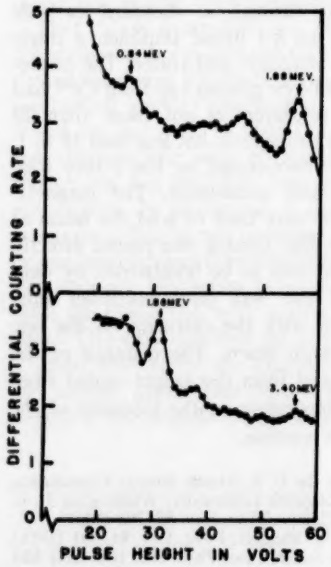

FIG. 2. Pulse-height distribution obtained from $N^{14}+d$.

[6] F. Ajzenberg and T. Lauritsen, Revs. Modern Phys. **24**, 321 (1952); see p. 354.
[7] See reference 6, p. 371.
[8] R. Malm and W. W. Buechner, Phys. Rev. **80**, 771 (1950).
[9] W. M. Gibson and E. E. Thomas, Proc. Roy. Soc. (London) **210**, 543 (1952).
[10] See reference 6, p. 363.

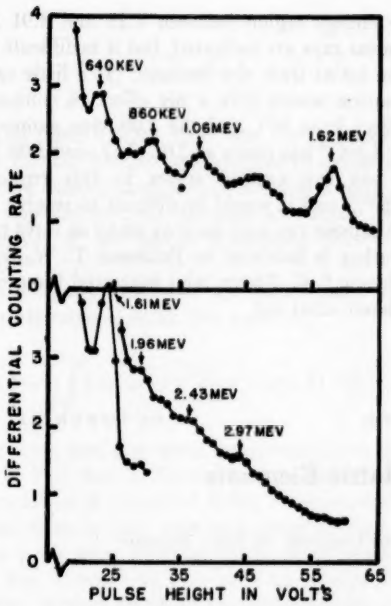

FIG. 3. Pulse-height distribution obtained from $F^{19}+d$.

presumably comes from the decay of the 3.68-Mev level in C^{13} to the ground state. It was thought interesting to see if this higher energy component could be detected at deuteron bombarding energies below 2 Mev.

At 1.35-Mev deuteron bombarding energy this higher energy component could not be detected. At 1.60 Mev a component of about 3.7-Mev energy was detected with an intensity about 1/20 that of the well-known 3.08-Mev gamma ray.

$F^{19}+d$

The F^{19} target was made by evaporating CaF off a tungsten filament upon a silver blank. The pulse-height distribution obtained from $F^{19}+d$ at a deuteron bombarding energy of 1.05 Mev is shown in the upper half of Fig. 3. The peak marked 1.62 Mev corresponds to the photoelectric peak of a gamma ray of 1.62-Mev energy. It results from the decay to the ground state of the 1.63-Mev level[11] in Ne^{20}. This level may be excited directly in the $F^{19}(d,n)Ne^{20}$ reaction, but most of its intensity comes from the beta decay of F^{20} [12] made in the $F^{19}(d,p)F^{20}$ reaction to the 1.63-Mev level in Ne^{20}. From intensity studies with beam "on" and "off", it was concluded that the peak was due almost entirely to the $F^{19}(d,p)F^{20}$ reaction.

The peaks marked 640 kev and 1.06 Mev may be attributed to the decay to the ground state of the 0.65- and 1.06-Mev levels[12] of F^{20}. This result seems logical since the proton groups to these levels are more intense than to any other low-lying levels in F^{20}.[13]

The gamma ray marked 860 kev may be due to the decay to the ground state of O^{17} made in the $F^{19}(d,\alpha)O^{17}$ reaction. On the other hand, this same gamma ray may arise from an oxygen impurity in the target and come from $O^{16}(d,p)O^{17}$. Below 640 kev the only intense lines were the 0.11- and 0.19-Mev gamma rays of F^{19} from inelastic scattering. The relative intensities of the 640-kev, 1.06-Mev, and 1.62-Mev gamma rays are 1, 2.5, and 9.

The lower curve in Fig. 3 was made on the 6-Mev Van de Graaff at a bombarding energy of 3.97 Mev. The results suggest a gamma ray of 2.97-Mev energy upon almost a continuum of gamma-ray energies. So many gamma rays are possible from $F^{19}+d$ that it is almost impossible to determine with any certainly what transition the 2.97-Mev gamma ray represents.

QUARTZ+d

A block of quartz $\frac{3}{4}$ in.$\times\frac{3}{4}$ in.$\times\frac{1}{4}$ in. was used as a target. Quartz is almost pure SiO_2. Silicon is 92 percent Si^{28}. Therefore, the target was largely one atom of Si^{28} to two atoms of O^{16}.

This target was bombarded with 1.35-Mev deuterons. At this bombarding energy, no gamma rays from O^{16} except the 875-kev gamma ray from $O^{16}(d,p)O^{17}$ are expected. The most intense higher energy gamma rays would be expected from $Si^{28}+d$.

The pulse-height distribution above 1-Mev gamma-ray energy from quartz+d at 1.35-Mev bombarding energy is shown in Fig. 4. The three peaks in the lower curve marked 3.91, 4.39, and 4.86 Mev all are pair peaks of the same gamma ray and probably represent the decay to the ground state of any or all of the

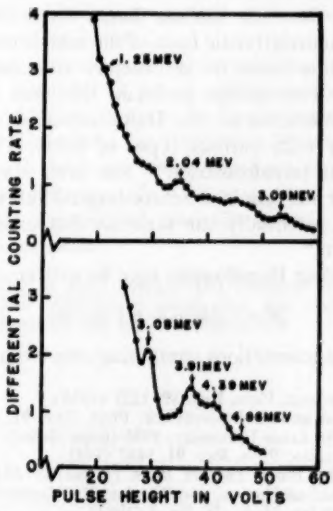

FIG. 4. Pulse-height distribution obtained from quartz+d.

[11] See reference 6, p. 390.
[12] See reference 6, p. 388.
[13] H. A. Watson and W. W. Buechner, Phys. Rev. 88, 1324 (1952).

4.84-, 4.90-, and 4.93-Mev levels[14] in Si^{29}. Below 1.2 Mev the curve rises because the 875-kev gamma ray from O^{16} is much stronger than any of the gamma rays from Si^{28}. When the region in the neighborhood of the change of slope marked 1.25 Mev in the upper curve was investigated under more favorable conditions of counting rate and window width, a peak was found at a gamma-ray energy of 1.25 Mev. This probably comes from the $Si^{28}(d,p)Si^{29}$ reaction and represents the decay to the ground state of the 1.28-Mev level[14] in Si^{29}.

[14] Endt, Van Patten, Buechner, and Sperduto, Phys. Rev. 83, 491 (1951).

In the energy region between 1.25 and 3.91 Mev, other gamma rays are indicated, but it is difficult to be conclusive for at least two reasons: (1) a little carbon contamination would give a big effect in comparison to the effect from Si^{28}, and the 3.08-Mev gamma ray from $C^{12}(d,p)C^{13}$ has peaks at 2.06, 2.57, and 3.08 Mev; (2) Si^{29} has five excited states in this region by $Si^{28}(d,p)Si^{29}$,[14] and it would be difficult to resolve them since one gamma ray may have as many as three peaks.

The author is indebted to Professor T. W. Bonner and Professor J. R. Risser, who suggested the problem and rendered other aid.

PHYSICAL REVIEW VOLUME 96, NUMBER 2 OCTOBER 15, 1954

Nuclear Forces and β Decay Matrix Elements

ROLAND F. HERBST
Argonne National Laboratory, Lemont, Illinois and St. Louis University, St. Louis, Missouri

(Received July 15, 1954)

The matrix elements of β decay are reduced to nonrelativistic form under the assumption that the nuclear Hamiltonian contains interactions involving odd operators. Particular attention is given to an interaction which gives rise to a spin orbit effect.

THE effect of nuclear forces on the β-decay matrix elements which involve odd operators has been discussed by a number of authors.[1–7] The matrix element of prime interest in these papers has been the pseudoscalar matrix element.

Peaslee[3] and Rose and Osborn[6] have shown that if the nuclear forces are due to two-body interactions and if these interactions are limited to even-even or odd-odd operators, then the nuclear forces have little effect upon the nonrelativistic form of the matrix elements.

Since there exists no satisfactory treatment of the relativistic two-nucleon problem, this note is limited to a consideration of the Hamiltonian of a nucleon interacting with various types of fields. The Foldy-Wouthysen transformation[8,9] has been employed to reduce the problem to a Schroedinger-Pauli form. This method is essentially the same as that used by Rose and Osborn.[6]

The nuclear Hamiltonian may be written as

$$H=-\beta M-\boldsymbol{\alpha}\cdot\mathbf{p}+\mathcal{E}+\mathcal{O}; \tag{1}$$

$\mathcal{E}$ indicates interactions containing only even operators and $\mathcal{O}$, odd operators.[10] Interactions involving only even operators affect the nonrelativistic form to the matrix elements by adding only terms of order $1/M^2$, and these should be negligible.[6] However, Konopinski[7] has suggested that if the nuclear "Thomas" term,[11] a second-order term, is for some reason large enough to account for the nuclear inverted doublets, then one would also expect the effect, also second order, on the pseudoscalar matrix element of the scalar nuclear potential to be enhanced. Rather than consider such anomalous effects, we will consider only contributions of terms in $\mathcal{O}$ which are of first order in $1/M$.

In general $\mathcal{O}$ has the form

$$\mathcal{O}=\boldsymbol{\alpha}\cdot\mathbf{V}+i\beta\boldsymbol{\alpha}\cdot\mathbf{F}+\gamma_5\theta+i\beta\gamma_5\varphi. \tag{2}$$

The $\mathbf{V}$, $\mathbf{F}$, θ, and φ are field quantities with the proper transformation properties.

In the low energy limit, the β decay matrix elements become[2]

$$\int\boldsymbol{\alpha}\approx-(1/M)\int[\mathbf{p}-\mathbf{V}-\boldsymbol{\sigma}\times\mathbf{F}-\theta\boldsymbol{\sigma}], \tag{3a}$$

$$i\int\beta\boldsymbol{\alpha}\approx(1/M)\int[\boldsymbol{\sigma}\times\mathbf{p}+\boldsymbol{\sigma}\times\mathbf{V}-\mathbf{F}-\varphi\boldsymbol{\sigma}], \tag{3b}$$

$$\int\gamma_5\approx(1/M)\int[\boldsymbol{\sigma}\cdot\mathbf{p}-\boldsymbol{\sigma}\cdot\mathbf{V}-\theta], \tag{3c}$$

[1] M. Ruderman, Phys. Rev. 89, 1227 (1953).
[2] R. Herbst and A. Bushkovitch, Phys. Rev. 91, 442 (1953); also thesis, St. Louis University, 1953 (unpublished).
[3] D. C. Peaslee, Phys. Rev. 91, 1447 (1953).
[4] H. Takebe, Progr. Theoret. Phys. (Japan) 10, 673 (1953).
[5] Alaga, Kofoed-Hansen, and Winther, Kgl. Danske Videnskab. Selskab, Mat-fys. Medd. 28, No. 3 (1953).
[6] M. E. Rose and H. K. Osborn, Phys. Rev. 93, 1315 (1954).
[7] E. J. Konopinski, Phys. Rev. 94, 492 (1954).
[8] L. L. Foldy and S. A. Wouthysen, Phys. Rev. 78, 29 (1950).
[9] W. Barker and Z. Chraplyvy, Phys. Rev. 89, 446 (1953).

[10] We have set $\hbar=c=m=1$, where m is the mass of the electron.
[11] D. R. Inglis, Phys. Rev. 50, 783 (1936); H. W. Furry, Phys. Rev. 50, 784 (1936).

and

$$i\int\beta\gamma_5\approx-(1/M)\int[\sigma\cdot\mathbf{F}-\varphi]. \qquad (3d)$$

The first terms in (3a), (3b), and (3d) are independent of the nuclear interactions and are in agreement with Rose and Osborn[6] and Ahrens and Feenberg.[12] No such term appears in (3d) because all terms containing derivatives of the lepton covariants have been discarded.[13]

The obvious extension to higher-order forbidden matrix elements is valid. For example,

$$\int\alpha\times\mathbf{r}\approx\frac{1}{M}\int[\mathbf{r}\times\mathbf{p}-\mathbf{r}\times\mathbf{V}-\mathbf{r}\times(\sigma\times\mathbf{F})-\theta\mathbf{r}\times\sigma]. \qquad (3c)$$

One must now give some interpretation to the quantities $\mathbf{V}$, $\mathbf{F}$, θ, and φ. These could be considered as the field variables of quantized fields. Ruderman[1] discussed the last term in (3d) from this point of view. In this case φ is the wave function of the pseudoscalar meson field. Any attempt to give such an interpretation is, however, subject to all of the uncertainties of meson field theories.

As a first approximation one may attempt to treat $\mathbf{V}$, $\mathbf{F}$, θ, and φ as classical fields. However, it is difficult to understand how θ or φ can be central and still conserve parity. Vector interactions ($\mathbf{V}$) give rise to velocity-dependent forces, and little is known about the existence of such forces in the nucleus. The tensor interaction ($\mathbf{F}$) lends itself to the most immediate interpretation.

Gaus[14] has shown that if the nuclear Hamiltonian contains a term $i\beta\boldsymbol{\alpha}\cdot\mathbf{F}$, then the nonrelativistic Hamiltonian will contain a spin-orbit term. If $\mathbf{F}$ is set equal to $f(r)\mathbf{r}$, then in the nonrelativistic limit the Hamiltonian will contain the terms

$$-[f(r)/M]\boldsymbol{\sigma}\cdot\mathbf{r}\times\mathbf{p}-(1/2M)[f^2(r)r^2+f'(r)r+3f(r)]. \qquad (4)$$

The last terms contribute only a small amount to the central nuclear potential, and so in a phenomenological theory the magnitude of $f(r)$ may be adjusted to fit known spin orbit energies.

If such a term is considered, (3d) becomes

$$i\int\beta\gamma_5\approx-(1/M)\int f(r)\boldsymbol{\sigma}\cdot\mathbf{r}. \qquad (3d')$$

This is of the same form as the matrix element derived by Konopinski[7] in connection with the "Thomas" term. If we use the estimate for the spin-orbit energies that the average of $f(r)/M$ lies between 2 and 4, then we see that the pseudoscalar matrix element and also the terms in (3a) and (3b) involving $\mathbf{F}$ are not negligible.

It might be mentioned here that a term $i\beta\boldsymbol{\alpha}\cdot\mathbf{r}f(r)$ also affects the electromagnetic properties of a proton. In an electromagnetic field a new term appears in the low energy limit*

$$(e/M)f(r)\boldsymbol{\sigma}\cdot\mathbf{r}\times\mathbf{A}. \qquad (5)$$

If $\mathbf{A}$ were, for example, the vector potential of a constant magnetic field, the magnetic moment of the proton may be calculated, and the g factor becomes

$$g=1\pm\frac{2\mu_p-1}{2l+1}\mp\langle f(r)r^2\rangle\frac{j+\frac{1}{2}}{j(j+1)};\ j=l\pm\tfrac{1}{2}. \qquad (6)$$

The first two terms are the usual g factor while the last is a correction due to the tensor interaction. Since $\langle f(r)r^2\rangle\approx1$, this effect tends to lower the $j=l+\frac{1}{2}$ Schmidt line and raise the $j=l-\frac{1}{2}$ line by about $\frac{1}{2}$ a nuclear magneton. This "suppression" of proton moments does not seem large enough to be discerned among the many uncertainties about nuclear moments.

These considerations indicate that the nonrelativistic form of the β-decay matrix elements is quite dependent upon the assumptions about nuclear forces and that even an order of magnitude calculation to the pseudoscalar matrix element must wait until much more is known of nuclear forces.

The author would like to express his gratitude to Dr. A. V. Bushkovitch for his advice on that part of this work which was done at St. Louis University, and also to the University for sponsoring his appointment as a Research Associate under Argonne's Participating Institutions Program. He also wishes to thank Dr. Coester, Dr. Hamermesh, and Dr. Kurath for many valuable discussions.

[12] T. Ahrens and E. Feenberg, Phys. Rev. **86**, 64 (1952).
[13] Ahrens, Feenberg, and Primakoff, Phys. Rev. **87**, 663 (1952).
[14] H. Gaus, Z. Naturforsch. **7a**, 44 (1952).

* *Note added in proof.*—Jensen and Goeppert-Mayer, Phys. Rev. **85**, 1040 (1952), have shown that this electromagnetic effect should exist for any spin-orbit interaction.

Elastic Scattering of Alpha Particles by Carbon*

J. W. Bittner† and R. D. Moffat
Department of Physics, University of Wisconsin, Madison, Wisconsin
(Received June 7, 1954)

By using a propane gas target and 4.0- to 7.6-Mev alpha particles from an electrostatic generator the elastic scattering differential, cross section of carbon has been measured with high resolution at five angles. A phase-shift analysis of the data indicates levels in O^{16} with the following energies, angular momenta, and parities: 10.36 Mev, $J=4$, +; 11.25 Mev, $J=0$, +; 11.51 Mev, $J=2$, +; 11.62 Mev, $J=3$, −; and 12.43 Mev, $J=1$, −. Reduced widths of the 10.36, 11.25, and 11.62 Mev levels approach the Wigner limit for single-particle excitation. Comparison is made with levels predicted by the alpha-particle nuclear model.

I. INTRODUCTION

THE study of a variety of reactions involving O^{16} has permitted assignment of numerous energy levels in that nucleus.[1] One of these processes is the elastic scattering of alpha particles by C^{12}, in which the compound nucleusO^{16*} is an intermediate state. In the light of dispersion theory,[2] anomalies in the elastic differential scattering cross section may be interpreted in terms of energy levels of the compound nucleus. Elastic scattering is a particularly desirable method for levels below 11.6 Mev in O^{16} since no other reactions can compete with the elastic scattering to cause ambiguity in the determination of level widths.

Hill[3] has reported such a scattering experiment performed with high resolution in the energy range 0.5 to 4.0 Mev. Resonances lying immediately above this range have been reported[4] but assignment of angular momenta and widths was not possible because of limitations in resolution. Recently a new He^{++} ion source[5] in the Wisconsin electrostatic generator has made available a beam of doubly charged alpha particles with energy up to 7.6 Mev. It seemed desirable therefore to extend the high-resolution experiments beyond 4 Mev.

Since C^{12} and He^4 are both nuclei of zero spin, the compound nucleus can be formed only in states with parity and total angular momentum equal to those of the colliding pair. Thus only O^{16} states with parity and angular momentum both even or both odd will be detected by elastic scattering.

II. EXPERIMENTAL PROCEDURE

The doubly charged alpha-particle beam from the electrostatic generator was passed through the magnetic and 90° electrostatic analyzer, which was operated at 0.15 percent energy resolution, i.e., full width at half-maximum intensity. The beam then entered a differentially pumped scattering chamber containing the propane gas target and was collected in a Faraday cup for integration. This apparatus has been described in the literature.[6]

Two proportional counters, separated from the target gas by side windows of 0.01-mil Ni foil, were used simultaneously to detect the alpha particles scattered at two angles. Pulse height was monitored with the aid of an oscilloscope and the discrimination level was set to avoid counting small noise and background pulses. For most of the energy range, an additional 0.02-mil Al foil was placed over the forward angle counter to stop recoil protons from the propane.

For convenience in analysis of the data four center-of-mass angles were selected for which the Legendre polynomials of order one to four vanish. These angles were: 147.9°, 140.8°, 123.2°, and 90.0°; at which vanish (or nearly so) the polynomials of order: $l=4$, $l=3$, $l=2$, and both $l=1$ and 3, respectively. At the extreme back angle of 171.2° all partial waves contribute to the scattering.

The propane gas pressure was varied between 0.25 and 1.1 cm Hg, depending on the magnitude and rate of variation of the scattered intensity. For 6-Mev alpha particles these pressures produced an effective target thickness of from 2.5 to 10 kev at 90° and 10 to 45 kev at 171.2°.

In order to make corrections for energy lost by the beam between the differential pumping entrance slits and the target volume, the resonances at 4.3 and 7.0 Mev were measured using various gas pressures. It was assumed that the beam energy loss was proportional to the gas pressure, for a given incident energy. This permitted calculation of the energy loss per unit gas pressure at the two energies 4.3 and 7.0 Mev. Since these rates were proportional to Bethe's[7] energy-loss cross section curves for alpha particles at these energies, the same proportionality was assumed for all incident energies. Energy loss in traversing the chamber varied with gas pressure and energy from 30 to 160 kev. At no energy is the uncertainty in energy greater than 10 kev. The 0.15 percent resolution of the electrostatic

* Work supported by the Wisconsin Alumni Research Foundation and the U. S. Atomic Energy Commission.
† Now at the Brookhaven National Laboratory, Upton, Long Island, New York.
[1] F. Ajzenberg and T. Lauritsen, Revs. Modern Phys. 24, 321 (1952).
[2] E. P. Wigner and L. Eisenbud, Phys. Rev. 72, 29 (1947).
[3] R. W. Hill, Phys. Rev. 90, 845 (1953).
[4] A. J. Ferguson and L. R. Walker, Phys. Rev. 58, 666 (1940).
[5] J. W. Bittner, Rev. Sci. Instr. (to be published).
[6] H. L. Jackson *et al.*, Phys. Rev. 89, 365 (1953).
[7] M. S. Livingston and H. A. Bethe, Revs. Modern Phys. 9, 245 (1937).

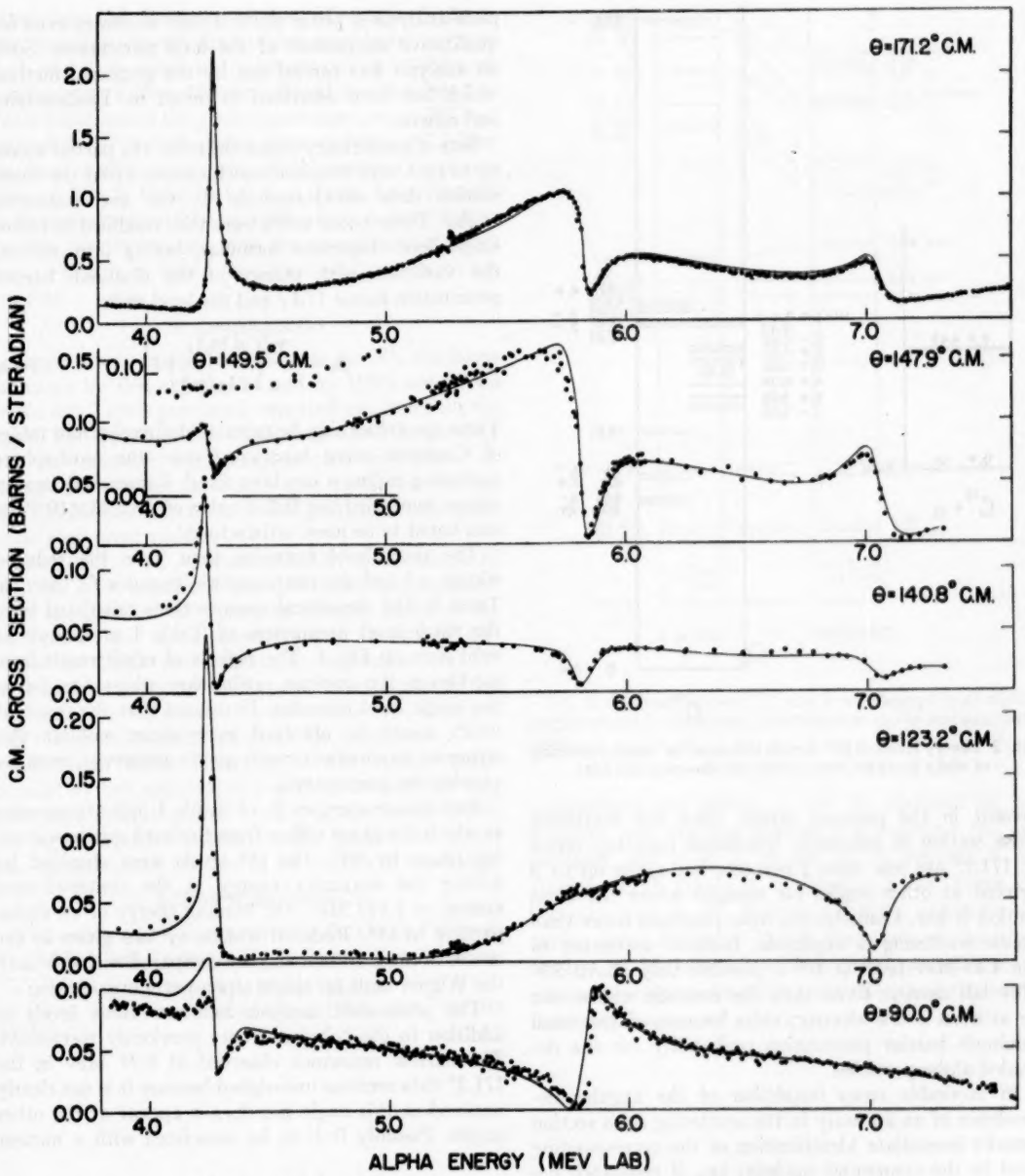

FIG. 1. Differential elastic scattering cross section of carbon for alpha paticles. The points are experimental data. The solid lines are a theoretical fit.

analyzer resulted in a spread of 6 to 11.4 kev about the central value. At the extreme back angle of 171.2° points were spaced at intervals of 8.5 kev for energies between 3.8 and 6.0 Mev, 11.4 kev from 6.0 to 6.6 Mev, and at 18-kev intervals above 6.6 Mev. At other angles points were taken less frequently except in regions where structure was expected because of the back-angle data.

III. DATA AND ANALYSIS

The points of Fig. 1 show the center-of-mass cross sections as a function of laboratory alpha-particle energy. For compactness the 171.2° cross sections are reduced in scale by a factor of ten relative to the others. Corrections have been applied for counter geometry and energy loss in the gas. No correction has been made for the one percent natural isotopic abundance of C^{13}

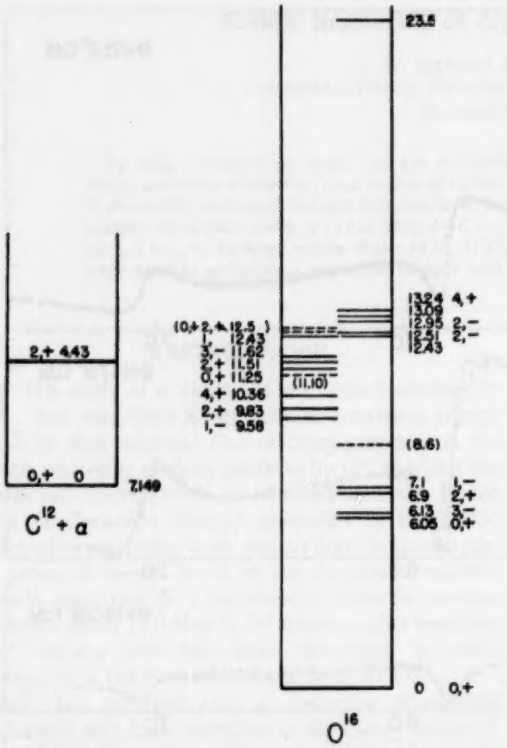

FIG. 2. Energy levels of O^{16}. Levels indicated by elastic scattering of alpha particles from carbon are shown at the left.

present in the propane target, since the scattering cross section is unknown. Statistical counting errors at 171.2° are less than 2 percent, but range up to 5 percent at other angles for energies where the cross section is low. Contribution from processes other than elastic scattering is negligible. Inelastic scattering to the 4.43-Mev level of C^{12} is possible only above 5.9-Mev lab energy. Even then the inelastic widths can be at most a few electron volts because of the small Coulomb barrier penetration probability for the degraded alpha particles.

In favorable cases inspection of the angular dependence of an anomaly in the scattering cross section permits immediate identification of the corresponding level in the compound nucleus; i.e., if resonance behavior is apparent at all angles except one, then the level must have the angular momentum and parity of the Legendre polynomial which vanishes at this angle. Such cases are the resonance at 4.28 Mev which vanishes only at 149.5° and is assigned $J=4, +$; the level at 5.82 Mev missing at 123.2° and hence $J=2, +$; and the $J=1, -$ level at 7.04 Mev identified by its absence at 90°.

However, the effect of any very broad level or of a $J=0$ level, which has a small effect at all angles, may be too subtle to be recognized so easily. A more complete analysis of phase shifts is then necessary even for qualitative assignment of the level parameters. Such an analysis was carried out by the graphical method which has been described in detail by Laubenstein[8] and others.

Sets of preliminary phase shifts for the partial waves up to $l=4$ were obtained which exactly fitted the cross-section data simultaneously at the five scattering angles. These phase shifts were then modified to follow single level dispersion formulas, taking into account the variation with energy of the Coulomb barrier penetration factor $1/A_l^2$ and the level shift

$$\Delta_\lambda = -\frac{\gamma_\lambda^2}{a}\left[\frac{d\ln A_l}{d\ln(kr)}+l\right] \qquad r=a.$$

These quantities may be calculated directly from tables of Coulomb wave functions,[9] once the hard-sphere scattering radius a has been fixed. Larger and smaller values were tried but Hill's[3] value of $a=5.43\times10^{-13}$ cm was found to be most satisfactory.

The single-level formulas then gave the reduced widths γ_λ^2 and the characteristic energies E_λ listed in Table I. The theoretical cross sections calculated from the single-level parameters of Table I are shown as solid lines on Fig. 1. The regions of misfit result from modifying the various preliminary phases to follow the single level formulas. It seemed that the exact fit which could be obtained everywhere without this stringent requirement could not be preserved, even by varying the parameter a.

Reseonance energies E_r of Table I indicate energies at which the phase differs from the hard sphere scattering phase by 90°. The O^{16} levels were obtained by adding the resonance energy in the center-of-mass system to 7.149 Mev, the binding energy of an alpha-particle in O^{16}. Reduced widths γ_λ^2 are given in the center-of-mass system and are compared with $\frac{3}{2}(\hbar^2/\mu a)$, the Wigner limit for single alpha-particle excitation.

The phase-shift analysis indicates three levels in addition to the "obvious" ones previously mentioned. The narrow resonance observed at 5.27 Mev in the 171.2° data remains unassigned because it is not clearly resolved at this angle nor does it appear at the other angles. Possibly it is to be associated with a nucleus

TABLE I. Summary of resonances.

J, Π	E_λ(lab) (Mev)	E_r(lab) (Mev)	Γ(lab) (kev)	γ_λ^2(c.m.) (Mev-cm)	O^{16*} (Mev)	Percent $\frac{3\hbar^2}{2\mu a}$
4, +	4.37	4.28	36	0.99×10^{-12}	10.36	26
(?)	···	5.27	10	···	11.10(?)	···
0, +	5.20	5.47	3300	3.0×10^{-12}	11.25	76
2, +	5.85	5.82	106	0.13×10^{-12}	11.51	3
3, −	6.82	5.96	1600	2.8×10^{-12}	11.62	73
1, −	7.07	7.04	230	0.17×10^{-12}	12.43	4

[8] R. A. Laubenstein and M. J. W. Laubenstein, Phys. Rev. **84**, 18 (1951).

[9] I. Bloch *et al.*, Revs. Modern Phys. **23**, 147 (1951).

other than O^{16}. Behavior of the $l=0$ and $l=2$ phases near the upper energy limit of this experiment suggests 0, + and 2, + levels in the vicinity of 12.5 Mev with widths greater than 100 kev. These are not listed in Table I because of the great uncertainty, but a 35° $l=2$ and nearly 90° $l=0$ resonant phase increase at 7.0 Mev has been used in calculating the theoretical cross sections of Fig. 1. Energies listed in Table I are thought to be correct within 20 kev, while errors in level widths are less than 10 percent, with the exception of the $l=0$ level, which is so broad that greater uncertainties are possible.

IV. CONCLUSION

Figure 2 is an energy level diagram for O^{16}. The levels indicated by this experiment and by Hill's are shown at the left. Levels previously reported are shown on the right. The broad 10.36, 11.25, and 11.62 levels may well be identified with single-particle excitation, although there is the possibility of a fortuitous overlap of wave functions for a number of particles which could cause such great widths.

The 10.36 $J=4$, + level is surely to be associated with the 4, + rotational level predicted by Dennison[10] from consideration of the alpha-particle model of the nucleus. In the accompanying paper Dennison[11] discusses in detail the remarkable agreement for O^{16} between the observed levels and those predicted by the alpha-particle model. Figure 3 shows the observed and theoretically predicted levels for comparison.

Additional levels occurring in the energy range covered by this experiment would not be found if they have even J values and odd parity or vice versa. Levels having experimental widths of less than 5 kev would also be undetected because of limitations in resolution.

V. ACKNOWLEDGMENTS

The authors wish to express their thanks to Professor R. G. Herb and Professor H. T. Richards for their encouragement and advice, to Dr. W. Haeberli for his guidance and untiring assistance throughout the experiment, and to R. L. Becker, E. D. Berners, S. E. Darden, R. H. Davis, A. S. Divatia, K. W. Jones, A. Okazaki, and R. B. Walton for their assistance in taking data. Professor D. M. Dennison of the University of Michigan has been most cooperative in communicating results of his calculations and discussing their pertinence.

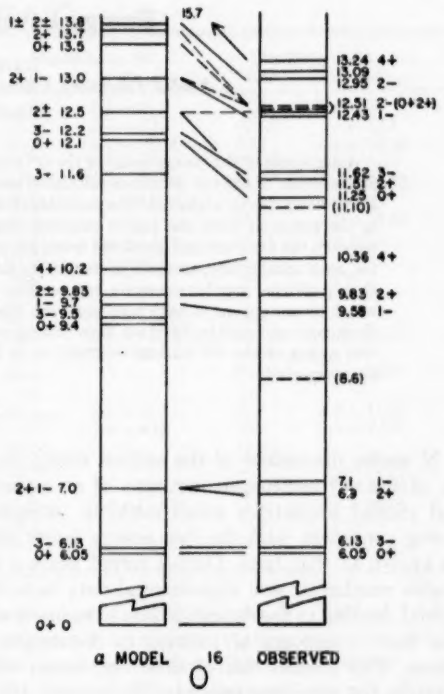

FIG. 3. Observed levels of O^{16} and levels obtained from alpha-particle model by Dennison. [Identification (a) of accompanying paper].

[10] D. M. Dennison, Phys. Rev. **57**, 454 (1940).
[11] D. M. Dennison, following paper [Phys. Rev. **96**, 378 (1954)].

Energy Levels of the O^{16} Nucleus

DAVID M. DENNISON
Randall Laboratory, University of Michigan, Ann Arbor, Michigan
(Received June 7, 1954)

A discussion of the energy levels of the O^{16} nucleus is given on the basis of an α-particle model. A considerable number of excited states are calculated under the assumption that the higher order rotation-vibration interactions can be neglected. The positions of the levels depend upon four parameters, three of which relate to the potential while the fourth measures the effective radius of the nucleus. Two possible correlations between the observed and predicted levels are made. The first identification, which appears to be somewhat the more satisfactory, succeeds in correlating sixteen levels in the range from 0 to 13.25 Mev with regard to their positions, angular momenta and parities. Five levels are predicted in the range from 9.5 to 13.8 Mev which do not appear to have been observed. However, three levels have been found in this range but as yet their spins and parities have not been determined and no attempt has been made to assign them. The effective radius of the O^{16} nucleus is found to be 2.5×10^{-13} cm which is somewhat smaller than might have been expected.

AN earlier discussion[1] of the excited energy states of the O^{16} nucleus on the basis of an α-particle model yielded predictions which could be interpreted as being consistent with the two energy levels which were known at that time. During recent years a considerable number of new experimental data have been obtained, leading to the determination of so many more levels that it appears of interest to re-examine the problem. The present list of observed levels, which is given in the preceding paper by Bittner and Moffat[2] contains (including the normal state) seventeen levels whose angular momenta and parities have been meaured together with three levels of unknown momentum and parity. As will appear, the agreement between the observed and predicted levels, while by no means perfect, seems sufficiently good to suggest that the α-particle model when applied to this particular nucleus, may well contain some elements of correctness. This result is rather surprising since it is not believed that the nucleons within a nucleus have any strong tendency to form α-particle groups, as shown by the fact that, in the overwhelming majority of cases, the α-particle model fails as conspicuously as the shell model succeeds.

It is possible that the reasons for the applicability of the α-particle model in the case of O^{16} may be of the following sort. The nucleus in its normal state is undoubtedly almost spherical in form. If the spherical volume is divided into four equal parts, each part will, on the average contain two protons and two neutrons. Thus even a weak tendency on the part of the nucleons to form α particles can result in imposing a tetrahedral symmetry on the sphere and this is all that is required, at least for the qualitative applicability of the α-particle model. Tetrahedral symmetry is very close to spherical symmetry and it is for this reason that one may expect that the validity of the model may be greater for O^{16} than, for example, for C^{12} or Ne^{20}. In one sense a model consisting of four mass particles at the corners of a regular tetrahedron represents an approximation to the more complex situation of sixteen masses filling a volume which is predominantly spherical but which possesses a certain amount of tetrahedral symmetry. The advantage of employing the simpler model is that the methods of obtaining its energy levels are all well known from the theory of polyatomic molecules and the results may be written down at once. Experience in approximating the vibrations and rotations of a continuum by dividing the region into a series of discrete masses indicates that the model should predict the lower energy states reasonably well but that it will fail to account for all of the higher states.

The model to be discussed is subject to the following assumptions: (1) the O^{16} nucleus is replaced by four α particles with equilibrium positions at the corners of a regular tetrahedron, (2) the vibration rotation levels will be calculated using the molecular approximation and neglecting all higher order interactions, (3) only those levels will be considered whose wave functions are invariant under an interchange of any two α particles. (Bose-Einstein statistics.)

These assumptions are identical with those employed in the earlier paper[1] and the same notation will be retained here. A number of extensions and comments should be made.

1. The Coriolis interaction between the internal angular momentum $\zeta\hbar$ associated with the vibration ω_3 and the total angular momentum $J\hbar$ was only given for one particular case. In general, when these momenta are parallel, perpendicular, or antiparallel, $I_{n_3J}=[-2J\zeta+2\zeta^2-2\zeta]\hbar^2/2A$, $[2\zeta^2-2\zeta]\hbar^2/2A$, or $[2J\zeta+2\zeta^2]\hbar^2/2A$, respectively. For the vibrational levels[3] $\omega_3\hbar$, $(\omega_1+\omega_3)\hbar$, and $(\omega_2+\omega_3)\hbar$, $\zeta=-1/2$; while for that part of $2\omega_3\hbar$ possessing an internal angular momentum, $\zeta=+1/2$. For all of the other states listed, $\zeta=0$.

2. The motions corresponding to the three normal vibrations may be described as follows. In ω_1 (the

[1] D. M. Dennison, Phys. Rev. **57**, 454 (1940).
[2] J. W. Bittner and R. D. Moffat, preceding paper [Phys. Rev. **96**, 374 (1954)].
[3] M. Johnston and D. M. Dennison, Phys. Rev. **48**, 868 (1935). Shaffer, Nielsen, and Thomas, Phys. Rev. **56**, 1051 (1939).

TABLE I. The energy levels of O^{16}.

						Identification (a)		Identification (b)	
n_1	n_2	n_3	J	p	$E/\hbar$	E_{calc}	E_{obs}	E_{calc}	E_{obs}
0	0	0	0	+	0	0	0+=0	0	0+=0
0	0	0	3	−	$6R$	(6.13)	3−=6.13	(6.13)	3−=6.13
0	0	0	4	+	$10R$	10.2	4+=10.36	10.2	4+=10.36
1	0	0	0	+	ω_1	(6.05)	0+=6.05	(6.05)	0+=6.05
1	0	0	3	−	ω_1+6R	12.2	3−=11.62	12.2	3−=11.62
0	1	0	2	±	ω_2+3R	(9.83)	2+=9.83	(6.9)	2+=6.9
0	1	0	4	±	ω_2+10R	17.0	···	14.0	4+=13.25
0	0	1	1	−	$\omega_3+9R/4$	(7.0)	1−=7.1	(7.1)	1−=7.1
0	0	1	2	+	$\omega_3+9R/4$	(7.0)	2+=6.9	7.1	···
0	0	1	3	−	$\omega_3+19R/4$	9.5	···	9.6	···
0	0	1	3	−	$\omega_3+27R/4$	11.6	···	11.7	···
0	0	1	4	+	$\omega_3+43R/4$	15.7	4+=13.25	15.8	···
2	0	0	0	+	$2\omega_1$	12.1	0+=11.25	12.1	0+=11.25
0	2	0	0	+	$2\omega_2$	13.5	0+=12.51	7.6	···
0	2	0	2	±	$2\omega_2+3R$	16.6	···	10.7	2+=9.83
0	0	2	0	+	$2\omega_3$	9.4	···	9.6	···
0	0	2	2	±	$2\omega_3+3R$	12.5	2+=11.51	12.7	2+=11.51
0	0	2	1	−	$2\omega_3+R/4$	9.7	1−=9.58	9.9	1−=9.58
0	0	2	2	+	$2\omega_3+17R/4$	13.7	···	13.9	···
1	1	0	2	±	$\omega_1+\omega_2+3R$	15.9	···	12.9	2−=12.51
1	0	1	1	−	$\omega_1+\omega_3+9R/4$	13.0	1−=12.43	13.1	1−=12.43
1	0	1	2	+	$\omega_1+\omega_3+9R/4$	13.0	2+=12.51	13.0	2+=12.51
0	1	1	1	±	$\omega_2+\omega_3+9R/4$	13.8	···	9.9	···
0	1	1	2	±	$\omega_2+\omega_3+9R/4$	13.8	2−=12.95	9.9	···

so-called breathing motion) $q_1=q_2=q_3=q_4=q_5=q_6$. In ω_2, which may be described as a two-dimensional torsional motion in which all particles move on the surface of a sphere, $q_1=q_2$, $q_3=q_4$, $q_5=q_6$ subject to the condition $q_1+q_3+q_5=0$. In the triple degenerate motion ω_3, $q_1=-q_2$, $q_3=-q_4$, and $q_5=-q_6$.

3. The tunnel motion, by which two of the α particles are interchanged, is more intimately connected with ω_2 rather than with ω_3 as stated in reference 1. It is expected that the tunnel energy will be larger for the state $n_2=1$ than for the normal state and larger still if $n_2=2$. A reconsideration of the tunnel energy appears to lead to the conclusion that with the present information regarding the nucleus, it is almost impossible to make a reliable estimate of its magnitude but that it is probably very small, presumably in the kev range. For this reason the tunnel energy has been omitted from the table of levels. When both of the tunnel levels are allowed by the statistics, the parity is designated ±.

4. A rather complete discussion of the symmetry species of the various vibrational and rotational wave functions is given by Jahn[4] for the methane molecule. The adaptation to the present model can be made by simply omitting the fourth methane frequency ω_4 and by setting the spin of each particle (α particle) equal to zero.

The energy expressions for the levels, together with their vibrational numbers $n_1\ n_2\ n_3$, angular momenta J, and parities are listed in the first six columns of Table I. As an abbreviation R is written in place of $\hbar/A$.

There appear to be two more or less obvious ways of correlating the predicted and observed levels. In both identifications (a) and (b), the 3− level at 6.13 Mev is interpreted as a pure rotation state, the 0+ level at 6.05 becomes the first vibrational state of ω_1, while the 1− level at 7.1 is associated with the first vibrational state of ω_3. Under identification (a) the 2+ level at 6.9 is set equal to the 2+ level of the first excited state of ω_3. The zeroth-order theory predicts that this level should coincide with the 1− level but of course small perturbations could easily account for the difference between 6.9 and 7.1. The last identification is the 2+ level at 9.83 which becomes the first excited level of ω_2. The four constants R, ω_1, ω_2, and ω_3 have now been determined and all the remaining levels are now fixed, at least, in zeroth approximation. In the first column under Identification (a) in Table I, the predicted levels are given while in the second column the observed levels are listed. Predicted levels higher than about 16 Mev are not given since this is both above the present range of observations (13.24 Mev) as well as being of dubious significance from the point of view of the validity of the theory.

The second column under Identification (a) lists those observed levels which can readily be accounted for. In all but one case (4+=10.36 which will be discussed later), the measured energies lie below the predicted positions by amounts which for the most part are less than 1 Mev. These displacements are in the direction that would be given by higher order interaction terms and their magnitudes are not unreasonably large. A study of Table I shows that with the aid of four parameters, sixteen levels have been correlated (although perhaps not wholly unambiguously) with regard to their positions, angular momenta and parities. Five levels are predicted in the range from 9.5 to 13.8 Mev which do not appear to have been observed. On

[4] H. A. Jahn, Proc. Roy. Soc. (London) **A168**, 469 (1938).

TABLE II. The parameters of O^{16}.

	R	ω_1	ω_2	ω_3	a	b	c
Identification (a)	1.02	6.05	6.77	4.7	3.42	−0.94	1.73
Identification (b)	1.02	6.05	3.8	4.8	1.86	−0.13	0.09

the other hand in this range, three levels (at 8.6, 11.10, and 13.09 Mev) have been found but their spins and parities are not known and hence no attempt has been made to assign them. Only one observed level, $2-=12.51$, finds no obvious counterpart in the predicted list although it may possibly be the other member of the pair $2\pm$ predicted at 12.5 Mev. It should perhaps be pointed out that the experimental method employed by the Wisconsin group of investigators would not have revealed the existence of the $2-$level in the pairs $2\pm$ even if the splittings were large enough to be observed.

Identification (b) differs from (a) in only one respect: the level $2\pm$ associated with the first excited state of ω_2 is assigned $2+=6.9$. Fifteen of the observed levels are accounted for. Many of the correlations are the same as under (a) but there are some differences. Eight levels in the range from 7.1 to 13.9 Mev are predicted but not assigned. Three of these might correspond to the three observed levels of unknown spin and parity. On the whole there seems to be little reason to choose between (a) and (b), although perhaps (a) is slightly superior in that it predicts fewer low-lying levels which are not observed.

The four parameters R, ω_1, ω_2, and ω_3, in Mev for both identifications are given in Table II together with the potential constants a, b, and c described in reference 1. These latter are given in units of 10^{20} dynes/cm. Both sets of potential constants are not unreasonable. The set under (b), where b and c are both negligible in comparison with a ,would describe a potential function between the α particles which would correspond to almost pure central forces.

Although four parameters have been used in describing the energy levels, one of these, $R=\hbar/A$, is adjustable only within a very narrow range since it is closely connected with the dimensions of the nucleus. The moment of inertia A may be set equal to $2\sum Mr_0^2/5$, the formula for the moment of inertia of a uniformly dense sphere of radius r_0 and total mass $\sum M$. In this calculation the tetrahedral symmetry superimposed upon the sphere has been disregarded. A substitution of $R=1.02$ Mev yields $r_0=2.5\times10^{-13}=1.0\times10^{-13}\mathfrak{A}^{\frac{1}{3}}$ cm, where $\mathfrak{A}=16$, the atomic weight. This figure is not too far out of line with recent measurements[5] of nuclear radii using electron diffraction methods although it is about 10 to 15 percent smaller.

The general agreement shown in Table I between the observed and predicted levels appears to be fairly satisfactory, but there exist a number of causes for uneasiness in taking it at its face value. Among these are the following.

1. The assumption of the grouping of nucleons into α particles within a nucleus receives so little confirmation in the over-all picture of nuclear structure.

2. The two levels $3-=6.13$ and $4+=10.36$ Mev have been assigned to states of pure rotation. Their energies, on the basis of a rigid rotator should be in the ratio of 3 to 5. Thus, if the $3-$ level is taken to be correct, the $4+$ level should lie at 10.22 Mev. If the nucleus is not rigid, the centrifugal distortion, at least for any of the usual types of restoring forces, will always tend to lower the energy. In disagreement with this prediction the observed $4+$ level is slightly higher than 10.22 Mev. The next higher pure rotation level $6\pm$ would lie well outside the present range of observation at about 21 Mev.

3. The molecular approximation implies that the Hamiltonian can be developed as a power series in a parameter of smallness. This parameter may be chosen in a number of ways, one of which is to take the ratio of a rotational to a vibrational frequency, for example, R/ω_i. From Table II this is seen to be of the order of 0.2. In the case of the tetrahedral molecule of methane, $R/\omega_i\simeq0.004$. The higher order interaction terms for methane are approximately one or two percent of the zeroth-order terms, and on this basis one would expect that the agreement between the observed and calculated levels of O^{16} might be substantially worse than appears to be the case. It is, however, difficult to assess the reliability of these considerations since the forces between the particles in a molecule are essentially long range forces. Shorter-range, more abruptly varying, forces will tend to increase the rigidity of the nucleus and this in turn may substantially decrease the magnitude of the interaction terms.

I would like to express my thanks to Professor Hugh T. Richards for suggesting a re-examination of the α-particle model and to Professor T. Venkatarayudu for his help in preparing the list of energies, spins, and parities predicted by the model.

[5] Pidd, Hammer, and Raka, Phys. Rev. 92, 436 (1953).

Inelastic Neutron Scattering in Iron*

D. L. Lafferty, L. A. Rayburn, and T. M. Hahn
Department of Physics, University of Kentucky, Lexington, Kentucky
(Received February 23, 1954; revised manuscript received June 1, 1954)

The gamma-ray spectrum from the inelastic scattering of *D-D* neutrons in iron has been obtained using an unshielded single-crystal NaI spectrometer. A ring-type geometry permitted subtraction of the background rate from the total rate: this yields a complex spectrum attributed to the inelastic scattering in iron. Energies have been assigned to the peaks of the complex spectrum indicating gamma-rays of 2.66, 2.10, 1.76, 1.59, 1.42, 1.24, 0.989, 0.851, 0.634, and 0.462 Mev.

MONOENERGETIC neutrons of 2.7 Mev were used to excite iron nuclei through inelastic collision. The de-excitation gamma rays were detected by a single-crystal NaI spectrometer consisting of a 1 in. by 1½ in. diameter NaI crystal mounted on a Du Mont 6292 photomultiplier tube. A ring-type geometry, previously described,[1] permitted the subtraction of the background counting rate from the total rate. The iron ring had an inside diameter of 3 in., an outside diameter of 6 in., and a thickness of 1 in. The neutron flux, about 10^7–10^8 neutrons per second, was monitored by a pair of BF_3 counters and all counting rates were normalized to this monitor rate.

The energy calibration was obtained from the 0.661-Mev line of Cs^{137} and the 0.511-Mev line of Na^{22}. The resolution is about 9 percent as determined from the 0.661-Mev line of Cs^{137} and should improve with increasing energy to the extent that the resolution at 2.5 Mev should be about 4–5 percent; this is the order of the closest line spacing observed.[2] The pulse-height distribution as determined by a single-channel analyzer is given in Fig. 1. The number and intensity of the lines differ somewhat from those contained in a previous report;[3] however, some indication of the complexity of the iron spectrum is given in a more recent work.[4]

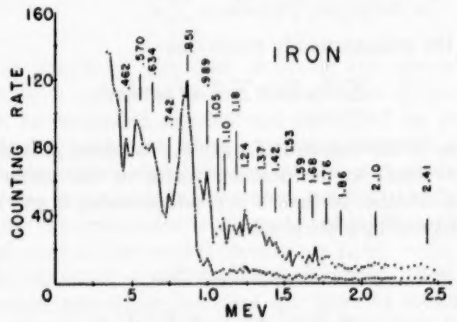

FIG. 1. The energy distribution of the gamma rays from inelastic scattering of fast neutrons in iron. The probable errors in the counting rates are about the magnitude of the dots denoting the experimental points. Energies assigned the individual peaks are as indicated.

Figure 1 also shows the energies assigned the individual peaks and presents the higher energy portion of the spectrum in greater detail. The curves of Fig. 1 represent the average of a number of independent runs; the individual runs show no essential differences. In several of the independent runs the broad peak at 0.570 Mev breaks into two single peaks of energies of 0.527 and 0.570 Mev. Also, the 1.05-Mev peak frequently appears resolved. Although the break at the top of the large 0.851-Mev photoelectric peak appears consistently it has not been separated as a single peak. There is considerable evidence of further structure; however, the limit imposed by resolution does not permit analysis of these unresolved peaks. The probable errors of the energy assignments are about 2 or 3 percent.

The possibility that some of the peaks might arise from elastic scattering into the crystal from the iron has been investigated. The iron spectrum was obtained under the same conditions except that a carbon ring was substituted for the iron ring during background counting. The spectrum obtained in this manner is similar to the curves of Fig. 1; in particular it does not allow any of the original peaks to be discarded.

Difficulties of interpretation are an ineluctable consequence of the complexity of the spectrum. However, an analysis based on a knowledge of the energies of the peaks and the relative cross sections for the photoelectric, Compton, and pair processes in NaI as a function of gamma-ray energy enables one to make judicious choices concerning the origin of certain of the experimental peaks. The division of the peaks among the three fundamental processes is indicated in Table I.

TABLE I. Probable energy assignments for the peaks of Fig. 1. Values denoted by * indicate peaks that do not appear resolved. Energies are in Mev.

Photoelectric	Compton	Pair
2.66*	2.41	1.68
2.10	1.86	1.10
1.76	1.53	0.74
1.59	1.37	0.57
1.42	1.18	...
1.24	1.05*	...
0.989	0.770*	...
0.851	0.656*	...
0.634	...	...
0.462	...	...

* Sponsored by the Office of Ordnance Research, U. S. Army.
[1] Rayburn, Lafferty, and Hahn, Phys. Rev. 94, 1641 (1954).
[2] G. G. Kelley, Nucleonics 10, No. 4, 34 (1952).
[3] Garrett, Hereford, and Sloope, Phys. Rev. 92, 1507 (1953).
[4] R. M. Kiehn and C. Goodman, Phys. Rev. 93, 177 (1954).

Some Properties of Nuclear Normal Modes*

INGRAM BLOCH AND YÜ-CHANG HSIEH
Vanderbilt University, Nashville, Tennessee
(Received May 10, 1954)

Energy levels and antisymmetric eigenfunctions are calculated, with the aid of normal coordinates, for a nuclear Hamiltonian containing inter-nucleon potentials of the Hooke's law type. Such a nuclear model exhibits the same shell structure as do the same nucleons moving without interaction in a common harmonic-oscillator central field. Modifications in the Hamiltonian—use of force parameters which depend on A, cutting off of forces at finite range, inclusion of spin-orbit forces—are discussed in connection with shell structure and the nuclear photoeffect.

I. INTRODUCTION

DESPITE the more fundamental status of meson theory, it remains interesting to study approximate nuclear Hamiltonians which depend on nucleon variables only. Even in this approximation the complexity of the many-body problem has led to the use of various simplifications, such as the single-particle (or central-field) model, the alpha-particle model, the liquid-drop model, and various other collective models. The occurrence of nuclear shells has refocused attention on the single-particle model,[1] whose recent successes do not seem to be wholly understood.

The purpose of this paper is to discuss a nuclear model first proposed by Houston,[2] studied by Margenau and Warren,[3] and, more recently, by Krook, by Rosen, by Post, and independently by the present authors.[4] The nuclear forces are assumed, in first approximation, to be ordinary central forces, obeying Hooke's law, between all pairs of nucleons. These forces do not exhibit saturation, and in fact correspond to infinite binding energy. The one important advantage of studying them is that one does not need to ignore the fact that the nucleus is a many-body system; the eigenfunctions and eigenvalues of such a Hamiltonian can be readily calculated with complete accuracy.

II. TRANSFORMATION TO NORMAL COORDINATES

The Hamiltonian used as a first approximation is

$$H_0=\sum_{k=1}^{A}\frac{1}{2m}\mathbf{p}_k^2+\sum_{k>j=1}^{A}[\tfrac{1}{2}b_{kj}(\mathbf{r}_k-\mathbf{r}_j)^2-D_{kj}], \quad (1)$$

where $\mathbf{p}_k$ and $\mathbf{r}_k$ are, respectively, the momentum and the position vectors of the kth nucleon, D_{kj} is a positive constant, m is the mass of a neutron or a proton, A is the nuclear mass number, and $b_{kj}=b_n$, b_p, or b_{np} according as nucleons k and j are both neutrons, both protons, or one of each.

It is possible in general to find normal coordinates $\xi_\alpha, \eta_\alpha, \zeta_\alpha$ ($\alpha=1\cdots A$), linear homogeneous functions of the Cartesian coordinates x_k, y_k, z_k of the nucleons, such that H_0 is a sum of squares of the normal coordinates and their conjugate momenta;[5] a possible form is

$$H_0=\sum_{\alpha=1}^{A}\frac{\pi_\alpha^2}{2m}+\sum_{\alpha=1}^{A}\tfrac{1}{2}\beta_\alpha\rho_\alpha^2-D, \quad (2)$$

where the β_α are constants, D is the sum of all the D_{kj}, $\rho_\alpha^2=\xi_\alpha^2+\eta_\alpha^2+\zeta_\alpha^2$, and π_α^2 is the sum of squares of the momenta conjugate to $\xi_\alpha, \eta_\alpha, \zeta_\alpha$. One can deal with this Hamiltonian by converting the x_k to the ξ_{α_1} the y_k to the η_α, and the z_k to the ζ_α all by the same unitary transformation, which can thus be written

$$\mathbf{r}_k=\sum_{\alpha=1}^{A}T_{k\alpha}\boldsymbol{\varrho}_\alpha, \quad (3)$$

with its inverse

$$\boldsymbol{\varrho}_\alpha=\sum_{k=1}^{A}\mathbf{r}_kT_{k\alpha}, \quad (4)$$

and the orthonormality conditions

$$\sum_\alpha T_{k\alpha}T_{j\alpha}=\sum_\alpha T_{\alpha k}T_{\alpha j}=\delta_{jk}.^6 \quad (5)$$

One of the constants β_α, say β_1, vanishes; $\boldsymbol{\varrho}_1$ is then proportional to the position vector of the center of mass. Another of the β's is nondegenerate; it and the corresponding $\boldsymbol{\varrho}$ are given by

$$\beta_{Z+1}=Ab_{np}\equiv\beta_{np}, \quad (6)$$

and

$$\boldsymbol{\varrho}_{Z+1}=\left(\frac{N}{AZ}\right)^{\frac{1}{2}}\sum_{k=1}^{Z}\mathbf{r}_k-\left(\frac{Z}{AN}\right)^{\frac{1}{2}}\sum_{k=Z+1}^{A}\mathbf{r}_k, \quad (7)$$

where the protons are numbered from 1 to Z, and the neutrons from $Z+1$ to $A=Z+N$. The remaining $(A-2)$

* Assisted by the Carnegie Foundation for the Advancement of Teaching, and the Office of Ordnance Research of the U. S. Army.

[1] M. G. Mayer, Phys. Rev. **75**, 1969 (1949); Haxel, Jensen, and Suess, Phys. Rev. **75**, 1766 (1949); Feenberg, Hammack, and Nordheim, Phys. Rev. **75**, 1968 (1949).

[2] W. V. Houston, Phys. Rev. **47**, 942 (1935); **49**, 206 (1936).

[3] H. Margenau and D. T. Warren, Phys. Rev. **52**, 790 (1937); D. T. Warren and H. Margenau, Phys. Rev. **52**, 1027 (1937).

[4] Max Krook, 1951 (private communication); Nathan Rosen, 1953 (private communication); H. R. Post, Proc. Phys. Soc. (London) **A66**, 649 (1953); I. Bloch, Phys. Rev. **80**, 138 (1950); I. Bloch and Y. C. Hsieh, Phys. Rev. **91**, 240 (1953).

[5] H. Goldstein, *Classical Mechanics* (Addison-Wesley Press, New York, 1950), Chap. 10.

[6] In the most general form of the homogeneous normal-coordinate transformation, the $T_{k\alpha}$ are tensors of second rank.

normal-mode oscillators have only two distinct β's:

$$\beta_2=\beta_3=\cdots=\beta_Z=Zb_p+Nb_{np}\equiv\beta_p,$$
$$\text{and}\qquad \beta_{Z+2}=\beta_{Z+3}=\cdots=\beta_A=Zb_{np}+Nb_n\equiv\beta_n. \tag{8}$$

The corresponding normal-mode vectors ϱ are thus highly arbitrary. It develops that the sum of coefficients in each of them vanishes, that $\varrho_2\cdots\varrho_Z$ depend only on proton coordinates, and that $\varrho_{Z+2}\cdots\varrho_A$ depend only on neutron coordinates.

III. WAVE FUNCTIONS AND ENERGY LEVELS

The Hamiltonian in Eq. (2) is easily separable; the eigenfunctions can be taken as products of plane-wave functions of ξ_1, η_1, ζ_1 by Hermite functions of the variables $a_2\xi_2, a_2\eta_2, a_2\zeta_2, \cdots a_A\zeta_A$, where $a_\alpha=(m\beta_\alpha/\hbar^2)^{\frac{1}{4}}$. The energy values are sums of the energies inherent in the separate normal coordinates with their conjugate momenta. The internal energy of the nucleus, excluding energy of motion of the center of mass, is

$$E=\sum_{\alpha=2}^{A}(l_\alpha+m_\alpha+n_\alpha+\tfrac{3}{2})\hbar(\beta_\alpha/m)^{\frac{1}{2}}-D, \tag{9}$$

where the $(3A-3)$ quantum numbers $l_\alpha, m_\alpha, n_\alpha$ are non-negative integers. These energies are, of course, independent of spins. Any energy eigenfunction can be made spin dependent through being multiplied by a product of single-particle spin functions.

It is expected that the exclusion principle rules out many of the lower energies permitted in Eq. (9). This matter has been investigated by means of antisymmetrized wave functions, which can be obtained with the aid of the generating function for the Hermite functions:[7]

$$f(u,a\xi)=\exp(-u^2+2ua\xi-\tfrac{1}{2}a^2\xi^2)$$
$$=\sum_{n=0}^{\infty}\exp(-\tfrac{1}{2}a^2\xi^2)H_n(a\xi)u^n/n!. \tag{10}$$

Such generating functions involving the normal coordinates associated solely with protons $(2\leq\alpha\leq Z)$ can be multiplied together and multiplied by proton spin functions; they then generate a complete set of spin-dependent eigenfunctions of the part of H_0 involving protons alone. The most general procedure is to use one independent auxiliary variable (like u above) with each of the normal coordinates $\xi_2, \eta_2, \cdots\zeta_Z$. The neutron states can be dealt with similarly. These two product generating functions can then be multiplied together to generate the product eigenfunctions for all the normal-mode oscillators except No. 1 (center of mass) and No. $Z+1$ (n vs p).

[7] Obviously one would like, if possible, to choose the normal coordinates in such a way that interchange of two similar particles is equivalent to interchange of two normal-mode oscillators, perhaps with some of the normal coordinates also changed in sign. E. B. Shanks of the Vanderbilt Mathematics Department has proven that such choices are impossible except in a few physically uninteresting cases.

The antisymmetrizing procedure is applied to the product generating functions rather than the wave functions themselves. The omitted oscillators (1 and $Z+1$) do not need to be included because their coordinates are invariant under permutation of similar particles. To antisymmetrize the product generating function for (say) the protons, one forms the usual sum of products with permuted nucleon coordinates and spins. The determinant form is convenient; e.g., for the proton oscillators,

$$G_p=\exp[-\sum_{\alpha=2}^{Z}(U_\alpha^2+\tfrac{1}{2}a_\alpha^2\rho_\alpha^2)]\Delta, \tag{11}$$

where Δ is a $Z\times Z$ determinant with elements

$$\Delta_{mn}=s_n(m)\exp(2\sum_{\alpha,\beta=2}^{Z}T_{m\beta}T_{n\alpha}a_\beta\mathbf{U}_\alpha\cdot\varrho_\beta). \tag{12}$$

Here $\mathbf{U}_\alpha$ is the vector whose Cartesian components are the independent auxiliary variables $u_\alpha, v_\alpha, w_\alpha$. The spin function $s_n(m)$ is the nth (i.e., first or second) of two independent spin functions for the mth particle; for example, $s_1(m)$ and $s_2(m)$ might correspond to the spin of the mth particle having a z component of $\hbar/2$ and $-\hbar/2$, respectively.

The generating function G_p for the proton normal modes $2\cdots Z$ is so defined as to be antisymmetric under interchange of space and spin coordinates of any two protons. Thus, if G_p is expressed as a power series in the components of the U_α, the coefficient of each separate product of powers of all these components is an (unnormalized) antisymmetric energy eigenfunction for the normal modes $2\cdots Z$, with the corresponding energy

$$E_p=\sum_{\alpha=2}^{Z}(l_\alpha+m_\alpha+n_\alpha+\tfrac{3}{2})\hbar(\beta_\alpha/m)^{\frac{1}{2}}-\sum_{k>j=1}^{Z}D_{kj}. \tag{13}$$

The quantum numbers $l_\alpha, m_\alpha, n_\alpha$ are, respectively, the powers of the u_α, v_α, and w_α in the term in question. Because of the β_α here are all equal [Eq. (8)], the energy E_p depends only on the sum K_p of these quantum numbers and is in general degenerate.

If the power series representing G_p is regarded as a Taylor series in the $u_\alpha, v_\alpha, w_\alpha$, one can see that any one of the antisymmetrized eigenfunctions mentioned above is proportional to one of the derivatives of G_p with respect to the $u_\alpha, v_\alpha, w_\alpha$ evaluated with these variables all equal to zero; the order of differentiation with respect to any one of the variables is equal to one of the quantum numbers $l_\alpha, m_\alpha, n_\alpha$; the total order of the derivative is thus the total excitation of the proton oscillators $2\cdots Z$ above their apparent ground-state energy, in units of $\hbar(\beta_p/m)^{\frac{1}{2}}$. Examination of the derivatives of G_p reveals that all vanish below a certain total order K_p, which depends on how many protons are present and on how equally they are divided between the two spin functions. For a given number of protons with given spin functions, K_p is just the same as it would be if the protons moved independently as iso-

tropic harmonic oscillators. A similar result holds for the neutron oscillators $Z+2, \cdots, A$. The center-of-mass oscillator (No. 1) and the neutron-proton oscillator $(Z+1)$ are unaffected by antisymmetry.

The fact that the Pauli exclusion principle affects the ground-state energy of the set of interacting nucleons in just the same way as if they did not interact, suggests that nuclear shell behavior may be a property of independent collective modes of motion rather than of independent particles moving in an average central field. However, the Hamiltonian H_0 (which gives closed shells at N or $Z=2$, 8, 20, 40, 70, and 112) needs to be modified if it is to give the correct shells, perhaps through inclusion of spin-orbit interactions of the type $\mathbf{r}\times\mathbf{p}\cdot\mathbf{s}$, or tensor forces.

IV. PARITIES, ANGULAR MOMENTA, AND MAGNETIC MOMENTS

It is easily seen that any energy eigenfunction for the internal oscillators (excluding center-of-mass functions) has a parity which is that of the sum of all the quantum numbers, $\sum_{a=2}^{A}(l_a+m_a+n_a)$. Also, from Eqs. (3)–(6), although the "orbital angular momentum" $\mathbf{y}_a=\boldsymbol{\rho}_a\times\boldsymbol{\pi}_a$ of a given normal-mode oscillator cannot be expressed in terms of the orbital angular momenta $\mathbf{M}_k=\mathbf{r}_k\times\mathbf{p}_k$ of the nucleons, the total orbital angular momentum of the nucleus with respect to a fixed origin can be expressed either as $\sum_{k=1}^{A}\mathbf{M}_k$ or as $\sum_{a=1}^{A}\mathbf{y}_a$, for these sums are equal.

Furthermore, if $\mathbf{M}$ is the angular momentum of the nucleus with respect to its center of mass,

$$\mathbf{M}=\sum_{a=2}^{A}\mathbf{y}_a=\mathbf{M}_p+\mathbf{M}_n+\mathbf{M}_{np}, \tag{14}$$

where $\mathbf{M}_p\equiv\sum_{a=2}^{Z}\mathbf{y}_a$ and $\mathbf{M}_n\equiv\sum_{a=Z+2}^{A}\mathbf{y}_a$ are the angular momenta of protons and neutrons about their respective centers of mass, and $\mathbf{M}_{np}\equiv\mathbf{y}_{Z+1}$ is the angular momentum of relative motion of neutrons and protons.

It is well known that a single three-dimensional isotropic harmonic oscillator with Cartesian quantum numbers l, m, n is in a mixture of angular momentum states with eigenvalues given by $L=l+m+n$, $l+m+n-2$, $l+m+n-4$, $\cdots 0$ or 1. Therefore, an energy eigenfunction for the proton normal modes $2\cdots Z$, with total quantum number K_p, is in general a mixture of eigenfunctions of M_p^2 and M_{pz} (with eigenvalues $L_p\cdot(L_p+1)\cdot\hbar^2$, and $L_{pz}\hbar$, respectively), with L_p assuming all integral values from 0 to K_p, and L_{pz} ranging between $\pm L_p$. A complete set of simultaneous eigenfunctions of proton energy, M_p^2, and M_{pz} can be formed as linear combinations of proton oscillator eigenfunctions with a common K_p but various values of the separate l_a, m_a, n_a. For any given Z, the ground state splits into the same eigenstates of M_p^2 and M_{pz} as if the protons moved independently in a harmonic-oscillator well; likewise, M_n^2 and M_{nz} for a given N. $M_{np}^2=0$ in the ground state.

If the spin functions s_n are chosen to correspond to spin "up" and spin "down," the wave functions generated are eigenfunctions of S_z, the z component of total spin. Linear combinations of generating functions which differ through interchange of spin functions can be chosen so that they generate eigenfunctions of S_z and S^2. The antisymmetrized ground state of H_0 always has S_p and S_n each equal to 0 or $\frac{1}{2}\hbar$, according as Z and N are even or odd.

Thus parity, and orbital and spin angular momenta, for the ground state of any nucleus are just the same as if the nucleons of each type moved without interacting in their own harmonic-oscillator central fields. Because H_0 does not lead to interaction moments,[8] the same statement applies to ground-state magnetic moments.

V. RADIATIVE TRANSITIONS

The n *vs* p oscillator $(Z+1)$ in the present treatment resembles the oscillator discussed by Goldhaber and Teller *et al.*[9] in connection with the nuclear photoeffect. In fact, the only nonvanishing electric-dipole matrix elements from the ground state are those which correspond to single excitation of this oscillator. To first order, then, the electric dipole transitions have the integrated cross section,

$$\int\sigma dE=(\pi e^2h/mc)(NZ/A), \tag{15}$$

with the excited state being at an energy above ground of

$$E-E_g=\hbar(Ab_{np}/m)^{\frac{1}{2}}. \tag{16}$$

If one calculates b_{np} and D for the deuteron so as to get the correct binding energy (2.23 Mev) and a reasonable wave function (mean separation of 3.16×10^{-13} cm as in a square well of radius 2×10^{-13} cm), one obtains

$$\begin{aligned} &b_{np}=3.37\times10^{25}\ \text{Mev/cm}^2,\\ &D=10.15\ \text{Mev},\\ &V=0\ \text{at}\ r=7.76\times10^{-13}\ \text{cm},\\ &h\nu=5.28\ \text{Mev}. \end{aligned} \tag{17}$$

The fact that $h\nu$ is in the neighborhood of the calculated energy of maximum photoelectric cross section[10] (4.46 Mev) is little better than a coincidence in the case of the deuteron, in which no transfers of energy need to occur before disintegration (i.e., the lifetime of the intermediate state is extremely short).

[8] R. G. Sachs and N. Austern, Phys. Rev. **81**, 705 (1951).

[9] M. Goldhaber and E. Teller, Phys. Rev. **74**, 1046 (1948); J. S. Levinger and H. A. Bethe, Phys. Rev. **78**, 115 (1950); Ferentz, Gell-Mann, and Pines, Phys. Rev. **92**, 836 (1953).

[10] See, for example, H. A. Bethe, *Elementary Nuclear Theory* (John Wiley and Sons, Inc., New York, 1947).

Equation (16) implies that the resonant energy of the photoeffect varies as $(Ab_{np})^{\frac{1}{2}}$. Experiment[11] reveals a proportionality to approximately $A^{-1/6}$ in the medium and heavy range, so one must assume that b_{np} is approximately proportional to $A^{-4/3}$, i.e., that many-body forces are present. Inasmuch as the form of H_0 rules out exchange forces and velocity-dependent forces with saturation properties, it is not surprising that many-body forces should need to be invoked here, even though their form is oversimplified. In keeping with the assumed form, one should take D_{kj} for each pair of nucleons to be a decreasing function of A, also, so that the ground states of heavy nuclei are not too negative in energy (zero energy being defined as the lowest energy at which one or more nucleons can escape to infinity from an actual nucleus).

A nucleus with the Hamiltonian H_0, having absorbed a photon, is unable to disintegrate; it can only return to ground by re-emission of the photon. The fact that actual nuclei emit particles or undergo fission upon absorbing gamma rays indicates not only that the Hooke's-law forces should be cut off at some finite range, but also that the normal-mode oscillators interact with each other strongly enough to permit the *n vs p* oscillator to share its energy with the others in most cases before emitting a photon. Possibly the same perturbation can produce both effects. A complete account of the process would explain how the energy goes into the particular mixture of normal-mode states which corresponds to emission of one nucleon, emission of two nucleons, or fission. The fact that in an emission process the center of mass of the neutrons moves away from that of the protons indicates that the *n vs p* oscillator remains excited with a certain probability. One would expect the same effect in photofission to produce an unequal division of charge between the fragments. A perturbation now being studied is

$$H'=\sum_{k>j=1}^{A}\{D_{kj}-\tfrac{1}{2}b_{kj}(\mathbf{r}_k-\mathbf{r}_j)^2 -\tfrac{1}{2}B_{kj}\exp[(\mathbf{r}_k-\mathbf{r}_j)^2/\lambda_{kj}^2]\}, \quad (18)$$

which replaces the quadratic inter-nucleon potentials by Gaussian potentials. The effect of such a perturbation is difficult to calculate because the Gaussian terms involve all the products of the nucleon position vectors or of the normal-mode vectors. It is tempting to cut off the forces by means of an H' which, like the original V_0, is a sum of terms for the different normal-mode oscillators, or to start with a V which is such a sum. However, it does not seem easy to find such a sum which is still symmetric under interchange of like particles, and even if available, such a potential would not contain the interaction of normal-mode oscillators needed to account for emission of one or two particles.

According to the nuclear model under discussion, by far the most probable photon absorption raises the *n-p* oscillator to its first excited state. If, as seems likely, *n-n*, *n-p*, and *p-p* forces are approximately equal, the Hooke's-law nucleus has no other excited levels much below this one. But actually the energy of this level is positive, or in the continuum. Thus it would appear that H_0, unmodified, cannot possibly account for the many excited states of nuclei which are stable against nucleon emission. Possibly the cutting-off procedure discussed above will sufficiently lower some of the other excited states in relation to the first excited state of the *n-p* oscillator, or maybe the spin-orbit forces needed to produce the correct shells will resolve much of the degeneracy of the present ground energy and thus lead to the proper excited states.

The fact that neutron capture by a nucleus is more often followed by several gamma rays in cascade than by a single gamma ray to ground[12] suggests that the photon-excited nucleus from which a neutron is emitted is in a state orthogonal to some of those produced by neutron capture. Possibly some of the latter have their excess energy mainly in excitation of other oscillators than the *n-p* oscillator. If so, their gamma rays do not arise from electric dipole transitions. In fact, because the *n-p* oscillator is the only one which can ever undergo an electric dipole transition, and its excited states are in the continuum, the present model indicates that $E1$ transitions will not be observed at all, except in conjunction with emission or capture of one or more nucleons.[13] This is true, however, only if the relative energies of the nuclear states are not much changed by perturbations. If H_0 is perturbed as in Eq. (18), or by spin-orbit couplings (e.g., $\sum_{k=1}^{A}\mathbf{s}_k\cdot\mathbf{M}_k$ or $\mathbf{S}_p\cdot\mathbf{M}_p$), some of the ground states of H_0 may be raised and some of the "first excited" states (of opposite parity) may be lowered to negative energies, so that a nucleus which cannot emit a particle can still emit an $E1$ γ ray, followed by another γ ray which is associated with no change of parity.

VI. CONCLUSIONS

It appears that ordinary inter-nucleon forces obeying Hooke's law lead to a nuclear model having the same ground-state energy, parity, angular momentum, and magnetic moment as the single-particle harmonic-oscillator model. The model exhibits saturation if the force parameters depend properly on A. Cutting off of the forces at finite range and addition of spin-orbit coupling seem likely to give correct shells, may also yield correct excited bound states, and will affect magnetic moments in ways as yet unknown. Possibly, too, such considerations may provide a new point of view toward such other phenomena as surface vibrations, fission, and nuclear reactions and scattering.

[11] Montalbetti, Katz, and Goldemberg, Phys. Rev. **91**, 659 (1953).

[12] J. M. Blatt and V. F. Weisskopf, *Theoretical Nuclear Physics* (John Wiley and Sons, Inc., New York, 1952).

[13] See M. G. Mayer, Phys. Rev. **78**, 16 (1950).

Gamma Radiation from Interaction of 3.2-Mev Neutrons with Various Materials

V. E. SCHERRER, B. A. ALLISON, AND W. R. FAUST
Naval Research Laboratory, Washington, D. C.

(Received June 21, 1954)

Gamma radiation arising from 3.2-Mev neutron bombardment of 30 elements has been observed and calculations made of the gamma-ray production cross section for 15 of these elements.

A DETAILED investigation of gamma radiation arising from 3.2-Mev neutron bombardment has been made of thirty elements picked more or less uniformly from the periodic table. Calculations have been completed of the gamma-ray production cross sections for half of the elements examined. Some of the gamma rays reported have been observed in similar experiments,[1-3] although most of the data is essentially new. Gamma radiation observed is consistent with level information where available.

Use of a 12.7-cm diameter by 5.1-cm thick crystal of NaI(Tl) as a detector simplified analysis of the complex pulse-height distributions. Because of the large dimensions of the crystal, a large fraction of the secondary radiation is absorbed, thereby augmenting the photopeak.

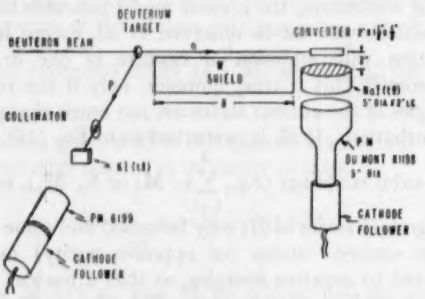

FIG. 1. Basic geometry of the experiment.

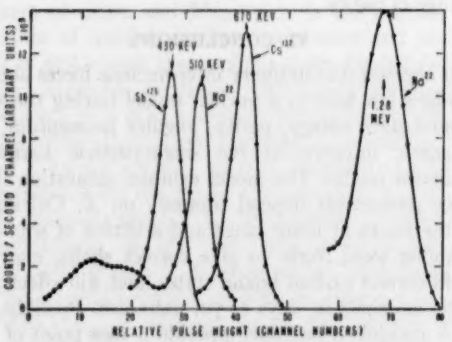

FIG. 2. Spectrometer calibration curves.

DESCRIPTION OF EXPERIMENTS

Neutrons were obtained from the $D(d,n)He^3$ reaction produced in a Cockcroft-Walton accelerator operated at 350 kv. The target was formed by adsorption of deuterium on aluminum and a KI(Tl) scintillation detector served as a monitor by counting protons from the $D(d,p)T$ companion reaction. A converter, made of the material of interest, was placed about 25 cm from the accelerator target and in line with the deuteron beam as shown in Fig. 1. Estimates of the neutron energy distribution were made by a method described previously[4] which indicated that the neutrons were distributed asymmetrically about the average energy of 3.2 Mev and that the width of the distribution at half-maximum was 0.2 Mev. The spectrometer was placed 2.5 cm below the converter and was shielded from the target by a tungsten bar. Counting data was taken first with the converter in position and then with it removed. The difference between these two conditions yielded net counting data due to the presence of the converter.

The spectrometer consisted of a 12.7-cm diameter by 5.1-cm thick crystal of NaI(Tl) mounted on a DuMont K-1198 photomultiplier tube. Pulse-height distributions were recorded on a twenty-channel analyzer. Typical calibration curves of this spectrometer, which were obtained with extended sources placed in the converter position, are shown in Fig. 2.

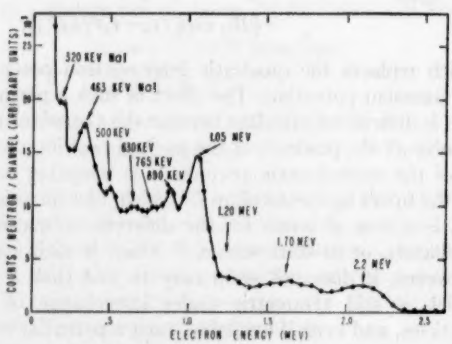

FIG. 3. Pulse-height distribution produced by 3.2-Mev neutron bombardment of Al.

[1] M. A. Rothman and C. E. Mandeville, Phys. Rev. **93**, 796 (1954).
[2] R. M. Kiehn and C. Goodman, Phys. Rev. **93**, 177 (1954).
[3] Scherrer, Allison, and Faust, Phys. Rev. **95**, 637 (1954).
[4] Shapiro, Scherrer, Allison, and Faust, Phys. Rev. **95**, 751 (1954).

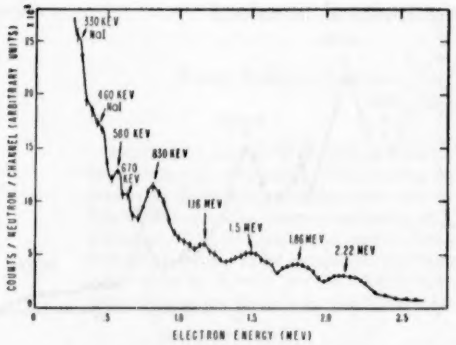

FIG. 4. Pulse-height distribution produced by 3.2-Mev neutron bombardment of Mn.

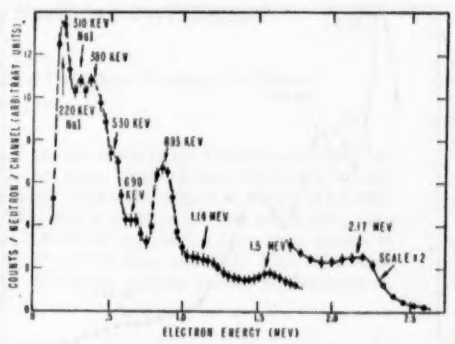

FIG. 5. Pulse-height distribution produced by 3.2-Mev neutron bombardment of Zr.

RESULTS

Pulse-height distributions obtained from Al, Mn, Zr, I, and Bi are shown in Figs. 3 through 7 and are typical of the general results. Data taken with a NaI(Tl) converter showed maxima near 210 kev, 330 kev, 420 kev, and 1.04 Mev, a distribution similar to the iodine distribution of Fig. 6. Maxima that occur at energies near the NaI(Tl) lines in the various figures probably arise from the interaction of scattered neutrons with the NaI(Tl) spectrometer crystal.

TABLE I. Gamma-ray production cross sections.

Element	Energy (Mev)	Cross section (Barns)	Element	Energy (Mev)	Cross section (Barns)
Cr	0.75 ±0.03	0.027	Mo	2.5 ±0.2	0.059
	0.97 ±0.04	0.10		1.4 ±0.06	0.33
	1.43 ±0.06	0.73		0.73±0.03	0.66
				plus unresolved lines	
Fe	0.835±0.015	1.18			
	1.17 ±0.05	0.39	Cd	0.57±0.02	0.69
	1.67 ±0.07	0.33		2.8 ±0.2	0.016
				plus unresolved lines	
Co	0.60 ±0.02	0.20		0.77±0.03	0.16
	1.15 ±0.04	0.82	In	0.88±0.04	0.27
	1.49 ±0.07	0.53			
	1.7 ±0.08	0.15		2.08±0.1	0.16
	2.5 ±0.1	0.19		1.15±0.05	0.10
Ni	0.59 ±0.02	0.047	Sn	0.69±0.02	0.14
	1.33 ±0.05	0.84		1.14±0.05	1.67
	1.49 ±0.06	0.54		2.0 ±0.1	0.21
	2.66 ±0.1	0.01			
Cu	0.66 ±0.03	0.21	Ta	0.46±0.03	1.26
	0.96 ±0.05	0.12		1.44±0.15	0.93
	1.37 ±0.06	0.81			
	1.9 ±0.1	0.16		plus unresolved lines	
			Pb	0.35±0.02	0.52
Zn	1.02 ±0.05	1.3		0.52±0.02	1.02
	1.3 ±0.06	0.03		0.80±0.03	1.05
	1.6 ±0.07	0.02		1.10±0.05	0.18
				1.40±0.10	0.25
Zr	0.690±0.04	0.038		2.20±0.10	0.16
	0.893±0.04	0.402			
	1.14 ±0.06	0.12	Bi	0.49±0.02	0.43
	1.5 ±0.07	0.14		0.94±0.05	1.2
	2.17 ±0.1	0.44		1.62±0.07	0.59
				2.6 ±0.1	0.37

Table I lists gamma rays definitely identified in the spectrum of each element examined. Also listed is the

TABLE II. Identified gamma rays for which no calculations have yet been made of corresponding production cross sections.

Element	Gamma-ray energy (Mev)	Element	Gamma-ray energy (Mev)
Be	none	Nb	0.27 ±0.02
			0.53 ±0.02
B	0.43*±0.02		0.69 ±0.03
	0.76 ±0.03		0.91 ±0.05
	1.02 ±0.05		
	1.17 ±0.05	Ag	0.74 ±0.03
	1.41 ±0.06		1.10 ±0.05
	1.61 ±0.08		1.50 ±0.06
	2.00 ±0.18		
		Te	0.72 ±0.04
C	none		1.10 ±0.05
			1.43 ±0.06
Mg	0.38 ±0.02		2.30 ±0.18
	0.59 ±0.02		
	1.30*±0.05	I	0.21 ±0.01
	1.79 ±0.08		0.33 ±0.01
			0.42*±0.02
Al	0.05 ±0.02		0.63*±0.03
	0.89 ±0.03		1.04 ±0.05
	1.05 ±0.05		
	1.20 ±0.05	Ba	0.47*±0.02
	1.70 ±0.08		0.60 ±0.03
	2.20 ±0.18		0.78 ±0.04
			1.06 ±0.05
P	1.0 ±0.05		1.19 ±0.05
	1.24*±0.05		1.41*±0.06
	1.60 ±0.07		1.51 ±0.06
	1.75 ±0.08		2.10 ±0.1
	2.05 ±0.18		
		Ce	0.48 ±0.03
Ti	0.92*±0.05		0.90 ±0.05
	1.30 ±0.06		1.50 ±0.06
	2.2 ±0.18		2.50 ±0.20
V	0.33*±0.02	Hg	0.38*±0.02
	0.97 ±0.05		0.54 ±0.03
	1.67 ±0.07		0.90 ±0.05
			1.21 ±0.05
Mn	0.58 ±0.02		2.0 ±0.18
	0.67 ±0.03		
	0.83*±0.04		
	1.16 ±0.05		
	1.50 ±0.06		
	1.86*±0.08		
	2.22*±0.17		

* Indicates strong lines.

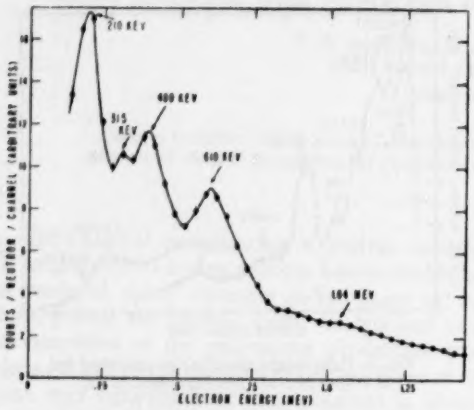

FIG. 6. Pulse-height distribution produced by 3.2-Mev neutron bombardment of I.

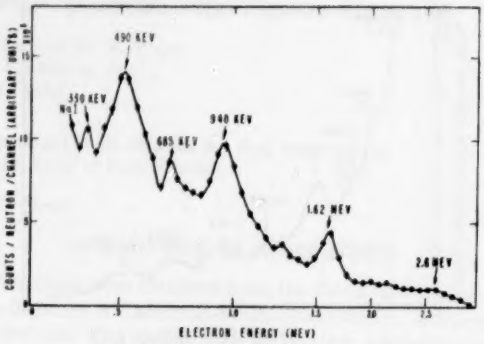

FIG. 7. Pulse-height distribution produced by 3.2-Mev neutron bombardment of Bi.

cross section σ_γ for the production of a gamma ray of that particular energy. These cross sections were obtained by measuring the total number of counts per neutron under each photoabsorption peak and correcting for attenuation of both neutrons and gamma rays in the converter. Some auxiliary experiments with carbon converters, similar to those described by Rothman and Mandeville,[1] indicated that the contribution to the area under the photopeaks from the NaI background was generally small. Absolute calibrations of the detector was carried out by placing extended sources of known energy and disintegration rate at the converter position. Calibration data similar to those of Fig. 2 indicated the number of photons in the photoabsorption peaks as a function of gamma-ray energy. It is estimated that the average error in the cross section calculation is ± 20 percent.

Table II lists gamma rays identified in the spectrum of elements for which no calculations have yet been made of the corresponding production cross sections.

ACKNOWLEDGMENT

The authors wish to express their appreciation to Dr. P. Shapiro and Dr. C. V. Strain for their active interest and support and to thank Mr. A. P. Flanick for invaluable aid given during the course of the experiments.

Inelastic Scattering of Alpha Particles by Lithium*

C. W. Li and R. Sherr†
Kellogg Radiation Laboratory, California Institute of Technology, Pasadena, California
(Received July 12, 1954)

The inelastic scattering of alpha particles by Li^7 leading to the formation of the 478-kev state of Li^7 has been studied by observation of the gamma ray emitted from that state. Singly charged helium ions accelerated by an electrostatic generator were used to determine the yield of the reaction up to an energy of 2.8 Mev. The excitation curve shows a resonance at 1.889±0.010 Mev, with a width of 200 kev and a peak cross section of 0.11±0.02 barn, and another broad resonance at 2.50±0.03 Mev with a peak cross section of 0.08±0.015 barn. These resonances correspond to levels of B^{11} at 9.86 Mev and 10.23 Mev. The thick target yield at $E_\alpha=2.3$ Mev is $1.5\times10^{-6}\gamma/\alpha$. The Doppler shift of the emitted gamma ray furnishes an upper limit of the lifetime for the 478-kev excited state of Li^7.

INTRODUCTION

THE excited state of Li^7 at 478 kev is the most extensively studied excited state in light nuclei.[1,2] The existence of this state was first indicated by the detection of gamma rays from lithium under bombardment of natural alpha particles by means of the process $Li^7(\alpha,\alpha')Li^{7*}$ used by Bothe and Becker and others.[3] Later, it was studied with different methods by means of the reactions (d,p), (p,p'), (d,d'), (n,α), and the K capture of Be^7. In the present work, the inelastic process $Li^7(\alpha,\alpha')Li^{7*}$ has been investigated by measurements on the 478-kev gamma ray emitted by the Li^{7*}. The results give information on the levels of the compound nucleus (B^{11}) in the region of excitation above 9.28 Mev. This region in B^{11} and the corresponding region in its mirror C^{11} have not been adequately investigated.

EXPERIMENTAL ARRANGEMENT

Singly-charged helium ions produced in a radio-frequency ion source[4] were accelerated by an electrostatic generator up to an energy of 2.8 Mev. The ion beam coming down the accelerating column was first separated into its different beam components with a magnetic field and then resolved and maintained homogeneous by an electrostatic analyzer of resolution 0.1 percent or better. The energy was calibrated by the 873.5-kev resonance in $F^{19}(p\alpha,\gamma)$. The beam current incident on the target was measured by a current integrator that has been in use for several years and is believed to be reliable to a few percent.

Targets were made by evaporating natural lithium metal onto a copper plate. The furnace consists of a strip of tantalum electrically heated and located inside the vacuum system. The copper plate could be moved over the furnace for evaporation and then retracted into the beam tube without breaking the vacuum. As lithium is notorious for its readiness to become contaminated, fresh, shiny targets were prepared from time to time during a day of measurements. The lithium furnace was first thoroughly outgassed and the deposit of lithium made as quickly as possible. A liquid nitrogen trap was located between the exit of the electrostatic analyzer and the target chamber. Both thick and thin targets have been used. The latter ranged in thickness from 5 to 30 kev for 2-Mev alpha particles. Thick targets of lithium hydroxide were used to check the yield.

The gamma rays were counted by means of a sodium iodide scintillation counter in conjunction with a ten-channel differential discriminator.[5] The counter consisted of a NaI(Tl) crystal 1½ inches long and 1½ inches in diameter mounted in a thin aluminum case with a quartz window, and placed on the flat top of a DuMont 6292 photomultiplier with silicone grease. Pulses from the photomultiplier were amplified and displayed in the ten channels. Usually, the bias was set so that the whole "photo" peak of the 478-kev gamma ray was displayed in the middle channels with the first and last channels indicating any background present.

The 478-Kev Gamma-Ray

Figure 1 shows the gamma-ray spectrum observed with a Li target 15 kev thick at $E_\alpha=2.5$ Mev with the counter at 90° to the beam. The annihilation radiation from Na^{22} was used as calibration of the gamma-ray energy. The resolution of the photopeak is seen to be 10 percent, and the peak-to-valley ratio for the 478-kev gamma ray is better than 20. The spectrum consists of the photopeak, the Compton plateau and two superposed peaks. Both the latter ones were produced by the lead shield which covers the top of the target and around the counter. The one at higher energy is due to

* Assisted by the joint program of the U. S. Office of Naval Research and the U. S. Atomic Energy Commission.
† On sabbatical leave from Princeton University, Princeton, New Jersey.
[1] Brown, Snyder, Fowler, and Lauritsen, Phys. Rev. **82**, 159 (1951), and the references listed there.
[2] F. Ajzenberg and T. Lauritsen, Revs. Modern Phys. **24**, 321 (1952).
[3] W. Bothe and H. Becker, Z. Physik **66**, 289 (1930); H. C. Webster, Proc. Roy. Soc. (London) **136**, 428 (1932).
[4] Thonemann, Moffatt, Roaf, and Sanders, Proc. Phys. Soc. (London) **61**, 483 (1948); Moak, Reese, and Good, Nucleonics **9**, No. 3, 18 (1951); C. W. Li (to be published).
[5] Hugh J. Woodbury, thesis, California Institute of Technology, 1953 (unpublished).

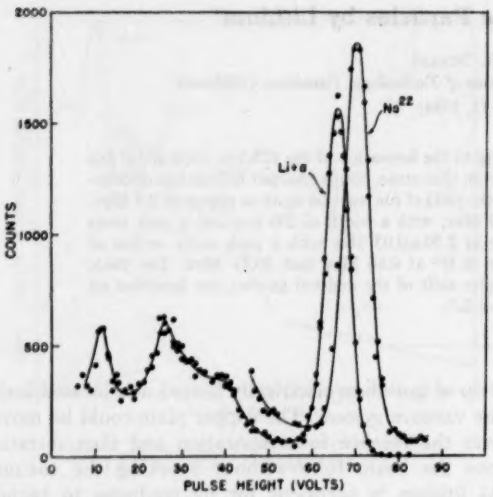

FIG. 1. Pulse-height spectrum of the gamma rays from lithium under bombardment of 2.5-Mev alpha particles. The photopeak of the 511-kev annihilation radiation of Na^{22} is shown for comparison.

the gamma radiation emitted from the target and back-scattered by the lead shield into the crystal. The other one is the Pb K x-ray generated in the lead shield, following absorption of the gamma rays from the target. Using Cs^{137} and the annihilation radiation of Na^{22} as calibration points, we obtained the value 484 ± 10 kev for the Li gamma ray, in adequate agreement with other measurements,[1,6,7] which average to 478.5 kev.

The angular distribution of the 478-kev gamma ray is known to be isotropic both from direct measurements and from the spin and parity assignment of the levels involved which are $\frac{3}{2}^-$ for the ground state of Li^7 and $\frac{1}{2}^-$ for the first excited state.[2] By measuring the relative intensity of gamma rays emitted from a thin target at angles from 0° to 160° relative to the alpha-particle beam at 1.9 Mev, we also obtained an isotropic distribution (within 10 percent).

Because of their relatively large mass, alpha particles are effective in producing Doppler shifts in the energy of the emitted gamma ray. By the comparison of the gamma-ray energy observed with the counter at 0° and at 160°, we obtained a rough measurement of the Doppler shift of the Li^7 gamma ray at a bombarding energy of 1.9 Mev. In this measurement, the NaI crystal subtended an angle of 15° at the target, which was a layer of lithium about 150 kev thick. As shown in Fig. 2, there was a shift of approximately 0.8 volt in the peak position, with the mean gamma-ray energy corresponding to a pulse height of 45 volts. The gain of the amplifier was monitored by the spectrum of Cs^{137} taken immediately before and after each measurement. The error of the shift can be set as ±0.3 volt. Therefore the Doppler shift is 1.8 ± 0.7 percent, in rough agreement with the calculated Doppler shift (2.3 percent) corresponding to a spherical distribution of recoil. From estimates on the stopping power, the time for an average recoil Li^7 to slow down to half of its initial speed will be of the order of 3×10^{-13} sec. Thus, assuming that we observed the full Doppler shift, this measurement indicates an upper limit for the lifetime of the first excited state of Li^7 of approximately 3×10^{-13} sec. Better estimates might be obtained with a very thin target of lithium on backing material of high density and large stopping power, like gold, under bombardment by high-energy alpha particles. Elliott and Bell,[8] by a comparison of the Doppler broadening of the 478-kev gamma ray in different materials using the reaction $B^{10}(n,\alpha)Li^{7*}$, concluded a lifetime of $(0.75\pm0.25)\times10^{-13}$ sec for the first excited state of Li^7.

Excitation Function

The thick target yield (for natural lithium metal) was measured with the counter set at 90° to the direction of the bombarding beam. The result is shown in Fig. 3 where the yield is that integrated over a solid angle of 4π, assuming an isotropic distribution of the emitted gamma ray. Because of the large increase in yield toward higher bombarding energies, we had to move the detector away from the target correspondingly in order not to overload the counting equipment. Thus, the curve given in Fig. 3 is the result of normalizing and matching several sections of yield curves for different energy ranges. As a check on the purity of

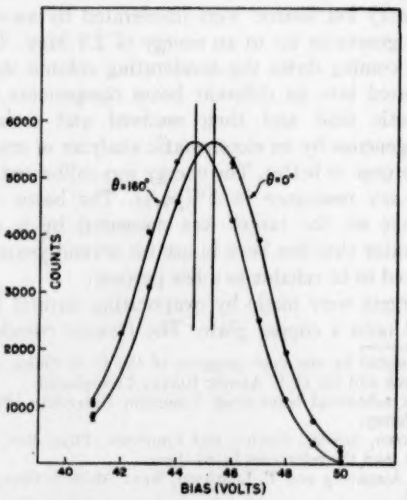

FIG. 2. The Doppler shift of the 478 gamma ray between the angles of observation, 0° and 160°, relative to the beam of incident alpha particles. $E_\alpha=1.9$ Mev. Target thickness = 150 kev.

[6] Williamson, Browne, Craig, and Donahue, Phys. Rev. 84, 731 (1951).
[7] R. G. Thomas and T. Lauritsen, Phys. Rev. 88, 969 (1952).
[8] L. G. Elliott and R. E. Bell, Phys. Rev. 76, 168 (1949).

the target, we measured the yield from a target of fused LiOH known to be clean from measurements on scattering of protons. The yield obtained with this target had a similar energy dependence and was 3.5 times as small as the yield from lithium metal at same bombarding energies. This ratio of 3.5 is what we should expect from the stopping powers of lithium and LiOH. For the lithium metal target used, the possibility cannot be excluded that a surface layer a few kev thick for the alpha particles might have built up during the experiment. By leaving a thick target of lithium metal overnight in the untrapped vacuum system, we observed that the surface layer can grow to a thickness as large as 60 kev to alpha particles of 2 Mev. However, this possible source of error would introduce only a small correction to the resultant absolute yield. Also, the increment of the thick target yield with bombarding energy is, in general, quite reliable and is useful in estimating the thickness of thin targets from their yields.

Since the efficiency of the particular NaI crystal in use was known as a function of γ-ray energy[5] the counting rates were readily converted to give absolute disintegration rates. Correction for absorption (6 percent) in the target housing has been included in determining the yields of Fig. 3.

To obtain more accurate excitation data the yield from several thin targets of lithium was measured. Figure 4 shows the result obtained with two targets, matched at 2.3 Mev. The target for the portion of the curve below 2.3 Mev was 21 kev for 2.3-Mev alpha particles, as estimated from a comparison of the counting rate with the slope of the thick target yield curve. The other target was 35 kev thick for 2.3-Mev alpha particles. The excitation curve was corrected for target thickness. The dashed curve shown in Fig. 4 is obtained by differentiating the thick target yield with respect to energy and multiplying it with corresponding stopping cross sections. In view of the broadness of the resonance and the uncertainty in the stopping cross section of lithium for alpha particles of these

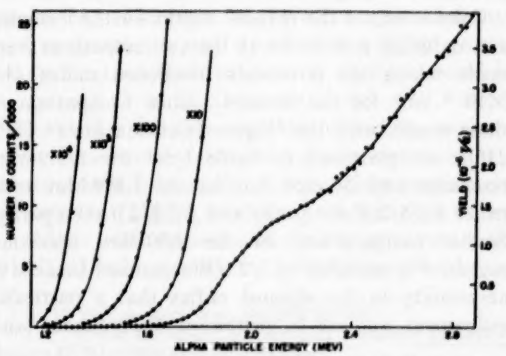

FIG. 3. Thick target yield of natural lithium metal for the 478-kev gamma ray.

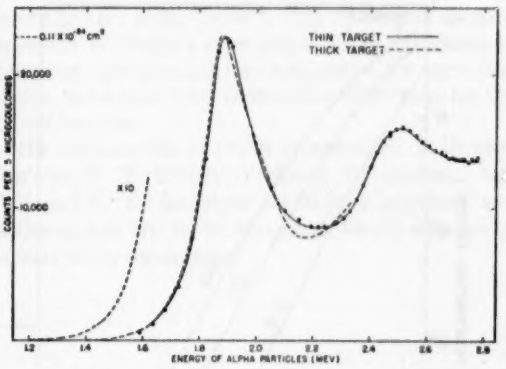

FIG. 4. Excitation function of $Li^7(\alpha,\alpha'\gamma)Li^7$. Solid curve: thin target results corrected for target thickness. Dashed curve: results of differentiating the thick target yield with respect to E_α and corrected for stopping power of the target for different E_α.

energies, the agreement of this differential curve with the corrected thin target curve seems reasonable.

The stopping cross sections of different materials for alpha particles at the low-energy range are poorly known. In view of the uncertain capture and loss of electrons by the alpha particles and other difficulties, the energy loss at low energy is essentially not calculable.[9] In the present calculations we have used the range-energy relation of air for alpha particles given by Bethe[10] and a stopping power of 0.5 for a lithium atom relative to an air atom. The absolute cross sections given in Fig. 4 for the excitation curve has also been corrected for the concentration of Li^7 in natural lithium. These cross sections are believed to be accurate to 20 percent, the main uncertainty being the efficiency of the counter and the stopping cross section of lithium.

From Fig. 4 we see that there are two resonances for $Li^7(\alpha,\alpha')Li^{7*}$ in the energy range studied. The first peak is at 1.889 ± 0.010 Mev with width of 200 kev and cross section at peak 0.11 ± 0.02 barn, and the second broad peak at 2.50 ± 0.03 Mev, with a cross section of 0.08 ± 0.015 barn. Subtracting the tail of the first resonance we have the cross section of the second resonance $\sigma_R\approx0.03$ barn. The part of the excitation curve for bombarding energy below 1.6 Mev was obtained by differentiation of the thick target yield which was taken with steps of about 20 kev. The regions around both peaks, as well as the region $E_\alpha=2.3$ to 2.8 Mev, have been measured with targets as thin as 6 kev for 2.3-Mev alpha particles and with comparable steps. No structure other than background fluctuations was seen. The results are to be compared with the recent work of Heydenburg and Temmer[11] in which they reported strong resonances at

[9] See, for example, E. Segrè, *Experimental Nuclear Physics* (John Wiley and Sons, Inc., New York, 1953), Vol. I, p. 166.

[10] H. A. Bethe, Revs. Modern Phys. 22, 213 (1950); also reference 9.

[11] N. P. Heydenburg and G. M. Temmer, Phys. Rev. 94, 1252 (1954).

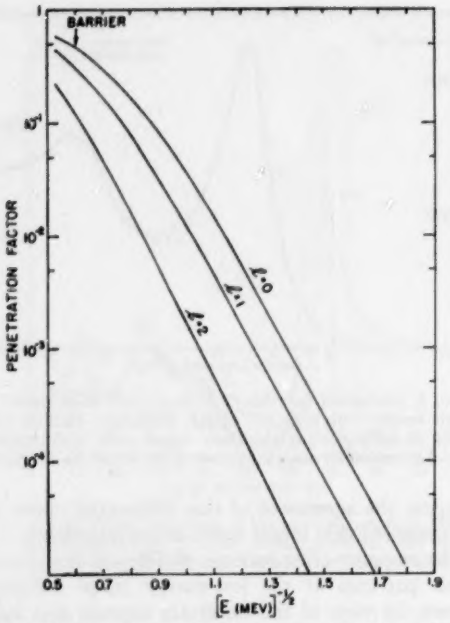

FIG. 5. Penetration factor of alpha particles for Li^7 for a channel radius of 4.9×10^{-13} cm. E_{Mev} is the energy of incident alpha particles in the laboratory system in Mev.

1.91, 2.46, and 3.06 Mev and some indication of weak resonances at 2.60 and 2.70 Mev.

DISCUSSION

In order to evaluate the level parameters it is convenient to remove the penetration factors from the excitation function. First, for purpose of reference, we give in Fig. 5 a plot of the barrier penetration factor of alpha particles in Li^7, following the style of Christy and Latter[12] for the case of protons. In Fig. 5, $P_l=1/[F_l^2(R)+G_l^2(R)]$ is the barrier penetration factor for alpha particles of orbital angular momentum l; $F_l(R)$ and $G_l(R)$, the usual Coulomb wave functions at the channel radius R. In making the computation, R was taken to be $1.4\times(7^{\frac{1}{3}}+4^{\frac{1}{3}})\times10^{-13}$ cm $=4.9\times10^{-13}$ cm, and tabulated Coulomb wave functions[13] were used.

Figure 6 shows the experimental excitation curve with the barrier penetration factors of the incoming and outgoing alpha particles removed. The combination $l=1$ for the incoming particle and $l'=1$ for the outgoing particle was used with the channel radius given above. The use of other orbital angular momenta and a different value of the channel radius would change the position and the width of the peaks only slightly. It can be seen that the width estimated directly from the experimental curve in the previous section is roughly right. We shall adopt the values 1.87 Mev and 2.45

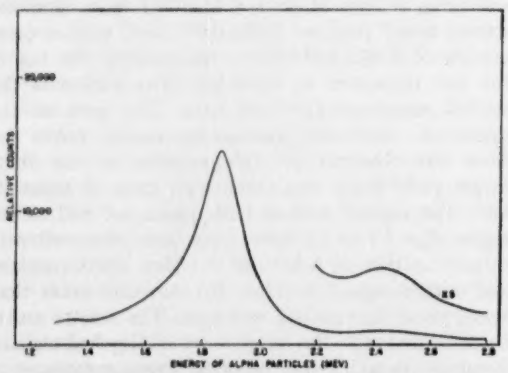

FIG. 6. Experimental excitation curve with the barrier penetration factors of the incoming and outgoing alpha particles removed. The combination of $l=1$ for the incoming particle and $l'=1$ for the outgoing particle is assumed.

[12] R. F. Christy and R. Latter, Revs. Modern Phys. 20, 185 (1948).

TABLE I. Table of reduced widths for the incident and inelastically scattered α-particles at the 1.889-Mev resonance. The first column gives the spin and parity of the B^{11*} compound state; the second and third columns give the angular momenta of the incident and emerging α particles. The fourth and fifth columns give the reduced widths divided by $\frac{3}{2}\hbar^2/MR$.

1.889-Mev resonance J	l_1	l_2	$2MR\gamma_1^2/3\hbar^2$	$2MR\gamma_2^2/3\hbar^2$
1/2+	1	1	0.12	0.85
1/2−	2	0	0.48	0.31
3/2+	1	1	0.20	0.27
			0.037	1.44[a]
3/2−	0	2	0.108	1.76
	2	2	0.79	1.97
5/2+	1	3	0.22	6
5/2−	2	2	0.87	1.08
7/2+	3	3	5	6

[a] We have assumed that the incident α particle has the larger partial width; the second sets given for a particular compound state give the results for the reverse assumption.

Mev as the position of peaks without barrier. These correspond to levels of B^{11} at 9.86 Mev with $\Gamma=125\pm10$ kev, and 10.23 Mev with $\Gamma\approx155$ kev, after changing from laboratory system to center-of-mass system.

Calculations of the reduced widths for the incoming and outgoing α particles at the two resonances were made taking the previously mentioned radius (4.9×10^{-13} cm) for the channel radius. Comparison of these results with the Wigner-Teichman limit[14] ($3\hbar^2/2MR$) are presented in Table I for the 1.889-Mev resonance and indicate that for the 1.889-Mev resonance $J\leq5/2$ if odd parity and $J\leq3/2$ if even parity. Similar computations for the 2.50-Mev resonance suggest J is probably $\leq7/2$. (We assumed because of uncertainty in the channel radius that a particular assignment was not in significant disagreement with

[13] Bloch, Hull, Broyles, Bouricius, Freemen, and Breit, Revs. Modern Phys. 23, 147 (1951).

[14] T. Teichman and E. P. Wigner, Phys. Rev. 87, 123 (1952).

theory if the reduced width was not more than a factor of two greater than the Wigner-Teichman limit.) Elkind[16] reports a new level of B^{11} at 10.32 ± 0.02-Mev excitation with width 54 ± 17 kev from the reaction $B^{10}(d,p)B^{11}$. This level is too narrow to be identified with our level at 10.23 Mev. From the limits of observation given by Elkind one can infer that if the intensities of groups corresponding to our broad levels at 9.86 and 10.23 Mev were less than half of the intensity of the 10.32-Mev group (at 90°), they would have escaped detection in Elkind's experiment. From our measurements we conclude that the cross section for excitation of the 10.32-Mev level is less than 0.006 barn for the $Li^7+\alpha$ reaction.

[16] M. M. Elkind, Phys. Rev. **92**, 127 (1953).

The authors wish to thank Professor W. A. Fowler, Professor R. F. Christy, Professor T. Lauritsen, and Professor C. C. Lauritsen for their suggestions and criticism, and Mr. R. W. Kavanagh for aid with many aspects of the experiment.

PHYSICAL REVIEW VOLUME 96, NUMBER 2 OCTOBER 15, 1954

Range of Nitrogen Ions in Emulsion

H. L. Reynolds and A. Zucker
Oak Ridge National Laboratory, Oak Ridge, Tennessee
(Received June 17, 1954)

The range of nitrogen ions in Ilford C-2 emulsion was measured for energies from 4 to 28 Mev. The rate of energy loss over this entire energy region is approximately 1.5 Mev per micron.

INTRODUCTION

THE range-energy characteristics of particles heavier than helium are difficult to predict from theory because such particles pick up electrons as they near the end of their range. In general, charge pickup and loss is observed when the ion velocity is comparable to the velocities of orbital electrons. Experimentally determined ranges of lithium and boron in emulsion[1] have illustrated the process of charge pickup, although the range over which charge pickup occurs for these particles is rather short. Miller[2] has measured the range of carbon ions in emulsion but his results apply mainly to energies higher than 30 Mev, which is above the region of charge pickup.

The range-energy relation for nitrogen ions in nickel below 30 Mev has been discussed previously.[3] It was shown that as nitrogen ions slow down in nickel they pick up electrons in such a manner that dE/dx remains nearly constant. Such behavior in emulsion would be in contrast to a calculation by Freier *et al.*,[4] which indicates that the observable thinning of the tracks of heavy nuclei as they slow down in emulsion is due to a decrease in dE/dx as the charge of the particle decreases. The range in emulsion of nitrogen ions from 4 to 28 Mev was measured with the nitrogen beam of the ORNL 63-inch cyclotron by methods described below.

[1] W. H. Barkas, Phys. Rev. **89**, 1019 (1953).
[2] J. F. Miller, University of California Radiation Laboratory Report UCRL-1902, 1952 (unpublished).
[3] Reynolds, Scott, and Zucker, Phys. Rev. **95**, 671 (1954).
[4] Freier, Lofgren, Ney, and Oppenheimer, Phys. Rev. **74**, 1818 (1948).

EXPERIMENTAL METHOD

Since the range of nitrogen ions in nickel is known for energies from 8 to 28 Mev, this portion of the range-energy curve was obtained by exposing 50-micron Ilford C-2 emulsions in the deflected cyclotron beam. To vary the energy, thin nickel foils were placed directly in front of the emulsions. The initial beam energy was determined as before[3] by observing the energy of recoil protons from a gas target. The emulsions were exposed in an evacuated chamber which was mounted on the exit port of the cyclotron. A $\frac{1}{4}$-in. brass plate with a $\frac{1}{32}$-in. slit was used as a shutter. The shutter was mounted on a Lucite rod which extended through a seal in the vacuum chamber. The shutter, thus insulated from ground, was used as a beam monitor. When a satisfactory current struck the plate the slit was rotated rapidly by means of the Lucite rod, thus exposing the emulsion to a short burst of ions. Results obtained in this manner are indicated by crosses in Fig. 1.

The low-energy portion of the curve was determined as follows: Plates exposed to the direct full-energy beam were scanned for nitrogen-proton elastic collisions. From conservation of momentum and energy it can be shown that

$$E_N=\frac{E_P[1-(M_P/M_N)]^2}{4(M_P/M_N)\cos^2\alpha},$$

where E_N and E_P are the nitrogen and proton energies after the collision, M_N and M_P are the nitrogen and proton masses, and α is the angle between the recoil proton and continuing nitrogen ion. E_P was determined

from the measured proton range and the range-energy curves for protons published by Rotblatt.[6] Particle ranges were measured with a filar eyepiece which was calibrated with a Bausch and Lomb stage micrometer. The projected angle was measured with a rotating microscope stage. By measuring the dip of both tracks and the emulsion shrinkage coefficient, the "dip" angle was determined. The projected angle and the dip angle were combined to determine α, the true angle between the nitrogen and proton tracks. All measurements were repeated by a second observer.

The errors in this second type of experiment are quite large. The percentage error in E_N due to inaccuracies in measuring α is proportional to $\tan\alpha\Delta\alpha$. For an angle α of 50 degrees and an error $\Delta\alpha$ of ± 2 degrees, the percentage error in E_N is nearly 9 percent. Because of the rapid increase of the error with increasing angle, an upper limit was set for the angles of events used. All events with a dip angle greater than 20 degrees and a projected angle greater than 50 degrees were discarded. These criteria, together with the imperfect events found, resulted in the discarding of approximately 80 percent of the proton recoil events located in the survey. The useful events remaining were grouped in ½-micron intervals; a statistically weighted mean was used for each interval. Approximately 90 events were used to obtain the results shown as circles in Fig. 1. Ilford C-2, 50-micron plates at a relative humidity of approximately 25 percent were used for both types of measurements.

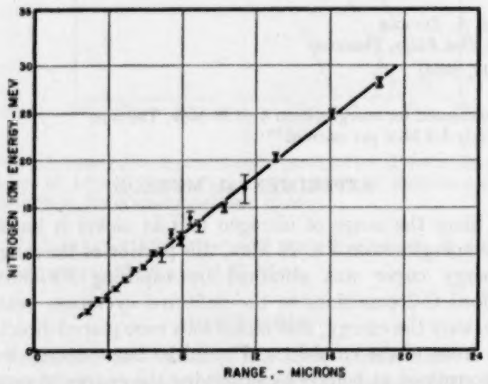

FIG. 1. Range-energy curve for nitrogen ions in Ilford C-2 emulsions. The crosses were obtained by bombardment of the plates with nitrogen ions of known energy; the dots are the results of proton-scatter events observed in the emulsion. Probable errors are shown on all points.

[6] J. Rotblatt, Nature **165**, 387 (1950).

DISCUSSION

The curve in Fig. 1 represents the experimental range-energy curve of nitrogen ions in emulsion. Probable errors are shown on all points. A calculation by Lonchamp[6] predicts a range approximately 10 percent smaller from 10 to 30 Mev with a somewhat larger dE/dx than our data indicate below 10 Mev. The difference is probably due to inaccurate charge-velocity relations used by Lonchamp.

Lonchamp[7] has concluded from considerations of the photographic process that the thinning down of the tracks of heavy ions as they approach the end of their range can be explained by the fact that the thickness of the developed track is due mainly to δ rays which at low ion velocities no longer have sufficient range to broaden the track. This conclusion is supported by our evidence that the rate of energy loss is nearly constant over the region of thin-down for ions with masses near that of nitrogen.

We wish to thank Mrs. W. Bowelle for her assistance in scanning and Professor L. D. Wyly for many helpful discussions.

[6] J. P. Lonchamp, J. phys. radium **14**, 89 (1953).
[7] J. P. Lonchamp, J. phys. radium **14**, 433 (1953).

Beta Spectra of C^{14} and S^{35}

A. Moljk and S. C. Curran
Glasgow University, Glasgow, Scotland
(Received June 28, 1954)

The beta spectrum of carbon 14 was measured with radioactive methane as the source in a proportional counter. To reduce end and side wall effects a pressure of 6 atmos (argon) was employed and a magnetic field of 3500 gauss was applied parallel to the counter axis. The spectrum of sulfur 35 was observed with the same equipment. The theoretical allowed spectrum for this source was modified according to calculations made to take into account the instrumental limitations. The modified theoretical form agreed excellently with the observations down to energies below 5 kev. With the sulphur spectrum as an experimental standard for an allowed shape very accurate empirical correction factors could be obtained, and these were applied to the data for C^{14}. The adjusted data for C^{14} were found to follow the theoretical shape for an allowed transition to within 1 percent accuracy at energies above about 3 kev.

INTRODUCTION

THE beta decay of C^{14} has been investigated by many,[1] but some unsatisfactory features remain. The spins of both C^{14} and N^{14} have been measured directly, giving $I=0$ and $I=1$, respectively. A spin change of unity is involved in the transition which is allowed, unfavored, according to Gamow-Teller rules. The observed comparative half-life ft is 1.9×10^9 sec, which exceeds the average value by a factor of about 10^4, and suggests empirical classification among second forbidden. Feenberg[2] suggested that an explanation of the anomaly was possible on the basis of a transition from an S state in C^{14} to a pure D state of N^{14} where LS coupling prevails. A small admixture of ^3S, less than 10^{-2}, to account for the large ft value may dominate the beta decay and produce a close approximation to an allowed shape. The shape of the spectrum is of enhanced interest in this case. There is general agreement that the shape of the spectrum is allowed down to about 50 kev, but below that there is some disagreement. Wu[3] found the Fermi plot linear down to 25 kev. Recently Mize and Zaffarano,[4] with a thin source in a proportional counter, found that the intensity dropped below the theoretical value at energies below about 50 kev. Their method seemed to work correctly with S^{35} and Pm^{146}.

Most of the experimental difficulties in the low-energy region arise in the use of solid sources and here the proportional counter with a gaseous source can be applied most advantageously. In fact, C^{14} has been investigated in this way by Angus, Cockroft, and Curran[5] and their results showed a deficiency of low-energy particles. Since then the technique has improved very considerably. Thus field-correcting tubes have been introduced,[6] thereby removing much of the uncertainty associated with the elimination or control of end effect by other means. The use of strong axial magnetic fields to reduce wall effect has proved valuable. For these reasons it was clear that an accurate examination of the C^{14} spectrum with the improved proportional tube spectrometer was desirable.

CHARACTERISTICS OF THE SPECTROMETER

With field tubes at the correct potential the gas multiplication factor is effectively constant throughout the volume of the cylinder of length equal to that of the operating central wire. With radioactive gas as a constituent of the filling mixture the beta spectrum can be analyzed successfully, provided the quantity of such gas does not adversely affect resolution. A strictly accurate spectrum is observed, provided each beta particle spends the whole of its energy in the sensitive volume and no electrons enter from outside. This condition can be satisfied at best approximately at high energies. From this point of view both S^{35} and C^{14} must be regarded as intermediate cases (end points at 167 and 156 kev, respectively).

Suppose that ρ nuclei decay per second and per cm^3 and that the fraction of beta rays with energy between E and $E+dE$ is $N(E)dE$. In the sensitive volume V we have $N\rho VdE$ such electrons produced per second. If they expend their energy within the volume V they give rise to pulses proportional in amplitude to the energy E and they are counted with an analyzer as occupying the channel E of width dE. Some of them escape from the sensitive volume or they reach the cylinder and so give rise to smaller pulses which are counted in lower-energy channels. If R is the particle range corresponding to the energy E it can be shown that for the electrons $N\rho R/4$ escape per cm^2 per sec through the surface S of the sensitive volume. Thus, $N\rho VdE[1-\frac{1}{4}R(S/V)]=N\rho VdE(1-\delta_E)$ are counted correctly in channel E. Here δ_E is the fractional loss to lower channels. At both ends of the cylindrical counting volume V, the rate of entry into V of electrons of energy E is $N\rho R/4$ per cm^2. Again these electrons spend part of their energy in V and give rise to smaller

[1] Hollander, Perlman, Seaborg, Revs. Modern Phys. **25**, 478 (1953).
[2] E. Feenberg and K. C. Hammack, Phys. Rev. **75**, 1877 (1949).
[3] L. Feldman and C. S. Wu, Phys. Rev. **75**, 1286 (1949).
[4] Summary Report of the Indiana Conference on Nuclear Spectroscopy and the Shell Model, May, 1953 (unpublished).
[5] Angus, Cockroft, and Curran, Phil. Mag. **40**, 522 (1949).
[6] A. L. Cockroft and S. C. Curran, Rev. Sci. Instr. **22**, 37 (1951).

pulses. If the specific ionization of electrons can be assumed constant, pulses caused by electrons escaping from or entering the sensitive volume are spread uniformly into all channels below E. In the low-energy region this is too approximate an assumption, and the spreading has to be determined by numerical integration, applying the range-energy relationship.

For a cylindrical counter of radius r and length l, the fraction δ_E not counted correctly in channel E is, as shown above,

$$\delta_E = R/2l + R/2r,$$

so that r and l should be as large as practicable, while the range R of the beta rays should be small. A gas of high atomic number helps to restrict R but xenon is difficult to procure in adequate quantities. Here argon at pressures up to 7 atmos was used. The dimensions were $r=6.8$ cm, $l=19.5$ cm. At the pressure of 5.5 atmos of argon, frequently employed, the range of electrons of energy 100 kev is about 2 cm, not small compared with r. But the application of an axial magnetic field B, 3500 gauss, forces the primary particles to describe circles of radius $r_m=mv/eB$ and as the particle loses velocity v the radius r_m rapidly decreases. The wall effect is so reduced at least in the ratio $R/2r_m$. Table I shows some calculated corrections. Separate experiments showed that the end effect was reduced by the field to approximately half the value in the absence of field. This was ascribed to the influence of the field on the number leaving and entering the ends.

The fraction δ_E of electrons in channel E which give smaller pulses to the channels below E decreases with energy and is less than 2 percent below 25 kev, while that caused by more energetic electrons increases. The magnetic field effect makes the calculations rather approximate, but the results are satisfactory, since the correction refers to something like 5 percent of the particles. The nature of the particle trajectories, which are particularly irregular at low energies as a result of scattering, adds to the uncertainties. The corrections as applied to S^{35} yield very satisfactory agreement between the theoretical and experimental spectra, as is shown below. This allows us to proceed in an alternative manner with the study of C^{14}. The spectra of C^{14} and S^{35} have similar limiting energies and the latter has been shown, and is shown here, with the application of the corrections, to have a very straight Fermi plot down to energies below 5 kev. Taking the experimental

TABLE I. Correction factors at 5.5 atmos pressure and 3500 gauss.

Electron energy in kev	$R/2l$ %	r_m/r %
25	0.6	2.2
51	1.7	3.3
102	5.7	4.6
153	11.0	5.7

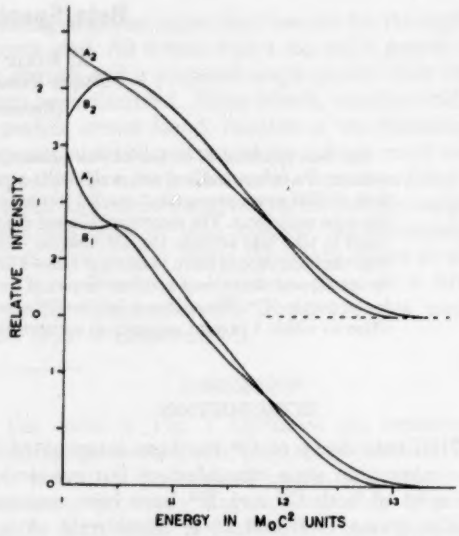

FIG. 1. Curves A_1 and B_1: observed spectra of S^{35} and C^{14} respectively; Curves A_2 and B_2: corresponding theoretical spectra, assuming the transitions allowed.

results for S^{35} as standard for an allowed source, we can deduce by comparison with the theoretical spectrum the precise correction to apply at any particular value of energy. In this way the observations for a spectrum such as that of C^{14} can be corrected accurately. The corrections throughout the range are relatively small and the corrected experimental data can be compared closely with the theoretical value. It is estimated that the true intensity is found to better than 1 percent accuracy in this manner. This technique is applied to C^{14} in Table I. It is worth stressing that this comparative method of study of beta spectra is one of fairly wide applicability. A number of accurately studied spectra, such as that of S^{35}, are available, and any instrument subject to errors and uncertainties as an absolute tool can nevertheless prove reliable in relative work. This is particularly true for the proportional counter as completely equivalent sources, as regards thickness, etc., may be difficult to make in solid form, but are readily produced as gaseous constituents of the gas mixture used in the counter.

EXPERIMENTAL ARRANGEMENT

The choice of a suitable gas for the analysis of C^{14} was determined solely on considerations of resolving power. Here methane suggested itself as eminently suitable. Carbon dioxide was liberated from barium carbonate by vacuum heating and converted to methane by adding hydrogen. Ruthenium was used as a catalyst; it was placed in a Pyrex tube and heated to 250°C. About 10 forced passages of the gases over the catalyst completed the reaction ($CO_2+4H_2 \rightarrow CH_4+2H_2O$). Excess hydrogen was removed through a heated

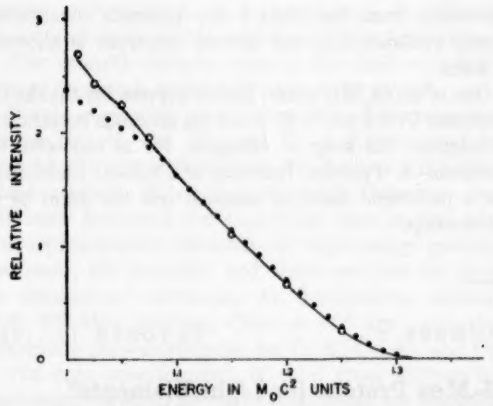

FIG. 2. The theoretical spectrum of S^{35}, shown by the filled circles, is modified, according to calculations of the instrumental effects, to the shape shown by the full curve. The open circles show the experimental results, indicating close agreement.

palladium tube. The radiomethane required in the counter was small in amount (<0.01 percent) and the main mixture consisted of methane to a pressure of 10 cm Hg and argon to a pressure of 6 atmos. Calcium turnings were used in the attached purifier. The width at half-height of the K_α line of silver was 15 percent. For the work on S^{35} labeled CS_2 vapor was used. Neither radioactive source reacted with the counter walls. The voltage on the counter was about 6500 volts. A nickel wire delay line kicksorter of the Hutchinson-Scarrott[7] type was used. This 100-channel pulse analyzer accepts pulses from 4.1 volts to 49 volts in amplitude. In this work it was mostly used on the 34-channel setting. Statistical errors of less than 2 percent could be achieved in a run lasting a few minutes. The kicksorter channels were calibrated in volts using the builtin pulse generator and calibrated attenuator. In energy units the calibration was effected with the fluorescence x-rays of silver. The counting rate was adjusted to about 14 000 per min. The background rate was about 450 per min. The complete spectra and various parts were analyzed many times and the results were self-consistent. The theoretical spectra were calculated using the Bethe-Bacher approximation for the Coulomb (Fermi) factor.

RESULTS AND DISCUSSION

In Fig. 1, one set of measurements for S^{35} and C^{14} are shown. In the upper figure the theoretical spectra for both are given. It is clear that the experimental results differ from the theoretical in the same way in each case. There is obviously about the same amount of distortion produced at low energies where some excess of particles caused by the end and wall effects already discussed are apparent. Both the calculated and experimental spectra crossover in the same energy channel. It is obvious that the distortion is about the same in amount for each spectrum and we can say that if S^{35} is allowed in form the experimental data for C^{14} is such as to indicate, to a fairly close approximation, that C^{14} is allowed in form.

For more detailed comparison of theory and experiment graphical calculation of the correction per channel was made for S^{35} and C^{14}. The results of this treatment, along the lines discussed above, are given in Fig. 2 for S^{35} only. The results for C^{14} not reproduced here took a very similar form, but we prefer to apply the alternative method of correction to this source as indicated below. In making the graphical calculations the spectrum was plotted in terms of range R rather than energy E, using the range-energy relationship for argon. It should be remarked that the total fraction of electrons entering the sensitive volume if no magnetic field is applied is $[(1/2l)\int_0^R NRdR]/\int_0^R NdR$, which in the present case is 3 percent. If magnetic field is applied this fraction becomes 1.6 percent as shown above. This must be doubled to 3.2 percent, since an equal percentage of the detected electrons pass out of the volume. The wall effect falls from about 9 percent (expressed in the same way) to about 2 percent in the case of field applied. Hence the total of wrongly analyzed pulses amounts to approximately 5 percent. This total agrees well with the sum of those spread into lower channels. The validity of the correction procedure was checked at different values of gas pressure and magnetic field strength.

It can be seen from Fig. 2 that S^{35} yields results entirely consistent with an allowed type of decay. This gives, in conjunction with earlier results, complete confidence in adopting S^{35} as a standard allowed spectrum for comparison with that of C^{14}.

To compare the results for C^{14} with theory the experimental curve for S^{35} was superimposed on the theoretical curve for the same source (curves A_1 and

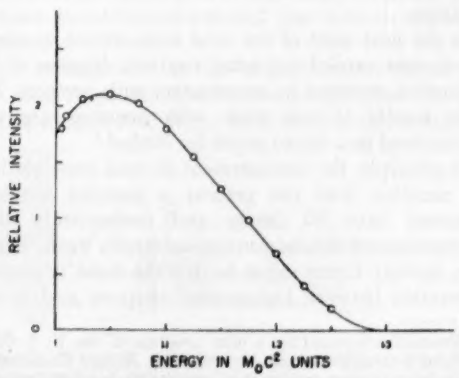

FIG. 3. The full curve represents the theoretical spectrum of C^{14}, assumed allowed. The circles show the corrected experimental data.

[7] G. W. Hutchinson and G. G. Scarrott, Phil. Mag. 42, 792 (1951).

A_2 of Fig. 1) normalizing for the same number of particles. In this way an accurate correction factor for beta intensity observed at any particular energy was deduced. This factor was then applied to the experimental data for C^{14} (curve B_1 of Fig. 1), and in Fig. 3 we show separately a plot of this corrected data. The full curve in Fig. 3 represents the theoretical form of the C^{14} spectrum, if the decay is allowed. It is seen to fit excellently the adjusted experimental values and the agreement from less than 3 kev upwards constitutes strong evidence that the carbon spectrum is allowed in form.

One of us (A.M.) would like to express his thanks to Professor P. I. Dee, F. R. S. for his generous hospitality throughout his stay in Glasgow. He is indebted to Professor A. Peterlin, Institute of Physics, Ljubljana, for a prolonged leave of absence and the grant of a scholarship.

PHYSICAL REVIEW VOLUME 96, NUMBER 2 OCTOBER 15, 1954

Total Cross Sections of 208-Mev and 315-Mev Protons for Light Elements*

HERVASIO G. DE CARVALHO†
Institute for Nuclear Studies, The University of Chicago, Chicago, Illinois
(Received June 25, 1954)

Transmission measurements were performed with an external collimated proton beam of The University of Chicago 170-inch synchrocyclotron. Total cross sections of the neutron and ten light elements (H and D, Li, B, Be, C, N, O, Al, S, and Cl) were measured by coincidence and anticoincidence methods at proton energies of 208 and 315 Mev at several subtended angles.

The cross sections obtained include all processes except the Coulomb scattering, for which corrections were applied. The corrected cross sections, measured at different subtended angles ("poor geometries") were plotted with their statistical uncertainties as a function of the solid angle subtended or of the angle, and extrapolated to zero degrees ("good geometry").

Only a limited number of previous investigations of the light elements at high particle energies have been made. The results found in the present study for the proton total cross sections for the various elements were comparable to the available published neutron total cross sections measured at the same energies.

It was found, by application of the transparent optical model, that cross sections measured were consistent with a nuclear radius $R=1.23A^{\frac{1}{3}}\times10^{-13}$ cm and an absorption coefficient $K=0.5\times10^{13}$ cm^{-1}.

I. INTRODUCTION

THE measurement of the total cross section of nuclei for high-energy nucleons gives information about the nuclear radius and the behavior of the high-energy nucleons within nuclear matter. In particular it gives information about the Serber[1] transparency effect of nuclear matter to high-energy nucleons which up to the present time has been studied mainly with neutrons.

In the past most of the total cross-section measurements were carried out using neutrons because of the difficulties involved in experiments with protons. The main results of this work with neutrons are well summarized in a recent paper by Nedzel.[2]

In principle, the measurement of total cross sections for neutrons does not present a complex problem. Neutrons have no charge and consequently their electromagnetic interactions are extremely weak. Therefore, nuclear forces cause by far the most important interaction between high-energy neutrons and nuclei. The measurements of neutron total cross sections are not complicated by the large contribution of the nuclear Coulomb field, which in the case of proton scattering is responsible for a fast rise of cross section at small angles.

In general one expects that the cross section depends on the energy. Since as a rule high-energy neutrons are not monoenergetic it is useful to calculate an effective neutron energy $\bar{E}_{\text{eff}}$. This is an involved problem, which is a serious handicap for the interpretation of the measurements. A second disadvantage follows from the fact that high-energy neutrons are detected indirectly by nuclear reactions or by recoil protons produced in neutron-proton scattering.

In contrast to the neutron situation, collimated monoenergetic beams of protons are readily obtained at high energies. Owing to energy loss by ionization, however, protons of several-hundred Mev energy are not able to cross even one entire nuclear interaction mean free path. In order to measure the nuclear interaction at a given energy it consequently becomes necessary to use relatively thin absorbers. As another difficulty, Coulomb scattering does not allow the direct "good geometry" measurements of total nuclear cross sections, but these can be obtained indirectly by a

* Research supported by a joint program of the U. S. Office of Naval Research and the U. S. Atomic Energy Commission.
† On leave of absence from the Conselho Nacional de Pesquisas of Brazil.
[1] R. Serber, Phys. Rev. 72, 1114 (1947).
[2] V. A. Nedzel, Phys. Rev. 94, 175 (1954).

precise extrapolation of measurements at different "poor geometries" to the condition of "good geometry."

The research already done in this field with high-energy protons is covered by only a few papers.

Proton absorption cross sections have been measured for Be, C, Al, Cu, Pb, and U by Kirschbaum[3] for protons of average energies of 305, 240, and 185 Mev. More recently Birnbaum, Crandall, Schecter, and Millburn[4] measured the absorption cross section of a few representative elements for high-energy protons, deuterons, He^3 particles, and alpha particles by using an attenuation technique. At Brookhaven, working with 870-Mev protons, Chen *et al.*[5] are measuring absorption cross sections for Be, C, Al, Cu, Sn, and Pb.

The only measurements of total cross sections for high-energy protons are the ones published by Marshall, Marshall, and Nedzel[6] at 410 Mev and of Chen[5] at 870 Mev. Consequently, following a suggestion of Professor John Marshall, it was decided that this study would be devoted to measuring total cross sections for protons on selected elements at energies between 200 and 400 Mev.

II. GENERAL FEATURES OF THE EXPERIMENT

For reasons mainly related to the Coulomb scattering, the elements of low atomic number were chosen for investigation. Hydrogen and deuterium have a very special importance since p-p and n-p scattering cross-section data are essential for the study of the nature of nuclear forces, and for this reason careful experiments to obtain their cross sections were carried out.

The elements for which high-energy proton scattering was studied were hydrogen and deuterium, lithium, beryllium, boron, carbon, nitrogen, oxygen, aluminum, sulfur, and chlorine.

A. Nature of the Samples

The cross section of hydrogen for 315-Mev protons was measured directly by using liquid hydrogen; the cross section for 208-Mev protons was obtained from the difference of the measured cross sections of carbon and polyethylene. The proton-neutron cross section for hydrogen was obtained from the difference between the measured cross sections of equal thicknesses of heavy and light water. The oxygen, sulfur, and chlorine cross sections were obtained from the differences, respectively, between those of water and hydrogen, carbon disulfide and carbon, and carbon tetrachloride and carbon. The nitrogen cross section was measured in liquid nitrogen, by using a special Styrofoam container. For the remaining elements, solid samples were used, with the best available purity. The lithium absorber was specially prepared as follows: Li metal was cleaned under kerosene, pressed in an aluminum die under 50 atmospheres, and sealed into an aluminum can with windows 0.003 inch thick. When not in use, the sample was kept under kerosene to prevent oxidation. The boron sample was very finely powdered amorphous boron in a thin-walled Lucite cylinder.

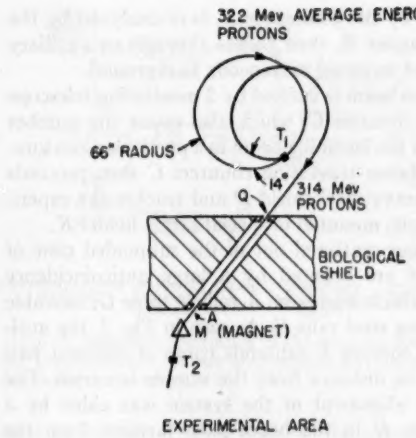

FIG. 1. Method used to select proton energy and to collimate proton beam.

B. Experimental Layout

An external well-collimated monoenergetic beam of protons was scattered out of the Chicago 170-inch synchrocyclotron from an internal beryllium target at 66 inches radius. The scattered protons were analyzed energy-wise by deflection in the fringing field of the cyclotron magnet, and then were defined as a beam by passing through two collimators in the heavy shield, (Fig. 1). The first collimator Q, located inside of the synchrocyclotron room, was a $\frac{1}{4}$-inch vertical slit obtained with stainless steel bricks. Outside of the biological shield was a second collimator A of $\frac{3}{8}$-inch diameter brass tube inside a lead brick. Following this the beam was deflected a second time with an auxiliary magnet B.

The arrangement of the experiment is shown in Fig. 2. The proton beam already analyzed in the fringing magnet field of the cyclotron enters the experi-

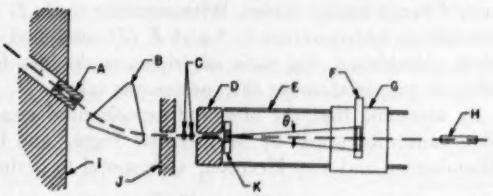

FIG. 2. Schematic arrangement of experimental apparatus (not to scale). A-collimator, B-auxiliary magnet, C-monitor telescope coincidence counters, D-shield, E-rails, F-anticoincidence counter, G-rolling table, H-cathetometer, I-heavy shield, J-auxiliary shield, K-target holder.

[3] A. J. Kirschbaum, thesis, University of California Radiation Laboratory Report UCRL-1967, 1952 (unpublished).
[4] Millburn, Birnbaum, Crandall, and Schecter, Phys. Rev. **95**, 1268 (1954).
[5] Chen, Leavitt, and Shapiro, Phys. Rev. **94**, 784 (1954).
[6] Marshall, Marshall, and Nedzel, Phys. Rev. **91**, 767 (1953).

mental area by the collimator A, is re-analyzed by the auxiliary magnet B, then passes through an auxiliary shield J used to avoid extraneous background.

The proton beam is defined by 2 monitoring telescope coincidence counters C, which also count the number of protons in the incoming beam in a particular measurement. The beam traversing counters C then proceeds through a heavy steel shield D and reaches the experimental sample, mounted in special target holder K.

The protons scattered out of the subtended cone of half angle θ are counted by a large anticoincidence counter F which stands on a rolling table G, movable on two strong steel rails E. As seen in Fig. 2, the anticoincidence counter F subtends cones of different half angles θ as its distance from the sample is varied. The preliminary alignment of the system was aided by a cathetometer H in the beam path farthest from the cyclotron in the end of the experimental area.

C. The Principle of Measurement

The thin sample inserted in the proton beam attenuates it exponentially. The cross section corresponding to a particular subtended angle θ is given by

$$\sigma = (1/N) \log_e(I_0/I), \tag{1}$$

where N is the number of nuclei per cm^2 in the sample, I_0 is the beam intensity at the detector counter with no sample, or for a particular measurement is the number of protons inside the subtended angle θ. I_0 is given by: $(M-B_0)$, where M is the monitoring count and B_0 is the flux of protons removed from the chosen angle. Protons passing through the telescope monitoring coincidence counters undergo both nuclear and Coulomb scattering along the path which disturbs somewhat the beam collimation. A number of protons B_0 are therefore scattered out of the subtended cone angle. I is obtained by measuring by anticoincidence the total number of protons B removed from the beam with the experimental sample in position, *viz.*: $M-B$. Therefore the cross section is given by

$$\sigma = (1/N) \log_e[(M-B_0)/(M-B)]. \tag{2}$$

D. Energy and Homogeneity of the Proton Beam

The energy of the highly collimated beam was measured from copper range measurements by using Aron's[7] range energy tables. With counters C (1, 2) in coincidence and counters 1, 2 and F (3) combined in triple coincidence, the ratio of triples *vs* doubles for different copper absorber thicknesses was taken.

By assuming that the observed experimental straggling values in copper by Mather and Segrè,[8] and by Bloembergen and Van Heerden,[9] correspond to perfect monochromatic proton beams, and using the straggling measured from the number-distance range curves in this experiment, an energy inhomogeneity of about 4 Mev for the 208-Mev proton beam and 8 Mev for the 315-Mev proton beam was obtained.

III. APPARATUS

A. Counting Rate

Since the precision of results depends on the statistical uncertainty and on the reliability of the counting system, careful attention was directed toward obtaining strict linearity and maximum stability in the counting apparatus, and at the same time minimum sensitivity to any extraneous radiation.

The arrangement of counters is shown in Fig. 2.

The protons produced by the synchrocyclotron are produced in bursts of short duration, and the counting circuits must detect, resolve, and count all protons in the beam used in the experiment.

For a cyclotron pulse length of 150 microseconds and repetition rate of 60 cycles, in order to avoid losses greater than 1 percent in the monitoring system, the resolving time of the scaling system to determine coincidences between different counters must be no less than about 10^{-7} second for a rate of about 1000 counts per second in counters 1 and 2. Losses have been tested experimentally by running the same measurement at different counting rates. At the rate of a few thousand protons per second, the cross-section measurements were only slightly higher and it was found that for counting rates of less than 600 protons the results were constant within the statistical uncertainty. Three hundred counts per second, therefore, was chosen as a safe counting rate. In this condition, the counting losses had no appreciable effect on the cross-section measurements.

B. Counters

When protons pass through the beam-monitoring counters 1 and 2 of the telescope arrangement, as stated earlier, the collimation of the beam is somewhat disturbed by Coulomb and nuclear scattering produced by the nuclei of the materials in the counters, the result being that about 1 percent of the total protons are scattered out of the beam. It happens, also, that some protons are backscattered or absorbed by the thick walls of the anticoincidence counter; furthermore, some protons are scattered by the air between the monitors and the detector. This scattered loss of beam together with accidental counts caused by stray radiation in the experimental area constitutes B_0, the anticoincidence background of our measurements. The ratio I_0/I is obtained by taking into account this background. If B_0 is the total number of protons removed from the beam without the absorber and recorded by counter F by the anticoincidence method, I_0 is obtained by subtraction of the background B_0

[7] Aron, Hoffman, and Williams, AECU-663, University of California Radiation Laboratory Report UCRL-12, 1949 (unpublished).

[8] R. L. Mather and E. Segrè, Phys. Rev. 84, 191 (1951).

[9] N. Bloembergen and J. Van Heerden, Phys. Rev. 83, 561 (1951).

from the monitoring counting rate M, *viz.*: $I_0 = M - B_0$. In order to obtain I_0 close to M it is necessary to minimize B_0. This is in part obtained by reducing the thickness of the scintillation counter required for sufficient pulse size.

The monitoring counters were circular counters made of plastic scintillator "Pilot B" with $\frac{1}{8}$-inch thickness and 1-inch diameter. This thickness appeared to be very satisfactory. The anticoincidence counter F is a large circular liquid scintillator ($9\frac{1}{4}$-inch diameter by 1 inch thick) made of a solution of 3 g/liter of terphenyl in phenylcyclohexane with 10 mg/liter of diphenylhexatriene in a Lucite cell enclosed in a light-tight aluminum box. The light produced in the scintillating material by energy loss of the proton going through it is conducted by a tapered Lucite light pipe to two photomultiplier tubes in parallel which convert the scintillation into an electric pulse.

C. Electronics

The adjustment of the electronic circuits will be described later and only the general description of the equipment used will be given here. Fast counting systems and fast resolving time coincidence circuits are necessary in order to obtain reliability with the counting rate used and in order to minimize background caused by accidental coincidence.

The negative pulse coming from the anode of the photomultiplier tube, Fig. 3, with a space charge limiter circuit developed by J. Fischer, is transmitted by a condenser to a coaxial cable, of 180-Ω characteristic impedance, and to a fast distributed amplifier. The coaxial cables, in order to prevent reflections of the signal, were each properly terminated at least on one end.

In order to correct for the time of flight of the particles, and transit time of signals in the tubes, amplifiers and connecting cables, the signal was transmitted through an adjustable cable delay with a 180-Ω impedance line switch box, capable of giving integral time delays from 1 to 63 millimicroseconds. The signal pulses from the monitor counters were each amplified through two and a half distributed amplifiers of 200-megacycles band width and voltage gain of 10 each. The pulses were clipped to 8×10^{-9} second by shorted cables of proper length and fed into a two-channel crystal diode coincidence circuit developed at the University of Chicago by J. Fischer. The output of the coincidence circuit was connected to a calibrated wide-band attenuator box and fed to a Hewlett-Packard 10 megacycle (scale of one hundred) scaler through two distributed amplifiers.

The anticoincidence pulse, from the two photomultiplier tubes of the anticoincidence counter was amplified by three distributed amplifiers and connected without clipping to a diode coincidence-anticoincidence circuit which also received the pulses from the first two counters by parallel connection to the first coincidence circuit. The output of the coincidence-anticoincidence was fed to a Hewlett-Packard 10 megacycle scaler. Both fast scalers were followed by slower scalers (scale of one thousand) and a mechanical register.

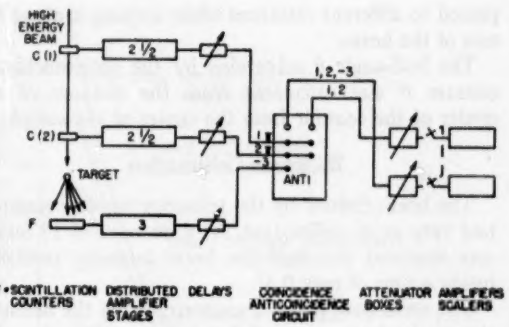

FIG. 3. Schematic illustration of the counting system, showing the anticoincidence counter arrangement and the block-diagram of the electronic system.

IV. PROCEDURE

The precision of the measurement depends on: (a) the geometrical alignment of the apparatus, (b) proper operation of the electronic equipment, (c) the correction for the effect of Coulomb scattering, and (d) the determination of the magnitude of errors inherent in the procedure chosen.

A. Geometrical Alignment

The geometrical alignment of the apparatus began with the proper location of the narrow collimating slit in the fringing magnetic field of the synchrocyclotron for a particular position of the internal beryllium target which provided protons of the desired energy. The proton beam was then located by searching horizontally and vertically, using the telescope coincidence counters on a rolling table which would also be displaced vertically.

Once the beam was located at two points, reasonably far apart, it was possible to set the optical axis of a cathetometer, so as to coincide exactly with the line through these two points. By the use of the cathetometer the telescope monitoring counters and the steel shield D, Fig. 2, were then aligned.

The two coincidence monitoring scintillation counters were fastened to the steel shield by special rails so that they could be removed and reinserted in the line of the beam. Each counter was marked with a dot at its center. This allowed a quick check of alignment of the counters by the cathetometer. An automatic sample holder K was also set on the axis of the beam providing a means of changing the different experimental samples with automatic alignment. The rails of the rolling table were located parallel to the proton beam in such a way that the anticoincidence counter could be dis-

placed to different distances while keeping it along the axis of the beam.

The half-angle θ subtended by the anticoincidence counter F was calculated from the distance of the center of the counter from the center of the sample.

B. Beam Collimation

The beam defined by the telescope monitor counters had very good collimation. At a distance of 12 feet it was observed that half the beam intensity remained inside a cone of only 0.3°.

The number of protons scattered out of the beam by the monitoring counters C, by the air, and by the thick walls of counter F was 1.3 percent at 10°, 2.2 percent at 3°, and 4 percent at 1°. Air attenuation makes an appreciable contribution to this effect.

C. The Adjustment and Operation of the Electronic Equipment

The electronic circuits were turned on and allowed to reach their equilibrium temperature condition. The monitoring counters C were connected in coincidence and counter F in anticoincidence. The adjustment of the electronics was carried out in the following steps. The counters C (1 and 2) were placed in the collimated proton beam and connected in double coincidence. In order to assure the time alignment of the two monitoring counters the delay of counter 1 with respect to 2 was varied; the coincidences per second were plotted as functions of the delay in millimicroseconds added to the channel of counter 2.

With the system operating on a plateau both with respect to pulse attenuation and photomultiplier voltage, the delay of counter 2 with respect to 1 was set to the value at the center of its delay curve.

Then counter F (3) was connected in anticoincidence with counters 1 and 2. The anticoincidence rate per unit of double coincidence $(1, 2, -3)/(1, 2)$ was plotted *vs* delay of counter F, for various values of voltage of the photomultiplier of F, and for various attenuations of pulse $(1, 2, -3)$ as it entered the scaler which recorded it. For the anticoincidence delay curve, a large inverted plateau curve was obtained. The delay of counter F (channel No. 3) was set to the value at the center of this delay curve. Counter F moves with the rolling table, and for each chosen distance from counters 1 and 2 the delay was adjusted to the value at the center of the corresponding new delay curve.

The shape and the width of this plateau curve gives good information about the proper operation of the over-all system including the coincidence circuit.

D. The Coulomb Scattering

The precision of the measurement of proton total nuclear cross sections depends on the accuracy of the extrapolation to zero degree angle, corresponding to the "good geometry" measurement condition. In order to obtain the best extrapolation, one must know the corrections in measurements at various angles due to Coulomb scatterings (single, plural, multiple, and the interference effect between Coulomb and diffraction scatterings).

This correction was obtained in the following way: The single Coulomb scattering correction was calculated from the Rutherford formula corrected for each special case and only this correction was applied. The remainder of the Coulomb scattering was kept to a magnitude which does not disturb the measurements and the precision of the extrapolation by a proper choice of the thickness of the target and of the angles used in the extrapolation. The multiple and plural scatterings give a large contribution only at very small angles and fall off very rapidly with increase of the subtended angle. One cannot obtain equations precise enough for corrections of these scatterings at very small angles, but by using formulas from the theory of multiple scattering it is possible to establish at which angle this scattering starts to give an appreciable contribution to the measured total cross section.

By assuming a Gaussian distribution for the multiple Coulomb scattering, and calculating the mean square deflection by the Rossi-Greisen[10] equation for the target thicknesses used in the measurement, it is found that for angles four times the mean square deflection the corresponding multiple Coulomb scattering effect is smaller than one percent of the total nuclear cross section measured.

In order to verify these results experimentally and to determine the contribution of the plural scattering and of an interference term, arising from a cross product of nuclear and Coulomb scattering, it was decided to investigate experimentally the magnitude of these Coulomb scattering effects for the worst condition; the lowest energy used, thickest target with highest Z and small angles. For that purpose the total cross section of a lead scatterer of a thickness of 7.63 g/cm^2 was measured, using protons of 214 Mev in a range of 1.4° and 15°.

From neutron cross-section data, from the measurements of Marshall, Marshall, and Nedzel,[6] and from the present measurements of total nuclear cross sections for protons on light elements one can infer the proton total cross section of lead at 214 Mev within ±10 percent precision. At angles of the order of 1.4° the nuclear part of the total cross section is only three percent of the measured total cross section, and therefore an error of 10 percent of the nuclear cross section amounts to only 0.3 percent of the total measured cross section. Therefore, it is possible by subtraction of the nuclear cross section and single Coulomb scattering (integrated from 1.4° to 180°) from the measured total cross sections to obtain a curve corresponding

[10] B. Rossi and K. I. Greisen, Revs. Modern Phys. 13, 240 (1941).

to the sum of the multiple plus the plural Coulomb scattering and the interference effect between Coulomb and diffraction scattering, and therefore to verify the contribution of these scatterings on the total cross section measurements.

Figure 4 shows plots of the above curves as a function of $\langle\theta^2\rangle_{Av}^{\frac{1}{2}}$. It can be seen that at four times $\langle\theta^2\rangle_{Av}^{\frac{1}{2}}$ the contribution of Coulomb scatterings is not appreciable. One can therefore safely extrapolate to zero the cross section from angles greater than $4\langle\theta^2\rangle_{Av}^{\frac{1}{2}}$. Since $\langle\theta^2\rangle_{Av}^{\frac{1}{2}}$ is a function of the square root of the thickness of absorber, one concludes that thin absorbers allow better extrapolations. However, in order to obtain good statistics with thin samples, longer cyclotron running time is needed. Hence it is necessary to compromise. It is also apparent that measurements of total cross sections of light elements provide best conditions for such extrapolations since one can use reasonably thick absorbers. With a target thickness of about 1 g/cm² and proper running time, it is possible to measure the cross section of elements heavier than chlorine provided appropriate corrections and careful extrapolation to "good geometry" is carried out.

The beam-monitoring coincidence counters with their light-tight shields have a thickness of about 1 g/cm². Therefore, by nuclear and Coulomb scattering they disturb the beam and remove about one percent of the total beam intensity at a distance of about three feet from the detector counter. During the measurements of cross section at subtended angles of about 3°, the protons have to traverse about 10 feet of air (about 0.4 g/cm²) which also attenuates the beam. These two effects constitute part of background measurements B_0 and put a limit to the minimum thickness of sample used, since the sample extenuation should not be much smaller than the inevitable background.

E. Errors

No correction was made for charged particle production because at the energies used the total cross section for pion production is much smaller than the measured total cross section.

Since the over-all accuracy was limited by the total number of counts obtained in the attenuation measurements, because of the statistical error of counting, it was decided to have for each sample an attenuation number of counts B exceeding the normal background B_0 by at least 10 000 counts.

The beryllium attenuation at different times during the one set of measurements was observed. By this process it was verified whether drifts occur in the linearity of the equipment. When several cross sections at the same energy were to be measured, but at different running times the beryllium attenuation at 15° was observed and its consistency with the previous results within the statistical errors was assured.

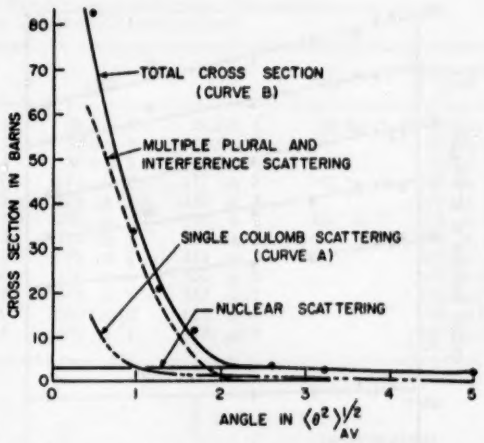

FIG. 4. The total absorption cross sections (curve B) of a lead target (with a 7.6 g/cm² thickness), plotted as functions of the mean square deflection produced by multiple Coulomb scattering as calculated from the Greisen-Rossi equation. (The multiple, plural, and interference scattering curve is obtained from the difference between the experimental curve B and the calculated Rutherford scattering plus the nuclear scattering curves.)

In order to detect electronic drifts the background measurement B_0 was very useful. During an experiment the background with its statistical deviation was plotted against the total number of counts and it was possible to observe abnormal deviations, if any, corresponding to drifts of the electronic circuit.

As a check against systematic errors, the cross sections were measured using the coincidence method at 315 Mev for 15°. The results by the two methods, within the statistical uncertainty, were consistent with each other. However, it is believed that experimentally the anticoincidence method is a more reliable method.

V. RESULTS

A. The Extrapolation to "Good Geometry"

To obtain the total nuclear proton cross section it is necessary to extrapolate the absorption cross section (corrected for the Rutherford scattering), measured at various angles, to zero degrees. In the range of energies used, and at the half-angle θ subtended in the measurements, most of the cross-section dependence with θ is due to the elastic scattering. The differential elastic cross section varies with the scattering angle and shows an interference pattern with a first minimum at angles which depend on the atomic mass and on the proton energy.

For energies of 208 and 315 Mev chosen for the present measurements, and for the light elements, the first-order diffraction pattern has its minimum outside of the maximum subtended angle θ and it is possible by the proper choice of a variable, such as the solid angle (in the case of the 208-Mev proton cross-section measurement), or the subtended half-angle θ (which

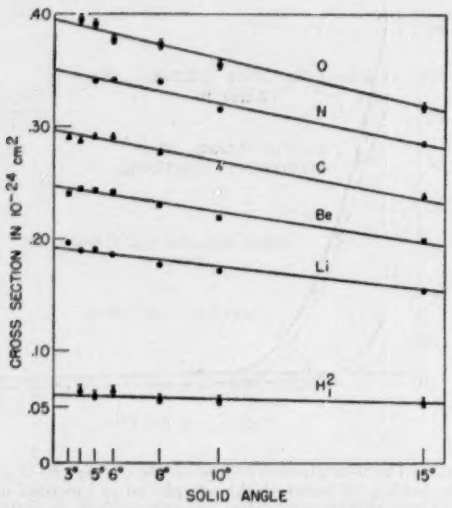

FIG. 5. Corrected cross sections for 208±4 Mev protons as a function of the laboratory-system solid angle subtended by the detector counter, showing extrapolations to zero steradians.

is more convenient for energies higher than 300 Mev) to find an almost linear relationship between the cross sections measured and the independent variable used for the extrapolation to zero degrees.

Those extrapolations are illustrated in Figs. 5 and 6.

For elements heavier than oxygen the differential cross section varies very strongly at angles much smaller than 15°, and the extrapolation loses the precision that it has for the light elements. For this reason the measurements were carried out only for elements of Z as high as chlorine, where this effect is already very pronounced. With copper, the extrapolation method used lost its precision completely.

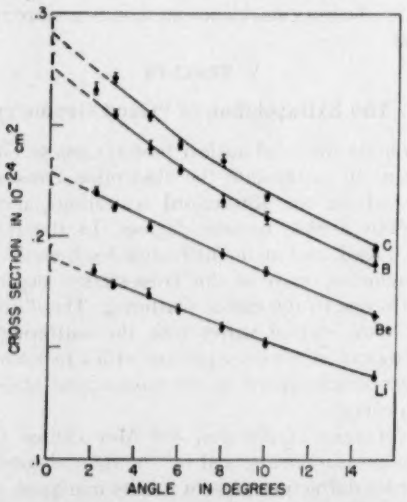

FIG. 6. Illustration of the method of extrapolation to "good geometry" used to obtain the total cross sections for 315±8 Mev protons. (The corrected cross sections measured at different geometries are plotted against the laboratory-system subtended angle θ and extrapolated to zero degrees.)

B. The Proton-Proton Scattering Cross Section

In the present work, two different methods were used to measure the total cross section of proton-proton scattering at 315±8 Mev. In the first method, following the procedure already described, the difference in the cross section in polyethylene and in graphite (with targets containing the same number of carbon atoms per square centimeter) was measured. The second method was a more precise experiment carried out with a large liquid hydrogen target. The hydrogen (with a thickness of 2.8 g/cm^2) was contained in a special Styrofoam target Dewar designed and built by

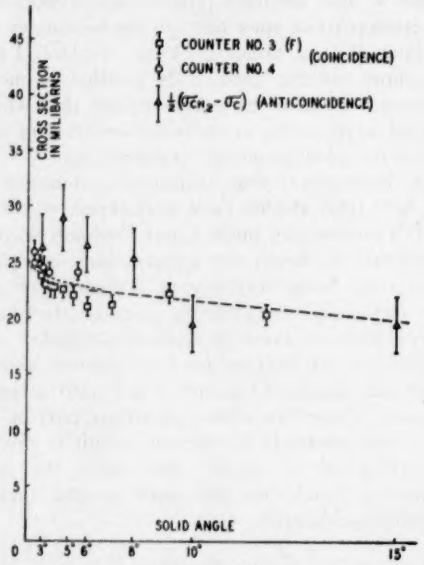

FIG. 7. Proton-proton scattering cross sections at 315±8 Mev plotted against solid angle in the laboratory system. (The dotted straight line between 6 and 15° corresponds to an average differential cross section, in the center-of-mass system, equal to 3.6 $\times 10^{-27}$ cm^2/sterad.)

Yodh[11] from a method developed at The University of Chicago by J. Marshall and L. Marshall.

At a proton energy of 208±4 Mev only the difference method (polyethylene-graphite) was used.

The cross sections obtained (corrected only for Rutherford scattering) are shown in Figs. 7 and 8. For the liquid hydrogen target the multiple Coulomb scattering correction was small even in the vicinity of two degrees, and for this reason several measurements were made at small angles in order to allow a precise extrapolation to zero degrees.

The counting system used at 315 Mev for the p-p scattering measurement in liquid hydrogen was some-

[11] G. B. Yodh (to be published).

TABLE I. Total nuclear cross sections for 315±8-Mev protons in millibarns. Corrected for single Coulomb scattering. Measured at different subtended angles θ.

Nucleus	15°	10°	8°	6°	4.65°	3°	2°	Extrapolated to 0°
Proton	20.2± 1	21.9± 1	22.4± 1	23.1± 1	23.8± 1	24.1± 1	24.2± 1	24.3± 1
Neutron	19.5± 5	26.5± 4	25.0± 4	31.8± 5	32.8± 4	26.5± 7		32.5± 4
Deuteron	39.7± 6	48.4± 5	47.4± 5	54.9± 5	56.6± 5	50.6± 8		56.8± 5
Lithium	137 ± 2	152 ± 2	159 ± 2	167 ± 2	173 ± 2	177 ± 2	185 ± 2	190 ± 6
Beryllium	164 ± 2	184 ± 2	192 ± 2	204 ± 2	213 ± 2	220 ± 2		229 ± 6
Boron	188 ± 3	208 ± 3	216 ± 4	230 ± 3	240 ± 3	255 ± 2	266 ± 3	276 ± 6
Carbon	194 ± 2	218 ± 2	234 ± 3	241 ± 2	254 ± 2	271 ± 2		292 ± 6
Nitrogen	226 ± 5	248 ± 5	267 ± 5	285 ± 5	298 ± 6	313 ± 5		340 ± 7
Oxygen	252 ± 5	277 ± 6	296 ± 6	307 ± 6	323 ± 6	350 ± 6		379 ±10
Aluminum	358 ± 6	402 ± 8	435 ± 8	472 ± 8	508 ± 9	553 ±11		580 ±16
Sulfur	408 ± 8	458 ± 9	494 ± 9	540 ±10	580 ±10	624 ±15		686 ±18
Chlorine	438 ±10	493 ±10	532 ±10	590 ±11	630 ±11	678 ±18		749 ±20

what different from that used in other measurements. Instead of the anticoincidence method, the coincidence method was used and not only one, but two counters, one behind the other on the axis of the beam, were used as detector counters for the measurement of the ratio (I_0/I). With this arrangement it was possible to measure simultaneously the cross sections corresponding to two different subtended angles θ, with economy of running time. I_0 was obtained with the Styrofoam target placed in the beam but no liquid hydrogen in it, and I was obtained with the hydrogen in.

Since the ratio of solid angle in the laboratory system to solid angle in the center-of-mass system, $(d\Omega/d\omega)_\theta$, does not vary much in the range of angles used, one can assume for it an average value. Between 6° and 15° this average value of $(d\Omega/d\omega)_\theta$ is about 0.231. It is possible to fit a straight line to the p-p scattering measurements, which is consistent with a slope corresponding to a $\langle d\sigma/d\omega\rangle_{av}$ equal to 3.6×10^{-27} cm²/sterad. However, at angles smaller than 6° the differential cross section seems to increase. The slope of the straight line fitted to 208-Mev data corresponds to an average value of $\langle d\sigma/d\omega\rangle_{av}$ equal to 3.4×10^{-27} cm²/sterad between 6° and 15° (see Figs. 7 and 8).

Within the experimental error the total cross sections of p-p scattering obtained in the present experiments do not vary with energy and are in good agreement with

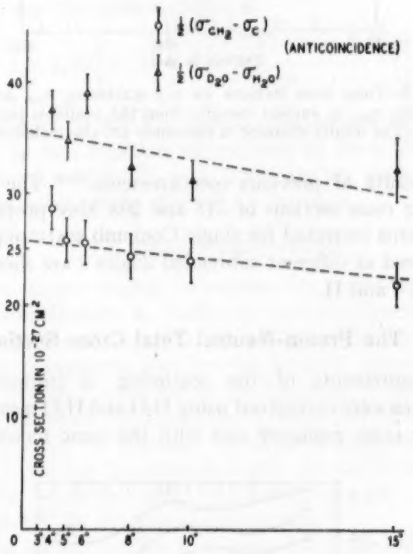

FIG. 8. Proton-proton scattering cross sections at 208±4 Mev plotted against solid angle in the laboratory system. Lower curve, proton-proton; upper curve, proton-neutron. (The dotted straight line fitting the experimental proton-proton values is consistent with an average value of 3.4×10^{-27} cm²/sterad for the differential cross section in the center-of-mass system.)

TABLE II. Total nuclear cross sections for 208±4-Mev protons in millibarns. Corrected for single Coulomb scattering. Measured at different subtended angles θ.

Nucleus	15°	10°	8°	7°	6°	5°	4°	3°	Extrapolated to 0°
Proton	22.0±2	24.0±2	24.4±2		25.6±2	25.8±2	28.7±2		25.8± 2.0
Neutron	32.2±3	31.2±2	32.4±2		39.0±2	34.7±2	36.5±2		37.0± 2.0
Deuteron	54.2±5	55.2±4	56.8±4		64.8±4	60.5±4	65.2±4		62.8± 3.0
Lithium	153 ±1	172 ±1	177 ±1		186 ±1	191 ±1	189 ±1	197±1	192 ± 3
Beryllium	198 ±1	219 ±1	231 ±1		242 ±2	243 ±2	245 ±1	240±2	247 ± 6
Boron	206 ±3	232 ±3	245 ±2	260±3	253 ±3	272 ±3	270 ±3	275±3	276 ± 9
Carbon	238 ±1	264 ±1	277 ±1		291 ±1	291 ±1	287 ±1	290±2	296 ± 3
Nitrogen	285 ±1	314 ±3	330 ±2		341 ±2	341 ±2			350 ±10
Oxygen	320 ±7	355 ±6	373 ±6		378 ±6	392 ±6	396 ±6		395 ±10
Aluminum	467 ±4	485 ±3	506 ±3		528 ±3	556 ±2	588 ±3		592 ±10
Sulfur	494 ±4	530 ±7	560 ±9		591 ±8	608 ±9	666 ±7		680 ±20
Chlorine	515 ±3	563 ±6	571 ±6		619 ±6	659 ±7	687 ±4		740 ±20

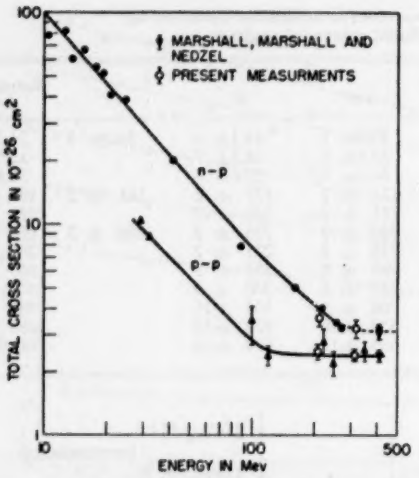

FIG. 9. Total cross sections for n-p scattering, σ_{np}, and p-p scattering, σ_{pp}, at various energies from the available published values. (The results obtained in this study are also included.)

the results of previous measurements.[19,13] The total nuclear cross sections of 315 and 208 Mev protons in millibarns corrected for single Coulomb scattering and measured at different subtended angles θ are shown in Tables I and II.

C. The Proton-Neutral Total Cross Section

Measurements of the scattering of protons by neutrons were carried out using D_2O and H_2O measured in the same geometry and with the same number of molecules per cm². The neutron cross sections were then $\frac{1}{2}[\sigma(D_2O)-\sigma(H_2O)]$.

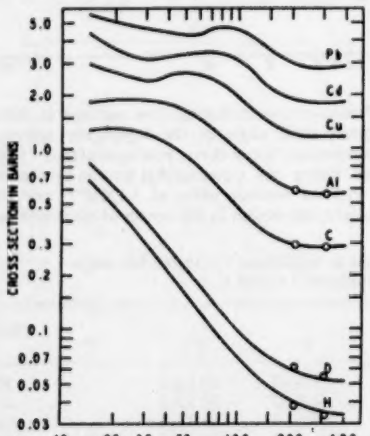

FIG. 10. Total neutron cross sections as a function of energy as compared with the proton cross sections measured at the same energies.

In Fig. 9 the results are compared with the previous work done at different energies.[14–20] One can observe that for energies lower than 100 Mev, σ_{np} has a $1/E$ dependence. At energies higher than 100 Mev the energy dependence appears to vary somewhat more slowly than $1/E$, and from the result of the present measurement it seems that the cross sections tend to be energy-independent for energies higher than 300 Mev.

D. Comparison with Neutron Cross Sections

From a compilation by Nedzel[2] of the available neutron cross sections it was possible to draw smooth curves fitting the experimental data, showing how the neutron cross section varies with the neutron energy. The proton cross sections are compared with those neutron cross sections at the same energy in Fig. 10 and in Table III.[2,6,20,21]

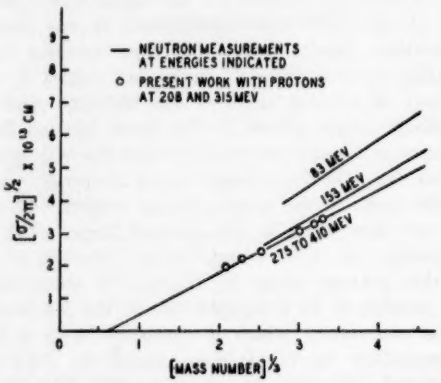
NEUTRON MEASUREMENTS AT ENERGIES INDICATED
PRESENT WORK WITH PROTONS AT 208 AND 315 MEV
83 MEV
153 MEV
275 TO 410 MEV
[σ/2π]^½ x 10¹³ CM
[MASS NUMBER]^⅓

FIG. 11. The effective nuclear radii for nucleons $(\sigma/2\pi)^{\frac{1}{2}}$ plotted as functions of $A^{\frac{1}{3}}$. (For neutrons of the energies indicated and for protons at 208 Mev and 315 Mev, for comparison. The negative intercept is clearly shown.)

The comparison shows evidence for support of the charge symmetry hypothesis.

From the results of measurement of the total cross section for fast neutrons the nuclear radius is expressed by the equation

$$R=a+r_0A^{\frac{1}{3}}, \tag{3}$$

which is consistent with the hypothesis of constant density of the nuclear matter. A positive intercept may be related to range of nuclear forces. If this range is

[13] Chamberlain, Pettengill, Segrè, and Wiegand, Phys. Rev. 93, 1424 (1954).
[19] Marshall, Marshall, and Nedzel, Phys. Rev. 85, 416 (1952).
[14] W. Sleator, Phys. Rev. 72, 207 (1947).
[15] R. Sherr, Phys. Rev. 68, 240 (1945).
[16] R. H. Hildebrand and C. E. Leith, Phys. Rev. 80, 842 (1950).
[17] Hadley, Kelly, Leith, Segrè, Wiegand, and York, Phys. Rev. 75, 351 (1949).
[18] Kelly, Leith, Segrè, and Wiegand, Phys. Rev. 79, 96 (1950).
[19] J. De Juren and B. J. Moyer, Phys. Rev. 81, 919 (1951).
[20] Fox, Leith, Wouters, and MacKenzie, Phys. Rev. 80, 23 (1950).
[21] J. De Juren and N. Knable, Phys. Rev. 80, 27 (1950).

TABLE III. A summary of high-energy neutron and proton cross sections in millibarns. The first three columns show the published neutron cross sections for 410 Mev,[a] 280 Mev,[b] and 270 Mev.[c] The fourth column shows published value for 408-Mev[d] protons, and in the fifth and sixth columns the results of present work are given for 208-Mev and 315-Mev protons.

	Neutrons			Protons		
	410 Mev	280 Mev	270 Mev	408 Mev	315 Mev	208 Mev
H	33.7±1.3	33± 3	38±1.5	31.6±2	32.5± 4	36.5± 4
D	62 ±4	49± 5	57±3	55.6±3	56.8± 5	61.0± 4
Be	231 ±4	225± 4	229±3	242 ±6	229 ± 6	247 ± 4
C	297 ±3	279± 4	288±3	285 ±4	292 ± 6	296 ± 4
O	278 ±5	380± 8	372±7	406 ±3	379 ±10	395 ± 8
Al	587 ±7	566±18	555±8		580 ±16	592 ±10
S	672 ±9				686 ±18	680 ±20
Cl	742 ±9				740 ±20	740 ±20

[a] See reference 2.
[b] See reference 20.
[c] See reference 21.
[d] See reference 6.

a very short one the equation may be written as

$$R=r_0A^{\frac{1}{3}}. \tag{4}$$

A negative value for the intercept has no physical meaning if one assumes an opaque sphere model of the nucleus and a constant density of nuclear matter.

It was found in the present investigation that the radii R obtained from the measured cross sections (using the opaque sphere model) when plotted against $A^{\frac{1}{3}}$, show a negative intercept (see Fig. 11), and also that the slope of the straight line fitting the experimental data is consistent with a nuclear radius

$$R=-0.4+1.19\times A^{\frac{1}{3}}, \tag{5}$$

in units 10^{-13} cm, which may be considered as too small.

These results can be explained by a partial nuclear transparency to the high energy protons. The actual radius can be obtained from the optical model of Fernbach, Serber, and Taylor.

This model predicts a total cross section (when the refractive index of the nuclear matter is one) given by an equation depending only on K (absorption coefficient) and the nucleon radius R,

$$\sigma_t=2\pi R^2\left\{1-2\left[\frac{1-(1+KR)\exp(-KR)}{K^2R^2}\right]\right\}. \tag{6}$$

The best fit for the proton cross-section measurement to this equation corresponds to $R=1.23\times10^{-13}$ cm and $K=0.5\times10^{13}$ cm^{-1}. These are the same as the values calculated by Nedzel[3] for neutrons.

VI. ACKNOWLEDGMENTS

The author wishes to express his appreciation to Professor Herbert L. Anderson, from the Institute for Nuclear Studies of The University of Chicago, for his encouragement and for the author's appointment as a Research Associate in the Institute, to Professor John Marshall for his guidance, help and encouragement, to Dr. L. Marshall for valuable suggestions, to Mr. J. Fischer for assistance with the electronics and to the cyclotron staff, particularly to Mr. Lester Kornblith, Jr., for helpful cooperation.

The author wishes to express his appreciation to Mr. M. D. A. Anastacio, M. Campos, and E. Heiberg for help during the experiments.

Zeeman Effects in the Chlorine Nuclear Quadrupole Resonance in Sodium Chlorate*

YU TING, EDWARD R. MANRING, AND DUDLEY WILLIAMS
The Ohio State University, Columbus, Ohio

(Received May 21, 1954)

The Zeeman splitting of Cl^{35} nuclear quadrupole resonance lines in a single crystal of sodium chlorate has been studied in a magnetic field sufficiently large to permit detailed investigation of individual Zeeman components for various orientations of the crystal in the applied magnetic field. The observed patterns are in agreement with theoretical predictions based on a Hamiltonian involving an interaction of the nuclear electric quadrupole moment with a crystalline field having axial symmetry and the interaction of the nuclear magnetic moment with the applied magnetic field. The quadrupole interaction term e^2Qq was found to be 58.806±0.002 Mc/sec and the effective nuclear magnetic moment was found to be 0.8215±0.0001 nuclear magnetons. An upper limit for the electric asymmetry parameter η was found to be 0.0012. The intensity variations of individual Zeeman components for different orientations of the crystal relative to the magnetic field were studied. The line width of individual Zeeman components was of the order of 900 cps.

I. INTRODUCTION

A NEW field of radio-frequency spectroscopy was opened by Dehmelt and Kruger[1] when they observed direct transitions between nuclear quadrupole levels in solids. Since this early work, investigations of the subject have been made in many laboratories.[2,3] Extensive studies of chlorine nuclear quadrupole resonances in many crystals have been carried on and have yielded exact determinations of the ratio Q^{35}/Q^{37} for the nuclear quadrupole moments as well as precise measurements of the quadrupole coupling constants e^2Qq for various crystals.

The quadrupole resonance line in sodium chlorate $NaClO_3$ has been observed by Wang *et al.*[4]; this resonance line is intense and relatively narrow at room temperature. The effects of an external magnetic field on this line have been studied by Livingston[5] and by Manring,[6] who observed the Zeeman effect in a field of approximately 50 gauss.

The purpose of the present study was the investigation of the Zeeman splitting of the Cl^{35} line in $NaClO_3$ in very strong magnetic fields. By applying strong magnetic fields it is possible to separate the Zeeman components sufficiently to make accurate observations of the behavior of individual components as the magnetic field is varied and as the orientation of the crystal with respect to the magnetic field is changed. Thus, it is possible to test more precisely existing theories of the Zeeman effect.

II. THEORY

The problem of a nuclear quadrupole system coupled to a crystalline electric field and further subjected to an externally applied magnetic field has been discussed by several authors. Pound[3] and Volkoff[7] treated the case in which the quadrupole interaction is smaller than the magnetic interaction. The reverse case, in which the magnetic interaction is smaller has been treated by Kopfermann[8] and Bersohn.[9] A more general treatment has been given by Dean,[10] whose notation will be employed here.

The total Hamiltonian of a nucleus interacting with a uniform magnetic field $\mathbf{H}$ and with the gradient tensor of an electrostatic field is

$$\begin{aligned}\mathcal{H}=&\frac{e^2qQ}{4I(2I-1)}[3\mathcal{I}_z^2-\mathcal{I}^2+\tfrac{1}{2}\eta(\mathcal{I}_+^2+\mathcal{I}_-^2)]\\&-g\beta_n(H_x\mathcal{I}_x+H_y\mathcal{I}_y+H_z\mathcal{I}_z)\\=&-\delta[\mathcal{I}_z^2+\tfrac{1}{6}\eta(\mathcal{I}_+^2+\mathcal{I}_-^2)+2\xi\mathcal{I}_H]+\tfrac{1}{3}\delta\mathcal{I}^2,\end{aligned}\tag{1}$$

where $\delta=-3e^2qQ/[4I(2I-1)]$ is a measure of the electric quadrupole interaction; $\xi=g\beta_nH/2\delta$ is the ratio of magnetic interaction to electric quadrupole interaction; $\eta=(V_{xx}-V_{yy})/V_{zz}$ is the asymmetry factor of the electrostatic field; x, y, z are the principal axes of the gradient tensor of the electrostatic field; and $\mathcal{I}_\pm=\mathcal{I}_x\pm i\mathcal{I}_y$. It is assumed that η and ξ are much smaller than 1.

In the representation of eigenstates $|m\rangle$, the eigenstates of $\mathcal{I}_z$, the matrix elements of the Hamiltonian

* Supported by a contract between the O.S.U. Research Foundation and the Office of Scientific Research of the Air Research and Development Command, United States Air Force, Baltimore, Maryland.

[1] H. G. Dehmelt and H. Kruger, Naturwiss. **37**, 111 (1950); **37**, 398 (1950); Z. Physik **129**, 401 (1951).

[2] R. Livingston, Phys. Rev. **82**, 289 (1951); J. Chem. Phys. **19**, 803 (1951).

[3] R. V. Pound, Phys. Rev. **79**, 685 (1950); **82**, 343 (1951).

[4] Wang, Townes, Schawlow, and Holden, Phys. Rev. **86**, 809 (1952).

[5] R. Livingston, Science **118**, 61 (1953).

[6] E. R. Manring, Doctoral dissertation, Ohio State University, June, 1953; paper presented at Molecular Structure Symposium, Columbus, Ohio, June, 1953 (unpublished).

[7] G. N. Volkoff, Can. J. Phys. **31**, 820 (1953).

[8] H. Kopfermann, Physica **17**, 386 (1951).

[9] R. Bersohn, J. Chem. Phys. **20**, 1505 (1952).

[10] C. Dean, Doctoral dissertation, Harvard University, 1952 (unpublished).

(1) are, for $I=\frac{3}{2}$,

$$\|\langle m|\mathcal{H}|n\rangle\|=-\delta\cdot\begin{array}{c|cccc} & (3/2) & (1/2) & (-1/2) & (-3/2) \\ \hline (3/2) & 1+3\xi\cos\theta & \sqrt{3}\sin\theta\cdot e^{-i\phi} & \eta/\sqrt{3} & 0 \\ (1/2) & \sqrt{3}\xi\sin\theta\cdot e^{i\phi} & -1+\xi\cos\theta & 2\xi\sin\theta\cdot e^{-i\phi} & \eta/\sqrt{3} \\ (-1/2) & \eta/\sqrt{3} & 2\xi\sin\theta\cdot e^{i\phi} & -1-\xi\cos\theta & \sqrt{3}\xi\sin\theta\cdot e^{-i\phi} \\ (-3/2) & 0 & \eta/\sqrt{3} & \sqrt{3}\xi\sin\theta\cdot e^{i\phi} & 1-3\xi\cos\theta \end{array}, \tag{2}$$

where θ, ϕ are the polar coordinates of $\mathbf{H}$ with respect to x, y, z, and where the constant term $\frac{1}{3}\delta\beta^2$ is discarded. The eigenvalues E of this matrix, expressed in units of $(-\delta)$, will be given for the following cases:

(i) In the absence of an external magnetic field,

$$E=\pm(1+\tfrac{1}{3}\eta^2)^{\frac{1}{2}} \qquad (|m|=\tfrac{1}{2},\tfrac{3}{2}). \tag{3}$$

The transition frequency between these two pure quadrupole levels is then

$$f_0=(2|\delta|/h)(1+\tfrac{1}{3}\eta^2)^{\frac{1}{2}}, \tag{4}$$

where η may or may not be zero. If the electrostatic field to which the nuclear quadrupole is coupled is a crystalline field, f_0 is temperature-dependent.

(ii) For a nonzero magnetic field parallel to the z axis,

$$E=\begin{cases}[(1\pm 2\xi)^2+\frac{1}{3}\eta^2]^{\frac{1}{2}}\pm\xi, \\ -[(1\mp 2\xi)^2+\frac{1}{3}\eta^2]^{\frac{1}{2}}\mp\xi.\end{cases} \tag{5}$$

When $\eta=0$, this reduces to

$$E=\begin{cases}1\pm 3\xi & (m=\pm\frac{3}{2}), \\ -1\pm\xi & (m=\pm\frac{1}{2}).\end{cases} \tag{5a}$$

These four levels, hereafter labeled as D, C, B, A, correspond to the four points at $\theta_A=0$ in Fig. 1. The zero magnetic field line is split into two components with frequencies

$$f_{BD,AC}=(2\delta/h)(1\pm\xi), \quad (\eta=0,\ \delta>0) \tag{6}$$

$$=f_0(1\pm f_M/f_0)=f_0\pm f_M, \tag{7a}$$

where $f_M=2\delta\xi/h=g\beta_n H/h$ is the magnetic resonance frequency for the nucleus in question. When $\eta\neq 0$, the two Zeeman components are slightly shifted to higher frequencies:

$$f_{BD,AC}=f_0[1\pm(f_M/f_0)+\tfrac{2}{3}\eta^2(f_M/f_0)^2 +\text{higher powers of } \eta \text{ and } (f_M/f_0)]. \tag{7b}$$

The expansion is possible because ξ, η are assumed much smaller than 1.

(iii) For a nonzero magnetic field oriented at angle θ (except 90°) to the symmetry axis of an electric field ($\eta=0$),

$$E_{\{\frac{1}{2}\}B,\{\frac{1}{2}\}A}=-\Big[1\mp(1+3\sin^2\theta)^{\frac{1}{2}}\xi+\tfrac{3}{2}\sin^2\theta\cdot\xi^2 \mp\frac{\frac{3}{2}\sin^2\theta}{(1+3\sin^2\theta)^{\frac{1}{2}}}(1-3\sin^2\theta)\xi^3 +\tfrac{3}{8}(4\sin^2\theta-3\sin^4\theta)\cdot\xi^4 \mp\frac{3}{8}\frac{\sin\theta}{(1+3\sin^2\theta)^{\frac{1}{2}}}(4-45\sin^2\theta -81\sin^4\theta+162\sin^6\theta)\xi^5+\cdots\Big], \tag{8a}$$

$$E_{\{\frac{1}{2}\}D,\{\frac{3}{2}\}C}=-\Big[-1\mp 3\cos\theta\cdot\xi-\tfrac{3}{2}\sin^2\theta\cdot\xi^2 \pm\tfrac{3}{2}\sin^2\theta\cdot\cos\theta\cdot\xi^3-\tfrac{3}{8}(4\sin^2\theta-3\sin^4\theta)\cdot\xi^4 \mp\frac{3}{8}\frac{\sin^2\theta(-4+\sin^2\theta+4\sin^4\theta)}{\cos\theta}+\cdots\Big], \tag{8b}$$

where the levels A and B, C and D are still grouped as $[\frac{1}{2}]$ and $[\frac{3}{2}]$ levels because the magnetic energy is small compared to the quadrupole interaction energy (i.e., $\xi\ll 1$). The appearance of $\cos\theta$ in the denominator shows that the last series diverges if $\theta=90°$.

These four levels are plotted in Fig. 1 for $\theta=0°$ to 90° as the set of solutions as a whole is evidently symmetric about 90°. When $\theta\neq 0°$, the four Zeeman components $A\to D$, $A\to C$, $B\to D$, $B\to C$ are allowed magnetic-dipole transitions and their frequencies may be calculated from Eqs. (8a) and (8b). According to the original matrix equation (2), there is a particular orientation at which the two Zeeman components f_{BD}, f_{AC} coincide. For any value of η, this orientation is given by

$$2-3\sin^2\theta+\eta^2\sin^2\theta\cos 2\phi=0. \tag{9}$$

When $\eta=0$, or when $\phi=\pm 45°$, $\pm 135°$, coincidence occurs at $\theta=\sin^{-1}(\sqrt{\frac{2}{3}})=54.7°$.

(iv) For an external magnetic field perpendicular to the electric symmetry axis or $\theta=90°$ ($\eta=0$),

$$E_{\{\frac{1}{2}\}B,\{\frac{1}{2}\}A}=-(1\mp 2\xi+4\xi^2)^{\frac{1}{2}}\pm\xi=-\Delta_{\mp}\pm\xi, \tag{8c}$$

$$E_{\{\frac{1}{2}\}D,\{\frac{3}{2}\}C}=(1\mp 2\xi+4\xi^2)^{\frac{1}{2}}\pm\xi=\Delta_{\mp}\pm\xi, \tag{8d}$$

where

$$\Delta_{\mp}=(1\mp 2\xi+4\xi^2)^{\frac{1}{2}}. \tag{8e}$$

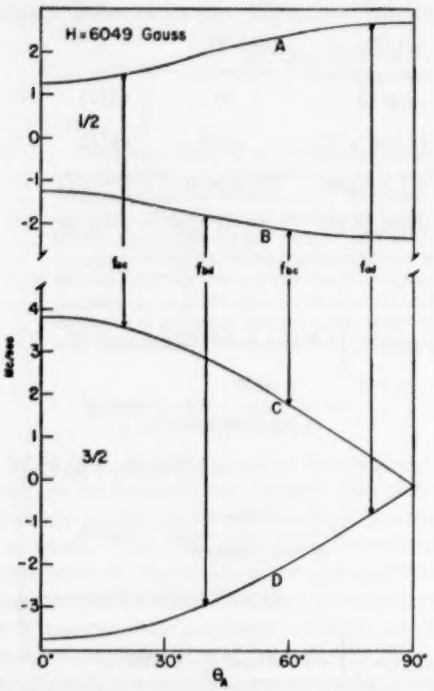

FIG. 1. Energy level diagram showing splitting of the nuclear quadrupole levels in a strong magnetic field for various angles θ_A between H field and the axis of electric symmetry. The separation between the $[\frac{1}{2}]$ and $[\frac{3}{2}]$ levels in the absence of a perturbing H field is 29.903 Mc/sec.

For $\xi \ll 1$, the spacing between levels A, B is approximately $4\xi\delta = 2f_M$, while that between levels C, D, is very small, approximately $3\xi^3\delta$. When $\eta \neq 0$, a term linear in magnetic field strength, that is, $\pm\eta\xi$, appears in the solutions of $E_{[\frac{1}{2}]}$. A comparison of level spacing C to D, as deduced from the frequencies of observed Zeeman components f_{BD}, f_{BC}, f_{AD}, f_{AC} at $\theta = 90°$, with $3\xi^3\delta$ therefore should yield an estimation of the asymmetry factor η.

The sodium chlorate crystal is a cubic crystal with four $NaClO_3$ molecules per unit cell.[11] The chlorine nucleus in each molecule is subject to a nonuniform intramolecular electric field with axial symmetry along the $Na^+ - ClO_3^-$ axis. Thus, for each Cl nucleus in the unit cell there is a different axis of electric symmetry. The arrangement of the $NaClO_3$ molecules in the unit cell is such that the axis of electric symmetry for each Cl nucleus is parallel to a body diagonal of the unit cell (i.e., perpendicular to the 111 plane).

Thus, for a single crystal in a magnetic field there are usually four Zeeman patterns corresponding to the four symmetry axes. Each pattern may contain four Zeeman components f_{AC}, f_{AD}, f_{BC}, and f_{BD} in the vicinity of the zero field line f_0 as indicated in Fig. 1. Thus, for weak magnetic fields, it is usually difficult to distinguish the lines of a given pattern from overlapping lines belonging to other patterns. For a few orientations, clear interpretations can be obtained[5,6] but it is not possible to follow unambiguously the detailed behavior of a given pattern as θ and H are varied. By employing strong magnetic fields, detailed studies of a given pattern were made possible.

[11] R. W. G. Wyckoff, *The Structure of Crystals* (Chemical Catalogue Company, New York, 1931), p. 276.

III. EXPERIMENTAL WORK

The $NaClO_3$ crystal employed in the present study was grown from a saturated aqueous solution. By cooling the solution at a rate of approximately 0.5°C per day, it was possible to obtain transparent cubic crystals measuring one inch on an edge in a period of two weeks. Newly prepared crystals were dried and then coated with a protective film of polystyrene. The crystal was mounted in a holder in such a way that one of the body diagonals could be rotated in a horizontal plane. The magnetic field H was horizontal. Since the diagonal of the crystal is along the axis of electric symmetry for one set of Cl nuclei, rotation of the crystal holder provided a method of obtaining all values of θ from 0° to 180° for this set of Cl nuclei. This angle θ will hereafter be denoted by θ_A. For every value of θ_A, there are also three other values of θ belonging to other sets of Cl nuclei; in strong H fields the Zeeman patterns belonging to these other sets of Cl nuclei are easily distinguishable from the pattern being investigated systematically.

The radio-frequency spectrograph utilized an oscillating detector and is similar in essentials to those employed in earlier studies.[12] The detector could be operated either as a super-regenerative detector with external quench or as a regenerative detector with audio

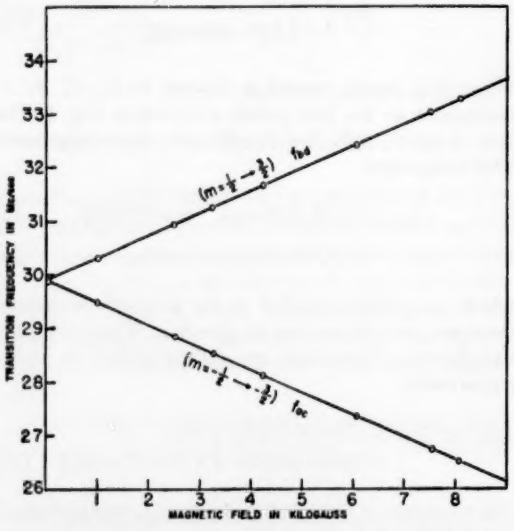

FIG. 2. Observed and calculated splitting of the zero-field quadrupole line as a function of magnetic field for $\theta_A = 0$.

[12] R. E. Sheriff and D. Williams, Phys. Rev. 82, 651 (1951).

feedback.[13] The frequency range covered by the spectrograph was 25 to 35 Mc/sec and a scanning rate as low as 1 kc/sec per minute was employed.

In most of the work, sinusoidal magnetic field modulation at 45 cps was used. However, for certain values of θ_A in the vicinity of 54.7°, frequency modulation of the detector was employed, since for f_{AC} and f_{BD} components Zeeman modulation produces only second-order effects at this value of θ_A; this may be seen from Eqs. (8a) and (8b).

Frequency measurements were made by means of a frequency standard calibrated by signals from WWV. When the super-regenerative detector was employed, the central frequency was determined by means of the frequency standard and an auxiliary receiver, which was used to "track" the central frequency. Under widely different quench conditions, the line frequency measurements were reproducible to within ±1 kc/sec.

Magnetic field measurements were made in terms of the magnetic resonance frequencies of H^1 in water and Li^7 in aqueous LiCl solution. In these measurements the following effective g-values were assumed: $g(H^1) = 5.58536$ and $g(Li^7) = 2.17063$. The resonance frequency values were reproducible to one part in 20 000.

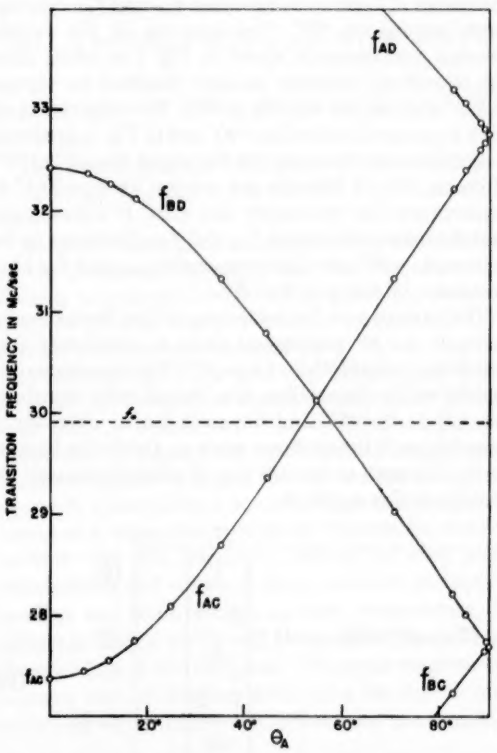

FIG. 3. Observed and calculated frequencies of Zeeman components of a field of 6049 gauss at various orientations θ_A.

[13] T. C. Wang, Doctoral dissertation, Columbia University, 1953 (unpublished).

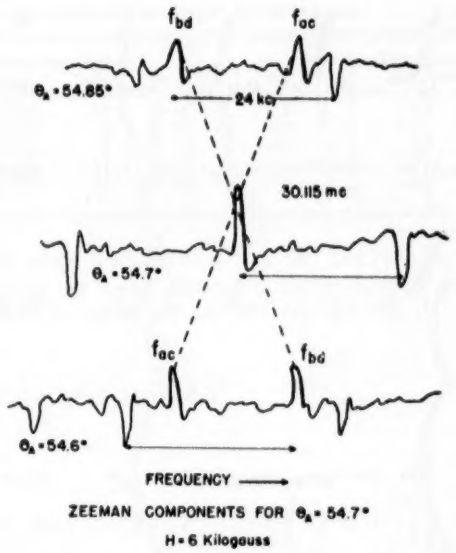

FIG. 4. Observed Zeeman components f_{AC} and f_{BD} in the vicinity of $\theta_A = 54.7°$. Super-regenerative sideband peaks spaced at 24-kc/sec intervals are useful for direct measurement of small frequency differences.

Values for angle θ_A could be determined from a divided circle mounted on the shaft of the crystal holder. From the divided circle, θ_A could be measured to ±0.1°. Near angles of special interest such as 54.7° and 90°, angle measurements with an auxiliary tangent-drive micrometer were used to measure $\Delta\theta_A$ to ±0.01°. The exact divided circle reading corresponding to $\theta_A = 0°$ was determined by observing the crystal orientation at which f_{AC} had its minimum value and f_{BD} had its maximum for a given strong H field.

All spectra were obtained with the sample at room temperature, which varied from 36°C to 25°C over a period of several months. As the quadrupole transition frequencies in a given sample show a slight variation with sample temperature, it was necessary to reduce all observed frequencies to the values corresponding to a sample at some arbitrary "standard" temperature. A temperature of 30°C was chosen for this purpose and a temperature coefficient of −4 kc/sec per °C was employed. This coefficient, which was actually obtained with the single crystal employed in most of the work, is in excellent agreement with that obtained in earlier studies.[6,13]

IV. RESULTS

The results of the present work for the case of zero external magnetic field give a value of $f_0 = 29.903$ ±0.001 Mc/sec for a single $NaClO_3$ crystal at 30°C. This value is in agreement with earlier work[6,13] and yields a value of $|\delta| = 14.952$ Mc/sec in Eq. (4), or a value of $|e^2Qq| = 59.806$ Mc/sec on the assumption that $\eta = 0$.

The results obtained for a crystal with orientation

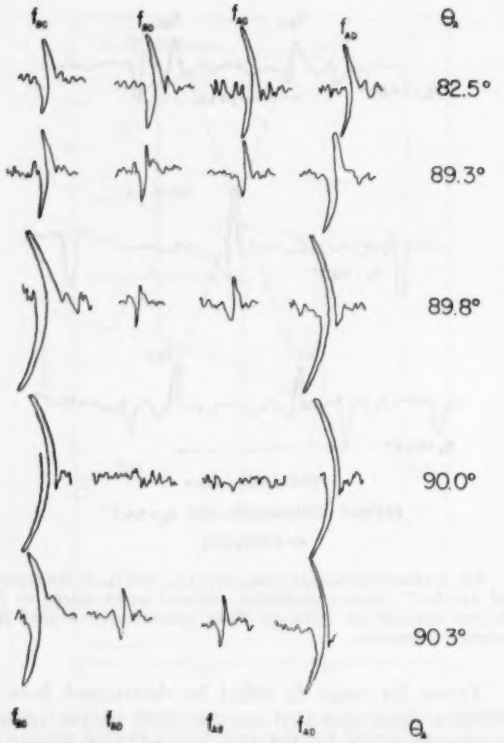

FIG. 5. Intensity variations of Zeeman components f_{AC}, f_{AD}, f_{BC}, and f_{BD} in the vicinity of $\theta_A=90°$ in a field of 6 kilogauss.

$\theta_A=0°$ in a magnetic field are summarized in Fig. 2. The solid curves give the frequencies predicted from Eq. (7a) when the value $\delta=14.952$ Mc/sec is used and when the magnetic moment $\mu_{Cl^{35}}=0.820896\pm0.000050$ n.m. obtained in measurements of LiCl solutions is employed without diamagnetic correction.[14] The circles in Fig. 2 represent the frequencies of the observed Zeeman components. The agreement between observed and predicted values is excellent and indicates that $\eta<0.08$ in Eq. (7b). Precise measurements at two widely different values of the H field suggests that agreement between observed and predicted values can further be improved by using a value $\mu_{Cl^{35}}=0.8215\pm0.0001$ n.m. This value of $\mu_{Cl^{35}}$ is closer to the diamagnetically corrected value $\mu_{Cl^{35}}=0.82180\pm0.00005$ n.m. than to the uncorrected value obtained in LiCl solutions.[14]

The frequencies of the Zeeman components obtained for various angles θ_A in a magnetic field of approximately 6 kilogauss are shown in Fig. 3. The solid curves represent frequencies calculated from Eqs. (8a) to (8d) with the same values for electric quadrupole and magnetic dipole interactions used to obtain the solid curves in Fig. 2. The circles represent observed frequencies. The agreement between observed and calculated frequencies is excellent without introducing an asymmetry factor.

It will be noted from Fig. 3 that f_{AC} and f_{BD} converge in the vicinity of 54.7°. The behavior of the Zeeman components in the vicinity of 54.7° is illustrated in Fig. 4, which shows recorder tracings for three angles near 54.7°. This convergence indicates that $\eta=0$ in Eq. (9) or $\phi=\pm45°$ or $\pm135°$. It seems very likely that η is extremely small or indeed zero, since the actual frequency as calculated for $\theta_A=54.7°$ is 30.116 Mc/sec if $\eta=0$ and the observed value is 30.115 ± 0.001 Mc/sec.

The Zeeman components f_{AD} and f_{BC} were observed between $\theta_A=80°$ and 90°; for $\theta_A=0$, these components are forbidden transitions for magnetic dipole radiation but become very intense as θ_A approaches 90°. The intensities of Zeeman components f_{AC} and f_{BD} decrease as θ_A approaches 90°. The behavior of the various Zeeman components is shown in Fig. 5 in which there are reproduced recorder tracings obtained for various values of θ_A in the vicinity of 90°. The behavior of all lines is symmetric about $\theta_A=90°$ and in Fig. 3, predicted frequencies are given only for the region from 0° to 90°. However, Fig. 5 includes one tracing for $\theta_A=90.3°$ to demonstrate that symmetry does exist. It will be noted that Zeeman components f_{AC} and f_{BD} disappear in the noise at $\theta_A=90°$ and that components f_{AD} and f_{BC} have maximum intensity at $\theta_A=90°$.

The variation in the intensities of the Zeeman components can be understood from a consideration of transition probabilities at $\theta_A=90°$. The transformation matrix which diagonalizes the Hamiltonian matrix of Eq. (2) at $\theta_A=90°$ and for $\eta=0$ can be obtained in closed form. If the arbitrary angle ϕ_A (arbitrary because $\eta=0$), is chosen to be zero (i.e., H along the x axis), the transformation matrix is

$$\|\langle i|m\rangle\|=\frac{\sqrt{3}\xi}{2}\cdot\begin{array}{c}\\(D)\end{array}\begin{array}{c}\left[\begin{array}{cc}(E_{D,B}-\xi)^{-\frac{1}{2}}(E_{D,B}-1)^{-\frac{1}{2}}\begin{pmatrix}1\\ \frac{E-1}{\sqrt{3}\xi}\\ \frac{E-1}{\sqrt{3}\xi}\\ 1\end{pmatrix}_{D,B} & (E_{A,C}+\xi)^{-\frac{1}{2}}(E_{A,C}-1)^{-\frac{1}{2}}\begin{pmatrix}1\\ \frac{E-1}{\sqrt{3}\xi}\\ \frac{1-E}{\sqrt{3}\xi}\\ -1\end{pmatrix}_{A,C}\end{array}\right]\\(B)\qquad\quad(A)\qquad\quad(C)\end{array}\begin{array}{c}(\tfrac{3}{2})\\(\tfrac{1}{2})\\(-\tfrac{1}{2})\\(-\tfrac{3}{2})\end{array}\tag{10}$$

[14] Yu Ting and D. Williams, Phys. Rev. 89, 595 (1953).

TABLE I. Frequencies (kc/sec) of Zeeman components in the neighborhood of 54.7°. $H=6049$ gauss.

	Observed frequency				Calculated frequency				Deviation (Obs.-Calc.)			
θ_A	f_{BD}	f_{AC}	Diff.	Mean	f_{BD}	f_{AC}	Diff.	Mean	f_{BD}	f_{AC}	Diff.	Mean
54.60°	30 126	30 108	18	30 117	30 125	30 106	19	30 115	1	2	−1	2
54.66°	30 118	30 111	7	30 115	30 120	30 112	8	30 116	−2	−1	−1	−1
54.70°	30 115	30 115	0	30 115	30 116	30 116	0	30 116	−1	−1	0	−1
54.85°	30 107	30 125	−18	30 115	30 108	30 125	−17	30 117	−1	0	−1	−2
55.20°	30 082	30 153	−71	30 118	30 085	30 152	−67	30 119	−3	1	−4	−1

where $|i\rangle=|A\rangle$, $|B\rangle$, $|C\rangle$, $|D\rangle$ are eigenstates belonging to the energy levels given in Eqs. (8c) and (8d). By the choice of $\phi_A=0$, the radio-frequency magnetic field is then along the y axis. Hence the matrix elements which determine the probability of magnetic-dipole transitions between the states $|B\rangle$ and $|C\rangle$, $|B\rangle$ and $|D\rangle$, $|A\rangle$ and $|C\rangle$, $|A\rangle$ and $|D\rangle$ are

$$\begin{aligned}
&\frac{1}{i}\langle C|I_y|B\rangle=\tfrac{1}{4}[(E_C+\xi)(E_B-\xi)(E_C-1)(E_B-1)]^{-\frac{1}{2}}[3\xi(E_C-E_B)+2(E_C-1)(1-E_B)]\\
&\qquad=\frac{\sqrt{3}}{2}(1+\xi+\cdots)=\frac{1}{i}[\langle C|I_y|A\rangle]_{\theta_A=0}(1+\xi+\cdots),\\
&\frac{1}{i}\langle B|I_y|D\rangle=\tfrac{1}{4}[(E_D-\xi)(E_B-\xi)(E_D-1)(E_B-1)]^{-\frac{1}{2}}\left[\frac{3\xi}{2}(E_D-1-E_D+1)+(E_B-E_B-1+1)\left(E_D-1-\frac{3\xi}{2}\right)\right]\\
&\qquad=0,\\
&\frac{1}{i}\langle C|I_y|A\rangle=\tfrac{1}{4}[(E_C+\xi)(E_A+\xi)(E_C-1)(E_A-1)]^{-\frac{1}{2}}\left[\frac{3\xi}{2}(E_C-1-E_C+1)+(E_C-1+1-E_C)\left(E_C-1-\frac{3\xi}{2}\right)\right]\\
&\qquad=0,\\
&\frac{1}{i}\langle A|I_y|D\rangle=\tfrac{1}{4}[(E_D-\xi)(E_A+\xi)(E_D-1)(E_A-1)]^{-\frac{1}{2}}[3\xi(E_D-E_A)-2(E_D-1)(1-E_A)]\\
&\qquad=\frac{\sqrt{3}}{2}(1-\xi+\cdots)=\frac{1}{i}[\langle B|I_y|D\rangle]_{\theta_A=0}(1-\xi+\cdots).
\end{aligned}\tag{11}$$

This shows that the intensities of the two Zeeman components f_{BD} and f_{AC} at $\theta_A=90°$ should indeed be zero.

Moreover this equation, together with considerations of the frequency values, shows that the other two Zeeman components at $\theta_A=90°$, f_{BC} and f_{AD}, should be equal in intensity (up to the second power of ξ) to the two allowed Zeeman components at $\theta_A=0$, f_{BD}, and f_{AC}, respectively. For a field of 6 kilogauss, $\xi=8$ percent, the f_{BC} component should be 16 percent stronger than the f_{AD} component. The recorded trace at 90° shows that they are of the same order of magnitude.

An attempt to measure the line widths of f_{AC} and f_{BD} at $\theta_A=0$ in fields of 3 and 6 kilogauss was made by means of a regenerative detector. The results obtained indicate that the frequency interval between points of maximum and minimum slope as shown on recorder tracings was 900±100 cps at room temperature. No difference in line width was noted when the field was changed from 3 to 6 kilogauss. This result suggests that a major part of the line width may be due to small variations in crystalline field throughout the sample.

V. DISCUSSION OF RESULTS

From the data presented in Figs. 2 and 3 it can be seen that there is excellent agreement between observed frequencies and frequencies calculated from theory on the assumption of complete axial symmetry with e^2Qq obtained from zero field measurements and μ from resonance experiments on LiCl solutions. In order to investigate possible differences between observed and calculated frequencies and to obtain an upper limit for the asymmetry factor η, details of the observations at two values of θ_A were given special attention.

Table I gives a comparison of observed and predicted frequencies near $\theta_A=54.7°$. The column headed "Diff." in the table of observed values gives precise frequency differences as obtained from the spacing of super-

TABLE II. Splitting of the $[\frac{3}{2}]$ level in 90° neighborhood (kc/sec).

	Observed splitting		Calculated splitting
θ_A	$f_{AD}-f_{AC}$	$f_{BD}-f_{BC}$	E_C-E_D
	($H=6049$ gauss)		
82.50°	982	983	985
89.32°	92	91	92
89.70°	48	47	47
89.80°	37	36	37
90.00°	(≈30)	(≈30)	27 ($=3\xi^2\delta$)
90.30°	48	48	47
90.88°	117	119	118
	($H=3024$ gauss)		
90.00°	(≈5.5)	(≈6.0)	3.5 ($=3\xi^2\delta$)

regenerative sideband resonances as displayed on the recorder tape. The part of Table I labeled "Deviation" shows that the average deviation between observed and calculated frequency was 1.2 kc/sec. This close agreement near $\theta_A=54.7°$ is to be expected from Eqs. (8a) and (8b), since the calculated frequencies f_{AC} and f_{BD} depend quadratically on ξ and hence are not influenced strongly by the choice of μ. An even closer agreement between observed and calculated frequencies is obtained if one compares the observed and calculated splitting of $[\frac{3}{2}]$ level near 90°, since in Eqs. (8d) and (8b) this splitting involves only ξ^3. Table II gives this comparison.

The splitting of the $[\frac{1}{2}]$ level near 90° depends linearly on ξ. Hence, a comparison of observed and calculated splitting provides a means of checking the value of μ obtained at $\theta_A=0$. Table III gives the comparison when the value of μ obtained with LiCl solutions is used in obtaining the calculated values. It will be noted that the observed splitting is consistently higher than the calculated splitting by approximately 5 kc/sec at 6049 gauss and 2.5 kc/sec at 3024 gauss. In order to bring the observed and calculated values into agreement, it is necessary to set $\mu=0.8216$ nm. This value is in essential agreement with the value $\mu=0.8215\pm0.0001$ nm obtained for $\theta_A=0$.

In connection with Eq. (8d), which was derived for $\eta=0$, it was pointed out that the calculated separation between levels C and D is $3\xi^3\delta$ for $\theta_A=90°$. If $\eta\neq0$, there should be a significant difference between observed splitting, given by $(f_{AD}-f_{AC})$ and $(f_{BD}-f_{BC})$, and calculated splitting at 90°. Unfortunately, the components f_{AC} and f_{BD} disappear at $\theta_A=90°$; however, an extrapolation beyond $\theta_A=89.8°$ is possible. This extrapolation gives a value slightly less than 30 kc/sec for the splitting, as shown in Table II for $H=6049$ gauss. This splitting is to be compared with $3\xi^3\delta=27$ kc/sec. This deviation gives an upper limit of 0.0012 for η. The corresponding comparison for $H=3024$ gauss gives an upper limit of 0.0018 for η. In view of the fact that extrapolation was necessary, η may in fact be zero.

It might be noted from Tables II and III that the agreement between four independent frequency measurements as recorded in the columns giving observed splitting for energy levels is within ±1 kc/sec. This more than justifies the initial estimation of accuracy in spectral line measurements.

TABLE III. Splitting of the $[\frac{1}{2}]$ level in 90° neighborhood (kc/sec).

θ_A	Observed splitting $f_{AD}-f_{BD}$	Observed splitting $f_{AC}-f_{BC}$	Calculated splitting E_A-E_B	Deviation
		($H=6049$ gauss)		
82.50°	4994	4995	4990	5
89.32°	5029	5028	5022.5	6
89.70°	5027	5026	5022	5
89.80°	5026	5025	5022	4
90.00°	...	...	5022	...
90.30°	5026	5028	5022	6
90.88°	5026	5028	5022	5
		($H=3024$ gauss)		
90.00°	2523.2	2523.5	2521.0	2.5

VI. SUMMARY

The results obtained in the present study may be summarized as follows: The total Hamiltonian given in Eq. (1) has proved adequate to account for all observed frequencies to approximately ±1 kc/sec in 30 000 kc/sec and for the observed intensity variations of the various Zeeman components. Three parameters δ, ξ, and η were employed; these parameters involve the following constants:

$$|e^2Qq|=59.806\pm0.002 \text{ Mc/sec},$$
$$\mu(Cl^{35})=0.8215\pm0.0001 \text{ n.m.},$$
$$\eta<0.0012.$$

In reducing all experimental data to a single temperature, a temperature coefficient of -4 (kc/sec) per °C was employed.

ACKNOWLEDGMENTS

The writers take pleasure in expressing their appreciation to Professor Preston Harris and Mr. Paul Splitstone of the Chemistry Department for advice on crystal growth, to Professor Duncan McConnell of the Mineralogy Department for advice on cutting of crystals, to Professor Jan Korringa and Dr. C. J. Tsao for helpful consultation on theoretical problems, and to Mr. John Hockenberry for assistance in certain parts of the experimental work.

Cross-Section Theorem

ROBERT A. MAPLETON
Air Force Cambridge Research Center, Air Research and Development Command, Cambridge, Massachusetts
(Received June 1, 1954; revised manuscript received July 7, 1954)

A cross-section theorem is derived for systems consisting of several identical particles. The total cross section for all processes; elastic, inelastic, and ionization is given in terms of the imaginary part of a linear combination of direct and exchange forward amplitudes.

IN a recent paper[1] the total cross section for the scattering of unpolarized low-energy electrons by hydrogen was estimated. This estimation was accomplished by using the relation

$$Q_1=\frac{4\pi}{k_0}\,\mathrm{Im}\,f_0(0)=\int d\Omega[|f_0(\theta,\phi)|^2+|g_0(\theta,\phi)|^2], \quad (1)$$

in which formula $k_0^2\hbar^2/2m$ is the energy of the incident electrons, f_0 and g_0 are the direct and exchange amplitudes for ground state scattering, and $d\Omega$ is the element of solid angle.

One of the early forms of the cross-section theorem was derived by Feenberg[2] for the case that exchange does not occur; the physical statement being that the integrated flux of current vanishes for steady state processes, the existence of sources and sinks being excluded as well as spin-dependent forces. It is easy to extend this conservation law for systems that include several identical particles, the electron-hydrogen problem being presented as the first application.

The antisymmetrical wave function is constructed from the unsymmetrized solutions of Schrödinger's equation and is

$$\Psi=(\psi_{12}-\psi_{21})\chi_S+(\psi_{12}+\psi_{21})\chi_A, \quad (2)$$

with χ_S and χ_A the symmetrical and antisymmetrical spin functions, respectively, and the asymptotic coordinate functions are:

$$\psi_{12}(r_1\to\infty)=e^{ik_0\mathbf{n}_0\cdot\mathbf{r}_1}\phi_0(\mathbf{r}_2)+\sum_n r_1^{-1}e^{ik_nr_1}\phi_n(\mathbf{r}_2)f_n(\theta_1,\phi_1),$$

$$\psi_{12}(r_2\to\infty)=\sum_n r_2^{-1}e^{ik_nr_2}\phi_n(\mathbf{r}_1)g_n(\theta_2,\phi_2),$$

$$\psi_{21}(r_2\to\infty)=e^{ik_0\mathbf{n}_0\cdot\mathbf{r}_2}\phi_0(\mathbf{r}_1)+\sum_n r_2^{-1}e^{ik_nr_2}\phi_n(\mathbf{r}_1)f_n(\theta_2,\phi_2),$$

$$\psi_{21}(r_1\to\infty)=\sum_n r_1^{-1}e^{ik_nr_1}\phi_n(\mathbf{r}_2)g_n(\theta_1,\phi_1).$$

ϕ_n are the hydrogen functions, $\mathbf{n}_0$ is the unit vector in the direction of incidence, and $\sum_n$ means a sum over all discrete states and an integration over the continuum.

One calculates the three-dimensional current $\mathbf{j}$ given by

$$\mathbf{j}=\mathrm{Im}(\hbar/m)\sum_{\text{spin}}\left(\int d\mathbf{r}_2\Psi^*\nabla_1\Psi+\int d\mathbf{r}_1\Psi^*\nabla_2\Psi\right), \quad (3a)$$

and requires that the integrated flux over spheres of infinite radius be zero; that is,

$$\mathrm{Im}\left(\int d\mathbf{r}_2\int\mathbf{j}\cdot d\mathbf{s}_1+\int d\mathbf{r}_1\int\mathbf{j}\cdot d\mathbf{s}_2\right)=0. \quad (3b)$$

The sum over the spin is effected to get

$$\mathrm{Im}\int d\mathbf{r}_2\int d\mathbf{s}_1\cdot[\psi_{12}^*\nabla_1\psi_{12}+\psi_{21}^*\nabla_1\psi_{21}-\tfrac{1}{2}(\psi_{12}^*\nabla_1\psi_{21}+\psi_{21}^*\nabla_1\psi_{12})]=0, \quad (3c)$$

the term $\int d\mathbf{r}_1\int\mathbf{j}\cdot d\mathbf{s}_2$ providing an identical contribution. The asymptotic forms of the wave functions are employed in (3c) to get

$$\int d\Omega\sum_n\frac{k_n}{k_0}[|f_n|^2+|g_n|^2-\tfrac{1}{2}|f_n^*g_n+f_ng_n^*)]$$
$$+\mathrm{Im}\int d\Omega r^2\left\{ik_0\cos\theta+e^{ik_0r(1-\cos\theta)}\left(\frac{ik_0}{r}-\frac{1}{r^2}\right)\right.$$
$$\times[f_0(\theta,\phi)-\tfrac{1}{2}g_0(\theta,\phi)]+\frac{ik_0}{r}\cos\theta[f_0^*(\theta,\phi)$$
$$\left.-\tfrac{1}{2}g_0^*(\theta,\phi)]e^{-ik_0r(1-\cos\theta)}\right\}=0. \quad (4)$$

In (4) terms in r^{-l} with $l>2$ are dropped. A partial integration is effected on the second integral of (4) to give the result

$$Q=(4\pi/k_0)\,\mathrm{Im}[f_0(0)-\tfrac{1}{2}g_0(0)], \quad (5)$$

with Q the total cross section for all processes: elastic, inelastic, and ionization, Q being given by the first integral of (4).

Equation (1) is obtained by omitting the cross terms in (3c), or the equivalent way by using $\Psi=\psi_{12}$ and omitting the spin summation in (3b), low-energy electrons being assumed.

For energies sufficiently low to insure purely elastic scattering, (5) takes a familiar form in terms of phase

[1] Howard Boyet and Sidney Borowitz, Phys. Rev. 93, 1225 (1954).
[2] Eugene Feenberg, Phys. Rev. 40, 40 (1932).

shifts as now demonstrated.

$$f_0(\theta)+g_0(\theta)=\frac{1}{2ik_1}\sum_{l=0}^{\infty}(2l+1)[\exp(i2\eta_l^+)-1]P_l(\cos\theta),$$

$$f_0(\theta)-g_0(\theta)=\frac{1}{2ik_0}\sum_{l=0}^{\infty}(2l+1)[\exp(i2\eta_l^-)-1]P_l(\cos\theta).$$

Consequently, from (5) Q becomes a well-known form:

$$Q=\frac{\pi}{k_0^2}\sum_{l=0}^{\infty}(2l+1)[3\sin^2\eta_l^-+\sin^2\eta_l^+]. \tag{6}$$

The derivation of (5) assumed infinite nuclear mass, consequently, (5) is only approximate. That this result is true for a nucleus of finite mass is now sketched for the scattering of protons by hydrogen, the result for electron scattering will then follow by the appropriate changes in charge and mass.

Let $\mathbf{r}_P$ and $\mathbf{r}_N$ be the proton coordinates and $\mathbf{r}_1$ the electron coordinate, all with respect to a fixed coordinate system. The following coordinate transformations are used[3,4]:

$$\xi_i=\mathbf{r}_1-\mathbf{r}_N,\quad \xi_f=\mathbf{r}_1-\mathbf{r}_P,$$

$$\mathbf{Z}=\frac{m\mathbf{r}_1+m(\mathbf{r}_P+\mathbf{r}_N)}{2M+m},$$

$$\boldsymbol{\gamma}_i=\mathbf{r}_P-\frac{M\mathbf{r}_N+m\mathbf{r}_1}{M+m},\quad \boldsymbol{\gamma}_f=\mathbf{r}_N-\frac{M\mathbf{r}_P+m\mathbf{r}_1}{M+m},$$

$$\boldsymbol{\gamma}_f=-\frac{\mu_1}{m}\boldsymbol{\gamma}_i-\frac{\mu_1}{\mu_2}\boldsymbol{\xi}_i,\quad \boldsymbol{\xi}_f=-\boldsymbol{\gamma}_i+\frac{\mu_1}{m}\boldsymbol{\xi}_i,$$

$$\boldsymbol{\gamma}_i=-\frac{\mu_1}{m}\boldsymbol{\gamma}_f-\frac{\mu_1}{\mu_2}\boldsymbol{\xi}_f,\quad \boldsymbol{\xi}_i=-\boldsymbol{\gamma}_f+\frac{\mu_1}{m}\boldsymbol{\xi}_f,$$

$$\mu_1=\frac{mM}{M+m},\quad \mu_2=\frac{M(M+m)}{2M+m},$$

where m = electron mass and M = proton mass.

The transformed Hamiltonian becomes

$$H-T_Z=T_{\gamma i}+H_i+V_i=T_{\gamma f}+H_f+V_f,$$

with

$$T_Z=-\frac{\hbar^2}{2(2M+m)}\nabla_Z^2,\quad T_{\gamma i}=-\frac{\hbar^2}{2\mu_2}\nabla_{\gamma i}^2,$$

$$H_i=-\frac{\hbar^2}{2\mu_1}\nabla_{\xi i}^2-\frac{e^2}{\xi_i},$$

$$V_i=-\frac{e^2}{|\boldsymbol{\gamma}_i-(\mu_1/m)\boldsymbol{\xi}_i|}+\frac{e^2}{|\boldsymbol{\gamma}_i+(\mu_1/M)\boldsymbol{\xi}_i|},$$

$$T_{\gamma f}=-\frac{\hbar^2}{2\mu_2}\nabla_{\gamma f}^2,\quad H_f=-\frac{\hbar^2}{2\mu_1}\nabla_{\xi f}^2-\frac{e^2}{\xi_f},$$

$$V_f=\frac{-e^2}{|\boldsymbol{\gamma}_f-(\mu_1/m)\boldsymbol{\xi}_f|}+\frac{e^2}{|\boldsymbol{\gamma}_f+(\mu_1/M)\boldsymbol{\xi}_f|}.$$

The three-dimensional current is

$$\mathbf{j}=\hbar\,\mathrm{Im}\sum_{\text{spin}}\Bigg(\frac{1}{2M+m}\int d\boldsymbol{\gamma}_i\int d\boldsymbol{\xi}_i\Psi^*\nabla_Z\Psi \times\frac{1}{\mu_1}\int d\mathbf{z}\int d\boldsymbol{\gamma}_i\Psi^*\nabla_{\xi i}\Psi +\frac{1}{\mu_2}\int d\mathbf{z}\int d\boldsymbol{\xi}_i\Psi^*\nabla_{\gamma i}\Psi\Bigg), \tag{6a}$$

and the conservation of integrated flux is

$$\mathrm{Im}\sum_{\text{spin}}\Bigg(\frac{1}{2M+m}\int d\boldsymbol{\gamma}_i\int d\boldsymbol{\xi}_i\int d\mathbf{s}_Z\cdot\Psi^*\nabla_Z\Psi +\frac{1}{\mu_1}\int d\mathbf{z}\int d\boldsymbol{\gamma}_i\int d\mathbf{s}_{\xi i}\cdot\Psi^*\nabla_{\xi i}\Psi +\frac{1}{\mu_2}\int d\mathbf{z}\int d\boldsymbol{\xi}_i\int d\mathbf{s}_{\gamma i}\cdot\Psi^*\nabla_{\gamma i}\Psi\Bigg)=0. \tag{6b}$$

The asymptotic form of the wave functions are

$$\begin{aligned}
\psi_{NP}(\boldsymbol{\gamma}_i\to\infty)&=e^{ik_0\mathbf{n}_0\cdot\boldsymbol{\gamma}_i}\phi_0(\boldsymbol{\xi}_i)+\sum_n\gamma_i^{-1}e^{ik_n\gamma_i}f_n(\theta_i,\phi_i)\phi_n(\boldsymbol{\xi}_i),\\
\psi_{NP}(\boldsymbol{\gamma}_f\to\infty)&=\sum_n\gamma_f^{-1}e^{ik_n\gamma_f}g_n(\theta_f,\phi_f)\phi_n(\boldsymbol{\xi}_f),\\
\psi_{PN}(\boldsymbol{\gamma}_f\to\infty)&=e^{ik_0\mathbf{n}_0\cdot\boldsymbol{\gamma}_f}\phi_0(\boldsymbol{\xi}_f)+\sum_n\gamma_f^{-1}e^{ik_n\gamma_f}f_n(\theta_f,\phi_f)\phi_n(\boldsymbol{\xi}_f),\\
\psi_{PN}(\boldsymbol{\gamma}_i\to\infty)&=\sum_n\gamma_i^{-1}e^{ik_n\gamma_i}g_n(\theta_i,\phi_i)\phi_n(\boldsymbol{\xi}_i),
\end{aligned} \tag{6c}$$

by noting that $(\boldsymbol{\gamma}_i,\boldsymbol{\xi}_i)$ are transformed into $(\boldsymbol{\gamma}_f,\boldsymbol{\xi}_f)$ upon interchanging proton coordinates. As in (2) the antisymmetric wave function is

$$\Psi=[(\psi_{PN}-\psi_{NP})\chi_S+(\psi_{PN}+\psi_{NP})\chi_A]\exp(i\mathbf{k}'\cdot\mathbf{z}). \tag{6d}$$

The first integral in (6b) gives no contribution since $\mathbf{Z}$ only appears as a plane wave coordinate. The second integral ($\xi_i\to\infty$) likewise gives no contribution. In fact, by the use of the integral equation formulation as in the paper by Borowitz and Friedman[5] it can be shown that this integral gives no contribution. Consequently

[3] J. D. Jackson and H. Schiff, Phys. Rev. **89**, 359 (1953).

[4] Edwin C. Kemble, *Fundamental Principles of Quantum Mechanics* (McGraw-Hill Book Company, Inc., New York, 1937), p. 64.

[5] S. Borowitz and B. Friedman, Phys. Rev. **89**, 441 (1953).

if (6d) is inserted in (6b), (6b) becomes

$$\mathrm{Im}\int d\mathbf{z}\int d\xi_i\int ds_{\gamma i}\cdot[\psi_{PN}^*\nabla_{\gamma i}\psi_{PN}+\psi_{NP}^*\nabla_{\gamma i}\psi_{NP}$$
$$-\tfrac{1}{2}(\psi_{PN}^*\nabla_{\gamma i}\psi_{NP}+\psi_{NP}^*\nabla_{\gamma i}\psi_{PN})]=0, \quad (6e)$$

and using (6c) ($\gamma_i\to\infty$) leads to (5) for the total cross section. That this, likewise, is valid for the electron-hydrogen problem follows immediately. (One could use the $[Z,\gamma_f,\xi_f]$ system with the corresponding functions from (6c) but the results are identical.)

The remaining system containing two identical particles that is easily treated is the two-body problem. The result is

$$Q=(8\pi/k_0)\ \mathrm{Im}[f(0)-\tfrac{1}{2}f(\pi)]. \quad (7a)$$

(The additional factor of 2 arises from the fact that in this problem there are two particles per unit area, i.e., one particle per unit area in each beam on the *same* surface.)[6] The cross section Q, for this case, is

$$Q=\int d\Omega[\tfrac{3}{4}|f(\theta,\phi)-f(\pi-\theta,\pi+\phi)|^2$$
$$+\tfrac{1}{4}|f(\theta,\phi)+f(\pi-\theta,\pi+\phi)|^2], \quad (7b)$$

It is perhaps interesting to conclude the applications of this conservation theorem by considering a three-electron problem; *viz.*, the scattering of electrons from helium for unpolarized incident electrons as before.

First, the initial state of the target is selected to be a singlet state. It is convenient to select the following eight orthonormal spin functions[7]:

$$\alpha(1)\alpha(2)\alpha(3),\quad \beta(1)\beta(2)\beta(3),$$
$$\frac{1}{\sqrt{3}}[\alpha(1)\alpha(2)\beta(3)+\alpha(1)\beta(2)\alpha(3)+\beta(1)\alpha(2)\alpha(3)],$$
$$\frac{1}{\sqrt{3}}[\beta(1)\beta(2)\alpha(3)+\beta(1)\alpha(2)\beta(3)+\alpha(1)\beta(2)\beta(3)],$$
$$\frac{1}{\sqrt{6}}[\alpha(1)\alpha(2)\beta(3)+\alpha(1)\beta(2)\alpha(3)-2\beta(1)\alpha(2)\alpha(3)], \quad (8a)$$
$$\frac{1}{\sqrt{6}}[\beta(1)\beta(2)\alpha(3)+\beta(1)\alpha(2)\beta(3)-2\alpha(1)\beta(2)\beta(3)],$$
$$\frac{1}{\sqrt{2}}\alpha(1)[\alpha(2)\beta(3)-\alpha(3)\beta(2)],$$
$$\frac{1}{\sqrt{2}}\beta(1)[\beta(2)\alpha(3)-\beta(3)\alpha(2)].$$

The first six of these spin functions are symmetrical in the coordinates and 2 and 3, while the last two are antisymmetrical in 2 and 3. The total wave function is constructed as

$$\Psi=\psi^{S,A}(123)\chi^{A,S}(123)+\psi^{S,A}(231)\chi^{A,S}(231)$$
$$+\psi^{S,A}(312)\chi^{A,S}(312), \quad (8b)$$

where the superscripts label the type of symmetry of the last two indices. χ are the spin functions given by (8a) and ψ are the asymptotic form for the wave functions on a sphere at infinity as given in (8c):

$$\psi^S(123)\underset{r_1\to\infty}{=}\exp(ik_0^S\mathbf{n}_0\cdot\mathbf{r}_1)\psi_0^S(2,3)$$
$$+\sum_n r_1^{-1}e^{ik_nr_1}\psi_n^S(2,3)f_n^S(\theta_1,\phi_1),$$
$$\psi^S(231)\underset{r_1\to\infty}{=}\sum_n r_1^{-1}\exp(ik_n^Sr_1)\psi_n^S(3,2)g_n^S(\theta_1,\phi_1),$$
$$\psi^S(312)\underset{r_1\to\infty}{=}\sum_n r_1^{-1}\exp(ik_n^Sr_1)\psi_n^S(3,2)g_n^S(\theta_1,\phi_1), \quad (8c)$$
$$\psi^A(123)=0,$$
$$\psi^A(231)\underset{r_1\to\infty}{=}\sum_n r_1^{-1}\exp(ik_n^Ar_1)\psi_n^A(3,2)g_n^A(\theta_1,\phi_1),$$
$$\psi^A(312)\underset{r_1\to\infty}{=}\sum_n r_1^{-1}\exp(ik_n^Ar_1)\psi_n^A(3,2)g_n^A(\theta_1,\phi_1).$$

In (8c) $\psi_n^S(3,2)=\psi_n^S(2,3)$ and $\psi_n^A(3,2)=-\psi_n^A(2,3)$, these coordinate wave functions being solutions of Schrödinger's equation for helium. The direct and exchange amplitudes f_n and g_n, as well as the propagation numbers k_n, are distinguished by superscripts in order to associate them with the proper helium wave functions; e.g., f_n^S, g_n^S, and k_n^S belong to ψ_n^S. It is assumed that ψ_n^S, and ψ_n^A form complete orthogonal sets of symmetrical and antisymmetrical solutions to the helium wave equation, and $\sum_n$ represents a summation over discrete states and integration over the continuum as before.

Exactly as before, one constructs the three-dimensional current vector and sets the total integrated flux equal to zero. This leads to the following results for the total cross section.

$$Q=(\pi/k_0^S)\ \mathrm{Im}[f_0^S(0)-g_0^S(0)], \quad (9a)$$

with

$$Q=\tfrac{1}{4}Q_{S\leftarrow S}+\tfrac{3}{4}Q_{T\leftarrow S},$$

and

$$Q_{S\leftarrow S}=\sum_n(k_n^S/k_0^S)\int d\Omega|f_n^S-g_n^S|^2,$$

for singlet-singlet transitions;

$$Q_{T\leftarrow S}=3\sum_n(k_n^A/k_0^S)\int d\Omega|g_n^A|^2$$

for singlet-triplet transitions.[8]

[6] N. F. Mott and H. S. W. Massey, *The Theory of Atomic Collisions* (Oxford University Press, London, 1950), p. 100.

[7] L. I. Schiff, *Quantum Mechanics* (McGraw-Hill Book Company, Inc., New York, 1949), p. 229.

[8] Bates, Fandaminsky, and Massey, Trans. Roy. Soc. (London) **A243**, 111 (1950).

Similarly, for the initial state a triplet state (of helium) the coordinate functions are obtained by changing superscripts in (8c). The results of this case becomes

$$Q=(3\pi/k_0{}^A)\ \mathrm{Im}[f_0{}^A(0)-g_0{}^A(0)], \tag{9b}$$

with

$$Q=\tfrac{3}{4}Q_{T\leftarrow T}+\tfrac{1}{4}Q_{S\leftarrow T},$$

and

$$Q_{T\leftarrow T}=\sum_n (k_n{}^A/k_0{}^A)\int d\Omega\{|f_n{}^A-g_n{}^A|^2+2|g_n{}^A|^2\},$$

for triplet-triplet transitions, and

$$Q_{S\leftarrow T}=\sum_n (k_n{}^S/k_0{}^A)\int d\Omega|g_n{}^S|^2$$

for triplet-singlet transitions.

From the examples considered, it is seen that the total cross section is given by an integral of interference terms consisting of plane and spherical waves; thus, the general structure can be displayed as

$$Q=(4\pi/k_0)\ \mathrm{Im}A(0)$$

$$=-2\pi\ \mathrm{Re}\int_0^\pi r^2\sin\theta d\theta(1+\cos\theta)A(\theta)e^{ikr(1-\cos\theta)},$$

with $A(\theta)$ some linear combination of direct and exchange amplitudes. It is instructive to transform the variable of integration by the substitution

$$u=r(1-\cos\theta),$$

and pass to the limit $r\to\infty$. Then, Q becomes

$$Q=-4\pi\ \mathrm{Re}A(0)\int_0^\infty due^{iku}.$$

Consider the quantity I defined by

$$I=-4\pi\ \mathrm{Re}A(0)\int_0^{\lambda/2} due^{iku}$$

with $\lambda=2\pi/k$. Transform this integral by the change of variable $u=v-r_0$ to obtain

$$I=-4\pi\ \mathrm{Re}A(0)e^{-ikr_0}\int_{r_0}^{r_0+\lambda/2} dve^{ikv}.$$

The integral that appears as a factor in I is of the same type (apart from angular dependence) that appears in the Kirchoff formulation of Huygen's principle.[9] This integral would then correspond to an integration over the first Fresnel zone (of a plane or spherical surface). An evaluation of I shows that $I=2Q$ and in scalar optics the integral over the first Fresnel zone is also twice the total contribution. Moreover, the phase of the contribution of the integral in I is shifted by $\pi/2$ with respect to the phase of the contribution from the center of the first zone, also as in scalar optics. Since $\cos(ku)$ is odd and $\sin(ku)$ is even on the range $0\leq u\leq\lambda/2$, it is clear why only $\mathrm{Im}A(0)$ appears in the expressions for Q.

ACKNOWLEDGMENTS

The author expresses his gratitude to Professor W. A. Furry of the Harvard Physics Department, for several stimulating conversations relevant to this paper.

[9] Max Born, *Optik* (Edwards Brothers, Inc., Ann Arbor, 1943), pp. 144–151.

Spatial Distribution of Energy Dissipation by High-Energy X-Rays*

HENRY BRYSK†
National Bureau of Standards, Washington, D. C.
(Received May 27, 1954)

The space distribution of energy dissipated by betatron x-rays results from the combined propagation of the x-rays and of their secondary electrons. This distribution has been calculated for a 40-Mev bremsstrahlung spectrum incident on a mass of water. The calculation is described and the results are compared with related experiments.

I. INTRODUCTION

WHEN an x-ray beam passes through a medium, it dissipates energy by ionization and excitation of the atoms. At depths in the medium greater than the range of secondary electrons, the different forms of radiation are, to a considerable extent, in equilibrium with each other and the energy dissipation follows approximately the x-ray spatial distribution, slightly displaced forward because of electron travel. Close to the entrance surface in the medium, on the other hand, there is little energy dissipation because the x-rays have not yet had much chance to produce secondary electrons which in turn dissipate the energy. Hence, the energy dissipation rises from a low value at the surface to a maximum further in (transition curve), then falls off with the x-ray distribution.

The transition curve is of considerable radiological interest because the energy dissipation is a measure of the biological effect. The position of the maximum depends on the x-ray energy and attains depths of the order of 1–10 cm for x-rays from multimillion volt accelerators. In medical applications requiring irradiation at a spot inside the body, it may be desirable to select a source such that the maximum of the transition curve will fall on the target, so as to minimize unnecessary irradiation of other areas. A certain number of measurements of transition curves have been made in the multimillion volt range[1] but there has been no previous attempt to perform a detailed theoretical calculation which takes into account the penetration, degradation, and diffusion of the x-rays and of their secondary electrons.

The equations that govern this phenomenon lend themselves to a straightforward calculation of the moments of the distribution of radiation, provided that the boundary effects can be schematized in the following manner: the x-ray beam will be assumed to be generated at the position of the entrance surface and to be perpendicular to the surface. The medium will be assumed to extend over all the space, even behind the entrance surface. The analytical transformations required to derive the moments have been given by Lewis[2] for electrons and by Spencer and Fano[3] for x-rays. For x-rays it has also been possible to utilize the values of a few moments and a rough knowledge of the trend of penetration to give a rather accurate description of the whole x-ray distribution.[3] Efforts to achieve the same results for the distribution of electrons derived from a collimated electron beam have not yet been successful. However, the combined penetration of x-rays and secondary electrons, which gives rise to the transition curve, offers a somewhat easier problem because the deep penetration is controlled by the x-rays rather than by the electrons. The solution of this problem for a typical example is reported in the present paper.

If the energy of the incident x-rays (or of incident electrons) is sufficiently high the electrons generate a large amount of bremsstrahlung and the bremsstrahlung a large amount of high-energy pair electrons which yield more bremsstrahlung. The transition curve goes over, then, into a shower curve. The work reported here concerns a combination of source energy and medium for which the bremsstrahlung of secondary electrons represents a minor effect which has been disregarded. The detailed calculation of a shower process would be only a little more complicated in principle and moderately more laborious in practice; it represents the next logical step in the program of this laboratory.

The experimental arrangement corresponding to the calculation described here is the following: A beam of 40-Mev electrons strikes a thin tungsten target in a betatron. Electrons leaving the target are removed (magnetically) and the (collimated) bremsstrahlung beam enters a tank of water. The calculation predicts the energy dissipation in a plane section, perpendicular to the direction of travel of the incident radiation, as a function of penetration distance in the water.

The calculation is accomplished in four stages: (1) spatial moments of the x-ray distribution resulting from scattering and absorption of the incident x-rays are calculated by the method of reference 3; (2) these moments are then used to calculate the spatial moments

* Work supported by the Office of Naval Research and the U. S. Atomic Energy Commission.
† Now at Oak Ridge National Laboratory, Oak Ridge, Tennessee.

[1] See, e.g., Koch, Kerst, and Morrison, Radiology **40**, 120 (1943). E. E. Charlton and H. E. Breed, Am. J. Roentgenol. Radium Therapy **60**, 158 (1948). Johns, Darby, Haslam, Katz, and Harrington, Am. J. Roentgenol. Radium Therapy **62**, 257 (1949). Laughlin, Beattie, Lindsay, and Harvey, Am. J. Roentgenol. Radium Therapy **65**, 787 (1951).

[2] H. W. Lewis, Phys. Rev. **78**, 526 (1950).

[3] L. V. Spencer and U. Fano, J. Research Natl. Bur. Standards **46**, 446 (1951).

of the electron and positron distribution which is produced directly by the x-rays through Compton scattering and pair production; (3) the moments resulting from (2) are used as the source in an electron diffusion equation the solution of which yields spatial moments of the electron distribution at various stages in the slowing-down process[2]; and (4) the moments resulting from (3) are used to construct the spatial distribution of electrons of each energy from which the energy dissipation as a function of depth is directly calculated.

It should be noted that the method of calculation affords the convenience of proceeding from one set of moments to the next, without actually reconstructing detailed spatial distributions until the final stage of the calculation.

II. X-RAY DIFFUSION

The spectrum of x-rays emerging from a betatron is not known in detail; however, the spectrum given by Bethe and Heitler[4] (or that of Schiff,[5] which is essentially the same) is believed to be reasonably accurate.[6] We assumed the (40-Mev) source spectrum striking the plane water barrier (perpendicularly) to be of this form.

Considering the integral of the radiation over an infinite plane perpendicular to the incident radiation renders the problem one-dimensional in space. This is equivalent to considering diffusion from a plane monodirectional source which is laterally infinite in extent. The diffusion equation for this situation is reduced in reference 3 to a set of interlinked integral equations. The solutions of these integral equations yield Legendre-Laguerre coefficients H_{ln} which are defined as follows:

$$H_{ln}(k)=\int dz L_n(\alpha z)\int_{4\pi} d\Omega P_l(\cos\theta)H(k,\theta,z), \quad (1)$$

where k is the photon energy in mc^2 units, θ is the angle between the photon direction and the direction of incidence, z is distance of the photon from the incident plane, α is a parameter which we take to be the narrow-beam attenuation coefficient of the 40-Mev radiation component, and $H(k,\theta,z)$ is the x-ray distribution function. P_l and L_n are the Legendre and Laguerre polynomials of the lth and nth degree, respectively.

It should be noted that the use of Laguerre coefficients instead of moments represents a convenience without loss of generality; the nth Laguerre coefficient is a linear combination of the first n moments and vice versa. (See Sec. V for further discussion.)

Our first objective was the calculation of H_{ln} for $l, n \leq 3$. This was accomplished by solving ten of the integral equations given in expression (10) of reference 3. The attenuation coefficients used were those of White[7]; and, as discussed at the beginning of this section, the source spectrum was that of Schiff. Straightforward numerical techniques were used, a detailed discussion of which can be found in a report by Berger and Doggett.[8] The solutions were carried to the lowest energy of x-rays which can give rise to electrons with 1 mc^2 kinetic energy (see Sec. III).

III. ELECTRON SOURCE

The next step in the calculation is to determine the Legendre-Laguerre coefficients of the electrons which are generated by the x-rays. We designate the distribution of these secondary electrons by $G(E,\theta,z)$ and write down the expression which relates $G(E,\theta,z)$ to the x-ray distribution $H(k,\theta,z)$, namely,

$$G(E,\theta,z)=\int dk\int d\Omega' p(k,E,\Theta)H(k,\theta',z), \quad (2)$$

where $p(k,E,\Theta)$ is the probability per unit photon path length per unit solid angle that a photon with energy between k and $k+dk$ produces an electron (or positron) of kinetic energy E traveling at an angle Θ with the photon direction. The integral over k includes all photon energies capable of producing an electron of energy E.

It is easy to see that (2) implies a similar relation between the Laguerre coefficients:

$$G_n(E,\theta)=\int dk\int d\Omega' p(k,E,\Theta)H_n(k,\theta'). \quad (3)$$

Further, by using the addition theorem of spherical harmonics, one obtains a convenient relation between the Legendre-Laguerre coefficients of G and H:

$$G_{ln}(E)=\int dk p_l(k,E)H_{ln}(k), \quad (4)$$

where

$$G_{ln}(E)=\int dz L_n(\alpha z)\int d\Omega P_l(\cos\theta)G(E,\theta,z), \quad (5)$$

$$p_l(k,E)=\int d\Omega P_l(\cos\theta)p(k,E,\theta).$$

Electrons of kinetic energy 1 mc^2 have a range of about 1 mm in water. Electrons of lower energy than this will be considered to lose all their energy at the point of origin. We, therefore, want to calculate $G_{ln}(E)$ only for $E \geq 1\ mc^2$. The processes which are effective in water in yielding electrons with such energies are pair production and recoil from Compton scattering.

The cross section per atom for recoil from Compton scattering (in units of the Thomson cross section) can

[4] H. Bethe and W. Heitler, Proc. Roy. Soc. (London) 146, 83 (1934).
[5] L. I. Schiff, Phys. Rev. 83, 252 (1951).
[6] H. W. Koch and R. E. Carter, Phys. Rev. 75, 1950 (1949).
[7] G. R. White, Natl. Bur. Standards Rept. 1003 (unpublished).
[8] M. J. Berger and J. A. Doggett, Natl. Bur. Standards Rept. 2224 (unpublished).

be obtained from the Klein-Nishina formula[9]:

$$\sigma^{KN}(k,E,Z) = \frac{3Z}{4}\frac{1}{k^2}\left\{1+\frac{E}{2k(k-E)}\left[(E-2)+\frac{E}{k(k-E)}\right]\right\}, \quad (6)$$

where the energies are expressed in mc^2 units and Z is the nuclear charge. In the Compton effect, fixing k and E also fixes the angle of scattering:

$$\cos\Theta = \frac{1+k}{k}\left(\frac{E}{E+2}\right)^{\frac{1}{2}}. \quad (7)$$

Hence

$$\sigma^{KN}(k,E,\Theta,Z) = (2\pi)^{-1}\sigma^{KN}(k,E,z)\delta\left[\cos\Theta-\frac{1+k}{k}\left(\frac{E}{E+2}\right)^{\frac{1}{2}}\right], \quad (8)$$

where δ is the Dirac delta function, and finally

$$\sigma_l^{KN}(k,E,Z) = \sigma^{KN}(k,E,z)P_l\left[\frac{1+k}{k}\left(\frac{E}{E+2}\right)^{\frac{1}{2}}\right], \quad (9)$$

where

$$0 \leq \frac{1+k}{k}\left(\frac{E}{E+2}\right)^{\frac{1}{2}} \leq 1.$$

For pair production, in water, at the range of energies of interest, the unscreened Born approximation as calculated by Bethe and Heitler[4] is adequate. The expression for the angular distribution[10] is, however, quite cumbersome and its Legendre expansion[11] is unwieldy. Fortunately, high-energy pair electrons are mostly produced within a cone of about angle $1/E$ with respect to the incident photon direction. This means that the coefficients of the Legendre expansion of the cross section tend to decrease in size quite slowly with l. Since we only need the first few coefficients, we assume for simplification that these coefficients are all equal, i.e., given by the Bethe-Heitler expression[4] integrated over all directions.

All coefficients would be equal if the electrons were generated traveling in the direction of the pair-producing photon. For low-energy electrons, the range is small and therefore the directional assumption is unimportant. A simple calculation indicates that the above approximation never displaces electrons more than about 1 mm from their true position.

We found it convenient to use Hough's simplified forms for the unscreened Bethe-Heitler cross section.[12] These are the following (in units of the Thomson cross section): For $k \geq 15$,

$$\sigma^{BH}(k,E,Z) = \frac{3}{2\pi}\frac{Z^2}{137}\frac{1}{k}\left[1-\frac{4}{3}\frac{(E+1)(k-E-1)}{k^2}\right] \times\left[\ln\frac{2(E+1)(k-E-1)}{k}-\frac{1}{2}\right], \quad (10)$$

and for $2 \leq k \leq 15$,

$$\sigma^{BH}(k,E,Z) = \frac{3}{8\pi}\frac{Z^2}{137}\Phi J\frac{1}{k-2} \times[1+0.135(\Phi-0.52)J(1-J)^2], \quad (11)$$

where

$$J = 2[x(1-x)]^{\frac{1}{2}}, \quad x = \frac{E}{k-2},$$
$$\Phi = 2.32\left(\frac{k-2}{k}\right)^2\ln\left(\frac{k}{2}\right)+A(k),$$

and $A(k)$ is a graphed correction term. The second term in the brackets of (11) is to be dropped when it becomes negative.

For our purpose no distinction need be made between electrons and positrons, since their diffusion properties do not differ appreciably in low-Z materials. The cross section for electron production should then be multiplied by two.

Pair production can also occur in the field of an electron, though it is less probable than pair production in the field of a nucleus by about a factor $(1/Z)$ at high energies. This cross section also falls off more rapidly at low energies and vanishes for $k \leq 4\ mc^2$. The angular distributions of the two kinds of pair production are closely similar.[13] We accounted for electronic pair production by increasing the nuclear pair production by 10 percent ($Z=10$). This is correct for high energies, and the overestimate at low energies is never more than 1 percent of the over-all electron-producing cross section[7] because the Compton effect then overshadows pair production from all sources.

Combining the over-all pair production cross section with the Compton recoil cross section, we have for the lth Legendre coefficient of the total probability for electron production

$$p_l(k,E) = \sum_i N_i\phi_0\sigma_l^{KN}(k,E,Z_i) + 2.2\sum_i N_i\phi_0\sigma^{BH}(k,E,Z_i), \quad (12)$$

where N_i is the number of atoms of each kind per unit volume and ϕ_0 is the Thomson cross section. In order to obtain the Legendre-Laguerre coefficients of the electron source, i.e., the G_{ln}, we entered these $p_l(k,E)$ into the integrals (4) and carried out the integration numerically.

[9] A. T. Nelms, Natl. Bur. Standards Circ. 542 (unpublished).
[10] F. Sauter, Ann. Physik (5) **20**, 404 (1934).
[11] H. Brysk, Natl. Bur. Standards Rept. 2277 (unpublished).
[12] P. V. C. Hough, Cornell report reproduced in part in Phys. Rev. **73**, 266 (1948).
[13] K. M. Watson, Phys. Rev. **72**, 1060 (1947).

IV. ELECTRON DIFFUSION

The diffusion of electrons is represented by the Lewis equation,[2] which relies on the approximation of continuous energy loss, according to which the energy of an electron at each point of its track is identified by its residual range r (i.e., by the initial range minus the path length s already traveled).[14] The Lewis equation pertinent to a problem in plane geometry is the following:

$$\left[-\frac{\partial}{\partial r}+\cos\theta\frac{\partial}{\partial z}\right]f(z,\theta,r)=(2\pi)^{-1}N\phi_0\int d\Omega'\times[f(z,\theta',r)-f(z,\theta,r)]\sigma^R(r,\Theta)+g(z,\theta,r), \quad (13)$$

where $f(z,\theta,r)$ is the distribution function and $g(z,\theta,r)$ is the source function. The corresponding Legendre-Laguerre coefficient equations are

$$-\frac{\partial}{\partial r}f_{ln}(r)+\frac{\alpha}{2l+1}\sum_{m=0}^{n-1}[(l+1)f_{l+1,m}(r)+lf_{l-1,m}(r)]=-k_l(r)f_{ln}(r)+g_{ln}(r), \quad (14)$$

where $k_l(r)=N\phi_0[\sigma_0{}^R(r)-\sigma_l{}^R(r)]$, and α is the scale factor already mentioned. Lewis obtains formally closed solutions of these equations in terms of the quantity $\exp\{-\int k_l(r)dr\}$. However, the integral cannot be performed analytically, and it turns out to be computationally simpler to convert the differential equations into Volterra integral equations of the second kind. These integral equations are similar to those in the gamma-ray diffusion problem and can be solved numerically in an analogous manner. We integrate (14) over the residual range from r to ∞. Since f is zero at the upper limit,

$$f_{ln}(r)=-\frac{\alpha}{2l+1}\sum_{m=0}^{n-1}\left[(l+1)\int_r^\infty f_{l+1,m}(r')dr'+l\int_r^\infty f_{l-1,m}(r')dr'\right]-\int_r^\infty k_l(r')f_{ln}(r')dr'+\int_r^\infty g_{ln}(r')dr'. \quad (15)$$

Changing over from residual range to energy as the variable for convenience we set

$$f_{ln}(r)dr=F_{ln}(E)dE,\quad g_{ln}(r)dr=G_{ln}(E)dE,\quad k_l(r)dr=K_l(E)dE. \quad (16)$$

Then

$$F_{ln}(E)\left(\frac{dE}{dr}\right)=-\frac{\alpha}{2l+1}\sum_{m=0}^{n-1}\left[(l+1)\int_E^\infty F_{l+1,m}(E')dE'+l\int_E^\infty F_{l-1,m}(E')dE'\right]-\int_E^\infty K_l(E')F_{ln}(E')dE'+\int_E^\infty G_{ln}(E')dE'. \quad (17)$$

For the electron scattering cross section, we used a screened Rutherford cross section with the relativistic correction in low-Z approximation[15]:

$$\sigma^R=\frac{Z(Z+1)}{p^2\beta^2}\left\{\frac{1-\beta^2\sin^2(\theta/2)}{[1-\cos\theta+2\eta]^2}\right\}. \quad (18)$$

Here the substitution of $Z(Z+1)$ for Z^2 accounts roughly for electron-electron deflections.[16] For η we used Molière's value,[17]

$$\eta=0.0000686[(1-\beta^2)/\beta^2]\times Z^{\frac{2}{3}}[1.13+3.76(Z/137\beta)^2]. \quad (19)$$

Correspondingly, we obtain for the $K_l(E)$,

$$K_l(E)=N\phi_0{}^2Z(Z+1)\left\{\frac{(E+1)}{E(E+2)}\right\}^2C_l(\eta), \quad (20)$$

where

$$C_l(\eta)=\int_{-1}^{1}\frac{1-\beta^2\sin^2(v/2)}{(1-\cos\theta+2\eta)^2}[1-P_l(\cos\theta)]d(\cos\theta). \quad (21)$$

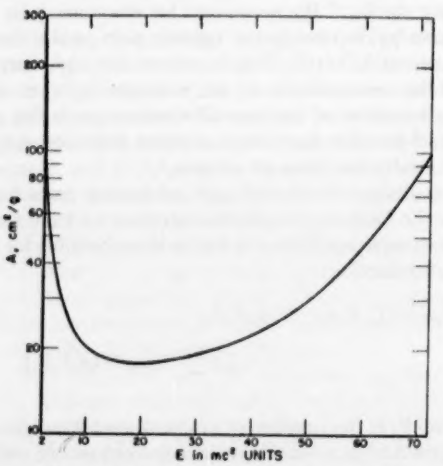

FIG. 1. The parameter A, whose reciprocal indicates the thickness required to bring electrons of different energies to equilibrium with the γ-ray spectrum.

[14] Lewis uses s as variable for an electron of given initial energy. For electrons of different initial energies, s no longer uniquely determines the energy, but r does—hence our modification.

[15] N. F. Mott and H. S. W. Massey, *The Theory of Atomic Collisions* (Oxford University Press, London, 1949), second edition, p. 80.

[16] This point was obtained in detail by Fano while the work was in progress [U. Fano, Phys. Rev. **93**, 117 (1954)]. The $Z(Z+1)$ approximation represents an underestimate of σ^R of the order of 4 percent. The error introduced in the final result is of course much less.

[17] G. Molière, Z. Naturforsch. **2a**, 133 (1947).

In the limit $l \leq \eta^{-1}$, which is obviously satisfied for all l's of interest, the integral becomes[18]

$$C_l(\eta) = \tfrac{1}{2}l(l+1)(1-\ln\eta - 2\sum_{m=1}^{l} m^{-1}) - \beta^2 \sum_{m=1}^{l} m^{-1}. \quad (22)$$

For the stopping power we used

$$\frac{dE}{dr} = \tfrac{3}{4}N\phi_0 Z \frac{(E+1)^2}{E(E+2)} B, \quad (23)$$

where the stopping number B is given by[19]

$$B = \ln[E^2(E+2)] - [1+(2E+1)/(E+1)^2]\ln 2 + (E+1)^{-2} + 2\ln\left(\frac{mc^2}{I}\right) - \delta. \quad (24)$$

The last two terms are taken from Sternheimer.[20]

Using these functions and the ten $G_{ln}(E)$ from the preceding stage of the calculation, we solved the corresponding ten equations (17) by standard numerical methods.

V. CONSTRUCTING THE DISTRIBUTION OF ELECTRONS

The calculations so far have been carried out in terms of Legendre-Laguerre coefficients. We now wish to use these coefficients to construct the distribution. The conceptual basis of the procedure is discussed in reference 3. In brief, we represent the distribution as the product of a weight function and a sum of polynomials orthonormal with respect to the weight function. The success of the procedure depends upon finding a weight function for which the polynomial series converges rapidly. This implies that the weight function bears sufficient resemblance to the actual distribution.

For the gamma-ray problem the distribution is basically exponential. The weight function can be chosen to be $\exp(-\mu_0 z)$, where μ_0 is the attenuation coefficient of the 40-Mev component of the radiation. The orthonormal polynomials are then the Laguerre polynomials $L_n(\mu_0 z)$.

For the electron distributions, our general knowledge of the shape of the transition curve led us to select a weight function of the form[21]

$$W(A,z) = e^{-\mu_0 z} - e^{-A\mu_0 z}. \quad (25)$$

[18] See reference 2, e.g., extended by C. H. Blanchard (private communication).

[19] H. Bethe, *Handbuch der Physik* (Springer, Berlin, 1933), Vol. 24, No. 1, p. 523.

[20] R. M. Sternheimer, Phys. Rev. **88**, 851 (1952).

[21] H. E. Johns *et al.*, Am. J. Roentgenol. Radium Therapy **62**, 257 (1949), have assumed that the energy dissipation is distributed in this manner on the basis of a qualitative picture of energy propagation as a two-step decay process. Since electron penetration does not follow a simple exponential law, this line of thought is not as convincing as one would like.

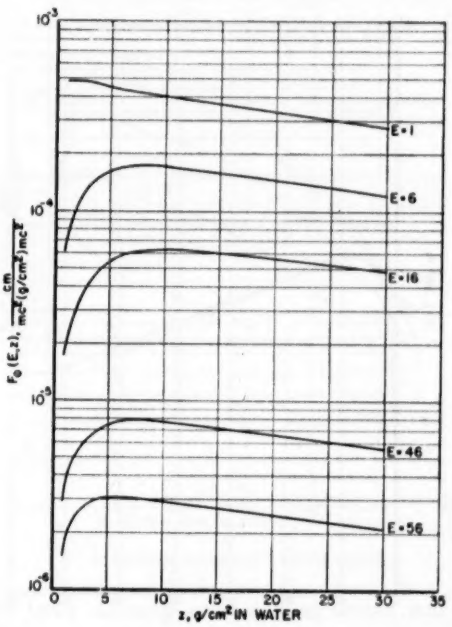

FIG. 2. The number flux of electrons as a function of z for various electron energies. $F_0(E,z)$ is expressed in units of track length (cm) per unit electron kinetic energy (mc^2) per unit thickness of medium (g/cm²) per unit incident γ-ray energy (mc^2).

To construct the spatial distribution of electrons of a given energy E, we constructed the orthonormal polynomials $w_n(A,z)$ associated with $W(A,z)$, and determined the coefficients $a_n(A,E)$ of the expansion $F_0(E,z) = W(A,z)\sum_n a_n(A,E)w_n(A,z)$, for $n=0, 1, 2, 3$, so that the distribution had the calculated values of F_{00}, F_{01}, F_{02}, and F_{03}.

For reasonable values of A, the $a_n(A,E)$ converged rapidly, so that the criterion for selecting A could be taken to be $a_3(A,E)=0$. Using this criterion, A's were obtained for different electron energies. Figure 1 shows a plot of A's so determined as a function of electron energy. The value of A affords a gauge of the departure of electron distributions from the gamma-ray distribution. For high-electron energies A is very large, signifying that electrons of these energies cannot, on the average, have traveled far from their point of origin. (Large path lengths mean large energy losses, which these electrons have obviously not undergone.) For low electron energies, A is again large, signifying that many of these electrons were produced with so little energy that they could not stray far from their point of origin. The electron energies slowest to come to equilibrium with the gamma rays (smallest values of A) are those of intermediate energies.

The behavior of A as a function of E and the numerical values for A are quite reasonable. We therefore gained some confidence in the fitting procedure and evaluated the polynomial sums representing electron

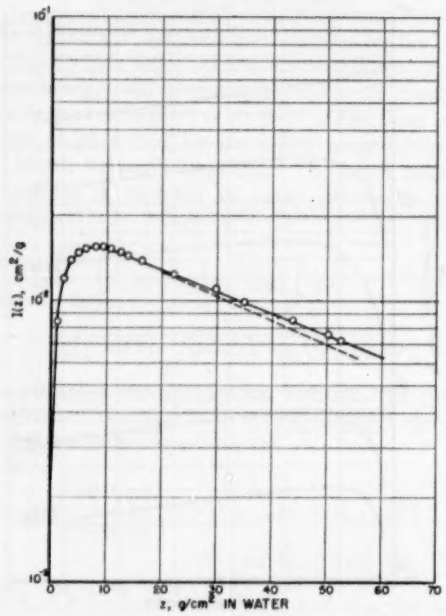

FIG. 3. The fraction of the incident γ-ray energy dissipated per unit thickness (g/cm²). The solid line is the theoretical energy dissipation distribution. The circles represent the measurements of Zendle and Koch corrected to include off-axis radiation. The dashed line represents the uncorrected Zendle-Koch data (normalized to agree with the theoretical value at the peak of the transition curve).

space distributions for each electron energy and for selected z's. Figure 2 shows the number of electrons as a function of z for various electron energies.

The energy dissipated by electrons of each energy E is obtained by weighting the number of electrons having energy E with the stopping power (dE/dr). The total energy dissipated at z is then given by the expression $I(z)=\int F_0(E,z)(dE/dr)dE$.[22] We evaluated these integrals for several values of z. The resulting distribution is shown in Figs. 3 and 4.

Figure 5 shows the electron spectra at several depths z. The quantity plotted is for convenience $(E/\beta)\times e^2F_0(E,z)$, and is proportional to the density of energy carried by electrons of energy E because $F_0(E,z)$, a flux, is proportional to the velocity β.

VI. CORRECTIONS AND CHECKS

A number of minor approximations were made in the course of performing the calculations which will be discussed in this section. Internal checks in the calculation are also mentioned briefly.

[22] Note that $F_0(E,z)$ has dimensions track length per unit thickness of medium per unit electron energy, per unit incident γ-ray energy so that $I(z)$ is the fraction of the incident energy dissipated per unit thickness. The integral $\int_0^\infty I(z)dz$ must therefore be unity. For a discussion of the units of the space integral of $F_0(E,z)$ see U. Fano, Phys. Rev. **92**, 328 (1953), or L. V. Spencer and U. Fano, Phys. Rev. **93**, 1172 (1954).

The detailed calculations described in the preceding sections were performed for electrons with kinetic energies greater than 1 mc^2 and for x-rays with photon energies sufficient to give rise to electrons with such energies ($k>1.37\ mc^2$). Electrons with kinetic energies lower than 1 mc^2, which are not penetrating and do not dissipate a large fraction of the total energy input, were treated in a cruder approximation. These low-energy electrons arise in several ways, namely:

(1) from source x-rays with energies below the "threshold" adopted for the detailed calculation or from x-rays achieving an energy below "threshold" through Compton scattering (8 percent of the total energy input),

(2) from high-energy x-rays directly by Compton recoil or pair production or from high-energy electrons which have lost most of their energy in electron diffusion (9 percent of the total energy input), and

(3) from annihilation radiation (2 percent of the total energy input).

We assumed that low-energy electrons contributed by (1) are distributed spatially exactly as are the lowest-energy *x-rays* treated in the detailed calculation of the x-ray distribution. We assumed that low-energy electrons contributed by (2) and (3) are distributed spatially like the 1 mc^2 electrons.

These assumptions should be quite adequate since low-energy x-rays and electrons tend to maintain a relative equilibrium with components of slightly higher energies. One may question whether this is the best way to treat annihilation radiation, which has an additional fairly large path length after the positrons are stopped. However, annihilation radiation represents only about 2 percent of the input energy and since the

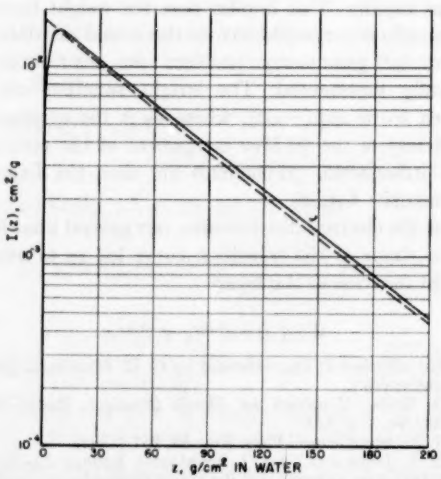

FIG. 4. A comparison between the energy dissipation curve $I(z)$ (solid line) and the energy dissipation curve calculated as if the electrons deposited their kinetic energy precisely where they are generated.

annihilation photons travel in opposite directions the "center of mass" of the radiation remains at the end of the positron range.

In order to determine the amount of energy contributed by (1), (2), and (3), we calculated the total energy generated in the form of x-rays or electrons above "threshold" at each stage of the calculation and made comparisons with the total input energy. This comparison of total energies generated at each stage of the calculation serves as an excellent internal check on the accuracy of the calculations.

Bremsstrahlung from the electrons was neglected because (a) the cross section is small because of the low atomic number of the medium, (b) the electron spectrum is strongly peaked at low energies, and (c) the bremsstrahlung cross section is also peaked at low energies.

The boundary would influence the x-ray calculation only for photons below 200 kev.[23] In the electron part of the calculation, low-energy electrons quite near the boundary would be affected. However, these are few—the electron distribution builds up from near zero at the boundary.

Inasmuch as this was a pilot calculation, many detailed considerations were included which represent refinements considerably beyond the accuracy required for the particular result. A discussion of the simplifications that can be made for a limited objective—and their justification—will be presented in a subsequent paper.

VII. COMPARISON WITH EXPERIMENT

An accurate experimental determination of the ionization depth dose of a betatron beam in water *along the axis of the beam* was made by Zendle and Koch.[24] On the other hand, the theoretical calculation is for the energy loss over the entire plane perpendicular to the direction of motion. To obtain the latter quantity, Boag and Zendle[25] complemented the Zendle-Koch results by measurements with annular beams. An *absolute* calibration of the experimental results was achieved. Figure 3 presents the theoretical transition curve (also absolute) together with the final experimental points. It is seen that excellent agreement is obtained both as to absolute intensities and variation with depth. For comparison (and caution), Fig. 3 also includes some of the Zendle-Koch data—the deviation is essentially due to the fact that in the latter case the crystal does not see radiation scattered away from the central axis. Figure 4 compares the depth variation (found for the energy loss) of the calculated energy dissipation with that which would result from a gamma-ray calculation disregarding electron travel. The two curves are seen to be parallel at greater depths, the correct curve being displaced some 4–5 cm deeper into the medium.

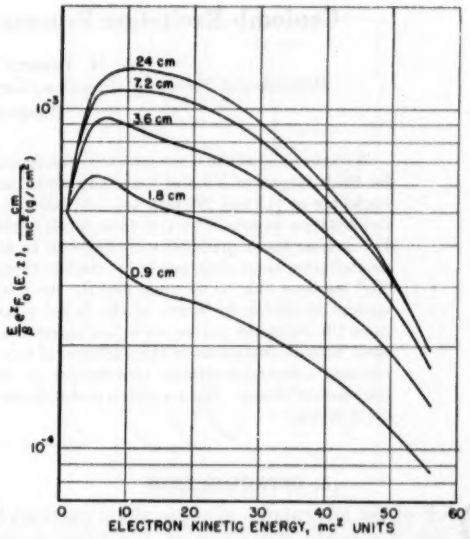

FIG. 5. Electron spectra at various depths z.

The interpretation of the electron spectra in Fig. 5 follows: The spectrum very near $z=0$ represents electrons immediately after their production by the x-rays. On the other hand, at 24 cm the electron spectrum has reached an equilibrium state which changes only as the x-ray spectrum changes, i.e., very slowly. The transition is characterized by an increase in the energy density carried by electrons of intermediate energies, which may be produced not only directly from the x-rays but by the slowing down of higher energy electrons.

The confluence of all curves on the left side seems to be accidental. The elementary calculation of electron spectra by Cormack and Johns[26] pertains in fact to zero depth, and the curve labeled "betatron" in their Fig. 7 resembles the 0.9-cm curve in Fig. 5 of this paper.

ACKNOWLEDGMENTS

This work was closely related to previous research and experience of members of the Nuclear Physics Section of the National Bureau of Standards, and the extent of their contributions is only partly reflected in the references. I wish to thank my colleagues M. J. Berger, C. H. Blanchard, U. Fano, L. V. Spencer, and G. R. White for many fruitful discussions. I am indebted to J. A. Doggett for the computation of the A values and for the figures. Access to the data of J. W. Boag, H. W. Koch, and B. Zendle of the Betatron Section in advance of publication was greatly appreciated. L. V. Spencer kindly undertook the unpleasant task of editorial review of the manuscript.

[23] M. J. Berger (private communication).
[24] B. Zendle and H. W. Koch (private communication).
[25] J. W. Boag and B. Zendle (private communication).
[26] D. V. Cormack and H. E. Johns, Brit. J. Radiol. 25, 369 (1952).

Coulomb Excitation Process in the Lighter Odd-Mass Nuclei*

G. M. TEMMER AND N. P. HEYDENBURG
Department of Terrestrial Magnetism, Carnegie Institution of Washington, Washington, D. C.
(Received June 21, 1954)

We have studied the Coulomb excitation functions for thin targets of F^{19}, Na^{23}, Ti^{47}, Mn^{55}, and Ge^{73}, and for thick targets of V^{51} and Fe^{57}, with alpha particles up to 3.5 Mev; the energy levels excited in these nuclei are at 113 and 196 kev, 446 kev, 160 kev, 128 kev, 68 kev, 320 kev, and 137 kev, respectively. The de-excitation gamma rays from these levels to the ground states were detected except for Fe^{57}, where a 123-kev gamma ray is predominantly emitted. In addition, we have excited the 182-kev level in Zn^{67}, whose de-excitation takes place partly by cascade through the 92-kev first excited state. In the cases of F^{19} and Na^{23} we were able to compare directly the relative contributions of Coulomb excitation and compound nucleus formation by means of the $(\alpha,p\gamma)$ reactions taking place via the same compound nuclei. In all cases the excitation curves are in fair agreement with the theoretical $E2$ curves at the lower energies, but show definite deviations in the direction of too much excitation at the higher energies, pointing to some resonant compound-inelastic contribution as well as possible penetration effects not accounted for by the classical theory. The transition probabilities of all transitions are about one-tenth of those in the rare earth region.

A. INTRODUCTION

ONE of the advantages of using alpha particles for the Coulomb excitation of low-lying nuclear energy levels[1-4] which became immediately apparent was the possibility of studying elements of low atomic number; our early results with Mn^{55} [1] encouraged us to pursue the present investigation. There are several reasons why ions heavier than protons are much better suited for the excitation of low-Z elements, and it might be useful to list them:

(a) The relation $2\eta=2Z_1Z_2e^2/\hbar v\gg 1$, which must hold in order to justify the classical orbit calculations,[5,6] is well satisfied to much lower values of Z_2, since Z_1/v (projectile charge over incident velocity) is larger for a given bombarding energy; for alpha particles this amounts to a factor of 4 over protons. As an example, $2\eta=8.00$ for 3-Mev alphas on $_{11}Na^{23}$.

(b) Because of the higher charge, the Coulomb barrier is higher and prevents appreciable interference of compound nucleus formation with the process of interest here until one goes to higher bombarding energies; we are thus allowed a range of energies over which Coulomb excitation is essentially the only mechanism contributing to the excitation of nuclear energy levels. This is important because (aside from lifetime determinations) Coulomb excitation is probably the best understood process today from which to extract nuclear transition matrix elements directly.

(c) Troublesome high-energy gamma radiation from light targets is almost entirely absent with alpha particles, whereas protons produce appreciable capture radiation in the (p,γ) process (E_γ of the order of 7 Mev) up to $Z\sim 40$, thus making the detection of low-energy gamma rays from the deexcitation of low-lying levels difficult if not impossible.

(d) Many of the nuclei between $Z=20$ and $Z=50$ have (p,n) thresholds lying between 1 and 2 Mev[7]; neutron background and induced positron activities then complicate the problem considerably. In some cases we have found the gamma radiation from the $(p,n\gamma)$ reaction, i.e., from the first excited state of the nucleus $(A, Z+1)$ when bombarding with protons. This is an interesting approach in itself but does not concern us in the present investigation.

(e) Targets which are available only as compounds, such as oxides and chlorides, can be used without difficulty when bombarding with alpha particles for the reasons discussed under (c) and (d); furthermore, the problem of finding a suitably inert backing material for thin target studies is minimized. Nickel turned out to be satisfactory in this respect, but not for protons (see Mn^{55} below).

(f) Finally, general background gamma radiation from the electrostatic generator is many times higher with protons than it is with alpha particles, mainly for the same reasons as listed under (c) and (d) above as applied to the walls of the accelerator tube.

It is for these reasons that we have experienced great difficulties in the few instances where we have attempted to measure Coulomb excitation cross sections with protons; this turns out to be necessary in order to determine the multipolarity of the transitions involved, when making use of the method suggested by Bjerregaard and Huus.[8] The lightest element so far where proton bombardment yielded useful results for us was rhodium ($Z=45$).

* A preliminary account of some of the results in this paper were presented at the Washington meeting of the American Physical Society [Phys. Rev. 95, 629 (1954)].
[1] G. M. Temmer and N. P. Heydenburg, Phys. Rev. 94, 351 (1954).
[2] N. P. Heydenburg and G. M. Temmer, Phys. Rev. 94, 906 (1954).
[3] G. M. Temmer and N. P. Heydenburg, Phys. Rev. 94, 1399 (1954).
[4] N. P. Heydenburg and G. M. Temmer, Phys. Rev. 95, 861 (1954).
[5] K. A. Ter-Martirosyan, J. Exptl. Theoret. Phys. (U.S.S.R.) 22, 284 (1952).
[6] K. Alder and A. Winther, Phys. Rev. 91, 1578 (1953).
[7] C. C. Trail and C. H. Johnson, Phys. Rev. 91, 474 (1953).
[8] J. H. Bjerregaard and T. Huus, Phys. Rev. 94, 204 (1954).

The largest cross sections for Coulomb excitation were found in F^{19} (196 kev), Na^{23} (446 kev), Ti^{47} (160 kev), Mn^{55} (128 kev), and Ge^{73} (68 kev). For these we were able to perform thin-target experiments successfully. Large cross sections do not necessarily imply large matrix elements for the transitions involved; in fact, the latter turn out to be small compared to the 137-kev transition in Ta^{181}. The cross sections are large only for strictly kinematical reasons having to do with the Coulomb excitation mechanism and not with the intrinsic excitability of nuclei under study.

B. EXPERIMENTAL DETAILS

The main features of our experimental setup have already been described.[9] In some cases we have used a

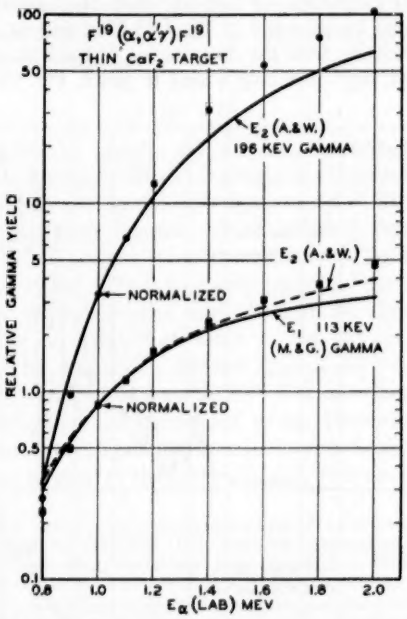

FIG. 1. Coulomb excitation by alpha particles of 113-kev and 196-kev levels in thin F^{19} target. Solid curves are theoretical $E1$ (113-kev) and $E2$ (196-kev) curves, according to Mullin and Guth (reference 13) and Alder and Winther (reference 6), respectively. Dashed curve is theoretical $E2$ curve for comparison. Experimental points are normalized to the curves at 1 Mev. For higher-energy region, see Figs. 3 and 4 of reference 9.

Note added in proof.—Recent calculations by K. Alder and A. Winther (to be published) using the WKB approximation for the $E1$ case have produced two major modifications: (a) the new definition of the parameter ξ (as discussed above); (b) the introduction of v_f (final relative velocity) in the place of v (unspecified) in their expression for the Coulomb excitation cross section (see reference 6). Modification (a) has been incorporated into this paper; modification (b) was not available in time. Suffice it to state that when this correction is applied to our results, essentially *all* the discrepancies between theory and experiment at the higher energies, seen in Figs. 3, 5, 6, 7, and 10, are removed. This correction is of course the larger, the greater ΔE. Only ~40 percent of the discrepancy disappears in the case of the 196-kev level in F^{19}.

[9] N. P. Heydenburg and G. M. Temmer, Phys. Rev. 94, 1252 (1954).

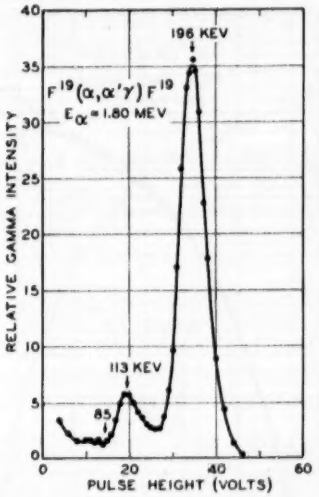

FIG. 2. Pulse-height distribution of gamma radiation from thin F^{19} target under 1.8-Mev alpha bombardment, using a well crystal. Note the absence of 83-kev cascade radiation. Note also that the peak below the 113-kev gamma ray (Fig. 5 of reference 9) has been eliminated.

2-in.×2-in. well-type NaI(Tl) crystal with a $\frac{3}{4}$-in. diameter hole $1\frac{1}{2}$ in. deep, the target being located at the bottom of the well.[10] In this arrangement, we approach 100-percent efficiency (including geometry) for radiations up to about 200 kev (see Fig. 1, reference 9). We were thus able to measure cross sections down to a fraction of a microbarn.

We prepared our thin targets by vacuum evaporation onto nickel backing. In the cases of Ti^{47}, Fe^{57}, Ge^{73}, and Zn^{67} we were able to obtain enriched isotopes.[11] We have no good measure of the target thicknesses for the thin targets, but we ascertained that they were thin enough for our purposes (~30 kev) by preparing targets yielding fewer gamma rays and comparing the shapes of the excitation curves. (Targets which are too thick produce characteristically steeper curves.)

C. EXCITATION FUNCTIONS

(a) F^{19}

We have previously reported some thin-target excitation functions for both the 113-kev and 196-kev levels of F^{19} under alpha-particle bombardment.[9] In this case, we know the target to be no thicker than the width of the narrowest resonance observed in the $(\alpha,p\gamma)$ reaction (see Fig. 6, reference 9). Some additional work, extending the energy range to lower values by using our high-efficiency well crystal, is plotted in Fig. 1. These curves are in essential agreement with the work of the group

[10] We are indebted to Dr. P. H. Abelson for the loan of this crystal.

[11] From the Oak Ridge National Laboratory, Oak Ridge, Tennessee.

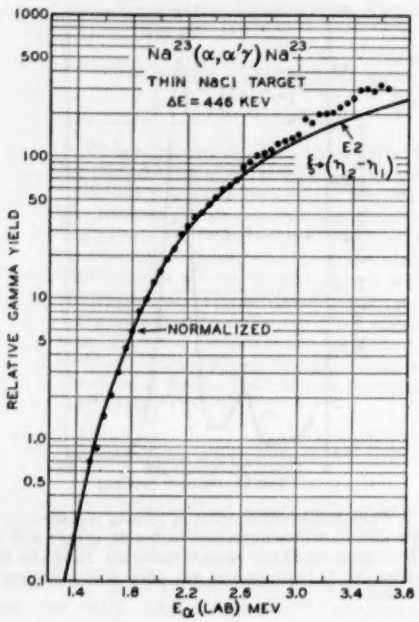

FIG. 3. Coulomb excitation function for thin NaCl target. Level energy is 446 kev. Solid curve is the theoretical $E2$ function (reference 6). Experimental points normalized at 1.8 Mev (see note added in proof, Fig. 1).

at the California Institute of Technology.[12] The theoretical curve for the electric dipole ($E1$) case is calculated according to Mullin and Guth;[13] the curves for the electric quadrupole ($E2$) case are calculated according to the expressions given by Alder and Winther;[6] it should be noted that the quantity $\eta_2-\eta_1$ ($\eta_1=Z_1Z_2e^2/\hbar v_1$; $\eta_2=Z_1Z_2e^2/\hbar v_2$, v_1 and v_2 being initial and final projectile velocities, respectively) rather than

$$\xi=(\Delta E/2E)(Z_1Z_2e^2/\hbar v)$$

[which is the limiting value of $(\eta_2-\eta_1)$ for $\Delta E/E \ll 1$, ΔE being the excitation energy, E the bombarding energy] has been used in all excitation curves, in accordance with prevailing theoretical preference. This is justified mainly by the results of the exact calculations for the electric dipole case;[13] furthermore, the Born approximation calculation for $E2$ employing $(\eta_2-\eta_1)$ as parameter[14] seems to agree with the exact (numerical) $E2$ calculations.[6] Incidentally, the fit with experiment is considerably improved when using the latter parameter. (Note, however, the discrepancy from theory at the higher energies.) Figure 2 shows the pulse-height distribution obtained from a thin CaF_2 target at 1.8-Mev alpha-particle energy, using the well crystal described above. Note that the satellite peak (see Fig. 5, reference 9) to the left of the 113-kev peak has disappeared. This peak seems to have also troubled Cal Tech[15] and Cavendish workers[16] when studying this reaction. The absence of cascade radiation from the 196-kev level to the 113-kev level is now very evident.

[12] Sherr, Li, and Christy, Phys. Rev. **94**, 1076 (1954).
[13] C. J. Mullin and E. Guth, Phys. Rev. **82**, 141 (1951).
[14] C. J. Mullin (private communication).

(b) Na^{23}

The excitation curve for the yield of the 446-kev gamma radiation from a thin NaCl target is shown in Fig. 3. The experimental points have arbitrarily been normalized to the theoretical $E2$ curve at 1.8 Mev. The agreement over a factor of 100 in cross section is seen to be excellent, leaving little doubt as to the $E2$ nature of the excitation process.† The disagreement with theory at the higher energies can be attributed to some compound nucleus formation (see note added in proof, Fig. 1). With the same target we were able to obtain the excitation function for the $Na^{23}(\alpha,p\gamma)Mg^{26}$ reaction as measured by the yield of the 1.83-Mev gamma radiation resulting from the deexcitation of the first excited state of Mg^{26} (see note added in proof, Fig. 1). This

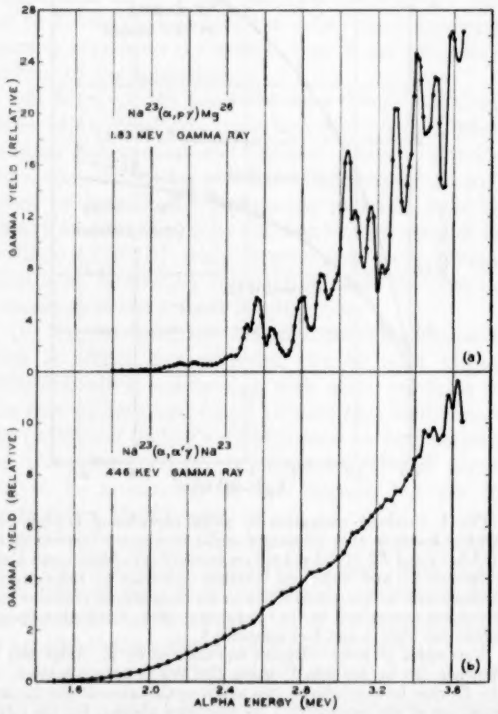

FIG. 4. (a) Excitation function for the reaction $Na^{23}(\alpha,p\gamma)Mg^{26}$, as detected by the 1.83-Mev gamma ray from Mg^{26}. Resonances are levels in the compound nucleus Al^{27}. (b) Excitation function for the reaction $Na^{23}(\alpha,\alpha'\gamma)Na^{23}$. Level energy is 446 kev. Same data as in Fig. 3. Thin NaCl target.

[15] Peterson, Barnes, Fowler, and Lauritsen, Phys. Rev. **93**, 951 (1954).
[16] G. A. Jones and D. H. Wilkinson, Phil. Mag. **45**, 230 (1954).

† *Note added in proof.*—The possibility that some of these transitions are of the $E1$ type cannot be completely ruled out; e.g., in the case of Na^{23} our data fall within ±5 percent of the theoretical $E1$ curve.

reaction takes place via the compound nucleus Al^{27}. The many peaks in Fig. 4(a) correspond to levels in that nucleus, and also show that we are dealing with a thin target. In Table I we list the resonances of $Na^{23}+\alpha$ and the corresponding levels in Al^{27}. The comparison with the $Na^{23}(\alpha,\alpha'\gamma)Na^{23}$ reaction plotted in Fig. 4(b) strikingly demonstrates the interplay of Coulomb excitation and compound nucleus formation. At the high-energy end the latter excitation curve begins to show irregularities which can be correlated with levels in the compound nucleus Al^{27} as indicated in the upper curve. One can say that 3.6 Mev are about 90 percent Coulomb excitation and 10 percent compound-inelastic excitation of the 446-kev state. Also, there is undoubtedly some nonresonant excitation over and above the classically expected Coulomb excitation at the higher energies because of the gradual breakdown of the assumption $2Z_1Z_2e^2/\hbar v \gg 1$ used in the derivation of the classical expressions.[6]

(c) Ti^{47}

The 160-kev gamma ray we reported earlier[1] was shown to belong to Ti^{47}. This gamma ray is presumably the one also seen in the beta decay of Sc^{47}.[17] The thin target excitation function for an enriched target of $Ti^{47}O_2$ (82.05 percent, natural abundance 7.75 percent) is shown in Fig. 5. In this case we know that the target is no more than 50 kev thick, because we observe a resonance of about that width in the $O^{18}(\alpha,n\gamma)Ne^{21}$ reaction by means of a 342-kev gamma ray[18] coming from the first excited state of Ne^{21}. The experimentally observed yields are normalized to the theoretical $E2$ curve[6] at 2 Mev. Again, the agreement with the theory is found to be good at the lower energies, with characteristic departures occurring around 2.5 Mev and above (see note added in proof, Fig. 1).

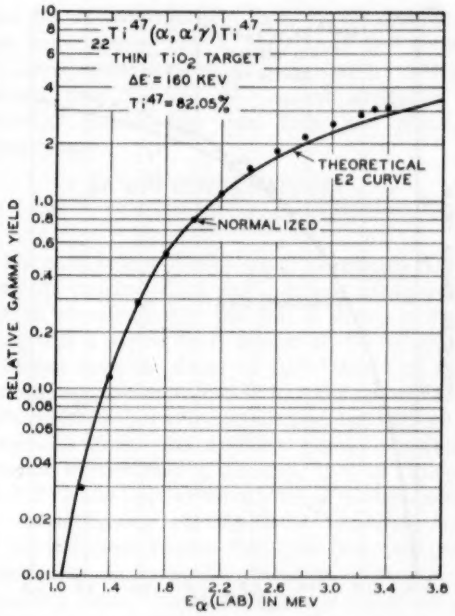

FIG. 5. Coulomb excitation function for thin enriched $Ti^{47}O_2$ target. Level energy is 160 kev. Solid curve is the theoretical $E2$ function (reference 6). Experimental points normalized at 2 Mev (see note added in proof, Fig. 1).

TABLE I. Levels in the compound nucleus Al^{27} as obtained from $Na^{23}(\alpha,p\gamma)Mg^{26}$, observing the 1.83-Mev gamma-ray yield. E_r = resonance energy in the laboratory system; $E_{c.m.}$ = resonance energy in the center-of-mass system; E^* = excitation energy of Al^{27}.

E_r (Mev)	$E_{c.m.}$ (Mev)	E^* (Mev)
1.95	1.66	12.08
2.15	1.83	12.24
2.43	1.98	12.40
2.51	2.14	12.56
2.56	2.18	13.60
2.64	2.25	12.67
2.80	2.39	12.79
2.90	2.47	12.87
3.04	2.59	13.01
3.07	2.62	13.04
3.16	2.69	13.11
3.23	2.75	13.17
3.29	2.80	13.20
3.40	2.90	13.32
3.50	2.98	13.40
3.58	3.05	13.47

[17] Cork, LeBlanc, Brice, and Nester, Phys. Rev. **92**, 367 (1953).
[18] This gamma ray is always present when we use oxide targets and represents the only observable effect ascribable to oxygen under alpha-particle bombardment.

(d) Mn^{55}

We have already reported our thick-target results for the excitation of the 128-kev line from this nucleus.[1] The main reason for investigating the thin-target yield was to establish how reliable our thick-target calculations were and how much detail is generally lost when we are forced, because of intensity considerations, to confine ourselves to thick-target excitation. Figure 6 shows the thin-target curve, along with the theoretical $E2$ function.[6] The agreement is again seen to be quite good at the lower energies, with deviations (excess over theory) becoming apparent at higher energies (see note added in proof, Fig. 1). The target used was electrolytic manganese metal evaporated on nickel foil. Generally speaking, not too much detail is lost when using thick targets, if the main objective is to measure absolute cross sections. It must be remembered that thin targets introduce the difficulty of having to know the target thickness absolutely.

In Mn^{55} we were able to make use of the comparison method[8] already mentioned. It turns out that if the thin-target yield of the gamma radiation is measured for protons and alpha particles having the same value of the parameter ξ, the ratio of the yields will always be either 16 for $E3$, 10 for $E2$, or 6.4 for $E1$ (numerical values approximate). In the case of Mn, 1.86-Mev

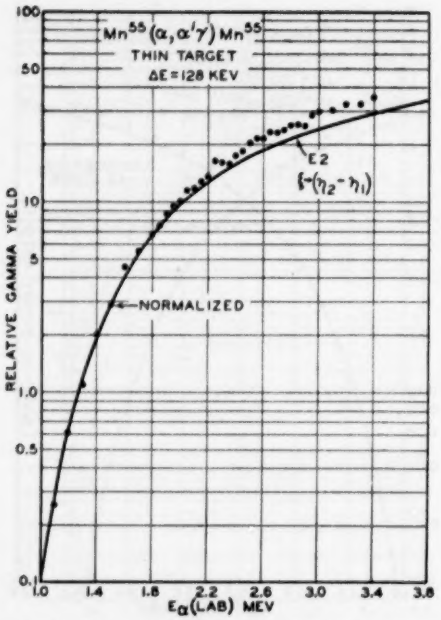

FIG. 6. Coulomb excitation function for thin Mn^{55} target. Level energy is 128 kev. Solid curve is the theoretical $E2$ function (reference 6). Experimental points normalized at 1.5 Mev. For thick-target excitation curve, see Fig. 2 of reference 1 (see note added in proof, Fig. 1).

alpha particles and 0.75-Mev protons have the same value of ξ. The experimentally observed ratio of alpha to proton yields at these energies was 10.8 ± 1.0, thus once again confirming the $E2$ nature of the excitation process. The thin target of Mn was deposited on niobium foil, using a 0.032-in. copper absorber to reduce the Nb x-rays. Niobium was found to have a lower background than nickel for proton excitation.

(e) Fe^{57}

Even with our enriched target of Fe^{57}(59.3 percent, natural abundance 2.25 percent) in the form of Fe_2O_3 and our 4π geometry we did not have enough intensity for thin target work. The previously reported 123-kev gamma ray[1] was shown to belong to Fe^{57} as expected. The oxide was reduced at about 1000°F in a hydrogen atmosphere, the resulting iron powder was compressed into a pure Fe^{57} foil 0.002 in. thick. This step facilitated the theoretical thick-target yield calculation. The excitation curve for a thick target of pure Fe^{57} for the 123-kev gamma ray is shown in Fig. 7. The insert in Fig. 7 shows the decay scheme as recently given by Alburger and Grace.[19] We are evidently exciting the second excited state of Fe^{57} at 137 kev. In order to show the sensitivity of the Coulomb excitation process to the value of the excitation energy ΔE, we have plotted the theoretical thick target yields for both $\Delta E=123$ kev and $\Delta E=137$ kev, both normalized to the experimental points at 2.0 Mev. The better agreement with the 137-kev curve is very evident. Although there is no doubt about the state of affairs in this particular instance, it is interesting to note that the excitation curve can in general decide whether a given gamma ray represents a transition to the ground state, even if the energy difference between excitation energy and gamma-ray energy were only about 10 percent.

In the gamma-ray spectrum of Fe^{57} we found evidence for gamma radiation at 14 kev, which is undoubtedly produced by cascade only, since that transition is known to be too slow ($t_{\frac{1}{2}}=1.1\times10^{-7}$ sec) and of the wrong multipolarity ($M1$) to be Coulomb excited. We also see some slight indication for the 137-kev crossover transition, which is known to be weak compared to the 123-kev radiation (ratio of $123/137=15\pm7$ as found by proportional counter measurement[19]). Our excitation of the 137-kev level confirms the electric quadrupole nature of the transition.

We also compared the thick-target yields for Fe^{57} and $Fe_2{}^{57}O_3$ at 3.0 Mev in order to have some empirical information on the stopping power effect of oxygen for cases (such as the rare earths) where only oxides are available. The ratio for the yields of the 123-kev radiation was 2.07. A similar thick-target comparison for Ta and Ta_2O_5 yielded a ratio of 2.00. We shall therefore use a factor of 2 to put oxides and pure substances on a correct relative basis.

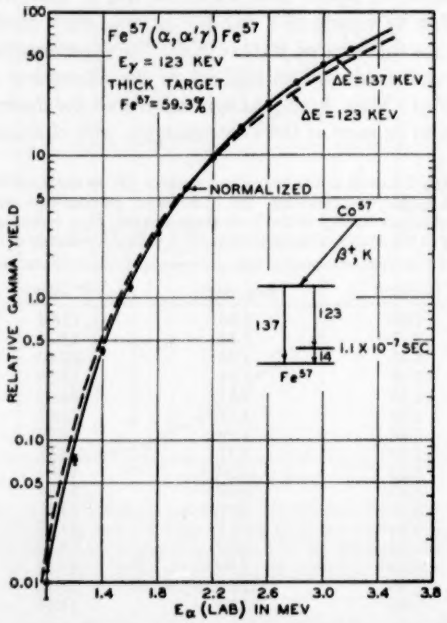

FIG. 7. Coulomb excitation function for thick enriched Fe^{57} target. Level energy is 137 kev, gamma ray detected is 123 kev. Solid curve is the theoretical $E2$ function for $\Delta E=137$ kev, dashed curve for $\Delta E=123$ kev. Experimental points normalized at 2 Mev. Insert shows level scheme as given in reference 19 (see note added in proof, Fig. 1).

[19] D. E. Alburger and M. A. Grace, Proc. Phys. Soc. A67, 280 (1954).

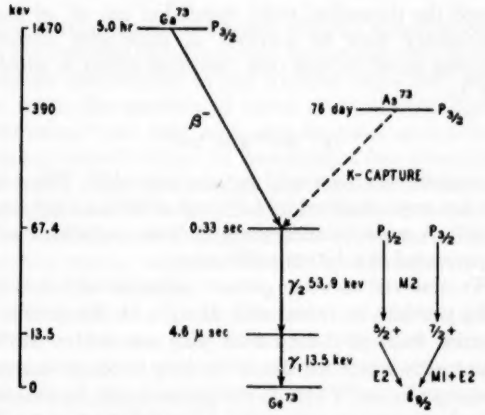

FIG. 8. Level scheme of Ge^{73} as given in reference 21. Level at 67.4 kev is not the one we excite (see text). Crossover transition to ground is less than 2×10^{-3} of the unconverted 54-kev radiation (reference 21).

(f) Ge^{72}

Our early work with ordinary GeO_2 revealed a strong gamma-ray line at 68 kev.[1] Since the only odd-A isotope of germanium is Ge^{73}, we suspected the line to belong to this isotope, since the even-even isotopes are either known or expected to have first excited states lying considerably higher (around 600 kev).[20] An enriched target of $Ge^{73}O_2$ (78.04 percent, natural abundance 7.67 percent) confirmed our expectation. Figure 8 shows the latest information given by Welker *et al.*,[21] on the level scheme of Ge^{73} as known from the decay of Ga^{73} and As^{73}. We see that a level exists at 67.4 kev; however, the crossover gamma ray has never been seen, with an upper limit on the intensity of 2×10^{-3} compared to the unconverted 53.9-kev radiation. Furthermore, the lifetime of that level is known to be 0.33 second, which implies a Coulomb excitation cross section (if it were an $E2$ transition) about 10^{-7} times that of the 137-kev transition in tantalum. On the other hand, we were unable to detect a trace of either the 53.9-kev or the 13.5-kev radiation. Figure 9 gives the pulse-height distribution as obtained with enriched $Ge^{73}O_2$. Three points locating the peak of the 67.8-kev gamma ray of ionium (Th^{230}), which is one of our calibration points, are also shown. We see that within the accuracy of our measurements the energy of the Ge^{73} line and the 68-kev ionium line is indistinguishable. We are forced to the conclusion that we are observing an energy level in Ge^{73} lying within less than 500 electron volts of a known level, but evidently having entirely different properties (spin, parity, lifetime).

Our thin-target excitation curve for this level is shown in Fig. 10. Again the agreement with the theoretical $E2$ curve[6] is very good. This also confirms the fact that the 68-kev transition leads to the ground state (see remarks under Fe^{57}). The case of Ge^{73} points up the necessity for some caution when we try to identify gamma rays observed in Coulomb excitation with "known" gamma rays from beta- and gamma-ray spectroscopy.

D. OTHER RESULTS

(a) Zn^{67}

The pulse-height distribution of the gamma radiation from an enriched thick $Zn^{67}O$ target (60.46 percent, natural abundance 4.11 percent) is shown in Fig. 11, along with a partial decay scheme of this nucleus as it is known from the decay of Ga^{67} [22] and Cu^{67}.[23] Two gamma rays, one at around 90 kev and one at 182 kev, were observed. Since the cascade from the 182-kev level involves a 90-kev and a 92-kev gamma ray (not resolvable by scintillation counter), it is of interest to see if the entire peak at around 90 kev can be accounted for without having to invoke direct Coulomb excitation of the first excited state. Using the best available information on internal conversion coefficients and branching ratios,[22] we find that this is indeed the case. That is to say, within the accuracy of our measurements all gamma radiation originated from the Coulomb excitation of the 182-kev level in Zn^{67}. We have further confirmation of this from the observation that the intensity ratio of (90+92)-kev gamma radiation to 182-kev gamma radiation is unchanged at 6 Mev (He^{++})

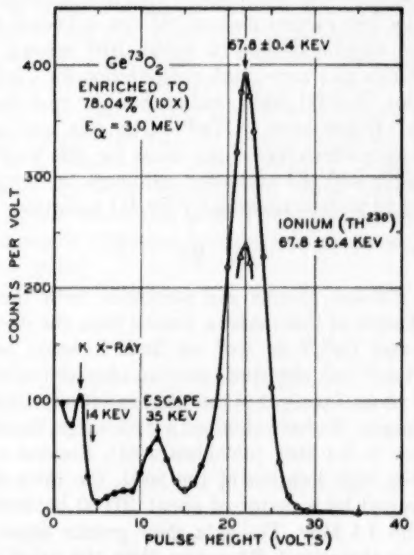

FIG. 9. Pulse-height distribution of gamma radiation from enriched $Ge^{73}O_2$ target, obtained with 3-Mev alpha particles. Three points under main peak locate the 67.8-kev known line from a Th^{230} calibration source. Note absence of 14-kev or 54-kev radiation.

[20] G. Scharff-Goldhaber, Phys. Rev. **90**, 587 (1953).
[21] Welker, Schardt, Friedlander, and Howland, Phys. Rev. **92**, 401 (1953).
[22] Meyerhof, Mann, and West, Phys. Rev. **92**, 758 (1953).
[23] H. T. Easterday, Phys. Rev. **91**, 653 (1953).

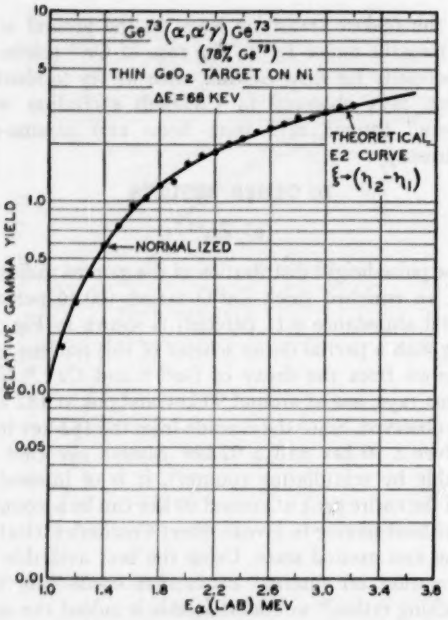

FIG. 10. Coulomb excitation function for thin enriched $Ge^{73}O_2$ target. Level energy is 68 kev. Solid curve is the theoretical $E2$ function (reference 6). Experimental points normalized at 1.4 Mev (see note added in proof, Fig. 1).

bombarding energy; the ratio would have been altered in favor of the 182-kev line, had some direct excitation of the 92-kev level taken place. This is as it should be, since the first excited state at 92 kev is known to be isomeric with a lifetime of about 10^{-5} second; this corresponds to a very small cross section for Coulomb excitation (~1000 times smaller than the cross section for the 137-kev level in Ta^{181}). The spin and parity assignments which have been made for this level[22] are compatible with $E2$ excitation, although the return to the ground state is presumably by $M1$ radiation.

(b) V^{51}

The 320-kev gamma ray associated with the first excited state of this nucleus, known from the decay of Ti^{51} [24] and Cr^{51},[25] as well as from inelastic proton scattering,[26] was observed, with an observed intensity of only about 5 percent of the other radiations discussed in this paper. We have obtained a thick-target excitation curve up to 3.4 Mev (not illustrated). Because of the relatively high location of the level, the thick-target yield varied by a factor of about 50 000 between 1.6 Mev and 3.4 Mev. The data show greater departures from the theoretical $E2$ curves than the other cases described in this paper, again in a direction so as to exceed the theoretical yield. Some, but not all, of this discrepancy may be ascribed to incorrectly known stopping power in this case (see note added in proof, Fig. 1).

(c) As^{75} and Se^{77}

As previously reported,[1] gamma rays of 68, 199, and 283 kev were observed in As^{75}, and of 237 and 445 kev in Se^{77}. A more detailed study of these radiations will be presented in a future publication.

We observed no other gamma radiation with 3-Mev alpha particles on nuclei with $22<Z<34$. We shall re-examine most of these nuclei with our 6-Mev He^{++} beam[4] with which we should be able to excite energy levels up to about 1 Mev in the lighter nuclei, and hence several of the even-even excited states in this region.[27]

E. CONCLUSIONS

In all cases we have studied we have verified the electric quadrupole nature of the transition involved.† We believe that on the strength of the Coulomb excitation function alone no choice can be made between the possible $E1$ or $E2$ character of the transition to the first excited state of F^{19} at 113 kev; in fact, the $E2$ curve is seen to fit somewhat better. However, the life-

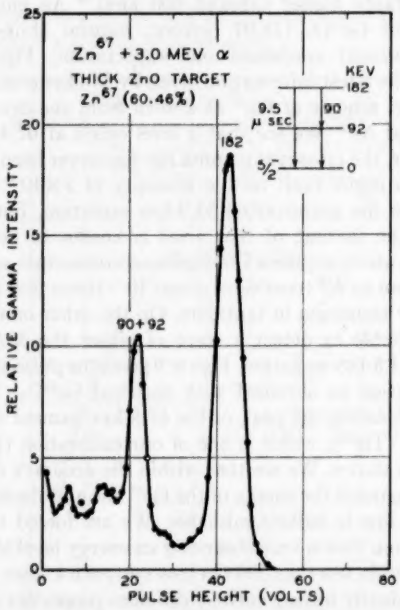

FIG. 11. Pulse-height distribution of gamma radiation from enriched $Zn^{67}O$ target, obtained with 3-Mev alpha particles. Peak marked 90+92 is entirely accounted for by cascade transitions from the 182-kev state, without direct excitation of the 92-kev level. Partial level scheme shown as insert is taken from reference 22.

[24] Koester, Maier-Leibnitz, Mayer-Kuckuk, Schmeiser, and Schulze-Pillot, Z. Physik 133, 319 (1952).
[25] W. S. Lyon, Phys. Rev. 87, 1126 (1952).
[26] Hausman, Allen, Arthur, Bender, and McDole, Phys. Rev. 88, 1296 (1952).
[27] We have already succeeded in detecting the gamma rays from the first excited states of the even-even isotopes of selenium.

time measurement[28] combined with the absolute value of the Coulomb excitation cross section and the isotropic angular distribution of the 113-kev radiation[12] seem to settle the question in favor of an electric dipole transition,[29] the only such case we have encountered among some 72 nuclei we have studied (see note added in proof, Fig. 1). Although the Coulomb excitation process favors $E1$ over $E2$ transitions by a factor of about 300 for 3-Mev alpha particles on F^{19}, the intrinsic nuclear matrix element for $E1$ is depressed about 1000-fold in this case.

Na^{23} provides a clear illustration of the interplay between Coulomb excitation and compound nucleus formation, since we have a comparison reaction proceeding via the compound nucleus Al^{27} at all energies. This case is similar to F^{19}, where we also have the $(\alpha,p\gamma)$ reaction taking place via the compound nucleus Na^{23}, as previously described.[9]

The deviations from the simple theory for $E2$ excitation evident at the high-energy end of most of these curves are presumably of two different origins: (a) compound nucleus contributions, as identified in certain favorable instances by the existence of resonances which agree with resonances of the respective compound nuclei; (b) barrier penetration effects due to the breakdown of "geometrical optics," and the existence of a finite nuclear radius (see note added in proof, Fig. 1). In view of the fact that the region of excitation in the compound nuclei involved in this investigation is completely unexplored (except for $F^{19}+\alpha$ and $Na^{23}+\alpha$) there is considerably difficulty in separating the two contributions experimentally. A more complete theory of the process can presumably hope to cope with (b) but not with (a).

In the way of spin assignments for the levels we excite, we can, of course, state that because of the $E2$ character of the transitions induced, the parities of the excited states are equal to the respective ground-state parities, and their spins differ by 0, ±1, or ±2 from the ground-state spins.

[28] Thirion, Barnes, and Lauritsen, Phys. Rev. **94**, 1076 (1954).
[29] D. H. Wilkinson (private communication) has obtained some independent evidence for the $1/2^-$ assignment for the 113-kev state from a study of the O^{19} beta decay.

TABLE II. Transition probabilities for some odd-A nuclei as found from Coulomb excitation. I_0 = ground-state spin and parity; I^* = spin of excited state (if known); ΔE = transition energy; $B_e(2)$ = reduced transition probability as defined in reference 13, obtained from thick-target yield Y_α at 3 Mev; F = ratio of observed to single-particle transition probability (using $r_0 = 1.2\times10^{-13}$ cm). Y_α is normalized to 1.00 for the 137-kev transition in Ta^{181}.

Nucleus	I_0	I^*	ΔE(kev)	$B_e(2)$ (10^{-48} cm^4)	Y_α	F
$_{11}Na^{23}$	$3/2^+$	$?^+$	446	0.041	1.6	71
$_{23}Ti^{47}$	$5/2^-$	$?^-$	160	0.047	4.5	31
$_{23}V^{51}$	$7/2^-$	$?^-$	320	0.013	0.41	8
$_{25}Mn^{55}$	$5/2^-$	$?^-$	128	0.070	10	38
$_{26}Fe^{57}$	$(3/2^-)$	$?^-$	137	0.051	7.5	26
$_{30}Zn^{67}$	$(5/2^-)$	$(5/2^-)$	182	0.043	3.7	18
$_{33}Ge^{73}$	$9/2^+$	$?^+$	68	0.042	5.8	16

Because of the good agreement with the $E2$ theory[6] over at least part of the energy range covered (see note added in proof, Fig. 1), we are justified in using the simple theory to estimate the relative sizes of the transition probabilities $B_e(2)$. Without making detailed corrections for variations in stopping power over the range of Z under investigation ($22\leqslant Z\leqslant 32$; Na^{23} corrected, however) nor for internal conversion, we list in Table II the approximate transition probabilities as well as F, the ratio of observed to single-particle transition probability (using $r_0 = 1.2\times10^{-13}$ cm). We note that in all cases the transition probabilities are at least an order of magnitude smaller than the (rotational) transition in Ta^{181} (or most rare-earth nuclei). Since the latter is about 100 times what is predicted from an independent-particle model estimate, our observed values are still very much larger than is expected for single-particle transitions (with the possible exception of V^{51}). This is *a fortiori* true when compared to empirical values of transition probabilities, which usually fall short of the theoretical ones. There also seems to be no systematic difference between odd-proton and odd-neutron nuclei.

Pressure Broadening of OCS in Foreign Gas Mixtures

F. A. Liuima,* A. V. Bushkovitch, and A. G. Rouse
Saint Louis University, St. Louis, Missouri
(Received June 1, 1954)

Line widths of the $J=1-2$ OCS line in mixtures with foreign perturbing gases have been measured. The perturbers were N_2O, He, and O_2 in three different percentages of mix, about 20 percent, 50 percent, and 75 percent of perturber. Systematic variation of collision diameters with mix ratio, previously reported, was not observed.

INTRODUCTION

In a previous investigation in this laboratory[1] pressure broadening of several lines of the microwave spectrum of ammonia in foreign gas mixtures was studied.[2] We have now measured line widths of the $J=1-2$ OCS line in mixtures of three different percentages with N_2O, He, and O_2 as perturbers, as well as in the case of self-broadening of this line. In this latter case the results are in good agreement with the value recently obtained by Smith,[3] our value being 9.20×10^{-8} cm as compared with the value of 9.28×10^{-8} cm given by Smith.

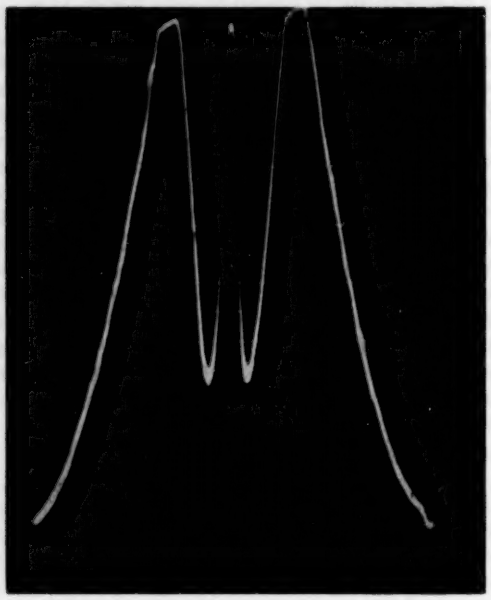

Fig. 1. Typical line; OCS at 100 microns pressure; the pattern is the absolute magnitude of the first derivative of the line contour superimposed on the U-shaped klystron mode.

OCS is a linear nonsymmetric molecule. This asymmetry gives to the molecule a dipole moment sufficient to cause relatively strong absorption lines. The line corresponding to $J=1-2$ rotational transition can be observed within the frequency limits of the 2K33 klystron. The absorption due to this transition takes place at a frequency of 24 325.92 Mc/sec[4] and has an intensity of 5.5×10^{-5} cm^{-1}. From the pressure-broadening data for this line the collision diameters have been obtained for both the mutual collisions of OCS molecules and for collisions with foreign perturbers by means of the formulas of reference 1.

EXPERIMENTAL

The spectrograph was of the unbalanced type, employing 45 feet of K-band wave guide for the absorption cell. The 2K23 klystron was swept over its mode by a saw-tooth voltage applied to its repeller grid. The same voltage was used for the horizontal sweep of the oscilloscope, so that a plot of absorption *versus* frequency was obtained. Upon this saw-tooth wave form there was superimposed a small sinusoidal voltage of 205 kc/sec, the effect of which was to sweep the klystron frequency rapidly over the region of varying absorption when it slowly passes the mode.[5] The line is then an effective frequency discriminator and can be detected by an AM reciever tuned to the same frequency. This receiver amplifies the signal from the crystal detector at radio-frequency, demodulates it, amplifies the resulting audio-frequency, and applies it to the vertical deflection plates of the oscilloscope. The amplification at the radio-frequency has the advantage of considerably improving the signal-to-noise ratio, with a good over-all sensitivity as a result. With this system the resulting pattern is the absolute magnitude of the first derivative of the line contour superimposed on the U-shaped klystron mode. The line width is the frequency difference between the two maxima multiplied by $\sqrt{3}$. Additional line broadening is introduced by the second modulation; it was corrected for by extrapolating the line widths to zero-frequency modulation. A resonant cavity wave meter was used to identify the line and to locate it on the oscilloscope.

* Now at Boston College, Chestnut Hill, Massachusetts.

[1] Potter, Bushkovitch, and Rouse, Phys. Rev. **83**, 987 (1951).

[2] For a general review of the subject of pressure broadening in microwave spectroscopy, see W. V. Smith, Ann. N. Y. Acad. Sci. **55**, 891 (1952); also Gordy, Smith, and Trambarulo, *Microwave Spectroscopy* (John Wiley & Sons, Inc., New York, 1953), Chap. 4.

[3] W. V. Smith, University of Delaware Research Report AF 18(600)-449 No. R-357-10-4 (unpublished). We should like to thank Dr. Smith for sending us a copy of this report.

[4] Dakin, Good, and Coles, Phys. Rev. **71**, 640 (1947).

[5] W. Gordy, Revs. Modern Phys. **20**, 668 (1948).

To provide horizontal frequency markers, a second identical klystron was coupled to the system by means of a 25-db Bethe hole coupler. The output of the two klystrons was fed into a crystal mixer, which in turn was connected to a 1-Mc/sec communications reciever. Selective tuning of this receiver provides two sharp pips on the oscilloscope, 2 Mc/sec apart.

The two signals, the line pattern and the pips, were fed into a Tektronix model 514AD oscilloscope via two separate inputs, either one of which can be selected by means of a switch. They were recorded separately on photographic film. The line widths were plotted against pressure for each mixture and the collision diameters calculated by means of the formulas of reference 1.

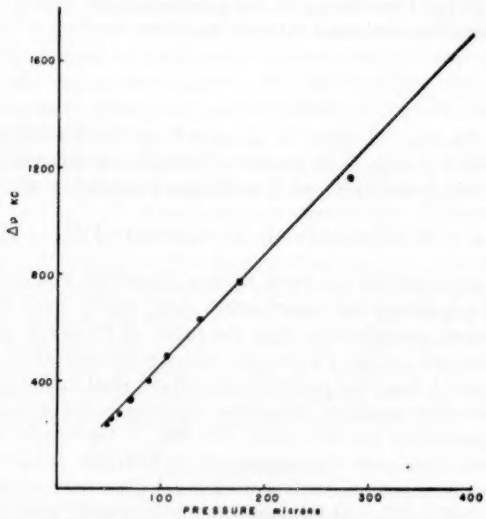

FIG. 2. Half-width *vs* pressure; OCS with 50.1 percent of O_2.

TABLE I. Collision diameters of OCS in mixtures ($\times 10^8$ cm).

OCS				Average 9.20
N_2O	22.6 percent 7.39	50.7 percent 7.49	74.4 percent 7.39	7.42
He	22.8 percent 3.13	50.4 percent 2.85	75.2 percent 3.11	3.03
O_2	20.2 percent 4.60	50.1 percent 4.95	77.5 percent 5.44	5.00

Figure 1 gives a typical line, while Fig. 2 is a typical plot of line half-width *versus* pressure.

The OCS gas was prepared in the laboratory through decomposition of ammonium thiocyanate with sulfuric acid.[6] Three different gases were used as perturbers: N_2O, He, and O_2, mixing each one of them with OCS in three different ratios. The mixing apparatus was the one described in reference 1.

RESULTS

The results are summarized in Table I. It is thought that the variations of the collision diameter with mix ratio are not significant, since the variation does not appear to follow a consistent pattern. This is contrary to reference 1 where there appeared to be a consistent decrease in collision diameter with increasing proportion of perturber. The results for self-broadening are thought to be accurate to within 1 percent; those for foreign broadening to within 10 percent. The substantially lower accuracy of foreign broadening results is thought to be due primarily to difficulties connected with the mixing process.

[6] We wish to thank Dr. Schaeffer and members of the Chemistry Department of St. Louis University for assistance in the preparation of OCS gas.

Pairing Effects in Coulomb Energies and the Radii of Mirror Nuclei*

B. C. CARLSON† AND I. TALMI‡
Palmer Physical Laboratory, Princeton University, Princeton, New Jersey
(Received June 16, 1954)

The Coulomb energy difference between the nuclei of a mirror pair exhibits an odd-even alternation with Z that is presumed to reflect the well-known pairing property of the short-range nuclear forces. By taking second differences of Coulomb energy (differences between successive mirror pairs), the alternation is seen to continue to at least $Z=15$, and additional irregularities appear that may be shell-structure effects. The analysis of Feenberg and Goertzel is discussed from the point of view of the shell model, and the pairing of spins is extended to the spherically symmetric pairing characteristic of the state of lowest seniority. A harmonic oscillator model with jj coupling is used to calculate the Coulomb energy, including exchange effects, in the state of lowest proton seniority. The single parameter of the model is determined by comparison with experimental data and remains constant to ± 1.5 percent through the $p_{1/2}$ and $d_{5/2}$ shells. The rms radius of the nuclear charge distribution is calculated by the same model. Between C^{13} and Al^{27}, the equivalent r_0 decreases fairly smoothly from 1.34 to 1.20. For $A \leq 11$ the model is not satisfactory, and for $A \geq 31$ there are some serious inconsistencies in the data. The most recent data indicate that r_0 may decrease to the range 1.1 to 1.15 for $A \cong 39$.

I. INTRODUCTION

THE Coulomb energy of a nucleus of atomic number Z has been written by Feenberg and Goertzel[1] in the form,

$$E_c(Z)=\tfrac{1}{2}Z(Z-1)a+[\tfrac{1}{2}Z]b, \qquad (1)$$

where $[\frac{1}{2}Z]$ denotes the largest integer not exceeding $\frac{1}{2}Z$. The first term represents the Coulomb energy of Z equivalent protons without consideration of symmetry effects. The second term arises ultimately from the Pauli exclusion principle and represents the correlation or pairing energy resulting from the fact that two protons have a larger probability of being found close together if their spins are oppositely directed. Unlike the force between electrons in atomic spectroscopy, the nuclear forces are attractive and favor the pairing of spins. The Coulomb forces between protons are far too weak to prevent pairing; however, since their energy depends on the spatial correlations, its odd-even alternation is a symptom and a rough measure of the pairing.

The parameters a and b are not expected to be exactly constant, but if only the ground states of the mirror nuclei are considered, one may hope that a and b will vary only slowly with Z. The difference in Coulomb energy between the two nuclei of a mirror pair will then be

$$\Delta_1(Z)=E_c(Z)-E_c(Z-1)$$
$$=(Z-1)a+\tfrac{1}{2}[1+(-1)^Z]b. \qquad (2)$$

Different mirror pairs can be conveniently compared[1] by dividing Δ_1 by $Z-1$, but this procedure has the disadvantage of making the pairing effects inconspicuous in the range of higher Z. In order to exhibit the pairing effects clearly, it is better to take second differences, in which the first term is no longer weighted by $Z-1$:

$$\Delta_2(Z)=\Delta_1(Z)-\Delta_1(Z-1)=a+(-1)^Z b. \qquad (3)$$

Equation (3) will serve, in Secs. II and III, as a guide in examining the experimental data, which have improved considerably since the paper of Feenberg and Goertzel. In Sec. IV we shall criticize the definitions of a and b from the point of view of the shell model and introduce modified definitions that seem to be more appropriate to this model. In Sec. V the crude but very convenient assumption of an isotropic harmonic oscillator potential will be used to calculate the modified a and b. The calculations will be compared with the experimental pairing effect; in addition, they will provide a prescription for obtaining nuclear radii from observed Coulomb differences.

II. EXPERIMENTAL DATA

The mass difference between the nuclei of a mirror pair can be obtained from experimental Q values of nuclear reactions, especially the (p,n) reaction, or from the β-decay end-point energy. After correction for the n-H^1 difference, the mass difference is then interpreted as the difference in Coulomb energy by the assumption of charge symmetry of the nuclear forces. In most cases, accurate Q values are available for low A ($A \leq 27$). For higher A, one must rely primarily on end-point determinations of the short-lived positron activities. If T_0 is the end-point kinetic energy of a positron spectrum, the first Coulomb energy difference Δ_1 is $T_0+(1.804\pm 0.001)$ Mev, since the n-H^1 mass difference is 0.782 ± 0.001 Mev and two electron masses account for 1.022 Mev. Alternatively, Δ_1 is just the negative of the Q value for a (p,n) reaction.

For $A \leq 21$, we have used the adjusted Q values

* This work was supported in part by the U. S. Atomic Energy Commission and the Higgins Scientific Trust Fund.
† Now at the Institute for Atomic Research and Department of Physics, Iowa State College, Ames, Iowa.
‡ Now at the Weizmann Institute of Science, Rehovoth, Israel.
[1] E. Feenberg and G. Goertzel, Phys. Rev. **70**, 597 (1946).

given by Li *et al.*[2] and Li.[3] For $A \geq 23$, a list of experimental values of Δ_1 is given in Table I. Where more than one measurement is available, the adopted value listed in the second column of Table II is an average weighted by the reciprocal squares of the quoted errors.[4] Thus, if the individual measurements are denoted by $a_i \pm \sigma_i$, where σ_i is the error quoted by the author, the adopted value is $\bar{a} \pm \bar{\sigma} = \sum_i w_i a_i \pm (\sum_i \sigma_i^{-2})^{-\frac{1}{2}}$, where $w_i = \bar{\sigma}^2/\sigma_i^2$. Measurements for which no limits of error are quoted are included in Table I for comparison, but have not been used in obtaining the adopted value. The averaging procedure is not entirely satisfactory when systematic errors are present, and $\bar{\sigma}$ tends to underestimate the actual uncertainty. In the cases of S^{31} and Ca^{39}, the values given by references Hu 54 and Br 53 are so much higher than the earlier measurements that it would be meaningless to take a weighted average. These higher-energy data have therefore been treated separately throughout, and are indicated by parentheses in Table II.

The second differences defined in Eq. (3) are listed in the third column of Table II and are plotted against Z in Fig. 1; it should be remembered that Z denotes the largest of the three atomic numbers involved in a second difference. The vertical line through a plotted point indicates the error of the second difference, computed from the errors of the two first differences by taking the square root of the sum of their squares. A vertical line is omitted when the computed error is less than 10 kev. Points for successive even (or odd) values of Z have been connected by straight lines.

III. DISCUSSION

The principal feature of Fig. 1 is that the line connecting points of even Z lies distinctly above the line for odd Z up to $Z=15$ (or 18, according to the recent measurement of S^{31} by Hunt *et al.*). This separation shows clearly the odd-even pairing effect up to this point; the less accurate data available to Feenberg and Goertzel[1] would have maintained the separation only up to $Z=8$.

The second point of interest is that between certain even values of Z, the fluctuations are conspicuously larger than between others. There are sharp drops between $Z=6$ and 8 and between 14 and 16, which might be associated with the closing of $p_{3/2}$ and $d_{5/2}$ shells at 6 and 14, respectively. In each case the next subshell to be filled ($p_{1/2}$ or $s_{1/2}$) contains two protons. The fluctuations in the line for odd Z are less marked, although there seems to be a distinct drop between $Z=7$ and 9, and another drop somewhere between 17 and 21. These drops suggest that the wave function of the ninth, and possibly the twenty-first, proton has a relatively small overlap with the core, as might be expected if a new shell begins after $Z=8$ or 20. These interpretations do not explain why changes occur after 6 and 14 in the line for even Z but not across 6 and 14 in the line for odd Z, and *vice versa* for 8. Moreover, the pattern is very different if the higher result for the

[2] Li, Whaling, Fowler, and Lauritsen, Phys. Rev. **83**, 512 (1951).
[3] C. W. Li, Phys. Rev. **88**, 1038 (1952).
[4] E. R. Cohen, Revs. Modern Phys. **25**, 709 (1953).

TABLE I. Coulomb energy differences Δ_1 for mirror pairs with $A \geq 23$. The end-point kinetic energy of the positron spectrum is $T_0 = \Delta_1 - (1.804 \pm 0.001)$ Mev.

Positron emitter	T_0 (Mev)	Δ_1 (Mev)	Method[a]	Reference[b]
Mg^{23}	2.82	4.62	cc	Wh 39
	2.78	4.58 ±0.3	pn	Wh 39
	3.17	4.97	pn	Bl 51
	2.99	4.79 ±0.09	scin	Bo 51
	3.073	4.877±0.010	pn	Wi 52
	2.95	4.75 ±0.07	scin	Hu 54
Al^{25}	3.23	5.03 ±0.06	d	Li 52, Go 53
Si^{27}	3.74	5.54	cc	Mc 40
	4.0	5.8 ±0.1	pn	Mc 40
	3.54	5.34 ±0.1	cc	Ba 40
	3.92	5.72	pn	Bl 51
	3.48	5.28 ±0.10	scin	Bo 51
	3.805	5.609±0.010	pn	Ki 53
	3.76	5.56 ±0.08	scin	Hu 54
P^{29}	3.63	5.43 ±0.07	cc	Wh 41
	5.25	7.05 ±0.1	d	Pe 48, Li 52
	4.16	5.96 ±0.04	d	Ma 52, Li 52
	3.945	5.749±0.010	s	Ro 53
	3.9	5.7 ±0.2	scin	Na 53
S^{31}	3.85	5.65 ±0.07	cc	Wh 41
	3.87	5.67 ±0.15	cc	El 41
	4.06	5.86 ±0.12	scin	Bo 51
	4.50	6.30 ±0.10	scin	Hu 54
Cl^{33}[c]	4.13	5.93 ±0.07	cc	Wh 41
	4.2	6.0 ±0.2	scin	Na 53
A^{35}	4.38	6.18 ±0.07	cc	Wh 41
	4.41	6.21 ±0.09	cc	El 41
K^{37}[c]	...	...		
Ca^{39}	5.13	6.93 ±0.15	scin	Bo 51
	6.7	8.5 ±0.5	a	Br 53
	6.10	7.90 ±0.15	scin	Hu 54
Sc^{41}	4.94	6.74 ±0.07	cc	El 41

[a] Methods: cc, cloud chamber; s, magnetic spectrometer; scin, scintillation spectrometer; a, absorption; pn, $\Delta_1 = -Q_{2n}$; d, $\Delta_1 = Q_{dp} - Q_{dn}$.
[b] We are indebted for several of the following references to a privately circulated list compiled by Professor H. T. Richards.

Ba 40 Barkas, Creutz, Delsasso, Sutton, and White, Phys. Rev. **58**, 383 (1940).
Bl 51 Blaser, Boehm, Marmier, and Scherrer, Helv. Phys. Acta **24**, 465 (1951).
Bo 51 F. I. Boley and D. J. Zaffarano, Phys. Rev. **84**, 1059 (1951).
Br 53 R. Braams and C. L. Smith, Phys. Rev. **90**, 995 (1953).
El 41 D. R. Elliott and L. D. P. King, Phys. Rev. **60**, 489 (1941).
Go 53 E. Goldberg, Phys. Rev. **89**, 760 (1953).
Hu 54 Hunt, Kline, and Zaffarano, Phys. Rev. **95**, 611 (1954) and W. A. Hunt, Ph.D. thesis, Iowa State College, 1954 (unpublished).
Ki 53 Kington, Bair, Carlson, and Willard, Phys. Rev. **89**, 530 (1953).
Li 52 C. W. Li, Phys. Rev. **88**, 1038 (1952).
Ma 52 Mandeville, Swann, Chatterjee, and Van Patter, Phys. Rev. **85**, 193 (1952).
Mc 40 McCreary, Kuerti, and Van Voorhis, Phys. Rev. **57**, 351 (1940).
Na 53 M. Nahmias and T. Yuasa, Compt. rend. **236**, 2399 (1953).
Pe 48 R. A. Peck, Jr., Phys. Rev. **73**, 947 (1948).
Ro 53 H. Roderick and C. Wong, Phys. Rev. **92**, 204 (1953).
St 53 P. Stähelin and P. Preiswerk, Nuovo cimento **10**, 1219 (1953).
St 53a P. Stähelin, Helv. Phys. Acta **26**, 691 (1953).
Wh 39 White, Delsasso, Fox, and Creutz, Phys. Rev. **56**, 512 (1939).
Wh 41 White, Creutz, Delsasso, and Wilson, Phys. Rev. **59**, 63 (1941).
Wi 52 Willard, Kington, and Bair, Phys. Rev. **86**, 259 (1952).

[c] Activities originally attributed to Cl^{33} and K^{37} in reference Bo 51 have been assigned to the ground states of Cl^{34} and K^{38} by references St 53, St 53a, and Hu 54.

TABLE II. Adopted values of Coulomb energy differences, Δ_1, and second differences, $\Delta_2(Z)=\Delta_1(Z)-\Delta_1(Z-1)$. Values of the energy parameter of the harmonic oscillator model, $e^2(\nu/\pi)^{\frac{1}{3}}=\Delta_1/\xi(A)$. Radii of the mirror nuclei of smaller Z in terms of $r_0=\sigma(A)/\Delta_1$. Values in parentheses refer to the higher-energy data for S^{31} (reference Hu 54 of Table I) and Ca^{39} (references Br 53 and Hu 54).

Nucleus of larger Z	Δ_1 (Mev)	Δ_2 (Mev)	$\xi(A)$	$e^2(\nu/\pi)^{\frac{1}{3}}$ (kev)	Nucleus of smaller Z	$\sigma(A)$	r_0
$_2He^3$	0.764±0.001	0.764±0.001	2.000	381.9±0.5	H^3	1.260	1.649±0.002
$_3Li^6$	0.8 ±0.3	0.04 ±0.3	3.000	270 ±100	He^6	1.593	2.0 ±1.0
$_4Be^7$	1.645±0.001	0.85 ±0.3	4.667	352.5±0.2	Li^7	2.450	1.489±0.001
$_5B^9$	1.852±0.002	0.207±0.002	5.667	326.8±0.4	Be^9	2.857	1.543±0.002
$_6C^{11}$	2.762±0.003	0.910±0.004	7.333	376.6±0.4	B^{11}	3.543	1.283±0.002
$_7N^{13}$	3.003±0.002	0.241±0.004	8.667	346.5±0.2	C^{13}	4.023	1.340±0.001
$_8O^{15}$	3.487±0.005	0.484±0.005	10.167	343.0±0.5	N^{15}	4.549	1.305±0.002
$_9F^{17}$	3.549±0.006	0.062±0.008	10.350	342.9±0.6	O^{17}	4.477	1.262±0.002
$_{10}Ne^{19}$	4.038±0.005	0.489±0.008	11.832	341.3±0.4	F^{19}	5.082	1.259±0.002
$_{11}Na^{21}$	4.30 ±0.03	0.27 ±0.03	12.643	340 ±3	Ne^{21}	5.373	1.248±0.009
$_{12}Mg^{23}$	4.873±0.010	0.57 ±0.03	14.125	345.0±0.7	Na^{23}	5.928	1.217±0.003
$_{13}Al^{25}$	5.03 ±0.06	0.16 ±0.06	14.937	337 ±4	Mg^{25}	6.186	1.230±0.015
$_{14}Si^{27}$	5.604±0.010	0.57 ±0.06	16.418	341.3±0.6	Al^{27}	6.706	1.197±0.002
$_{15}P^{29}$	5.767±0.010	0.163±0.010	18.113	318.4±0.6	Si^{29}	7.297	1.265±0.002
$_{16}S^{31}$	5.70 ±0.06	−0.07 ±0.06	19.477	293 ±3	P^{31}	7.727	1.356±0.015
	(6.30 ±0.10)	(0.53 ±0.10)		(323 ±5)			(1.23 ±0.02)
$_{17}Cl^{33}$	5.94 ±0.07	0.24 ±0.09	20.098	296 ±4	S^{33}	7.878	1.33 ±0.02
		(−0.36 ±0.12)					
$_{18}A^{35}$	6.19 ±0.06	0.25 ±0.09	21.508	288 ±3	Cl^{35}	8.320	1.344±0.013
$_{19}K^{37}$	...	...	22.311	...	A^{37}	8.520	...
$_{20}Ca^{39}$	6.93 ±0.15	...	23.721	292 ±6	K^{39}	8.944	1.29 ±0.03
	(7.95 ±0.14)			(335 ±6)			(1.13 ±0.02)
$_{21}Sc^{41}$	6.74 ±0.07	−0.19 ±0.17	22.985	293 ±3	Ca^{41}	8.562	1.270±0.013
		(−1.21 ±0.16)					
$_{22}Ti^{43}$	...	...	24.341	...	Sc^{43}	9.029	...

S^{31} end point is correct. The drop after 14 then disappears, and a large drop occurs between 15 and 17.

Since a large Coulomb energy indicates a close association between the protons, it suggests a strong nuclear interaction as well; in fact, the investigation of odd-even Coulomb effects was stimulated by the known pairing property of the nuclear energy. It is therefore of interest to compare the variations in Coulomb energy with variations in the nuclear binding energy of the last nucleon. Redlich[5] has plotted the binding energy of the last proton as a function of Z (for several fixed values of $N-Z$), and similarly that of the last neutron as a function of N. If allowance is made for the average trend of the curves, a neutron curve of given $N-Z$ shows a pattern of variations similar to that of the proton curve with the same value for $Z-N$. The average trend is of course different for protons and neutrons because of the Coulomb energy, but on the scale of energies of interest here, the Coulomb energy is a very smoothly varying quantity and has a negligible effect on irregularities in the binding energy. For the mirror nuclei, in particular, the binding energy of the last neutron for $N-Z=1$ is just the binding energy of the last proton for $N-Z=-1$ plus the first Coulomb energy difference $\Delta_1(Z)$.

The pattern of variations in the binding energy contains several features exhibited by the curves of Fig. 1. In Redlich's curves for even Z or N, there are sharp drops between 6 and 8 and between 14 and 16 (as well as between 28 and 30). In the curves for odd Z or N, there are dips at 9 and some indication of dips at 21.

[5] M. G. Redlich, Phys. Rev. **88**, 38 (1952).

IV. THEORY

The two-parameter expression [Eq. (1)] obtained by Feenberg and Goertzel for the total Coulomb energy represents in a very satisfactory way the two main features of the experimental data, namely, the average trend of the first differences and the even-odd alternation of the second differences. In order to describe finer details of the data, one could require a and b to be slowly varying functions of Z and proceed to determine them from the experimental values of Δ_1. However, this procedure will not give a satisfactory representation of the second differences, since these do not change slowly. In fact, the parameters of Eqs. (1), (2), and (3) can be identified with one another only insofar as they do vary slowly with Z. Rapid variations, whether large or small, will be enhanced by the process of taking differences. Perhaps the opposite point of view is more appropriate. The parameters of Eq. (3) may have a more direct interpretation and a greater interest than those of Eqs. (2) or (1), in which the variations have been smoothed out by the process of taking sums. Such is the case in the shell model, which we shall consider after a brief review of Feenberg and Goertzel's derivation of Eq. (1).

Their model is that of the supermultiplet theory. The wave function of the ground state has maximum orbital symmetry but is not specified in detail, and the total proton spin is a good quantum number with the value $\frac{1}{2}$ for odd Z and 0 for even Z. This means that

as many protons as possible are paired off with oppositely directed spins; there are $[\frac{1}{2}Z]$ such pairs, and one extra proton if Z is odd. A descriptive interpretation of the analysis can be given as follows. The total number of proton-proton bonds, or couplings, is $N_t=\frac{1}{2}Z(Z-1)$. Of these, $N_p=[\frac{1}{2}Z]$ are bonds between paired protons; they are completely antisymmetric in spin and symmetric in orbital coordinates. The remaining N_t-N_p are "statistical bonds," in the sense that each one is three-quarters spin-symmetric and one-quarter spin-antisymmetric, in accordance with the statistical weights of the triplet and singlet spin states. If L_c denotes the average Coulomb energy of a statistical bond, and L_s that of an orbitally symmetric bond, then the total Coulomb energy is

$$E_c=(N_t-N_p)L_c+N_pL_s=N_tL_c+N_p(L_s-L_c)$$
$$=N_tL_c+N_p\cdot\tfrac{3}{4}L_c', \quad (4)$$

where the last equality defines L_c'. This result is Eq. (1); the second term is expected to be different from zero because protons have a larger probability of being found close together if their spins are oppositely directed. Thus, we expect that L_s will be larger than $L_c=\frac{3}{4}L_a+\frac{1}{4}L_s$, where L_a is the average Coulomb energy of an orbitally antisymmetric bond (spins parallel).

In order to express the L's in terms of expectation values, we observe that if P_{ij} exchanges the spatial coordinates of protons i and j, then the total Coulomb energy of all the orbitally symmetric bonds is

$$N_sL_s=\sum_{i<j}\int\psi\frac{e^2}{r_{ij}}\frac{1}{2}(1+P_{ij})\psi d\tau. \quad (5)$$

The average energy L_s is just this sum divided by the number of symmetric bonds, $N_s=N_p+\frac{1}{4}(N_t-N_p)$. Similarly, L_a is obtained by changing the sign of P_{ij} and dividing by the number of antisymmetric bonds, $N_a=\frac{3}{4}(N_t-N_p)$.

It is clear that L_s and L_a, and therefore the a and b of Eq. (1), depend by definition on the state considered. The state is not uniquely specified by requiring that the total proton spin be 0 or $\frac{1}{2}$, and before making calculations with a detailed model, it will be necessary to make a further assumption about the wave function. We shall use the shell model and define Z' to be the number of protons in an unfilled shell, the remaining $Z-Z'$ protons being in lower closed shells. Then the total Coulomb energy can be written as a sum of three terms: the interaction of the protons in the closed shells, Z' times the interaction of one of the outer protons with the protons in the closed shells, and the interaction of the Z' outer protons among themselves. Anticipating that the last term will have a Z' dependence analogous to that of Eq. (1), as it certainly will formally if we apply Feenberg and Goertzel's procedure to the Z' outer protons, we can write

$$E_c=\alpha+\beta Z'+\tfrac{1}{2}Z'(Z'-1)a+[\tfrac{1}{2}Z']b, \quad (6)$$

where α and β are independent of Z'. Provided that a and b can be shown to vary slowly with Z' in the ground states of the mirror nuclei, the first Coulomb energy difference will be

$$\Delta_1=\beta+(Z'-1)a+\tfrac{1}{2}[1+(-1)^Z]b, \quad (7)$$

since $Z-Z'$ is even. The expression for the second differences obtained from Eq. (7) is then identical with Eq. (3). In order to discuss the second differences, it is therefore sufficient to consider the interaction of protons outside closed shells (except at a transition between shells). If the a and b of Eq. (1) were rigorously constant, then they would be identical with the a and b considered here. On the other hand, if the a and b considered here change from one shell to another, then the a and b of Eq. (1) will not be constant and will have a less direct interpretation in terms of the shell model.

Since the presence of neutrons outside closed shells introduces certain complications, let us first consider a hypothetical simplified problem in which all the nucleons outside closed shells are protons. If all these protons have the same orbital angular momentum, l, then the ground state determined by short range nuclear forces will be the state of lowest seniority, i.e., the state in which there are as many ^1S pairs as possible. In LS coupling, this uniquely determined state is ^1S for Z' even and ^2L, where $L=l$, for Z' odd.

The Coulomb energy in this state is given by a general formula of Racah[6] for the expectation value of any Wigner force, and is

$$E_c(l^{Z'})=\tfrac{1}{2}Z'(Z'-1)\epsilon+[\tfrac{1}{2}Z']\delta, \quad (8)$$

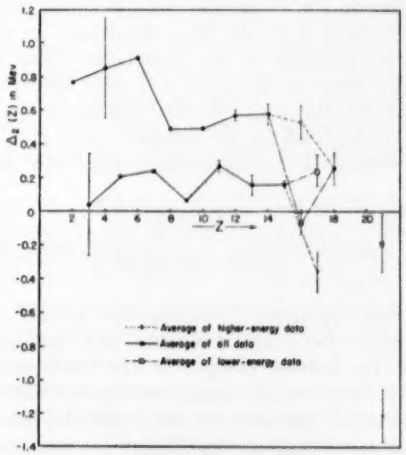

FIG. 1. Second Coulomb differences $\Delta_2(Z)=\Delta_1(Z)-\Delta_1(Z-1)$. Note that Z stands for the highest of the three atomic numbers involved; for instance, $\Delta_2(8)$ is the $O^{15}-N^{15}$ Coulomb energy difference minus the $N^{13}-C^{13}$ difference. Points for successive even (odd) values of Z are connected by straight lines. The points shown as "higher energy data" are those listed in parentheses in the third column of Table II.

[6] G. Racah, *L. Farkas Memorial Volume* (Research Council of Israel, Jerusalem, 1952), p. 294. See Eqs. (33) and (34).

where

$$\epsilon=(2l)^{-1}[(2l+1)F^0-E(l^2,{}^1S)], \tag{9a}$$

$$\delta=(2l+1)(2l)^{-1}[E(l^2,{}^1S)-F^0]. \tag{9b}$$

F^0 is the zero-order Slater integral and $E(l^2,{}^1S)$ is the interaction energy in the state $(l^2){}^1S$. The parameter ϵ vanishes in the limit of short-range forces, and δ vanishes in the long-range limit. Thus, in the state of lowest seniority, there is no pairing energy in the long-range limit, whereas all the energy is pairing energy in the short-range limit. For Coulomb forces, E_c has the expected form with values of a and b that are independent of Z' within a shell. Except at a transition between shells, Eq. (8) will give us a means of estimating the a and b of Eq. (3) after the effects of the neutrons outside closed shells have been discussed.

In jj coupling, also, E_c has the same form with constant a and b for the state of lowest seniority in the $j^{Z'}$ configuration. This state has $J=0$ for Z' even and $J=j$ for Z' odd. The expectation value of the Coulomb energy[7] is

$$E_c(j^{Z'})=\tfrac{1}{2}Z'(Z'-1)\frac{(2j+1)F^0-2E_0}{2j-1}+[\tfrac{1}{2}Z']\frac{2j+1}{2j-1}(E_0-F^0), \tag{10}$$

where E_0 now denotes the Coulomb energy in the state j^2, $J=0$.

However, the constants of Eq. (8) are not the L_c and L_c' obtained by applying Feenberg and Goertzel's definitions to the Z' protons outside closed shells. In order to obtain N_sL_s and N_aL_a separately, we can use a formula of Racah for the expectation value of any Majorana force in the state of lowest seniority.[8] In conjunction with Eq. (8), the expectation value of $\sum_{i<j}P_{ij}e^2/r_{ij}$ leads to the constant value $L_a=\epsilon$. But the expression for L_s depends in a complicated manner on Z':

$$L_s-L_a=\frac{4[\tfrac{1}{2}Z']\delta}{\tfrac{1}{2}Z'(Z'-1)+3[\tfrac{1}{2}Z']}=L_c'.$$

From these equations it follows that $L_c=\frac{1}{4}(L_s+3L_a)=L_a+\frac{1}{4}(L_s-L_a)$ is also a function of Z' and contains part of the pairing energy. In the state of lowest seniority, therefore, the quantities that are convenient for theoretical treatment are not L_c and L_c' but rather the constants ϵ and δ in Eq. (8).

The failure of L_c and L_c' to be independent of Z' may be interpreted by saying that the average Coulomb energy of a symmetrical bond changes with Z' when the state of lowest seniority is considered for each value of Z'. However, it is interesting that constant values of L_c and L_c' can be defined in terms of an average over all states in the $l^{Z'}$ configuration that have the same spin.

The possibility of taking an average with this property is shown by a procedure, due to Racah, for expressing the average energy over certain classes of states in the l^n configuration in terms of averages over similar classes in the l^2 configuration. The classes in question are characterized by the value of the Majorana operator $\sum_{i<j}P_{ij}$ (which is a good quantum number in LS coupling of protons only), or equivalently by the spin. In the l^2 configuration, the average Coulomb energy over all the space-symmetrical states (${}^1S$, ${}^1D$, $\cdots$, with $P_{12}=1$) is

$$\bar{L}_s=\epsilon+(l+1)^{-1}\delta. \tag{11}$$

The average Coulomb energy over all space-antisymmetrical states (${}^3P$, ${}^3F$, $\cdots$, with $P_{12}=-1$) is

$$\bar{L}_a=\epsilon; \tag{12}$$

this is the same L_a that we obtained before for the state of lowest seniority.[8]

The average energy over either class of states can be expressed in the unified form,

$$\bar{E}_c(l^2)=\bar{L}_s\tfrac{1}{2}(1+P_{12})+\bar{L}_a\tfrac{1}{2}(1-P_{12})=\bar{L}_c+\tfrac{1}{4}(1+2P_{12})\bar{L}_c'. \tag{13}$$

This equation cannot be regarded as an operator equation expressing the energy operator as a linear combination of 1 and P_{12}, since the energy operator has many more different eigenvalues in the l^2 configuration than does the right-hand side. Extra terms would be required to reproduce the expectation value of the energy in each individual state, but Eq. (13) shows that all these additional operators average to zero over all states with the same orbital symmetry.

In the l^n configuration the total interaction energy is simply a sum over all two-particle interactions:

$$[E_c(l^{Z'})]_{op}=\bar{L}_c\sum_{i<j}1+\tfrac{1}{4}\bar{L}_c'\sum_{i<j}(1+2P_{ij})+\cdots.$$

The additional terms that would be required to separate the energies of the individual states are indicated by dots; they are similarly sums of two-particle interactions over all pairs of particles. But just as in the l^2 configuration, they again average to zero over each class consisting of all states of a given orbital symmetry, as can be shown by group theoretical arguments.[9] The Coulomb energy, averaged in this sense, becomes

$$\bar{E}_c(l^{Z'})=\tfrac{1}{2}Z'(Z'-1)\bar{L}_c+\tfrac{1}{4}\sum_{i<j}(1+2P_{ij})\bar{L}_c', \tag{14}$$

[7] Reference 6, Eq. (44a).

[8] Racah's formula for the energy in the state of lowest seniority is obtained by a procedure that is similar to the one used here, but requires a more detailed classification of the states. However, no further subdivision of the space-antisymmetrical states of l^2 is introduced, and L_a is consequently the same in both cases.

[9] Reference 6, Sec. 3.

where

$$\bar{L}_c=\tfrac{1}{4}(\bar{L}_s+3\bar{L}_a)=\epsilon+\tfrac{1}{4}(l+1)^{-1}\delta, \quad (15)$$

$$\bar{L}_c'=\bar{L}_s-\bar{L}_a=(l+1)^{-1}\delta. \quad (16)$$

Equation (14) can be expressed in terms of the spin of the class of states over which the averaging process is extended. By use of the relation $P_{ij}=-\frac{1}{2}-2(\mathbf{s}_i\cdot\mathbf{s}_j)$, which is valid for protons, one obtains

$$\bar{E}_c(l^{Z'},S)=\tfrac{1}{2}Z'(Z'-1)\bar{L}_c+\tfrac{1}{2}[\tfrac{3}{4}Z'-S(S+1)]\bar{L}_c'. \quad (17)$$

In particular, the class with $S=\frac{1}{2}$ for Z odd or with $S=0$ for Z even contains the ground state according to the supermultiplet theory. For this class, the coefficient of $\bar{L}_c'$ is $\frac{3}{4}[\frac{1}{2}Z']$, and Eq. (17) takes the form of the last two terms of Eq. (6) with constant coefficients a and b.

When both protons and neutrons are present outside closed shells, the presence of proton-neutron forces will prevent the proton seniority from being a good quantum number, and Eq. (8) is no longer strictly applicable. The total proton spin is still a good quantum number (0 or $\frac{1}{2}$) in the lowest supermultiplet, but states of different proton seniority and orbital angular momentum will be mixed together, and the expectation value of the Coulomb energy will be a weighted average of contributions from these various states. Among them is the state of lowest proton seniority, with proton angular momentum $L=0$ for Z even and $L=l$ for Z odd. It seems implausible that states with other L values should have amplitudes so large as to justify taking the average over terms with a weighting factor $2L+1$, as was done in obtaining $\bar{L}_c$ and $\bar{L}_c'$. In fact, the state of lowest proton seniority is expected to have the predominant amplitude; consequently, it seems a reasonable approximation to use Eq. (8) for a theoretical estimate of the pairing effect even when neutrons are present outside closed shells. Likewise, in jj coupling, the state of lowest proton seniority is expected to predominate in the ground state of a mirror nucleus, and in this case the estimate will therefore be based on Eq. (10). Since lowest seniority implies maximum pairing, this approximation will give a larger odd-even effect than a calculation that takes account of the neutrons.

V. CALCULATIONS WITH A HARMONIC OSCILLATOR MODEL

We shall now inquire whether a nuclear shell model gives a satisfactory detailed account of the observed odd-even variations in Coulomb energy and of the additional irregularities that appear to be associated with shell closure. The model will also provide a means of calculating nuclear radii from experimental Coulomb energies, with inclusion of exchange effects.

The single-nucleon wave functions will be assumed for simplicity to be the stationary states of an isotropic harmonic oscillator well, $V(r)=\frac{1}{2}m\omega^2r^2=\hbar\omega\nu r^2$. In jj coupling the various shells will be filled in the order $0s_{1/2}$, $0p_{3/2}$, $0p_{1/2}$, $0d_{5/2}$, $1s_{1/2}$, $0d_{3/2}$, $0f_{7/2}$, and the Coulomb interaction between protons will be treated as a perturbation to first order. Since the model contains only one parameter, essentially the spring constant of the oscillator, the calculated Coulomb energy of any nucleus will be a numerical multiple of a single energy unit, $e^2\nu^{\frac{1}{2}}$.

As a preliminary test to see if the model gives the right order of magnitude for the pairing effect, we can calculate second Coulomb differences for values of Z from 10 to 14 by assuming ν to be constant through the $d_{5/2}$ shell in jj coupling (or the d shell in LS coupling). Within this shell the second differences should alternate between $a+b$ and $a-b$; the experimental data of Fig. 1 show roughly, though not exactly, this behavior, with a ratio $(a-b)/(a+b)$ of the order of 0.4 or 0.5. For the state of lowest proton seniority in jj coupling, we need only calculate the constants in Eq. (10). The symbol E_0 in that equation is a linear combination[10] of Slater integrals of the Coulomb potential, to be evaluated with the radial wave functions[11] of the isotropic harmonic oscillator. The integrals can be done analytically, and $(a-b)/(a+b)$ is found to be 0.55. With LS coupling in the state of lowest proton seniority, the value of this ratio is found to be 0.44 from Eqs. (8) and (9), in which $E(d^2,{}^1S)$ is likewise a linear combination[12] of Slater integrals. On the other hand, the averages $\bar{L}_c$ and $\bar{L}_c'$ over all states of the same proton spin in LS coupling, as calculated from Eqs. (15), (16), and (17), lead to a ratio $(a-b)/(a+b)=0.83$. This last result implies an odd-even effect considerably smaller than the observed one, and supports the assertion of Sec. IV that it is a better approximation to assume the state of lowest proton seniority. The choice between LS and jj coupling is less clear-cut; the larger pairing effect of LS coupling is perhaps in slightly better agreement with present experimental data, but the order of filling the d and s shells is ambiguous in LS coupling.

In further calculations it will therefore be assumed that jj coupling is in force and that the nucleons in an unfilled shell combine to form the state of lowest proton seniority. (The calculations can then be carried out as though neutrons were not present.) The parameter ν will be required to be the same for all protons in a given nucleus, and also the same in both nuclei of a mirror pair. Instead of attempting to reproduce the experimental second differences by suitable choice of ν, we shall calculate the first differences as multiples of $e^2\nu^{\frac{1}{2}}$; comparison of calculated and experimental first differences will then determine $e^2\nu^{\frac{1}{2}}$ as a function of A. The appropriateness of the model can be judged according

[10] G. Racah, Phys. Rev. **62**, 438 (1942), Eq. (54).

[11] I. Talmi, Helv. Phys. Acta **25**, 185 (1952). In Sec. I of this reference, the symbol ν is two times the ν of the present paper.

[12] E. U. Condon and G. H. Shortley, *The Theory of Atomic Spectra* (Cambridge University Press, Cambridge, 1935), p. 202.

to whether this parameter has a simple dependence on A or whether it still exhibits the odd-even effects and other irregularities that one would like to attribute to the amount of overlap of the wave functions rather than to variations of the nuclear potential well.

In order to calculate first differences, it is not enough to consider the protons outside closed shells. The addition of one proton to a nucleus not only increases the Coulomb energy of the unfilled shell, but also gives rise to energy of Coulomb interaction between the extra proton and each of the closed shells, as indicated by the symbol β in Eq. (7). Let $\beta(nl,n'l')$ denote the Coulomb interaction energy between one proton with quantum numbers nl and one $n'l'$ proton, averaged over all protons in the closed $n'l'$ shell. This quantity is independent of m_l and m_s. For example, any proton from the ninth to the fourteenth has a Coulomb interaction with the closed s and p shells amounting to $2\beta(0s,0d)+6\beta(0p,0d)$. The β's are linear combinations[13] of Slater integrals of both the direct and exchange varieties.

Besides the interaction of an extra proton with a shell that is closed in LS coupling, one needs in some cases the interaction with a subshell that is closed only in jj coupling. An easy method of calculating the latter is to observe that the energy of a closed (LS) shell minus one particle is independent of the coupling scheme. The energy of the $(p_{3/2})^4p_{1/2}$ configuration is therefore equal to that of $(p_{3/2})^3(p_{1/2})^2$, and by use of Eq. (10) one finds $\beta(0p_{3/2},0p_{1/2})=F^0-F^2/10=(17/12)\times e^2(\nu/\pi)^{\frac{1}{3}}$. Similarly, in terms of Slater integrals for the d shell, it is simple to obtain

$$\beta(0d_{5/2},0d_{3/2})=F^0-F^2/70-F^4/21=(489/400)e^2(\nu/\pi)^{\frac{1}{3}}.$$

By adding the increase of Coulomb energy of the unfilled shell [when Z' in Eq. (10) is increased by unity] to the interaction of the extra proton with the closed shells, we obtain the calculated first Coulomb difference as a numerical multiple of the energy parameter:

$$\Delta_1(Z)=\xi(A)e^2(\nu/\pi)^{\frac{1}{3}}. \tag{18}$$

Since the Slater integrals for harmonic oscillator wave functions can be evaluated analytically, $\xi(A)$ is obtainable as a rational number for each value of $A=2Z-1$ and is listed to three decimal places in the fourth column of Table II. By substituting the experimental Coulomb energy difference in the left side of Eq. (18), the energy parameter $e^2(\nu/\pi)^{\frac{1}{3}}$ is obtained as a function of A. Its values are listed in the fifth column of Table II and are plotted in Fig. 2.

The model is clearly unable to account for the large experimental odd-even effect in the $p_{3/2}$ shell; however, the eight points corresponding to the $p_{1/2}$ and $d_{5/2}$ shells have the same energy parameter to within ±1.5 percent. According to the older data, the parameter decreases 14 percent in two equal steps as the $s_{1/2}$ shell is filled, and then remains constant to within ±2 percent in the $d_{3/2}$ shell. The new data of Hunt and Zaffarano[14] for S^{31} and Ca^{39} make a radical change in this picture of the $s_{1/2}$ and $d_{3/2}$ shells, and throw some doubt also on the reliability of the early cloud-chamber determinations of the Cl^{33}, A^{35}, and Sc^{41} end points. Additional measurements of these end points by other methods would be of very great interest; it should also be emphasized that the K^{37} end point has never been measured.

Since the experimental Coulomb difference, for given A, determines the spring constant of the oscillator well, it also determines the single-nucleon wave functions and the shape of the charge distribution. In particular, the mean square radius of the nucleus can be obtained directly from the virial theorem. Since the energy of a single-particle state with quantum numbers n and l is $\hbar\omega(2n+l+\frac{3}{2})$, the expectation value of r^2 in this state is

$$\overline{r^2}=(4n+2l+3)/4\nu. \tag{19}$$

The mean square radius of the charge distribution for the stable member of a mirror pair is obtained by averaging Eq. (19) over the quantum numbers of the $Z_<=\frac{1}{2}(A-1)$ protons:

$$\langle r^2\rangle_{\text{av}}=\eta(Z_<)/4\nu, \tag{20}$$

where $\eta(Z_<)$ is an easily calculated rational number. We now define r_0 in the usual way in terms of the radius of an equivalent uniform charge distribution,

$$R_{\text{eq}}=[(5/3)\langle r^2\rangle_{\text{av}}]^{\frac{1}{2}}=r_0A^{\frac{1}{3}}\times10^{-13}\text{ cm}. \tag{21}$$

It follows from Eqs. (18), (20), and (21) that

$$r_0=\sigma(A)/(\Delta_1\text{ in Mev}), \tag{22}$$

where

$$\sigma(A)=0.5244A^{-\frac{1}{3}}\xi(A)[\eta(Z_<)]^{\frac{1}{2}}. \tag{23}$$

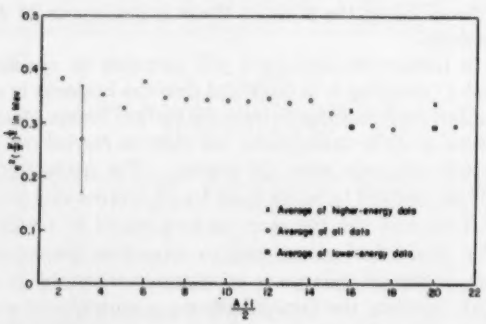

FIG. 2. The single parameter $e^2(\nu/\pi)^{\frac{1}{3}}$ of the harmonic oscillator model as a function of $\frac{1}{2}(A+1)=Z_>$. The radial wave functions of the oscillator model are completely determined by ν, which is related to the oscillator spring constant by the definition $V(r)=\frac{1}{2}m\omega^2r^2=\hbar\omega\nu r^2$. The plotted points are determined from Eq. (18) by using experimental Coulomb differences Δ_1 and values of ξ calculated with jj coupling. "Higher-energy" points are those listed in parentheses in the fifth column of Table II.

[13] Reference 12, p. 182.

[14] Reference Hu 54 following Table I.

The numbers σ are listed in the seventh column of Table II; the values of r_0 corresponding to the experimental Coulomb differences are given in the eighth column and are also plotted in Fig. 3. The radius of the charge distribution of the unstable member of a mirror pair can be obtained from Eq. (22) if desired by replacing $\eta(Z_<)$ by $\eta(Z_>)$ where $Z_>=\frac{1}{2}(A+1)$.

Figure 3 shows that in the region $13\leq A\leq 27$, where the constancy of the energy parameter encourages some confidence in the model, r_0 decreases fairly smoothly from 1.34 for C^{13} to 1.20 for Al^{27}.[15,16] According to the old data, the nucleus expands abruptly while the $s_{1/2}$ shell is being filled, and r_0 then decreases through the $d_{3/2}$ shell. The new data of Hunt and Zaffarano[14] again suggest a different picture, in which the abrupt increase of r_0 is much less pronounced and may be an artificial consequence of the model. Their results are consistent with a continued decrease of r_0 to values between 1.1 and 1.15 for the heaviest mirror nuclei, but until further measurements are made, the radii of the mirror nuclei with A between 31 and 41 remain uncertain by 10 or 15 percent and do not permit extrapolation to higher A.

The harmonic oscillator model can also be applied to isotopic-spin triplets if the assumption of charge symmetry is extended to charge independence. For mass numbers 10 and 14, all three members of the triad are known experimentally; in such a case, without appealing to data from nuclei of different mass number, we can compare the observed position of the $T_z=0$ state with its position as calculated from the difference in Coulomb energy between the $T_z=\pm 1$ states. When the $T_z=0$ state has an odd number of protons, it might be expected to lie lower than would be predicted by a model that does not take adequate account of the odd-even effect.

For example, the $C^{10}-B^{10}$ difference in Coulomb energy is 4.85 ± 0.10 Mev if the end point of the C^{10} positron spectrum is taken to be 2.10 ± 0.10 Mev.[17] The γ-ray energies and the Be^{10} end point are known to a few kilovolts.[18] According to the model of a uniform charge distribution, the position of the 0+ state of B^{10} should correspond to the ratio of Coulomb differences $(B^{10*}-Be^{10})/(C^{10}-B^{10*})=(5\times 4-4\times 3)/(6\times 5-5\times 4)$. The calculated energy of the 0+ state is then 1.93 ± 0.05 Mev; as expected, the experimental value of 1.739 ± 0.003 Mev is lower than this. The harmonic oscillator model also underestimates the pairing effect in the $p_{3/2}$ shell. Since the calculation of ξ depends only on the number of protons, the ratio of the Coulomb differences in jj coupling can be found from Table II to be 5.667/7.333, and the corresponding energy of the 0+ level is 1.89 ± 0.05 Mev. In LS coupling the ratio of Coulomb differences is lowered to 5.667/7.500 and the energy of the 0+ level is 1.86 ± 0.05 Mev.

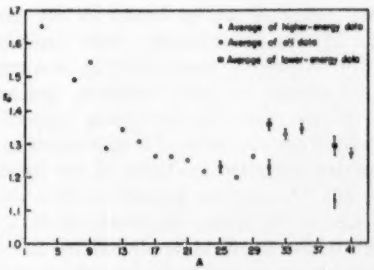

FIG. 3. Radii of the mirror nuclei of smaller Z. The point at $A=13$, for instance, is related to the rms radius of the nuclear charge distribution of C^{13} (not N^{13}) by the definitions $(5/3)^{\frac{1}{2}}\langle r^2\rangle_{Av}^{\frac{1}{2}}=R_{eq}=r_0A^{\frac{1}{3}}\times 10^{-13}$ cm. The plotted points are determined from Eq. (22) by using the experimental Coulomb differences Δ_1 and the values of σ calculated with jj coupling. "Higher-energy" points are those listed in parentheses in the last column of Table II.

The case of N^{14} benefits from more accurate experimental data as well as from slightly greater confidence in the oscillator model. The end point of the O^{14} spectrum has recently been measured as 1.835 ± 0.008 Mev,[19] and the γ-ray energy and the C^{14} end point are also known accurately[18]; the $O^{14}-C^{14}$ Coulomb difference is found to be 6.576 ± 0.015 Mev. The calculated ratio of Coulomb differences, $(N^{14*}-C^{14})/(O^{14}-N^{14*})$, is 6/7, 8.667/10.167, and 8.333/10.167 in the uniform density model, the oscillator model with jj coupling, and the oscillator model with LS coupling, respectively. The corresponding energies of the 0+ state in N^{14} are 2.408, 2.399, and 2.335 Mev, each with a computed error of 7 kev, as compared with the experimental value of 2.310 ± 0.012 Mev. Thus the jj model is scarcely better than the uniform density model in this instance, whereas the LS coupling result is almost in agreement with experiment. It may be worth mentioning that the energy parameter $e^2\nu^{\frac{1}{3}}$, calculated from the $O^{14}-C^{14}$ difference on the assumption of charge symmetry alone, lies between 1 percent and 1.5 percent higher, in both jj and LS coupling, than the average of its values for mass numbers 13 and 15.

VI. CONCLUSIONS

The odd-even effect in the Coulomb energies of mirror nuclei can be accounted for, in a manner that appears to be satisfactory except for the lightest nuclei ($Z\leq 6$), by a shell model with harmonic oscillator wave functions. It is not necessary to attribute the odd-even alternation of Coulomb energy to a similar alternation in the radius of the charge distribution; on the contrary,

[15] This value for Al is in very good agreement with preliminary data from electron scattering (private communication from Professor R. Hofstadter).

[16] The values of r_0 obtained from the uniform density model also show a steady decrease (superposed on a pronounced odd-even alternation) from 1.515 for O^{17} to 1.34 for Al^{27}. Professor R. K. Sheline of Florida State University informs us that he and Dr. N. R. Johnson have likewise observed a decrease of this kind and have attributed the subsequent discontinuity to shell structure.

[17] R. Sherr and J. B. Gerhart, Phys. Rev. **91**, 909 (1953).

[18] F. Ajzenberg and T. Lauritsen, Revs. Modern Phys. **24**, 321 (1952).

[19] J. B. Gerhart, Phys. Rev. **95**, 288 (1954).

a sufficient cause is to be found in the symmetry properties of the ground-state wave function. The permutation symmetry corresponding to a pairing of spins is not enough by itself, however, and has to be extended to the more thorough-going type of pairing described by Racah's notion of lowest seniority.

The results presented in Table II are based on jj coupling, but LS coupling appears to give an equally good account of the present experimental data. In fact, the larger odd-even effect predicted by LS coupling has the advantage of producing better accord between the assumption of charge independence and the observed energy of the 0+ state in N^{14}. Further measurements are needed to establish whether a discontinuity in Coulomb energy and radius occurs after $Z=14$.

The oscillator model gives appreciably smaller values for the rms radius of the nuclear charge distribution than does the uniform density model in which $E_c=(3/5)Z(Z-1)e^2/R_{eq}$ and $\Delta_1(Z)=(6/5)(Z-1)e^2/R_{eq}$. Part of the difference is due to the absence of exchange terms[20] in the latter case, but it is not clear that exchange effects are sufficient to account for the whole difference. For instance, if the Slater exchange integrals are completely omitted in calculating Δ_1 for $A=17$, the result obtained is $10.967e^2(\nu/\pi)^{\frac{1}{3}}$, only 6 percent larger than the value with exchange. The corresponding r_0 for O^{17} would be 1.34 without exchange, compared with 1.52 from the uniform density model. This remaining discrepancy is caused by the change in shape of the shell-model charge distribution when an outer proton turns into a neutron.

The values of r_0 listed in Table II show a steady decrease from C^{13} to Al^{27}. It is to be hoped that further measurements of Coulomb energies will soon determine whether this decrease continues without interruption in the heavier mirror nuclei, and that electron scattering experiments will provide an independent set of results for comparison.

It is a pleasure to express our gratitude to Professor E. P. Wigner for valuable discussions.

[20] The separation between direct and exchange terms is sometimes defined in a different way. When the wave function is taken to be a single determinant of one-particle functions, it is often formally convenient to add a sum of "self-energy" integrals, $\frac{1}{2}\sum_i\int\int|\psi_i(\tau_1)\psi_i(\tau_2)|^2(e^2/r_{12})d\tau_1 d\tau_2$, to the direct terms and subtract the same sum in the form of exchange contributions. We do not include such integrals in the definitions of "direct" and "exchange"; it seems superfluous to attribute direct and exchange Coulomb energies of equal magnitude and opposite sign to a system containing only one charged particle, and undesirable to attribute exchange energy to an unsymmetrized many-particle wave function with no positional correlations.

PHYSICAL REVIEW VOLUME 96, NUMBER 2 OCTOBER 15, 1954

Radiations from Ir^{192m}†

J. P. Mize, M. E. Bunker, and J. W. Starner
University of California, Los Alamos Scientific Laboratory, Los Alamos, New Mexico

(Received July 12, 1954)

The photon and electron spectra of Ir^{192m} (1.42 min) have been thoroughly investigated. Study of the photon spectrum with scintillation spectrometers and an aluminum-lined proportional counter spectrometer revealed the presence of a quantum continuum, iridium L x-rays, and a 58-kev gamma ray. The quantum continuum was shown to be bremsstrahlung engendered by conversion electrons from the isomeric transition. Previous to this study, the quantum continuum had been interpreted as possibly caused by "two-quantum" emission. A high-resolution, 180° permanent magnet spectrograph was employed for the examination of the conversion electron spectrum. The energy of the isomeric transition was found to be 58.0±0.4 kev from the conversion electron studies. Lifetime-energy considerations and the observed L-subshell conversion ratios show that the 58.0-kev gamma ray is $E3$. The L-shell conversion coefficient was determined from scintillation spectrometer data to be $\geqslant 870$.

I. INTRODUCTION

PREVIOUS investigations[1,2] have shown that the decay of Ir^{192m} (1.42 min) is accompanied by iridium L x-rays, L-shell conversion electrons from an ~60-kev gamma ray, and a quantum continuum with peak intensity at ~30 kev and upper energy end point at ~60 kev. Conversion electron analyses have been made by Hole,[3] Caldwell,[4] and Weber[5] yielding energy values for the isomeric transition of 55.5, 57.4, and 56.0 kev, respectively. The reported quantum continuum has been interpreted as possibly caused by "two-quantum" transitions.[1,2] Sachs[6] has suggested that nuclear decay through transitions of the type 0→0 (yes) can take place by simultaneous emission of two quanta, one quantum and one electron or two elec-

† Work performed under the auspices of the U. S. Atomic Energy Commission.

[1] Goldhaber, Muehlhause, and Turkel, Phys. Rev. **71**, 372 (1947).

[2] E. der Mateosian and M. Goldhaber, Phys. Rev. **82**, 115 (1951).

[3] N. Hole, Arkiv. Mat. Astron. Fysik **A36**, No. 9 (1948).

[4] R. L. Caldwell, Phys. Rev. **78**, 407 (1950).

[5] C. Weber and A. Flammersfeld, Z. Naturforsch. **A8**, 580 (1953); C. Weber, Z. Naturforsch. **A9**, 115 (1954).

[6] R. G. Sachs, Phys. Rev. **57**, 194 (1940).

trons. Transitions of these types would be characterized by the quantum or electron spectrum having a continuous energy distribution. Goldberger[7] has discussed the reported quantum continuum of Ir^{192m} in the light of simultaneous emission of one quantum and one electron according to the mechanism postulated by Sachs.

Since the Ir^{192m} quantum continuum seemed to be experimentally unique, it appeared worth while to investigate the continuum in further detail to gain additional insight as to the characteristics of its radiations. In view of the fact that the isomeric transition is believed to be either $E3$ or $M3$,[8] it also seemed desirable to undertake a new study of the L-subshell conversion electrons in order to arrive at a unique multipolarity assignment.

II. EXPERIMENTAL METHODS AND RESULTS

a. Photon Measurements

The isomeric state of Ir^{192} was prepared by irradiating IrO_2 (of natural isotopic abundance) with thermal neutrons. The Ir^{192m} photon spectrum was initially studied with a commercially packaged 2-in.×2-in. right circular cylinder of NaI(Tl) mounted on a Dumont 6292 photomultiplier tube. A ten-channel differential pulse-height analyzer was utilized for the recording of data. The photon spectrum (Fig. 1) measured with the above apparatus indicates the presence of a 58-kev gamma ray and a broad, low-energy photon distribution (A) which, from resolution considerations, cannot be attributed to a single monoenergetic gamma ray. A study of the 15–40 kev region with a proportional counter spectrometer revealed no additional fine structure. It was thus concluded that the pulse distribution A probably corresponds to the quantum continuum previously reported. The proportional counter data also indicated that the decay of Ir^{192m} is accompanied by intense iridium L x-rays. Since virtually no iridium L x-rays can be seen in the scintillation spectrum of Fig. 1, it was concluded that the commercially packaged NaI(Tl) detector possessed a relatively low quantum detection efficiency at low energies, caused in part by its ambient Al_2O_3 reflector.

To facilitate further study of the quantum continuum and iridium L x-rays, a scintillation spectrometer was designed which would be expected to have essentially constant detection sensitivity in the energy region 10 to 60 kev. The experimental arrangement of the spectrometer is shown in Fig. 2. Since the hygroscopic NaI(Tl) detector of Fig. 2 was exposed to the atmosphere throughout the experiment, a continual check was made of its resolution and detection sensitivity. It was established that after the sodium iodide crystal had been polished with alcohol, the resolution

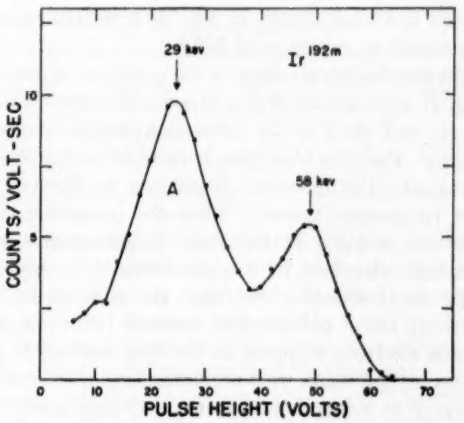

FIG. 1. Photon spectrum of Ir^{192m}, obtained with a commercially packaged NaI(Tl) crystal mounted on a Dumont type 6292 photomultiplier tube.

(~21 percent) and detection efficiency of the spectrometer for the 59.8-kev gamma ray of Am^{241} remained constant during each photon spectrum measurement.

Results of the Ir^{192m} photon spectrum measurements with the scintillation apparatus of Fig. 2 are presented in Fig. 3. The intense iridium L x-rays present in the Ir^{192m} decay necessitated the placement of a 0.020-inch thick aluminum absorber between source and detector for the studies shown in Fig. 3. The conversion electrons were stopped by either the 0.020-inch thick aluminum foil or by a 5.0-mg/cm² polyethylene film. The iridium sources were prepared from IrO_2 powder and were mounted on the aluminum foil or the polyethylene film. The surface densities of the IrO_2 sources were estimated from microscopic measurements of aggregate grain size. By this method an average surface density of ~70 mg/cm² was obtained for the thick sources, and an average surface density of ~0.7 mg/cm² was obtained for the thin sources. Since the IrO_2 was of questionable chemical purity, the decay of the 58-kev gamma ray was followed through seven half-lives. During that period no deviation was observed from the 1.42 minute half-life assigned to the isomeric transition. Since the quantum continuum and iridium L x-rays also decayed with a 1.42 minute half-life, the

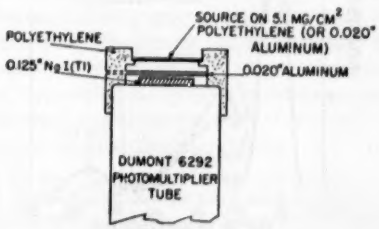

FIG. 2. Schematic diagram of the scintillation counter arrangement.

[7] M. L. Goldberger, Phys. Rev. **73**, 1119 (1948).
[8] M. Goldhaber and A. W. Sunyar, Phys. Rev. **83**, 906 (1951).

photon spectrum shown in Fig. 3 is unambiguously engendered by the decay of Ir^{192m}.

The amplitude and shape of the quantum continuum (Fig. 3) were measured as a function of source surface density and the Z of the conversion electron stopping material. The data have been normalized to the 58-kev photopeak. The quantum continuum is observed to have its greatest intensity when the conversion electrons are stopped in the thick iridium source and aluminum absorber; its weakest intensity is observed when the conversion electrons are stopped in the relatively low Z polyethylene material (with few conversion electrons stopping in the thin source). If the quantum continuum were of nuclear origin, its relative intensity as a function of source thickness would not behave in the above manner. Instead the intensity of the quantum continuum would exhibit a variation similar to that of the iridium L x-ray shown in Fig. 3, i.e., the intensity of the continuum (relative to that of the 58-kev gamma ray) would be a minimum for a thick source and a maximum for a thin source. Furthermore, if the continuum were of nuclear origin its magnitude and shape would not be dependent on the Z of the material in which the conversion electrons are stopped. It can be observed from Fig. 3 that the intensity of the continuum increases with the Z of the material in which the conversion electrons are stopped.

When the photon spectrum A of Fig. 3 is corrected for absorption in the aluminum foil, the peaked distribution of the quantum continuum at $\sim$30 kev is removed and the quantum continuum assumes the hyperbolic shape shown in Fig. 4.

Thus the above experimental evidence and evidence to be presented below strongly suggest that the quantum continuum is not of nuclear origin[9] but is in all probability bremsstrahlung engendered by conversion electrons from the isomeric transition

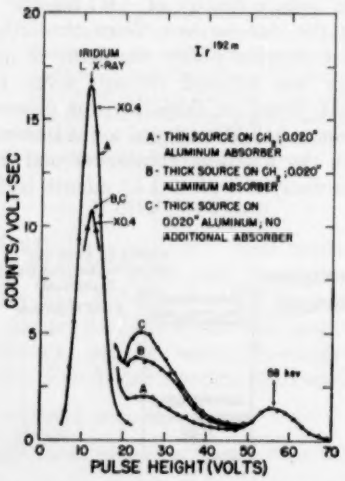

FIG. 3. Photon spectra of Ir^{192m}, obtained with the scintillation apparatus shown in Fig. 2.

b. Coincidence Experiment

To offer further proof that the quantum continuum of Ir^{192m} is indeed a bremsstrahlung distribution, a coincidence experiment was performed. Two scintillation spectrometers of the type shown in Fig. 2 were used in the coincidence measurements. Quanta in the energy region 17–57 kev were "gated" by quanta in the same energy region. The singles counting rate in each channel was recorded, and a coincidence rate of only 1 percent of the expected rate for two-quantum emission in the above energy region was observed. The observed coincidences could be attributed to Compton scattered events, bremsstrahlung—x-ray coincidences, and chance coincidences.

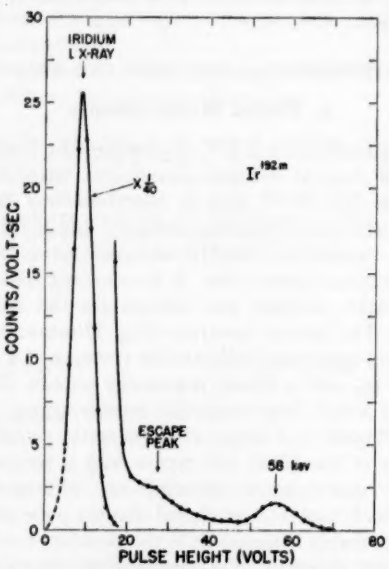

FIG. 4. Photon spectrum A of Fig. 3 corrected for absorption in the 0.020-inch thick aluminum absorber.

c. Internal Conversion Electron Measurements

A 77 gauss, 180° permanent magnet spectrograph of high resolution was employed for the analysis of

[9] Independent research carried out by Weber (reference 5) on Ir^{192m} came to our attention after we had reached the above conclusion concerning the nature of the quantum continuum. Weber utilized absorption techniques and found that under the assumption that the entire number of quantum transitions with $E>30$ kev are from the gamma-ray continuum:

$$N_{\text{cont.}}/N_{\text{I.T.}} \leqslant 10^{-3}.$$

Under the assumption that the entire number of quantum transitions with $E>30$ kev are unconverted 56.0-kev quanta, the resulting value for the total internal conversion coefficient of the gamma ray has a lower limit of 1000. From these intensity relationships, Weber concluded that he had found no evidence for Ir^{192m} decay by "two-quantum" emission.

conversion electrons accompanying the Ir^{192m} decay. The spectrograph was calibrated with K conversion electrons from the 80.133±0.005-kev transition in Xe^{131} [10] and the L and M conversion electrons from the 59.78±0.02-kev transition in Np^{237}.[11] The spectra were recorded on Eastman No-Screen X-Ray film. The spectrograph camera was constructed so that radioactive sources could be inserted through a vacuum gate without appreciable loss of the vacuum inside the chamber. At the conclusion of each iridium activation, approximately one minute was required to mount the source and insert it into the spectrograph. A suitable spectrogram of the internal conversion lines was obtained by performing seven successive bombardments and exposures.

Caldwell has observed two L-subshell conversion electron lines from Ir^{192m} by utilizing a high-resolution permanent magnet spectrograph.[4] These lines were interpreted to be L_I and L_{III} conversion electrons from a 57.4-kev transition. However, it has been pointed out by Mihelich[12] that the L_I line in Caldwell's data falls midway between the expected positions for the L_I and L_{II} lines on the spectrogram. The 57.4-kev transition has been classified as either $E3$ or $M3$ from lifetime-energy considerations.[8] Our measured values of the energies and intensities of the L-subshell conversion electrons (summarized in Table I) indicate that conversion takes place principally in the L_{II} and L_{III} subshells. By using the empirical L-subshell conversion ratios determined by Mihelich[12] and the recent calculations of L-subshell conversion coefficients by Rose *et al.*,[13] the radiation is unquestionably electric and must therefore be $E3$. An energy value of 58.0±0.4 kev was obtained for the isomeric transition from the data of Table I.

d. The Conversion Coefficient

The L-shell conversion coefficient for the Ir^{192m} transition was calculated from the expression

$$\alpha_L = \frac{A_1}{A_2}\left[\frac{F+G}{FD+GE}\right], \qquad (1)$$

where A_1 is the area of the L x-ray photopeak of Fig. 4, A_2 is the area of the gamma-ray photopeak occurring at ~57 volts in Fig. 4 (corrected for the 13-percent loss into the escape peak), D and E are the fluorescent yields of the iridium L_{II} and L_{III} shells, respectively,[14] and F and G are the relative intensities of the L_{II} and L_{III} conversion electrons, respectively (Table I). A value of $\alpha_L \geqslant 870$ was obtained from Eq. (1).

TABLE I. Energies and relative intensities of L-subshell conversion electron lines of Ir^{192m}.

Electron shell	Relative intensity	Electron energy (kev)	Binding energy (kev)	Transition energy (kev)
L_I	not observed		13.4	
L_{II}	1.1	45.2	12.8	58.0
L_{III}	1.0	46.8	11.2	58.0

It must be realized that the above measurement of α_L is fraught with serious uncertainties which arise from the questionable amount of L x-ray absorption in the thin iridum source and also in the assumption that the sodium iodide detector of Fig. 2 has a constant photon-detection efficiency from 10 to 60 kev. Therefore, the experimental value of α_L is only indicative of its proper order of magnitude. When the theoretical L-subshell conversion coefficient calculations of Rose *et al.* are completed, a more exact value of α_L can be determined and the above value checked.

III. CONCLUSIONS

The foregoing study has shown that Ir^{192m} is a well-behaved one-step isomer. The isomeric level decays by the emission of a 58.0±0.4-kev ($E3$) gamma ray. Although the isomer does not decay by "two-quantum" transitions which would engender a continuous gamma spectrum, the observed photon spectrum is somewhat unique in that the 58.0-kev gamma ray is converted to the extent ($\alpha_L \geqslant 870$) that the remaining nuclear radiation does not obscure the bremsstrahlung spectrum produced by conversion electrons. Furthermore it is clear that unless source thickness, conversion-electron stopping material, and photon-detection efficiency are well known parameters, the resulting bremsstrahlung distribution may not appear to have the characteristic hyperbolic shape. The total intensity of the observed bremsstrahlung distribution can only be crudely estimated because of the presence of the comparatively intense iridium L x-rays which completely obscure the continuum below ~20 kev. If the portion of the bremsstrahlung spectrum above 20 kev represents 10 percent of the total bremsstrahlung intensity, then there are <0.01 bremsstrahlung quanta emitted per ejected conversion electron. No attempt has been made to estimate what fraction of the observed bremsstrahlung spectrum is caused by continuous gamma radiation accompanying the internal conversion process[15,16] and what fraction is caused by external bremsstrahlung.

[10] Lind, Brown, Klein, Muller, and DuMond, Phys. Rev. **75**, 1544 (1949).
[11] C. I. Browne and I. Perlman, Phys. Rev. **85**, 758 (1952).
[12] J. W. Mihelich, Phys. Rev. **87**, 646 (1952).
[13] Privately circulated tables of L-shell conversion coefficients by Dr. M. E. Rose *et al.* We wish to thank Dr. Rose for making these values available before publication.
[14] B. B. Kinsey, Can. J. Research **A26**, 401 (1948).
[15] H. B. Brown and R. Stump, Phys. Rev. **90**, 1061 (1953).
[16] L. Spruch and G. Goertzel, Phys. Rev. **94**, 1671 (1954).

Model for Nuclear Reactions with Neutrons*

H. FESHBACH, C. E. PORTER,† AND V. F. WEISSKOPF
Department of Physics and Laboratory for Nuclear Science, Massachusetts Institute of Technology, Cambridge, Massachusetts
(Received June 28, 1954)

A simple model is proposed for the description of the scattering and the compound nucleus formation by nucleons impinging upon complex nuclei. It is shown that, by making appropriate averages over resonances, an average problem can be defined which is referred to as the "gross-structure" problem. Solution of this problem permits the calculation of the average total cross section, the cross section for the formation of the compound nucleus, and the part of the elastic-scattering cross section which does not involve formation of the compound nucleus. Unambiguous definitions are given for the latter cross sections.

The model describing these properties consists in replacing the nucleus by a one-body potential which acts upon the incident nucleon. This potential $V=V_0+iV_1$ is complex; the real part represents the average potential in the nucleus; the imaginary part causes an absorption which describes the formation of the compound nucleus. As a first approximation a potential is used whose real part V_0 is a rectangular potential well and whose imaginary part is a constant fraction of the real part $V_1=\zeta V_0$.

This model is used to reproduce the total cross sections for neutrons, the angular dependence of the elastic scattering, and the cross section for the formation of the compound nucleus. It is shown that the average properties of neutron resonances, in particular the ratio of the neutron width to the level spacing, are connected with the gross-structure problem and can be predicted by this model.

The observed neutron total cross sections can be very well reproduced in the energy region between zero and 3 Mev with a well depth of 42 Mev, a factor ζ of 0.03, and a nuclear radius of $R=1.45\times10^{-13}A^{\frac{1}{3}}$ cm. The angular dependence of the scattering cross section at 1 Mev is fairly well reproduced by the same model. The theoretical and experimental values for the ratios of neutron width to level distance at low energies and the reaction cross sections at 1 Mev do not agree too well but they show a qualitative similarity.

I. INTRODUCTION

THIS paper deals with the interaction of nuclear particles with complex nuclei in nuclear reactions. A model is proposed for the description of the energy exchange between the incoming particle and the target nucleus. The considerations are restricted to neutron reactions with incident energies between 0 and 20 Mev.

One usually describes the interaction of nuclear particles with complex nuclei by means of the concept of a compound nucleus which is formed after the nucleon has entered the nucleus. Before the striking success of the nuclear shell model was known, it was generally assumed that the quantum state formed by the particle entering the nucleus is one in which the motions of all particles are intimately coupled. We will refer to this assumption as the "strong-coupling model." These ideas led to certain general qualitative conclusions in regard to the cross sections for nuclear reactions. Several authors[1] have attempted in previous papers to derive approximate expressions for the cross sections of nuclear reactions with a minimum of special assumptions in addition to the main assumption of the validity of the strong-coupling model. We summarize the main results of these qualitative considerations.

1. Particle widths.—The particle widths of nuclear resonances with respect to particle emission are related in a general way to the average spacing D of the levels of the compound nucleus. For example, the width for the emission of neutrons with zero-orbital angular momentum is given approximately by

$$\Gamma_n\approx(2/\pi)(k/K)D, \tag{1.1}$$

and the widths for the emission of other particles are equal to the above expression multiplied by the penetration factor of the potential barrier. Here k is the wave number of the incoming particle, and K is the wave number in the interior of the nucleus; K is of the order of 10^{13} cm^{-1}.

2. Potential scattering.—The elastic scattering arises from a superposition of a resonance amplitude and a slowly varying potential scattering amplitude. The former is important only in the immediate vicinity of the resonance; the latter is equal to the scattering amplitude of an impenetrable sphere of a radius approximately equal to the nuclear radius.

3. Neutron total cross section.—The neutron total cross section averaged over resonances is equal to the total cross section of a spherical potential well whose depth is such as to give rise to an internal wave number $K\sim10^{13}$ cm^{-1} and which possesses an absorption for the incoming waves such that the waves are absorbed inside within distances of the order K^{-1}. These conditions were expressed approximately by Feshbach and Weisskopf[2] in the form of a boundary condition on the incoming wave function u/r at the nuclear boundary:

$$du/dr=-iKu.$$

Formula (1.1) and the other consequences of the strong-coupling model have been found correct as to the order of magnitude. However, as a consequence of point (3), the neutron total cross sections when averaged

* This work was supported in part by the U. S. Office of Naval Research and the U. S. Atomic Energy Commission.

† Now at Brookhaven National Laboratory, Upton, New York.

[1] H. Bethe, Phys. Rev. **57**, 1125 (1940); Feshbach, Peaslee, and Weisskopf, Phys. Rev. **71**, 145 (1947); H. Feshbach and V. F. Weisskopf, Phys. Rev. **76**, 1550 (1949); E. P. Wigner, Phys. Rev. **73**, 1002 (1948); E. P. Wigner, Am. J. Phys. **17**, 99 (1949).

[2] H. Feshbach and V. F. Weisskopf, Phys. Rev. **76**, 1550 (1949).

over resonances should all be smooth functions of the energy which decrease monotonically with increasing energy and whose form is rather similar for all atomic numbers A. Also the dependence on A at constant energy should show a continuous, slowly increasing trend with increasing A. The measurements of neutron total cross sections by the Wisconsin group and by others have clearly demonstrated that this is not so. The neutron total cross sections exhibit typical deviations from the predictions of the strong-coupling model. (See Fig. 3.) The shape of the energy dependence of the neutron cross sections changes significantly over the range of A; however, this change is not random but gradual. Nuclei with small differences in A show almost the same behavior. One concludes, therefore, that these characteristic shapes do not depend on detailed features of nuclear structure but on some general properties which vary slowly with A, say, the nuclear radius.

The success of the shell model has cast some doubt upon the fundamental assumptions of the strong-coupling model. Does the particle necessarily form a "compound state" after entering the nucleus? The shell structure furnishes much evidence that a nucleon can move freely within the nucleus without apparently changing the quantum state of the target nucleus. This is a consequence of observations made at the ground state and at low excitation energies, and it is questionable whether this apparent absence of interaction between one nucleon and the rest is valid also at those excitation energies ($\sim$8 Mev) which are created in nuclear reactions with neutrons of a few Mev. Furthermore, there is some reason to believe that at higher energies, 15 Mev and up, the interaction between the entering nucleon and the target is appreciable, since the reaction cross sections at those energies have been found[3] to be equal to the geometrical cross sections $[\pi(R+\lambda)^2]$. Hence, for such energies it happens rarely that a neutron enters the nucleus and leaves it again without sharing its energy with the rest.

It seemed worth while, therefore, to investigate the consequences of a reduced interaction between the nucleons for the theory of nuclear reactions in the energy region of a few Mev. This reduced interaction will manifest itself in the following way: The incident nucleon can penetrate into the nucleus and move within the boundaries of the nucleus *without* forming a compound state. Hence, in this case, the target nucleus acts upon the incoming nucleon as a potential well. The actual formation of a compound state occurs only with a probability smaller than unity, once the particle has entered the nucleus. It has a finite chance of leaving the nucleus without having formed a state in which it has exchanged energy or momentum with the rest of the nucleus. The formation of the compound state then would have the aspect of an absorption. Hence, the effect of the nucleus upon the incident particle could be described as the effect of a potential well with absorption, where the absorption coefficient within the well would be an adjustable parameter. It is obvious that this description represents an oversimplification which naturally cannot reproduce all features of nuclear reactions. Specifically, it will not reproduce any resonance phenomena which are connected with the many possible quantum states of the compound system. We therefore expect that this model will at best describe only the features of nuclear reactions after averaging over the resonances of the compound nucleus.

The formulation of this attempt to construct a simple model for nuclear reactions requires a study of the definitions of the various cross sections; in particular, the meaning of the cross section for the formation of a compound nucleus must be clarified.

We introduce the following cross sections: σ_t, the total cross section, which can be split into

$$\sigma_t=\sigma_{el}+\sigma_r,$$

where σ_{el} is the elastic scattering cross section, and σ_r is the "reaction cross section." The former is defined as the cross section for scattering without change of the quantum state of the nucleus. The particle leaves by the same channel by which it has entered. The elastic scattering has an angular dependence which we express by the differential cross section $d\sigma_{el}/d\Omega$,

$$\sigma_{el}=\int\frac{d\sigma_{el}}{d\Omega}(\theta)d\Omega.$$

The reaction cross section includes all processes in which the residual nucleus is different from or in a state different from that of the target nucleus. These are all processes whose exit channels differ from the entrance channel. It will be practical later on to subdivide the elastic cross section into two parts:

$$\sigma_{el}=\sigma_{se}+\sigma_{ce}.$$

We call the second part, σ_{ce}, the "compound elastic" cross section. It is the part of the elastic scattering which comes from the formation of the compound nucleus and the subsequent emission of the incident particle into the entrance channel. The first part we call "shape elastic" cross section; this is the part of the elastic scattering which occurs without the formation of a compound. The exact definition of this split will be given in Sec. II. We note that such definitions will be possible only for the average cross sections, averaged over an energy interval containing many resonances, if such resonances are present.

On the basis of the compound nucleus assumption, we consider all actual reactions to occur after compound formation. Hence, we introduce a cross section σ_c of compound nucleus formation:

$$\sigma_c=\sigma_{ce}+\sigma_r,$$

[3] Phillips, Davis, and Graves, Phys. Rev. 88, 600 (1952).

and obtain, naturally,

$$\sigma_t=\sigma_{se}+\sigma_c.$$

The nuclear model which we propose here is expected to predict only the cross sections σ_{se} and σ_c. It considers only the conditions in the entrance channel, that is, in that part of the phase space in which the target nucleus is in its initial state. Hence, the compound nucleus formation is considered as an *absorption* of the incident beam, although part of it, namely σ_{ce}, leads to an elastic scattering process. The model consists in describing these conditions by means of a one-particle problem. The nucleus is replaced by a complex potential,

$$V=V_0+iV_1, \tag{1.2}$$

acting upon the incoming neutron. The scattering which the neutron suffers in (1.2) should reproduce the shape elastic scattering σ_{se}; and the absorption which is caused by the imaginary part V_1 should reproduce the compound nucleus formation.

It is probable that the potential functions in (1.2) vary somewhat with the incident energy. For example, one might expect an increase of the imaginary part with increasing energy. If an approximate description of the facts is possible by means of a potential (1.2), the shape of the potential will be indicative of the type of nuclear interaction which a neutron suffers in the nucleus. The real part V_0 would describe the average potential energy of the neutron within the nucleus, and its shape would give indications as to the form of the potential "well" inside the nucleus. It is similar to the potential encountered in the shell model of the nucleus, although we do not pretend that an incident neutron of several Mev is faced with exactly the same potential which acts upon the nucleus in the ground state. The imaginary part V_1 would indicate the strength and location of the processes that lead to an energy exchange between the incoming neutron and the target nucleus.

We expect the potential V to depend in a simple way upon the mass number A. Its dependence on r should be similar for all nuclei. The simplest choice would be a square-well potential:

$$V_0=-U \quad \text{for} \quad r<R,$$
$$V_0=0 \quad \text{for} \quad r>R,$$
$$V_1=\zeta V_0.$$

In general, we might express it in the form $V=V(r/R)$, $R=r_0A^{\frac{1}{3}}$. However, there might be a region near $r=R$ in which the features depend on r and not on (r/R); the thickness of that part of the potential which represents the surface might be independent of the radius.

With a given $V(r)$ and its dependence on A, it is possible to calculate the cross sections σ_t, σ_{se}, and σ_c, each as functions of energy and mass number, and also the angular dependence of the scattering. The next section contains the definitions of the cross sections involved, and the following sections describe the technique of calculating the cross sections and their comparison with experimental material.

II. THEORY OF AVERAGE CROSS SECTIONS

All nuclear cross sections exhibit strong fluctuations with energy which are generally referred to as resonances, especially in the lower part of our energy range. As the energy increases, the width of the resonances increases too; and, for not too light nuclei, the width becomes comparable or larger than the level distance at energies above a few Mev. Hence, we find the cross sections at higher energies to be smooth functions of energy with little fluctuation. We will refer to the lower-energy region as the "resonance region" and the upper as the "continuum region."

The behavior of the cross sections in the resonance region does not lend itself to a description by a simple one-particle potential (1.2) because of the rapid fluctuations with energy. However, the averages of the cross sections taken over an interval I, which includes many resonances, will be shown to be the cross sections belonging to a new scattering problem with slowly varying phases, which we will call the "gross-structure" problem. In this problem it is possible to define cross sections for the formation of a compound nucleus which also includes the compound elastic scattering. *It is this gross-structure problem and not the actual rapidly varying cross sections which we intend to describe by means of a one-particle problem with the potential (1.2).*

We bombard a nucleus X with particles a and consider the total cross section σ_t, the elastic cross section σ_{el}, and the reaction cross section σ_r. $\sigma_t=\sigma_{el}+\sigma_r$. Each of these cross sections will be subdivided into their parts coming from different angular momenta l, e.g.,

$$\sigma_t=\sum_l \sigma_t^{(l)}. \tag{2.1}$$

These cross sections can be expressed in terms of the amplitudes of the wave which describes the situation in the entrance channel. We consider the subwave u_l/r in the entrance channel with the orbital angular momentum l (r is the channel coordinate), and we write the wave in the form for

$$r\to\infty,$$
$$\varphi_l\to\text{const}[\exp(-i(kr-\tfrac{1}{2}l\pi)) - \eta_l\exp(+i(kr-\tfrac{1}{2}l\pi))]. \tag{2.2}$$

The complex reflection factor η_l is connected with the complex phase shift φ_l by $\eta_l=\exp(2i\varphi_l)$, and the cross sections are given by the well-known expressions for the elastic cross section:

$$\sigma_{el}^{(l)}=\pi\lambda^2(2l+1)|1-\eta_l|^2, \tag{2.3}$$

and for the reaction cross section,

$$\sigma_r^{(l)}=\pi\lambda^2(2l+1)(1-|\eta_l|^2), \tag{2.3a}$$

where λ is the wavelength of the incoming particle divided by 2π.

The reflection factor η_l is a complicated function of the energy of the incoming particle. It exhibits rapid fluctuations coming from the numerous close-spaced resonances of the compound nucleus. We will make the assumption that one can average over these fluctuations; that is, we assume that the average reflection factor,

$$\bar{\eta}_l(\epsilon)=\frac{1}{I}\int_{\epsilon-I/2}^{\epsilon+I/2}\eta_l(\epsilon')d\epsilon', \tag{2.4}$$

is a smooth function of ϵ if the interval I contains many close-spaced resonances. We also define average cross sections in the same way, and we can write

$$\begin{aligned}\bar{\sigma}_{el}^{(l)}&=\pi\lambda^2(2l+1)\overline{|1-\eta_l|^2},\\ \bar{\sigma}_r^{(l)}&=\pi\lambda^2(2l+1)(1-\overline{|\eta_l|^2}),\end{aligned} \tag{2.5}$$

where the bar over an expression signifies its average over the interval I. It is also assumed that I is much smaller than the energy ϵ such that slowly varying functions of ϵ, like λ^2, need not be averaged.

One can easily verify the following relations:

$$\bar{\sigma}_{el}^{(l)}=\pi\lambda^2(2l+1)\{|1-\bar{\eta}_l|^2-|\bar{\eta}_l|^2+\overline{|\eta_l|^2}\}, \tag{2.6}$$

and especially

$$\bar{\sigma}_t^{(l)}=\pi\lambda^2(2l+1)\{|1-\bar{\eta}_l|^2+1-|\bar{\eta}_l|^2\}. \tag{2.7}$$

Hence, the average total cross section depends only upon the average reflection factor (2.4). [This follows directly from the fact that the total cross section is a *linear* function of the real part of the phase η_l.]

We now divide the average elastic cross section into two parts, the "shape elastic" cross section $\sigma_{se}^{(l)}$ and the "compound elastic" cross section[4] $\sigma_{ce}^{(l)}$, by writing

$$\begin{aligned}\sigma_{se}^{(l)}&=\pi\lambda^2(2l+1)|1-\bar{\eta}_l|^2,\\ \sigma_{ce}^{(l)}&=\pi\lambda^2(2l+1)\{\overline{|\eta_l|^2}-|\bar{\eta}_l|^2\}.\end{aligned} \tag{2.8}$$

Furthermore, we combine $\sigma_{ce}^{(l)}$ and $\bar{\sigma}_r^{(l)}$ into a new cross section $\sigma_c^{(l)}$, which we call the cross section for the formation of the compound nucleus

$$\sigma_c^{(l)}=\sigma_{ce}^{(l)}+\bar{\sigma}_r^{(l)}=\pi\lambda^2(2l+1)\{1-|\bar{\eta}_l|^2\}. \tag{2.9}$$

We can see from (2.3) and (2.3a) that $\sigma_{se}^{(l)}$ and $\sigma_c^{(l)}$ have just the form of a scattering and a reaction cross section of a new and different problem, whose phase is the slowly varying function $\bar{\eta}_l$. In other words, by replacing η_l with $\bar{\eta}_l$, we obtain a new problem, which we have called the "gross-structure problem." The elastic scattering cross section σ_{se} of *this* problem is only part of the actual scattering; it is the "shape elastic" scattering. The other part, the "compound elastic," appears incorporated into the absorption or reaction cross section σ_c of the gross-structure problem together with the actual reaction cross section.

One is therefore led to consider the "compound elastic" scattering as that part which comes from the formation of the compound nucleus and its subsequent decay into the entrance channel, hence its incorporation into σ_c. After the averaging, σ_{ce} appears as part of the absorption from the incoming beam, which corresponds to the idea that the formation of the compound nucleus can be considered as an absorption whatever happens afterwards, re-emission or not.

It is the gross structure problem which we intend to reproduce by the interaction of the incident particle with the potential (1.2). The resulting scattering cross section should represent the shape elastic scattering, and the resulting absorption cross section should represent the compound formation. The latter contains the part σ_{ce} of the actual scattering.

When the energy is high enough above the resonance region that the continuum region is reached, the cross sections and phases are no longer rapidly varying functions of energy. Then the gross-structure problem is equal to the actual one and $\bar{\eta}_l=\eta_l$. It follows from (2.9) that $\sigma_{ce}=0$. One also can see this from an application of the compound nucleus assumption to the continuum region. The overlap of the resonances can be interpreted as a consequence of the fact that the probability Γ_α^s of the decay of the compound nucleus in the state s into the entrance channel α is much smaller than the probability of the decay into other channels. This follows from the well-known relation that any channel width Γ_α^s cannot be larger than $D/2\pi$ (D is the distance between resonances of the same J value). Hence, if the total width is much larger than D, the contribution to Γ from decays other than the one through α must be overwhelming. In the continuum region, therefore, the cross section for the formation of the compound nucleus is identical to the average reaction cross section $\bar{\sigma}_r$, and σ_{ce} is negligible.

We now illustrate the averaging process described above by using cross sections as given by the Breit-Wigner formula. We consider a nucleus with resonances at the energies ϵ_s, and we restrict our considerations to neutrons with $l=0$. We also restrict the discussion to low energies so that the following two magnitudes are small: One is kR and the other is Γ/D, with R the nuclear radius, and Γ and D the average values of the total width of and the distance between neutron resonances.

[4] This terminology will become obvious later on. B. T. Feld [*Experimental Nuclear Physics*, edited by E. Segrè (John Wiley and Sons, Inc., New York, 1953), Vol. 2] calls σ_{ce} the "capture elastic" cross section.

We have derived in the Appendix exact and approximate expressions for the scattering amplitude η_0 and for the cross sections in this energy region. For the present purposes, we will use the following form (see A.14b), which is valid in a region D_s including a resonance ϵ_s as indicated:

$$\eta_0=e^{-2ikR'(\epsilon)}\left(1-\frac{i\Gamma_a^s}{\epsilon-\epsilon_s+i\Gamma^s/2}\right)+\eta_0^*,$$

$$\eta_0^*=e^{-2ikR'(\epsilon)}\left(\frac{\Gamma_a^s}{\epsilon-\epsilon_s+i\Gamma^s/2}G_1+iG_2+G_3\right), \quad (2.10)$$

for

$$\epsilon_s+\epsilon_{s-1}<2\epsilon<\epsilon_{s+1}+\epsilon_s.$$

Here R' is a length and a slowly varying function of the energy. (A function is slowly varying if it changes value appreciably only over intervals large compared to D.) The length R' is of the order of magnitude of nuclear dimensions. It plays the role of a scattering length and takes on both positive and negative values. The quantities Γ_a^s and Γ^s are the partial width and the total width, respectively. The terms G_1, G_2, and G_3 are real functions of ϵ of the following order of magnitude:

$$G_1\sim\Gamma/D,\ G_2\sim(\Gamma_a/D)[(\Gamma/D)+kR],\ G_3\sim\Gamma_a/D, \quad (2.11)$$

where the omission of the superscript signifies the average value of the magnitude in the interval I.

The first term in η_0 incorporates the contribution from the resonance level ϵ_s, whereas η_0^* contains the contribution from the other resonances; the first term in η_0^* represents interference effects between the resonance ϵ_s and other resonances. It will appear later that η_0^* contributes negligibly to the average of η_0.

The cross sections in the immediate neighborhood of the resonance ($|\epsilon-\epsilon_s|\ll D_s$) follow from (2.5) and (2.10) by neglecting η_0^*, since, in that region, they contribute terms much smaller than the others.

$$\sigma_r^{(0)}=\pi\lambda^2\frac{\Gamma_a^s(\Gamma^s-\Gamma_a^s)}{(\epsilon-\epsilon_s)^2+(\Gamma^s/2)^2},$$

$$\sigma_{el}^{(0)}=\pi\lambda^2\left|(e^{2ikR'}-1)+\frac{i\Gamma_a^s}{\epsilon-\epsilon_s+i\Gamma^s/2}\right|^2, \quad (2.12)$$

$$|\epsilon-\epsilon_s|\ll D.$$

The reaction cross section is just the sum over β of the one-level Breit-Wigner cross sections

$$\sigma_{a\beta}^{(0)}=\frac{\Gamma_a^s\Gamma_\beta^s}{(\epsilon-\epsilon_s)^2+(\Gamma^s/2)^2}\pi\lambda^2 \quad (2.13)$$

for the reaction leading from the entrance channel α to an exit channel β. (Γ_β^s is the partial width of decay into the channel β.)

The elastic cross section contains a "potential" scattering amplitude

$$P=e^{2ikR'(\epsilon)}-1,$$

which corresponds to a scattering at a hard sphere of a radius R', where R' is not identical to but only of the order of magnitude[6] of the nuclear radius and is a slowly varying function of the energy.

We now determine the average value of the scattering amplitude η_0 over the resonances in the interval I:

$$\bar\eta_0=\frac{1}{I}\int_I\eta_0 d\epsilon=\left\langle\frac{1}{D_s}\int_{D_s}\eta_0(\epsilon)d\epsilon\right\rangle_I,$$

where the symbol $\langle\ \rangle_I$ signifies an average taken over all resonances within I. The random position of resonances allows us to write

$$\bar\eta_0=\frac{1}{D}\int_{\epsilon_s-D/2}^{\epsilon_s+D/2}\eta_0(\epsilon)d\epsilon, \quad (2.14)$$

where D is the average level distance within the interval I; typical average values of Γ^s and Γ_a^s should be used in the expression (2.10) for η_0.

Evaluation of (2.14) gives

$$\bar\eta_0=e^{-2ikR'}[1-(\pi\Gamma_a/D)], \quad (2.15)$$

when all magnitudes of the order $(\Gamma_a\Gamma)/D^2$ or $(\Gamma_a/D)kR'$ or smaller are neglected. It is seen in each interval D_s that the main contribution to the average comes from the main resonance. The contribution of neighboring resonances which are expressed by η_0^* in (2.10) contribute only to expressions which are smaller than (2.14) by a factor of the order Γ/D or kR.

We now use (2.14) for the calculation of the "shape elastic" scattering and get, with the help of (2.8),

$$\sigma_{se}^{(0)}=\pi\lambda^2|(e^{2ikR'}-1)+\pi\Gamma_a/D|^2. \quad (2.16)$$

For small kR', this becomes

$$\sigma_{se}^{(0)}=4\pi R'^2[1+(\pi\Gamma_a/2kR'D)^2]. \quad (2.17)$$

The magnitude $[\pi\Gamma_a/2(kR'D)]^2$ is usually rather small. [It is of the order of 10^{-2}; see, for example, the estimate in Blatt and Weisskopf,[5] Chap. VIII, Eq. (7.14).] Hence, $\sigma_{se}^{(0)}$ is very nearly equal to $4\pi R'^2$ for $kR'\ll 1$.

We get the cross section for the formation of the compound nucleus according to (2.9),

$$\sigma_c^{(0)}=2\pi^2\lambda^2(\Gamma_a/D)(1-\tfrac{1}{2}\pi\Gamma_a/D). \quad (2.18)$$

[6] The appearance of the length R' is a consequence of our general treatment of the nuclear resonance in the Appendix. In the special derivation of the Breit-Wigner formula, as given in Feshbach, Peaslee, and Weisskopf (reference 1) or J. M. Blatt and V. F. Weisskopf, *Theoretical Nuclear Physics* (John Wiley and Sons, Inc., New York, 1952), assumptions are made which make R' constant and equal to the nuclear radius R. It is shown in this paper that these assumptions probably are valid only in special cases as in the case of strong coupling, for example.

The average total cross section then becomes

$$\sigma_t^{(0)}=\sigma_{ss}^{(0)}+\sigma_c^{(0)}=4\pi R'^2+2\pi^2\lambda^2\Gamma_a/D. \quad (2.19)$$

The second term in this expression is proportional to $(1/v)$.

It is interesting to compare σ_c with the average of σ_r, which, according to (2.12), is

$$\bar{\sigma}_r^{(0)}=2\pi^2\lambda^2(\Gamma_a/D)(\Gamma-\Gamma_a)/\Gamma. \quad (2.20)$$

Hence, the difference between the two, the "compound elastic" scattering, is [neglecting the small factor $\pi\Gamma_a/(2D)$]

$$\sigma_{ce}^{(l)}=2\pi^2\lambda^2\Gamma_n^2/D\Gamma. \quad (2.21)$$

This is just the average of that part of the elastic scattering (2.12) which corresponds to the resonance amplitude only, namely, of

$$\sigma=\pi\lambda^2\frac{(\Gamma_a^s)^2}{(\epsilon-\epsilon_s)^2+(\Gamma^s/2)^2}.$$

It is the cross section which one would get for the re-emission into the entrance channel from the Breit-Wigner expression (2.13).

It is significant that expressions (2.15), (2.18), and (2.19) do not contain the total width Γ but only the channel width Γ_a. The "gross" properties (total, shape elastic, and compound nucleus formation cross sections) are independent of the nature of the other exit channels. They would remain unchanged, for example, if the exit channels $\beta\neq\alpha$ were closed. It would only increase σ_{ce} at the expense of $\bar{\sigma}_r$, as seen in (2.20) and (2.21). This is connected with the fact that a change of Γ with constant Γ_a changes only the width of the resonance, but not its area.

At the energies considered here, the cross section for the formation of the compound nucleus contains only magnitudes (Γ_a and D), which can be determined by studying the neutron resonances. Hence, investigations of slow neutron resonances are useful to check the theoretical predictions of σ_c at low energy. The "shape-elastic" scattering, on the other hand, in this energy region is almost entirely given by $4\pi R'^2$ and is therefore essentially independent of the neutron resonance values. Apart from the small correction $\pi^3\lambda^2(\Gamma_a/D)^2$, it is equal to the potential scattering as shown in (2.12) and, therefore, can be measured also by studying the cross sections near and between resonances.

III. POTENTIAL-WELL MODEL

In this section we shall employ a potential-well model to determine the gross-structure cross sections. We have adopted for the purposes of a preliminary survey the simplest type of potential well:

$$\begin{aligned} V&=-V_0(1+i\zeta), \quad r<R,\\ V&=0, \qquad\qquad r>R, \end{aligned} \quad (3.1)$$

where V_0 and ζ are constants and R is the nuclear radius. The use of the complex potential is necessary to obtain nonzero values for the cross section for the formation of the compound nucleus. A similar model in which $\zeta\sim 1$ was employed by Bethe.[6] Fernbach, Serber, and Taylor[7] have used the same model in order to describe nuclear scattering at very high energies. A model in which $\zeta=0$ was used by Ford and Bohm[8] in discussing zero-energy cross sections. It is essential that the crudeness of this model be emphasized. We have, for example, omitted any spin-orbit terms which play an important role in the shell model, but which we expect will not affect the over-all qualitative features which we seek here. The constants in (3.1) may well turn out to be energy dependent. We particularly expect this for ζ, since we know that $\bar{\sigma}_r$ is large at high energies, while the success of the shell model indicates that ζ should be zero for the ground states of nuclei.

We give some of the details of the calculations with potential (3.1). For each l we calculate the value of the logarithmic derivative,

$$f_l=R(u_l'/u_l)_{r=R}. \quad (3.2)$$

The average reflection factor $\bar{\eta}_l$ is then

$$\bar{\eta}_l=e^{-2i\delta_l}\left(1-\frac{2s_l}{M_l+iN_l}\right), \quad (3.3)$$

where

$$\delta_l=\tan^{-1}(-j_l(x)/n_l(x)), \quad (3.4a)$$

$$\Delta_l+is_l=1+xh_l'(x)/h_l(x), \quad (3.4b)$$

$$M_l=s_l-\mathrm{Im}f_l, \quad N_l=-\Delta_l+\mathrm{Re}f_l. \quad (3.4c)$$

The functions j_l, n_l, and h_l are the spherical Bessel, Neumann, and Hankel functions, respectively, while x is, as usual, kR.[9] $h_l'(x)$ is the derivative of $h_l(x)$ with respect to x; Δ_l and s_l are both real magnitudes and are defined as the real and imaginary part of the expression on the right of (3.4b).

For potential (3.1), f_l may be written down directly

$$f_l=1+Xj_l'(X)/j_l(X), \quad (3.5)$$

where

$$X^2=x^2+X_0^2(1+i\zeta), \quad X_0^2=(2m/\hbar^2)V_0R^2.$$

This is, however, not the most convenient form for determining the real (Re) and imaginary (Im) parts of f_l. We have instead employed recurrence relations for these quantities based on recurrence relations for j_l.

[6] H. Bethe, Phys. Rev. **57**, 1125 (1940).
[7] Fernbach, Serber, and Taylor, Phys. Rev. **75**, 1352 (1949).
[8] K. W. Ford and D. Bohm, Phys. Rev. **79**, 745 (1950).
[9] This follows the notation of Morse, Lowan, Feshbach, and Lax, U. S. Navy Department of Research and Inventions Report No. 62.1R, 1945 (unpublished).

For $l=0$, we get

$$f_0=X\cot X,$$
$$\mathrm{Re}f_0=\frac{X_1\sin 2X_1+X_2\sinh 2X_2}{\cosh 2X_2-\cos 2X_1},\tag{3.6}$$
$$\mathrm{Im}f_0=\frac{X_2\sin 2X_1-X_1\sinh 2X_2}{\cosh 2X_2-\cos 2X_1},$$

where $X=X_1+iX_2$. The recurrence relations which follow from

$$f_l=\frac{X^2}{l-f_{l-1}}-l$$

are

$$\mathrm{Re}f=\frac{(X_1^2-X_2^2)(l-\mathrm{Re}f_{l-1})-2X_1X_2\,\mathrm{Im}f_{l-1}}{(l-\mathrm{Re}f_{l-1})^2+(\mathrm{Im}f_{l-1})^2}-l,\tag{3.7}$$

$$\mathrm{Im}f_l=\frac{(X_1^2-X_2^2)\,\mathrm{Im}f_{l-1}+2X_1X_2(l-\mathrm{Re}f_{l-1})}{(l-\mathrm{Re}f_{l-1})^2+(\mathrm{Im}f_{l-1})^2}.\tag{3.8}$$

The asymptotic expression for f_l,

$$f_l\underset{X\to\infty}{\longrightarrow}X\cot(X-\tfrac{1}{2}l\pi),\tag{3.9}$$

unfortunately cannot be generally employed. The fractional error in (3.9) is $l(l+1)/(X\sin 2X)$, from which we learn that (3.9) is not sufficiently accurate for $l\geqslant 2$, while for $l=1$ it will fail for small X or for $X=n\pi$.

The total cross section, as well as the cross section for the formation of the compound nucleus, may be easily obtained

$$\frac{\bar\sigma_l^{(l)}}{\pi R^2}=\frac{4}{x^2}(2l+1)\left[\sin^2\delta_l+s_l\frac{M_l\cos 2\delta_l-N_l\sin 2\delta_l}{M_l^2+N_l^2}\right],$$
$$\frac{\sigma_c^{(l)}}{\pi R^2}=\frac{4}{x^2}(2l+1)s_l\left[\frac{-\mathrm{Im}f_l}{M_l^2+N_l^2}\right]\equiv\frac{(2l+1)T_l}{x^2},\tag{3.10}$$
$$\bar\sigma_l=\sum_l\bar\sigma_l^{(l)},\quad\sigma_c=\sum_l\sigma_c^{(l)},$$

where the T_l may be interpreted as penetrabilities.

These cross sections will have characteristic large-scale resonances, which are present in the experimental data. In the $l=0$ case, these resonances occur when

$$X_1=(X_0^2+x^2)^{\frac{1}{2}}=(n+\tfrac{1}{2})\pi+\frac{X_0^2\zeta^2}{2(2n+1)\pi},$$

where n is an integer and where we have assumed that $\zeta X_0^2/n\pi\ll 1$. The width of the large-scale resonance is $2x\hbar^2/mR^2$, which in the experimental range is of the order of Mev. For a given energy, the $l=0$ cross section will give maxima as a function of R. The width of these maxima against changes in R is approximately $(2xR/X^2)$, independent of R.

The angular distribution for shape elastic scattering is

$$\frac{d\sigma_{se}}{d\Omega}=\frac{\lambda^2}{4}\Big|\sum_l(2l+1)(1-\bar\eta_l)P_l(\cos\theta)\Big|^2.$$

Therefore

$$\frac{1}{R^2}\frac{d\sigma_{se}}{d\Omega}=(\mathrm{Re}\sum)^2+(\mathrm{Im}\sum)^2,\tag{3.11}$$

where

$$\mathrm{Im}\sum=\frac{x}{4}\sum_l\frac{\sigma_t^{(l)}}{\pi R^2}P_l(\cos\theta),\tag{3.12}$$
$$\mathrm{Re}\sum=\frac{1}{2x}\sum_l(2l+1)\left[\sin 2\delta_l-2s_l\frac{M_l\sin 2\delta_l+N_l\cos 2\delta_l}{M_l^2+N_l^2}\right].$$

Before we can compare the theory with the experimental data on angular distributions, it is necessary to add the compound elastic scattering. From our general qualitative ideas, we may break the process up into the formation of the compound nucleus and the re-emission of the incident particle into a particular l state, which will naturally have a very definite associated angular distribution. The result is particularly simple in the case of a target nucleus of spin zero and an incident particle of spin zero, since here the angular momentum of the incident particle cannot change in an elastic scattering process. We may therefore write

$$\frac{d\sigma_{ce}}{d\Omega}=\sum\sigma_c^{(l)}|Y_{l0}|^2w_l,\tag{3.13}$$

where Y_{l0} are the normalized spherical harmonics and w_l is the probability that the compound nucleus formed by the absorption of a particle of angular momentum l will decay by emission of the same particle without loss of energy or change in angular momentum.

This simple result cannot be applied to the neutron case because of the possibility of spin changes of the neutron and re-orientation of the spin of the target nucleus without any change in the energy of either the neutron or the target nucleus. The formalism which needs to be used here has been worked out by Hauser and Feshbach[10] and by Wolfenstein.[11] The target nucleus and neutron system is now characterized by the spin of the target nucleus I, its z component m, and spin of the neutron i, the channel spin $s(\mathbf{s}=\mathbf{i}+\mathbf{1})$, the angular momentum of the incident neutron l, and its z component which is zero, and of course the parity of the system. The compound nucleus will have a total angular momentum J, z component m, and will decay into a residual nucleus of spin I' and a particle of spin i'. These form a final channel spin $s'(\mathbf{s}'=\mathbf{i}'+\mathbf{1}')$, z component $m-m'$. The system will have an angular momentum l', z component m'.

[10] W. Hauser and H. Feshbach, Phys. Rev. **87**, 366 (1952).
[11] L. Wolfenstein, Phys. Rev. **82**, 690 (1951).

To obtain the desired cross section, we must now introduce the assumptions of the statistical nuclear theory. We assume that, upon appropriate averaging, the various J levels do not interfere, that there is no residual interference between the various l's which can form the given compound state J, or between the various l's into which it can decay. We then break up the process of compound elastic scattering into the cross section for the formation of the compound nucleus in state J, with incident particles of angular momentum l, multiplied by the probability that it will decay by emission of a particle of angular momentum l', leaving the residual nucleus in the ground state with spin I. The formation process is given first by the cross section for the formation of the compound nucleus which, because of our simple assumption (3.1), depends only on l and is $\sigma_c^{(l)}$. This must be multiplied by the probability of forming the system with angular momentum J, using incident particles of angular momentum l. Again, because of the absence of any spin-dependent forces, this is simply the square of the Clebsch-Gordan coefficient $|(ls0m|lsJm)|^2$. On the emission side, we will need the probability of forming J with particles of angular momentum l'. This is given by $|(l's'm'm-m'|l's'Jm)|^2$. We need the relative probability of decay with emission of l' particles leaving the nucleus in the ground state which we will denote by $w(l')\leqslant 1$. The limitations of the relative probability of different kinds of emission arising from angular momentum conservation are contained in the Clebsch-Gordan coefficients. The function w contains all the other dependence. Because of our assumption of spin-independent forces in Eq. (3.1), it will depend only on l' and the parity of the system. The angular distribution of the emitted particles is $|Y_{l'm'}|^2$. Combining these results, we have

$$\frac{d\sigma_{ee}}{d\Omega}=\frac{1}{(2i+1)(2I+1)}\sum\sigma_c^{(l)}|(ls0m|lsJm)|^2 \times|(l's'm'm-m'|l's'Jm)|^2w(l')|Y_{l'm'}|^2. \quad (3.14)$$

The indicated sums are over m, m', s, s', l, l', and J. The spin factor in front arises from the average over initial spin states, which involves the sum over m and m'.

By employing methods due to Racah[12] and discussed by Blatt and Biedenharn,[13] the sums over m and m' may be performed yielding

$$\frac{d\sigma_{ee}}{d\Omega}=\frac{1}{4\pi(2I+1)(2i+1)}\sum\frac{\sigma_c^{(l)}w(l')}{2l+1} \times Z(lJlJ;sL)Z(l'Jl'J;s'L)P_L(\cos\theta), \quad (3.15)$$

where the Z factors are defined by Biedenharn, Blatt, and Rose[14] and for which tables[15] are available. The sums are over J, l, l', and L. Only even L will occur. This result is given in reference 10.[16] We have not introduced a specific notation to describe the role of parity, so it should be understood that parity is conserved both in the formation and in the decay of the compound nucleus.

The total compound elastic cross section may be easily evaluated from (3.15) and gives the expected result

$$\sigma_{ee}=\sum\frac{2J+1}{(2I+1)(2i+1)(2l+1)}\sigma_c^{(l)}w(l').$$

Expression (3.15) simplifies considerably in two special cases (a) $I\gg 1$ and (b) $I=0$. In case (a), it follows from the sum rule (see reference 10),

$$\sum_{s'l'}(2s'+1)|Z(lJlJ;sL)Z(l'Jl'J;s'L)|P_L=(2J+1)^2(2l+1), \quad (3.16)$$

that $d\sigma_{ee}/d\Omega$ is approximately independent of angle. We note that if $I\gg 1$, the factor $2s'+1$ is approximately a constant, the error being of the order of $(1/I)$. In case (b) we note that $s=s'=\frac{1}{2}$ and that $l=l'$ because of parity conservation. We therefore find for this case (placing $i=\frac{1}{2}$)

$$\frac{d\sigma_{ee}}{d\Omega}=\sum_{l,L}\frac{\sigma_c^{(l)}w(l)}{4\pi(4l+2)}[Z^2(l,l+\tfrac{1}{2},l,l+\tfrac{1}{2};\tfrac{1}{2},L) +Z^2(l,l-\tfrac{1}{2},l,l-\tfrac{1}{2};\tfrac{1}{2},L)]P_L. \quad (3.17)$$

The factors w which may be computed as outlined in reference 10 depend on the details of the levels of the residual nucleus. There it is shown that

$$w(l')=T_{l'}(E)/\textstyle\sum_{pq}T_p(E_q'). \quad (3.18)$$

The quantity $w(l')$ lies between 0 and 1. The values of T_p are calculated in reference 10 under the assumption of strong coupling. The ideas underlying the present theory would change these factors to those given by Eq. (3.10). Since the compound elastic scattering is not very large compared to the shape elastic, we have only determined the upper limit for σ_{ee}, which is given by putting $w(l')=1$. We expect σ_{ee} to be near this upper limit at energies for which there is little inelastic scattering or capture, and to be near zero when inelastic scattering or other nuclear reactions are appreciable.

[12] G. Racah, Phys. Rev. **61**, 186 (1942); **62**, 438 (1942).
[13] J. M. Blatt and L. C. Biedenharn, Revs. Modern Phys. **24** 258 (1952).
[14] Biedenharn, Blatt, and Rose, Revs. Modern Phys. **24**, 249 (1952).
[15] L. C. Biedenharn, Oak Ridge National Laboratory Report ORNL-1501, May 28, 1953 (unpublished).
[16] It is worth while noting that Eq. (3.15) may be derived from the general analysis of Blatt and Biedenharn by combining the definitions of average cross section as given in Sec. II and the statistical assumptions. The chief elements of the latter are (1) nonoverlap of resonances and (2) random phases for the scattering matrix so that, upon averaging over possible ways of forming the compound nucleus, interference terms average to zero.

IV. ISOLATED RESONANCES

We should like to establish a correspondence between the parameters describing a single compound nucleus resonance and the parameters which describe the average potential (3.1). This is most easily done for the low-energy case. We evaluate the cross sections for very low energy on the basis of the potential (3.1) and by comparing them with the expressions for the average cross sections which were derived in Sec. II in terms of the resonance parameters. The only two resonance parameters entering here are the ratio Γ_a/D of neutron width[17] to level distance and the radius R' of the potential scattering.

We start with the evaluation of the results from (3.1). The only contribution comes from $l=0$ and we get from (3.3)

$$\eta_0=e^{-2ix}\frac{f_0+ix}{f_0-ix}=e^{-2ix(1-\alpha)}, \tag{4.1}$$

where α is a complex number:

$$\alpha=(1/x)\tan^{-1}(x/f_0)\cong 1/f_0,$$

and f_0 is given by the expressions (3.6).

This should be compared with (2.14) in order to express the two relevant magnitudes R' and Γ_a/D in terms of X_1 and X_2. Equating (2.14) and (4.1) gives in the limit of $k\to 0$, a limit which also implies $\Gamma_a/D\to 0$:

$$R'=R(1-\alpha_1), \quad (\pi/2x)(\Gamma_a/D)=\alpha_2,$$

where α_1 and α_2 are the real and imaginary parts of α.

From (3.6) we can easily obtain the following relations:

$$\alpha=f_0^{-1}=\alpha_1+i\alpha_2,$$

$$\alpha_1=\frac{1}{|X|^2}\frac{X_2B-X_1A\sin 2X_1}{B^2+2A\cos^2X_1},$$

$$\alpha_2=\frac{1}{|X|^2}\frac{X_1B-X_2A\sin 2X_1}{B^2+2A\cos^2X_1},$$

with $A=1/(2\cosh^2X_2)$, $B=\tanh X_2$.

We now distinguish two limiting cases: the cases of strong and weak coupling. In the first case the absorption is so strong that the neutron is completely absorbed in a distance of a nuclear radius within nuclear matter: $\exp(-X_2)\ll 1$. In the case of weak coupling we assume $X_2\ll 1$.

Hence we get, for strong coupling: $A\to 0$, $B\to 1$, and

$$\alpha_1=X_2/|X|^2=1/X_2', \quad \alpha_2=X_1/|X|^2=1/X_1',$$

and $R'=R(1-1/X_2')$, $\Gamma_a/D=2x/\pi X_1'$. The length R' is almost equal to R since $(X_2')^{-1}$ is a small magnitude. The expression for Γ_a/D is the same as that used by Feshbach, Peaslee, and Weisskopf with the only exception that X_1' replaces X_1. The former magnitude is somewhat larger than X_1.[18]

Strong coupling therefore leads essentially to the same results as Feshbach, Peaslee, and Weisskopf: The potential scattering length is roughly equal to R and $\Gamma_a/D=2(x/\pi X_1')$.

In the weak coupling approximation we get

$$A=\tfrac{1}{2}, \quad B=X_2\ll 1, \quad |X|^2=X_1^2,$$

and hence

$$R'=R\left(1-\frac{1}{2X_1}\frac{\sin 2X_1}{X_2^2+\cos^2X_1}\right),$$

$$\frac{\Gamma_a}{D}=\frac{2x}{\pi X_1}\beta, \quad \beta=X_2\frac{1-(1/2X_1)\sin 2X_1}{X_2^2+\cos^2X_1}.$$

Here R' and β are functions of X_1, and hence of R, with a characteristic resonance denominator. The shapes of these functions are reminiscent of optical dispersion and absorption curves, respectively. The maximum in β occurs when $X_0\cong(n+\frac{1}{2})\pi$ (n integer), the value of β being $2/[(n+\frac{1}{2})\pi\zeta]$ and the width of the peak at half-maximum $(n+\frac{1}{2})\pi\zeta$. The minimum value of β is about $(n+\frac{1}{2})\pi\zeta/2$. Figure 1 shows both magnitudes plotted as a function of X_0 for a value of $\zeta=0.03$.

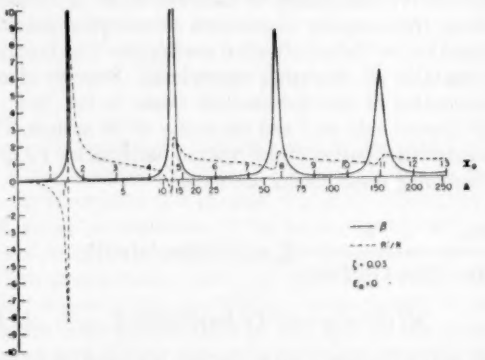

FIG. 1. Potential scattering length R' and the ratio Γ_a/D of the neutron width to the level distance at low energy as a function of $X_0=K_0R$ for $\zeta=0.03$. R' is plotted in units of R and Γ_a/D is given in the form of the parameter $\beta=(\pi/2)(V_0/\epsilon)^{\frac{1}{2}}(\Gamma_a/D)$, where ϵ is the energy of the neutron. The atomic-weight scale corresponding to X_0 is shown also for a potential-well depth $V_0=42$ Mev and radii $R=1.45\times 10^{-13}A^{\frac{1}{3}}$ cm.

[17] From here on we use the symbol Γ_a for "neutron width" since the entrance channel a is a *neutron* channel in all cases which we treat in this paper.

[18] It is plausible to assume that, in the case of strong coupling, the imaginary part of the potential is of the same order as the real part. An imaginary part that is much larger than the real one would imply that the absorption takes place over distances small compared to the wavelength in the interior. Hence X_1' is about twice as large as X_0 which leads to a Γ_a/D half as large as in Feshbach, Peaslee, and Weisskopf. This strong coupling result is somewhat more consistent than the result in Feshbach, Peaslee, and Weisskopf. In the latter paper the boundary condition was chosen such that the wave inside the nucleus is a sine wave $\sin(Kr-\delta)$, an assumption that is contrary to the idea of strong compound nucleus formation. In fact, a wave $\exp(+\Omega r)\sin(Kr-\delta)$ with $\Omega\sim K$ would be more consistent and does lead to the same result as the one above.

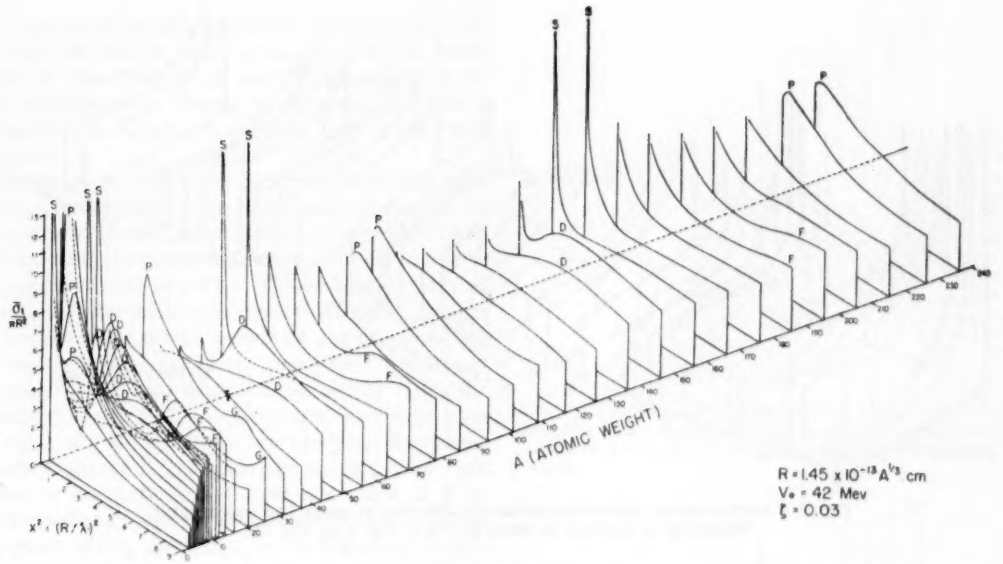

(a)

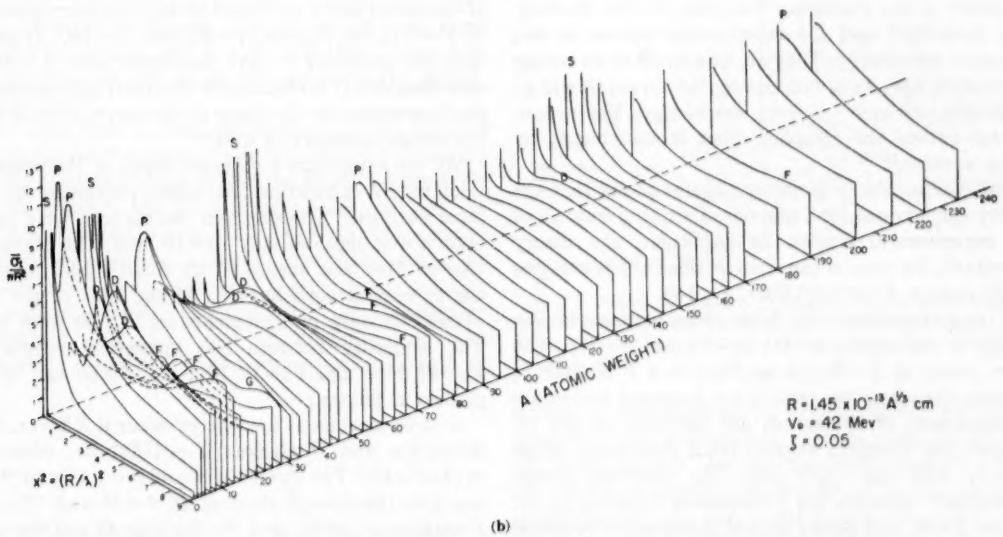

(b)

FIG. 2. (a) Calculated neutron total cross sections as a function of energy and mass number, for a well depth $V_0=42$ Mev, radius $R=1.45\times10^{-13}A^{\frac{1}{3}}$, $\zeta=0.03$. The energy ϵ is expressed in terms of

$$x^2=[A^{\frac{1}{3}}\cdot A/10(A+1)]\epsilon,$$

where ϵ is in Mev. (b) The same for $\zeta=0.05$.

V. COMPARISON WITH EXPERIMENTAL RESULTS

Figure 2a shows a profile presentation of the calculations of the neutron total cross sections on the basis of the potential (3.1) with a depth $V_0=42$ Mev and a radius $R=1.45\times10^{-13}A^{\frac{1}{3}}$ cm. The constant ζ is assumed to be 0.03 which corresponds to an absorption coefficient of $\kappa=4.2\times10^{11}$ cm^{-1} in nuclear matter for neutrons of zero energy in free space. This means that the intensity of a beam of slow neutrons is reduced in nuclear matter to $1/e$ at a distance of $\kappa^{-1}=2.4\times10^{-12}$ cm. The cross sections are plotted as a function of the energy in units of $x^2=(R/\lambda)^2$ and of the atomic weight. The letters denoting the maxima indicate the character of the resonance causing the maximum. Figure 3 contains a profile presentation of the observed cross sections plotted against the same coordinates.

The experimental curves in Fig. 3 are averages over resonances. For higher A and small level distance this

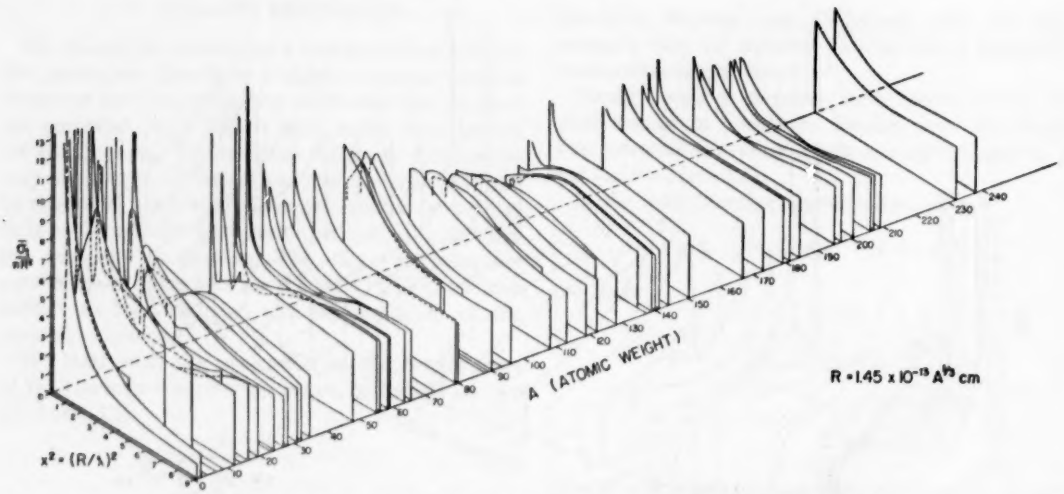

FIG. 3. Observed neutron total cross sections as a function of energy and mass number. The energy is expressed in terms of x^2 as in Fig. 2, (a) and (b).

average was done by the measuring apparatus itself, for lower A the averaging was done in the drawing. The theoretical and the experimental curves do not extend to zero energy. They are broken off at an energy of about 50 kev. As is well known, the curves should go approximately as $\epsilon^{-\frac{1}{2}}$ at very low energy. The experimental curves are compiled from measurements by many workers.[19–25]

The comparison of these two figures shows that the theory can account for a number of striking features of the experimental results. In particular, the theory reproduces the drop of the cross sections at low energies in the regions $A\sim40$ and $100<A<140$.

It also reproduces the large cross sections at low energy in the regions $A\sim60$, $A\sim90$, and $A\sim150$. The large values at $A\sim90$ are ascribed to a P resonance; whereas the other two regions are supposed to contain S resonances. P resonances are expected to fall off towards low energies; whereas the S resonances merge directly with the $(1/v)$ rise. The observed energy dependence indicates the P-resonance behavior in the region $A\sim90$ and shows typical S-resonance behavior at $A\sim60$ and 150. There is an indication of P-resonance at low energies for $A\sim30$ as the theory predicts.

The theory also reproduces the type of maxima (D maxima) which are found for energies corresponding to $x^2\sim3$ in the regions $A\sim40$, and $A\sim140$. It seems that the predicted F-wave maximum near $A\sim200$ is also observed. It is remarkable that one finds reasonably good agreement in the shape of the curves even at very low atomic numbers: $A<20$.[26]

We are using here a different depth of the potential than in the calculations published previously by the same authors.[27] The previous calculations were based upon a well depth of only $V_0=19$ Mev. The change to $V_0=42$ Mev was suggested by Adair[28] and improves the agreement considerably. At the time of the first calculation only measurements for $A>60$ were used. The similarity between the theoretical results for $V_0=42$ Mev and $V_0=19$ Mev for $A>60$ can be explained as follows:

S-wave maxima at low energy occur if $RK_0=r_0A^{\frac{1}{3}}K_0\cong(n+\frac{1}{2})\pi$ and P maxima if $r_0A^{\frac{1}{3}}K_0\cong n\pi$, where $K_0=(2mV_0/\hbar^2)^{\frac{1}{2}}$. For $V_0=19$ Mev and $r_0=1.45\times10^{-13}$ cm, one gets therefore S maxima at $A\sim38$ and 170, and P maxima at $A\sim11$ and 90. For $V_0=42$ and the same r_0 one gets S maxima at $A\sim11$, 55, and 150; P maxima at $A\sim27$, 90, and 216. Hence, the P maximum near 90 and the S maximum near 160 are reproduced by both potential depths. The behavior of the curves in the neighborhood of these maxima also must be similar, in particular, the depression at low energy for values of A just below an S maximum. However, the experimental data for nuclei below $A=60$ definitely indicate another S maximum near 55 and a strong low-energy depression for $A\sim40$ as predicted by $V_0=42$. These features are

[19] H. H. Barschall, Phys. Rev. **86**, 431 (1952).
[20] Miller, Adair, Bockelman, and Darden, Phys. Rev. **88**, 83 (1952).
[21] Walt, Becker, Okazaki, and Fields, Phys. Rev. **89**, 1271 (1953).
[22] Okazaki, Darden, and Walton, Phys. Rev. **93**, 461 (1954).
[23] N. Nereson and S. Darden, Phys. Rev. **89**, 775 (1953); Phys. Rev. **94**, 1678 (1954); and unpublished data on Li and B (private communication).
[24] C. F. Cook and T. W. Bonner, Phys. Rev. **94**, 651 (1954); McCrary, Taylor, and Bonner, unpublished data on Li (private communication).
[25] *Neutron Cross Sections*, U. S. Atomic Energy Commission Report AECU-2040 (Technical Information Division, Department of Commerce, Washington, D. C., 1952), and three supplements (unpublished).
[26] See also C. E. Porter, Bull. Am. Phys. Soc. **29**, No. 5, 25 (1954).
[27] Feshbach, Porter, and Weisskopf, Phys. Rev. **90**, 166 (1953).
[28] R. K. Adair, Phys. Rev. **94**, 737 (1954).

not reproduced by the theoretical curves for $V_0=19$. We therefore believe that $V_0=42$ Mev yields a better model. It should be noted that the agreement is not very sensitive to a change of potential V_0 with a corresponding change of r_0 such that $V_0^{\frac{1}{3}}r_0$ stays constant.

The shapes of the total cross section curves are quite sensitive to the value of the absorption constant ζ. An increase of ζ flattens the maxima and minima. Strong fluctuations in the calculated curves occur only at lower energies for values of $x<1.5$. This is below 2 Mev at $A\sim60$ and below 0.6 Mev at $A\sim200$. At higher energies the contributions of the numerous angular momenta prevent the appearance of any pronounced maxima or minima. Therefore the determination of ζ by fitting the calculated curves to the experimental ones only gives the value of ζ for relatively low energies. We cannot exclude a change of ζ at energies of, say, more than 1 Mev or fluctuations in ζ from one value of A to another although below 1 Mev it seems that ζ cannot vary much as a function of A. In the low-energy region the determination is quite accurate. A change of ζ to 0.05 or to 0.02 would give rise to a worse agreement with experiments. Figure 2(b) shows the total cross sections for $\zeta=0.05$, and it is obvious that the maxima and minima are not as pronounced as in the experimental data.[29]

We now turn to the calculations of the angular distribution of the elastic scattering. Figure 4 shows the experimental results at 1 Mev as measured by Walt and Barschall.[30] The most characteristic features are the flat distributions around $A\sim60$, a very strong forward peaking and a rise at backward angles at $A\sim140$, and the appearance of a second maximum at 90° around $A\sim180$. The calculation of the angular dependence (Fig. 5) is not unambiguous since the amount of compound elastic scattering is difficult to determine. Furthermore, the angular dependence of the compound elastic scattering depends upon the spin of the target nucleus. We therefore have shown in Fig. 5 the calculated angular distribution of the shape elastic scattering only. In Fig. 6 the compound elastic scattering is added in full which would correspond to the case in which the compound state decays exclusively via the entrance channel. The target spin was assumed to be zero. The actual $d\sigma_{el}/d\Omega$ must lie somewhere between Fig. 5 and Fig. 6. For nuclei with strong inelastic scattering, Fig. 5 should be the better approximation.

It is seen from Figs. 5 and 6 that some of the main features are again reproduced by the theory. The flatness of the distribution around $A\sim60$ comes from the fact that the P contribution is very weak in this region and, at small angles, of opposite phase to the S scattering. This occurs always at values KR somewhat below a P resonance. The second maximum at 90° at high mass numbers is not too well reproduced. The

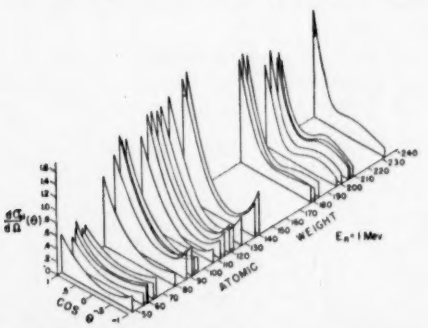

FIG. 4. Observed angular distribution (in barns/sterad) of the elastic 1-Mev neutron scattering as a function of $\cos\theta$ and the mass number A as measured by Walt and Barschall.

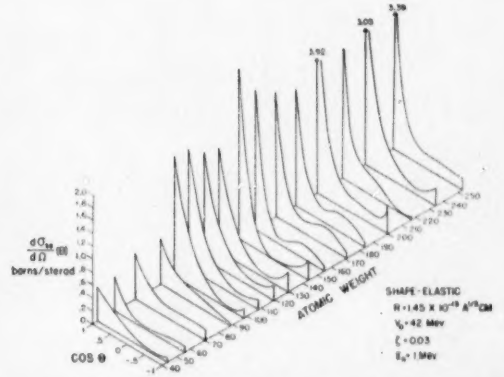

FIG. 5. Calculated angular distribution of the elastic neutron scattering (shape elastic only) as a function of $\cos\theta$ and the mass number A for a well $V_0=42$ Mev, $R=1.45A^{\frac{1}{3}}\times10^{-13}$ cm, and $\zeta=0.03$.

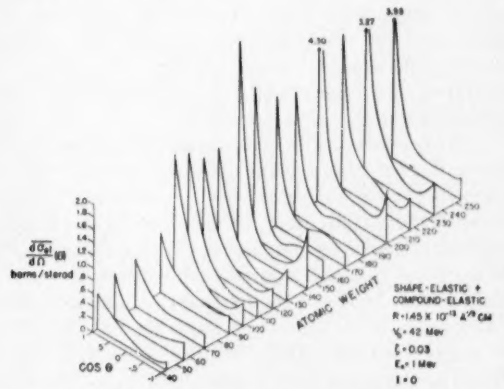

FIG. 6. Calculated angular distribution of the elastic neutron scattering (shape elastic plus maximum compound elastic) as a function of $\cos\theta$ and A for a well $V_0=42$ Mev, $R=1.45A^{\frac{1}{3}}\times10^{-13}$ cm, and $\zeta=0.03$.

[29] The disagreement is worse for high values of A. This might be an indication of a slight decrease of ζ with the mass number. If the absorption were concentrated in a surface layer of given thickness, one would expect a similar effect [see M. H. Johnson and E. Teller, Phys. Rev. **93**, 357 (1954)].

[30] M. Walt and H. H. Barschall, Phys. Rev. **93**, 1062 (1954).

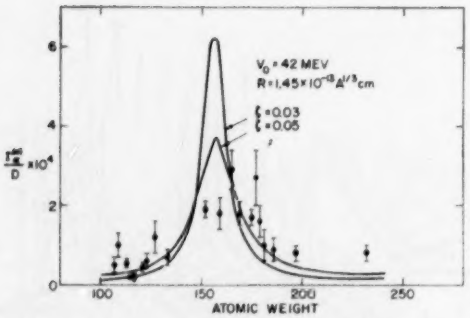

FIG. 7. Ratio $\Gamma_a^{(0)}/D$ of neutron width to level distance for low energies as a function of A. Here $\Gamma_a^{(0)}=\Gamma_a(\epsilon^{(0)}/\epsilon)^{\frac{1}{2}}$ is the "reduced" width, and $\epsilon^{(0)}$ is taken to be 1 ev. The curves represent the calculated values for $\zeta=0.03$ and 0.05. The points represent the observed values and the limits of error.

theory shows it only between $A=150$ and $A=200$. The angular dependence above $A=200$ does not seem to agree too well with the experiment. The angular distributions are not very sensitive to the choice of constants. The results with $V_0=19$ Mev are not very different from the ones shown here.

The agreement with experiments is also less satisfactory for the cross section σ_e for the formation of the compound nucleus. It is difficult to measure σ_e directly since it includes the compound elastic scattering besides the reaction cross section, and the former cannot easily be separated from the shape elastic scattering. At very low energies, however, the formation of the compound nucleus can be measured by studying the individual resonances (see Sec. III). The relevant magnitude is the ratio Γ_a/D of the neutron width to the level distance, averaged over a number of neighboring resonances. The theoretical values Γ_a/D expected on the basis of $V_0=42$ Mev are shown in Fig. 7 together with a compilation[31] of the measurements[32–41] of Γ_a/D. Only recently has it been possible to measure the neutron widths of several resonances in one isotope, so that the average Γ_a and the level distance can be determined to some degree of reliability. It is seen that the expected maximum of Γ_a/D at $A\sim155$ is noticeable, but it is not as strong as the theory predicts for the same value of ζ which gives the best fit for the total cross sections ($\zeta=0.03$). Also the values off peak are somewhat larger than predicted.

The fact that the resonance at $A\sim155$ is not as strong as expected might be connected with the large deviations from sphericity which are ascribed to the nuclei in this region.[42] If the shape of the potential well is ellipsoidal, one would expect results which roughly represent averages over the spherical results taken over radii which lie between the smallest and the largest axis. This would give rise to a flattening of the maxima and a rise of the wings in the theoretical curves of Fig. 7.[43]

Although no direct measurement of the formation of the compound nucleus is possible, the measurements of inelastic cross sections σ_{in} or reaction cross sections σ_r can be used to compare with the theoretical predictions of σ_c. Evidently σ_{in} and σ_r must be smaller than σ_c. The difference $\sigma_c-\bar{\sigma}_r$ is the compound elastic cross section which is expected to be rather small if inelastic scattering or other reactions are strong enough to compete for the decay of the compound state.

Walt and Barschall have determined inelastic scattering cross sections σ_{in} at 1 Mev by subtracting the elastic scattering from the total scattering. The values of σ_{in} should be less than or equal to the theoretical values of σ_c.

Figure 8 shows a comparison between the observed inelastic cross sections and the calculated σ_c at 1 Mev as functions of A. The observed values are of the expected order of magnitude, but they do not agree with the theoretical curve. The absence of the maximum at $A=50$ might be explained by the fact that the compound elastic scattering is relatively high for these nuclei. The same fact explains the low value of the inelastic cross section in lead and bismuth. However, the expected maxima at $A=90$ and 150 seem to occur at higher values of A. We have no explanation for these discrepancies.

There are many measurements of inelastic cross sections at somewhat higher energies. They all indicate that the values are not too far from $\pi(R+\lambda)^2$, which is

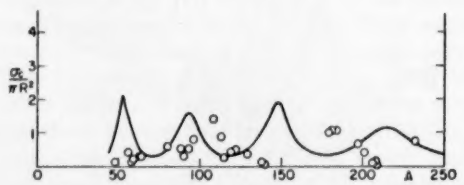

FIG. 8. The calculated cross section σ_c for compound nucleus formation at $E_n=1$ Mev and the observed reaction cross section at 1 Mev as determined by Walt and Barschall. R is taken to be $1.45\times10^{-13}A^{\frac{1}{3}}$ cm. In the calculations the parameters V_0 and ζ were taken to be 42 Mev and 0.03, respectively.

[31] R. S. Carter *et al.*, Phys. Rev. (to be published).
[32] F. G. P. Seidl, Hughes, Palvesky, Levin, Kato, and Sjöstrand, Phys. Rev. **95**, 476 (1954); and private communication.
[33] R. S. Carter and J. A. Harvey, Phys. Rev. **95**, 645(A) (1954).
[34] Foote, Landon, and Sailor, Phys. Rev. **92**, 656 (1953).
[35] Sailor, Landon, and Foote, Phys. Rev. **93**, 1292 (1954).
[36] Pilcher, Carter, and Stolovy, Phys. Rev. **95**, 645(A) (1954); and private communication.
[37] Hughes, Kato, and Levin, Phys. Rev. **92**, 1094 (1953); and private communication.
[38] R. L. Christensen, Phys. Rev. **92**, 1509 (1953).
[39] Melkonian, Havens, and Rainwater, Phys. Rev. **92**, 702 (1953).
[40] L. Bollinger, unpublished data on Sb (private communication). We wish to thank Dr. Bollinger for making his results available in advance of publication.
[41] V. E. Pilcher and R. S. Carter (private communication).
[42] A. Bohr and B. R. Mottelson, Kgl. Danske Videnskab. Selenskab Mat. fys. Medd. **27**, 16 (1953).
[43] This thought was suggested to us by A. Bohr and B. R. Mottelson.

the value one would expect if the neutron wave were totally absorbed in contrast to our findings of $\zeta \sim 0.03$. Especially the measurements at 14 Mev[3] indicate this fact. On the basis of this evidence one would conclude that the value of ζ is strongly energy dependent and reaches a value ($\zeta \gtrsim 0.12$) corresponding to almost total absorption in a medium-sized nucleus certainly at 14 Mev but most likely already at energies as low as 4.5 Mev. The latter conclusion is based upon measurements of inelastic cross sections by Lonsjo, Taylor, and Bonner.[44] In this connection it is interesting that the calculations of Morrison, Muirhead, and Rosser[45] also give a very strong increase with energy of the absorption of nucleons in nuclear matter just in the region which corresponds to incident neutrons of 1 Mev. These calculations are based on the Goldberger method[46] of the scattering of free particles with the application of the Pauli principle. The effect of the exclusion principle alone causes a sharp drop of the energy exchange with decreasing energy.[47]

It is apparent that our model is much less successful in reproducing the strength of compound nucleus formation than in reproducing the total and elastic scattering. It gives too much variation with A of Γ_a/D at low energies and probably too little compound nucleus production at 1 Mev and higher, although it is possible to explain the discrepancies at higher energy by assuming that ζ increases with energy above 1 Mev.

The discrepancies may come from two possible sources: (A) The potential $V(r)$ as given by (3.1) may not be the shape best fitted for the model. (B) The attempt of this paper, the description of the gross behavior of a nucleus by a complex one-particle potential, may be unsuccessful. In connection with (A) it must be noted that the potential (3.1) necessarily is an oversimplified version, since it is physically impossible that the potential well actually has a discontinuity in the form of a sudden jump at $r=R$. It might be that a rounding-off of the corners of the potential well will improve the agreement with experiments.

The smoothing of the edges of the square-well potential was of significance for the interpretation of the elastic proton scattering with heavy nuclei. This scattering has been measured with protons of an energy of about 18 Mev by Gugelot,[48] Burkig and Wright,[49] and by Cohen and Neidigh.[50] The results cannot be interpreted on the basis of a potential (3.1) with sharp edge, as shown by Chase and Rohrlich.[51] However, Woods and Saxon[52] have shown recently that a rounding-off even within the small interval of 0.5×10^{-13} cm changes the results considerably and brings them into much better agreement with the experiments.

It is possible, therefore, that the smoothing of the discontinuity of V at $r=R$ would also improve the agreement of theory and experiment in respect to compound nucleus formation. It would decrease the reflection of the neutron wave at the nuclear surface and hence increase the cross section σ_c when all other constants (V_0,R,ζ) are unchanged. It remains to be seen whether the rounding-off of the potential well improves the agreement with respect to σ_c and Γ_a/D and with respect to the angular distribution of the elastic cross section, without destroying the agreement of the total and elastic cross sections.

Calculations are under way to investigate these possibilities.

It must be pointed out that one should never expect any exact agreement between the predictions based upon a model of this type and the observed cross sections. The very nature of this attempt to describe a complicated many-body problem by a simple one-body potential implies that the model can only contain the main features of the situation. Apart from this general limitation it should be kept in mind that we have used here a potential which has a particularly simple dependence on the radius and on the mass number. We have assumed the same radial dependence for the real and imaginary part which is very probably too strict an assumption. We have neglected spin-dependent forces as observed by Adair and co-workers,[53] and we have excluded any special features connected with the shell structure.

The purpose of the proposed approach is to connect some characteristic salient features of the nuclear cross sections with simple nuclear properties rather than to construct a theory which will produce the exact quantitative details of the observations.

ACKNOWLEDGMENTS

We are greatly indebted to many experimental physicists who in the course of the last few years have discussed with us their results before publication and have helped us adjust our models to the latest values. In particular, we owe special gratitude to H. H. Barschall, M. Walt, and collaborators at Wisconsin; R. K. Adair, J. A. Harvey, D. J. Hughes at Brookhaven; N. Nereson of Los Alamos; and T. W. Bonner of the Rice Institute for their invaluable help and advice and readiness to furnish their newest results.

We also wish to express our gratitude to those who have participated in the important, but tedious, work of computing. Our thanks are offered to Fern Abrams,

[44] Lonsjo, Taylor, and Bonner (private communication). We are grateful to the authors for showing us their results before publication.
[45] Morrison, Muirhead, and Rosser, Phil. Mag. **44**, 1326 (1953).
[46] M. Goldberger, Phys. Rev. **74**, 1269 (1948).
[47] V. F. Weisshopf, Science **113**, 101 (1951).
[48] P. C. Gugelot, Phys. Rev. **87**, 525 (1952).
[49] J. W. Burkig and B. T. Wright, Phys. Rev. **82**, 451 (1951).
[50] B. L. Cohen and R. V. Neidigh, Phys. Rev. **93**, 282 (1954).
[51] D. M. Chase and F. Rohrlich, Phys. Rev. **94**, 81 (1954).
[52] R. D. Woods and D. S. Saxon (private communication). We are grateful to the authors for showing us their results before publication.
[53] Darden, Field, and Adair, Phys. Rev. **93**, 931 (1953).

Harvey Amster, Betty Campbell, Elgie Ginsburgh, Dr. A. Glassgold, Mida Karakashian, Barbara Levine, Edith Moss, Hannah Paul, Evelyn Walker, and Hannah Wasserman at the Massachusetts Institute of Technology; Elaine Scheer at Nuclear Development Associates, Inc.; and Jane Levin and Phyllis Levy at Brookhaven National Laboratory.

One of us (C.E.P.) wishes to acknowledge the helpful cooperation he received at Brookhaven National Laboratory during the final stage of this work prior to publication.

APPENDIX

The Scattering Amplitude at Low Energies

The scattering amplitude η is the diagonal element $S_{\alpha\alpha}$ of the scattering matrix, where the index α refers to the entrance channel. The matrix S is given by the following expression [see Blatt and Weisskopf, formula (X, 4.11)]:

$$S_{\alpha\beta}=\exp[-i(k_\alpha+k_\beta)R]S_{\alpha\beta}'. \tag{A.1}$$

Here R is the nuclear radius, and

$$S'=(1+i\mathfrak{R}')/(1-i\mathfrak{R}'), \tag{A.1a}$$

where $\mathfrak{R}'$ is connected with the derivative matrix $\mathfrak{R}$ by

$$\mathfrak{R}_{\alpha\beta}'=(k_\alpha k_\beta)^{\frac{1}{2}}\mathfrak{R}_{\alpha\beta},$$

and k_α, k_β are the channel wave numbers at the energy E. The matrix $\mathfrak{R}$ is defined on page 545 of Blatt and Weisskopf. It can be expressed in the following form [see Sec. X (4.22)]:

$$\mathfrak{R}_{\alpha\beta}=\sum_s \frac{y_{s\alpha}y_{s\beta}}{E_s-E}, \tag{A.2}$$

where E_s are the resonance energies and the $y_{s\alpha}$ are magnitudes which are connected with the channel widths $\Gamma_\alpha{}^s$ (partial widths for the decay via the channel α):

$$\Gamma_\alpha{}^s=2k_\alpha y_{s\alpha}{}^2. \tag{A.3}$$

Each $y_{s\alpha}$ is real but its sign might be positive or negative. We make the reasonable assumption that the signs are distributed at random.

In what follows we will assume that we work in an energy region for which, first, $k_\alpha R\ll 1$, and, second, $\Gamma^s\ll D_s$, where D_s is the interval

$$D_s=\tfrac{1}{2}(E_{s+1}-E_{s-1}),$$

which includes the resonance E_s from mid-point to mid-point. We also assume that the values $\Gamma_\alpha{}^s$ and D_s have the same order of magnitude for all resonances in an energy interval I which includes many resonances but which is small compared to energy intervals occurring in single-particle problems (say $I\sim 10$ kev for heavy nuclei).

Let us surround each resonance E_s by an energy interval D_s from $\frac{1}{2}(E_{s-1}+E_s)$ to $\frac{1}{2}(E_s+E_{s+1})$. In this interval we can write the matrix $\mathfrak{R}_{\alpha\beta}'$ in the form

$$\mathfrak{R}_{\alpha\beta}'=\frac{y_{s\alpha}'y_{s\beta}'}{E_s-E}+g_{\alpha\beta}, \tag{A.4}$$

where $y_{s\alpha}'=(k_\alpha)^{\frac{1}{2}}y_{s\alpha}$. The matrix $g_{\alpha\beta}$ has no singularities in D_s and is given by

$$g_{\alpha\beta}=\sum_{t\neq s}\frac{y_{t\alpha}'y_{t\beta}'}{E_t-E}. \tag{A.4a}$$

We now estimate the order of magnitude of $g_{\alpha\beta}$. Here it is important to take into account that the signs of the $y_{t\alpha}'$ are distributed at random over the different resonances t and the different channels α.

First we split $g_{\alpha\beta}$ into the contributions of neighboring and far-off levels:

$$\begin{aligned} g_{\alpha\beta}&=g_{\alpha\beta}'+r_{\alpha\beta},\\ g_{\alpha\beta}'&=\sum_{t\neq s}{}'\frac{y_{t\alpha}'y_{t\beta}'}{E_t-E},\\ r_{\alpha\beta}&=\sum_{t\neq s}{}''\frac{y_{t\alpha}'y_{t\beta}'}{E_t-E}, \end{aligned} \tag{A.4b}$$

where the prime on the summation sign means that the sum should be extended only over resonances within the interval I, and the double prime means extension over the resonances outside I. Because of the random signs of $y_{t\alpha}'$, the terms in the sums (A.4b) have random signs for $\alpha\neq\beta$ and only the immediate-neighbor resonances contribute appreciably to $g_{\alpha\beta}$; on the same grounds $r_{\alpha\beta}$ can be neglected. We, then, obtain the estimate:

$$|g_{\alpha\beta}'|\cong|g_{\alpha\beta}|\sim(\Gamma_\alpha\Gamma_\beta)^{\frac{1}{2}}/D,\quad r_{\alpha\beta}\approx 0,\quad \alpha\neq\beta. \tag{A.5}$$

We understand by Γ_α (without superscript) the average value of $\Gamma_\alpha{}^s$ in the interval I. For $\alpha=\beta$, all terms have the same sign for $E_t>E$ or $E_t<E$. Since there are roughly an equal number of levels above and below E_s in the interval I, we get the following estimate:

$$g_{\alpha\alpha}'\sim\Gamma_\alpha/D. \tag{A.5a}$$

The order of magnitude of the contribution $r_{\alpha\alpha}$ from the faraway levels is quite undetermined. However, the scattering cross section between resonances turns out to be $4\pi R^2(1+r_{\alpha\alpha}/x)^2$. Experimentally, we know that this cross section is of the order of $4\pi R^2$, and hence we conclude $r_{\alpha\alpha}\sim k_\alpha R\equiv x$.

It follows from (A.5) and (A.5a) that the $g_{\alpha\beta}$ are all small compared to unity in the energy region considered, and we proceed to expand (A.1) in powers of g. For this purpose we introduce the *factorable* matrix

$$T_{\alpha\beta}=-y_{s\alpha}'y_{s\beta}'/\Delta,\quad \Delta=E-E_s. \tag{A.6}$$

The following relation holds:

$$T^n = B^{n-1}T, \quad n \geqslant 1, \qquad B = \sum_\beta T_{\beta\beta}. \tag{A.7}$$

The quantity B is a number and it is connected with the total width. $\Gamma^s = \sum_\beta \Gamma_\beta{}^s$ of the resonance s:

$$B = -\tfrac{1}{2}\Gamma^s/\Delta. \tag{A.8}$$

Hence, if a matrix is a function of T which can be expressed as a power series with *powers larger than zero*

$$A(T) = \sum_{n=1}^{\infty} a_n T^n,$$

we get the relation

$$A_{\alpha\beta} = B^{-1}A(B)T_{\alpha\beta}. \tag{A.9}$$

We may now expand (A.1), noting that $\mathfrak{R}' \dashv g$:

$$S' = -1 + \frac{2}{1-i(T+g)}$$

$$= -1 + \frac{2}{1-iT} + \frac{1}{1-iT}(2ig)\frac{1}{1-iT} - \frac{2}{1-iT}g\frac{1}{1-iT}g\frac{1}{1-iT} + \cdots.$$

From (A.9) we have $1/(1-iT) = 1 + T/(1-iB)$, so that

$$S' = 1 + \frac{2iT}{1-iB} + 2ig - 2g^2 - 2\frac{(gT+Tg)}{1-iB} + S^*,$$

$$S^* = -2i\frac{TgT}{(1-iB)^2} - 2i\frac{Tg^2+gTg+g^2T}{(1-iB)} - 2\frac{TgTg+Tg^2T+gTgT}{(1-iB)^2} + 2i\frac{TgTgT}{(1-iB)^3}. \tag{A.10}$$

The scattering amplitude η_0 is the diagonal element S_{aa}. We first note the cross sections which would follow from (A.10) when we put $g=0$: ($x = k_a R$)

$$\eta_0 = e^{-2ix}\left(1 + \frac{2iT_{aa}}{1-iB}\right) = e^{-2ix}\left(1 - \frac{i\Gamma_a{}^s}{\Delta + i\Gamma^s/2}\right), \tag{A.11}$$

and hence we get the well-known expressions:

$$\sigma_{el}{}^{(0)} = \pi\lambda^2\left|2x + \frac{\Gamma_a{}^s}{\Delta + i\Gamma^s/2}\right|^2, \qquad \sigma_r{}^{(0)} = \pi\lambda^2\frac{\Gamma_a{}^s(\Gamma^s - \Gamma_a{}^s)}{\Delta^2 + (\Gamma^s/2)^2}. \tag{A.12}$$

We now proceed to neglect all terms in the expansion (A.10) which would give rise to terms in σ_{el} and σ_r of the order of $\delta\sigma_r$ and $\delta\sigma_{el}$, respectively, with

$$\delta\sigma_r = \sigma_e{}^{(0)} f, \quad \delta\sigma_{el} = \sigma_e{}^{(0)} f, \tag{A.13a}$$

where $\sigma_e{}^{(0)} = \pi\lambda^2\Gamma_a\Gamma/[\Delta^2 + (\Gamma^2/4)]$ and f is a small number,

$$f \sim x \quad \text{or} \quad f \sim \Gamma/D. \tag{A.13b}$$

This means we will neglect cross sections which are small by a factor Γ/D or x, compared to $\sigma_e{}^{(0)}$, which can be regarded as the one-level value of the cross section for the formation of the compound nucleus.

It will be shown below that all terms of (A.10) contained in S^* give rise to corrections in the cross sections of the order (A.13) or smaller. Hence, within the accuracy (A.13), we can write S' in the form:

$$S' = 1 + \frac{2iT}{1-iB} + 2ig - 2g^2 - \frac{2(gT+Tg)}{1-iB}. \tag{A.14}$$

To prove this point, we first examine the effect of a small addition $\Delta\eta'$ to $\eta' = S_{aa}'$ on the cross sections: We get

$$\Delta\sigma_{el} = \pi\lambda^2 2\,\mathrm{Re}[(e^{2ix} - \eta')\Delta\eta'^*] \lesssim 4\pi\lambda^2|\Delta\eta'|, \qquad \Delta\sigma_r = \pi\lambda^2 2\,\mathrm{Re}[\eta'^*\Delta\eta'] \leqslant 2\pi\lambda^2|\Delta\eta'|, \tag{A.15}$$

where $\mathrm{Re}(a)$ is the real part of a. The former relation follows from the fact that $|e^{2ix} - \eta'| \leqslant 2$ and the latter relation from the fact that $|\eta'| \leqq 1$. As an example, we discuss the omission of the first term in the expression S^* in (A.10). We find according to (A.5) and (A.5a)

$$|\Delta\eta'| \sim |(TgT)_{aa}/(1-iB)^2| \approx \frac{\Gamma_a\Gamma}{\Delta^2 + (\Gamma^s/2)^2}[(\Gamma/D) + x],$$

and hence the contributions to the cross section of this term are negligible according to (A.15) and (A.13). Similar considerations show that the other neglected terms in (A.10) contribute the same or less to the cross sections.

We now single out the diagonal element of S' because of its significance for the scattering amplitude. We can write S_{aa}' from (A.14) and (A.13b) in the following form:

$$S_{aa}' \cong \exp(2ir_{aa})\left[\left(1 + \frac{2iT_{aa}}{1-iB}\right) + 2ig_{aa}' - 2(g'^2)_{aa} - \frac{4(g'T)_{aa}}{1-iB}\right].$$

This expression differs from the diagonal element of (A.14) by terms which are of the order S^* and therefore negligible, as, for example, $r_{aa}(g'T)_{aa}/(1-iB)$. We

can write it in the form

$$S_{\alpha\alpha}'=\exp(2i\mathbf{r}_{\alpha\alpha})\times\left[1+\frac{2iT_{\alpha\alpha}}{1-iB}+\frac{T_{\alpha\alpha}}{1-iB}G_1+iG_2+G_3\right], \quad \text{(A.14a)}$$

or, according to (A.1)

$$S_{\alpha\alpha}=\eta_0=\exp(-2ik_aR')\times\left[1+\frac{2iT_{\alpha\alpha}}{1-iB}+\frac{T_{\alpha\alpha}}{1-iB}G_1+iG_2+G_3\right], \quad \text{(A.14b)}$$

where

$$R'=R-\mathbf{r}_{\alpha\alpha}/k_a. \quad \text{(A.16)}$$

$$G_1=4\sum_{t\neq s}'\sum_{\beta}\frac{y_{t\alpha}'y_{t\beta}'(y_{s\beta}'/y_{s\alpha}')}{E_t-E},$$
$$G_2=2g_{\alpha\alpha}', \qquad \text{(A.17)}$$
$$G_3=-2(g'^2)_{\alpha\alpha}.$$

This is the form which is used in the text. The orders of magnitude of these real functions are given by (2.11).

The following simplification can be used if one calculates the scattering cross section σ_{el} and the transfer cross sections $\sigma_{\alpha\beta}$ (cross section of the reaction $\alpha\rightarrow\beta$):

$$\sigma_{\alpha\beta}^{(0)}=\pi\lambda^2|S_{\alpha\beta}'|^2 \quad \text{(A.18)}$$

within the limits of accuracy (A.13). It turns out that the last two terms in (A.14) give rise to nonnegligible contributions only to σ_r when expression (2.3a) is used. In expression (2.3) for σ_{el} and in expression (A.18) for $\sigma_{\alpha\beta}$, the two last terms of (A.14) give rise to contributions which can be neglected according to (A.13).[54] Hence for the calculation of $\sigma_{\alpha\beta}^{(0)}$ and $\sigma_{el}^{(0)}$ we may use the shorter form

$$S'=1+[2iT/(1-iB)]+2ig,$$

or

$$S_{\alpha\beta}'\simeq\delta_{\alpha\beta}\exp(2i\mathbf{r}_{\alpha\alpha})+2i\sum_r'\frac{y_{r\alpha}'y_{r\beta}'}{E-E_r+i\Gamma^r/2}, \quad \text{(A.19)}$$

where the sum is extended over all resonances within the interval I. Actually the imaginary part $+i\Gamma^r/2$ in the denominator of (A.16) should be found only in the term $r=s$, but the addition in the other terms leads only to errors smaller than (A.13). We then get for the cross section $\sigma_{\alpha\beta}$

$$\sigma_{\alpha\beta}=\pi\lambda^2|S_{\alpha\beta}'|^2=4\pi\lambda^2\left|\sum_r'\frac{y_{r\alpha}'y_{r\beta}'}{E-E_r+i\Gamma^r/2}\right|^2, \quad \text{(A.20)}$$

and for the scattering cross section,

$$\sigma_{el}=\pi\lambda^2|e^{2i\mathbf{s}}-S_{\alpha\alpha}'|^2,$$
$$=\pi\lambda^2\left|\exp(2ik_aR')-1+\sum_r\frac{i\Gamma_\alpha{}^r}{E-E_r+i\Gamma^r/2}\right|^2. \quad \text{(A.21)}$$

According to (A.19), the value of $\sigma_{\alpha\beta}$ goes to zero between two resonances E_s and E_{s+1} if the sign of $y_{s\alpha}'y_{s\beta}'$ is the same for both resonances. If the sign is opposite, no zero occurs. Note that this statement is good only to the accuracy (A.13). At the zero of (A.17) the actual cross section might still be of the order (A.13).

We note in (A.21) that the potential scattering amplitude $\exp(2ikR')-1$ corresponds to the scattering by an impenetrable sphere of radius R' as given by (A.16). The quantity R' itself is a function of the energy, which is slowly varying and changes only over intervals much larger than D.

The forms (A.15) and (A.16) correspond to the Breit-Wigner formulas used in the literature before the more exact investigations by Wigner and Eisenbud.[55] The amplitudes contain characteristic sums over the contributions of the different resonances with the imaginary contribution $i\Gamma^r/2$ in the denominator. It has been pointed out repeatedly that the forms (A.17) and (A.18) are not exactly correct. We have shown, however, that they are valid within the errors given by (A.13).

[54] At first sight this seems puzzling since $\sigma_r=\Sigma_\beta\sigma_{\alpha\beta}$. It must be remembered that Eq. (2.3a) uses the diagonal element of S; whereas (A.18) uses off-diagonal elements. The connection between these elements is established by the unitary nature of S: $1-|S_{\alpha\alpha}|^2=\Sigma_{\beta\neq\alpha}(S_{\alpha\beta})^2$. In order to insure the validity of this equation up to the order g^2, one must include the last two terms of (A.14) in $S_{\alpha\alpha}$, but it is not necessary to include them in $S_{\alpha\beta}'$.

[55] E. P. Wigner and L. Eisenbud, Phys. Rev. 72, 29 (1947).

Long-Lived Radioactivity of Eu^{152} and Eu^{154}

R. E. SLATTERY, D. C. LU, AND M. L. WIEDENBECK
Randall Laboratory of Physics, University of Michigan, Ann Arbor, Michigan
(Received May 10, 1954)

The long-lived activity of $Eu^{152,154}$ has been examined by means of a thin-lens coincidence spectrometer and a crystal-summing spectrometer. Decay schemes are given for Eu^{152} and Eu^{154}.

NATURAL europium consists of two isotopes, Eu^{151}(47.77 percent) and Eu^{153}(52.23 percent), which when subject to neutron irradiation transform to Eu^{152} and Eu^{154} by means of the (n,γ) reaction. Both Eu^{152} and Eu^{154} have half-lives of the order of years, with the exact values being uncertain at present.[1–3] In addition, Eu^{152} has a second, 9.2-hour decay, which seems fairly well understood.[4,5]

The decay of the long-lived $Eu^{152,154}$ mixture has been examined by many authors,[5–9] but up to now, no satisfactory decay scheme has existed. Previous workers have identified at least two beta decays and many gamma transitions. These latter are commonly assigned the following energies: 122, 123, 244.3, 336.4, 344, 412, 720, 778, 964, 1086, 1116, and 1402 kev.

In the present work, the beta spectra of the $Eu^{152,154}$ mixture were re-examined, and coincidence studies were made between conversion lines, the conversion lines and the beta spectra, and between the gamma radiations. This information, combined with a knowledge of isotopic assignments drawn from other sources, permits a reasonable ordering of the Eu^{152} and Eu^{154} decay schemes.

APPARATUS

The information gathered here was obtained by means of two separate instruments: a thin-lens coincidence spectrometer and a crystal-summing spectrometer.

The thin-lens coincidence spectrometer consists of two thin-lens spectrometers on a common axis and tube, and with a common source. The individual thin-lens instruments are of conventional design, utilize ring focusing,[10] and are each capable of resolutions of about 2.0 percent. The instrument proper is horizontally mounted in a north-south direction to reduce effects due to the horizontal component of the earth's field. The vertical component is compensated by means of Helmholtz coils. It was found that during operation, the individual focusing coils of the two component spectrometers coupled with each other. The total coupling was less than one percent, and could be easily compensated for in practice. A Garwin circuit[11] of 0.28 microseconds resolving time was used to register coincidences between the Geiger tube detectors of the individual thin-lens instrument.

With a thin-lens coincidence spectrometer of this type, it is possible to utilize either of the component thin-lens instruments in the normal fashion, and to measure coincidences between conversion lines and also between conversion lines and the continuous beta spectrum. A feature of this instrument is the narrowing of coincidence peaks due to source thickness and source size. (A similar effect has been noted for the 180° coincidence spectrometer of Fowler and Shreffler.[12])

Coincidences between gamma rays were observed by means of the crystal summing technique previously described.[13] A thallium-activated sodium iodide crystal, with a 3-mm diameter hole drilled to its center, is coupled to a Dumont 6292 phototube, and the pulses are examined by means of a single-channel discriminator. The gamma-ray spectrum is first examined with the source outside the crystal (i.e., in the normal fashion) and then with the source inserted into the hole. Coincident gamma rays or x-rays, which appear as individual peaks in the first case, add in the second to show a new peak, whose energy is the sum of the contributing peak energies. Similar results are obtained for triple and quadruple coincidences. When this "summing" process takes place, the individual contributing peaks disappear in whole or in part.

The source used in this work was generously provided by Professor J. M. Cork of this university, and is the remains of the material used by Cork, Shull, and Fowler, and is at least five years old. In the thin-lens spectrometer work, the source was evaporated onto a double-layer zapon backing (0.034 mg/cm²) and covered with a double layer of zapon. In the case of the crystal summing study, the source was enclosed in a Lucite container.

[1] Hayden, Reynolds, Inghram, Phys. Rev. **75**, 1500 (1949).
[2] Karraker, Hayden, and Inghram, Phys. Rev. **87**, 901 (1952).
[3] E. E. Lockett and R. H. Thomas, Nucleonics **11**, No. 3, 15 (1953).
[4] H. B. Keller and J. M. Cork, Phys. Rev. **84**, 1079 (1951).
[5] J. M. Hill and L. R. Shepherd, Proc. Phys. Soc. (London) **A63**, 126 (1950).
[6] Cork, Shreffler, and Fowler, Phys. Rev. **72**, 1209 (1947) **73**, 78 (1948).
[7] F. B. Shull, Phys. Rev. **74**, 917 (1948).
[8] Cork, Keller, Rutledge, and Stoddard, Phys. Rev. **77**, 848 (1950).
[9] L. J. Shavtvalov, J. Exptl. Theoret. Phys. (U.S.S.R.) **21**, 1123 (1950).
[10] Keller, Koenigsberg, and Pashin, Rev. Sci. Instr. **21**, 713 (1950).
[11] R. L. Garwin, Rev. Sci. Instr. **21**, 569 (1950).
[12] C. Fowler and R. Shreffler, Rev. Sci. Instr. **21**, 740 (1950).
[13] D. C. Lu and M. L. Wiedenbeck, Phys. Rev. **94**, 501 (1954).

RESULTS

Figure 1 shows the beta spectrum of $Eu^{152,154}$ as measured by the south thin-lens spectrometer. The resolution is 2.2 percent as determined from the K conversion line of the 663-kev transition in Cs^{137}. The conversion peaks are identified. It will be noted that there is a large difference in height between the unresolved 122- and 123-kev peaks and the remainder of the conversion lines. The energies of the unobscured peaks are 244.0 and 343.3 kev in good agreement with previous authors.

Figure 2 is a Kurie plot of the beta spectrum. The high-energy end point is at 1.45±0.05 Mev, followed by a second spectrum with a 0.70±0.03-Mev end point. These values are somewhat lower than those measured by previous workers. (Shull quotes 1.575±0.15 and 0.75±0.015, respectively.) In addition, a third beta spectrum with an end-point energy of 0.330±0.100 Mev is seen. This last beta spectrum must be classified as doubtful, since a second Kurie plot subtraction leads to greatly increased errors. Also, the region in which it is measured contains many conversion electrons, with the accompanying possibility of scattering. In order to minimize this scattering, the beta spectrum has been plotted exclusively from points near the high-energy edge of conversion lines.

Using the thin-lens coincidence spectrometer, coincidences between the conversion lines and the beta spectrum were examined. No coincidences were found between either the 122- or 123-kev L conversion lines and the beta spectrum, or between the 244-kev K conversion line and the beta spectrum. Coincidences were found between the 344-kev K conversion line and the continuous beta spectrum. The coincidence beta spectrum was plotted by fixing the north thin-lens spectrometer on the 344-kev K conversion line and sweeping the south thin-lens spectrometer across the beta spectrum. The resulting Kurie plot is shown in Fig. 3. It will

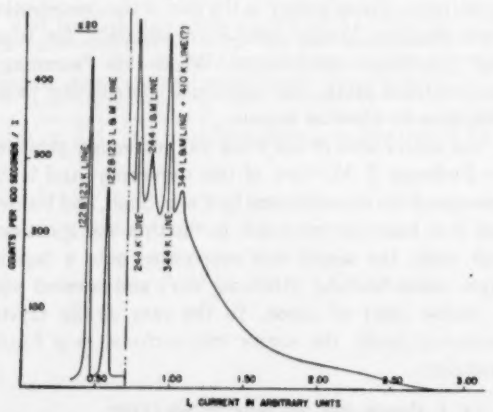

FIG. 1. The beta spectrum of $Eu^{152,154}$. Note the difference in height between the 122+123 conversion peaks and all other peaks.

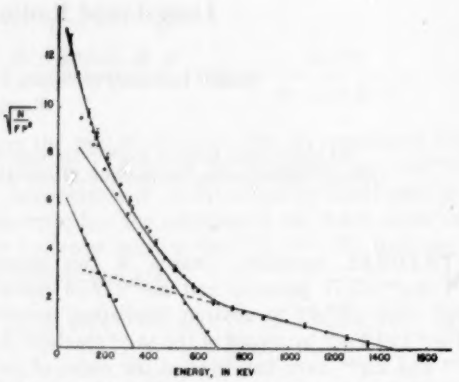

FIG. 2. Kurie plot of the beta spectrum of $Eu^{152,154}$.

be seen that the 344-kev transition is unambiguously in coincidence with the 0.70-Mev end-point beta spectrum. Shavtvalov[9] has noted similar coincidences, which he attributed to either the 336- or 344-kev gamma-ray line. Examination of our data and Shull's data indicates that the 336-kev gamma ray is not contributing to the coincidences. In fact, we have not seen any such transition.

Coincidences were then sought between conversion peaks. Either the 122- or 123-kev gamma ray (unresolved in this work) was found to be in coincidence with the 244-kev transition. No other coincidences were noted. This disagrees with certain previous workers, but has been confirmed by the crystal summing data.

The crystal summing data with the principal peaks identified are shown in Fig. 4. Due to the Lucite source container, a certain amount of the continuous beta spectrum is detected in the "summing" spectrum; this accounts for the increased background. From this data, the following results will be noted:

1. Part of the 122- and 123-kev peak (unresolved) is in coincidence with a 39-kev x-ray from K capture, as indicated by the sum peak at 162 kev on the "summing" spectrum.

2. Part of the 122- and 123-kev peak is *not* in coincidence with an x-ray, since it fails to disappear completely on the "summing" spectrum as would otherwise be required. Hence one of the 122- and 123-kev radiations follows K capture; the other does not. This is further indicated by the fact that no coincidence was observed between the 122- and the 123-kev radiations, a fact confirmed by both instruments.

3. The 244-kev transition appears to be in coincidence with an x-ray. (It disappears completely in the "summing" spectrum, and hence must be in coincidence with something of *low* energy.)

4. The 244-kev gamma ray is in coincidence with 122- or 123-kev gamma ray.

5. The 344-kev gamma ray is not in coincidence with anything (i.e., it is unchanged in the two spectra).

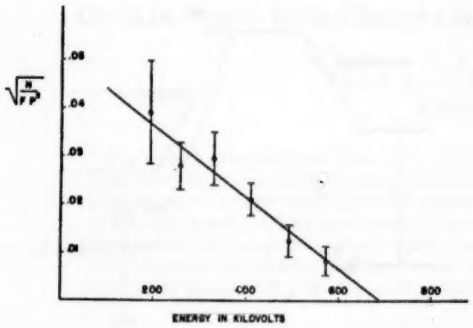

FIG. 3. Kurie plot of the beta spectrum with 0.70-Mev end point plotted from coincidences with the K conversion of the 344-kev transition.

6. An indication of the 410-kev gamma ray is seen, but if any coincidences with it occur, they are obscured by other peaks.

7. A 720-kev peak occurs in the normal spectrum, but any possible coincidences with lower-energy gamma rays are obscured by other peaks in the "summing" spectrum.

8. A large sum peak appears in the "summing" spectrum at ~1140 kev. It will be noted that 720+244 +122 or 123+39≈1140, and that 964+122 or 123+39 is also ≈1140. In these sums, 39 kev is the K x-ray energy of samarium.

9. A 778-kev line occurs, but it is not in coincidence with anything.

10. A 964-kev line is seen in the normal spectrum. Its partial disappearance in the "summing" spectrum assures that it is in coincidence with something. The broadening at the low-energy base of the 1140-kev sum peak indicates that it is probably in coincidence with an x-ray (also see 8 above).

11. The 1086- and 1116-kev peaks are seen in the normal spectrum, but are unresolved.

12. Sum peaks equal to 1086 kev plus two x-rays and to 1086 plus 122 or 123 kev plus an x-ray are seen.

13. A 1415-kev peak is seen in the normal spectrum.

14. Sum peaks equal to 1415 kev plus an x-ray and to 1415 plus 122 or 123 are seen. No peak equal to 1415 plus 122 or 123 plus an x-ray is seen. Hence 1415 is in coincidence with 122 or 123 or its conversion x-ray, but not with a K-capture x-ray.

ISOTOPIC ASSIGNMENTS

The following isotopic assignments are made by Katz and Lee[14] and shall be adhered to in constructing the decay schemes: the 344, 244, and 122-kev gamma rays belong to the isotope of mass 152; the 1116- and 123-kev gamma rays belong to the isotope of mass 154. This is confirmed by the coincidence measurements made here and by information received privately from Church.[15] Katz's results are based on enriched isotopes, and Church's upon the relative intensity of conversion lines from bombarded and from fission product sources. Church also finds that the 123-kev line is internally converted in gadolinium. In addition, Hill and Shepherd[5] found no positrons from the $Eu^{152,154}$ mixture to one part in four thousand.

This information, combined with the data described above, allows decay schemes to be drawn for Eu^{152} and Eu^{154}.

DECAY SCHEME OF Eu^{152}

The decay scheme for Eu^{152} is shown in Fig. 5. The 122- and 244-kev gamma rays are known to belong to the isotope of mass 152; hence the 244-kev transition must be in coincidence with the 122- and not the 123-kev transition. Since neither the 122- nor the 244-kev gammas are in coincidence with the beta decay, and since they are in coincidence with an x-ray, they are assigned to the K-capture branch of the 152 isotope. The quadruple coincidence of 720, 244, and 122-kev

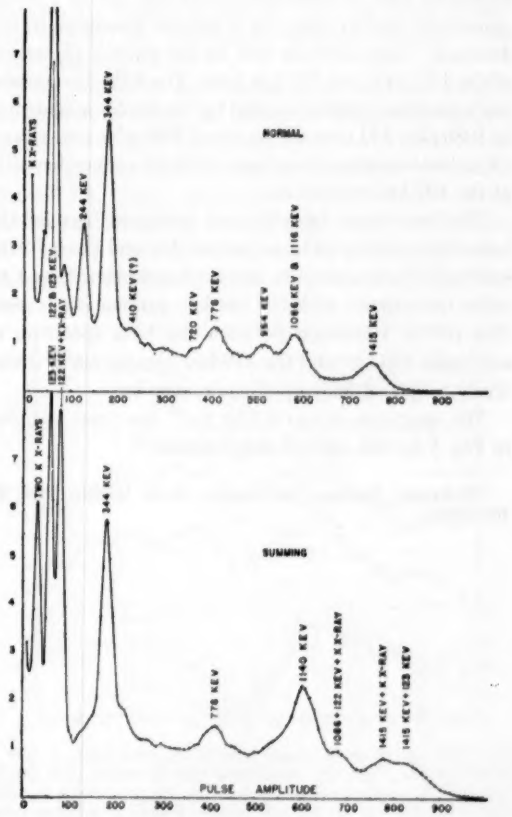

FIG. 4. The normal gamma-spectrum (upper curve) and "summing" spectrum (lower curve) of $Eu^{152,154}$ measured with a crystal summing spectrometer.

[14] R. Katz and M. R. Lee, Phys. Rev. **85**, 1038 (1952).

[15] E. L. Church, Argonne National Laboratories (private communication).

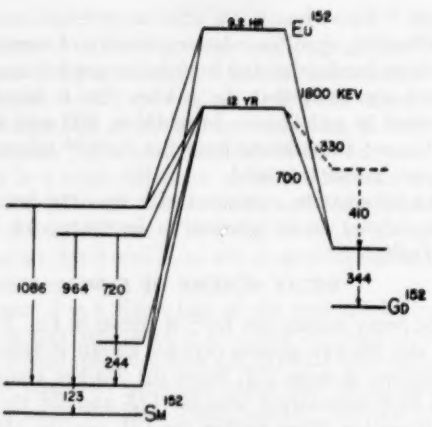

FIG. 5. Proposed decay scheme for Eu^{152}.

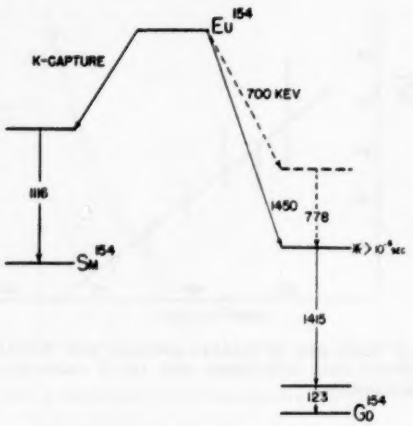

FIG. 6. Proposed decay scheme for Eu^{154}.

gamma rays with the x-ray places them in the position shown. The energy fit of the 964-kev gamma ray, combined with its coincidence with the 122- or 123-kev gamma ray and an x-ray, fits it into the scheme as drawn. Intensity considerations lead to the relative placement of the 122, 244, and 720-kev lines. The 1086-kev gamma ray's position is demonstrated by the triple coincidences of 1086 plus 122 plus an x-ray and 1086 plus two x-rays. (The latter comes about from the high conversion ratio of the 122-kev transition.)

The beta-decay branch is as indicated because the coincidence of the 344-kev gamma ray and the 0.7-Mev end-point beta spectrum has been established, and no other coincidence with the 344-kev gamma ray is seen. The dotted transition between the beta spectrum of end point 300 kev and the 410-kev gamma ray is tentatively proposed because of the energy fit.

The spectrum of the 9.2-hr Eu^{152} has been included in Fig. 5 for the sake of completeness.[16]

[16] Hollander, Perlman, and Seaborg, Revs. Modern Phys. 25, 469 (1943).

DECAY SCHEME FOR Eu^{154}

The decay scheme for Eu^{154} is shown in Fig. 6. The coincidence of the 123- and 1415-kev gamma rays has been demonstrated. However no coincidences between the 123-kev gamma ray and either a K-capture x-ray or the continuous beta spectrum exists. Since the 123-kev gamma ray is converted in Gd^{154},[15] the beta-decay branch is constructed as shown with the *delay* indicated. The dotted transition is made purely on the basis of energy fit and represents the possibility that the beta spectrum of 0.7-Mev end point actually consists of two spectra of almost identical end points, one occurring in Eu^{152}, the other in Eu^{154}. Both the 778- and 410-kev gamma transitions are dotted in this work. They have been seen only by Cork, Shull, and ourselves using the same source material, and could be due to contamination caused by other rare earths.

Although no coincidences between the 1116-kev gamma ray and an x-ray are seen, they would be obscured by the large 1140-kev "sum" peak. This gamma ray is known to belong to the isotope of mass 154 and does not fit into the beta decay branch. Hence it probably results from K capture in Eu^{154}.

Cycle of World-Wide Changes in the Daily Variation of Meson Intensity

V. SARABHAI, U. D. DESAI, AND D. VENKATESAN
Physical Research Laboratory, Ahmedabad, India

(Received May 13, 1954)

The study by Sarabhai and Kane of the world-wide changes in the daily variation of meson intensity has been extended by an analysis of unpublished Carnegie Institution data, kindly supplied by Dr. Forbush. Comparison of Carnegie Institution measurements at Huancayo and Cheltenham for the period 1937 to 1952 reveals high correlation between changes of the times of maxima at the two stations. The changes of amplitudes of the daily variations are not equally consistently related. The change of intensity of the coronal 5303A emission line exhibits the major features seen in the change of the daily variation of meson intensity. Both follow the usual 11-year solar cycle of activity.

SARABHAI and Kane,[1] in a paper later referred to in this article as I, have shown, by an examination of the Carnegie Institution data[2] for the period 1937 to 1946, large world-wide changes in the amplitude and the time of maximum of the daily variation of meson intensity, corrected for barometric pressure. These changes were found to follow the broad pattern of the eleven-year solar cycle. In a later communication, Thambyahpillai and Elliot[3] have drawn attention to the progressive change, from 1940 to 1952, of the time of maximum of the daily variation to earlier hours. They have compared data from different types of instruments at different periods and have suggested a twenty-two-year cycle of change.

Directional studies made at Stockholm and Manchester and recent work at Ahmedabad clearly reveal the dependence of the time of maximum $M\phi^D$ and the amplitude M^D of the diurnal component of the daily variation of mesons on the sensitive cone of the measuring instrument and its orientation. The treatment of results from ionization chambers and counter telescopes on a directly comparable basis therefore appears questionable. A test of this, and further extension of our earlier studies have now been made possible by the supply of unpublished data covering 1946 to 1953 from the Carnegie Institution stations, through the kind generosity of Dr. Forbush.

Figures 1 (a) and (b) show the changes of M^D and $M\phi^D$ computed from the annual mean daily variation centered at successive bimonthly epochs. Unlike the treatment in I the present authors have not smoothed out their results by taking moving averages over three successive bimonthly values. Uninterrupted data are available for Huancayo and Cheltenham from 1936 to 1953, while for Christchurch there is a large gap from 1st July 1942 to 30th April 1946 due to irregular stoppages.

An examination of Fig. 1 reveals that:

(1) The changes in the amplitude M^D at the different stations do not appear to be well correlated except during the period 1940–1946. For Christchurch and Cheltenham which are sea-level stations at comparable latitudes south and north of the equator, respectively, the changes in amplitude are better related than between either station and Huancayo. The prominent disturbance in 1943 followed by a quiet period in 1944 is strikingly revealed in all curves.

(2) The changes in time of maximum $M\phi^D$ at all stations are highly correlated. For the entire fifteen-year period, the correlation between Huancayo and Cheltenham is 0.93.

The change in the annual mean relative sunspot number R, centered at successive bimonthly epochs, is shown in Fig. 1 (c). Alongside are also given corresponding values of the total solar emission of the coronal line 5303 A. These have been computed, after interpolating at bimonthly intervals, from the observations of Waldmeier[4] at different epochs. It is clearly seen that changes of $M\phi^D$ follow the normal solar cycle, there

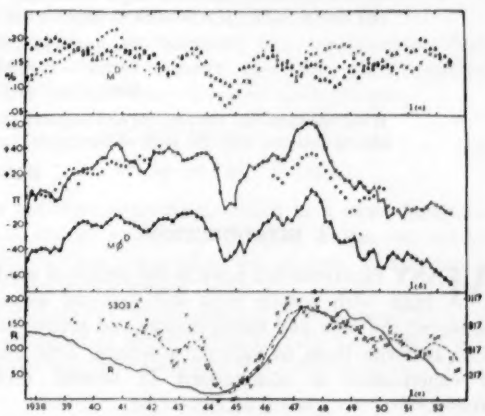

FIG. 1. Time series for annual mean values during 1937–1953 of (a) M^D, meson diurnal amplitude; (b) $M\phi^D$, meson diurnal time of maximum; (c) R, Zurich relative sunspot number and total emission of 5303-A coronal line. In (a) and (b) the results from individual stations are indicated by ▲ for Huancayo, × for Cheltenham, and ● for Christchurch. In (c), × indicate the values of coronal emission reported by Waldmeier. In (b), π in the ordinate relates to 1300 hours instead of noon.

[1] V. Sarabhai and R. P. Kane, Phys. Rev. **90**, 204 (1953).
[2] I. Lange and S. E. Forbush, Carnegie Institution of Washington Publications, No. 175, 1948.
[3] T. Thambyahpillai and H. Elliot, Nature **171**, 918 (1953).
[4] M. Waldmeier, Z. Astrophys. **26**, 264 (1949).

being no evidence for a twenty-two year period. While the mechanism of solar control is still obscure, we have earlier interpreted the new results as indicative of continuous solar emission of cosmic rays and changes of $M\phi^D$ as caused by magnetic bending of the trajectories of charged solar particles. The consistent world-wide character of changes of $M\phi^D$ is then not surprising.

Coronal emission in 5303 A is the most satisfactory index we know for activity in solar cosmic-ray emission. This is demonstrated strikingly in 1943, and in the pronounced shift of $M\phi^D$ in 1947 to later hours. Therefore, Simpson's observations with neutrons relating to low-energy primaries and the daily variation of mesons related to a more energetic primary component both lead to the same conclusion. They must focus our attention on the solar corona for an understanding of the processes of continuous cosmic-ray emission from the sun.

We are deeply indebted to Dr. S. E. Forbush and to Professor Waldmeier for furnishing the unpublished data, which have made the present study possible. It is a pleasure to acknowledge assistance from Mr. K. A. Gidwani, Mr. Duggal, and Mr. Bhatt, and support from the Atomic Energy Commission of India.

PHYSICAL REVIEW VOLUME 96, NUMBER 2 OCTOBER 15, 1954

Precision Measurement of the Negative Pion Mass from Its Radiative Absorption in Hydrogen*†

KENNETH M. CROWE‡ AND ROBERT H. PHILLIPS§
Radiation Laboratory, Department of Physics, University of California, Berkeley, California
(Received March 9, 1954)

The gamma-ray spectrum of the reaction

$$\pi^- + p \rightarrow n + \gamma$$

has been remeasured with an improved design of the high-energy pair spectrometer. This design has taken advantage of one of the focusing properties of a 90-degree wedge-shaped magnetic field to minimize the effect on the resolving power of multiple scattering of the pair fragments in the converter. The theory of the spectrometer is developed in detail. The accuracy of the energy scale depends on magnetic field measurements and the calculation of orbits, aberrations, and resolving power. By the determination of the mesonic absorption gamma-ray energy, a precise mass value for the negative pion has been found:

$$M_{\pi^-} = 272.7 \pm 0.3 m_e.$$

From the $\pi^- - \pi^0$ mass differences already obtained by Panofsky, Aamodt, and Hadley (PAH), by Chinowsky, Sachs, and Steinberger (CSS), and the $\pi^- - \mu^-$ mass difference obtained by Lederman, Tinlot, and Booth (LTB), it is possible to improve the mass values for the π^0 and the μ^- mesons.

From $\pi^- - \pi^0$ (PAH): $M_{\pi^0} = 262.2 \pm 2.0\ m_e$;
from $\pi^- - \pi^0$ (CSS): $M_{\pi^0} = 263.9 \pm 0.7\ m_e$;
from $\pi^- - \mu^-$ (LTB): $M_{\mu^-} = 206.7 \pm 3.0\ m_e$.

If one assumes that the positive and negative pions have the same mass, the mass of the positive muon can also be deduced from the work of Birnbaum, Smith, and Barkas:

$$M_{\mu^+} = 206.3 \pm 0.3\ m_e.$$

I. INTRODUCTION

MANY experimenters have in the course of studies both with cosmic rays and artificial sources, measured the pion and muon masses and several relations between them to varying accuracy. This group of experiments is summarized in several review articles.[1-3]

To date only one of these experiments, other than the present work, has been carried to an accuracy better than a half percent (~1 electron mass). This experiment was started by the late Dr. Eugene Gardner several years ago, and has been carried on by the nuclear emulsion group at Berkeley[4]; results have appeared at various stages of completion.[5]

Since the mass relations obtained in this manner will

* Presented by K. M. Crowe in partial fulfillment of the degree of Doctor of Philosophy.
† This work was done under the auspices of the U. S. Atomic Energy Commission.
‡ Now at Stanford University, Stanford, California.
§ Now at Brookhaven National Laboratory, Upton, New York.
[1] C. F. Powell, Repts. Progr. Phys. **13**, 350 (1950).
[2] Hugh Bradner, University of California Radiation Laboratory Report No. UCRL-486, 1949 (unpublished).
[3] W. K. H. Panofsky and K. M. Crowe in *Experimental Nuclear Physics*, edited by E. Segrè (John Wiley and Sons, Inc., New York), Vol. III (in preparation).
[4] Smith, Barkas, Bradner, and Gardner, Phys. Rev. **78**, 86 (1950); Bradner, Smith, Barkas, and Bishop, Phys. Rev. **77**, 462 (1950); Barkas, Smith, and Gardner, Phys. Rev. **82**, 102 (1951).
[5] Birnbaum, Smith, and Barkas, Phys. Rev. **83**, 895 (1951); Phys. Rev. **91**, 765 (1953); and W. Birnbaum (to be submitted to Revs. Modern Phys.).

be used to derive the muon mass, we will briefly sketch the methods involved and give their current results.

The basic method of the Gardner mass-measurement technique assumes that one can compare directly the purely electromagnetic interactions of the meson and the proton. This is done by a precise measurement of the ratio of the ranges in the same nuclear emulsions and at the same time measuring the ratio of the momenta as defined by the orbits in the cyclotron magnetic field (Fig. 1).

By choosing the proper orbits it is possible to eliminate from the mass calculation the details of the energy loss relations if one makes the usual assumption that the energy loss depends only on the velocity of the particles.

A comprehensive summary of the theory for this method is described by Barkas.[6] It will suffice to point out that the major source of error appearing in the measurement is statistical and results from the range straggling producing a distribution in the final mass ratio. The results of these measurements are as follows[7]:

$$M_{\pi^+}=273.3\pm0.2\ m_e, \tag{1}$$

$$M_{\pi^-}=272.7\pm0.3\ m_e. \tag{2}$$

An additional experiment which compares positive decay muons with pions permits the accurate evaluation of mass difference. One assumes the decay reaction to be

$$\pi^+\rightarrow\mu^++\nu. \tag{3}$$

The derived $\pi^+-\mu^+$ mass difference depends on the decay momentum and the mass ratio and is found to be[5]

$$M_{\pi^+}-M_{\mu^+}=66.41\pm0.07\ m_e. \tag{4}$$

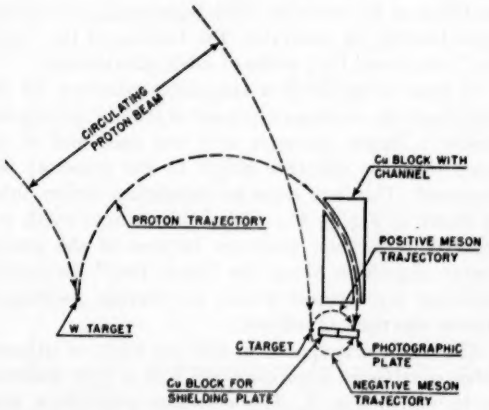

FIG. 1. Diagram illustrating geometry of experiment to measure meson to proton mass ratios by the Gardner technique.

[6] Walter H. Barkas, University of California Radiation Laboratory Report No. UCRL-2327, 1953 (to be submitted to Revs. Modern Phys.); Walter H. Barkas, Am. J. Phys. **20**, 5 (1952).

[7] Frances M. Smith, University of California Radiation Laboratory Report No. UCRL-2371, 1954 (to be submitted to Revs. Modern Phys.).

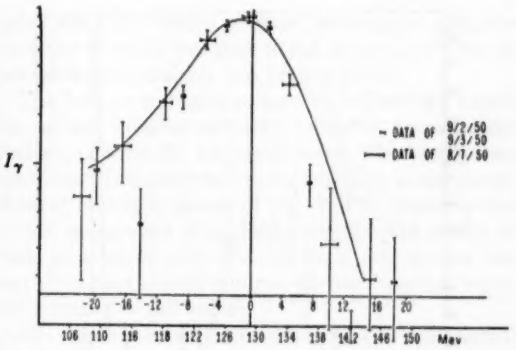

FIG. 2. The gamma-ray energy spectrum with the theoretical resolving power used in previous π^- mass measurements. The resolution does not include ionization loss, converter horizontal width corrections, or energy scale corrections due to fringe field. Probable errors are shown.

The error of this measurement involves the statistical distribution caused by range fluctuations. An absolute field measurement is necessary for calculating the decay momentum and was made with a nuclear induction fluxmeter.

The decay in flight of π^- mesons has been observed in a cloud chamber by Lederman, Tinlot, and Booth.[8] The momenta of the π^- and μ^- were measured and from the kinematics they obtained a mass difference for negative mesons,

$$M_{\pi^-}-M_{\mu^-}=66.0\pm3.0\ m_e. \tag{5}$$

Since the current measurement of the negative pion mass was an outgrowth of the work of Panofsky *et al.*,[9] we shall also briefly summarize their mass measurement results.

By using a multichannel pair spectrometer, they measured the gamma-ray spectrum which resulted when π^- mesons came to rest in hydrogen gas.

$$\begin{aligned}&\pi^-+p\rightarrow n+\gamma,\\ &\pi^-+p\rightarrow n+\pi^0,\quad \pi^0\rightarrow 2\gamma.\end{aligned} \tag{6}$$

The radiative absorption results in a monochromatic line of energy approximately equal to the rest energy of the pion less the recoil of the neutron. The spectrum they obtained is shown in Fig. 2.

The energy of this gamma ray was evaluated knowing the geometry of the detectors and the magnetic field of the spectrometer, and from this they obtained a mass

$$M_{\pi^-}=275.2\pm2.5\ m_e. \tag{7}$$

In the subsequent analysis of the spectrometer used in the current measurement, several small corrections were made which were omitted in the above mass value, the major one being the ionization loss of the pair frag-

[8] Lederman, Tinlot, and Booth, Phys. Rev. **81**, 281 (1951).

[9] Panofsky, Aamodt, and Hadley, Phys. Rev. **81**, 565 (1951), and private communications; Phys. Rev. **80**, 94, 282 (1950); Panofsky, Aamodt, and York, Phys. Rev. **78**, 89 (1950).

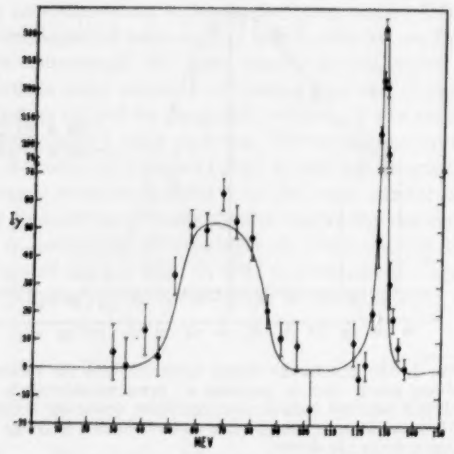

FIG. 3. Composite plot of γ-ray spectrum resulting from the capture of negative pions in hydrogen. Note that the scale of the ordinate is expanded by a factor of five below $I_\gamma=75$ Mev to show details of the π^0 peak.

ments leaving the converter. The corrected value should be $\sim 278\ m_e$. The error of this measurement has not been reanalyzed since there is considerable uncertainty in such an analysis without extensive remeasurements of the magnetic field.

From the branching into π^0 and subsequent Doppler shift of the decay gamma rays, they were able to establish the difference between the masses of the charged and neutral pion,

$$M_{\pi^-}-M_{\pi^0}=10.5\pm 2\ m_e. \tag{8}$$

The error of this measurement results almost entirely from the small number of events as seen from Fig. 3, a composite plot of the previous results and the present radiative capture line. A further improvement in the accuracy of neutral meson mass would be possible by a remeasurement of this π^0 spectrum.

Chinowsky, Sachs, and Steinberger[10] have studied the angular correlation of the gamma rays of the reaction Eq. (6). The aberration of the decay gamma rays caused by the motion of the π^0 has yielded a precise measure of the mass difference,

$$M_{\pi^-}-M_{\pi^0}=8.8\pm 0.6\ m_e. \tag{9}$$

II. THE FOCUSING PAIR SPECTROMETER AND THE EXPERIMENTAL METHOD

The absorption equipment shown in Fig. 4 was the same as that used by Panofsky *et al.*[9] Mesons which are produced at the cyclotron target stop in a vessel (Fig. 5) filled with hydrogen. The resulting gamma-ray spectrum is measured with a pair spectrometer. A background spectrum is measured when the vessel is evacuated, and this is subtracted off.

The improvement in resolution of the spectrometer was accomplished by redesigning the detection array in such a way as to achieve a refocusing in the horizontal plane for particles which have multiply scattered when leaving the converter. The location of the "focus line" was found by a series of orbit calculations.

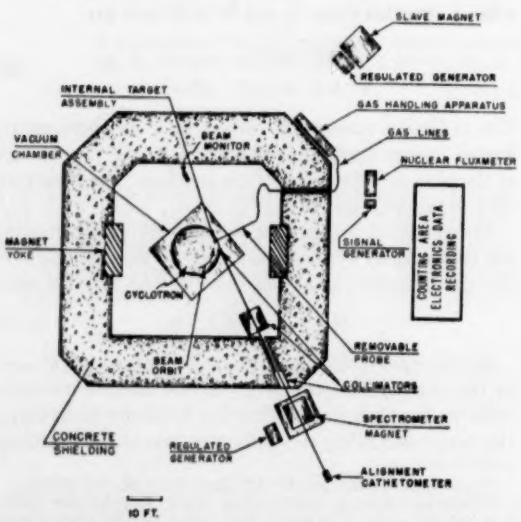

FIG. 4. The general layout of the experimental apparatus.

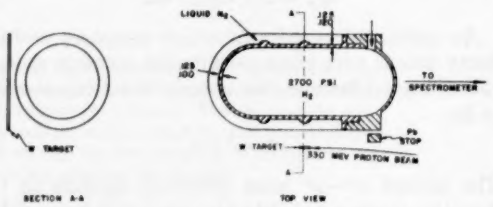

FIG. 5. Internal hydrogen target assembly. The vessel walls are stainless steel.

In order to maintain a reasonable efficiency for the spectrometer—necessary because of the low gamma-ray yields—a larger converter area was used and at the same time the effective height of the detectors was increased. This was done by paralleling Geiger tubes as shown in Fig. 6. The size of the channel width was reduced in the new geometry because of the greater energy dispersion along the "focus line." To further minimize the channel width, an overlap coincidence system was used as follows:

The tubes were spaced so that the edges of adjacent tubes overlapped approximately $\frac{1}{3}$ of a tube diameter as shown in Fig. 7. The detection electronics were arranged so that events in which a particle passed through the overlap portion of the tube could be distinguished from those passing through the central $\frac{1}{3}$ or nonoverlap portion of the tube.

The block diagram of the electronics is shown in Fig. 8. The gating of Geiger-tube outputs by the require-

[10] Chinowsky, Sachs, and Steinberger, Phys. Rev. **93**, 917 (1954).

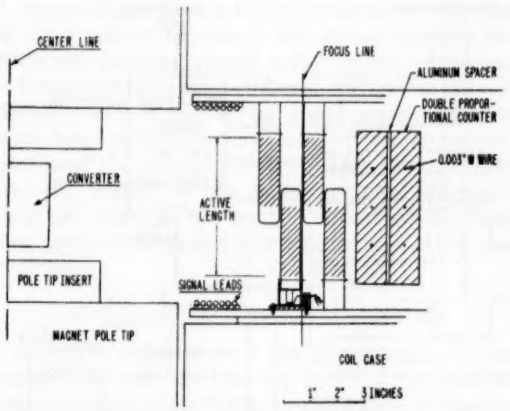

FIG. 6. The side view (cross section) of the tube holder, magnet pole tip, and multiwire proportional counter. The Geiger counters straddle the focus line.

ment of a quadruple coincidence between proportional counters backing up the Geiger-tube banks was used to eliminate accidental background as in the previous spectrometer design of Panofsky *et al.*[9] The Geiger-tube outputs were observed visually with numbered neon lights. The losses which occurred because of rapid flurries of counts (less than 10 percent of total counts) presumably are a random sample of events. The numbering system for the Geiger-tube channels is not easily converted by the observer to the gamma-ray energy so that the observer is in no way prejudiced in which energy events he rejects or misses.

The design of the counter holder and the location of tubes was made from a series of preliminary orbits the accuracy of which was later found to be $\pm 1/10^3$ by the precision orbit analysis (see Section III B).

The background gamma rays we believe are caused by neutral mesons probably produced by scattered protons striking the hydrogen vessel. The background spectrum when corrected by the statistics of the energy channel matrix is shown in Fig. 9. The normalization of the background which is subtracted was chosen so that, in a region well removed from the capture line and the neutral meson gamma-ray flux from hydrogen, the intensity would vanish.

The dependence of these results on the background-subtraction method and variations of efficiency for various energy channels has been considered in detail for the spectrum obtained with deuterium[11] where, because of the relative width and intensities of the spectra, the effect on the energy scale is exaggerated. These effects are negligible in this experiment.

To establish the resolution experimentally, a preliminary measurement of the meson-capture gamma rays was made using several size converters. These spectra, shown in Figs. 10–12, corrected for background, can be analyzed to give a crude mass value and a resolving-power width. Although the statistics are poor, the agreement of the energy scale as obtained with the thin converter (0.010 in.) and the check of the resolution theory is most gratifying. (See Table I.)

The converters were supported on thin slabs of beryllium. The amount of conversion obtained with no tantalum is 10 percent of the total counts as determined with neutral mesons produced at the primary

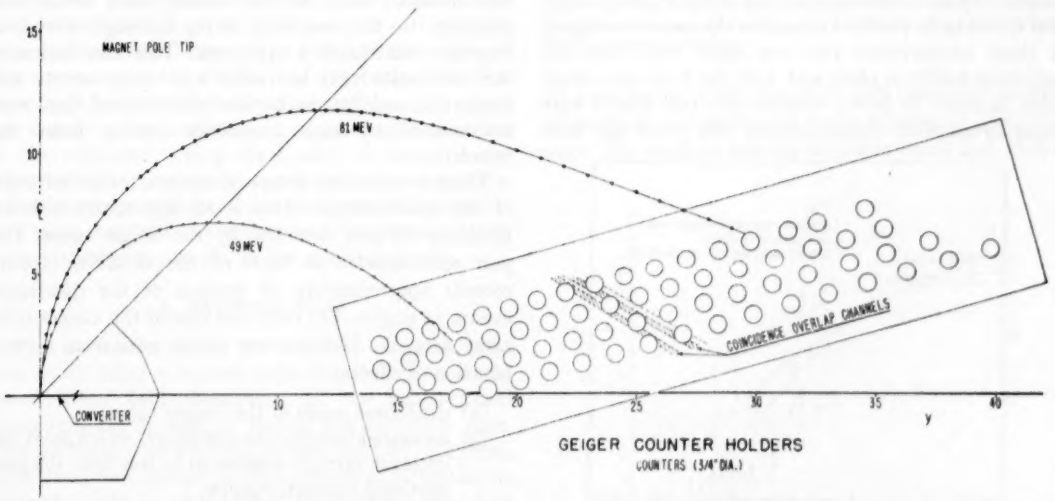

FIG. 7. Top view of counter holder in relation to magnet pole tip. The orbits for 49- and 81-Mev electrons are shown. The overlap channels defined by coincidences between adjacent Geiger tubes are shown for the central energy of the spectrometer. The scale is in inches.

[11] R. H. Phillips and K. M. Crowe, University of California Radiation Laboratory Report No. UCRL-1845 Rev. Following paper [Phys. Rev. **96**, 484 (1954)].

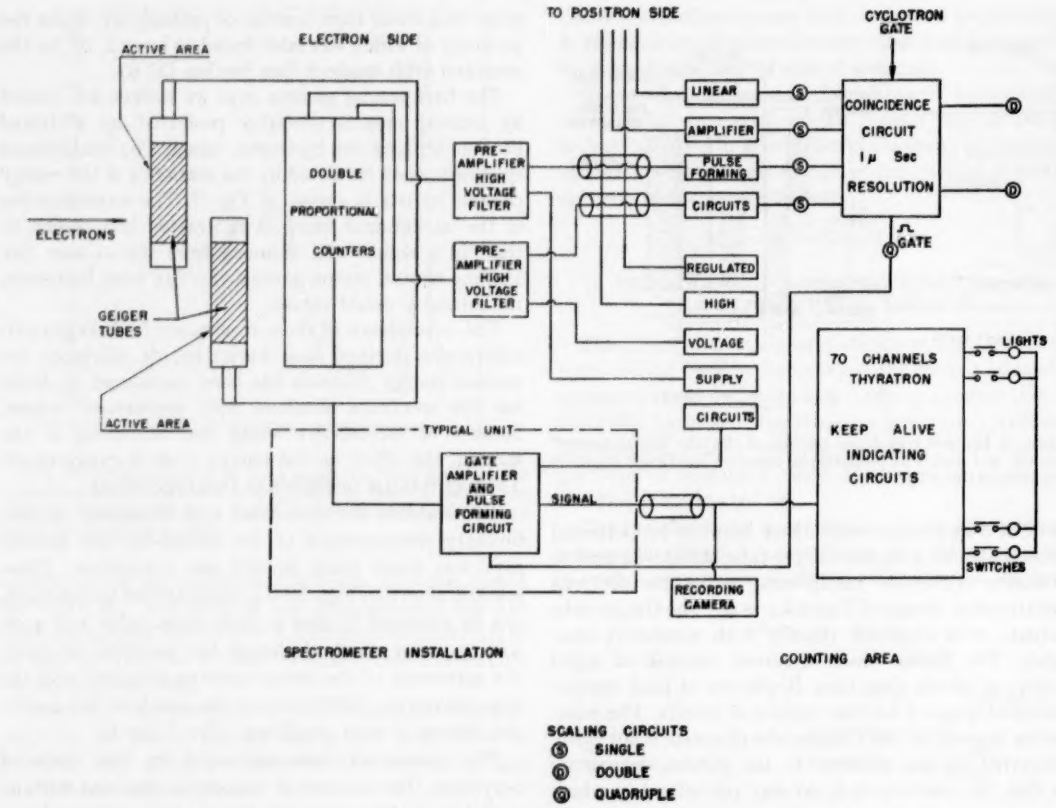

FIG. 8. The electronic block diagram.

target. The no-converter spectrum of the π^0 gamma rays was found to be similar in shape to the converter signal. A short no-converter run was made with only the beryllium holder in place and with the hydrogen vessel filled in order to detect whether any odd effects were being overlooked. Approximately one count per hour was obtained and the few counts were distributed similarly to the converter data, although the data scarcely constituted a spectrum. This run indicated the electronics were not subject to stray counts and cross talk, and that no accidentals occurred that were not caused by pair fragments coming from the converter.

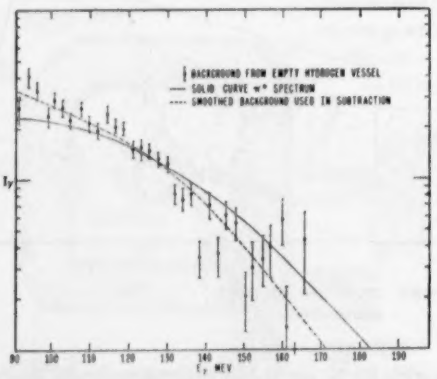
BACKGROUND FROM EMPTY HYDROGEN VESSEL
SOLID CURVE π⁰ SPECTRUM
SMOOTHED BACKGROUND USED IN SUBTRACTION
80 100 110 120 130 140 150 160 170 180 190
E_γ, MEV

FIG. 9. Gamma-ray background from the empty hydrogen vessel. Probable errors are shown. The solid line is obtained from the π^0 decay gamma's which are produced at the primary target with 340-Mev protons. The dotted line shows the smooth background that was subtracted from the hydrogen data.

There is one other source of concern in the behavior of the spectrometer. This is an apparently reduced efficiency for pair detection by the Geiger tubes. The pair spectrometer in both of the detector layouts records approximately 50 percent of the quadruple events as singles, i.e., only one side of the Geiger-tube array fires. We believe these events arise from a combination of effects:

(a) dead time losses of the Geiger tubes,
(b) measured Geiger-tube end effects which limit the detector vertical window to be less than the proportional counter window,
(c) random variations in the plateau characteristics of the 140-odd Geiger tubes, which were all run at the same voltage, and
(d) accidental gating signals from the proportional counters.

None of these effects is believed to have any influence on the spectrum because of the unique identification of the real events as opposed to the random distribution of the assumed processes. Although the overlap channel efficiency will be affected by a and c, measurements again indicate that the reduction is at most 10 percent. In general the average energy obtained from the data does not depend on the individual tube efficiencies since the counts in any energy channel are averaged over many combinations of energy division of the pair fragments.

III. THEORY OF THE SPECTROMETER

A complete discussion of the determination of the energy scale and the resolving power is not possible here because of space limitations. We shall summarize the major features with special references to those effects which bear on the energy scale. A more detailed account of this subject is to be submitted to the *Review of Scientific Instruments*.[12]

The energy scale of the spectrometer was established in the following manner. The magnetic field was measured in the median plane throughout the regions of interest. A numerical integration of the equations of motion was carried out at three energies of both electron and positron. These orbits began at the center of the converter in the direction of the beam axis. The equations for perturbation of these orbits were solved for various initial conditions, i.e., positions and angles at the converter. Using the known or observed distributions for these initial conditions, the energy distributions were calculated for each type of aberration and these were folded together with the other types of energy aberrations to obtain the resolving power.

TABLE I. Energy values obtained with various converter sizes.

Converter	Theoretical resolution full width at half-maximum	Observed resolving power width	Gamma-ray energy	π^- mass
0.050″ Ta	...	4.5 ±1 Mev	130.0 ±1	274.5±2.2
0.020″ Ta	3.3 Mev	3.5 ±1 Mev	129.3 ±0.3	273.0±0.6
0.010″ Ta	2.3	2.45±0.2	129.19±0.12	272.7±0.3

A. Magnetic Field

The determination of the absolute magnetic field was made using a nuclear induction fluxmeter in the spectrometer field throughout all the relative field measurements as well as during the cyclotron runs. The uniformity of the magnet was mapped in a mesh which was fine enough so that numerical interpolation methods could be used to find the field for any place in the median plane without increasing the error appreciably above the value at the mesh points.

[12] Kenneth M. Crowe, University of California Radiation Laboratory Report No. UCRL-2050 Rev. I, 1952 (unpublished).

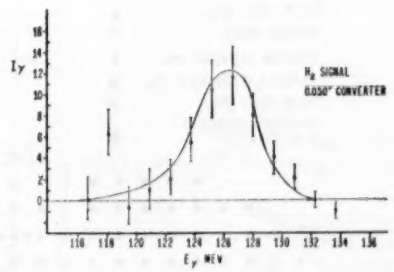

FIG. 10. The pion capture γ-ray spectrum which is obtained by using a 0.050-in. tantalum converter. Probable errors are shown. The solid curve is the estimated resolution. The effects caused by scattering out losses are difficult to include.

The location of the grid was determined by a precision aluminum template. The template was positioned relative to the pole tip insert (indicated in Figs. 6 and 7), which in turn was pinned to the pole tip base.

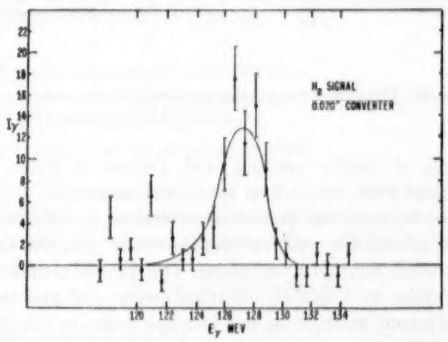

FIG. 11. The capture spectrum obtained by using a 0.020-in. tantalum converter. Probable errors are shown. The solid curve is the calculated resolution.

All positioning of the detectors and converter as well as the main alignment was made relative to this template. The smallest spacing of points was ½ inch in the

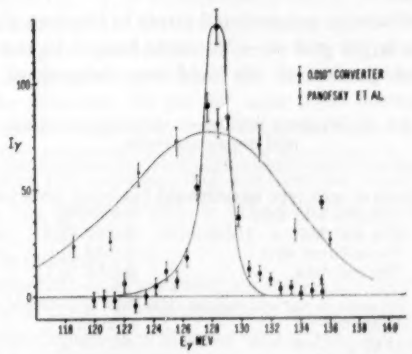

FIG. 12. The capture spectrum measured with the thin target, 0.010-in. tantalum, compared to the spectrum obtained by Panofsky *et al.* The solid curves are theoretical resolution curves. Probable errors are shown.

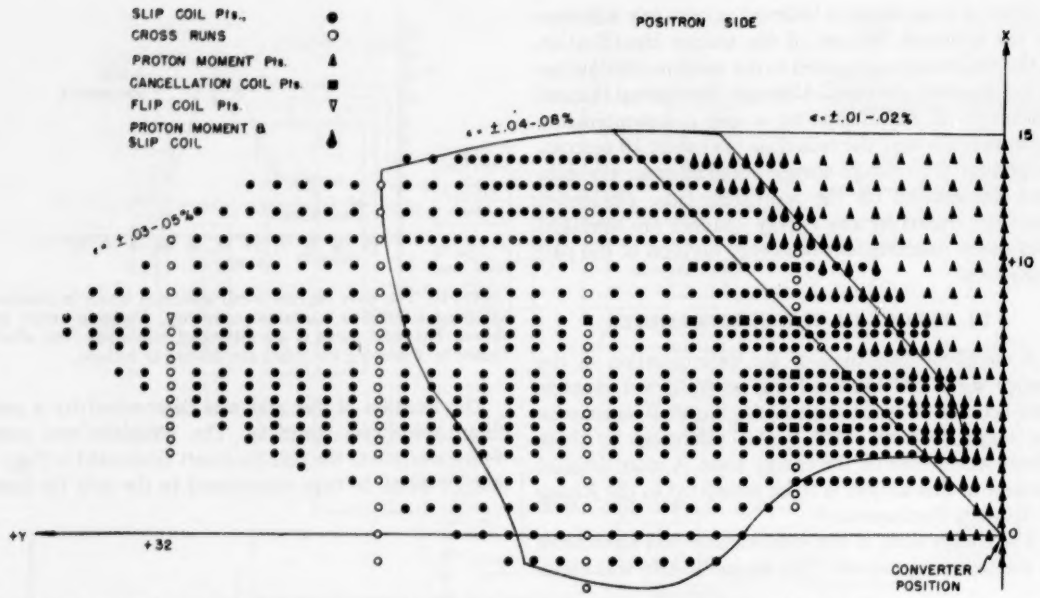

FIG. 13. The grid of field measurements positron side; ϵ's indicate the range of errors in percent of H_0 which are estimated to be associated with each of the regions in the field. The scale is in inches.

regions of rapidly varying field. Figure 13 shows the field grid with the various types measurements.

The bulk of the field measurements (~1000) consisted of relative uniformity runs made with the usual search coil, fluxmeter technique. The slip coil is mounted in a holder such that its electrical center and axis could be adjusted relative to the locating holes in the template. Care was taken to check and eliminate drifts and every measurement was an average of at least three independent measurements.

At a low value of field (~1 percent of the field at the converter), a coil of known area was flipped and the fluxmeter calibrated against a known field. The accuracy of these standards was considerably higher than required.

To eliminate accumulated errors in the long slip-coil runs, a larger grid of ~30 points located in the high-gradient portion of the field was determined by a cancellation method. This was done by rotating two bucking search coils, one in the unknown field and the other in a slave magnet which could be controlled and measured with the proton resonance fluxmeter. The coils were rotated slowly by a geared selsyn system and the difference signal measured with the search coil fluxmeter. These measurements were used in conjunction with the proton resonance data and the data at the low field to calibrate the sensitivity of the slip coil readings, thereby distributing the accumulated errors over short segments of the field.

The errors of the field measurements are summarized in Table II.

TABLE II. Magnetic field errors, expressed as percent of field at pair converter.

A. Errors of each type measurement (standard deviation):	
1. Uniform field data	±0.015%
2. Flip coil data	±0.02 %
3. Cancellation data	±0.03 %
4. Slip coil data	±0.03 %
B. Total error in various regions (standard deviation):	
1. Uniform field	±0.015%
2. High-gradient field	±0.060%
3. Low fields	±0.035%
C. The errors when weighted over these regions averaged over various orbits (probable error)	±0.035%

B. Precise Orbits

The precise energy scale at the detectors was established by computing orbits for particles which were produced at the center of the converter along the beam direction. The numerical method of computation of orbits was chosen keeping the field grid in mind. The radius-of-curvature equation in rectangular coordinates was integrated stepwise. The form of the differential equation for the orbit was

$$\frac{d^2y/dx^2}{[1+(dy/dx)^2]^{\frac{1}{2}}}=-\frac{1}{\rho}=-\frac{cH(x,y)}{(E^2-(mc^2)^2)^{\frac{1}{2}}}, \tag{10}$$

where dy/dx and d^2y/dx^2 are the first and second derivatives at the orbit in rectangular coordinates, ρ is the radius of curvature, $H(x,y)$ is the magnetic field at (x,y). The field measured at the converter was $H(0,0)=9.12261$ kilogauss, E is the total relativistic

energy and mc^2 the rest energy of the electron or positron; and c is the velocity of light.

The Bessel central difference extrapolation and interpolation formulas were used[13] and the step size ($\sim\frac{1}{2}$ inch to 2 inches) was chosen so that the number of higher differences required for the accuracy necessary was convenient. Six figures were carried throughout the computation. The field values were interpolated from the grid by using four-point Lagrangian interpolation coefficients.[14] An entire orbit averaged 80 steps and seven orbits were carried out (four on one side and three on the other).

The accuracy of the numerical approximations used in the computations was sufficient to give $\sim 1/10^4$ accuracy in the final energy so that the precision of these orbits rested upon the knowledge of the magnetic field. The energy scale along the detector line was fitted to a polynomial to interpolate between calculated orbits. The error introduced because of this procedure was estimated from the relative size of the polynomial coefficients to be $\sim 1/10^4$.

C. Perturbation Orbits

To determine the effect of the large size converter, calculations were made in various approximations for the orbits which deviated from the central or precise orbits. The first approximation to the deviated orbits was obtained by solving the Kerst-Serber vertical and horizontal perturbation equations[15] on the Berkeley differential analyzer.[16]

The equations for the horizontal and vertical motion are

$$\xi_1''+\frac{1-n_1(s)}{\rho^2}\xi_1=0, \tag{11}$$

$$Z_1''+\frac{n_1(s)}{\rho^2}Z_1=0. \tag{12}$$

The definitions of terms which appear in Eqs. (11) and (12) and subsequent equations follow:

ρ, ρ', ρ'' are the radius of curvature and its derivatives along the orbits;
s is the arc length measured along the zero order orbit (primes are derivatives with respect to s);
ξ is the displacement in the horizontal plane normal to the orbit;
Z is the displacement in the vertical plane normal to the orbit;

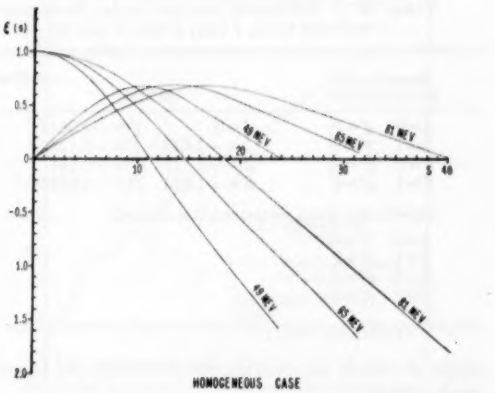

FIG. 14. The family of ξ solutions for the horizontal motion for typical particle energies. For the solutions for which $\xi(s=0)=0$, the initial slope $\xi'(s=0)=\tan\theta_0$. For the other solutions, $\xi'(s=0)=0$ and $\xi(s=0)=1$. s is the arc length measured along the zero order orbit. ξ is the displacement in the horizontal plane normal to the zero order orbit. The scale is in inches and the trajectories end along the focus line.

ξ and Z are small compared to ρ,
$n_1(s)=-(\rho/H)(dH(x,y)/d\eta)$, the first normal derivative of the field, and
η is taken as the outward normal.

In this approximation ξ and Z are uncoupled and satisfy linear second-order differential equations. Thus, for example, the general solution for ξ will be of the form

$$\xi_1(s)=A\xi_A(s)+B\xi_B(s), \tag{13}$$

where ξ_A and ξ_B are the solutions with the initial conditions,

$$\xi_A(s=0)=\xi_0 \quad \text{and} \quad \xi_A'(s=0)=0, \tag{14}$$

and

$$\xi_B(s=0)=0 \quad \text{and} \quad \xi_B'(s=0)=\tan\theta_0, \tag{15}$$

where θ_0 is the initial angle to the beam axis.

Typical solutions for these initial conditions are shown in Fig. 14 for various energy central orbits. From these solutions the first-order focusing against multiple scattering in the horizontal plane can be seen. Also, one can see how the width of the converter is magnified at the detectors. In the 90° apex style spectrometer this width would be in focus along the edge of the tip and this crossover can be seen in the figure. In Fig. 15 we have the corresponding solutions for vertical motion, i.e., perpendicular to the horizontal or medium plane. The strong defocusing action of the fringe field is indicated.

These first-order perturbation results are summarized in Table III A. If one uses these orbits together with the distribution of scattering angles, one can calculate what fraction of the total flux of pair fragments arrives within the vertical window in the detector. This yield will vary for pairs produced at various converter thicknesses. The characteristic scattering parameter is the

[13] J. B. Scarborough, *Numerical Mathematical Analysis* (Johns Hopkins Press, Baltimore, Maryland, 1930); L. J. Comrie, *Interpolation and Allied Tables* (His Majesty's Stationery Office, London, 1936).
[14] *Tables of Lagrangian Interpolation Coefficients* (Columbia University Press, New York, 1944).
[15] D. W. Kerst and R. Serber, Phys. Rev. **60**, 53 (1941).
[16] E. G. Sorenson, University of California Radiation Laboratory Report No. UCRL-1717, 1952 (unpublished); John Killeen, University of California Radiation Laboratory Report No. UCRL-2239, 1953 (unpublished).

TABLE III A. Differential analyzer results. Homogenous solutions of ξ and Z equations $\xi(0)$, $\xi'(0)$, $Z(0)$, $Z'(0)$ are initial conditions $\xi(S_f)$, $\xi'(S_f)$, $Z(S_f)$, $Z'(S_f)$ are terminal values in inches or radians as measured at the focus line.

Negative side initial condition	Final displacement and slope for typical energies 49 Mev	65 Mev	81 Mev
$\xi=0$ $\xi'=\theta_0$	$\xi=0$ $\xi'=-0.0615$	$\xi=-0.026$ $\xi'=-0.0435$	$\xi=+0.0245$ $\xi'=-0.0327$
$\xi=1$ $\xi'=0$	$\xi=-1.630$ $\xi'=-0.127$	$\xi=-1.665$ $\xi'=-0.0992$	$\xi=-1.683$ $\xi'=-0.0840$
$Z=0$ $Z'=\theta_0$	$Z=+3.125$ $Z'=+0.144$	$Z=+3.212$ $Z'=+0.125$	$Z=+3.360$ $Z'=+0.044$
$Z=1$ $Z'=0$	$Z=+1.810$ $Z'=+0.0522$	$Z=+1.860$ $Z'=+0.0486$	$Z=+1.913$ $Z'=+0.0163$
Positive side (check on symmetry of magnet)			
$\xi=0$ $\xi'=\theta_0$		$\xi=+0.024$ $\xi'=-0.0442$	
$\xi=1$ $\xi'=0$		$\xi=-1.651$ $\xi'=-0.0974$	
$Z=0$ $Z'=\theta_0$		$Z=+3.189$ $Z'=+0.1250$	
$Z=1$ $Z'=0$		$Z=+1.795$ $Z'=+0.0458$	

angle at which the distribution has fallen to $1/e$ of the peak value[17]:

$$\theta_m=\left[\frac{4\pi Nz(z+1)e^4}{p^2v^2}\ln\left\{4\pi z^{4/3}Nt\left(\frac{\hbar}{mv}\right)^2\right\}\right]^{\frac{1}{2}}$$
$$\doteq\left(\frac{15}{E}\right)\left(\frac{t}{x_0}\right)^{\frac{1}{2}}. \quad (16)$$

The symbols have the usual meanings: x_0 is the radiation length of the converter material. The value $(21/E)(t/x_0)^{\frac{1}{2}}$ which is commonly used in calculation of this type, is in error owing to plural scattering.[17]

Averaging over energies and converter depths, the calculated yield is obtained as shown in Fig. 16.

The other yield variations which bear indirectly on the aberration corrections are yield *vs* width and yield *vs* height. In the first approximation the yield should be proportional to the area for the same thickness converter. This, of course, assumes that there was a uniform flux of gamma rays over the converter. This last condition was checked visually in the alignment and with 90-Mev neutrons coming from deuterons on the internal target moved in line with the collimating system. A gross check was also made with neutral mesons from this target, although unfortunately the statistics of counts obtained with the various converter sizes were poor. Because of the lack of accuracy of these checks, a small uncertainty has been calculated and included with the final evaluation of errors.

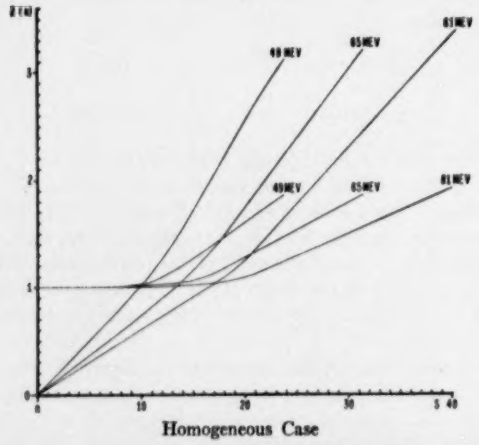

Homogeneous Case

FIG. 15. The family of Z solutions which determines the vertical motion in the first-order theory for typical particle energies. Initial conditions correspond to those in Fig. 14. Z is the displacement in the vertical plane normal to the zero order orbit. The scale is in inches and the trajectories end along the focus line.

It should be noted that effects or yields caused by the second-order perturbations in the Z motion have not been included. The justification for this will become apparent in the following section.

The next approximation calculated was that in which the terms which were neglected in Eqs. (11) and (12) were included as a perturbation to the first-order solution. The form of these terms has been developed by Judd,[18] and the results for motion in the horizontal plane with second-order terms is

$$\xi_2''+\left(\frac{1-n_1}{\rho^2}\right)\xi_2=-\left[\frac{1-2n_1+n_2}{\rho^3}\right]\xi_2^2$$
$$+\left[\frac{-n_1+2n_2+2\rho'^2-\rho\rho''}{2\rho^3}\right]Z_2^2+\left[\frac{1}{2\rho}\right](\xi_2'^2-Z_2'^2)$$
$$+\left[\frac{\rho'}{\rho^2}\right](\xi_2\xi_2'+Z_2Z_2'). \quad (17)$$

$n_2=(\rho^2/2H)(d^2H/d\eta^2)$, the second normal derivative.

The other symbols are the same as in Eqs. (11) and (12).

The method of solution of this equation was to treat the right-hand side of the equations as a driving term for the first-order equation substituting in the right-hand side the first-order solutions corresponding to the particular kind of orbit perturbation being solved. The

[17] B. Rossi and K. Greisen, Revs. Modern Phys. **13**, 240 (1941); J. Ashkin and H. A. Bethe in *Experimental Nuclear Physics*, edited by E. Segrè (John Wiley and Sons, Inc., New York, 1953), Vol. I, Part 2; Hansen, Lanzl, Lyman, and Scott, Phys. Rev. **84**, 634 (1951).

[18] David Judd (private communication).

equations thus became

$$\xi_2''+A(s)\xi_2=R(s,\xi_1(s),Z_1(s),\cdots). \quad (18)$$

The first-order solution can be subtracted off since it satisfies Eq. (18) with $R=0$. Thus we obtain the second-order displacement at the final value of s, i.e., the detector position for various combinations of ξ_1 and Z_1 where these in turn are the result of the initial conditions set by Eqs. (14) and (15).

Let us take for example the second-order perturbation in ξ for motion in the Z direction. Figure 17 shows the result obtained for $R(s)$ with the initial conditions $Z_1(0)=1$, $Z_1'(0)=0$, for three energies. Figure 18 shows the solution for $\xi_2(s)$. Notice that the perturbations begin at zero ($\xi=0$ and $\xi'=0$) corresponding to the assumed initial conditions and the final value is obtained by following the solution to the intersection of the central orbit with the detector line. With this solution one can calculate the apparent energy shift which results from the complicated behavior in the fringing field off the median plane of the particle which has started at the converter 1 inch above the center.

TABLE III B. Second-order results. The cases correspond to the solution of the ξ equation with higher-order terms as explained in text.[a] Final displacement is in inches at the focus line.

Case	Initial conditions ξ	ξ'	Z	Z'	Final displacement $\xi(S_f)49$	$\xi(S_f)65$	$\xi(S_f)81$
1	1	0	0	0	−0.0011	−0.0039	+0.0013
2	0	θ_0	0	0	−0.0786	−0.0496	−0.0259
3	1	θ_0	0	0	−0.0734	−0.0447	−0.016
4	−1	θ_0	0	0	−0.0689	−0.0545	−0.033
5	0	0	1	0	−0.1293	−0.1232	−0.0837
6	0	0	0	θ_0	−0.3355	−0.2369	−0.2125
7	0	0	1	θ_0	−0.8117	−0.6235	−0.5040
8	0	0	−1	θ_0	−0.1244	−0.0835	−0.0792
9	0	0	1	$\theta_0/2$	−0.3939	−0.2515	−0.2496
10	0	0	−1	$\theta_0/2$	−0.0463	−0.0396	−0.0364
11	1	θ_0	1	θ_0	−0.7122	−0.6570	−0.556
12	−1	θ_0	1	θ_0	−0.7058	−0.6915	−0.580
13	1	θ_0	−1	θ_0	−0.1300	−0.1300	−0.158
14	−1	θ_0	−1	θ_0	−0.1646	−0.1383	−0.086

[a] Kinetic energy: θ_0 = 49 Mev: 0.100; 65 Mev: 0.0750; 81 Mev: 0.0600

This procedure is carried out for each initial condition and the various combinations, to explore mixing of the various effects. The results of these calculations are shown in Table III B.

The same kind of procedure can be followed with the Z motion in second order. The vertical equation is

$$Z_2''+(n_1/\rho_2)Z_2=[(-2n_1+2n_2)/\rho^3]\xi_2Z_2 +[1/\rho](\xi_2'Z_2')+[\rho'/\rho^2](\xi_2'Z_2-Z_2'\xi_2). \quad (19)$$

By inspection, one can see that in the method used in solving the equation there is a simplification in the extent of these perturbations. For cases where either $Z_1(s)$ and $Z'(s)$ or $\xi_1(s)$ and $\xi_1'(s)$ vanish, the driving term also vanishes. Therefore the Z solutions consist entirely of mixing terms. The maximum size of Z_2 is of the same order as the other second-order perturbations

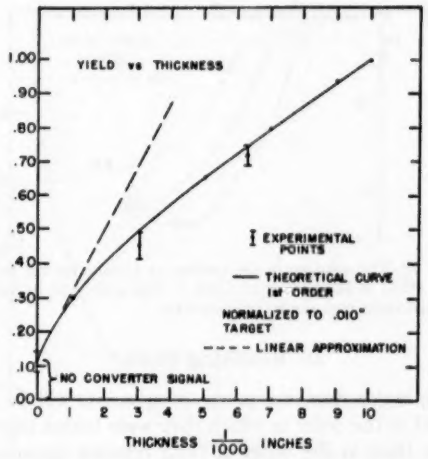

FIG. 16. The theoretical and experimental yields for various converter thicknesses. The theoretical curve has been used to weight all the effects in the resolution which depend upon converter thickness. The experimental points were measured with neutral meson γ rays; probable errors are shown.

so that the first-order theory for detector window is in error by a small amount. The Z solutions thus effect the energy scale only by introducing a small change in the distribution for orbits which have both large Z and ξ displacements. This correction has been estimated and it has been included among sources of error for the second-order energy correction.

Finally, the accuracy of these perturbation solutions is estimated both from the reproducibility of the differential analyzer results and the accuracy of the field gradients which come into the calculations, to be approximately 1 to 5 percent of the final displacement, depending on the initial conditions. The errors introduced in the neglect of the higher terms in the perturbation calculation as well as that introduced by neglect of still higher terms in the differential equations were checked in the important cases and the effects were found to be well within the accuracy of the perturbation solutions.

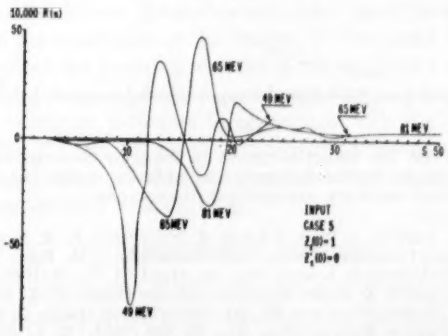

FIG. 17. The analyzer input function for the initial displacement in the vertical direction $Z(0)=1$, $Z'(0)=0$; Case 5. The scale is in inches and the trajectories end along the focus line.

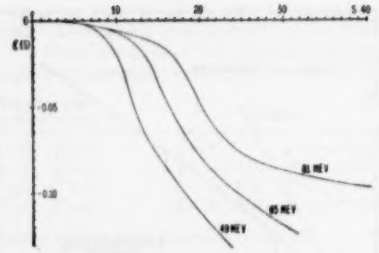

FIG. 18. The solution in the median or ξ plane for the vertical height effect of the converter. Case 5. The scale is in inches and the trajectories end along the focus line.

D. Resolving Power

The major resolving power components will be considered in the order in which they were folded together rather than in the order of their relative importance. In evaluating the energy of the gamma ray, the relevant quantity is the average shift (the first moment) of the resolving power which can be shown[12] to be the algebraic sum of the shifts of the components. In Table IV the energy shifts for each effect are shown for comparison.

Pairs that are produced in the converter lose energy traversing the converter by both ionization and radiation. The theory of these processes is discussed thoroughly by Ashkin and Bethe.[17]

In computing the resolving width caused by variation in the energy loss we have included the following effects:

1. A Landau type distribution[19] for the fluctuations of ionization loss.

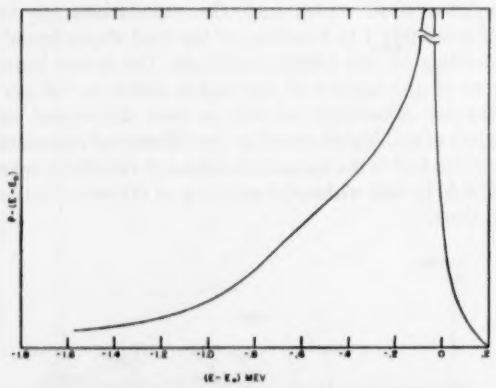

FIG. 19. The resolution caused by first-order converter thickness effects: ionization energy loss, radiation energy loss, and horizontal scattering, averaged over the converter.

2. Sternheimer's correction[20] because of the density effect for ionization loss in the converter.

3. The mean ionization potential for the converter (tantalum) interpolated from Bakker and Segrè.[21]

4. The correction in the bremsstrahlung[22] cross section as indicated from recent experiments ($\sim$7.5 percent in tantalum).

5. The moments of the distribution were computed by cutting off the tails of the radiation straggling curves at 6 Mev and including the reduction in detection efficiency along with the purely geometrical effects for each converter thickness. This cutoff procedure was used in calculating the first moment of the data to eliminate the dependence of the moment on the assumed cutoff. The same procedure was then repeated by cutting off at 12 Mev and the results agreed within the statistical error.

These distributions were then combined with the scattering in the horizontal plane which was deduced from the perturbation orbit calculations. The shape of this distribution is based on the Gaussian angular distribution for multiple scattering. The errors in the assumed distribution are not consequential. In fact, due to a fortuitous cancellation of several opposing effects, the net moment of the resolution was found to be almost independent of the assumed mean-square scattering angle.

TABLE IV. Shifts in the energy scale.

1. Ionization loss	
Converter	−0.509 Mev
Air	−0.174 Mev
2. Radiation (cut off at 6 Mev)	−0.411 Mev
3. Horizontal scattering	
First-order theory	+0.003 Mev
Second-order perturbation	−0.100 Mev
4. Converter horizontal width	
First-order theory	+0.709 Mev
Second-order perturbation	−0.002 Mev
5. Converter vertical height and scattering	
Second-order theory	−0.310 Mev
6. Detector channel location	
(tube positions and central orbits)	−0.146 Mev
Net moment −0.940 Mev	

The resolutions for these effects were averaged together over the converter thickness and the resulting curve is shown in Fig. 19.

The channel width was calculated knowing the precise central energy scale and the accurate counter locations. In the positioning (made before the precise

[19] L. Landau, J. Phys. U.S.S.R. **8**, 201 (1944); K. R. Symon, Harvard University, thesis, 1948 (unpublished); A. Bohr, Kgl. Danske Videnskab. Selskab, Mat.-fys. Medd. **24**, No. 19 (1948); T. Bower and F. X. Roser, Phys. Rev. **83**, 689 (1941); F. X. Roser and T. Bower, Phys. Rev. **82**, 284 (1951); **85**, 992 (1952); R. Hofstader and A. Hudson, Phys. Rev. **88**, 589 (1952); W. L. Wittemore and J. C. Street, Phys. Rev. **76**, 1786 (1949); Goldwasser, Mills, and Hansen, Phys. Rev. **88**, 1137 (1952); Igo, Clark, and Eisberg, Phys. Rev. **89**, 879 (1953).

[20] W. F. G. Swann, J. Franklin Inst. **226**, 598 (1938); E. Fermi, Phys. Rev. **56**, 1242 (1939); **57**, 485 (1940); G. C. Wick, Nuovo cimento **1**, 302 (1943); Ricerca sci. **11**, 273 (1940); O. Halpern and H. Hall, Phys. Rev. **57**, 459 (1940), Phys. Rev. **73**, 477 (1948); R. M. Sternheimer, Phys. Rev. **88**, 851 (1952).

[21] R. L. Mather and E. Segrè, Phys. Rev. **84**, 191 (1951); C. J. Bakker and E. Segrè, Phys. Rev. **81**, 489 (1951).

[22] C. R. Emigh, Phys. Rev. **86**, 1028 (1952); DeWire, Ashkin, and Beach, Phys. Rev. **82**, 447 (1951); Phys. Rev. **83**, 233, 476, 505 (1951); J. L. Lawson, Phys. Rev. **75**, 433 (1949); C. D. Curtis, Phys. Rev. **81**, 308 (1951); C. D. Curtis, Phys. Rev. **89**, 123 (1953).

orbits were completed) an uncertainty was present in the approximate energy scale which was later accurately determined. The resolution width which resulted from this uncertainty is shown in Fig. 20. This resolution was folded in with the previous result.

The distribution because of the width of the converter was computed assuming uniform flux and equal detection efficiency. The main effect here is obtained from the first-order calculations for the orbits which are produced in the strip of converter in the horizontal plane which leave normally to the converter. One can show that the displacement at the detector $\delta\xi(s_f)$, can be approximated by the expression

$$\delta\xi(s_f)\cong\xi_1(s_f)\xi_1'(s_f)/\tan\phi, \tag{20}$$

where s_f refers to the final value for the arc length ξ_1, ξ_1' the first order solution and its derivative, and ϕ is the angle of intersection between the counter line and the central unperturbed orbit.

Since $\xi_1(s_f)$ and $\xi_1'(s_f)$ are both proportional to the initial conditions $\xi(s=0)$, one obtains that the energy

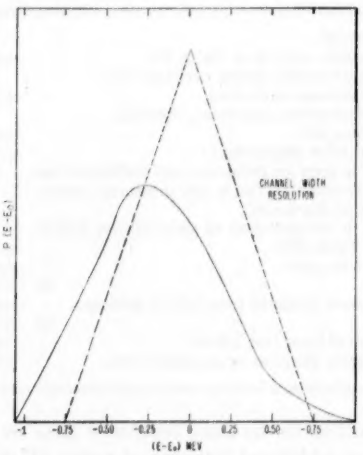

FIG. 20. The finite detector channel width resolution. The dotted curve is the ideal resolution for a single pair of counters located at positions such that $E^+ + E^- = E_0$. The solid curve is the actual resolution when averaged over slight errors in location and in channel widths.

shift is given by

$$\Delta E\propto\xi(0)^2. \tag{21}$$

The distribution can be found to be

$$P(\Delta S)\propto(\Delta E)^{-\frac{1}{2}}. \tag{22}$$

One must average properly over the division of the pairs and the result is shown in Fig. 21.

The second-order effect of multiple scattering in the horizontal plane can be calculated in a manner similar to the horizontal width calculations.

The last major effect results from the vertical motion. These calculations were complex since in obtaining

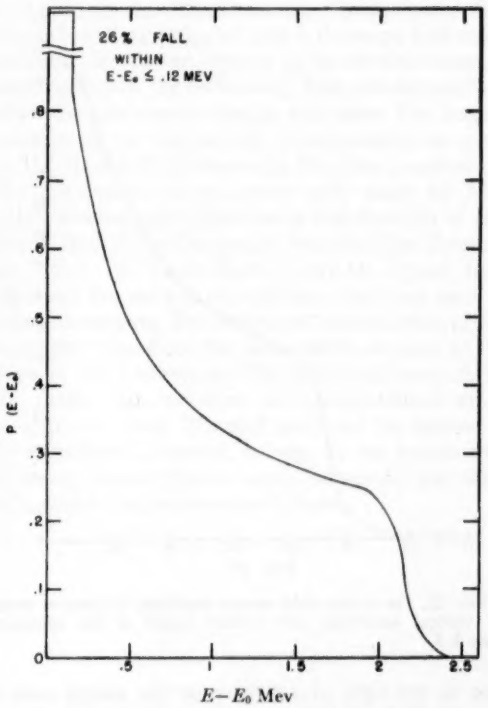

FIG. 21. Resolving power resulting from the finite lateral width of the converter. This depends only upon the first-order solutions to the orbit perturbation problem. (The small effects of the second-order orbit perturbation theory have not been included in this curve.)

the distribution of initial conditions, the motion resulting from vertical displacement and vertical scattering is not at all separable either in the manner in which the perturbation effects occur or in the way the initial conditions are restricted by the counter acceptance windows. The calculation, although lengthy, followed closely the method outlined in the previous calculations. The resulting distribution is shown in Fig. 22. Fortunately for the accuracy required, the detailed analysis was necessary only to assure that there were no larger nonlinear effects present which may have resulted from the complexity of the motion. In fact, none were large and the resulting moment is not sensitive to the complex features of the calculations. The final fold of the resolution is shown in connection with the data in Fig. 23. The vertical normalization is arbitrary. The energy scale is labeled to correspond to the channels in which the data were recorded.

IV. EXPERIMENTAL RESULTS

To arrive at the value for the gamma-ray energy, the first moment of the data was obtained. The resolution has a net moment as determined algebraically in Table III. In addition the zero of the resolution appears on the folded curve and this is indicated by the arrow

FIG. 22. The second-order energy resolution component caused by vertical scattering and vertical height of the converter; Case 4, 5.

just to the right of 129 Mev on the energy scale of Fig. 23. The value for the energy which results from a visual fit of the resolution to the data agrees well with the value obtained by the moments. We obtain for the gamma-ray energy:

$$E_\gamma = 129.19 \pm 0.12 \text{ Mev}. \tag{23}$$

The relation between the pion mass and the gamma-ray energy is given as follows:

$$E_\gamma = M_\pi c^2 - \frac{E_\gamma^2}{2M_n c^2} + \frac{1}{8}\frac{E_\gamma^4}{(M_n c^2)^3} - (M_n - M_p)c^2 - \left(\frac{\alpha^2}{2}\right) M_\pi c^2 + \cdots. \tag{24}$$

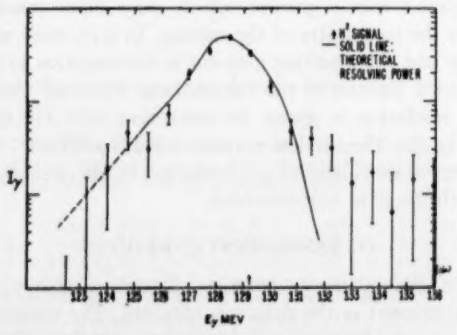

FIG. 23. The resolution curve which includes all the first and second-order effects calculated by folding together the resolution components. The data is shown with probable errors.

The terms in order of importance are the meson rest mass, the recoil energy of the neutron, the neutron-proton mass difference, and the Bohr K-shell energy. In calculating the meson mass we have used the electronic rest mass from DuMond and Cohen,[23] and the neutron-proton mass difference from Robson's work[24]:

$$(M_n - M_p)c^2 = 1.293 \pm 0.013 \text{ Mev}. \tag{25}$$

In calculating the radius of curvature (Eq. 10), the absolute field was measured using the magnetic moment as obtained by Thomas, Driscoll, and Hipple.[25]

The errors have already been discussed in some detail and they appear in summary in Table V.

In evaluating the statistical error (G), we can fit the data with a gaussian of root-mean-square width of 1.0 Mev. This fit is satisfactory if one ignores all points which are three or more standard deviations from the mean. Making the usual analysis based on the total number of events, we arrive at a probable error of ±0.048 Mev.

TABLE V. Summary of errors in mass measurement.

A	Field errors: (probable error from Table II)	$\pm 3.5/10^4$
B	Field fluctuations during cyclotron run: (½-maximum deviation)	$\pm 1.0/10^4$
C	Geometry errors, templates, counters, leveling, etc:	$\pm 3.5/10^4$
D	Central orbit calculations:	$\pm 1.0/10^4$
E	Probable error in ionization and radiation loss due to uncertainties in the measured corrections to the theory:	$\pm 2/10^4$
F	Errors in computations of perturbation orbits: (see Table III):	$\pm 3/10^4$
G	Statistical error:	±0.048 Mev
	or	$\pm 3.7/10^4$
H	Total error obtained from known sources:	±0.095 Mev
	or	$\pm 0.21\ m_e$
I	Additional error (see below):	$\pm 6/10^4$
J	Total error assigned by experimentors:	$\pm 0.27\ m_e$

In addition to the usual sources of error we have included an additional estimate of errors (I) which fall into two classes.

(1) There are a number of small sources of error which were calculated to be negligible which it was not possible to investigate with sufficient accuracy because of the low counting rates. Although the theory indicates these effects to be unimportant (that is, less than $1/10^4$) these may contribute in a systematic rather than random manner.

(2) We also are including here the contribution which represents an estimate of uncertainties of the error estimates. For example, there are uncertainties in the

[23] J. W. M. DuMond and E. R. Cohen, Am. Scientist **40**, 447 (1952).

[24] J. Robson, Phys. Rev. **83**, 349 (1951); Hornyak, Lauritsen, Morrison, and Fowler, Revs. Modern Phys. **22**, 291 (1950).

[25] Thomas, Driscoll, and Hipple, Phys. Rev. **75**, 902 (1949); Phys. Rev. **78**, 787 (1950); N. F. Ramsey, Phys. Rev. **77**, 567 (1950); H. A. Thomas, Phys. Rev. **80**, 901 (1950).

background normalization, the yield runs, vertical scattering losses in higher order, etc.

Our result is

$$M_{\pi^-}=272.74\pm0.27\ m_e. \tag{26}$$

The π^0 mass which is derived from Eq. (9) is

$$M_{\pi^0}=263.9\pm0.7\ m_e. \tag{27}$$

The μ^+ mass is derived from Eq. (4) to be

$$M_{\mu^+}=206.33\pm0.28\ m_e. \tag{28}$$

The last value assumes the π^+ and π^- to have the same mass.

V. ACKNOWLEDGMENTS

The authors take pleasure in acknowledging the assistance so generously offered by members of the Radiation Laboratory Staff. Professor W. K. H. Panofsky, now at Stanford University, has guided the entire program.

The Magnetic Measurements Group, under Mr. Duane Sewell, contributed over a thousand field measurements. Mr. Robert Teeters set up the field measurements and made the preliminary field calculations from which the spectrometer design was made. The lengthy reduction of the precise field measurements was made by Mr. Harold B. Knowles and Mr. Glen Lambertson. The calculations of the orbits were made by Mrs. Ardith Kenney and others under the direction of Mr. John Killeen of the Computing Section of the Theoretical Group. Dr. Louis Henrich and Dr. David Judd suggested the method of approach that was used in these calculations. The design and construction of the equipment represents the joint effort of most of the shops of the Laboratory. The cyclotron crew, under Mr. James Vale, provided the bombardments which lasted over a week. The real credit for the success of the experiment, however, belongs to the people who did many hours of tedious work, accurately and skillfully, within the groups named above.

An Indirect Measurement of the n-n Interaction*†

ROBERT H. PHILLIPS‡ AND KENNETH M. CROWE§
Radiation Laboratory, Department of Physics, University of California, Berkeley, California
(Received March 9, 1954)

The gamma-ray spectrum from the process $\pi^-+d\rightarrow 2n+\gamma$ has been remeasured using a high resolution 110-channel pair spectrometer. The negative pions produced in an internal target by 335-Mev protons of the Berkeley 184-inch cyclotron, are captured at rest in a high-pressure deuterium vessel. Comparison of the spectrum with the gamma-ray spectrum from the process $\pi^-+p\rightarrow n+\gamma$ measured with the same apparatus shows the effect of the n-n interaction as a broadening of approximately three times the resolving width. In spite of the low counting rates and resulting statistical inaccuracy, it is possible to establish limits for the scattering length "a" for S-state neutron-neutron scattering. The experimental data are analyzed by evaluating a weighted first moment of the spectrum. Comparison of the weighted first moments of the theoretical spectra with that of the data leads to a value of $a=-15.9\times10^{-13}$ cm with limits, based on the probable error, of $a=-8.5\times10^{-13}$ cm and $a=-\infty$ cm. The value $a=-15.9\times10^{-13}$ cm corresponds to an unbound state ($\sim$160 kev positive) for the hypothetical dineutron. The bound dineutron of more than 50 kev is less than 0.1 percent probable. This result is consistent with the n-p and p-p scattering data and is in agreement with the theory of charge independence of nuclear forces.

I. INTRODUCTION

THE p-p interaction for low-energy scattering has been successfully treated by the evaluation of the scattering length and the effective range.[1] The scattering results predict[2] that the lowest singlet state for two protons is unstable and to date no He^2 or diproton has been found. Furthermore, if charge symmetry[3] is assumed, the parameters derived from the low-energy p-p scattering experiments when applied to the n-n system predict that the ^1S state of the dineutron would not be stable either. Since the low-energy scattering parameters for the p-p and n-p systems are also in agreement within experimental error, the more general theory of charge independence[3] would predict an unstable ^1S state for the deuteron as is known to be the case.[4] The low-neutron fluxes available at present, however, have precluded the use of scattering experiments to study the n-n forces. The n-d scattering would in principle give information about the n-n interaction but the theoretical interpretation of the experimental work "is still in a very preliminary state"[5] because of the complications inherent in the three body problem.

Evidence for charge symmetry from other fields of investigation is good, so results contrary to those we have found would have been surprising. However, it is worthwhile to supply direct verification and derive whatever quantitative information that is possible with the present experimental techniques.

Two further approaches have been used to obtain experimental evidence concerning the n-n force: (1) a search for the dineutron; (2) analysis of the energy spectrum of "C" resulting from the reaction $A+B\rightarrow C+2n$. If "C" is a particle, its nuclear interaction with the two neutrons makes a quantitative analysis very difficult. This is again a three-body problem and if "C" is a complex nucleus the results will depend on the model for "C". If, however, "C" is a gamma ray an accurate analysis is possible.[6] It should also be noted that, in both cases, even if there is no bound state the system will be peaked if the neutrons are emitted singly under the action of an attractive potential. The present experiment permits the indirect evaluation, within rather broad limits, of the scattering length for the n-n interaction.

Using the first approach Kundu and Pool[7] bombarded Co^{59} and Rh^{103} with tritium. The observed half-lives of the products and the energies of the decay betas established the fact that the reaction had proceeded by capture of two neutrons. From the behavior of the cross section for various triton energies they concluded that the mechanism involved was probably the Oppenheimer-Phillips[8] process with l rather than a compound nucleus mechanism. This suggests that the two neutrons may be captured as a group, which would imply that a dineutron could have at least transient existence in the instant between the polarization of the tritium nucleus and the capture. As yet, the experiment has a rather remote bearing on the actual occurrence of an observable dineutron since the detailed theoretical analysis of this process and its implications concerning the n-n interaction have not been made.

* Presented by R. H. Phillips in partial fulfillment of the requirements for the degree of Doctor of Philosophy.
† This work was done under the auspices of the U. S. Atomic Energy Commission.
‡ Now at Brookhaven National Laboratory, Upton, New York.
§ Now at Stanford University, Stanford, California.
[1] J. M. Blatt and J. D. Jackson, Phys. Rev. **76**, 18 (1949).
[2] H. A. Bethe and R. F. Bacher, Revs. Modern Phys. **8**, 133 (1936).
[3] G. Breit and E. Feenberg, Phys. Rev. **50**, 850 (1936); K. M. Watson, Phys. Rev. **85**, 852 (1952).
[4] H. A. Bethe, *Elementary Nuclear Theory* (John Wiley and Sons, Inc., New York, 1947), first edition, p. 52 ff; J. M. Blatt and V. F. Weisskopf, *Theoretical Nuclear Physics* (John Wiley and Sons, Inc., New York, 1952), p. 93.
[5] See Blatt and Weisskopf, reference 4, p. 206.
[6] K. Watson and R. Stuart, Phys. Rev. **82**, 738 (1951).
[7] D. N. Kundu and M. L. Pool, Phys. Rev. **73**, 22 (1948); Phys. Rev. **82**, 305 (1951).
[8] J. R. Oppenheimer and M. Phillips, Phys. Rev. **48**, 500 (1935).

Feather[9] has established an upper limit on the binding energy of the dineutron. By consideration of a group of known reactions for which the Q values have been experimentally established he is able to deduce

$$\mathrm{He}^6 \rightarrow \mathrm{He}^4 + 2n - 0.7 \text{ Mev}.$$

Since He^6 is known to decay instead by β emission, one concludes that the binding energy of the dineutron is less than 0.7 Mev.

Acting on a suggestion by Feather[9] that the dineutron might be emitted in the process of fission, and if so could be detected by subsequent capture in Bi^{209}, Fenning and Holt[10] irradiated Bi^{209} in the Harwell pile. The thermal flux of neutrons was about 10^{12} neutrons per sq cm per sec. Denoting the flux of dineutrons by ϕ and the capture cross section by σ, they reported that no activity ascribable to AcC'' or Tl^{207} was observed and set $\phi\sigma < 1.5\times10^{-21}$ per sec.

Feather gave a preliminary report[11] on an experiment by Fenning in which he had irradiated He^4 in the Harwell pile and apparently observed the approximately one-second activity from He^6 in the reaction $\mathrm{He}^4 + n^2 \rightarrow \mathrm{He}^6 \rightarrow \beta^-$. It was later concluded[12] that the observed activity was a result of contamination of the He^4. A limit of $\phi\sigma < 10^{-18}$ per sec was set, where σ is now the capture cross section of helium for dineutrons.

The experiments so far described only yield evidence on the existence of the dineutron. Beyond the establishment of limits on the "binding energy" of this hypothetical particle, they have given no detailed information on the n-n interaction.

Los Alamos Scientific Laboratory[13] using the second approach mentioned above has reported evidence for the production of dineutrons in the reaction $t^3 + t^3 \rightarrow \mathrm{He}^4 + n^2$. A. Hemmendinger[14] gives more detail on this experiment. The reaction may proceed in three alternative ways:

$$\begin{aligned}
&(1)\quad t^3 + t^3 \rightarrow \mathrm{He}^4 + 2n,\\
&(2)\quad t^3 + t^3 \rightarrow \mathrm{He}^4 + n^2,\\
&(3)\quad t^3 + t^3 \rightarrow \mathrm{He}^5 + n\\
&\qquad\qquad\quad\ \ \rightarrow \mathrm{He}^4 + n.
\end{aligned}$$

The first process will give a continuous distribution of alpha-particle energies. The second process would give a peak of alpha-particle energies depending on the angle of observation. A detailed kinematic analysis of the third process shows that two or more peaks of alpha-particle energies, associated with a given angle, would be expected. But if the He^5 nucleus is in its ground state as determined by n He^4 scattering measurements[15] the number of peaks for the He^5 process would be limited to two and one of these peaks would be of too low energy to be observed by their apparatus. At all angles the peak resulting from process (2) would appear at a higher energy than any of the peaks from process (3). Since two peaks are observed, the high-energy peak is attributed to the emission of interacting neutrons. Hemmendinger states that "the dineutron appears to be unbound by a few hundred kev," although no detailed calculations, based on the absolute energy calibration from the $d(t,n)\mathrm{He}^4$ reaction, are given.

The fact that two of the $d(t,n)\mathrm{He}^4$ alpha-energy peaks almost coincide on the pulse-height scale with the two attributed to the emission of interacting neutrons suggests the possibility that either beam or target contamination by deuterium in the t-t reaction might account for the observed results. Hemmendinger[16] reports that a careful mass spectrograph analysis was carried out to eliminate this possibility and the results showed negligible deuterium contamination.

Another group at Chalk River[17] have also investigated the t-t reactions by measurement of the disintegration products. They observe no alpha-particle group with an energy equal or greater than 3.8 Mev. They therefore conclude that a dineutron of zero or greater binding energy can exist in less than one percent of the disintegrations. They also place an upper limit of one percent on the disintegrations as resulting from the existence of the dineutron in a virtual state of energy, $|E_B| \leq 0.6$ Mev, and of lifetime $\geq 3\times10^{-21}$ sec. Deuterium contamination of the target prevents them from making more detailed observations in the energy region corresponding to the unstable dineutron.

Experimental work with mesons has brought about a theoretical simplification of this general method for investigating the n-n interaction. Panofsky, Aamodt, and Hadley[18] have shown that the capture of negative pions in deuterium may lead to either of the following processes:

$$\begin{aligned}
&\pi^- + d \rightarrow 2n,\\
&\pi^- + d \rightarrow 2n + \gamma.
\end{aligned}$$

Tamor and Marshak[19,20] and Brueckner, Serber, and Watson[21] have pointed out that the gamma spectrum from the radiative capture is influenced by the n-n interaction.

Watson and Stuart,[6] using a singlet S state for the

[9] N. Feather, Nature **162**, 213 (1948).
[10] F. W. Fenning and F. R. Holt, Nature **165**, 722 (1950).
[11] N. Feather, Report of an International Conference on Elementary Particles, Tata Institute of Fundamental Research, December, 1950 (Commercial Printing Press, Bombay, India).
[12] F. W. Fenning (private communication to W. K. H. Panofsky). We wish to thank Dr. Fenning for his kindness in keeping us informed of his results.
[13] Los Alamos Scientific Laboratory, Phys. Rev. **79**, 238 (1950).
[14] A. Hemmendinger, Oak Ridge National Laboratory Report TID-372, 1950 (unpublished).
[15] Bashkin, Petree, Mooring, and Peterson, Phys. Rev. **77**, 748 (1950).
[16] We are grateful to Dr. Hemmendinger for giving us this information on the work at Los Alamos.
[17] Allen, Almquist, Dewan, Pepper, and Sanders, Phys. Rev. **82**, 262 (1951).
[18] Panofsky, Aamodt, and Hadley, Phys. Rev. **81**, 565 (1951).
[19] S. Tamor and R. Marshak, Phys. Rev. **80**, 766 (1950).
[20] S. Tamor, thesis, University of Rochester, 1950 (unpublished).
[21] Brueckner, Serber, and Watson, Phys. Rev. **81**, 575 (1951).

final state of the two neutrons, have calculated the theoretical spectra based on the phase shift which is directly related to the low-energy n-n scattering cross section through the equation $\sigma_{n-n}=4\pi/k^2\sin^2\delta$. Schwinger[23] has shown that δ may be related, through the equation $k\cot\delta\approx-1/a+\frac{1}{2}r_0k^2$, to the two parameters used to describe the low-energy scattering: a, the scattering length and r_0, the effective range. Since the spectra are not very sensitive to the exact value of r_0, they assign to it the value obtained from p-p scattering: $r_0=2.65\times10^{-13}$ cm.[23] $\alpha=1/a$ becomes the convenient parameter in this description of the n-n interaction. If α is positive the possibility of forming the bound state exists and the spectrum will be composed of a continuous part and a monochromatic line separated from the continuum by approximately the binding energy.

Previous experimental results[24] using the basic method described in this paper lead to a nominal value of $+1.2$ Mev for the lowest energy of the n-n system at which the phase shift is $\pi/2$, equivalent to a value of $hc\alpha\simeq34$ Mev. The energy resolution was such that the effect of the interaction was evident only as a change in the energy scale. The resulting uncertainty in the scattering length, however, was too poor to exclude either the bound or no-interaction case. The present work is an attempt to extend these results by improving the resolving power of the spectrometer.

II. EXPERIMENTAL METHOD

A. Basic Method

The capture of negative pions[18] at rest in hydrogen yields a monoenergetic gamma ray since it is a two-body process: $\pi^-+p\rightarrow n+\gamma_p$. The capture of negative pions at rest in deuterium[18] yields a spectrum of gamma rays

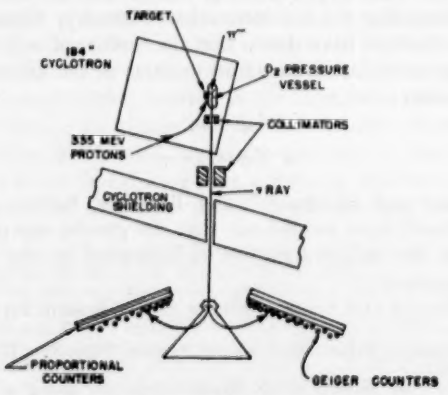

FIG. 1. Schematic diagram of geometrical arrangement of apparatus.

influenced by the n-n interaction: $\pi^-+d\rightarrow2n+\gamma_d$. The case where the two neutrons come off together, but without interaction determines the energetic upper limit for an unbound state. Conservation of energy and momentum gives, for the two processes:

$$E_{\max}(\gamma_d)=M_\pi c^2+M_d c^2-2M_n c^2[1+\tfrac{1}{4}(E_{\max}(\gamma_d)/M_n c^2)^2]^{\frac{1}{2}}=\frac{(M_\pi c^2+M_d c^2)^2-(2M_n c^2)^2}{2(M_\pi c^2+M_d c^2)} \quad (1)$$

$$E(\gamma_p)=M_\pi c^2+M_p c^2-M_n c^2[1+\tfrac{1}{2}(E(\gamma_p)/M_n c^2)^2]^{\frac{1}{2}}=\frac{(M_\pi c^2+M_p c^2)^2-(M_n c^2)^2}{2(M_\pi c^2+M_p c^2)}. \quad (2)$$

$E_{\max}(\gamma_d)-E(\gamma_p)$ determines the position of the upper limit of the continuous part of the theoretical spectra on the energy scale relative to $E(\gamma_p)$. The dependence of this position on an error in the meson mass can be shown to be

$$d[E_{\max}(\gamma_d)-E(\gamma_p)]\simeq(1/M_n c^2)[E(\gamma_p)-\tfrac{1}{2}E_{\max}(\gamma_d)]dE(\gamma_p)\simeq0.06dE(\gamma_p)\ \text{(Mev)}. \quad (3)$$

Using the value[25] $E(\gamma_p)=129.2\pm0.12$ leads to

$$\Delta[E_{\max}(\gamma_d)-E(\gamma_p)]\simeq\pm0.007\ \text{Mev}.$$

This will be seen to be a negligible factor in the present measurement. The theoretical spectra, corrected for the resolution of the instrumentation, may thus be compared with the experimental data for $\pi^-+d\rightarrow2n+\gamma_d$ without exact evaluation of the absolute energy scale provided both capture processes are observed with identical instrumentation. A mere change of the gas used as the capturing substance made this possible in the present instance.

B. General Arrangement

Negative pions are produced by bombarding a heavy-element target (in this case thorium) with the internal proton beam of the 184-inch Berkeley synchrocyclotron. Some of the pions are then absorbed in deuterium gas at 2700 psi. The gas is confined in a vessel contiguous to the primary (proton beam) target. Gamma rays emitted in the reaction $\pi^-+d\rightarrow2n+\gamma_d$ are permitted to enter a pair spectrometer through a collimating system which shields the spectrometer from the primary target (Fig. 1). A detailed description of this experimental arrangement is given in the paper by Panofsky *et al.*[18]

The events comprising the data are Geiger-tube co-

[23] J. Schwinger, Phys. Rev. **72**, 742 (1947); hectographed notes on nuclear physics, Harvard, 1947 (unpublished).
[23] J. D. Jackson and J. M. Blatt, Revs. Modern Phys. **22**, 77 (1950).
[24] Aamodt, Panofsky, and Phillips, Phys. Rev. **83**, 1057 (1952).
[25] K. M. Crowe, paper to be submitted to *Review of Scientific Instruments;* K. M. Crowe, thesis, University of California (unpublished); K. M. Crowe and R. H. Phillips, preceding paper [Phys. Rev. **96**, 470 (1954)].

incidences resulting from detection of the pair fragments (see Fig. 1). The Geiger tubes are gated by a quadruple coincidence between both sides of both proportional counters in coincidence with a beam-pulse gate. A measurement of the energy of the pair fragments determines the energy of the incident gamma ray.

The present pair spectrometer has been redesigned from that used by Panofsky to improve the energy resolution. This was accomplished by changing the location of the Geiger tubes to reduce the defocusing effects of multiple scattering in the converter. Figure 2 is a schematic drawing showing how first-order horizontal angular focusing results from the geometry used. In addition an increased number of detector channels (110) were used with the energy defining aperture reduced to 0.75 Mev (Fig. 2).

The same equipment has been used in a precision measurement of the mass of the π^- meson as described in the companion paper.[25] The magneto-optical features have been described in that paper and the detailed theory of the spectrometer is being submitted for publication in the *Review of Scientific Instruments*.[25] Since the experimental results have been shown to be essentially independent of an absolute energy scale, a more detailed analysis of the pair spectrometer is unnecessary except insofar as the resolution or detection efficiency is energy dependent (see Sec. F).

C. Operation of the Runs

The entire running time extended continuously over a period of ten days. The net data collection time was 37.8 hours for deuterium, 26.0 hours for hydrogen, and 22.1 hours for background. The background runs were made by evacuating the high-pressure vessel. Total counts were 421 hydrogen gammas, 432 deuterium gammas, and 824 background gammas.

Plateaus for the proportional counters and associated electronics were established using the gamma-ray flux from neutral pion decay[26] by moving the primary target into the collimated line of observation. The 140 odd Geiger tubes and their associated electronics were individually checked at the beginning of the runs and at the end of each day by means of a radioactive source. No replacements were necessary. The magnetic field was maintained constant to ± 0.02 percent throughout the experiment by monitoring with a nuclear fluxmeter.

D. Background Effects

The observed background is attributed to decay gammas from neutral pions produced by scattered protons which strike the high-pressure vessel. The shape of the background spectrum substantiates this. Consideration must be given to the fact that processes other than the radiative capture of the negative pion may have taken place when the deuterium was introduced. Besides negative pions, positive and neutral pions, protons, neutrons, and gamma rays are produced by the 335-Mev protons incident on the heavy-element primary target. Some of these particles can give rise to high-energy gamma rays when they interact with the deuterium. These interactions are now listed in order of their importance.

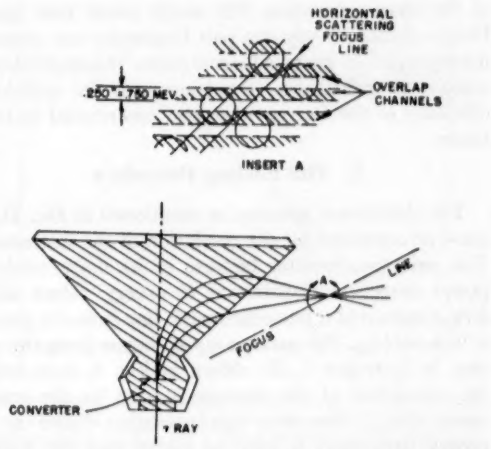

FIG. 2. Schematic diagram to show how first-order horizontal angular focusing of the pairs is achieved. The Geiger-tube array is grouped about the focus line as shown in the insert. The region of constant magnetic field is shaded; region of no magnetic field is unshaded. (Fringing field is neglected in this approximation.)

Charge exchange scattering of either positive or negative pions can produce neutral pions with their consequent high-energy decay gammas. A calculation based on the charge exchange cross section for negative pions reported by workers at Rochester[27] gives an effect which is less than one percent of the measured radiative capture. A search for charge exchange scattering of negative pions stopped in deuterium[28] gave a negligible upper limit for this process. Evidence that charge exchange scattering is negligible in the present experiment is also given by the result of previous experimental work on the capture of negative pions in deuterium.[18,29] Attempts to observe gamma emission from neutral pions resulted in a null effect (-2.5 ± 7.2 percent of the radiative capture intensity).

Any decay gammas from neutral pions produced by stray high-energy particles incident on the deuterium would also have shown up in the previous deuterium capture experiments. The null effect mentioned above rules this out.

The data showed no evidence of being influenced by accidentals. Coincidences between three or more Geiger channels and other multiple events, not caused by a single gamma-ray pair, comprised less than ten percent

[26] Bjorklund, Crandall, Moyer, and York, Phys. Rev. **77**, 213 (1950).

[27] R. Wilson and J. P. Perry, Phys. Rev. **84**, 163 (1951); Roberts, Spry, and Tinlot, Phys. Rev. **90**, 343 (1954).

[28] J. Steinberger and W. Chinowsky, Phys. Rev. **95**, 623(A) (1954).

[29] R. L. Aamodt, thesis, University of California, 1951 (unpublished).

of the observed events. The single count rate (gated Geiger counts of only one pair fragment) was approximately equal to the rate for real pairs. This is attributed mainly to end effects. Deadtime and the individual efficiency of the Geiger tubes also contributed to these losses.

E. The Folding Procedure

The theoretical spectra, as mentioned in Sec. II, A, must be corrected for the resolution of the instrument. The pair spectrometer because of its finite resolving power detects a distribution of energy values about $E(\gamma_p)$ instead of a monochromatic line from the process $\pi^-+p\rightarrow n+\gamma_p$. The gamma-ray spectrum from the capture in hydrogen $I_\gamma(E)$ shown in Fig. 3, thus defines the resolution of the instrumentation at the energy value $E(\gamma_p)$. Provided this resolution curve is not energy dependent it may be folded into the various theoretical spectra for comparison with the experimental results.

The folding operation is

$$\phi(E)=\int_{-\infty}^{+\infty} I(t)R(t-E)dt,$$

where $I(t)$ is the theoretical spectrum, and $R(t)$ is the resolution curve (the kernel) which describes the distribution of energy values around an origin defined by the setting of the instrument. In general, this origin must be determined by a theoretical analysis of the characteristics of the instrumentation which produce the spread in energy values. As has been shown [Eq. (3)], no exact evaluation of the energy scale is necessary for evaluation of the final result of this experiment. The method of correcting the data for the resolution of the instrumentation is also independent of any error in determining the origin of the kernel. Physically this independence follows from the fact that the value $E(\gamma_p)$ chosen for the origin is also the value which determines the position of $I(t)$ on the energy scale. This may be shown as follows. The origin of the kernel is the measured value $E(\gamma_p)$ and is thus the origin in a plot of $R(t)=I_\gamma\{-[E-E(\gamma_p)]\}$. An error $(-\Delta E)$ in the measured value of $E(\gamma_p)$ thus results in a change $(+\Delta t)$ in the origin of the kernel. The kernel now becomes $R(t+\Delta t)$. But this change in $E(\gamma_p)$ also changes the position of the spectrum $I(t)$ by an amount Δt. The resulting fold is

$$\phi(E)=\int_{-\infty}^{+\infty} I(t+\Delta t)R[(t+\Delta t)-E]dt.$$

Thus $\phi(E)$ is independent of Δt.

Equation (3), gives the error in the position of the theoretical spectra caused by an error in the origin, $E(\gamma_p)$, of the kernel. Watson and Stuart[6] assumed a value $E_{\max}(\gamma_d)=132.00$ Mev which corresponds to an

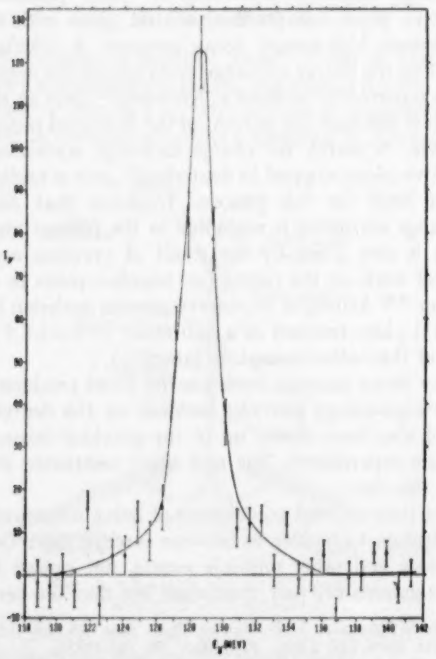

FIG. 3. $I_\gamma(E)$, the energy spectrum of the gamma ray from the process: $\pi^-+p\rightarrow n+\gamma_p$ with background subtracted. The data have been corrected for energy dependent factors (Sec. II, F).

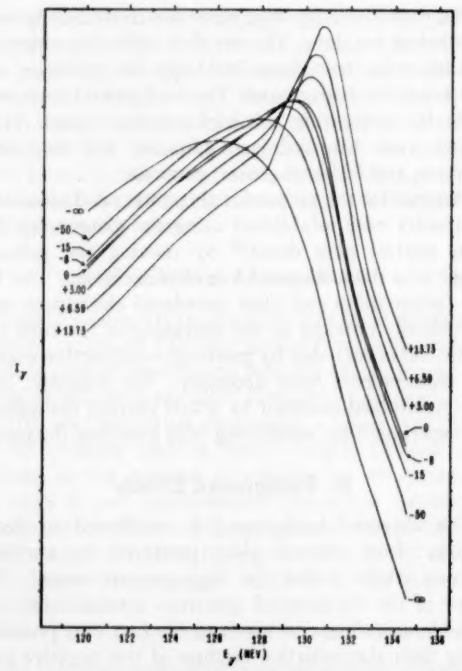

FIG. 4. Plot of the folded theoretical spectra; i.e., the theoretical spectra as deduced by Watson and Stuart (see reference 6) folded with the resolution function, $R(t-E)$.

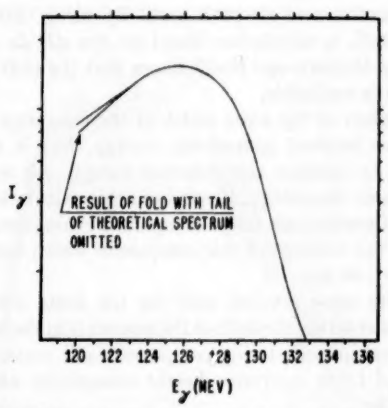

FIG. 5. Fold of the resolution function with the theoretical spectrum for $\hbar c\alpha = -\infty$ showing result of omitting the tail below 120 Mev of the theoretical spectrum.

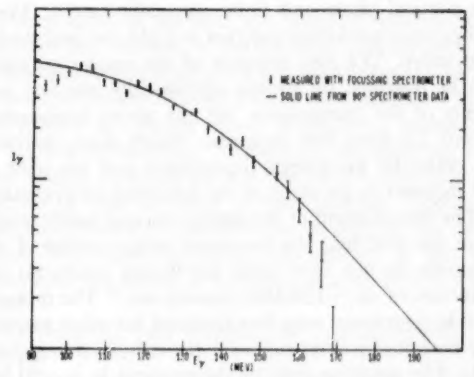

FIG. 6. Neutral meson gamma-ray spectrum obtained with the pair spectrometer by bombarding wolfram with 340-Mev protons. The observation angle is 180°. The solid curve is the same spectrum as obtained by Crandall (see reference 30) with the conventional nonfocusing 90° wedge-spectrometer geometry.

origin at $E(\gamma_p)=129.9$ Mev. For the purposes of this analysis the error introduced by using the calculated curves is negligible since the measured value[25] of $E(\gamma_p)$ is 129.2 ± 0.12. The folded theoretical spectra are shown in Fig. 4.

The theoretical curves[6] are uncertain in the energy region below 120 Mev, but this should result in an insignificant error in the final folded theoretical curves because both the theoretical curves and the kernel have low values of $I_\gamma(E)$ in this region. The effect was checked by a fold performed omitting the entire tail (below 120 Mev) of one of the theoretical spectrum. The spectrum for the case $\hbar c\alpha = -\infty$ was used for this check. It would show the maximum effect since it has the largest values of $I_\gamma(E)$ in this region of any of the theoretical spectra. The result is shown in Fig. 5. A calculation based on the analysis of the data as described in Part G below shows that this procedure results in less than a three percent error in evaluating the spectrum for $\hbar c\alpha = -\infty$ for comparison with the experimental results. Thus even a large error in the theoretical data below 120 Mev would have a very small effect on the fold.

F. Energy Dependence of Efficiency and Resolving Power

It is important that no energy-dependent errors distort the observed gamma-ray spectra. A major source of energy dependence of the detection efficiency of the pair spectrometer results from its finite size, since it detects a variable fraction of the possible pair combinations for a given E_γ. A correction for this effect is easily calculated from the known geometry of the Geiger counter[29,30] array.

A correction was made for the variation of the pair production cross section as a function of energy. The maximum effect was less than $1\frac{1}{2}$ percent for I_γ from capture in deuterium. No correction is necessary for I_γ from capture in hydrogen since $E(\gamma_p)$ is monochromatic.

Multiple scattering in the converter is a source of energy-dependent losses in the observed intensity of gamma rays. The defocusing effect of the fringing field is not independent of the energy of the vertically scattered electrons. As a result they are scattered into a solid angle which is energy dependent whereas the vertical defining aperture of the Geiger tubes is constant. The rather large (three square inches) converter used will magnify this effect. A measurement of the relative efficiency was made with π_0 decay gammas of known intensity to determine the magnitude of this effect (Fig. 6). The details are given in the paper dealing with the associated experiment.[25] It is shown that no significant losses occur except at the ends of the spectrum which are far from the region of interest for both capture processes as will become apparent later in this section.

The resolution, as has been pointed out, must not be energy dependent if it is to be used in the folding operation over the range of energy values of the theoretical spectra. The final analysis of the data (see Sec. II, G), is based on evaluation of the first moment of the folded theoretical curves. The fold with $R(l-E)$ will only result in an error in the evaluation of the first moment of the folded theoretical curves if the first moment of $R(l)$ is energy dependent. A theoretical analysis of the resolution curve of the pair spectrometer[25] involves consideration of (1) energy channel width, (2) multiple scattering of the pair in the converter, (3) radiation straggling of the pair in the converter, (4) energy loss resulting from ionization by the pair, (5) lateral width of the converter, and (6) higher-order defocusing effects resulting from (a) multiple scattering of pair fragments in the horizontal plane, (b) motion in

[30] W. E. Crandall, thesis, University of California, 1952 (unpublished).

the vertical plane and finite converter height. These components are folded together to yield the final resolution curve. The first moment of the resolution curve can be obtained by adding algebraically the first moments of the components. All the above components except (2) have first moments, which must therefore be examined for energy dependence and the shift of the moment in the range of the fold must be evaluated.

The first moment of the energy-channel width results from the fact that the measured energy values of the channels do not agree with the design values for the detection of an ~129-Mev gamma ray.[25] The moment of this component may be calculated for other gamma-ray energies by averaging over the corresponding channels. The resulting shift of the moment is ~−30 kev for the extreme range of the fold.

The radiation straggling component can be derived from Heitler's expression[31] for the probability, $W(y)dy$, that an electron will retain ϵ^{-y} times its initial energy in traversing a thickness l of converter. By a change of variable the probability $W(E/E_0)dE$ that the electron retains a fraction E/E_0 of its initial energy E_0 is

$$W(E/E_0)dE \simeq \frac{[\Gamma(bl)]^{-1}}{E_0(\ln E_0/E)^{1-bl}}dE \quad bl \leq 0.1.$$

The first moment can be shown to be

$$M(W) \simeq E_0 - \frac{bl}{1+bl}(E_0 - E_e),$$

where E_e is the cutoff value assumed for this component of the resolution. Comparison of the values of $M(W)$ for extreme values of E_0 in the range of the fold shows the shift in $M(W)$ is negligible.

The probability of energy loss from ionization is approximately constant up to a value of ~1.4 Mev for the converter and air path used. By using this value as a cutoff, a calculation based on the dE/dx curves given by Halpern and Hall[32] shows that the shift of the moment is negligible.

The effect of the finite width of the converter varies with the incident gamma-ray energy, but is always such as to increase the observed energy, the more so the greater the energy. Results of orbit calculations for different energy pair fragments permit evaluation of the shift in the moment of this component which turns out to be ~−80 kev.

By the same method used for the finite converter width calculation the shift of the moments in the second-order multiple scattering component and vertical motion and finite converter height component are each ~−30 kev.

The resultant shift thus adds to ~−170 kev. However, two important factors tend to minimize any effects of this shift. First, the intensity of the theoretical curves is in general low outside a region within approximately 3 Mev of the energy value (~129 Mev) at which the resolution curve is determined, whereas the above shifts are computed on the basis of the extreme range of the fold (~12 Mev). Second, the method of treating the data (II, G) weights the folded curves inversely as the distance from this energy value (~129 Mev). We therefore conclude that the influence of these shifts on the final data is negligible as compared with the other sources of error (see the next section).

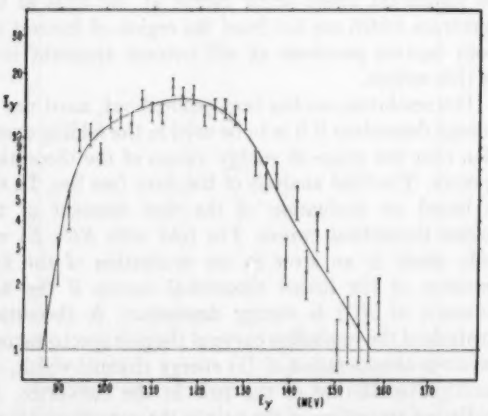

FIG. 7. Smoothed background spectrum uncorrected for energy dependent factors (Sec. II, F). The statistical probable error of the combined points is shown.

G. Treatment of the Data

The reduction of the raw data from the pion capture reactions requires the normalization of the background counts to those of the γ_p and γ_d signal data. Any normalization procedure depends on some method of evaluating the relative beam intensity and detection efficiency from one type of run to another. The beam monitoring methods attempted were not found to be internally consistent to better than ±10 percent over the ten day run.

An alternative procedure based on the data itself was used to obtain the normalization for the background subtraction. The background data were averaged over three energy channels using a simple arithmetical mean and a smooth curve was drawn through the result. The curve was adjusted to the data by balancing probable errors. This process was repeated independently for the two other possible ways of combining the results of three energy channels. The values of all three smoothed curves were averaged to give the values for the final smoothed background curve. This curve was then plotted on semilog paper (Fig. 7) to permit normalization by visual matching of slopes. This same procedure was carried out for the γ_p and γ_d signal data.

The theoretical resolution curve[25] mentioned above and the actual data show that the full width at half-

[31] W. Heitler, *The Quantum Theory of Radiation* (Oxford University Press, London, 1944), second edition, p. 225.

[32] O. Halpern and H. Hall, Phys. Rev. **73**, 484 (1948).

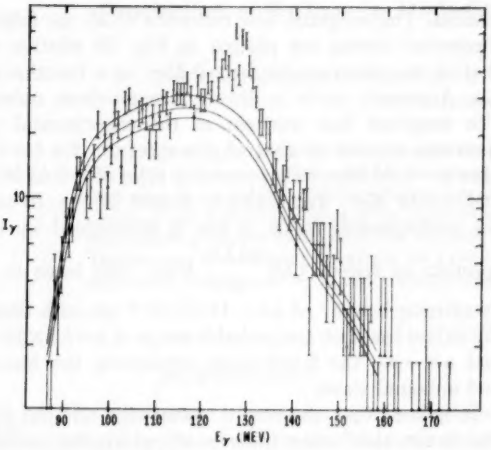

FIG. 8. Unadjusted data showing gamma-ray spectra from $\pi^-+d\rightarrow 2n+\gamma_d$. The data are uncorrected for energy-dependent factors (Sec. II, F). All three normalizations of the smoothed background spectrum are shown. The "best" fit is the middle curve.

maximum of the γ_p signal is approximately two Mev and the signal is below one percent of its peak value beyond ten Mev on either side of the peak. It is, therefore, possible to normalize the background to the γ_p signal by matching slopes of the two curves excluding the region within ten Mev of the peak of the γ_p signal. Because of the strong peaking of the signal as a result of the improved resolution, the resulting folded theoretical spectra are insensitive, within the statistical error, to a five percent change in the normalization factor.

The observed resolution curve (I_γ, Fig. 3), which was used in the fold is in good agreement with the theoretical resolution curve[25] and does not have any significant uncertainty resulting from background normalization.

In the normalization of the γ_d signal no assumption may be made regarding the limitation of signal intensity in the energy region below the peak since the shape of the spectrum is unknown. The background was therefore normalized using three different factors: (1) "best" fit, (2) fit to high-energy signal, and (3) fit to low-energy signal (Fig. 8). The final result was evaluated using all three factors to check the sensitivity of the data to the background normalization. The high and low normalization gives a final result in disagreement by 0.18 Mev at most, with the result calculated on the basis of "best" fit normalization. This effect is included in the probable error. It will be noted that the region of energy dependent losses as shown in Fig. 6 lies beyond any significant γ_d signal for any of the three normalization factors.

The final γ_d signal with background subtracted and the correction made for energy dependent factors (Sec. II, F) is shown in Fig. 9.

The analysis of the data was made by evaluating a weighted first moment of this net experimental data for comparison with the weighted first moment of the folded theoretical curves. The deuterium spectrum has a long tail toward low energy which is relatively insensitive to the n-n interaction. The method of weighting has been chosen to minimize this tail with a resulting reduction in the accuracy of the moment. Although elaborate statistical methods can be applied, we have chosen the weighting factor proportional to the reciprocal of the square of relative probable error at each point.

The weighted first moment, M, was determined as follows:

$$M=\Sigma\frac{N_iF_i}{W_i^2}E_i\Big/\Sigma\frac{N_iF_i}{W_i^2},$$

where

$$W_i^2=\frac{\{[\frac{1}{3}(0.675)(m_{i-1}+m_i+m_{i+1})^{\frac{1}{2}}\mathfrak{N}]^2+(0.675)^2n_i\}}{N_i^2},$$

n_i = number of counts in channel i of the γ_d spectrum, m_i = number of counts in channel i of the background effects, $N_i=n_i-\mathfrak{N}m_i$, F_i = energy dependent correction factor (Sec. II, F), $\mathfrak{N}$ = background normalization factor. The same weights, W_i, were used in the determination of the weighted moment of the experimental data and the theoretical curves. The probable error of the calculated value of M was determined by the method of propagation of errors to be $\delta M=\pm 0.39$ Mev. M was considered as a function of one variable only, N_i. The contribution to the error in M from the error in the combined probable error of the signal and background is of the second order and was neglected.

M was determined for all three background normalization factors for the γ_d spectrum. The quoted value of M is based on the "best" fit normalization (see above). The two other normalization factors resulted in M values differing by $\Delta M=+0.18$ Mev (using background fit to high-energy signal) and $\Delta M=-0.13$

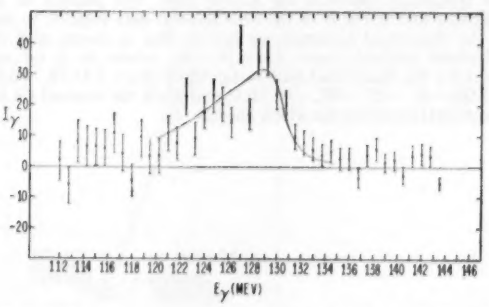

FIG. 9. Gamma-ray spectrum from $\pi^-+d\rightarrow 2n+\gamma_d$ with background subtracted. The data have been corrected for energy-dependent factors (Sec. II, F). The statistical probable error is shown. The solid line is the theoretical spectrum for $\hbar c\alpha=-15$ Mev. Of the calculated theoretical spectra, this is the one for which $\hbar c\alpha$ is closest to the experimentally measured $\hbar c\alpha=-12.4$.

Mev (using background fit to low-energy signal). The final error was evaluated as

$$[(\delta M)^2+(\Delta M)^2]^{\frac{1}{2}}=\begin{matrix}+0.43\\-0.41\end{matrix}\text{ Mev.}$$

III. RESULTS AND CONCLUSIONS

The parameter chosen for comparison of the experimental data with the theory is the weighted first moment as defined above. The position of Watson and Stuart's theoretical spectra[6] on the energy scale, relative to the observed γ_d spectrum, is established by the observed γ_p spectrum as described in Sec. II, A. The most probable value of $\hbar c\alpha$ corresponding to the observed γ_d spectrum is then determined in the following manner. The weighted first moments of all the folded theoretical curves are plotted in Fig. 10 relative to that of the spectrum for $\hbar c\alpha=0$ Mev as a function of $\hbar c\alpha$. A smooth curve is drawn through these points. The weighted first moment of the experimental γ_d spectrum relative to that of the spectrum for $\hbar c\alpha=0$ Mev is -0.43 Mev with a probable error of $+0.43$ Mev and -0.41 Mev. This value is plotted in Fig. 10 and the corresponding value of $\hbar c\alpha$ is determined by inspection as $\hbar c\alpha=-12.4^{+12.4}_{-10.9}$ Mev. This leads to a "scattering length" of $a=-15.9\times10^{-13}$ cm with limiting values based on the probable errors of $a=8.5\times10^{-13}$ and $a=-\infty$, the latter value separating the bound and unbound states.

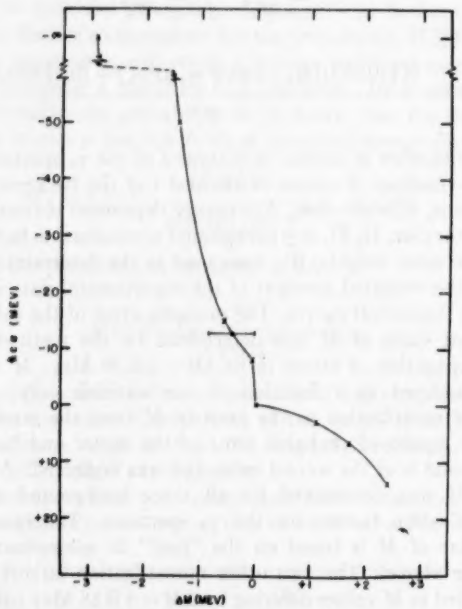

FIG. 10. Plot of the shift of the weighted first moment of the theoretical gamma-ray spectra from $\pi^-+d\rightarrow 2n+\gamma_d$ relative to the theoretical spectrum for $\hbar c\alpha=0$ Mev. The position of the weighted first moment of the experimental data relative to that of the theoretical spectrum for $\hbar c\alpha=0$ Mev is shown with the calculated probable error. $\Delta M=M_i-M_0$, where M_i is the moment for the theoretical spectra for which $\hbar c\alpha=+13.73$, $+6.59$, $+3.00$, -8, -15, -50, $-\infty$ Mev, and M_0 is the moment for the theoretical spectrum for which $\hbar c\alpha=0$.

It is seen that the results essentially rule out the "no interaction" case ($\hbar c\alpha=-\infty$) which lies outside the measured value by six probable errors. The probable error is still too large, however, to conclude definitely that there is no bound state of the n-n system. The probability is less than 0.1 percent that the dineutron is bound by more than 50 kev.

The results are consistent with the p-p and n-p scattering data and are thus in agreement with the theory of charge independence of nuclear forces.

IV. ACKNOWLEDGMENTS

We are indebted to Dr. W. K. H. Panofsky of Stanford University for his inspiration and patient assistance throughout this work. The basic experimental arrangement was conceived by him for the pioneer negative pion capture experiments. Dr. Watson and Dr. Stuart kindly made available their original data for the "folding" process. Much valuable information was gained from discussions with Dr. Warren Heckrotte, Dr. Louis Henrich, and Dr. Herbert York. Mrs. Ardith Kenney graciously devoted many hours of her spare time to the tedious calculations. Mr. John Kohot was of special aid in the detailed design of the equipment. The cyclotron crew under Mr. James Vale and Mr. Lloyd Hauser was especially cooperative. The complexity of the experiment required much help during the collection of the data and the assistance of the many who are not specifically mentioned above is gratefully acknowledged.

Production of Tritons in High-Energy Deuteron-Deuteron Collisions*

C. S. GODFREY
Radiation Laboratory, Department of Physics, University of California, Berkeley, California
(Received July 6, 1954)

The differential cross section for the process $d+d\rightarrow H^3+p$ has been measured at six angles extending from 20° to 85° in the center-of-mass system. Deuterons of 190 Mev from the Berkeley 184-inch synchrocyclotron were used. A coincidence counting system, consisting of scintillation counters for both particles, was employed. Time of flight and range of the particles were made use of, both in identifying the process and in discriminating against background. The resulting cross section is highly peaked in the forward direction. The behavior is explained qualitatively by a theoretical calculation based on an extension of the stripping mechanism first proposed by Serber. The total cross section for the reaction is estimated to be 4.1 millibarns.

INTRODUCTION

WHEN high-energy deuterons in the Berkeley 184-inch synchrocyclotron were first allowed to strike a target, it was found that an intense cone of high-energy neutrons was projected in the same direction of motion as the incident deuterons. Serber[1] proposed a "stripping" mechanism to explain its formation. In this process, one nucleon of the deuteron interacts suddenly with the target nucleus while the other nucleon is largely unaffected in its motion. It was felt that the formation of H^3 and He^3 particles in deuteron-deuteron collisions might be considered as a stripping process in which the neutron or proton, respectively, of one deuteron might interact with and "stick to" the other deuteron—leaving its partner to continue with essentially the same momentum it had at the instant of stripping. A theoretical calculation by Heckrotte and Bludman[2] obtained the general shape of the angular distribution for the pure stripping process. The present experiment was designed to measure the absolute differential cross section for the process $d+d\rightarrow H^3+p$ over as wide a range of angles as possible and compare it with that expected of a stripping process.

EXPERIMENTAL PROCEDURE

Since the external deuteron beam is essentially monoenergetic, the kinematics of the above process can be calculated uniquely for any scattering angle by applying the laws of conservation of energy and momentum. This calculation was carried out relativistically. Since the colliding deuterons are indistinguishable, the cross section must be symmetric about 90° center of mass. It is necessary to measure the scattering only from 0° to 90° to obtain the complete differential cross section.

The high background in the Berkeley "cave" has been one of the major difficulties to be overcome for any low-cross-section experiment. Recently, time-of-flight techniques have been used successfully in the cave to reduce the effect of this background. The range of energies and angles required in this experiment seemed quite suitable for the application of similar methods in the above process. Since the time of flight of the tritons over an eleven-foot path (the usable length of the cave) from target to detector was the order of 30 millimicroseconds, it was necessary to use a coincidence circuit considerably faster than this. The circuit used had a resolving time of about 3 millimicroseconds. As a further aid in discriminating against background and providing identification, absorbers were used in front of the detectors.

The experimental arrangement for a typical scattering angle is shown in Fig. 1. The apparatus, electronics, and experimental procedure are so similar to those described by Frank[3] in measuring the differential cross section for the reaction $p+d\rightarrow H^3+\pi^+$, that they need not be repeated here.

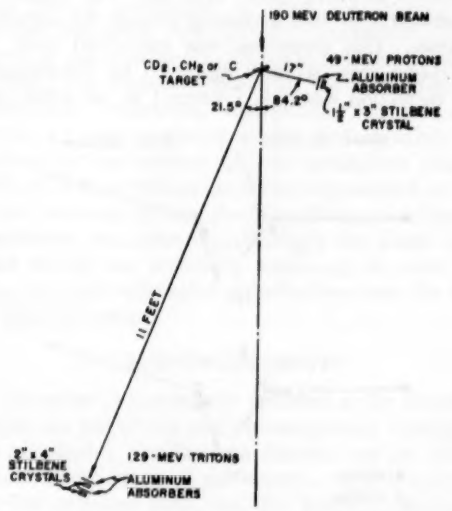

FIG. 1. Experimental arrangement for observing the process $d+d\rightarrow H^3+p$.

* This work was performed under the auspices of the U. S. Atomic Energy Commission.

[1] Robert Serber, Phys. Rev. 72, 1008 (1947).

[2] W. Heckrotte and S. Bludman (private communication).

[3] Frank, Bandtel, Madey, and Moyer, Phys. Rev. 94, 1716 (1954).

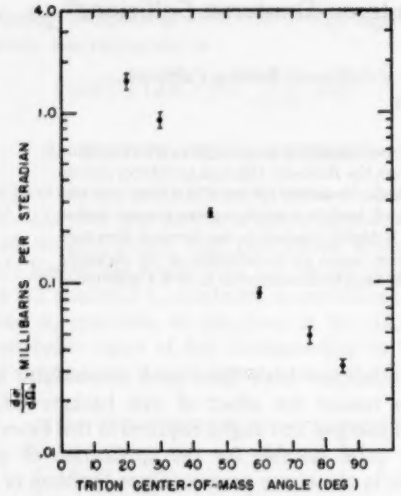

FIG. 2. Experimental angular distribution for the process $d+d \rightarrow H^3+p$ on semilog coordinates.

RESULTS AND CORRECTIONS

Data for an angular distribution were taken at six laboratory angles chosen to cover as nearly as possible the center-of-mass scattering range of 0° to 90°. These uncorrected data are summarized in Table I. This difference rate is the counting rate R that appears in the cross-section formula. The apparent high counting rates for the last two readings are due to use for these data of a monitor having a calibration differing by a factor of ten from that used for the other data.

Three corrections were applied to the original difference counting rate. The first was caused by absorption of protons in passing through the aluminum absorber. This correction was calculated from the absorption cross sections measured by Kirschbaum.[4] The correction was only 7 percent in the worst case.

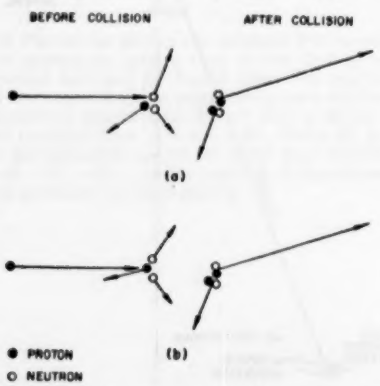

FIG. 3. Diagram showing typical laboratory momenta of particles before and after collision in the $p+H^3 \rightarrow d+d$ process: (a) for pure pickup interaction, (b) for indirect pickup interaction resulting in same external momenta.

[4] Albert J. Kirschbaum, thesis, University of Californai Radiation Laboratory Report No. UCRL-1967 (unpublished).

TABLE I. Counting rate with CD_2 target minus counting rate with C target in counts per volt of integrated beam.

Triton c.m. angle	Difference between CD_2 and C rates	Ratio of CD_2 to C rates
20°	7.69±0.85	2.3:1
30	6.88±0.76	5.3:1
45	10.31±0.65	7.4:1
60	5.23±0.36	5.3:1
75	24.7 ±2.9	7.5:1
85	10.9 ±1.0	12.0:1

The second correction was necessitated by absorption of the tritons in the aluminum absorbers or in the first stilbene crystal. It is not possible to make a rigorous correction for this effect. The following attack was employed to give an estimate of the correction. Crandall[5] has measured the total inelastic cross section of high-energy He^3 particles for various elements. By assuming that the probability of a nuclear event at high energy is the same for a H^3 as for a He^3, it is possible to calculate the attenuation of the tritons in going through the absorber. The majority of the inelastic events, however, constitute stripping processes in approximately two-thirds of which a fast deuteron continues in the forward direction. Since these deuterons, in general, still produce a pulse in the triton detector, only something of the order of one-third of the inelastic events are lost. Since the inelastic attenuation in the worst case was 21 percent, the maximum correction is around 7 percent.

The third correction was that for small-angle scattering losses. These losses were minimized by having the proton detector subtend a considerably larger solid angle than the triton detector. Under these conditions, the worst correction amounted to 8 percent.

The correction factors are summarized in Table II.

The center-of-mass differential cross section is obtained from the relation

$$d\sigma/d\Omega_0 = RC/N_b N_t \Delta\Omega_0.$$

The numerator is the product of the original difference rate R and the total correction factor C. N_b is the deuteron beam flux in deuterons per integrated beam unit; it is calculated from the ion-chamber calibration factor and the capacitance of the integrating condenser. N_t is the target particle density in deuterons per cm^2; it depends on the weight, area, and composition

TABLE II. Correction factors for proton and triton absorption and scattering

Triton c.m. angle	Proton absorption	Triton absorption	Scattering	Total
20°	1.00	1.07	1.07	1.14
30	1.00	1.06	1.03	1.09
45	1.00	1.05	1.08	1.13
60	1.01	1.03	1.07	1.11
75	1.04	1.02	1.08	1.15
85	1.07	1.01	1.08	1.17

[5] Walter E. Crandall (private communication).

of the target and the angle made by the target with respect to the beam. $\Delta\Omega_0$ is the center-of-mass solid angle subtended by the triton detector; it is calculated from the laboratory solid angle by means of the calculated relativistic transformation. The final results are given in Table III and plotted in Fig. 2.

The errors shown are the statistical deviations related to the number of counts constituting the original data. The errors in N_b, N_t, and $\Delta\Omega_0$ have been neglected as far as relative angular distribution data are concerned, since they are the same for each angle and affect only the total absolute cross section. The error in N_b is estimated to be several percent; in N_t about 1 percent or 2 percent; and in $\Delta\Omega_0$ around 5 percent. The corrections to the data are relatively small, but if it is assumed that they could contribute an error of 5 percent, one can estimate that the absolute results have an uncertainty of about 15 percent. When a smooth curve is drawn through the data of Fig. 2, the integrated total cross section is estimated to be 4.1 millibarns.

TABLE III. Corrected experimental differential cross section for the process $d+d\rightarrow H^3+p$.

Triton c.m. angle	$\frac{d\sigma}{d\Omega_0}$ (millibarns/steradian)
20°	1.54 ±0.17
30	0.905 ±0.100
45	0.258 ±0.016
60	0.0871±0.0060
75	0.0486±0.0057
85	0.0317±0.0029

CONCLUSION

A discussion of the mechanism for the production of tritons in the reaction $d+d\rightarrow H^3+p$ can be facilitated by considering instead the inverse process $p+H^3\rightarrow d+d$. This merely changes one's point of view; i.e., we now consider a pickup mechanism instead of a stripping mechanism. By the law of detail balance, however, the interaction matrix remains the same. One postulates that there is a sudden interaction between the proton and one of the H^3 nuclei, and further that the momenta of the other two nuclei of the H^3 are essentially unaffected by the interaction. Two cases are of interest: (a) where the two interacting nuclei end up in the same deuteron, and (b) where they end up in different deuterons. Momentum diagrams for these two interactions are shown in Fig. 3. Both these processes have been observed in the proton bombardment of nuclei. The first situation is identical to the pickup mechanism proposed by Chew and Goldberger[6] to explain the presence of fast deuterons in the forward direction when matter is bombarded with high-energy protons or neutrons. The second situation might be called an indirect pickup, as it consists of a proton's scattering in a nucleus and then finding a pickup partner of momentum compatible to the formation of a deuteron. This indirect pickup process could contribute to the scattering process at wide angles where the pure pickup cross section would be negligible. Using 360-Mev protons, Wilmot Hess is measuring the indirect pickup cross section for various elements. Preliminary results[7] indicate that a substantial fraction of the deuterons observed at 40° laboratory system for p-d scattering are a result of indirect pickup rather than pure pickup. In the $p+H^3\rightarrow d+d$ process, one would expect a comparatively low cross section, since the momenta must be compatible to the formation of two deuterons instead of just one. In the pure pickup interaction, for example, not only must the two interacting particles form a deuteron, but also the two remaining nuclei of the H^3 must be left in a state corresponding to that of a deuteron.

Using the Born approximation, Dr. Bludman and Dr. Heckrotte set up the integrals for the matrix elements of the cross sections for the $d+d\rightarrow H^3+p$ reaction. There were two integrals involved; one corresponding to the pure pickup and the other corresponding to the indirect pickup contribution. The pure pickup cross section was readily solved in terms of the momentum distributions of the deuteron and the triton. On the assumption of the Hulthén wave function for the deuteron, and the wave function proposed by Messiah for the triton, the distribution of the $d+d\rightarrow H^3+p$ cross section was calculated. It was found to behave exponentially in the forward direction in a manner similar to the experimental data. The slope of the theoretical curve, however, was greater than that of the experimental curve. The contribution of the pure pickup calculation at wide scattering angles became negligible, whereas the experimental curve shows an appreciable contribution at these angles.

Hess's experiments suggest that the indirect pickup mechanism contributes substantially to the cross section at wide scattering angles. Unfortunately, the integral for the indirect pickup interaction was too difficult to solve without an undue expenditure of time.

One can conclude that the pure pickup (or stripping) mechanism can explain qualitatively the shape of the cross section for scattering angles up to about 45° c.m., but that substantial contributions must be made by other processes.

ACKNOWLEDGMENTS

The author is particularly indebted to Dr. Burton J. Moyer for his advice and encouragement throughout the experiment. Dr. Kenneth Bandtel and Dr. Wilson Frank shared much of the onerous work of carrying out the cyclotron runs, and Dr. Richard Madey led the development of the electronic equipment used. Thanks are due the graduate students of Dr. Moyer's group for their help in executing the cyclotron runs. Paul Nikonenko has fabricated much of the electronic equipment used.

[6] G. F. Chew and M. L. Goldberger, Phys. Rev. **77**, 470 (1950).
[7] Wilmot N. Hess (private communication).

Absorption of Positive Pions by Deuterium at 76 and 94 Mev*

HENRY L. STADLER
Institute for Nuclear Studies, The University of Chicago, Chicago, Illinois
(Received June 28, 1954)

The absorption of positive pions by liquid deuterium has been studied with scintillation counters, using a collimated pion beam from the Chicago synchrocyclotron. The differential cross sections for the production of protons at angles of 35°, 45°, 60°, and 90° are 1.189±0.076, 0.926±0.058, 0.643±0.061, and 0.442±0.052 millibarns per steradian at 94 Mev and 1.010±0.102, 0.718±0.081, 0.431±0.073, and 0.300±0.058 millibarns per steradian at 76 Mev in the center-of-mass system. The angular distribution can be represented by $a+\cos^2\theta$ with the following values of a: 0.268±0.089 at 76 Mev and 0.388±0.082 at 94 Mev. The total cross sections are 7.38±1.21 millibarns at 76 Mev and 9.70±1.03 millibarns at 94 Mev.

I. INTRODUCTION

THE theory of the pion absorption reaction, $\pi^+ + d \rightarrow p + p$, has been investigated by many authors[1–12] and measurements of its cross section have been made at 23, 25, 40, and 53 Mev.[13,14] (All energies mentioned in this section refer to pion energy in the center-of-mass system.) In addition, the inverse reaction, pion production, $p+p \rightarrow \pi^+ + d$, has been measured at a number of energies between 10 and 64 Mev.[15–19] A review of the measurements of both the absorption and production reactions is contained in Rosenfeld.[12] The angular distributions at pion energies between 19 and 64 Mev appear to be representable as $d\sigma/d\omega \propto a+\cos^2\theta$, where a represents the isotropic contribution to the differential cross section. a seems to decrease from about 0.3 at 20 Mev to less than 0.2 at 64 Mev. This paper reports measurements of the angular distribution and total cross section of the absorption reaction at somewhat higher energies than have been studied before.

The following section describes the arrangement of the experimental equipment and explains how the reaction $\pi^+ + d \rightarrow p + p$ was measured without interference from any other processes. Section III indicates the method of determining the energy and composition of the incident beam. Sections IV and V describe the liquid deuterium container and the counting equipment and Secs. VI and VII outline the calculation of the cross sections and angular distributions from the observed data.

II. EXPERIMENTAL METHOD

The measurement was made by bombarding liquid deuterium with positive pions from the Chicago synchrocyclotron. The arrangement is essentially the same as that used in previous work on pion scattering.[20] Pions are produced inside the cyclotron by the collision of 450-Mev protons with a beryllium target. The positive pions which are emitted backward from the proton beam direction are deflected outward by the cyclotron magnetic field and emerge from the vacuum chamber through a thin aluminum window. The fringe magnetic field of the cyclotron focusses some of the pions of each energy into a roughly parallel beam. Several of these beams of various nominal energies, 66 to 165 Mev, are allowed to pass through narrow channels cut through the 12-foot thick steel and concrete shield wall into the experimental room. For this experiment the 122-Mev pion channel was left open; all others were plugged with lead and steel blocks. The pion beam emerging from the channel was deflected by a secondary magnet through about 45° to remove neutrons and gamma rays and passed through a 1-inch polyethylene sheet to stop low-energy protons. After being thus purified the beam was defined and monitored by two 2-inch diameter scintillation counters, No. 1 and No. 2, and passed through the center of the liquid deuterium cell, as shown in Fig. 1.

The aim of this experiment was to measure only the nonradiative absorption of positive pions by deuterium, $\pi^+ + d \rightarrow p + p$, and to avoid counting any other reaction. The two protons formed in the pion absorption are emitted 180° apart in the center-of-mass system. The method of this experiment was to detect the two protons in coincidence with each other as well as in coincidence with the incident pion. Thus, the two proton counters,

* Research supported by a joint program of the U. S. Office of Naval Research and the U. S. Atomic Energy Commission.

[1] K. A. Brueckner, Phys. Rev. **82**, 598 (1951).
[2] C. Morette, Phys. Rev. **76**, 1432 (1949).
[3] Gunn, Power, and Touschek, Phys. Rev. **81**, 277 (1951).
[4] K. M. Watson and K. A. Brueckner, Phys. Rev. **83**, 1 (1951).
[5] K. M. Watson and C. Richman, Phys. Rev. **83**, 1256 (1951).
[6] W. B. Cheston, Phys. Rev. **83**, 1118 (1951).
[7] Brueckner, Serber, and Watson, Phys. Rev. **84**, 258 (1951).
[8] Chew, Goldberger, Steinberger, and Yang, Phys. Rev. **84**, 581 (1951).
[9] A. M. L. Messiah, Phys. Rev. **86**, 430 (1952).
[10] L. Van Hove and R. Marshak, Phys. Rev. **88**, 1211 (1952).
[11] K. M. Watson, Phys. Rev. **88**, 1163 (1952).
[12] A. H. Rosenfeld, Phys. Rev. **96**, 139 (1954).
[13] Clark, Roberts, and Wilson, Phys. Rev. **85**, 523 (1952).
[14] Durbin, Loar, and Steinberger, Phys. Rev. **84**, 581 (1951).
[15] A. G. Schulz, Jr., University of California Radiation Laboratory Report UCRL-1756 (unpublished).
[16] F. S. Crawford, Jr., and M. L. Stevenson, Phys. Rev. **91**, 468 (1953).
[17] Cartwright, Richman, Whitehead, and Wilcox, Phys. Rev. **91**, 677 (1953).
[18] Fields, Fox, Kane, Stallwood, and Sutton, Phys. Rev. **95**, 638(A) (1954).
[19] A. H. Rosenfeld, Phys. Rev. **96**, 130 (1954).
[20] Anderson, Fermi, Martin, and Nagle, Phys. Rev. **91**, 155 (1953).

No. 3 and No. 4, were placed on opposite sides of the deuterium cell and an event was recorded only when both of them fired in coincidence with the incident beam counters, No. 1 and No. 2. Counter No. 4 was large enough and was placed close enough to the cell that if one proton from a pion absorption hit counter No. 3, the other one hit No. 4 more than 99 percent of the time. The positions of the proton counters for each measurement are shown in Table I. Figure 1 is an illustration of the counters and deuterium container during the measurement of the protons at 60° in the center-of-mass system for pions of 114 Mev in the laboratory system. The double coincidences of counters No. 1 and No. 2 were recorded simultaneously with the quadruple coincidences of all four counters. The fraction of the incident beam which caused pion absorption reactions was indicated by the ratio of quadruple to double coincidences, Q/D.

Reactions involving incident particles other than pions were prevented by purifying the beam of gamma rays, neutrons, and protons, as already described. The muons and electrons which remained in the pion beam after purification were assumed not to cause any reactions leading to quadruple coincidences. Reactions of pions with the deuterium were distinguished from those of pions with the metal walls and other surrounding materials by taking repeated measurements with the cell alternately full and empty of liquid deuterium. The difference of Q/D for these two cases was attributed to reactions of pions with the deuterium. Thus, the main problem in measuring the pion absorption was to discriminate against the other pion-deuteron reactions. The pion-deuteron reactions considered possible in this experiment were:

nonradiative absorption	$\pi^+ + d \rightarrow p + p,$	(1)
elastic scattering	$\pi^+ + d \rightarrow \pi^+ + d,$	(2)
inelastic scattering	$\pi^+ + d \rightarrow \pi^+ + p + n,$	(3)
charge exchange scattering	$\pi^+ + d \rightarrow \pi^0 + p + p,$	(4)
radiative absorption	$\pi^+ + d \rightarrow \gamma + p + p.$	(5)

The protons formed in reaction (1) have greater energy, hence greater range, than the protons and deuterons scattered in reactions (2), (3), and (4). A plastic absorber just thick enough to stop the most

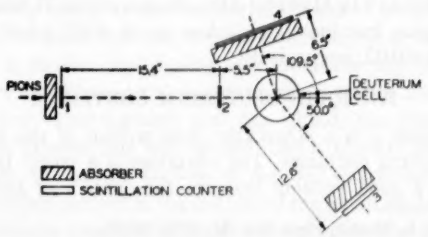

FIG. 1. Experimental arrangement for angular distribution measurement.

TABLE I. Positions of proton counters and absorber thicknesses (see Fig. 1).

Laboratory energy of incident pion (Mev)	Barycentric angle between pion and proton (degrees)	Counter No.[a]	Laboratory angle between counter axis and incident beam (degrees)	Thickness in g/cm² and composition of absorber in front of counter
		Run No. 1		
114	45	3	37.0	5.25 Lucite
114	45	4	−125.5	2.62 Lucite
114	60	3	50.0	4.87 Lucite
114	60	4	−109.5	3.93 Lucite
114	90	3	77.8	4.12 Lucite
114	90	4	−82.5	4.87 Lucite
		Run No. 2		
114	35	3	29.0	5.81 polyethylene
114	35	4	−131.7	2.07 polyethylene
114	45	3	37.0	5.81 polyethylene
114	45	4	−125.5	2.36 polyethylene
114	90	3	77.8	4.29 polyethylene
114	90	4	−82.5	4.01 polyethylene
91	35	3	29.5	4.72 polyethylene
91	35	4	−135.0	1.37 polyethylene
91	45	3	38.2	4.01 polyethylene
91	45	4	−124.2	1.65 polyethylene
91	60	3	51.5	3.73 polyethylene
91	60	4	−110.0	1.93 polyethylene
91	90	3	79.1	2.92 polyethylene
91	90	4	−80.4	2.92 polyethylene

[a] Counter No. 3 was always 12-5/8 inches from the center of the deuterium cell; counter No. 4 was always 6-1/2 inches from the cell.

energetic protons and deuterons from reactions (2), (3), and (4) was placed in front of each of the two proton counters, No. 3 and No. 4. The protons from reaction (1) always had enough range to penetrate the absorbers and counters, but the other reactions were almost completely prevented from counting. The thickness and composition of these absorbers for the different counters and angles measured are given in Table I and their position during a typical count is shown in Fig. 1.

The absorbers discriminated against reaction (2) very well. The scattered pion of reaction (2) has a long range and frequently triggered one of the two proton counters during the measurement. However, the recoil deuteron from the same reaction was prevented by the absorbers from reaching the other proton counter, whose simultaneous activation was required for the recording of an event.

The absorbers did not discriminate completely against reactions (3), (4), and (5) and a few quadruple coincidences are caused by them. The rest of this section is a discussion of the corrections required to compensate for these spurious counts (which constituted about 3 percent of the quadruples).

The recoil proton of reaction (3) was always stopped by the absorbers, but both the scattered pion and the recoil neutron could penetrate the absorbers. The pion frequently fired one of the proton counters and it was possible for the neutron, by causing a star in the counter or by knocking a proton from either the counter or its

absorber into the counter, to fire the second proton counter simultaneously. Whenever this chain of events occurred it was recorded as a quadruple coincidence. The frequency of this type of event has been calculated from the measured cross section for negative pion scattering by deuterium at this energy[21] to be about 2.7 percent of the net Q/D rate.

The protons formed in reaction (4) are both prevented from reaching the counters. However, there is a small chance that the two gamma rays formed by the decay of the neutral pion[21] will each create a pair directed at one of the two proton counters. The contribution of this occurrence to the net counting rate was calculated to be 0.2 percent.

The radiative absorption, reaction (5), is a very slow reaction at the energy of this experiment. If it is assumed that the radiative absorption of positive pions by deuterons is the same as that by neutrons, then reaction (5) is the inverse reaction of the photoproduction of positive pions from protons. On this assumption, the cross section of reaction (5) was estimated by detailed balancing from the measured cross section for the photoeffect[22] to be 1.8×10^{-2} mb/sterad. Reaction (5) usually forms a high-energy gamma ray and protons too slow to be counted. Occasionally it forms a low-energy gamma ray and two oppositely directed, high-energy protons which penetrate both proton counters and cause an event to be recorded. The contribution of reaction (5) to the total counting rate was estimated to be 0.1 percent. On the basis of the above considerations is was concluded that reaction (1) was counted with very good efficiency (calculated in Sec. VI) and that all other reactions contributed only a very small number of counts.

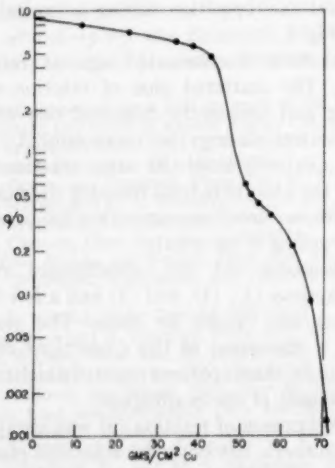

FIG. 2. Range curve of π^+ in copper.

[21] D. E. Nagle, Phys. Rev. **93**, 918 (1954).
[22] Bishop, Steinberger, and Cook, Phys. Rev. **80**, 291 (1950).

III. ENERGY OF THE PION BEAM

The energy of the pion beam is determined by the position of the beryllium target inside the cyclotron, by the strength of the cyclotron magnetic field, and by the position of the channel cut in the shield wall through which the pions are permitted to emerge into the experimental area.[23] These parameters were set before the experiment to give approximately the desired energy of positive pions in the channel. The exact energy of the pions was measured by range curves taken immediately before each set of angular distribution measurements. Figure 2 shows a representative range curve. For this measurement counters No. 1 and No. 2 and the polyethylene absorber between the secondary magnet and counter No. 1 were left in their standard positions (see Fig. 1). The deuterium cell was removed and counters No. 3 and No. 4 were placed in line with and behind counters No. 1 and No. 2. (counter No. 4, the larger one, was placed last to reduce losses caused by multiple scattering.) Copper absorbers 10 inches high by 10 inches wide and of various thicknesses were inserted between counter No. 2 and counter No. 3. Attenuation measurements were made by recording double coincidences of counters No. 1 and No. 2, and quadruple coincidences of all four counters. Figure 2 is a plot of the ratio of quadruple to double coincidences *versus* thickness of copper absorber used. The curve shows a sharp drop corresponding to the end of the pion range with a secondary plateau and another sharp drop corresponding to the end of the range of the remaining muons. The uncorrected mean range of the pions from the curve is 46.2 g/cm² of copper. The residual range of the pions at the center of the deuterium cell during the angular distribution measurement is obtained by adding to the copper the thickness of counter No. 3 plus one-half the thickness of counter No. 4 minus one-half the thickness of the deuterium cell, including walls. This corrected range is then converted to energy, by means of the range energy tables of Aron[24] and by adopting 6.72 [25] as the mass ratio of the proton to the pion, which gives an energy of 114 ± 5 Mev in the laboratory system.

The range curves were also used to estimate the contamination of the beam by muons and electrons. The total contamination was estimated to be 4.3 ± 2.0 percent at 114 Mev and 5.0 ± 2.0 percent at 91 Mev, so the pion fractions were taken to be 0.957 ± 0.02 and 0.950 ± 0.02, respectively.

IV. LIQUID DEUTERIUM CONTAINER

Figure 3 is a schematic cross section of the liquid deuterium container. The container is a metal Dewar with a good vacuum between the outer wall and the

[23] R. L. Martin, Phys. Rev. **87**, 1052 (1952).
[24] W. A. Aron, University of California Radiation Laboratory Report UCRL-1325 (unpublished).
[25] Smith, Birnbaum, and Barkas, Phys. Rev. **91**, 765 (1953).

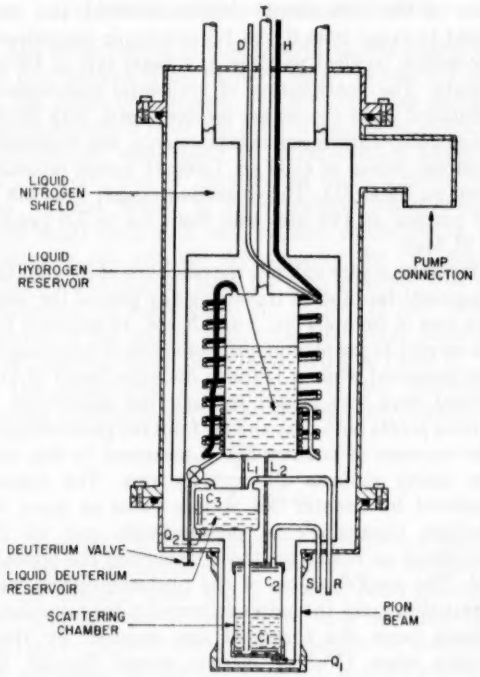

FIG. 3. Liquid deuterium container.

inner containers of hydrogen and deuterium. A metal radiation shield, kept at liquid nitrogen temperature, is suspended between the outside wall and the inner containers to reduce heat radiation to the deuterium and hydrogen. Deuterium gas is cooled and liquefied in a heat exchanger which surrounds the liquid hydrogen reservoir. The liquid deuterium trickles down through the deuterium valve into the liquid deuterium reservoir and scattering chamber where it remains throughout the experiment. The walls surrounding the scattering cell were made thin to reduce background scattering. The outside wall was 0.030-inch aluminum and the radiation shield was 0.002-inch aluminum. The cell wall was 0.005-inch brass, in its thin-walled part, which was $4\frac{1}{4}$ inches in diameter and $4\frac{1}{4}$ inches high. The cell had a capacity of 1.14 liters; the reservoir, which had a slightly greater capacity than the cell, was connected to it by a tube extending from the bottom of the reservoir nearly to the bottom of the cell. There was a vapor exhaust tube leading out from the top of the cell and a similar one leading out from the top of the reservoir. Whenever it was required to empty the cell, the cell vapor exhaust line was closed, the reservoir vapor exhaust line was opened, and a 15-watt electric heater, Q_1, at the bottom of the cell was turned on. The vapor evolved in the cell forced the liquid deuterium up into the reservoir in about two minutes. The heater power was then reduced to the two watts required to hold the deuterium up in the reservoir. When it was desired to refill the cell, the cell exhaust line was opened, the reservoir line closed, the cell heater turned off, and a 15-watt heater, Q_2, at the bottom of the reservoir was turned on. The liquid then returned to the cell under the vapor pressure in the reservoir and gravity in a similar time. By this method successive counts were taken with the cell alternately full and empty of deuterium liquid.

The indication that the cell was full of liquid deuterium was the increase in capacity of four micromicrofarads in a horizontal parallel plate condenser, C_2, at the top of the cell, above the thin-walled section. The indication that the cell was empty was the decrease in capacity of the same amount in a similar condenser, C_1, at the bottom of the cell.

The path length of the pions through the cylindrical deuterium cell was averaged over the beam using a beam profile measured at the position of the scattering cell, and the mean path length was found to be 10.2 cm. The liquid deuterium contained $(4.84\pm0.04)10^{22}$ atoms per cm^3. When the cell was empty of liquid it contained deuterium vapor amounting to (0.08 ± 0.01) 10^{22} atoms per cm^3. The difference, (4.76 ± 0.05) 10^{22}, multiplied by the mean path length, gives (4.87 ± 0.05) 10^{23} deuterium atoms per cm^2. The uncertainty in the densities of the liquid and vapor is the result of uncertainty about their temperature.

V. COUNTING EQUIPMENT

Liquid and plastic scintillation counters were used in this experiment because they can be made nearly 100 percent efficient for meson and proton counting over a large sensitive area and because they are quite fast. The scintillating liquid used in counters No. 1 and No. 3 was phenylcyclohexane with 3 grams per liter of *p*-terphenyl and 10 milligrams per liter of diphenylhexatriene.[26] The cell of No. 1 was 1/4-inch thick overall with 1/32-inch Lucite windows cemented into a Lucite frame, holding a cylindrical volume of scintillating liquid 2 inches in diameter by 3/16 inch thick. The cell of No. 3 was 1/2-inch thick overall, with 1/16-inch windows, holding a cylindrical volume of liquid 4 inches in diameter and 3/8 inch thick. One end of each Lucite cell was shaped to fit the photocathode of an RCA 5819 photomultiplier tube. The cell was pressed against the tube and a thin layer of silicone grease between them assured good optical contact.

Counters No. 2 and No. 4 used plastic scintillators, cut from scintillating plastic sheet. Counter No. 2 had a sensitive volume 2 inches in diameter and 1/8 inch thick, clamped tightly inside one end of a Lucite light pipe shaped to fit the lateral surface of the plastic cylinder. The other end of the light pipe made good optical contact with the RCA 5819 photocathode. Counter No. 4 had a 6 inches high by 8 inches wide by 1/8 inch thick plastic scintillator clamped to one end of

[26] H. Kallman and M. Furst, Phys. Rev. **81**, 853 (1951).

TABLE II. Observed values of Q/D, the fraction of pions non-radiatively absorbed, in units of 10^{-4}.

Run No.	Pion energy in laboratory frame (Mev)	Barycentric angle between pion and proton (degrees)	With deuterium	Without deuterium	Net
1	114	45	85.4±6.5	12.0±4.0	73.4±8.3
1	114	60	61.5±3.9	8.0±3.0	53.5±4.9
1	114	90	32.0±4.0	2.3±1.5	29.7±4.3
2	114	35	124.0±6.0	12.0±4.0	112.0±7.1
2	114	45	104.3±5.6	15.2±4.0	89.1±6.9
2	114	90	37.5±4.3	5.4±3.8	32.1±5.7
2	91	35	111.9±7.0	17.5±6.0	94.4±9.2
2	91	45	75.3±6.0	10.9±4.0	64.4±7.1
2	91	60	50.3±5.0	13.4±3.3	36.9±6.0
2	91	90	24.2±3.5	1.9±1.9	22.3±4.0

a Lucite light pipe whose other end made good optical contact with an RCA 5819 photocathode. The scintillators and light pipes of all the counters were covered with thin aluminum foil sealed with black electrical Scotch Tape to keep stray light out and to increase the collection of scintillated light. The photomultiplier tube of each counter was surrounded by a cylindrical iron shield to protect it from the stray magnetic field of the cyclotron.

The photomultiplier anode of each counter was connected to a preamplifier which clipped the pulses into a fairly square shape 2×10^{-8} second wide. These pulses were amplified by four stages of distributed amplification[27] before being delivered to the coincidence circuits.[27] The pulses from counters No. 1 and No. 2 were fed into a coincidence circuit A; the pulses from No. 2 and No. 3 were fed into a circuit B; and the pulses from No. 1 and No. 4 were fed into a coincidence circuit C. The output pulses from circuits A, B, and C were counted in triple coincidence and recorded by a cascade combination of a Hewlett Packard high-speed scaler and an Atomic Instrument decade scaler as Q, the quadruple coincidences of all four counters. The output pulses of coincidence circuit A were simultaneously counted by a similar cascade of scalers and recorded as D, the double coincidences of counters No. 1 and No. 2. Coincidence circuits A, B, and C were double coincidence circuits with triggered output pulses about 5×10^{-8} second long.[27] The counting rates were low enough (10^4 per second during cyclotron pulses) and the dead time of the counting equipment short enough (10^{-7} second) that counting losses were negligible.

There was enough stray radiation in the experimental room to cause some accidental coincidences even though the resolving time of the coincidence equipment for quadruple coincidences was 6×10^{-8} second. These were computed from the measured singles, doubles, and triples rates of all counters and the measured resolving time of the coincidence circuits involved and were found to range from 0.8 to 1.3 quadruple coincidences per million incident particles at a beam rate of 10^4 per minute. The contribution of accidental coincidences, calculated from the actual incident-beam rate during the angular-distribution measurements, was subtracted from the values of Q/D on Table II before recording them on Table III. The correction ranged from 0.8 to 2.0 percent at 114 Mev and from 2.3 to 7.6 percent at 91 Mev.

It was necessary to know the efficiency of the counting equipment for protons traversing any part of the sensitive area of counters No. 3 and No. 4. To estimate this the current at the photomultiplier anode of each counter was measured while a 1/4-inch diameter beam of Co^{60} gamma rays was passed through the scintillator at various points both near and far from the photocathode. The response of counter No. 3 measured in this way was nearly uniform all over its area. The current produced by counter No. 4 was twice as great for particles traversing the photocathode end of the scintillator as it was for those traversing the opposite end. The amplifications of the photomultipliers were adjusted to make the pulses delivered to the coincidence circuits twice the threshold size required by those circuits when 110-Mev mesons passed through the center of the counters. The efficiency of counters No. 3 and No. 4 for these mesons was measured directly, by placing them in line with and between counters No. 1 and No. 2 in the meson beam. The ratio of quadruple coincidences of all counters to double coincidences of counters No. 1 and No. 2 was (0.975±0.002). The protons counted during the angular distribution measurement gave up four times as much energy to the counters as did these mesons, so it was assumed that they were counted with 100 percent efficiency all over the counter area.

TABLE III. Differential cross sections for pion absorption.

$$\frac{d\sigma}{\omega d}=\frac{Q}{D}\frac{1-r}{2n\Omega lefb},$$

where $n=4.87\times10^{23}$ deuterium atoms/cm³, $\Omega=0.0776$ steradian, $f=0.957$ at 114 Mev and 0.950 at 91 Mev = pion content of the beam, $b=0.994$ = correction for absorption of the beam by deuterium, and $r=0.030$ = fraction of quadruple coincidences due to pion scattering reactions.

E Mev	θ degrees	$10^4\times$Net Q/D[a] Fraction of pions absorbed	ϵ detection efficiency	Differential cross section $d\sigma/d\omega$, (10^{-27} cm² per steradian) Laboratory system	Barycentric system
114	35	111.0±7.1	0.895	1.680±0.107	1.189±0.076
114	45	82.6±5.3	0.883	1.267±0.080	0.926±0.058
114	60	52.6±5.0	0.866	0.823±0.078	0.643±0.061
114	90	29.8±3.5	0.860	0.470±0.055	0.442±0.052
91	35	91.7±9.3	0.907	1.380±0.140	1.010±0.102
91	45	62.9±7.1	0.905	0.949±0.107	0.718±0.081
91	60	35.2±6.0	0.897	0.536±0.091	0.431±0.073
91	90	20.6±4.0	0.894	0.315±0.061	0.300±0.058

[a] Corrected for accidental coincidences.

[27] Glicksman, Anderson, and Martin, Proc. Natl. Electronics Conf. 9, 483 (1954).

VI. DIFFERENTIAL CROSS SECTIONS

The measurement of pion absorption was carried out for two energies of the primary beam, 91 and 114 Mev in the laboratory system. At each of these energies measurements of Q/D, the ratio of quadruple to double coincidences, were made at center-of-mass angles of 35°, 45°, 60°, and 90° between the forward proton and the incident beam. At each position measurements were made both with and without deuterium in the scattering cell and the difference of the two results attributed to protons from the pion absorption by the deuterium. It was pointed out in Sec. II that only 3 percent of the counts were caused by other processes. The observed values of Q/D are listed in Table II.

The differential cross section in the laboratory system is found from Q/D by the following formula:

$$\frac{d\sigma}{d\omega}=\frac{Q}{D}\frac{1-r}{2nfb\Omega e}.$$

In this formula n is the number of deuterium atoms per cm², 4.87×10^{23}, as computed in Sec. IV; f is the fraction of the incident beam which is pions, 0.957 ± 0.020 at 114 Mev and 0.950 ± 0.020 at 91 Mev (see Sec. III); and the factor $b=0.994$ is a correction for the absorption of the beam by the deuterium. r is the fraction of quadruples counts caused by various scattering reactions (calculated to be 3.0 percent in Sec. II). Ω is the effective solid angle accepted by counters No. 3 and No. 4 and e is their combined efficiency. Counter No. 3 is 4 inches in diameter and was placed 12 5/8 inches from the center of the scattering cell; counter No. 4 is 6 inches high by 8 inches wide and was placed 6 1/2 inches from the cell. Thus, counter No. 3 nearly defined the solid angle accepted by both counters, which was 0.0776 steradian.

The efficiency of counters No. 3 and No. 4 for counting a pair of protons that geometrically should have been accepted by both counters was not 100 percent, even though every proton had sufficient range to penetrate the counters, because of nuclear absorption in the deuterium cell and the absorbers. In order to compute this loss, the cross sections of these materials for the absorption of protons were assumed to be the same as their absorption cross sections for neutrons, i.e., one half their total cross sections for neutrons, except for hydrogen whose proton absorption was assumed to be nil. The neutron cross sections were found by interpolation between the values of Cook *et al.*,[28] De Juren and Knable,[29] and Taylor *et al.*[30] The loss of quadruple coincidences caused by absorption was found to be from 10.0 percent to 14.1 percent, depending on the proton energy and absorber thickness. Diffraction scattering by the deuterium also reduced the efficiency a small amount (0.7 to 0.9 percent at the various angles). Both the total efficiency, e, and the differential cross sections, for the various angles and incident pion energies, are given in Table III.

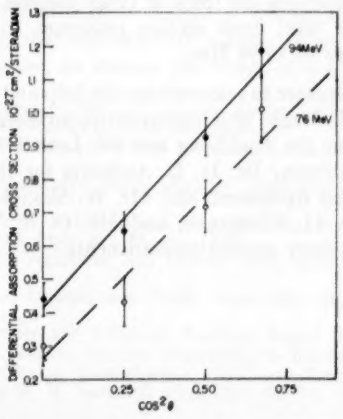

FIG. 4. Differential cross sections at 94 and 76 Mev in the barycentric system plotted *versus* $\cos^2\theta$.

TABLE IV. Angular distributions and total cross sections.

$$\frac{d\sigma}{d\omega}=\alpha_1+\alpha_2\cos^2\theta.$$

E Pion energy in Barycentric system Mev	α_1 10^{-27} cm²/sterad	α_2 10^{-27} cm²/sterad	$a=\frac{\alpha_2}{\alpha_1}$	M Least squares sum	σ Integrated total cross section 10^{-27} cm²
76	0.262 ± 0.053	0.978 ± 0.150	0.268 ± 0.089	2.40	7.38 ± 1.20
94	0.415 ± 0.047	1.071 ± 0.120	0.388 ± 0.082	1.45	9.70 ± 1.03

VII. ANGULAR DISTRIBUTIONS AND TOTAL CROSS SECTIONS

In Fig. 4, the differential cross sections in the barycentric system are plotted against $\cos^2\theta$, where θ is the barycentric angle between the pion and proton directions. At the energies of this experiment there may be small interactions in the d state as well as those in the s and p states found at lower energies. Thus, the differential cross sections can be represented by

$$\frac{d\sigma}{d\omega}=\alpha_1+\alpha_2\cos^2\theta+\alpha_3\cos^4\theta.$$

If α_3 is assumed zero, a least-squares analysis of the data gives values of M, the least-squares sum, of the order of the difference between the number of points and the number of parameters, indicating a good fit. However, this does not rule out even a fairly substantial α_3, since a wide range of positive values of α_3 give better fits than $\alpha_3=0$. The actual value of α_3 is not determined well by this experiment because the statistical errors are fairly large and because the $\cos^4\theta$ term would not contribute very much at the large angles

[28] Cook, McMillan, Peterson, and Sewell, Phys. Rev. **75**, 7 (1949).
[29] J. De Juren and N. Knable, Phys. Rev. **77**, 606 (1950).
[30] Taylor, Pickavance, Cassels, and Randle, Phil. Mag. **42**, 20 (1951).

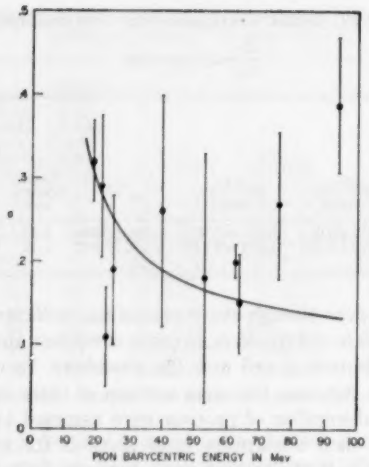

FIG. 5. The coefficient a plotted *versus* pion energy. The curve is proportional to η^{-2} where η is the pion momentum divided by μc. It is fitted to the experimental values below 70 Mev. (See reference 12.)

(35° and larger) which could be measured without interference from the incident beam. The value of α_2 given by the least-squares analysis depends very strongly on the assumed value of α_3, because the observed anisotropy of the angular distribution can be assumed dependent on either $\cos^2\theta$ or $\cos^4\theta$. On the assumption that α_3 is zero, one obtains values of $a=\alpha_1/\alpha_2$ of 0.268 ± 0.089 and 0.388 ± 0.082 at pion energies of 76 and 94 Mev in the center-of-mass system. Table IV shows the values found for α_1, α_2, a, and the least-squares sum, M, on the assumption that α_3 is zero.

The differential cross sections were integrated over solid angle to give the total cross sections shown in Table IV. As an over-all check the integrated total cross section found in this experiment at 114 Mev in the laboratory system was added to the sum of the integrated cross sections for ordinary and charge exchange scattering of negative pions at 120 Mev[21] and compared to the total cross section of deuterium for pions found by transmission measurements. The two values agree within experimental errors.

In Fig. 5 the parameter $a=\alpha_1/\alpha_2$, where $d\sigma/d\omega=\alpha_1+\alpha_2\cos^2\theta$, is plotted against pion energy in the center-of-mass system. The values shown have been taken from both the direct reaction,[13,14] $\pi^++d\rightarrow p+p$, and its inverse.[15–19] It has been suggested[11,12] that at low energies the parameter a should decrease with increasing energy as η^{-2}. However, the value of a found at 94 Mev in the present experiment is considerably larger than is predicted by an η^{-2} dependence. The smooth variation of a with energy from 65 Mev to 94 Mev through values measured under identical experimental conditions indicates that the increase of a with energy is real. This in turn indicates that the region in which a is proportional to η^{-2} is limited to pion energies of less than 90 Mev in the barycentric system.

In Fig. 6 the integrated total cross section, σ, is plotted against barycentric energy of the pion. The values have been taken from measurements of both the absorption reaction [13,14] and, by detailed balancing, from those of its inverse, the pion production reaction.[15–19] The two highest-energy points, the results of the present experiment, lie on a smooth exptrapolation of the excitation function found by earlier workers.

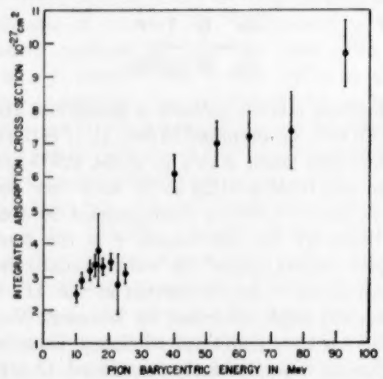

FIG. 6. Integrated total cross sections plotted *versus* pion energy.

The present measurements of the reaction $\pi^++d\rightarrow p+p$ at 76 and 94 Mev in the barycentric system show:

(a) The angular distribution of the protons can be represented by $a+\cos^2\theta$. The angular distribution becomes more isotropic with increasing energy above 70 Mev, reversing the trend at lower energies.

(b) The total cross section continues to increase with energy up to 94 Mev.

It is a pleasure to acknowledge the help and guidance of Dr. D. E. Nagie, who suggested this problem. Thanks are also due Dr. Earl Long and Dr. Lothar Meyer for liquid hydrogen, Dr. H. L. Anderson for the use of his counting equipment, and Mr. W. Skolink, Mr. C. Cohn, Dr. M. Glicksman, and Mr. G. B. Yodh for helping to carry out the measurements.

Scattering of Polarized Neutrons from Heavy Nuclei*

R. K. ADAIR,† S. E. DARDEN, AND R. E. FIELDS‡
University of Wisconsin, Madison, Wisconsin

(Received April 13, 1954)

The polarization of 400-kev Li(p,n) neutrons emitted at a laboratory angle of 50° with respect to the incident proton beam was measured to be 53±6 percent by determining the left-right asymmetry in the intensity of neutrons scattered at 90° from oxygen. Oxygen scattering phase shifts necessary for this calculation were derived from the results of previous experiments.

Left-right scattering asymmetries were measured for 11 elements, ranging in atomic weight from copper to bismuth. From these asymmetries the magnitudes of the polarizations caused by the heavy nuclei were determined. The variation of the polarization with atomic number appeared similar to that expected from the square well-with-absorption nuclear model of Feshbach, Porter, and Weisskopf, modified by the addition of a spin-orbit term equal to −1.5 Mev ($\mathbf{l}\cdot\mathbf{s}$).

I. INTRODUCTION

FESHBACH, Porter, and Weisskopf[1] have shown that the results of measurements of the total neutron cross sections of nuclei as a function of atomic number and of neutron energy[2–4] are in good agreement with the predictions of a simple nuclear model. Furthermore, observed angular distributions of elastically scattered neutrons have been found to be similar to predictions employing this model.[5,6] The model uses a square well with a range of $1.45\times10^{-13}\,A^{\frac{1}{3}}$ cm and a depth $V_0(1+i\zeta)$, where v_0 is taken as 19 Mev and ζ, which represents the effect of absorption of the neutron to form a compound state, is equal to 0.05. Such a description of the nucleus appears reasonable in view of the success of the independent particle model,[7,8] since the small absorption coefficient, ζ, results in a long mean-free path of the nucleon in nuclear matter. In addition to assuming the presence in the nucleus of single-particle orbits, the shell model introduces spin-orbit coupling. It appeared desirable to investigate the presence and strength of the nuclear spin-orbit forces which would be expected to have an effect on scattering in addition to their effect on bound states[7,8] of nuclei. The spin-orbit forces will affect the angular distributions of neutrons scattered from nuclei and the variation of total neutron cross sections with energy. It would be difficult, however, to deduce the effect of spin-orbit forces from measurements of these quantities. On the other hand, the presence of spin-orbit forces can be observed in a reasonably unambiguous manner by measuring the polarization of neutrons scattered from nuclei.[9,10] The magnitude of the polarization and the variation with nuclear size should provide information concerning the strength of spin-orbit forces.

II. PRODUCTION AND ANALYSIS OF POLARIZED NEUTRONS

Polarizations P resulting from scattering of neutrons by heavy nuclei were determined by measuring the left-right asymmetry in the scattering of neutrons, which have an initial polarization P'. The neutrons, scattered through an angle ϑ, were observed in a plane perpendicular to the direction of polarization of the incident beam. The left-right asymmetry, which is the ratio of the neutron flux scattered to the right to that scattered to the left, will be

$$(1+PP')/(1-PP'). \qquad (1)$$

In order to achieve sufficient intensity it appeared desirable to use polarized neutrons produced by a nuclear reaction rather than by scattering. Since the effects of polarization are present only in the interaction of neutrons having an orbital angular momentum greater than zero, fast neutrons must be used; on the other hand, interpretation of any observed effects in scattering is much simpler if the neutron energy is so low that only neutrons with low orbital angular momenta are strongly affected by the interaction. At neutron energies near 500 kev, only S and P waves will be important. Further, a study of the 19.8-Mev excited state of Be^8 indicated[11] that it was probable

* Work supported by the U. S. Atomic Energy Commission and the Wisconsin Alumni Research Foundation.

† Now at Brookhaven National Laboratory, Upton, Long Island, New York.

‡ Now at Consolidated Vultee Aircraft Corporation, Fort Worth, Texas.

[1] Feshbach, Porter, and Weisskopf, Phys. Rev. **90**, 166 (1953).

[2] H. H. Barschall, Phys. Rev. **86**, 431 (1952).

[3] Miller, Adair, Bockelman, and Darden, Phys. Rev. **88**, 83 (1952).

[4] Walt, Becker, Okazaki, and Fields, Phys. Rev. **89**, 1271 (1953).

[5] Feshbach, Porter, and Weisskopf, Technical Report No. 62, Laboratory for Nuclear Science, Massachusetts Institute of Technology, Cambridge, Massachusetts, 1953 (unpublished).

[6] M. Walt and H. H. Barschall, Phys. Rev. **90**, 714 (1953); **93**, 1062 (1954).

[7] M. G. Mayer, Phys. Rev. **75**, 1969 (1949).

[8] Haxel, Jensen, and Suess, Phys. Rev. **75**, 1766 (1949).

[9] Nucleon polarization has been discussed theoretically by J. Schwinger, Phys. Rev. **69**, 681 (1946); L. Wolfenstein, Phys. Rev. **75**, 1664 (1949); J. Lepore, Phys. Rev. **79**, 137 (1950); R. S. Blin-Stoyle, Proc. Phys. Soc. (London) **64**, 700 (1951); A. Simon and T. A. Welton, Phys. Rev. **90**, 1036 (1953); and others. The calculations in this paper were made following procedures of Wolfenstein.

[10] E. Baumgartner and P. Huber, Helv. Phys. Acta **26**, 420, 545 (1953); R. Ricamo, Helv. Phys. Acta **26**, 423 (1953); R. Ricamo, Nuovo cimento, **10**, 12, 1607 (1953).

[11] R. K. Adair, Phys. Rev. (to be published).

that the Li(p,n) reaction produces, at certain angles, strongly polarized neutrons of about this energy.

Since it is not possible to calculate reliably the magnitude of the polarization of the neutrons from the Li(p,n) reaction, it was necessary to find a suitable analyzer to measure the polarization. There is a neutron scattering resonance of oxygen, at about 435-kev neutron energy associated with a state in O^{17} of spin 3/2 and odd parity.[12] At this neutron energy the only scattering phase shifts expected to be important are the S and $P_{\frac{1}{2}}$ phases. From slow neutron interference measurements the S-wave phase shift, δ_0, is known to be negative. Its magnitude is easily calculable as a function of energy using the relation

$$\sigma = 4\pi k^{-2} \sin^2\delta_0, \tag{2}$$

where σ is the nonresonant scattering cross section. The $P_{\frac{1}{2}}$ phase shift can be calculated using the relation[13]

$$\delta(P_{\frac{1}{2}}) = \delta_+ = \tan^{-1}(\Gamma/2(E_r - E)), \tag{3}$$

where $\Gamma = \Gamma_r x^3(1+x_r^2)/[x_r^3(1+x^2)]$. In this expression Γ represents the width of the resonance, equal to 42 kev at resonance; E_r is the resonance energy, 435 kev; x stands for kR, where R is the nuclear radius taken as 5×10^{-13} cm; and k is the neutron wave number. The subscript r denotes the value of a quantity at the resonance energy. At 90° in the c.m. system, the polarization of neutrons scattered in the neighborhood of this resonance will be equal to

$$P = \frac{2\sin\delta_0 \sin\delta_+ \sin(\delta_+ - \delta_0)}{\sin^2\delta_+ + \sin^2\delta_0}, \tag{4}$$

where P refers to polarization of the neutron spin in the X direction, for neutrons scattered in the Y direction. The direction of the incident unpolarized beam is taken in the Z direction. The solid curve in Fig. 1 shows the polarization of neutrons scattered at 90° from oxygen as a function of neutron energy calculated using Eqs. (2), (3), and (4). The large values of the polarization make oxygen a useful analyzer of polarized neutrons in this energy region.

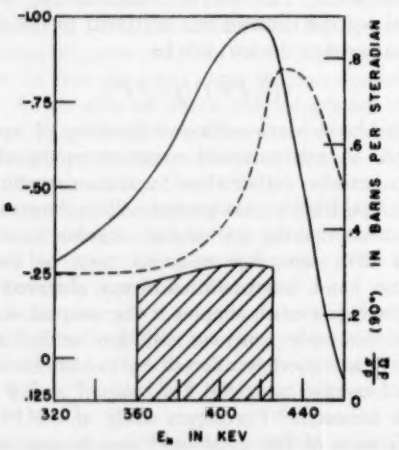

FIG. 1. Curves used to calculate Li(p,n) polarization from oxygen scattering data. The ruled area represents the shape of the neutron energy spectrum from the Li(p,n) reaction as it was used in the measurement. The solid curve shows the polarization of neutrons scattered at 90° in the c.m. system from oxygen, and the dashed curve represents the oxygen differential scattering cross section at 90°, all as a function of neutron energy.

A schematic diagram of the experimental arrangement used to measure the polarization of Li(p,n) neutrons is shown in Fig. 2. Protons from the electrostatic generator with an energy of 2.262 Mev strike a thin lithium target evaporated in place, which has a stopping power of 65 kev for protons of this energy. Neutrons emitted at a laboratory angle of 50° with respect to the incident proton beam pass through a collimating hole in the paraffin shield, and strike a thin-walled metal Dewar filled with liquid oxygen. Neutrons scattered at 90° in the c.m. system by the Dewar and oxygen are counted by a hydrogen recoil proportional counter. Intensity of the scattering by the oxygen was determined by finding the counting rate with the Dewar full and subtracting the background counting rate measured with the Dewar empty. This background counting rate was about 60 percent. The neutron beam was monitored by measuring the charge incident on the lithium target with a current integrator.

The paraffin shield was designed to block the direct beam from the counter and to shield the counter from as much of the room scattered flux as possible. Collimation of the neutron beam was such that the beam did not strike any part of the shield exposed to the counter. A metal Dewar constructed with an inside wall of 0.005-in. stainless steel and an outside wall of 0.015-in. brass served to contain the liquid oxygen. The inside diameter of the Dewar was 1.3 cm and the inside depth was 12 cm. The height of the liquid oxygen column would stay above 7 cm for about 15 minutes after filling. Since the diameter of the neutron beam was 5 cm, measurements could be made safely for nearly 15 minutes without refilling the Dewar. A recoil proportional counter filled with 4 atmos of hydrogen, and having an active volume 2.5 cm in diameter and about 10 cm long, was used as a neutron detector. Counts were recorded at two discriminator settings. One discriminator was set to count all pulses from proton recoils of energy greater than 250 kev, the other was biased at 175 kev.

The scatterers were placed about 25 cm from the neutron source. This position was reproducible within 2 mm. The position of the center of the active volume of the counter was about 10 cm from the scatterer

[12] Adair, Barschall, Bockelman, and Sala, Phys. Rev. **75**, 1124 (1949); R. K. Adair, Phys. Rev. **92**, 1491 (1953).
[13] Feshbach, Peaslee, and Weisskopf, Phys. Rev. **71**, 145 (1947).

and was reproducible within 1 mm. In order to ascertain that no pronounced asymmetries would result from a difference in the effective geometry of the experiment when the counter was moved from one side to the other, the left-right asymmetry in the scattering of neutrons from carbon was measured. Since there is no broad P-wave or D-wave resonance for the scattering of neutrons from carbon near this energy, it is probable that the contribution to the scattering of neutrons with angular momentum greater than zero is small, and hence that there is no appreciable polarization of the scattered neutrons. Therefore, the measured left-right asymmetry of 1.000 ± 0.029 indicates that the experimental procedure introduces no strong bias. For the oxygen scatterer the measured left-right asymmetry was 1.92 ± 0.12. From this value, corrected for multiple scattering, and the oxygen polarization, plotted in Fig. 1, one can calculate the average polarization of the beam of neutrons from the Li(p,n) reaction using Eq. (1). The asymmetries were corrected for multiple scattering following the procedure used by Walt.[14,15] Corrected for mutiple scattering, the left-right asymmetry in the scattering from oxygen is $2.52_{-0.30}^{+0.35}$, where the error includes the uncertainty in the multiple scattering correction and estimated errors in the alignment and geometry. Neutrons multiply scattered into the counter first by the scatterer and then by the paraffin shield will lose, on the average, enough energy so that they will not be counted. If an appreciable number were counted, the counting efficiency will be higher for the low bias than the high bias. Since both biases gave about the same left-right asymmetry, it appears that effects caused by neutrons scattered by the shield are not important.

The effective polarization produced by the oxygen scatterer is an average over the neutron energy spread, weighted according to the differential Li(p,n) cross section at a laboratory angle of 50°, and according to the oxygen scattering cross section at 90°. Both the neutron energy spectrum calculated from the Li(p,n) reaction cross sections measured by Taschek and Hemmendinger[16] and the oxygen scattering cross section at 90°, calculated from the phase shifts of Eqs. (2) and (3), are shown in Fig. 1. By taking P, the average polarization from the oxygen scattering, as -0.82, a value which is a little smaller than the average taken from Fig. 1 because of the small deviation from 90° of most of the neutrons scattered into the counter, a polarization of -0.53 ± 0.06 for the neutron beam from the Li(p,n) reaction was obtained. This value is somewhat higher than a value of -0.35 deduced from theoretical considerations.[11] Although some of the neutrons in the beam from the collimation hole will have been scattered at small angles from the paraffin walls of the collimater, no correction was made for this effect as such collisions will not depolarize the neutrons.

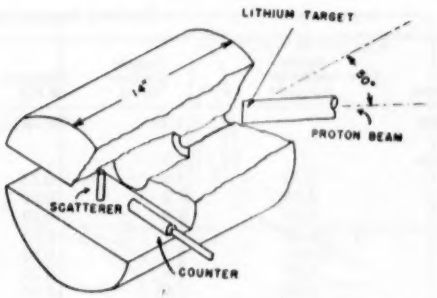

Fig. 2. Schematic view of experimental setup.

III. POLARIZATION OF NEUTRONS SCATTERED FROM HEAVY NUCLEI

The polarization of neutrons scattered from heavy nuclei was determined by measuring the left-right asymmetry in the scattering of 400-kev polarized neutrons under the same conditions as described in the preceding section. Scatterers of various materials which had been procured for another experiment[6] were available. All of the scatterers were cylinders 6.3 cm long. Table I lists the elements measured, the diameters of the samples, and the ratio of the diameter of the sample to the mean free path of the neutron in the sample. The choice of diameters chosen for the scatterers was influenced by three considerations; the diameter should not be greater than 2 cm in order to avoid an asymmetry which might be caused by the variation with angle of the neutron intensity from the Li(p,n) reaction, and hence a variation of flux across the scatterer; the diameter should not be greater than 80 percent of the mean free path to keep multiple scattering from becoming objectionably large; and, within the first two restrictions, the sample should be as large as possible in order to get a reasonably large counting rate.

Some of the nuclei will scatter both elastically and inelastically. If inelastic scattering with large degradation in energy were important, the ratio of the counting rates at the two different discriminator biases would be different, as at the lower bias inelastically scattered neutrons would be counted relatively more efficiently than at the higher discriminator bias. There seemed to be no evidence of such an effect. For each heavy element the counting rate at the low bias was about twice the rate at the high bias. For carbon and oxygen the ratio was higher than two to one, presumably because of the loss of energy in elastic scattering.

Measured left-right asymmetries for the different nuclei are listed in Table I, together with values corrected for multiple scattering. The multiple scattering corrections were made in the same manner as the corrections for scattering by oxygen. Both the

[14] Martin Walt, thesis, University of Wisconsin, 1953 (unpublished).
[15] M. Walt and H. H. Barschall, Phys. Rev. **93**, 1062 (1954).
[16] R. F. Taschek and A. Hemmendinger, Phys. Rev. **74**, 373 (1948).

TABLE I. Sample parameters and experimental results.

Elements	Nuclear radius in cm $\times 10^{13}$	Sample diameter in cm	Diameter M.F.P.	Left-right scattering asymmetry	Left-right asymmetry corrected for multiple scattering	Polarization
Oxygen		1.35	0.79 0.275	1.92 ±0.12	2.52 $^{+0.35}_{-0.25}$	−0.82
Carbon		1.9		1.000±0.029		0
Cu	5.76	1.9	0.73	1.003±0.023	1.003±0.023	−0.003±0.02
Zn	5.85	1.9	0.61	1.006±0.025	1.005±0.025	−0.006±0.02
Zr	6.51	1.9	0.69	0.967±0.022	0.954±0.026	+0.044±0.026
Nb	6.56	1.7	0.72	0.894±0.023	0.854±0.032	+0.148±0.031
Mo	6.65	1.6	0.82	0.895±0.027	0.850±0.032	+0.153±0.031
Ag	6.89	1.8	0.79	0.920±0.029	0.888±0.031	+0.112±0.033
Cd	6.98	1.9	0.65	0.859±0.039	0.817±0.039	+0.190±0.047
Sn	7.10	1.9	0.49	0.866±0.029	0.834±0.034	+0.174±0.034
Ta	8.19	1.27	0.51	1.036±0.038	1.045±0.041	−0.038±0.041
W	8.22	1.27	0.56	1.036±0.033	1.040±0.033	−0.037±0.033
Bi	8.59	1.9	0.42	1.024±0.023	1.027±0.023	−0.025±0.023

statistical standard error and an estimate of the multiple scattering error are included in the quoted uncertainty. Polarizations calculated from Eq. (1) are listed in the last column of Table I together with the probable error. In Fig. 3 these polarizations are plotted against the nuclear radius, taken as 1.45×10^{-13} $A^{\frac{1}{3}}$ cm.

IV. INTERPRETATIONS AND CONCLUSIONS

The elastic scattering of neutrons from nuclei can be described, in this energy region, as the result of two separate processes,[17] potential or body elastic scattering, and resonance or capture elastic scattering. Feshbach, Porter, and Weisskopf have pointed out that the resonance scattering is incoherent with body elastic scattering if the energy spread of the incident beam is sufficiently broad. It can be seen from the uncertainty principle that the interaction time is well defined for a scattering measurement made with a neutron beam which has a large energy spread. Therefore, scattering which results from the formation and decay of narrow long-lived compound states will interfere with neither the incident beam or the body elastic scattering. This condition should obtain for most of the elements measured as the neutron energy spread of 65 kev which was used should be much greater than the level widths. There may be small effects due to individual resonances, however, for the closed shell nuclei, zirconium, tin, and bismuth which are likely to form shorter-lived compound states. Polarization of scattered neutrons occurs through interference between scattering amplitudes of neutrons with their spins reversed and the amplitudes of neutrons whose spin directions were unchanged by the scattering interaction. Since compound elastic scattering will not, when averaged over resonances, interfere with the body elastic scattering, the polarization cannot be due to the effect of narrow resonances but must result from the body scattering or potential scattering itself.

The nuclear model of Feshbach *et al.*[1] explains the strongly varying patterns of average neutron cross sections in terms of the variations in the potential scattering. While this model of the nucleus will not account for polarization, the addition of a spin-orbit term to the potential well, as required by the shell model, will produce a polarization of the scattered neutrons. Calculations of the expected polarization were made using such a modification. The potential used was

$$V(r)=-V_0(1+i\zeta)-V'(\mathbf{l}\cdot\mathbf{s}),\ r<R$$
$$=0,\ r>R,$$

where, from reference 1, $V_0=19$ Mev, $\zeta=0.05$, and $R=1.45\times10^{-13}$ $A^{\frac{1}{3}}$ cm. Values of 1 and 2 Mev were chosen for V' in an attempt to fit the experimental polarization data.

Effects of neutrons of angular momentum greater than one were not considered in these calculations. These considerations do not take into account the spin of the scattering nucleus but describe the interaction of neutrons with the spinless nuclear core, and disregard the nucleons in the outer orbits which, according to the shell model, give the nucleus as a whole its spin. Consequently, the calculation is similar to that described previously[18] for a special case of neutrons scattered by a spinless nucleus. States of the neutron-nuclear core system are formed with a well-defined total angular momentum and scattered amplitudes are determined for S, $P_{\frac{1}{2}}$, and $P_{\frac{3}{2}}$ waves. The polarization is defined as $P=(A^*|\sigma_x|A)/d\sigma/d\omega$, where A is the body elastic scattering amplitude in the Y direction and $d\sigma/d\omega$, the differential cross section for scattering in the Y direction, is the sum of the body elastic scattering and the capture elastic scattering. The body elastic scattering intensity is just $|A|^2$. Although the total cross section for incoherent processes is determined by the potential, the division into capture elastic scattering and inelastic scattering, and the angular distributions of these processes must be estimated from other considerations. Polarizations were

[17] Feshbach, Porter, and Weisskopf (private communication).

[18] R. K. Adair, Phys. Rev. **86**, 155 (1952).

calculated under the assumption that the incoherent processes result entirely from capture elastic scattering, and that the angular distribution of these resonance-scattered neutrons is that characteristic of the decay of pure states, isotropic for $P_{\frac{1}{2}}$ and S waves, and of the form $1+3\cos^2\vartheta$ for $P_{\frac{3}{2}}$ neutrons. Coupling of the angular momentum with the nuclear spin will tend to make the $P_{\frac{1}{2}}$ distribution more nearly isotropic. Since the contribution of the capture scattering to the total scattering at this energy is not large, the uncertainties involved in these assumptions will not affect the calculated values of the polarization strongly.

Polarizations calculated in the manner described are shown by the solid and dashed lines in Fig. 3. There is qualitative similarity between the experimental values and the calculated curves. The position of the calculated curves as a function of the nuclear radius R is determined primarily by the value of V_0; a value of 18.5 Mev instead of 19 Mev would shift the whole curve towards higher values by about 0.1×10^{-13} cm and might give a better fit to the experimental points. While other small changes, notably an increase in the absorption coefficient, might also result in a better fit to the data, such changes may not be warranted by either the accuracy of the experiment or the reliability, as far as such detailed predictions are concerned, to be expected of so simple a description of the nucleus.

It appears that a value of V of about 40 Mev instead of 19 Mev may be more nearly correct.[19] All of the important scattering phase shifts are then increased almost exactly 360°, and there is very little difference in the physical scattering results. However, the values of V' deduced from these measurements must be multiplied by about $(40/19)^{\frac{1}{2}}$ if the deeper potential is correct.

The width of the resonance-like maxima and minima of the polarization curve increases with V'. While the magnitude of V' is not too well determined by the limited experimental data, a value larger than 2.5 Mev or smaller than 1.0 Mev would not appear to be in agreement with the measurements. It must be emphasized that since the value of V' is deduced primarily from measurements of nuclei of $A\approx100$, at energies and angles where only S and P waves are important, a value of 1–2 Mev for V' properly refers only to the interaction of P neutrons with nuclei having a mass of about 100. Calculations[20–22] concerning the value of the potential V' indicate that it may depend on the orbital angular momentum l and the nuclear radius R. Because of this it is difficult to compare the spin-orbit energy indicated from these scattering measurements with that deduced from the shell model and the bound states of nuclei. However, a value of 1.5 Mev for V' in the scattering calculation would result in a splitting of about 2.25 Mev for a bound single P-wave nucleon outside of a closed shell, which is about what might be anticipated from the shell model.[21,23]

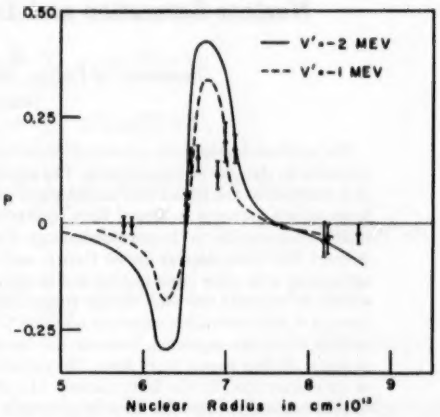

FIG. 3. The points show the measured polarizations of 400-kev neutrons produced by scattering from heavy nuclei as a function of nuclear radius, R. The solid curve shows values obtained when a potential term equal to -2 Mev $(\mathbf{l}\cdot\mathbf{s})$ is added to the potential used by Feshbach, Porter, and Weisskopf. The dashed curve represents the results of calculations for a spin-orbit term of -1 Mev $(\mathbf{l}\cdot\mathbf{s})$.

When plotted as a function of atomic weight, the experimental total cross sections at a neutron energy of 400 kev exhibit a resonance-like behavior in the region of atomic weights around 100. This general variation can be reproduced using the potential of Feshbach, Porter, and Weisskopf, where the rise in the cross section is attributed to a virtual P level. Total cross section calculations were made using S and P waves only, since the D-wave contribution is expected to be quite small at this energy. If no spin-orbit coupling is introduced, the predicted peak in the total cross section appears too high and narrow, while calculations which include a spin-orbit term -1.5 Mev $(\mathbf{l}\cdot\mathbf{s})$ in the potential are in fair agreement with the data in the neighborhood of the peak.

No detailed calculations concerning the effect of the spin orbit term on the angular distributions have been made.[5] Somewhat more isotropic angular distributions might be expected since terms in the angular distribution proportional to $P^{\pm1}(\cos\vartheta)$ will be introduced by spin-orbit coupling.

The basic ideas for this experiment were developed in the course of a conversation of one of the authors with Dr. C. K. Bockelman.

[19] K. W. Ford and D. Bohm, Phys. Rev. **79**, 745 (1950). R. K. Adair, Phys. Rev. **94**, 737 (1954).
[20] C. H. Blanchard and R. Avery, Phys. Rev. **81**, 35 (1951).
[21] J. Hughes and K. J. LeCouteur, Proc. Phys. Soc. (London) **A63**, 1219 (1950).
[22] D. R. Inglis, Revs. Modern Phys. **25**, 390 (1953).
[23] M. G. Mayer, Phys. Rev. **78**, 16 (1950).

Nuclear Saturation and Two-Body Forces. II. Tensor Forces

K. A. Brueckner
Department of Physics, Indiana University, Bloomington, Indiana
(Received June 7, 1954)

The method developed in a previous paper for the treatment of the problem of nuclear saturation has been extended to the case of tensor forces. The general result obtained expresses the many-body potential energy as a function of the triplet and singlet eigen phase shifts for scattering. One consequence is that the tensor force, which averages to zero if Born approximation is used to evaluate the scattering, now gives a very sizable contribution to the potential energy. Phase shifts have been determined for a specific potential model derived from pseudoscalar meson theory, and are shown to give scattering up to 90 Mev which is in good agreement with total cross section and in approximate agreement with angular distributions. Use of these results to evaluate the total energy (neglecting Coulomb effects) in heavy nuclei shows that for a typical case ($A=300$) saturation occurs at a radius $1.15\times10^{-13}A^{\frac{1}{3}}$ with a binding energy of 10 Mev per particle. If surface effects are neglected, however, the density at saturation increases by a factor of 1.74 with an increase in mean binding energy to 39 Mev. The potential energy per particle has also been determined as a function of its momentum. In the finite nucleus ($A=300$) the potential depth varies from -82 Mev for a particle of zero momentum to -32 Mev for a particle at the top of the Fermi momentum distribution. Arguments are presented which suggest that this effect is to a large extent independent of the model used.

I. INTRODUCTION

In a previous paper[1] (to be referred to as I) the relation of nuclear saturation to two-body forces was discussed making use of an approximation method which allowed an exact treatment of the coherent particle motion in the nucleus. This method is in essence an "optical model" approximation in that the potential felt by a particle is expressed as an average of the forward scattering amplitudes over the nuclear momentum states. In such an approximation, coherent modes of motion appear which are particle-like but which are not simply related (except in an average sense) to the motion of a "bare" nucleon. Thus the "independent particle" given by the model does not refer to "independent nucleon" motion but rather refers to a type of collective aspect of the nuclear state. The detailed relationship of the approximation methods of I and of this paper to other models and methods will form the content of a paper to be published separately.

In I it was found that if tensor forces (which average to zero in first approximation) and surface effects were neglected, two-body potentials derived from meson theory[2] and in agreement with low-energy scattering parameters were sufficient in themselves to give saturation with about the correct values of density and binding energy, i.e., $R=1.15\times10^{-13}A^{\frac{1}{3}}$ cm, $E=-12$ Mev. It is the purpose of this paper to consider the effects of tensor forces and also to compare the scattering amplitudes used with the nucleon-nucleon scattering over the range of energies which are important in the saturation problem. We shall also discuss some of the simplest surface effects which arise from the modification (by the finite surface) of the nuclear states. We shall not, however, in this paper discuss the Coulomb effects or the tendency of the tensor force to distort the nucleus.

In Sec. II we shall summarize briefly the formulas which we shall need in our consideration of the saturation problem with tensor forces and discuss the computational techniques used in determining the phase shifts for scattering; in Sec. III we shall compare with experiment the scattering predicted by the potentials we have used; in Sec. IV the effects of finite nuclear size will be discussed; in Sec. V the saturation problem will be evaluated; and finally in Sec. VI some concluding remarks will be made.

II. FORMALISM

In I it was shown that in order to determine the effective "potential" in the saturation problem, it was sufficient to evaluate the sum

$$\langle V\rangle=\tfrac{1}{2}\sum[(\mathbf{k}_i,\mathbf{k}_j|t'_{\rm ord}|\mathbf{k}_i,\mathbf{k}_j)-(\mathbf{k}_j,\mathbf{k}_i|t'_{\rm exch}|\mathbf{k}_i,\mathbf{k}_j)], \quad (1)$$

where the t''s are the scattering amplitudes in the momentum states $\mathbf{k}_i$, $\mathbf{k}_j$ evaluated at the kinetic energies in the nuclear medium. $t'_{\rm ord}$ and $t'_{\rm exch}$ are, respectively, the ordinary and exchange matrix elements of the scattering amplitudes. This result is further expressible in terms of the scattering amplitudes in the forward direction in the substates of spin and isotopic spin, which we denote by $a_{s\lambda}$ where s indicates the spin state and λ the isotopic spin state. As a function of these, the potential energy is

$$V=-\frac{4A}{\pi m}\int_0^{k_F}P(k)dk[a_{ss}+3a_{ts}+3a_{st}+9a_{tt}], \quad (2)$$

with $P(k)$ the probability (unnormalized) of finding the relative momentum k in the nuclear ground state. It is this integral which we wish to express in terms of the

[1] Brueckner, Levinson, and Mahmoud, Phys. Rev. **95**, 217 (1954).
[2] K. A. Brueckner and K. M. Watson, Phys. Rev. **92**, 1023 (1953).

phase shifts for scattering with the tensor force effects included. It is clear that in this treatment we do not consider the possible effects on the energy arising from spin polarization and distortion of the nucleus from a spherical shape; these are specifically surface effects and small compared with both the volume energy and with the simple surface effect which we discuss in Sec. V.

We further remark here that any contribution to the scattering which is due to the tensor force and which can be legitimately treated in Born approximation gives no contribution to the integral of Eq. (2). This result is the consequence of the averaging to zero of the tensor force operator upon spin averaging and is the analog in our method of the absence of a tensor force contribution in an uncorrelated medium.

It is next convenient to summarize formulas for tensor scattering which express the phase shifts in terms of the eigen phase shifts of the scattering matrix. In this we make use of results which are implicit in the work of Blatt and Biedenharn.[3] An explicit derivation of these formulas is given in Appendix A. For the singlet scattering and for the uncoupled triplet states (with $L=J$), this introduces no change from the usual results. For the coupled triplet states with $L=J\pm1$, however, application of the results of Blatt and Biedenharn leads to useful relations between the usual phase shifts (functions of LJm) and the eigen phase shifts. In the notation of Blatt and Biedenharn, we have (see Appendix A):

$$\begin{aligned}
\eta_{J-1}{}^{J,\pm1}&=(\tan\epsilon+\cot\epsilon)^{-1}\{\cot\eta_\alpha+\tan\eta_\beta\\
&\qquad-[J/(J+1)]^{\frac{1}{2}}(\eta_\alpha-\eta_\beta)\},\\
\eta_{J+1}{}^{J,\pm1}&=(\tan\epsilon+\cot\epsilon)^{-1}\{\tan\eta_\alpha+\cot\eta_\beta\\
&\qquad+[J/(J+1)]^{-\frac{1}{2}}(\eta_\alpha-\eta_\beta)\},\\
\eta_{J-1}{}^{J,0}&=(\tan\epsilon+\cot\epsilon)^{-1}\{\cot\eta_\alpha+\tan\eta_\beta\\
&\qquad+[J/(J+1)]^{-\frac{1}{2}}(\eta_\alpha-\eta_\beta)\},\\
\eta_{J+1}{}^{J,0}&=(\tan\epsilon+\cot\epsilon)^{-1}\{\tan\eta_\alpha+\cot\eta_\beta\\
&\qquad-[J/(J+1)]^{\frac{1}{2}}(\eta_\alpha-\eta_\beta)\},
\end{aligned}\tag{3}$$

where

$$\eta_L{}^{Jm}=\sin\delta_L{}^{Jm}e^{i\delta_L{}^{Jm}},\quad \eta_\alpha=e^{i\delta_\alpha}\sin\delta_\alpha,\quad \text{etc.}\tag{4}$$

The eigen phase shift δ_α is the $L=J-1$ dominant phase shift; at low energy as the mixing parameter ϵ goes to zero, the scattering in a given J state is dominated by the $L=J-1$ state.

Application of the formulas of Eq. (3) leads to simple expressions for the forward scattering amplitudes averaged over spins. We denote the coupled phase shifts by $\eta^\pi{}_{J\sigma}(\sigma=\alpha,\beta)$ where $\pi=-(-1)^J$ is the parity, and the uncoupled states by $\mu^\pi{}_{JL}$. Application of the usual scattering formulas[4] then gives for the four substates of spin and isotopic spin:

$$\begin{aligned}
ka_{ss}&=\sum_{J\text{ odd}}\mu^-{}_{JJ0}(2J+1),\\
ka_{st}&=\sum_{J\text{ even}}\mu^+{}_{JJ0}(2J+1),\\
3ka_{ts}&=\sum_{J\text{ odd}}(2J+1)(\eta^+{}_{J\alpha1}+\eta^{+*}{}_{J\beta1})\\
&\qquad+\sum_{J\text{ even}\geq2}(2J+1)\mu^+{}_{JJ1},\\
3ka_{tt}&=\sum_{J\text{ even}}(2J+1)(\eta^-{}_{J\alpha1}+\eta^-{}_{J\beta1}+\mu^+{}_{JJ1})\\
&\qquad+\sum_{J\text{ odd}}(2J+1)\mu^-{}_{JJ1}.
\end{aligned}\tag{5}$$

For the triplet odd states (a_{tt}) the scattering is rather weak and may be treated in Born approximation; for this reason the tensor contribution averages out in the saturation calculation for this state. Thus we may write for a_{tt} the simpler expression

$$ka_{tt}=\sum_{L\text{ odd}}(2L+1)\mu^-{}_L(c),\tag{6}$$

where $\mu^-{}_L(c)$ is determined by the central odd-state potential alone.

We note that the results of Eq. (5) depend on the eigen phase shifts alone, the parameter ϵ having dropped out on performing the spin sum. We also remark at this point that we take proper account of the standing wave boundary condition[5] which is correct in the saturation problem by replacing the complex $e^{i\delta}\sin\delta$ by $\tan\delta$. It is here that the convenience of expressing the scattering in terms of the eigen phase shifts is apparent since it is only in terms of the eigen states that a stationary description of the problem is possible.

The phase shifts for the coupled $J=1$ even parity state were determined by numerical integration of the coupled equations; as a check, an iteration in the integral equations was made. Two independent solutions were constructed by so choosing the amplitudes and slopes at the core as to satisfy the orthogonality condition.[6] From these two solutions, the eigen states and mixing parameter were determined following the methods of Appendix A. For the remaining states, the potential for the uncoupled D waves is quite strong so that this phase shift was determined by numerical integration. The other D phase shifts were determined by Born approximation, as were the quite small P-wave phase shifts, both coupled and uncoupled.

III. SCATTERING RESULTS

The intimate connection between the saturation calculation and the scattering phase shifts which is characteristic of the methods used in I and in this paper makes a parallel discussion of both desirable. We shall

[3] J. Blatt and L. C. Biedenharn, Phys. Rev. **86**, 399 (1952).
[4] See, for example, J. Ashkin and Ta-You Wu, Phys. Rev. **73**, 973 (1948).
[5] B. A. Lippmann and J. Schwinger, Phys. Rev. **79**, 469 (1950).
[6] W. Rarita and J. Schwinger, Phys. Rev. **59**, 436 (1941).

therefore in this section describe the scattering[7] which is predicted by the phase shifts we are to use in the discussion of saturation. These have been determined for the meson theory potentials we have specifically considered.[2] First, we shall qualitatively describe the p-p scattering as given by our results and the comparison with experiment.[8,9] The calculated cross section together with the experimental results are shown in Fig. 1. The potentials we use are characterized by quite short range in the singlet state and by a nonmonotonic quite strong tensor force together with a weak central force in the odd state. The combined effect of these is the following: at 32 Mev, the small D-wave scattering (0.80° D phase shift) is almost completely masked by the quite appreciable tensor scattering (peaked at 90°) which combines with the central scattering (peaked at 0°) to give an almost isotropic scattering. The magnitude of the scattering is slightly larger than the experimental results; the tendency of the S-wave repulsion to diminish the S-wave scattering is only slightly felt at this energy. At 90 Mev, the central scattering now shows very pronounced S-D interference which, however, is still masked completely by the tensor scattering which gives a quite appreciable fraction of the scattering. The resulting cross section (nuclear scattering only) is still quite isotropic; the cross section is rather small with the rapidly dropping S phase showing the core effect. The magnitude of the scattering is perhaps

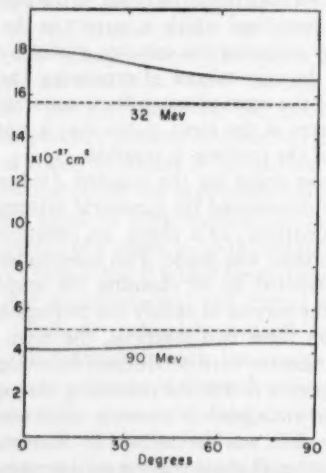

FIG. 1. Differential cross sections in the center-of-mass system for p-p scattering at 32[8] and 90[9] Mev, neglecting Coulomb effect. The experimental results are well fitted by pure S-wave nuclear scattering; the magnitudes of the nuclear scattering alone which agree with the experimental results are shown by the dashed curves.

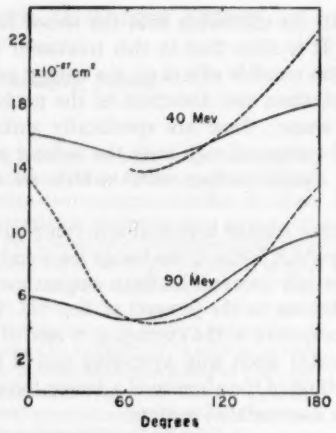

FIG. 2. Differential cross sections in the center-of-mass system for n-p scattering at 40[11] and 90[12] Mev. The solid curves are calculated; the dashed curves represent an approximate fit to the experimental results.

slightly too small although not outside of the experimental errors, and is actually in good agreement with a recently reported value[10] of 4.6 millibarns for the differential cross section at 90 degrees. These results show certainly a good agreement with the high-energy p-p scattering and, of course, agree with the low-energy scattering data which were used in determining the parameters of the potential.

The situation is not quite so satisfactory in the n-p scattering. The potentials in this case are more complicated than in the p-p case with twice as many states (because of the effects of the exclusion principle) and the even-odd state interference makes the analysis less simple. Qualitatively, the potentials which did not act on the p-p system are characterized by the dominant tensor force in the triplet even state and the strong repulsion in the singlet odd state. The even-state tensor force gives most of the scattering of the partial waves of high angular momenta since it is of considerably larger range than the very short-tailed central triplet even force. The cross section drops quite rapidly in magnitude as the repulsive cores affect the S-wave scattering quite appreciably even at 40 Mev.

The quantitative results of the scattering at 40 and 90 Mev are given in Fig. 2. It is apparent that although the cross sections in magnitude agree very well with the experimental results,[11,12] they are in error to some extent in having somewhat too much exchange scattering and too little scattering of high partial waves; i.e., the odd-state potentials are somewhat too strongly repulsive, and the even-state potentials are not long-tailed enough. It is possible that these difficulties might

[7] In this section we have drawn extensively on the ideas and results of R. Christian and E. Hart, Phys. Rev. **77**, 441 (1950); R. Christian and H. P. Noyes, Phys. Rev. **79**, 85 (1950).

[8] W. K. H. Panofsky and F. L. Fillmore, Phys. Rev. **79**, 57 (1950); Cork, Johnson, and Richman, Phys. Rev. **79**, 71 (1950).

[9] R. W. Birge, Phys. Rev. **80**, 490 (1951); R. W. Birge, Phys. Rev. **83**, 274 (1951).

[10] V. E. Kruse and J. M. Teem, Phys. Rev. **95**, 662 (A) (1954).

[11] Hadley, Kelley, Leith, Segrè, Wiegand, and York, Phys. Rev. **75**, 351 (1949); R. Hildebrand and C. E. Leith, Phys. Rev. **76**, 587 (1949).

[12] O. Chamberlain and J. W. Easley, Phys. Rev. **94**, 208 (1954). This paper gives a list of references to earlier work.

be eliminated by alteration of the potentials we have used. In view of the semiquantitative agreement, however, and of the great arbitrariness which enters in much alteration of the interactions, we have not at present made further investigation of the origin of the detailed discrepancies. It might be pointed out, however, that the difficulty appears to originate in the too short-tailed character of the triplet even-state potentials which can be altered without upsetting the good agreement of the predicted p-p scattering with experiment.

In concluding this section, we remark that the agreement with experiment of the scattering predicted by the phase shifts we have calculated is quantitatively quite good, particularly in the p-p scattering. We therefore feel that the use of these scattering amplitudes in the saturation discussions of Sec. V will not introduce appreciable errors. This is particularly true since most of the contribution to the potential energy comes from rather low relative momenta (corresponding to energies in scattering of less than 40 Mev) where the agreement with experiment is particularly good.

IV. SURFACE EFFECTS

Before proceeding to a discussion of the saturation problem, we shall develop some results which we use in the next section. Specifically, we shall discuss a surface effect which in this model appears to be of particular importance, i.e., the effect of the finite nuclear volume on the distribution of momentum states. This effect appears very directly in the kinetic energy which is increased when the nuclear particles are localized in a finite volume. A further effect arises from the alteration of the distribution of states of relative momentum for two colliding particles which has a pronounced effect on the potential energy.

To account for this effect in an approximate (and very simple) way, we make use of a result of Wheeler and Hill[13] who show approximately that the number of states per momentum interval (assuming spherical symmetry) is given by

$$N(k)d\mathbf{k}=\left(\frac{v}{2\pi^2}-\frac{S}{16k\pi}\right)\frac{d\mathbf{k}}{4\pi}, \tag{7}$$

where v is the total volume and S is the surface area. In this expression a small term linear in the nuclear dimensions has been dropped. For a spherical nucleus, this can be written

$$N(k)d\mathbf{k}=v\frac{d\mathbf{k}}{(2\pi)^3}[1-3\pi/4kR], \tag{8}$$

where R is the nuclear radius. We note that the number of states goes to zero at

$$k=3\pi/4R\equiv k_0, \tag{9}$$

which is reasonable since

$$\lambda_0=2\pi/k_0=8R/3, \tag{10}$$

is approximately the longest wavelength which can have nodes in the nuclear volume ($\frac{1}{2}$ wave falling in the nucleus). (The factor $8R/3$ appearing instead of $4R$ represents a crude correction for the surface curvature.) Thus, we write

$$N(k)d\mathbf{k}=\frac{vd\mathbf{k}}{(2\pi)^3}\left(1-\frac{k_0}{k}\right). \tag{11}$$

The total number of particles (with 4 per momentum state) is

$$A=\frac{4v}{(2\pi)^3}\frac{4\pi}{3}k_F^3(1-\tfrac{3}{2}k_0/k_F), \tag{12}$$

defining K_F as a function of A, the density, and of k_0 (or of R). Further, we have for the mean kinetic energy

$$T=\frac{4}{A}\int\frac{k^2}{2M}N(k)d\mathbf{k}=\frac{vk_F^5}{5AM\pi^2}\left(1-\frac{5}{4}\frac{k_0}{k_F}\right). \tag{13}$$

These results can be expressed conveniently in terms of the limiting case of $A\to\infty$ for constant density. In this case we introduce the dimensionless density parameter η by the relation

$$v=(4/3)\pi R^3=(4/3)\pi r_0^3\eta^3A, \tag{14}$$

where r_0 is the mean spacing between nuclear particles ($r_0=1.40\times10^{-13}A^{\frac{1}{3}}$ cm) and η is accordingly of the order of one. In terms of this parameter, the Fermi momentum for an infinite medium is

$$k_\infty=(9\pi/8)^{\frac{1}{3}}(r_0\eta)^{-1}=1.52\mu/\eta. \tag{15}$$

Using Eq. (9) for k_0, we finally find

$$\frac{k_F}{k_\infty}=\left[1-\tfrac{3}{4}(3\pi^2)^{\frac{1}{3}}\frac{k_\infty}{k_F}A^{-\frac{1}{3}}\right]^{-\frac{1}{3}}, \tag{16}$$

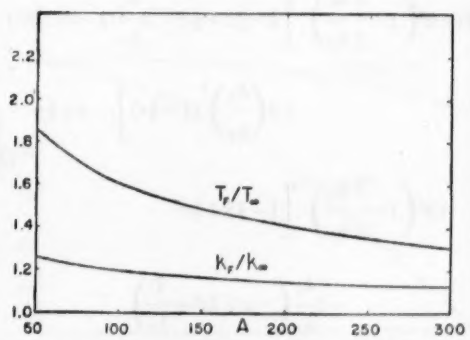

FIG. 3. Effects at constant density of finite nuclear size on the maximum momentum k_F and the average kinetic energy T_F in the degenerate Fermi gas. The ratios of k_F and T_F to k_∞ and T_∞ (k_F and T_F for an infinite medium) are given.

[13] D. L. Hill and J. A. Wheeler, Phys. Rev. **89**, 1102 (1953).

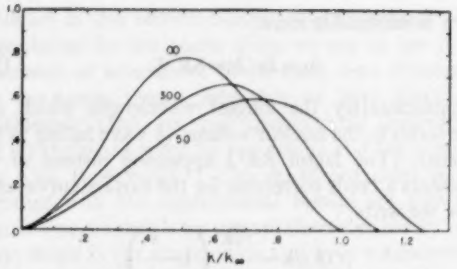

FIG. 4. Probability of the relative momentum k in a degenerate Fermi gas, showing surface effect. The vertical scale is arbitrary; the horizontal scale is in units of k_∞.

and

$$\frac{T_F}{T_\infty}=\left(\frac{k_F}{k_\infty}\right)^5\left[1-\tfrac{5}{8}(3\pi^2)^{\frac{1}{3}}\frac{k_\infty}{k_F}A^{-\frac{1}{3}}\right]^{\frac{1}{3}}. \tag{17}$$

These results for k_F/k_∞ and T_F/T_∞ are given in Fig. 3 as a function of A.

We next need the effect from this change in the momentum distribution on the distribution of relative momenta. In evaluating the potential energy, we encounter an integral of the form

$$\int N(k_1)d\mathbf{k}_1N(k_2)d\mathbf{k}_2f(\tfrac{1}{2}\mathbf{k}_1-\tfrac{1}{2}\mathbf{k}_2)\Big/\int N(k_1)d\mathbf{k}_1. \tag{18}$$

Transforming to relative and total momentum coordinates and introducing the results of Eq. (11), we find for this integral

$$32\pi\int_0^{k_F}dk f(k)P(k), \tag{19}$$

where $P(k)$ is the probability (unnormalized) of finding a relative momentum k, and is equal to (with $x=k/k_F$)

$$\begin{aligned}P(k)=k^2\left(1-\frac{3}{2}\frac{k_0}{k_F}\right)^{-1}&\left[1-\tfrac{3}{2}x+\tfrac{1}{2}x^3-3\frac{k_0}{k_F}(1-x-\tfrac{3}{5}x^2)\right.\\&\left.+3\left(\frac{k_0}{k_F}\right)^2(1-\tfrac{3}{5}x)\right],\quad x\leqslant\tfrac{1}{2};\\=k^2\left(1-\frac{3}{2}\frac{k_0}{k_F}\right)^{-1}&\left[1-\tfrac{3}{2}x+\tfrac{1}{2}x^3\right.\\&-3\frac{k_0}{k_F}\left(-x+\tfrac{3}{5}x^2+\frac{1}{3x}\right)\\&\left.+3\left(\frac{k_0}{k_F}\right)^2\frac{1}{2x}(1-x)^2\right],\quad x\geqslant\tfrac{1}{2}.\end{aligned} \tag{20}$$

This distribution is given in Fig. 4 for several values of A. The shift to higher values of relative momentum with decreasing radii is evident.

V. SATURATION

A. Average Energies

We now proceed to relate the results of the preceding sections to the saturation problem. The phase shifts which we need are simplified by the averaging out of all tensor force contributions which need be considered only in Born approximation. For this reason, the tensor force affects only the coupled ^3S-^3D and the remaining D phase shifts. The contributing states are shown in Figs. 5, 6, and 7. In evaluating the integrals over relative momenta which give the potential energy, the passage of the large phase shift δ_α through 90° at a relative momentum of about 0.64 μc gives rise to a singularity in the integrand (as $\tan\delta_\alpha$ passes through the singularity at $\delta_\alpha=\pi/2$). This does not give any difficulty, however, since the integral about this point has the character of a principal value and the integration through the pole gives a finite result, the contribution from the vicinity of the pole actually giving only a small contribution to the result. It might be remarked that the occurrence of this pole is a consequence of the presence of a bound state for the triple even state.

The energy is finally determined as a function of the number of particles and of the density by use of Eqs. (2), (5), (6), (20), and the values for the phase shifts. These results are given in Fig. 8. They show the remarkably large effect of the surface, not only in the kinetic energy but also to about the same extent in the volume energy. It is perhaps not possible to take these results entirely seriously since the treatment in which surface effects are so important is probably less reliable than the treatment of a volume effect alone. Nevertheless, it is difficult to believe that these effects do not exist to a very considerable extent in nuclear structure in any model. They represent qualitatively very reasonable modifications in the kinetic energy (due to restriction in volume) and in volume energy (due to shift to population to higher momenta and hence to less strongly interacting states).

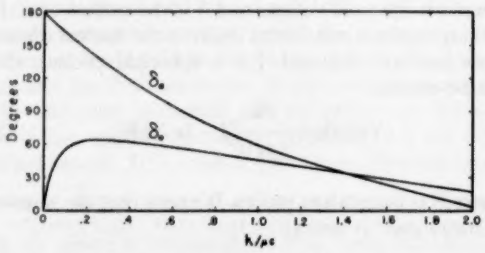

FIG. 5. Singlet $S(\delta_0)$ and S-dominant $J=1$ even-parity (δ_α) phase shifts. The abscissa is in units of $\mu c=140$ Mev/c.

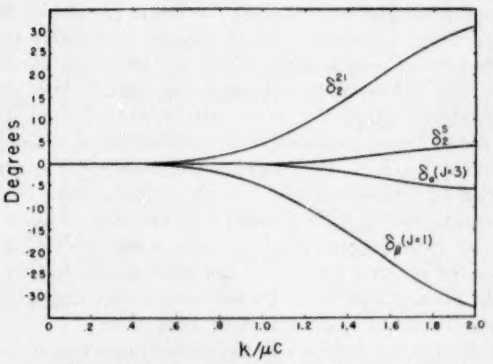

FIG. 6. D phase shifts for coupled [$\delta_\beta(J=1)$ and $\delta_\alpha(J=3)$] and uncoupled (δ_2^{21}) triplet states and for singlet state (δ_2^{s}).

B. Energies as a Function of Particle Momentum*

We can also obtain more detailed information about the characteristics of particle motion in the nuclear medium. A particularly interesting result is the dependence of the interaction energy on the momentum of the particle being considered. We get this result by integrating in the potential energy only over the momenta of one of the colliding particles. This gives an expression:

$$V(k)=\frac{2}{\pi M}\int_0^{\frac{1}{2}(k+k_F)} f(k')P(k',k)dk', \qquad (21)$$

where $f(k')$ is the same statistically weighted sum of amplitudes that appears in the integral of Eq. (2), and $P(k,k')$ is the probability of finding the relative momentum k'; using Eq. (11) for the density of momentum states, this function is

$$P(k',k)=\mu_{\max}-\mu_{\min}-(k_0/k)[(k^2+4k'^2+4kk'\mu_{\max})^{\frac{1}{2}} - (k^2+4k'^2+4kk'\mu_{\min})^{\frac{1}{2}}], \qquad (22)$$

where

$$\mu_{\max}=\text{lesser of}\left\{1,\frac{k_F^2-k^2-4k'^2}{4kk'}\right\},$$
$$\mu_{\min}=\text{greater of}\left\{-1,\frac{k_0^2-k^2-4k'^2}{4kk'}\right\}. \qquad (23)$$

* *Note added in proof.*—Because of an oversight by the author, a factor of two was omitted in Eq. (21) for $V(k)$ which should read

$$V(k)=\frac{4}{\pi M}\int_0^{\frac{1}{2}(k+k_F)} f(k')P(k',k)dk'. \qquad (21')$$

This factor is necessary since in calculating the average potential energy, it is necessary to take account of the origin of the potential energy in two-body forces. Thus the correct relation between $\bar{V}$ and $V(k)$ is

$$\bar{V}=\frac{1}{2}\int_0^{k_F} V(k)k^2dk \Big/ \int_0^{k_F} k^2dk, \qquad (21'')$$

the factor $\frac{1}{2}$ arising from the fact that the integrations of Eqs. (21′) and (21″) are equivalent to summing over all particles twice. $\bar{V}$ defined by Eqs. (21′) and (21″) is identical with that given by Eq. (2).

As a result of this correction, all values for $V(k)$ in Fig. 9 and Fig. 10 should be multiplied by two. Consequently the anomaly of unbound surface particles discussed in the conclusion does not arise.

The result of the integration of Eq. (21) for the potential energy as a function of k is given in Figs. 9 and 10 for the cases of 300 nucleons and of an infinite number. The rapid change of the depth with energy reflects the much stronger scattering at low values of relative momentum.

C. Discussion

The tensor force makes its presence strongly felt in the saturation, even when nuclear distortion is not considered, through its marked enhancement of the low energy triplet even state scattering. This effect, which is absent in the conventional saturation calculation without correlation, increases the average potential energy per particle by roughly 40 percent and at the same time increases the rate of increase of potential energy with increasing density. The net effect relative to the calculation neglecting tensor effects is not only to increase considerably the average binding in an infinite medium (from 12 Mev to 39 Mev) but also to decrease the equilibrium radius from $1.15\times10^{-13}A^{\frac{1}{3}}$ cm to $0.85\times10^{-13}A^{\frac{1}{3}}$ cm. These effects for an infinite medium are, however, to some extent compensated in a finite medium by the effects of the surface on both the kinetic and potential energies so that in a heavy nucleus ($A=300$) the binding energies and equilibrium radius again take on reasonable values.

VI. CONCLUSIONS

We have derived formulas which relate the many-body potential energy to the characteristics of two-body scattering, for the general case of central and noncentral forces. We have also evaluated approximately the effects of the nuclear surface when the number of interacting nucleons is finite. Combining these results with a set of phase shifts derived from an explicit potential model (which gives scattering in semiquantitative agreement with experiment), we obtain the energy per particle in nuclear matter as a function of the density, the number

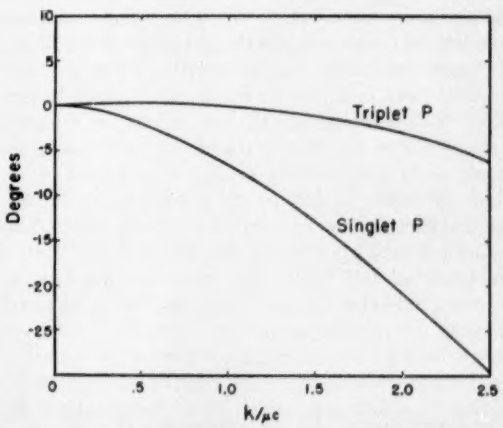

FIG. 7. P phase shifts neglecting tensor force. The core radius in the triplet states has been taken to be $0.4\hbar/\mu c$.

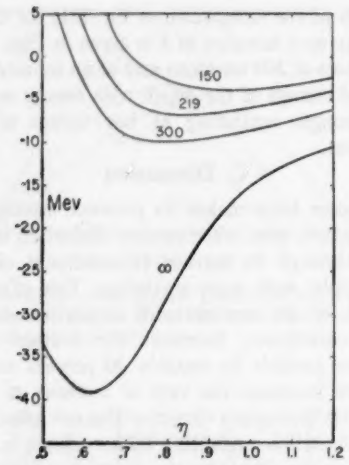

FIG. 8. Average energy per particle as a function of density and of total number of particles. The density parameter η is defined in Eq. (14).

of nucleons, and the momentum of the particle. These results show that in the absence of surface effects, the binding energy per particle is 39 Mev at an equilibrium radius of $R=0.85\times10^{-13}A^{\frac{1}{3}}$ cm, and thus that saturation in the usual sense does not occur at normal density. These results differ markedly from the results of I, where central forces alone were considered, in that the strong low energy scattering arising from the tensor force considerably increases the interaction energy for low momentum encounters. This effect is, of course, absent in a method which treats the scattering in Born approximation and which further assumes uncorrelated nucleon positions.

If, however, a finite nucleus is considered (as, for example, with 300 nucleons) the surface effects increase the kinetic energy and decrease the potential energy with the net result that a more reasonable value of binding energy of 10 Mev per particle results at an equilibrium radius of $1.15\times10^{-13}A^{\frac{1}{3}}$ cm. These modifications are the consequence of the alteration in the density of momentum states (compared with a Fermi gas), and are analogous to a surface energy with origin in both kinetic and potential effects. Such effects are a natural consequence of the specific model used but would also appear in a qualitatively similar way in any model which attempts to deduce the potential of an "independent particle" model from the two-body interactions.

Another striking effect is the strong dependence of the potential felt by a particle on the particle momentum, reflecting the decrease in the scattering amplitudes as the relative momentum in collision increases. This behavior almost certainly is present, in a qualitative form at least, in any nuclear model treating particle motion to a first approximation as independent. The size of the effect can be seen in Fig. 10 which shows the decrease in potential energy from -82 Mev at zero momentum to -32 Mev at the top of the Fermi distribution. A curious anomaly appears here also in that the relatively weak potential felt by the rapidly moving particles of maximum kinetic energy results in a positive total energy; i.e., these particles are unbound. The precise meaning of this result depends on a thorough understanding of the nature of the nuclear surface, and more particularly, of the relation to the nucleons of the independent particle modes of the coherent motion. It is not clear, for example, that the requirement of binding for the physical nucleons is not more closely related to the average binding of the coherent modes than to the binding of the mode of highest momentum.

In conclusion we would like to comment that further extension of the methods of the previous paper (I) and of this paper cannot be made until the nature of the nuclear surface and of the "particle" coupling to the surface is understood. The strikingly large effect of the surface considered somewhat crudely in this paper shows the importance of a quantitative understanding of the surface phenomena. These topics form a subject outside of the scope of this paper; it is expected that work along these lines will be published separately in the near future.

The author is indebted to Dr. C. A. Levinson and Dr. H. Mahmoud for helpful discussions of some of the topics of this paper, and to Professor John A. Wheeler for a very stimulating discussion of the implications of these results. The author would also like to acknowledge the computational aid of Dr. John Chappelear.

APPENDIX A. TENSOR SCATTERING AND EIGEN PHASE SHIFTS

We consider the scattering in a state with total angular momentum J, parity $\pi=-(-1)^J$, and with two coupled orbital angular momentum states with $L=J\pm1$. We introduce the eigenstates of the scattering

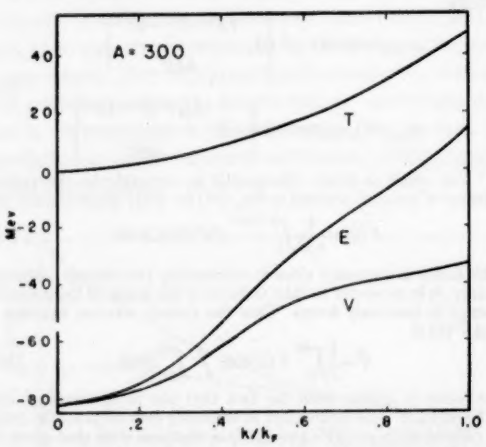

FIG. 9. Potential, kinetic, and total energy per particle in an infinite medium as function of momentum. The abscissa is measured in units of the Fermi momentum. The evaluation has been carried out at the equilibrium density indicated in Fig. 8.

matrix which are characterized by the fact that in scattering, such states experience the same phase shift in the two coupled states with $L=J\pm1$. These states we call $g_{J\alpha}{}^m$ and $g_{J\beta}{}^m$; they have, respectively, the asymptotic forms

$$g_{J\alpha}\sim\frac{\mathcal{Y}_{J,J-1}{}^m-\tan\epsilon\,\mathcal{Y}_{J,J+1}{}^m}{1+\tan^2\epsilon}\,\frac{\sin[kr-\frac{1}{2}\pi(J-1)+\delta_\alpha]}{kr},$$
$$g_{J\beta}\sim\frac{\mathcal{Y}_{J,J-1}{}^m+\cot\epsilon\,\mathcal{Y}_{J,J+1}{}^m}{1+\cot^2\epsilon}\,\frac{\sin[kr-\frac{1}{2}\pi(J-1)+\delta_\beta]}{kr}, \tag{A1}$$

where ϵ is the real parameter which determines the asymptotic ratio of $L=J-1$ and $L=J+1$ states in the eigenstate and δ_α, δ_β are the eigen phase shifts. We use these equations to define generalized spherical harmonics

$$I_{J\alpha}{}^m(\epsilon)=(\mathcal{Y}_{J,J-1}{}^m-\tan\epsilon\,\mathcal{Y}_{J,J+1}{}^m)(1+\tan^2\epsilon)^{-1},$$
$$I_{J\beta}{}^m(\epsilon)=(\mathcal{Y}_{J,J-1}{}^m+\cot\epsilon\,\mathcal{Y}_{J,J+1}{}^m)(1+\cot^2\epsilon)^{-1}, \tag{A2}$$

or collectively, introducing the transformation coefficients $B(JLm|J\sigma m)$,

$$I_{J\sigma}{}^m=\sum_L B(JLm|J\sigma m)\mathcal{Y}_{JL}{}^m,\quad \sigma=\alpha,\beta, \tag{A3}$$

and their inverses

$$\mathcal{Y}_{JL}{}^m=\sum_{\sigma=\alpha,\beta} B(J\sigma m|JLm)I_{J\sigma}{}^m. \tag{A4}$$

With this notation it is now simple to get expressions for the phase shifts in terms of the eigen phase shifts and the transformation coefficients $B(JLm/J\sigma m)$. First we write the total wave function in the asymptotic region

$$\psi_J{}^m=\sum_{\sigma=\alpha,\beta} A_\sigma I_{J\sigma}{}^m\sin[kr-\tfrac{1}{2}\pi(J-1)+\delta_\sigma]/kr. \tag{A5}$$

The incoming wave is

$$\psi_0{}^m=\sum C_L Y_L{}^0\chi_1{}^m\sin(kr-\tfrac{1}{2}\pi L)/kr$$
$$=\sum C_L C(JLm|SL0m)B(J\sigma m|JLm)I_{J\sigma}{}^m\times\sin(kr-\tfrac{1}{2}\pi L)/kr, \tag{A6}$$

where the $C(SLm_Lm_S|JLm)$ are the usual Clebsch-Gordan coefficients. Using this result and choosing the coefficients A_σ in such a way as to have only outgoing spherical waves, we find

$$\psi_J{}^m=\psi_{0J}{}^m+\psi_J{}^m-\psi_{0J}{}^m$$
$$=\psi_{0J}{}^m+\frac{e^{ikr}}{kr}\sum C_L C(JLm|SL0m)\times B(J\sigma m|JLm)(-i)^L I_{J\sigma}{}^m(e^{2i\delta\sigma}-1)/2i. \tag{A7}$$

To get the conventional expression in terms of the usual phase shifts, we re-express the $I_{J\sigma}{}^m$ in terms of the spherical harmonics to find

$$\psi^m=\psi_0{}^m+\frac{e^{ikr}}{kr}\sum C_{L'}\times C(JL'm|SL'0m)B(J\sigma m|JL'm)(-i)^{L'}\times B(JLm|J\sigma m)C(SLm-m_s'm_s'|JLm)\times\frac{e^{2i\delta\sigma}-1}{2i}Y_L{}^{m-m_s'}\chi_1{}^{m_s'}. \tag{A8}$$

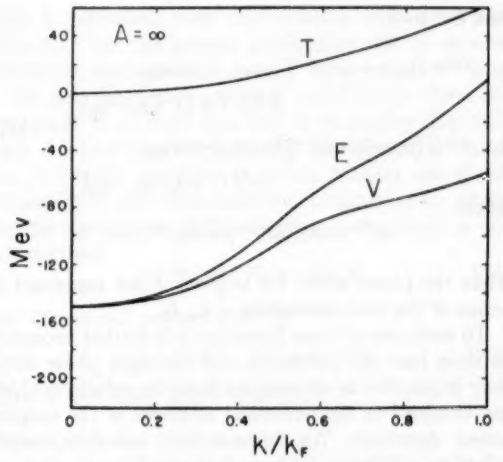

FIG. 10. Potential, kinetic, and total energy per particle for a "nucleus" made up of 300 nucleons (with $Z=N$) as a function of momentum. The evaluation is at equilibrium density.

In terms of the usual complex phase shifts $\delta_L{}^{Jm_s}$, the wave function has the form

$$\psi^m=\psi_0{}^m+\frac{e^{ikr}}{kr}\sum C_L i^L\frac{[\exp(2i\delta_L{}^{Jm_s})-1]}{2i}\times C(SLm_s-m_s'm_s'|JLm_s)\times C(JLm|SL0m)Y_L{}^{m_s-m_s'}\chi_1{}^{m_s'}. \tag{A9}$$

Comparison of Eqs. (A8) and (A9) gives:

$$\frac{\exp(2i\delta_L{}^{Jm_s})-1}{2i}=\sum_{L'\sigma}\frac{C(JL'm|SL'0m)}{C(JLm|SL0m)}\times B(J\sigma m|JL'm)B(JLm|J\sigma m)\times\left(\frac{2L'+1}{2L+1}\right)^{\frac{1}{2}}\frac{e^{2i\delta\sigma}-1}{2i}. \tag{A10}$$

Using the transformation coefficients $B(J\sigma m|JLm)$ and their inverses, we finally get for $m=\pm1$,

$$\eta_{J-1}{}^{J,\pm1}=(\tan\epsilon+\cot\epsilon)^{-1}[\cot\eta_\alpha+\tan\eta_\beta-(J/J+1)^{\frac{1}{2}}(\eta_\alpha-\eta_\beta)],$$
$$\eta_{J+1}{}^{J,\pm1}=(\tan\epsilon+\cot\epsilon)^{-1}[\tan\eta_\alpha+\cot\eta_\beta+(J/J+1)^{-\frac{1}{2}}(\eta_\alpha-\eta_\beta)]. \tag{A11}$$

And for $m=0$

$$\eta_{J-1}{}^{J,0}=(\tan\epsilon+\cot\epsilon)^{-1}[\cot\epsilon\eta_\alpha+\tan\epsilon\eta_\beta+(J/J+1)^{-\frac{1}{2}}(\eta_\alpha-\eta_\beta)],$$
$$\eta_{J+1}{}^{J,0}=(\tan\epsilon+\cot\epsilon)^{-1}[\tan\epsilon\eta_\alpha+\cot\epsilon\eta_\beta-(J/J+1)^{\frac{1}{2}}(\eta_\alpha-\eta_\beta)], \quad \text{(A12)}$$

where

$$\eta_L{}^{J\,m}=\exp(i\delta_L{}^{J\,m})\sin\delta_L{}^{J\,m}, \text{ etc.}$$

Thus the phase shifts for a given J are expressed in terms of the real parameters ϵ, δ_α, δ_β.

To make use of these formulas, it is further necessary to show how the parameter and the eigen phase shifts may in practice be determined from the solutions which are obtained in the numerical solutions of the coupled tensor equations. We suppose that two independent solutions satisfying the boundary conditions have been determined, as for example by so choosing the amplitudes and slopes at the core as to satisfy the orthogonality condition.[6] These solutions are asymptotically of the form (we consider the $J=1$ even parity state)

$$\psi_i{}^m=\sin(kr+\delta_i)\mathcal{Y}_{101}{}^m+\beta_i\sin(kr-\pi+\sigma_i)\mathcal{Y}_{121}{}^m, \quad \text{(A13)}$$

where δ_i and σ_i are the (in general unequal) phase shifts for the S and D waves and β_i is a parameter determining the relative asymptotic amplitude of S and D waves. From these two solutions we construct the linear combinations

$$\psi_\rho{}^m=\psi_1{}^m+\rho\psi_2{}^m. \quad \text{(A14)}$$

If we now impose the condition that the phase shift in the S and D waves be equal, thus determining the eigen phases, we find a condition on ρ and further an expression for $\tan\delta_\rho$,

$$\frac{\sin\delta_1+\rho\sin\delta_2}{\cos\delta_1+\rho\cos\delta_2}=\frac{\beta_1\sin\sigma_1+\rho\beta_2\sin\sigma_2}{\beta_1\cos\sigma_1+\rho\beta_2\cos\sigma_2}=\tan\delta_\rho. \quad \text{(A15)}$$

This gives a quadratic equation for ρ; the two roots determine the two eigen phase shifts. Thus we can write for the solution $\psi_\alpha{}^m$:

$$\psi_\alpha{}^m=A_\alpha[\sin(kr+\delta_\alpha)\mathcal{Y}_{101}{}^m+\tan\epsilon\sin(kr+\delta_\alpha-\pi)\mathcal{Y}_{121}{}^m], \quad \text{(A16)}$$

where $\tan\epsilon$ from comparison with Eq. (A1) is, using Eq. (A15),

$$\tan\epsilon=\frac{\beta_1\sin\sigma_1+\rho_\alpha\beta_2\sin\sigma_2}{\sin\delta_1+\rho_\alpha\sin\delta_2}. \quad \text{(A17)}$$

This completes the construction from the two original solutions of the necessary parameters.

PHYSICAL REVIEW VOLUME 96, NUMBER 2 OCTOBER 15, 1954

Space-Time Representation in Wave Mechanics: Illustration of the Method

MALCOLM K. BRACHMAN
Texas Instruments Incorporated, Dallas, Texas
(November 12, 1953)

The basic equations of a new space-time representation are derived in a heuristic fashion, and a simple application is presented to illustrate the point of view.

A NEW space-time representation has been developed by Hellund and the present author.[1] This paper provides a heuristic derivation of the Schrödinger equation in the new representation and illustrates its solution by considering the square-well potential.

THE SCHRÖDINGER EQUATION

We consider a one-dimensional system with a Hamiltonian $H(-i\hbar\partial/\partial x, x)$ in the Schrödinger representation. The Hamiltonian is assumed to have the form

$$H=\frac{\hbar^2}{2m}\frac{\partial^2}{\partial x^2}+V(x)=T+V. \quad (1)$$

The wave function $\Psi(x,t)$ satisfies the Schrödinger equation

$$H\Psi=i\hbar(\partial\Psi/\partial t). \quad (2)$$

Our task is to find the form of this equation in the new representation.

The one-dimensional space is split into cells by the points of division $x=L_\sigma$, $\sigma=0,\pm1,\pm2,\cdots$, with $L_0=0$. The σth cell is bounded by the abscissas L_σ and $L_{\sigma-1}$, and its length is $l_\sigma=L_\sigma-L_{\sigma-1}$. In the σth cell there is an orthonormal set of functions, $\varphi_{j\sigma}(x)$, which is defined only within the cell. These functions may be conveniently chosen to be of exponential form, and may be written

$$\varphi_{j\sigma}(x)=\frac{h(\sigma)}{\sqrt{l_\sigma}}e^{ik_jx}, \quad j=0,\pm1,\pm2,\cdots. \quad (3)$$

[1] E. J. Hellund and M. K. Brachman, Phys. Rev. 92, 822 (1953).

The k's satisfy the fundamental relationship,

$$k_{j\sigma}l_\sigma = 2\pi j, \tag{4}$$

and the function $h(\sigma)$ is defined as follows:

$$h(\sigma) = S(x-L_{\sigma-1}) - S(x-L_\sigma), \tag{5}$$

where

$$S(x) = 1, \quad x>0, \tag{6a}$$

$$= 0, \quad x<0. \tag{6b}$$

Thus $S(x)$ is the Heaviside unit function, and $h(\sigma)$ is seen to equal unity for $L_{\sigma-1}<x<L_\sigma$ and to vanish otherwise. We now abandon rigor and proceed, finding that it will become necessary to discard infinite terms. We note first that (5) may be differentiated to yield

$$dh(\sigma)/dx = \delta(x-L_{\sigma-1}) - \delta(x-L_\sigma), \tag{7}$$

where $\delta(x)$ is the Dirac delta function. We define

$$C_{j\sigma} = \int_{-\infty}^{\infty} \varphi_{j\sigma}^*(x)\Psi(x,t)dx, \tag{8}$$

and assume the validity of the expansion

$$\Psi(x,t) = \sum_j C_{j\sigma}\varphi_{j\sigma}. \tag{9}$$

The basic task is to project the Schrödinger equation (2) into the σth cell, or more properly, to evaluate both sides of the equation

$$(\varphi_{j\sigma}, H\Psi) = (\varphi_{j\sigma}, i\hbar\partial\Psi/\partial t), \tag{10}$$

where the customary notation for a scalar product has been employed.

The result will have the form

$$\sum_{j'\sigma'} \{(j\sigma|T|j'\sigma') + (j\sigma|V|j'\sigma')\}C_{j'\sigma'} = i\hbar\frac{\partial}{\partial t}C_{j\sigma}. \tag{11}$$

We have written

$$(j\sigma|A|j'\sigma') = \int_{-\infty}^{\infty} \varphi_{j\sigma}^* A \varphi_{j'\sigma'}dx, \tag{12}$$

where A is any operator. We remark that it is an obvious requirement of any consistent representation that it be isomorphic, in the sense that

$$(j\sigma|AB|j'\sigma') = \sum_{j''\sigma''} (j\sigma|A|j''\sigma'')(j''\sigma''|B|j'\sigma'), \tag{13}$$

where A and B are any appropriate operators. For convenience we introduce the notation

$$(j\sigma \,\vdots\, A \,\vdots\, j'\sigma') = (l_\sigma l_{\sigma'})^{\frac{1}{2}} \int_{-\infty}^{\infty} \varphi_{j\sigma}^* A \varphi_{j'\sigma'}dx. \tag{14}$$

This is patterned after the notation of Condon and Shortley,[2] but the present application will be to non-Hermitian operators.

We now proceed to calculate $(j\sigma|T|j'\sigma')$. There are two ways to do this. The first is to employ Eq. (11) with $A = (-\hbar^2/2m)(\partial^2/\partial x^2)$, and the second is to use Eq. (13) with $A = B = -i\hbar(\partial/\partial x)$. Making use of the properties of the delta function, integrating by parts, and taking account of Eq. (4) give as the result of the first method

$$(j\sigma \,\vdots\, \partial^2/\partial x^2 \,\vdots\, j'\sigma') = R + W_1, \tag{15}$$

and the second method leads to

$$(j\sigma \,\vdots\, \partial^2/\partial x^2 \,\vdots\, j'\sigma') = R + W_2. \tag{16}$$

Here R (for right) is the expression

$$R = -k_{j\sigma}^2 l_\sigma \delta_{jj'}\delta_{\sigma\sigma'} + i(k_{j'\sigma'} + k_{j\sigma}) \times [e^{i(k_{j'\sigma'}-k_{j\sigma})L_\sigma}\delta_{\sigma',\sigma+1} - e^{i(k_{j'\sigma'}-k_{j\sigma})L_{\sigma-1}}\delta_{\sigma',\sigma-1}], \tag{17}$$

and

$$W_1 = e^{i(k_{j'\sigma'}-k_{j\sigma})L_\sigma}[\delta(L_\sigma - L_{\sigma'-1}) - \delta(L_\sigma - L_{\sigma'})] - e^{i(k_{j'\sigma'}-k_{j\sigma})L_{\sigma-1}}[\delta(L_{\sigma-1}-L_{\sigma'-1}) - \delta(L_{\sigma-1}-L_{\sigma'})], \tag{18a}$$

$$W_2 = [(l_{\sigma+1})^{-1}\{\delta_{\sigma',\sigma+2}e^{i(k_{j'\sigma'}L_{\sigma+1}-k_{j\sigma}L_\sigma)} - \delta_{\sigma',\sigma}e^{i(k_{j'\sigma'}-k_{j\sigma})L}\} - (l_{\sigma-1})^{-1}\{\delta_{\sigma',\sigma}e^{i(k_{j'\sigma'}-k_{j\sigma})L_{\sigma-1}} - \delta_{\sigma',\sigma-2}e^{i(k_{j'\sigma'}L_{\sigma-2}-k_{j\sigma}L_{\sigma-1})}\}]\sum_{j''} 1. \tag{18b}$$

To obtain (16) we note that

$$(j\sigma \,\vdots\, \partial/\partial x \,\vdots\, j'\sigma') = ik_{j\sigma}l_\sigma\delta_{jj'}\delta_{\sigma\sigma'} + \delta_{\sigma',\sigma+1}e^{i(k_{j'\sigma'}-k_{j\sigma})L_\sigma} - \delta_{\sigma',\sigma-1}e^{i(k_{j'\sigma'}-k_{j\sigma})L_{\sigma-1}}, \tag{19}$$

and

$$(j\sigma \,\vdots\, \partial^2/\partial x^2 \,\vdots\, j'\sigma') = \sum_{j''\sigma''} (l_{\sigma''})^{-1} \times (j\sigma \,\vdots\, \partial/\partial x \,\vdots\, j''\sigma'')(j''\sigma'' \,\vdots\, \partial/\partial x \,\vdots\, j'\sigma'). \tag{20}$$

The expression R is, apart from a factor $-\hbar^2/2m$, that given in reference 1 for $(j\sigma|T|j'\sigma')$. The terms W_1 and W_2 arise from the nature of the mathematical processes we have used, and we discard them, remarking only that the technique discussed in reference 1 avoids these difficulties.

We now write the Schrödinger equation for our representation by combining Eqs. (9) and (17). For simplicity we limit ourselves to the case $L_\sigma = a\sigma$, *viz.*, uniform cells of length a. This restriction will be observed for the remainder of this paper, but it is, of course, unnecessary. Then Eq. (9) becomes

$$i\hbar\frac{dC_{j\sigma}}{dt} = \frac{\hbar^2}{2m}k_j^2 C_{j\sigma} + \frac{\hbar^2 i}{2ma}\sum_{j'}(k_{j'}+k_j) \times \{C_{j'\sigma-1} - C_{j'\sigma+1}\} + \sum_{j'\sigma'}(j\sigma|V|j'\sigma')C_{j'\sigma'}. \tag{21}$$

[2] E. U. Condon and G. H. Shortley, *The Theory of Atomic Spectra* (Cambridge University Press, Cambridge, 1935), p. 62.

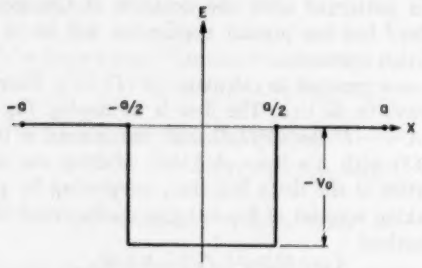

FIG. 1. The square-well potential.

Note that it is now possible to drop the subscript σ from the k's, which are the same in all cells.

An interpretation of Eq. (21) has been given in reference 1. We illustrate its use and our point of view with a simple problem and defer further development of the theory.

THE SQUARE-WELL POTENTIAL

We consider a stationary state, and write

$$C_{j\sigma}=b_{j\sigma}\exp[-(iE/\hbar)t]. \tag{22}$$

Equation (21) becomes

$$\left(\frac{\hbar^2}{2m}k_j^2-E\right)b_{j\sigma}+\frac{\hbar^2 i}{2ma}\sum_{j'}(k_{j'}+k_j)\{b_{j'\sigma-1}-b_{j'\sigma+1}\}+\sum_{j'\sigma'}(j\sigma|V|j'\sigma')b_{j'\sigma'}=0. \tag{23}$$

The problem is the familiar eigenvalue one, and requiring the determinant of the coefficients to vanish gives the secular equation for the eigenvalue of E.

For the square well of Fig. 1, the potential energy is

$$V=-V_0, \quad |x|<a/2, \tag{24a}$$

$$=0, \quad |x|>a/2. \tag{24b}$$

In accordance with our convention the σth cell extends from $(\sigma-1)a$ to σa. We have chosen the cell width equal to the width of the potential hole, but this is not a serious restriction. (On the other hand, our method requires continuity of potential at the cell boundaries.) We are interested primarily in cells 0 and 1, and a first approximation to the energy may be obtained by considering the states $j=0,\pm1$ in both cells. We write minus one as $\bar{1}$. The requisite matrix elements obtained from Eq. (11) are diagonal in σ and take the values

$$(j0|V|j'0)=\frac{V_0}{2\pi i(j-j')}[(-1)^{j-j'}-1], \quad j'\neq j, \tag{25a}$$

$$(j0|V|j0)=-\tfrac{1}{2}V_0, \tag{25b}$$

and

$$(j1|V|j'1)=(-1)^{j'-j}(j0|V|j'0). \tag{25c}$$

For brevity we introduce

$$(\hbar^2/2ma)\epsilon=E, \tag{26}$$

and

$$(\hbar^2/2ma)v=V_0. \tag{27}$$

Inserting these into Eq. (23) yields

$$\begin{pmatrix}
(2\pi)^2-\frac{1}{2}v-\epsilon & iv/\pi & 0 & 4\pi i & 2\pi i & 0\\
-iv/\pi & -\frac{1}{2}v-\epsilon & iv/\pi & 2\pi i & 0 & -2\pi i\\
0 & -iv/\pi & (2\pi)^2-\frac{1}{2}v-\epsilon & 0 & -2\pi i & -4\pi i\\
-4\pi i & -2\pi i & 0 & (2\pi)^2-\frac{1}{2}v-\epsilon & -iv/\pi & 0\\
-2\pi i & 0 & 2\pi i & iv/\pi & -\frac{1}{2}v-\epsilon & -iv/\pi\\
0 & 2\pi i & 4\pi i & 0 & iv/\pi & (2\pi)^2-\frac{1}{2}v-\epsilon
\end{pmatrix}\begin{pmatrix}b_{\bar{1}0}\\ b_{00}\\ b_{10}\\ b_{\bar{1}1}\\ b_{01}\\ b_{11}\end{pmatrix}=0. \tag{28}$$

From the symmetry we find that the substitution

$$b_{j0}=b_{\bar{j}1} \tag{29}$$

reduces Eqs. (28) from six equations in six unknowns to three equations in three unknowns. Replacing $\epsilon+(v/2)$ by λ and employing (29) gives the secular equation

$$\begin{vmatrix}
(2\pi)^2-\lambda & [(v/\pi)+2\pi]i & 4\pi i\\
-[(v/\pi)+2\pi]i & -\lambda & [(v/\pi)+2\pi]i\\
-4\pi i & -[(v/\pi)+2\pi]i & (2\pi)^2-\lambda
\end{vmatrix}=0. \tag{30}$$

Setting $(2\pi)^2-\lambda$ equal to η and $(v/\pi)+2\pi$ equal to ω, we obtain

$$(\eta^2-16\pi^2)(\eta-4\pi^2)-2\omega^2\eta=0. \tag{31}$$

For the case $\omega\gg1$, we find

$$\eta=\pm\sqrt{2}\omega=\pm(\sqrt{2}/\pi)v, \tag{32}$$

or

$$\epsilon=-[\tfrac{1}{2}+(\sqrt{2}/\pi)]v=-0.95v. \tag{33}$$

This corresponds to the quantum-mechanical solution,

$$E=-V_0, \tag{34}$$

which is the lowest level for the case $2ma^2V_0/\hbar^2\gg1$.

This solution can be improved by including states of higher (absolute) j value. It is obvious that the labor involved is excessive, since the difficulty of solving the secular equation increases rapidly with its order.

Among further applications of the method that may be contemplated are the Zeeman effect, the simple harmonic oscillator, the hydrogen atom, and the Kronig-Penney model of a solid.

Application of Variational Principles to Scattering Problems*

H. E. Moses
Institute of Mathematical Sciences, New York University, New York, New York
(Received May 20, 1954)

The Schwinger and Kohn-Hulthén variational principles are adapted to scattering problems in which only a part of the scattering potential is small.

I. INTRODUCTION

SEVERAL authors[1-3] have discussed the problem of scattering by a potential, only part of which is to be considered small. It is found that the scattering operator can be written as the sum of two terms: the first is the scattering operator which would be obtained if the small part of the potential vanished and the second is a term involving the eigenfunction of the entire Hamiltonian. The first term is assumed known. Hence to find the scattering operator of the problem one needs to find the second term only. In the present paper it is our objective to show how the Schwinger and Kohn-Hulthen variational principles can be used to find approximate expressions for this term.

II. THE VARIATIONAL PRINCIPLES

We shall briefly review the scattering operator formalism and indicate the usual form of the variational expressions. In scattering problems the total Hamiltonian H is broken up into two parts,

$$H=K+V, \tag{1}$$

where K is the unperturbed Hamiltonian and V is the scattering potential. Usually the eigenvalues of K are degenerate. It will thus be convenient to introduce additional operators collectively denoted by B which together with K form a complete set of commuting variables. Using a slightly modified form of Dirac's bra and ket notation[4] we denote the eigenvector of K and B belonging to the eigenvalue E of K and a of B by $|K,B;E,a\rangle$. Hence,

$$K|K,B;E,a\rangle=E|K,B;E,a\rangle. \tag{2}$$

Assuming the eigenfunctions normalized we have

$$\langle K,B;F,b|K,B;E,a\rangle=\delta(E-F)\delta(a,b), \tag{3}$$

where $\delta(a,b)$ is a suitably generalized δ function defined by

$$\int_R f(a)\delta(a,b)da=f(b),$$

if the range of integration R includes b;

$$\int_R f(a)\delta(a,b)da=0,$$

if R does not include b. Integration over a is to be interpreted as summation when a lies in a discrete spectrum.

The completeness of the set of eigenfunctions $|K,B;E,a\rangle$ is expressed by the relation

$$\int |K,B;E,a\rangle dEda\langle K,B;E,a|=I, \tag{4}$$

where I is the identity operator.

We shall assume that the continuous spectrum of H coincides with that of K and hence that the degeneracy of the continuous spectrum of H is the same as that of K. We can therefore introduce operators, collectively denoted by A, which together with H form a complete set of commuting variables such that the eigenvalues of A have the same range as those of B. We shall concern ourselves with two sets of eigenfunctions belonging to the continuous spectrum of H. One set is commonly called the set of "outgoing eigenfunctions." Eigenfunctions of this set are denoted by $|H,A;E,a\rangle_-$. They satisfy the equation

$$|H,A;E,a\rangle_-=|K,B;E,a\rangle+\gamma_-(E-K)V|H,A;E,a\rangle_-, \tag{5}$$

where

$$\gamma_-(x)=\lim_{\epsilon\to 0}[1/(x+i\epsilon)]=-i\pi\delta(x)+(P/x). \tag{6}$$

Here P/x means the principal part should be used in integrations over x. The second set of eigenfunctions which we denote by $|H,A;E,a\rangle_+$ are called the "incoming eigenfunctions." They satisfy the equation

$$|H,A;E,a\rangle_+=|K,B;E,a\rangle+\gamma_+(E-K)V|H,A;E,a\rangle_+, \tag{7}$$

where

$$\gamma_+(x)=\lim_{\epsilon\to 0}[1/(x-i\epsilon)]=+i\pi\delta(x)+(P/x). \tag{6a}$$

The operators $\gamma_-(E-K)$ and $\gamma_+(E-K)$ are the

* The research reported in this article was done at the Institute of Mathematical Sciences, New York University, and has been made possible through support and sponsorship extended by Geophysics Research Directorate, Air Force Cambridge Research Center.

[1] K. Watson, Phys. Rev. **88**, 1163 (1952).
[2] M. Gell-Mann and M. L. Goldberger, Phys. Rev. **91**, 403 (1953).
[3] G. Breit and H. A. Bethe, Phys. Rev. **93**, 888 (1954).
[4] The author is indebted to Professor K. O. Friedrichs for suggesting this notation.

Hermitian adjoints of each other. We note the identity,

$$\lim_{t\to\pm\infty} e^{i(K-E)t}\gamma_\pm(E-K)=0, \tag{8}$$

$$\lim_{t\to\mp\infty} e^{i(K-E)t}\gamma_\pm(E-K)=\pm 2\pi i\delta(E-K). \tag{9}$$

We should note that we have reversed the usual convention of denoting outgoing and incoming eigenfunctions. In the usual convention outgoing eigenfunctions are denoted by $+$ and incoming eigenfunctions by $-$. We have reversed the convention because in a more rigorous treatment[5] the outgoing and incoming eigenfunctions are specified in a time-dependent fashion by conditions at $t=-\infty$ and $t=+\infty$, respectively. It can be shown from (8) and (5) and (6) that

$$\lim_{t\to\pm\infty} e^{iKt}e^{-iHt}|H,A;E,a\rangle_\pm = \lim_{t\to\pm\infty} e^{i(K-E)t}|H,A;E,a\rangle_\pm = |K,B;E,a\rangle. \tag{10}$$

This means that for values of $t\to-\infty$ we have

$$e^{-iHt}|H,A;E,a\rangle_-\cong e^{-iKt}|K,B;E,a\rangle.$$

Thus the outgoing eigenfunction $|H,A;E,a\rangle_-$ is specified by the condition that the solution $e^{-iHt}|H,A;E,a\rangle_-$ of the time-dependent Schroedinger equation with the Hamiltonian H shall behave at $t=-\infty$ like the solution $e^{-iKt}|K,B,E,a\rangle$ of the equation with the Hamiltonian K. A similar statement can be made with respect to the relation

$$e^{-iHt}|H,A;E,a\rangle_+\cong e^{-iKt}|K,A;E,a\rangle$$

for $t=+\infty$.

The scattering operator S is defined by

$$\lim_{t\to+\infty} e^{iKt}e^{-iHt}|H,A,E,a\rangle_- = \lim_{t\to+\infty} e^{i(K-E)t}|H,A;E,a\rangle_- = S|K,B;E,a\rangle. \tag{11}$$

The state $e^{-iKt}S|K,B;E,a\rangle$ represents the final state (which like the initial state is an eigenstate of K) when the initial state is $e^{-iKt}|K,B;E,a\rangle$. From (9) and (5) it is clear that

$$\lim_{t\to+\infty} e^{i(K-E)t}|H,A;E,a\rangle_- = |K,B;E,a\rangle - 2\pi i\delta(E-K)V|H,A;E,a\rangle_-, \tag{12}$$

and hence from (11) the scattering operator in the K representation is given by

$$\langle K,B;F,b|S|K,B;E,a\rangle=\delta(E-F)\delta(a,b) - 2\pi i\delta(E-F)\langle K,B;E,b|V|H,A;E,a\rangle_-. \tag{13}$$

Similarly, the inverse scattering operator S^{-1} is defined by

$$\lim_{t\to-\infty} e^{i(K-E)t}|H,A;E,a\rangle_+=S^{-1}|K,B;E,a\rangle, \tag{14}$$

and

$$\langle K,B;F,b|S^{-1}|K,B;E,a\rangle=\delta(E-F)\delta(a,b) + 2\pi i\delta(E-F)\langle K,B;E,b|V|H,A;E,a\rangle_+. \tag{15}$$

It can also be shown that

$$\langle K,B;E,b|V|H,A;E,a\rangle_+=\langle K,B;E,a|V|H,A;E,b\rangle_-^*, \tag{16}$$

where the asterisk means complex conjugate. Equation (16) is called the reciprocity theorem. A final identity which might be noted is

$$_+\langle H,A;F,b|H,A;E,a\rangle_-=\langle K,B;F,b|S|K,B;E,a\rangle, \tag{17}$$

$$_-\langle H,A;E,a|H,A;F,b\rangle_+=\langle K,B;F,b|S|K,B;E,a\rangle^* =\langle K,B;E,a|S^{-1}|K,B;F,b\rangle. \tag{18}$$

From Eq. (13) it is seen that if we knew $\langle K,B;E,b|V|H,A;E,a\rangle_-$, we should know the scattering operator. Both the Schwinger and the Kohn-Hulthén variational principles are concerned with finding this quantity.

The Schwinger variational principle is based upon the two equations

$$a=Ry, \quad a'=R'y', \tag{18}$$

where a and a' are given vectors, y and y' unknown vectors, and R and R' are given operators which are the Hermitian adjoints of each other. We define λ and $\lambda(v',v)$ by

$$\lambda=1/(a',y)=1/(y',a) \tag{19}$$

and

$$\lambda(v',v)=(v',Rv)/(a',v)(v',a), \tag{19a}$$

respectively, where (w,v) indicates the Hermitian inner product of the vectors w and v. It can be shown that the first variation of $\lambda(v',v)$ due to variations of v' about y' and v about y is zero. Hence, since $\lambda(y',y)=\lambda$ we have

$$1/(a',y)\cong(v',Rv)/(a',v)(v',a), \tag{20}$$

where v' and v approximate y' and y, respectively.

We can write (5) and (7) as

$$V|K,B;E,a\rangle=V|H,A;E,a\rangle_- - V\gamma_-(E-K)V|H,A;E,a\rangle_- \tag{21}$$

and

$$V|K,B;E,b\rangle=V|H,A;E,b\rangle_+ - V\gamma_+(E-K)V|H,A;E,b\rangle_+. \tag{22}$$

We identify a and a' with $V|K,B;E,a\rangle$ and $V|K,B;E,b\rangle$, respectively; y and y' with $|H,A;E,a\rangle_-$ and $|H,A;E,b\rangle_+$, respectively; and R and R' with $V-V\gamma_-(E-K)V$ and $V-V\gamma_+(E-K)V$, respectively.

[5] H. E. Moses, New York University, Institute of Mathematical Sciences, Research Report CX-12, 13, 1953 (unpublished).

Hence relation (20) becomes

$$[\langle K,B;E,b|V|H,A;E,a\rangle_-]^{-1}\cong\frac{{}_+\langle H,A;E,b|V|H,A,E,a\rangle_{-t}-{}_+\langle H,A;E,b|V\gamma_-(E-K)V|H,A;E,a\rangle_{-t}}{\langle K,B;E,b|V|H,A;E,a\rangle_{-t}+{}_t\langle H,A;E,b|V|K,B;E,a\rangle},\tag{23}$$

where $|H,A;E,b\rangle_{+t}$ and $|H,A;E,a\rangle_{-t}$ are states which approximate $|H,A;E,b\rangle_+$ and $|H,A;E,a\rangle_-$, respectively.

In the Kohn-Hulthén variational principle one introduces the functional $A(|H,A,E,a\rangle_{-t},|H,A;E,b\rangle_{+t})$ defined by

$$A(|H,A;E,a\rangle_{-t},|H,A;E,b\rangle_{+t})=\lim_{F\to E}{}_+\langle H,A;F,b|H-E|H,A;E,a\rangle_-+\langle K,B;E,b|V|H,A;E,a\rangle_{-t}.\tag{24}$$

Here

$$|H,A;E,a\rangle_{\pm t}=|K,B;E,a\rangle+\gamma_\pm(E-K)V|H,A;E,a\rangle_{\pm t}.$$

It can be shown[6] that the first variation of $A(|H,A;E,a\rangle_{-t},|H,A;E,b\rangle_{+t})$ due to variations of $|H,A;E,a\rangle_{-t}$ and $|H,A;E,b\rangle_{+t}$ about $|H,A;E,a\rangle_-$ and $|H,A;E,b\rangle_+$, respectively, is zero. Hence, as can be shown, since

$$A(|H,A;E,a\rangle_-,|H,A;E,b\rangle_+)=\langle K,B;E,b|V|H,A;E,a\rangle_-,$$

we have

$$\langle K,B;E,b|V|H,A;E,a\rangle_-\cong A(|H,A;E,a\rangle_{-t},|H,A;E,b\rangle_{+t}),\tag{25}$$

where $|H,A;E,a\rangle_{-t}$ and $|H,A;E,b\rangle_{+t}$ approximate $|H,A;E,a\rangle_-$ and $|H,A;E,b\rangle_+$, respectively. By rewriting the expression for A one can get a more useful expression, namely:

$$\begin{aligned}\langle K,B;E,b|V|H,A;E,a\rangle_-\cong&\langle K,B;E,b|V|K,B;E,a\rangle\\&+{}_+\langle H,A;E,b|V\gamma_-(E-K)V|K,B;E,a\rangle\\&+\langle K,B;E,b|V\gamma_-(E-K)V|H,A;E,a\rangle_{-t}\\&-{}_+\langle H,A;E,b|V\gamma_-(E-K)V|H,A;E,a\rangle_{-t}\\&+{}_+\langle H,A;E,b|V\gamma_-(E-K)V\gamma_-(E-K)V|H,A;E,a\rangle_{-t}.\end{aligned}\tag{26}$$

III. FINAL FORM OF THE VARIATIONAL PRINCIPLES

We shall now give the form of the variational principles for the case discussed in the introduction, namely, when the scattering potential is the sum of two parts, one of which is to be considered small. Accordingly we write

$$V=V_1+V_2,\tag{27}$$

where V_2 is to be considered the small part of the potential. We define L by

$$L=K+V_1.\tag{28}$$

Hence H, as defined in (1), is also given by

$$H=L+V_2.\tag{29}$$

Let us denote the incoming and outgoing eigenvectors of L with respect to K by $|L,C;E,a\rangle_\pm$, where

$$|L,C;E,a\rangle_\pm=|K,B;E,a\rangle+\gamma_\pm(E-K)V_1|L,C;E,a\rangle_\pm.\tag{30}$$

We assume these eigenvectors are known. In reference 2, it is shown that the quantity $\langle K,B;E,b|V|H,A;E,a\rangle_-$ which we seek can be written as

$$\langle K,B;E,b|V|H,A;E,a\rangle_-=\langle K,B;E,b|V_1|L,C;E,a\rangle_-+{}_+\langle L,C;E,b|V_2|H,A;E,a\rangle_-.\tag{31}$$

Equation (31) is the decomposition of the scattering operator referred to in the introduction. It is our objective to obtain variational expressions for ${}_+\langle L,C;E,b|V_2|H,A;E,a\rangle_-$ only, instead of the entire quantity $\langle K,B;E,b|V|H,A;E,a\rangle_-$. The possibility of obtaining such expressions is based on the fact that the eigenvectors $|H,A;E,a\rangle_\pm$ which satisfy (5) and (7) can be shown also to satisfy the equations,

$$|H,A;E,a\rangle_\pm=|L,C;E,a\rangle_\pm+\gamma_\pm(E-L)V_2|H,A;E,a\rangle_\pm.\tag{32}$$

The equation of (32) with the minus subscript is proved in reference 2. The equation with the plus subscript is proved analogously.

The Schwinger variational principle for

$${}_+\langle L,C;E,b|V_2|H,A;E,a\rangle_-$$

is obtained by rewriting (32) as follows:

$$\begin{aligned}V_2|L,C;E,a\rangle_-&=V_2|H,A;E,a\rangle_--V_2\gamma_-(E-L)V_2|H,A;E,a\rangle_-,\\V_2|L,C;E,b\rangle_+&=V_2|H,A;E,b\rangle_+-V_2\gamma_+(E-L)V_2|H,A;E,b\rangle_+.\end{aligned}\tag{32a}$$

We identify a and a' of Eq. (18) with $V_2|L,C;E,a\rangle_-$ and $V_2|L,C;E,b\rangle_+$, respectively; the vectors y and y' with $|H,A;E,a\rangle_-$ and $|H,A;E,b\rangle_+$; and R and R' with $V_2-V_2\gamma_-(E-L)V_2$ and $V_2-V_2\gamma_+(E-L)V_2$. Then Schwinger's variational principle yields

$$[{}_+\langle L,C;E,b|V_2|H,A;E,a\rangle_-]^{-1}\cong\frac{{}_+\langle H,A;E,b|V_2|H,A;E,a\rangle_{-t}-{}_+\langle H,A;E,b|V_2\gamma_-(E-L)V_2|H,A;E,a\rangle_{-t}}{{}_+\langle L,C;E,b|V_2|H,A;E,a\rangle_{-t}+{}_t\langle H,A;E,b|V_2|L,C;E,a\rangle_-},\tag{33}$$

[6] H. E. Moses, Phys. Rev. **92**, 817 (1953).

where $|H,A;E,a\rangle_{\pm t}$ approximate $|H,A;E,a\rangle_{\pm}$ respectively. Incidentally, equations (32a) yield a reciprocity theorem, namely,

$$
\begin{aligned}
&{}_{+}\langle L,C;E,b|V_2|H,A;E,a\rangle_{-} \\
&\qquad = {}_{+}\langle H,A;E,b|V_2|L,C;E,a\rangle_{-} \\
&\qquad = {}_{-}\langle L,C;E,a|V_2|H,A;E,b\rangle_{+}^{*}. \quad (34)
\end{aligned}
$$

Borowitz and Friedman[7] use this form of the Schwinger variational principle in a special case.

The Kohn-Hulthén variational principle uses the functional $\tilde{A}(|H,A;E,a\rangle_{-t},|H,A;E,b\rangle_{+t})$ defined by

$$
\begin{aligned}
&\tilde{A}(|H,A;E,a\rangle_{-t},|H,A;E,b\rangle_{+t}) \\
&\qquad = \lim_{F\to E} {}_{+t}\langle H,A;F,b|H-E|H,A;E,a\rangle_{-t} \\
&\qquad\qquad + {}_{+}\langle L,C;E,b|V_2|H,A;E,a\rangle_{-t}, \quad (35)
\end{aligned}
$$

where $|H,A;E,a\rangle_{\pm t}$ are defined by

$$
\begin{aligned}
|H,A;E,a\rangle_{\pm t} &= |L,C;E,a\rangle_{\pm} \\
&\quad + \gamma_{\pm}(E-L)V_2|H,A;E,a\rangle_{\pm t}. \quad (35a)
\end{aligned}
$$

As in reference 6, it can be shown that the first variations of $\tilde{A}$ due to variations of $|H,A;E,a\rangle_{\pm t}$ about $|H,A;E,a\rangle_{\pm}$, respectively, vanish. Since also

$$
\begin{aligned}
&\tilde{A}(|H,A;E,a\rangle_{-},|H,A;E,b\rangle_{+}) \\
&\qquad = {}_{+}\langle L,C;E,b|V_2|H,A;E,a\rangle_{-}, \quad (36)
\end{aligned}
$$

we have

$$
\begin{aligned}
&{}_{+}\langle L,C;E,b|V_2|H,A;E,a\rangle_{-} \\
&\qquad \cong A(|H,A;E,a\rangle_{-t},|H,A;E,b\rangle_{+t}), \quad (37)
\end{aligned}
$$

where $|H,A;E,a\rangle_{\pm t}$ approximates $|H,A;E,a\rangle_{\pm}$ respectively. Using an alternative form for $\tilde{A}$ obtained by substituting (35a) into (35) we have

$$
\begin{aligned}
&{}_{+}\langle L,C;E,b|V_2|H,A;E,a\rangle_{-} \cong {}_{+}\langle L,C;E,b|V_2|L,C;E,a\rangle_{-} \\
&\quad + {}_{+t}\langle H,A;E,b|V_2\gamma_{-}(E-L)V_2|L,C;E,a\rangle_{-} \\
&\quad + {}_{+}\langle L,C;E,b|V_2\gamma_{-}(E-L)V_2|H,A;E,a\rangle_{-t} \\
&\quad - {}_{+t}\langle H,A;E,b|V_2\gamma_{-}(E-L)V_2|H,A;E,a\rangle_{-t} \\
&\quad + {}_{+t}\langle H,A;E,b|V_2\gamma_{-}(E-L)V_2\gamma_{-}(E-L)V_2|H,A;E,a\rangle_{-t}. \\
&\qquad\qquad\qquad\qquad\qquad\qquad\qquad\qquad\qquad\qquad (38)
\end{aligned}
$$

If we assume that $V_1=0$, that is $V=V_2$, then the Kohn-Hulthén and the Schwinger variational principles (38) and (33) reduce to (26) and (23), respectively, as required, for in this case $L=K$ and

$$|L,C;E,a\rangle_{\pm} = |K,A;E,a\rangle.$$

[7] S. Borowitz and B. Friedman, Phys. Rev. **89**, 441 (1953).

Radiative Effects in a Constant Field

ROGER G. NEWTON*
Institute for Advanced Study, Princeton, New Jersey
(Received June 17, 1954)

A method of avoiding all infrared divergencies in the radiative effects of a constant electromagnetic field is developed. It is used, without the necessity of resumming a nonintegrable series, to calculate the one photon mass operator up to the third order in the external field. The magnetic susceptibility and field dependence of the rest mass of an electron are thereby exhibited to lowest order. The result is then shown in a simple way to provide charged particles with strong short-range forces against the Coulomb field. Particles of unrealistically small mass and charge would carry a large repulsive core, if Coulomb attractive, or a large attractive shell, if Coulomb repulsive.

I. INTRODUCTION

THE present problem is to calculate the one-photon mass operator[1] for the Dirac equation in the presence of a uniform external magnetic field. It was found previously[2] that in the expansion of the mass operator in powers of the uniform external field strength, terms higher than the first contain infrared divergencies. If one asks for the radiative contribution to the behavior of an electron in such a field, one has no other effects which, if properly taken into account, could be expected to cancel such divergencies (such as bremsstrahlung contributions which cancel infrared divergencies in the elastic scattering by a central potential). These divergencies are therefore either real or else due to faulty mathematical technique. Since infrared divergencies are not expected to be real, the latter is the only alternative. It is one of the purposes of this paper to exhibit the faults of the previously used techniques of expanding the mass operator in powers of the external field and to correct them for the present case. Admittedly, the procedure used for this correction in the simple case of a uniform field is not directly applicable to the general one of an arbitrary electromagnetic field. But then, in all other cases of interest one has been able to eliminate the effects of the incorrect expansion by different means (e.g., the introduction of a finite photon mass, which could be allowed to vanish only after other effects, such as inelastic contributions to scattering, were added).

The fact that the customary technique of expanding all terms in powers of the external field is incorrect manifests itself in the proper result by means of a logarithmic dependence on the electromagnetic field. Such a logarithm was first obtained by Gupta[3] and also by Demeur.[4] Both authors, however, used entirely different and less general methods than the one employed here, and their results differ numerically from the present one. (See discussion in Sec. III.)

The renormalized (one-photon) mass operator may be written[5]

$$\Delta M=-ie^2\int_0^\infty ds\,s\int_0^{'} du\,u^{-2}\int(dK)^4(2\pi)^{-4}\times\exp(-ism^2-isu^{-1}K^2)(\mathfrak{M}_1-\mathfrak{M}_0), \quad (1)$$

$$\mathfrak{M}_0=\{2m+(1-u)\gamma\pi,\exp[is(1-u)(\gamma\pi)^2]\},$$

$$\mathfrak{M}_1=\tfrac{1}{2}\exp(isK^2)\gamma_\mu\{m-\gamma(\pi-K),\exp[is(\gamma(\pi-K))^2]\}\gamma_\mu, \quad (2)$$

where $u=s(s+t)^{-1}$ and t is the "proper time" variable (corresponding to s) for the photon.[6]

After the photon summations (i.e., the K integration and the summation over μ in $\gamma_\mu\cdots\gamma_\mu$) are carried out, ΔM cannot be expressed in a closed form as a function of the external field $F_{\mu\nu}$ and $\gamma\pi$ in such a way that matrix element between electron states can be taken directly. The customary technique is therefore to expand the exponentials in powers of eA and then exhibit the result in gauge invariant form. But it will be noticed that eA occurs in the exponentials in two ways: multiplied by s alone, and multiplied by us. If the former are expanded in powers of eA, correspondingly higher and powers of s occur. The K integration and subsequent vanishing of $(\gamma\pi+m)$ (or $\gamma p+m$) on the extreme left and right by virtue of the Dirac equation introduce a factor of $\exp(-isum^2)$ everywhere, instead of the previous $\exp(-ism^2)$. The s integration will therefore produce higher and higher powers of u^{-1} and consequently divergencies of arbitrarily high order at $u=0$.

This is the origin of the infrared divergencies. They are clearly due to an unallowed expansion in which it is assumed that $seA\ll sum^2$, an expansion in powers of $eAm^{-2}u^{-1}$ rather than the alleged eAm^{-2}. As soon as a small photon mass is introduced, however, the expansion is correct. Such a mass causes, via the photon Green's function, an additional factor of $\exp(-isu^{-1}\epsilon^2)$. The expansion then becomes one in powers of $eA(m^2u$

* Frank B. Jewett Fellow.
[1] J. Schwinger, Proc. Natl. Acad. Sci. U. S. **37**, 452 (1951).
[2] R. G. Newton, Phys. Rev. **94**, 1773 (1954).
[3] S. N. Gupta, Nature **163**, 686 (1949).
[4] M. Demeur, Acad. roy. Belg., Classe sci., Mem. **28** (1953).
[5] See reference 2, for example.
[6] The notation is the usual one, with $\hbar=c=1$, $\pi=p-eA$; the Dirac matrices used are such that the Dirac equation reads $(\gamma\pi+M)\psi=0$.

$+\epsilon^2)^{-1}$, which for fixed ϵ can be made uniformly small by assuming eA small enough. If the expansion is done in the presence of a finite photon mass, therefore, as it has been in the past for the purposes of cancelling the divergencies of separate calculations, it is correct (provided the resulting series of finite terms converges). But it is, at least partly, an expansion in powers of $eA\epsilon^{-2}$.

In order to correct this situation one must, then, avoid any expansion in powers of s alone, while one in powers of us is permissible. Such a technique will be introduced below in the special case of a uniform field.

II. CALCULATION

The starting point of the calculation is the following theorem which holds for any uniform electromagnetic field $F_{\mu\nu}=-ie^{-1}[\pi_\mu,\pi_\nu]$ and any 4-vector K_μ, all of whose components commute with all components of π_μ:

$$\exp[-is(\pi-K)^2]$$
$$=\exp(-is\pi^2)\exp(-isKEK)\exp(2isKE\pi)$$
$$=\exp(2is\pi EK)\exp(-isKEK)\exp(-is\pi^2), \quad (3)$$

where

$$\mathrm{E}'(s)_{\mu\nu}=(e^{2esF})_{\mu\nu}, \quad \mathrm{E}(s)=s^{-1}\int_0^s ds\mathrm{E}'$$
$$=(e^{2esF}-1)/(2esF). \quad (4)$$

To prove (3) we first observe that

$$[\pi_\mu,\exp(-is\pi^2)]=-is\int_0^1 dv\exp(-is(1-v)\pi^2)$$
$$\times[\pi_\mu,\pi^2]\exp(-isv\pi^2)$$
$$=2es\int_0^1 dv\exp(-is(1-v)\pi^2)F_{\mu\nu}\pi_\nu\exp(-isv\pi^2)$$
$$=2es\exp(-is\pi^2)F_{\mu\nu}\pi_\nu+(2es)^2\int_0^1 dv_1\int_0^1 dv_2v_1$$
$$\times\exp(-is(1-v_1v_2)\pi^2)F_{\mu\lambda}F_{\lambda\nu}\pi_\nu\exp(-isv_1v_2\pi^2)$$
$$=\cdots=\exp(-is\pi^2)[\exp(2esF)-1]_{\mu\nu}\pi_\nu.$$

Therefore,

$$\pi_\mu\exp(-is\pi^2)=\exp(-is\pi^2)\mathrm{E}'_{\mu\nu}\pi_\nu. \quad (5)$$

Similarly,

$$\exp(-is\pi^2)\pi_\mu=\pi_\nu\mathrm{E}_{\nu\mu}'\exp(-is\pi^2). \quad (5')$$

By means of (5) one then obtains

$$\frac{\partial}{\partial s}\exp(-is(\pi-K)^2)=-i(\pi^2+K^2-2K\pi)$$
$$\times\exp(-is(\pi-K)^2)=-i(\pi_l^2-2K\mathrm{E}'\pi_r+2K\mathrm{E}'K-K^2)$$
$$\times\exp(-is(\pi-K)^2), \quad (6)$$

where the subscripts l and r indicate that π is to stand to the left and right, respectively, of the exponential.

It is well known that

$$\frac{\partial}{\partial s}e^{f(s)}=e^{f(s)}\left\{f'+\frac{1}{2!}[f',f]+\frac{1}{3!}[[f',f],f]+\cdots\right\}.$$

Therefore

$$e^{-2isKE\pi}\frac{\partial}{\partial s}e^{2isKE\pi}=2i\{K\mathrm{E}'\pi+is[K\mathrm{E}'\pi,K\mathrm{E}\pi]\}$$
$$=2i(K\mathrm{E}'\pi-esK\mathrm{E}'F\mathrm{E}^TK)$$
$$=2i(K\mathrm{E}'\pi+\tfrac{1}{2}K(1-\mathrm{E}')K). \quad (7)$$

Equations (6) and (7) yield

$$\frac{\partial}{\partial s}\exp(-is(\pi-K)^2)=\left[\frac{\partial}{\partial s}(-is\pi^2-isKEK)\right]$$
$$\times\exp(-is(\pi-K)^2)+\exp(-is(\pi-K)^2)$$
$$\times\exp(-2isKE\pi)\frac{\partial}{\partial s}\exp(2isKE\pi). \quad (8)$$

The differential equation (8) is clearly solved by the first line of (3), with the correct boundary value at $s=0$. The second line of (3) is proved similarly by means of (5').

Equation (3) allows us to separate out the factor $\exp(-is\pi^2)$ from $\mathfrak{M}_1$ in (2) before the K integration is carried out. For a constant field, then

$$\exp[is(\gamma(\pi-K))^2]=\exp(\tfrac{1}{2}ies\sigma F)\exp(-isKEK)$$
$$\times\exp(-is\pi^2)\exp(2isKE\pi)$$
$$=\exp(\tfrac{1}{2}ies\sigma F)\exp(-isKEK)$$
$$\times\exp(2is\pi EK)\exp(-is\pi^2). \quad (9)$$

We shall now assume that the electric field vanishes and there is only a constant magnetic field H in the direction of the x axis:

$$F_{23}=-ie^{-1}[\pi_2,\pi_3]=\mathbf{H}_1=H,$$

while all other components and commutators vanish. This yields

$$\mathrm{E}'_{11}=1, \quad \mathrm{E}'_{22}=\mathrm{E}'_{33}=\cos(2esH),$$
$$\mathrm{E}'_{23}=-\mathrm{E}'_{32}=\sin(2esH),$$
$$\mathrm{E}_{11}=1, \quad \mathrm{E}_{22}=\mathrm{E}_{33}=\sin(2esH)/2esH,$$
$$\mathrm{E}_{23}=-\mathrm{E}_{32}=\sin^2(esH)/esH, \quad (10)$$

while all other components vanish. If we set

$$\pi'_\mu=\mathrm{E}_{\mu\nu}\pi_\nu, \quad (11)$$

then it is easily checked that

$$[\pi'_2,\pi'_3]=ieH\lambda^2, \quad \lambda=\sin(esH)/esH, \quad (12)$$
$$\pi'^2_2+\pi'^2_3=(\pi_2^2+\pi_3^2)\lambda^2. \quad (13)$$

In the following we shall use *a special summation convention: the subscripts "−" shall take the values* 1 *and* 4, *while "×" runs through* 2 *and* 3. One may thus handle π_- as c numbers. Because

$$e^{(A+B)}=e^Ae^Be^{-\frac{1}{2}[A,B]}, \tag{14}$$

if $[A,B]$ commutes with A and B, and because of (12), one easily obtains

$$\exp[-is(\pi-K)^2]=\exp(-is\pi^2)$$
$$\times\exp\{-is[K_-{}^2+K_\times{}^2\sin(2esH)/2esH]\}$$
$$\times\exp(2is^2\lambda^2K_2K_3eH)\exp(2isK_2\pi'_2)$$
$$\times\exp(2isK_3\pi'_3). \tag{15}$$

Consider the integral

$$I=\int_{-\infty}^{\infty}dK_2\int_{-\infty}^{\infty}dK_3\exp[is(1-u^{-1})K^2]$$
$$\times\exp(-is\mu u^{-1}K_\times{}^2)\exp(2isK_2\pi'_2)$$
$$\exp(2isK_3\pi'_3)\times\exp[2is^2\lambda^2K_2K_3eH], \tag{16}$$

where

$$\mu=1-u[1-(2esH)^{-1}\sin(2esH)]. \tag{17}$$

We first carry out the K_3 integration by shifting K_3 the amount $-u\mu^{-1}[\pi'_3+(esH)^{-1}\sin^2(esH)K_2]$ which is allowable since no commutation between π'_2 and π'_3 is necessary during this integration. Next all terms containing K_2 are moved onto the same exponential by means of (12) and (14), and then K_2 is shifted by the amount

$$-(\pi'_2+u\mu^{-1}\lambda^2eH\pi'_3)u\mu\mu'^{-2},$$

where

$$\mu'=[\mu^2+\lambda^4(useH)^2]^{\frac{1}{2}}. \tag{18}$$

The two K integrations are now ordinary Gaussian integrals. We obtain

$$I=-i\pi us^{-1}\mu^{-1}(\mu'^2/\mu^2)^{-\frac{1}{2}}$$
$$\times\exp[isu\mu\mu'^{-2}(\pi'_2+u\mu^{-1}\lambda^2eH\pi'_3)^2]$$
$$\times\exp(isu\mu^{-1}\pi'_3{}^2). \tag{19}$$

The equation[7] (for $[q,p]=i$),

$$f(p)g(q)=g(q-i\partial/\partial p)f(p), \tag{20}$$

whose consequence is

$$\exp(-ap^2)\exp(bq^2)\exp(ap^2)=\exp[b(q+2iap)^2], \tag{21}$$

allows us to write [since $\pi'_2s(eH)^{\frac{1}{2}}(\sin esH)^{-1}$ and $\pi'_3s(eH)^{\frac{1}{2}}(\sin esH)^{-1}$ obey the same commutation relations as q and p]

$$I=-i\pi s^{-1}\mu^{-1}(\mu'^2/\mu^2)^{-\frac{1}{2}}\exp(\tfrac{1}{2}isu\mu^{-1}\pi'_3{}^2)$$
$$\times\exp(isu\mu\mu'^{-2}\pi'_2{}^2)\exp(\tfrac{1}{2}isu\mu^{-1}\pi'_3{}^2). \tag{22}$$

[7] See reference 2, Eq. (2.7).

The order in which the integrations are done is, of course, arbitrary. Had we carried them out in the opposite order, π_2' and π_3' would have been interchanged in (22).

The K_1 and K_4 integrations are trivial, and we obtain

$$\int(dK)^4\exp[is(1-u^{-1})K^2]\exp[-is(\pi-K)^2]$$
$$=-i\pi^2u^2s^{-2}\mu^{-1}(\mu'^2/\mu^2)^{-\frac{1}{2}}\exp(-is\pi^2)\exp(ius\pi_-{}^2)$$
$$\times\exp(\tfrac{1}{2}isu\mu^{-1}\pi'_3{}^2)\exp(isu\mu\mu'^{-2}\pi'_2{}^2)\exp(\tfrac{1}{2}isu\mu^{-1}\pi'_3{}^2)$$
$$=(\pi'_2\text{ and }\pi'_3\text{ interchanged}). \tag{23}$$

So far no approximations have been used, but from this point on we shall restrict ourselves to terms up to the order $(eH)^3$, inclusively. A strict expansion will not be possible, but we shall drop terms which are $o(eH)^3$ as $eH\to0$.

Now $(\mu^2\mu'^{-2}-1)=\mu'^{-2}(useH)^2\lambda^4$ and $\lambda\leq1$; μ' and μ can vanish only for $u=1$ and $esH=\frac{1}{2}n\pi$. These zeros of μ' and μ will never cause divergencies.[8] The factor $(\mu^2\mu'^{-2}-1)$ may therefore be handled as one of the second order in eH, since expansion in $(useH)$ is allowed. Similarly $\{[\pi'_2,\pi'_3]us\}$ is of order (eH). Therefore, to the order $(eH)^3$ inclusively,

$$\exp(\tfrac{1}{2}ius\mu^{-1}\pi'_3{}^2)\exp(ius\mu\mu'^{-2}\pi'_2{}^2)\exp(\tfrac{1}{2}ius\mu^{-1}\pi'_3{}^2)$$
$$=\tfrac{1}{2}\{\exp[ius\mu^{-1}(\mu^2\mu'^{-2}-1)\pi'_2{}^2],\exp(\tfrac{1}{2}ius\mu^{-1}\pi'_3{}^2)$$
$$\times\exp(ius\mu^{-1}\pi'_2{}^2)\exp(\tfrac{1}{2}ius\mu^{-1}\pi'_3{}^2)\}. \tag{24}$$

It can easily be proved that near $a=0$,

$$\tfrac{1}{2}[\exp(\tfrac{1}{2}ap^2)\exp(aq^2)\exp(\tfrac{1}{2}ap^2)$$
$$+\exp(\tfrac{1}{2}aq^2)\exp(ap^2)\exp(\tfrac{1}{2}aq^2)]$$
$$=\exp[a(1-a^2/3!)(p^2+q^2)]+O(a^4), \tag{25}$$

$$\tfrac{1}{2}[\exp(\tfrac{1}{2}ap^2)\exp(aq^2)\exp(\tfrac{1}{2}ap^2)$$
$$-\exp(\tfrac{1}{2}aq^2)\exp(ap^2)\exp(\tfrac{1}{2}aq^2)]=O(a^3). \tag{26}$$

Equations (24) to (26) and the fact that $(\mu^2\mu'^{-2}-1)=O(eH)^2$ have as a consequence that

$$\tfrac{1}{2}[\exp(\tfrac{1}{2}ius\mu^{-1}\pi'_3{}^2)\exp(ius\mu\mu'^{-2}\pi'_2{}^2)$$
$$\times\exp(\tfrac{1}{2}ius\mu^{-1}\pi'_3{}^2)+(\pi'_2\leftrightarrow\pi'_3)]$$
$$=\exp[ius(1+\Lambda)\pi_\times{}^2]+o(eH)^3, \tag{27}$$

where

$$\Lambda=\lambda^2\mu^{-1}-1-\tfrac{1}{3}\mu^{-3}\lambda^6(useH)^2. \tag{28}$$

The integral appearing in (23) is also needed with a factor of K in the integrand. This is obtained in a manner similar to the above. By means of (27) and

[8] A simple way of proving this is to envisage the u integration as extending only up to $\frac{1}{2}$, say, for the purposes of the present procedure. The remaining u integration from $\frac{1}{2}$ to 1 is then handled by straightforward expansion in powers of the field, where no trouble at $u=1$ ever arises.

the relation

$$\gamma_\times\pi'_\times=\lambda\exp(\tfrac{1}{2}ise\sigma\cdot\mathbf{H})\gamma_\times\pi_\times\exp(-\tfrac{1}{2}ise\sigma\cdot\mathbf{H}),\quad(29)$$

which is easily proved, the result may be formulated as follows:

$$i\pi^{-2}u^{-2}s^2\int(dK)^4\exp[is(1-u^{-1})K^2]$$

$$\times\exp[-is(\pi-K)^2](1,\gamma K)=\mu^{-1}[1+\mu^{-2}\lambda^4(useH)^2]^{-\frac{1}{2}}$$

$$\times\exp(-is\pi^2)\exp(\tfrac{1}{2}ise\sigma\cdot\mathbf{H})C\exp(-\tfrac{1}{2}ise\sigma\cdot\mathbf{H})$$

$$+o(eH)^3=\mu^{-1}[1+\mu^{-2}\lambda^4(useH)^2]^{-\frac{1}{2}}\exp(-\tfrac{1}{2}ise\sigma\cdot\mathbf{H})C$$

$$\times\exp(\tfrac{1}{2}ise\sigma\cdot\mathbf{H})\exp(-is\pi^2)+o(eH)^3,\quad(30)$$

where

$$C=\tfrac{1}{2}\{\exp[ius(\pi^2+\Lambda\pi_\times^2)],\ (1,u\gamma\pi+u\mathrm{B}\gamma_\times\pi_\times)\},$$

$$\mathrm{B}=\lambda\mu^{-1}-1.\quad(31)$$

If (31) is substituted in (1) and (2), the $\gamma\cdots\gamma$ summation carried out, and one sets $\gamma\pi=-m$ on the outside by virtue of the zero-order Dirac equation, one obtains

$$\Delta M_1=-(\alpha/4\pi)\int_0^1du\int_0^\infty dss^{-1}\exp(-ius m^2)$$

$$\times\{\mu^{-1}[1+\mu^{-2}\lambda^4(useH)]^{-\frac{1}{2}}D+2m(1+u)\}+o(eH)^3,$$

$$D=\exp(-\tfrac{1}{2}ise\sigma\cdot\mathbf{H})$$

$$\times\tfrac{1}{2}\{\exp[ius(e\sigma\cdot\mathbf{H}+\Lambda\pi_\times^2)],4u(\gamma\pi+\mathrm{B}\gamma_\times\pi_\times)\cos(esH)$$

$$-\{\exp(ise\sigma\cdot\mathbf{H}),m+u\gamma\pi+u\mathrm{B}\gamma_\times\pi_\times\}\}\exp(-\tfrac{1}{2}ise\sigma\cdot\mathbf{H})$$

$$+2i\sin(esH)[\sigma\gamma_\times\pi_\times,$$

$$\exp[ius\Lambda\pi_\times^2-is(1-u)e\sigma\cdot\mathbf{H}]],\quad(32)$$

where

$$\sigma=\sigma_1=\sigma_{23}=i\gamma_2\gamma_3.$$

The following three relations, in which the zero-order Dirac equation has been used, are easily proved:

$$\{\sigma\gamma_-\pi_-,\exp(ius\Lambda\pi_\times^2)\}$$

$$=-\{\sigma m+\tfrac{1}{2}i\gamma_\times\pi_\times\sin(2useH\Lambda),\exp(ius\Lambda\pi_\times^2)\},\quad(33)$$

$$\{\gamma_\times\pi_\times,\exp(ius\Lambda\pi_\times^2)\}$$

$$=m^{-1}\{(\pi_\times^2-e\sigma\cdot\mathbf{H})[1-i\sigma\Lambda useH-(\Lambda useH)^2$$

$$+(5/3)i\sigma(\Lambda useH)^3],\exp(ius\Lambda\pi_\times^2)\}$$

$$-i(16m)^{-1}\sin^3(2\Lambda useH)$$

$$\times\{\gamma_\times\pi_\times,\sigma[\gamma_\times\pi_\times,\exp(ius\Lambda\pi_\times^2)]\},\quad(34)$$

$$[\sigma\gamma_\times\pi_\times,\exp(ius\Lambda\pi_\times^2-is(1-u)e\sigma\cdot\mathbf{H})]$$

$$=i\{\sin[s(1-u)eH]-\tfrac{1}{2}\cos[s(1-u)eH]\sin(2\Lambda useH)\}$$

$$\times\{\gamma_\times\pi_\times,\exp(ius\Lambda\pi_\times^2)\}.\quad(35)$$

Equations (33) to (35) are used to simplify D. The result is then expanded in powers of $(useH)$, with coefficients which are polynomials in u, whose coefficients in turn are bounded functions of (eHs). Since the integrals are still too complicated to be feasible, we also expand $\exp(ius\Lambda\pi_\times^2)$ in powers of $(us\pi_\times^2)$. We shall assume that $\pi_\times^2=O(eH)$ and retain terms accordingly. The zero-order Dirac equation yields

$$\pi_\times^2=e\sigma\cdot\mathbf{H}-(m^2-p_0^2+p_1^2).\quad(36)$$

Since p_1 and p_0 commute with everything in the present problem, they may be assigned arbitrary values, for example such that $p_0^2-p_1^2=m^2$. Our assumption, that $\pi_\times^2=O(eH)$, is therefore the assumption that

$$(p_0^2-m^2-p_1^2)\text{ is not }\gg eH.\quad(37)$$

After the expansion the u and s integrals can be carried out. They are all of the following form,

$$I=\int_0^1du\int_0^\infty dss^{-1}\exp(-ius m^2)(useH)^nf(u,eHs),\quad n\geq1$$

where f is a polynomial in u, $(eHs)^{-1}$, $\sin(eHs)$, and $\cos(eHs)$ in such a way that it is finite for $eHs=0$. I is easily evaluated by repeated partial integrations on u until all the inverse powers of s have disappeared. The boundary terms, coming from $u=1$, can be expanded in powers of eH, while the remaining double integral can be carried out in straightforward manner. One example will suffice to illustrate the procedure:

$$I=\int_0^1du\int_0^\infty dss^{-1}(useH)\exp(-ius m^2)$$

$$\times[(eHs)^{-1}-(eHs)^{-2}\sin(eHs)]$$

$$=\int_0^1du\int_0^\infty dse^{-ius K}(s^{-1}-s^{-2}\sin s);$$

by change of scale in s, $eHs\to s$, and $K=m^2(eH)^{-1}$.

I is to be evaluated to order K^{-3}. The s^{-1} term is once, and the s^{-2} term twice, partially integrated with respect to u:

$$I=-\frac{1}{2}\int_0^\infty dse^{-isK}(s^{-1}-s^{-2}\sin s-\tfrac{1}{3}iKs^{-1}\sin s)$$

$$+\tfrac{1}{2}iK\int_0^1duu^2\int_0^\infty dse^{-iusK}(1-\tfrac{1}{3}iuK\sin s)$$

$$=\frac{1}{2}\int_0^\infty dse^{-isK}\left(\frac{1}{6}s-\frac{1}{3}iK+\frac{1}{18}iKs^2+\cdots\right)$$

$$+\frac{1}{2}\int_0^1du\{\tfrac{2}{3}u-\tfrac{1}{6}K^{-1}[(uK+1)^{-1}+(uK-1)^{-1}]\}$$

$$=\tfrac{1}{6}(eH/m^2)^2(\tfrac{5}{6}-\log|eH/m^2|)+O(eH)^4.$$

After the evaluation of a number of integrals of the foregoing type the result obtained is given in the next section.

III. RESULT

We shall write the mass separator in the following form:

$$\Delta M=\Delta m-\Delta\mu\,\boldsymbol{\sigma}\cdot\mathbf{H}. \tag{38}$$

The suggestiveness of (38) is clear if the Dirac equation, including one-photon radiation processes, is multiplied by $(m-\gamma\pi)$ on the left to read

$$[\pi^2+(m+\Delta m)^2-2m\boldsymbol{\sigma}\cdot\mathbf{H}(\mu+\Delta\mu)]\psi=0,$$
$$\mu=\hbar/2mc.$$

Δm is a field-dependent change in the rest mass of the electron, while $\Delta\mu$ is a field-dependent anomalous magnetic moment. Their values are found to be

$$\frac{\Delta m}{m}=-\frac{\alpha}{4\pi}\left(\frac{eH}{m^2}\right)^2\left\{\frac{13}{9}+\frac{8}{3}\log\left|\frac{2eH}{m^2}\right|+\frac{p_0^2-m^2-(\mathbf{p}\cdot\mathbf{H}|H|^{-1})^2}{m^2}\left[-\frac{293}{45}+\frac{272}{15}\log 2+\frac{16}{3}\log\left|\frac{eH}{m^2}\right|\right]+O\left(\left(\frac{eH}{m^2}\right)^2\log\left|\frac{eH}{m^2}\right|\right)\right\}, \tag{39}$$

$$\frac{\Delta\mu}{\mu}=\frac{\alpha}{2\pi}\left\{1+\left(\frac{eH}{m^2}\right)^2\left[-\frac{83}{45}+\frac{332}{15}\log 2+\frac{28}{3}\log\left|\frac{eH}{m^2}\right|\right]+O\left(\left(\frac{eH}{m^2}\right)^4\log\left|\frac{eH}{m^2}\right|\right)\right\}. \tag{40}$$

The following part of $\Delta m/m$ comes from the expansion of $\exp[-ius(1-\lambda^2)(\pi_-^2+m^2)]$ in powers of $(\pi_-^2+m^2)/m^2$:

$$-\frac{\alpha}{4\pi}\left(\frac{eH}{m^2}\right)\frac{\pi_-^2+m^2}{m^2}\left(-\frac{119}{45}+\frac{116}{15}\log 2+\frac{4}{3}\log\left|\frac{eH}{m^2}\right|\right).$$

Notice that $0\leqslant(1-\lambda^2)\leqslant 1$, and therefore one could, instead of expanding in $(\pi_-^2+m^2)/m^2$, state that for *any* π_-^2, m^2 ought to be replaced everywhere by $m^2+\epsilon(p_0^2-p_1^2-m^2)$, with $0\leqslant\epsilon\leqslant 1$, which is always larger than m^2. But ϵ, of course, differs from integral to integral. It is, nevertheless, clear that for large energies the expansion is one in powers of $eH(p_0^2-m^2-p_1^2)^{-1}$ rather than eHm^{-2}.

The first term in (40) is the anomalous magnetic moment (first derived by Schwinger[9]), while the second is an induced magnetic moment, as a factor of H a field-dependent magnetic susceptibility of the electron.

A term proportional to $(eHm^{-2})^2\log(eHm^{-2})$ was first obtained by Gupta,[3] but his result differs from ours. Both terms proportional to $(eHm^{-2})^3\log(eHm^{-2})$ and to $(eHm^{-2})^3\log(eHm^{-2})$ were obtained by Demeur,[10] his second-order terms agree with the ones in (40), while our third orders disagree. Both these authors used methods significantly different from ours in two ways. They used a special state of the electron in which $p_0=m$ and $\mathbf{p}\cdot\mathbf{H}=0$, and a special gauge. Their results are therefore neither clearly gauge nor Lorentz invariant and they do not obtain the term in $(p_0^2-m^2-\mathbf{p}\cdot\mathbf{H}|H|^{-1})$. Furthermore, an expansion and later resummation of part of the series is used. This latter procedure is never necessary in the present method.

The process used to obtain (39) and (40) is clearly gauge invariant. Potentials, in fact, are never used. It is also evidently Lorentz invariant. Equations (39) and (40) are valid whenever $\mathbf{E}\cdot\mathbf{H}=0$, i.e., $F_{\mu\nu}F_{\mu\nu}^*=0$, while in the general Lorentz frame

$$H^2\to\tfrac{1}{2}F_{\mu\nu}F_{\mu\nu}$$

and

$$H^2[(\mathbf{p}\cdot\mathbf{H}|H|^{-1})^2-p_0^2]\to\pi_\mu F_{\mu\nu}F_{\nu\lambda}\pi_\lambda+\tfrac{1}{2}\pi_\mu^2F_{\lambda\nu}F_{\lambda\nu}.$$

Although there exists no physical transformation from a frame in which $E=0$, $H\neq 0$, to one in which $H=0$, $E\neq 0$, (39) and (40) are clearly valid also in the latter frame. With the Dirac equation,

$$[\pi^2+(m+\Delta m)^2+2m(\mu+\Delta\mu)\gamma_4\boldsymbol{\gamma}\cdot\mathbf{E}]\psi=0,$$

Δm and $\Delta\mu$ are obtained from (39) and (40) by the substitution $H^2\to-E^2$.

IV. DISCUSSION

In the presence of artificially produced fields, the corrections given in (39) and (40) are, of course, much too small to be measurable. The expansion parameter is

$$eHm^{-2}=2.36\times10^{-14}\times H \text{ in gauss},$$
$$eEm^{-2}=2.36\times10^{-14}\times E \text{ in esu}.$$

In the inner shell of heavy atoms or inside nuclei, however, such corrections are not negligible.

Because of the presence of the logarithms each term in the expansion of $\Delta\mu$ and Δm has an extremum. The maximal magnetic moment correction is attained for a magnetic field strength of about 6.3×10^{12} gauss and its value is -9.6 percent of the anomalous magnetic moment. In view of the fact that at this extremum the expansion parameter has the rather small value 2.06×10^{-2} the next terms will presumably not alter its value appreciably. The maximal correction to the mass has a value of

$$\Delta m/m\approx 2.4\times10^{-5},$$

[9] J. Schwinger, Phys. Rev. **73**, 416 (1948).

[10] See reference 4. The discrepancy between our results is presumably due to an error on his part. Starting from (22), p. 79, of Demeur's paper one obtains agreement with the present result if a method of expansion in $v\alpha$ alone is used, which obviates the necessity for resumming the series that leads to divergencies.

which is attained at $(eHm^{-2})^2=3\times10^{-2}$ (approximately 7.6×10^{12} gauss).

In the $2s$ level of hydrogen the addition to the anomalous magnetic moment is obtained from (40) in an approximate fashion by setting

$$eE/m^2=\alpha^3/n^4=2.44\times10^{-5},$$

and therefore

$$\Delta^2\mu/\mu=(\alpha/2\pi)\times0.9\times10^{-13}.$$

This is to be compared with the fourth-order radiative correction to the magnetic moment,[11]

$$-(\alpha/2\pi)\times1.38\times10^{-2}.$$

The contribution to the Lamb shift due to the second term in (40) is therefore entirely negligible.

Apart from a constant change in the magnetic moment, then, the lowest order radiative correction to the behavior of an electron in the presence of a uniform electric field manifests itself in the form of a rest mass change:

$$\frac{\Delta m}{m}=\frac{\alpha}{12\pi}\left(\frac{2eE}{m^2}\right)^2\left[\frac{13}{12}+\log\left(\frac{2eE}{m^2}\right)^2\right]. \tag{41}$$

Let us take this field dependence of the mass for the moment at face value and neglect all other radiative effects due to a spacial inhomogeneity of the field. We may then ask *classically* what the resulting forces between stationary charged particles are by simply taking the radial derivative of the energy. Due to the radiative effects now not only the Coulomb potential energy but also the rest mass is a distance dependent part (via its dependence on the Coulomb field) of the energy. Therefore, with the simplest radiative corrections classically incorporated, the radial derivative of the energy between two charged particles at rest,

$$\partial(m_1+m_2+e_1e_2r^{-1})/\partial r,$$

vanishes, provided that

$$R^3=K_1(\log R+K_2), \tag{42}$$

where

$$R=(mch^{-1})(2\alpha)^{-\frac{1}{2}}\exp(-25/48)\pi\mathfrak{m}|e_1e_2|^{-\frac{1}{2}}(1+\epsilon)^{-\frac{1}{2}},$$

$$K_1=(8/3\pi)(\alpha/2)^{\frac{1}{2}}\exp(-25/16)e_1^2|e_1e_2|^{-\frac{1}{2}}sgn(e_1e_2),$$

$$K_2=\tfrac{1}{2}\{\log(1+\epsilon)-\epsilon(1+\epsilon)^{-1}\log[\epsilon(e_1/e_2)^2]\},$$

$$\epsilon=(m_1/m_2)^3(e_2/e_1)^2,$$

and $\mathfrak{m}$ is the mass of particle 1 in units of electron masses, e_1 and e_2 being the two charges in units of the electronic charge.

At the distance which solves (42) two charged particles can stay at rest with respect to each other. The following can be shown easily (in case one particle is much heavier than the other, say): By *decreasing* the charges (in order not to increase the multiple photon effects) the expansion parameter eE/m^2 at the rest distance can be made as small as 0.18 in the case of opposite charges. By decreasing the mass of the lighter particle, we can make the rest distance as large as we please. Hence, if one believes in the convergence of the expansion at $eE/m^2\approx0.2$ one can conclude that oppositely charged particles of arbitrarily small charge and mass would have repulsive cores of arbitrary extension.

In the case of charges of equal sign, (42) has a solution only if $e_2<10^{-6}e_1^3$. Then there will be two solutions, representing the boundaries of an attractive shell. At the inner boundary $0.09<eE/m^2<0.18$, and at the outer, $eE/m^2<0.09$. Therefore, again, if there were particles of arbitrarily small charge and mass, they would, if of equal sign of charge, have attractive shells of arbitrarily large size.

For physically real particles conclusions as to the existence of a repulsive core cannot be drawn with any assurance because the expansion parameter becomes too large at the rest distance. The first term in the series will then no longer suffice, even if the series still converges. (For an electron-proton pair, $eE/m^2\approx11$ at the rest distance of $\sim10^{-12}$ cm.) It is, nevertheless, perhaps of some interest that even on the basis of such a very simple approximation the radiative effects provide charged particles with strong forces opposed to the Coulomb field.

The author would like to express his gratitude to Professor J. Robert Oppenheimer for the hospitality extended to him at the Institute for Advanced Study.

[11] R. Karplus and N. M. Kroll, Phys. Rev. **77**, 536 (1950).

Letters to the Editor

PUBLICATION of brief reports of important discoveries in physics may be secured by addressing them to this department. The closing date for this department is five weeks prior to the date of issue. No proof will be sent to the authors. The Board of Editors does not hold itself responsible for the opinions expressed by the correspondents. Communications should not exceed 600 words in length and should be submitted in duplicate.

Isotope Shift in λ4415 Cd II

E. C. WOODWARD AND D. R. SPECK
University of California, Berkeley, California
(Received August 23, 1954)

THE isotope shifts in λ4415 Cd II ($4d^{10}5p\ ^2P_{3/2} - 4d^9 5s^2\ ^2D_{5/2}$) have been reported by several workers[1–4] using either natural cadmium or separated isotopes, although all of the latter were not employed. In view of the complex structure of this line, it seemed desirable to study suitable mixtures of all the isotopes. By using a Schüler hollow-cathode discharge tube cooled with liquid nitrogen as a source, and a Fabry-Perot etalon in conjunction with a large prism spectrograph as the dispersive element, the following isotopes and their mixtures were studied: Cd^{110} and Cd^{114}, Cd^{110} and Cd^{116}, Cd^{112} and Cd^{116}, Cd^{113}, Cd^{113} and Cd^{116}, Cd^{111}, Cd^{111} and Cd^{116}, Cd^{108} and Cd^{114}, Cd^{106} and Cd^{114}, and Cd^{106} and Cd^{110}.

Table I lists the separations in millikaysers of the lines due to the various isotopes as compared to those of previous workers. A positive value indicates a shift toward the violet. The Cd^{110} line is taken as the origin.

From the consistency of the data the separations in the present work are accurate to ±1.5 mK.

Both Cd^{111} and Cd^{113} showed only two components in their hyperfine structure. The strong component lay toward the red in each case. The ratio of intensities was measured by photographic photometry to be 1.35±0.05. Thus the hyperfine structure of both Cd^{111} and Cd^{113} is due to two close-lying components in the $^2D_{5/2}$ state. This is analogous to the results of Ritschl[5] on the spectrum of Cu I and of Schüler and Westmeyer[6] on the spectrum of Zn II. Using the theoretical ratio of intensities of 1.40, the center of gravity of the Cd^{111} pattern is located at +7.3 mK with respect to the Cd^{110} line, and the center of gravity of the Cd^{113} pattern is located at +62.9 mK with respect to the Cd^{110} line, giving a relative shift between Cd^{111} and Cd^{113} of 55.6 mK. The anomalous shift of Cd^{113} reported by Woodward[2] was in error because of inadequate cleansing of the hollow cathode between use with different samples. The ratio of magnetic moments of Cd^{113} to Cd^{111} was found to be 1.046±0.027, in good agreement with the value 1.0461±0.0001 found by Proctor and Yu.[7]

TABLE I. Separations with respect to Cd^{110} line, in millikaysers (1 kayser = 1 cm^{-1}).

Cadmium isotope	Separation (mK) Present work	Schüler and Westmeyer[a]	Murakawa[b]	Hindmarsh, Kuhn, and Ramsden[c]
106	−112.2	...	−106	...
108	− 51.2	...	− 56	...
111 strong component	− 15.2	...	− 20	...
110	0.0	0	0	0.0
111 weak component(s)	38.8	...	33	...
	...	...	59	...
113 strong component	39.4	...	35	...
112	53.1	54	55	53.3
113 weak component(s)	95.9	...	91	...
	...	...	118	...
114	99.9	105	109	101.2
116	135.6	...	147	135.6

[a] See reference 1.
[b] See reference 3.
[c] See reference 4.

[1] H. Schüler and H. Westmeyer, Z. Physik **82**, 685 (1933).
[2] E. C. Woodward, Phys. Rev. **93**, 948 (1954).
[3] K. Murakawa, Phys. Rev. **93**, 1232 (1954).
[4] Hindmarsh, Kuhn, and Ramsden, Proc. Phys. Soc. (London) **A67**, 478 (1954).
[5] R. Ritschl, Z. Physik **79**, 1 (1932).
[6] H. Schüler and H. Westmeyer, Z. Physik **81**, 565 (1933).
[7] W. G. Proctor and F. C. Yu, Phys. Rev. **76**, 1728 (1949).

Quantum Theory of Cyclotron Resonance in Semiconductors

W. KOHN* AND J. M. LUTTINGER†
Bell Telephone Laboratories, Murray Hill, New Jersey
(Received September 2, 1954)

WE have investigated in detail the quantum theory of "cyclotron" resonance of holes in semiconductors such as Si and Ge. In the case of electrons the quantum theory of cyclotron resonance is identical with the classical theory.[1] This is connected with the fact that the classical or W.K.B. approximation gives *exactly* the correct quantum levels for a simple harmonic oscillator. For holes the situation is very different because of complications arising from the degeneracy at the top of the valence band.[2] In this case we have shown that the quantum theory leads to different energy levels and selection rules for low quantum numbers, though of course for high quantum numbers the classical results are again valid.[1] Under the conditions of experiments such as those of Lax *et al.*[3] conducted at liquid helium temperature, the mean quantum number is ~5. By lowering the temperature further (to say 1 or 1.5°K) it should be possible to enhance the quantum effects and observe additional resonances. In fact there may be some evidence of these resonances in the structure observed by Dresselhaus, Kip, and Kittel.[4]

The quantum result may be formulated as follows. Consider first the case of no spin-orbit coupling. Then it is known[2] that in the absence of an external magnetic field the energy surfaces are found by solving the secular

equation:

$$\begin{bmatrix} Ak_x^2+B(k_y^2+k_z^2) & Ck_xk_y & Ck_xk_z \\ Ck_xk_y & Ak_y^2+B(k_z^2+k_x^2) & Ck_yk_z \\ Ck_xk_z & Ck_yk_z & Ak_z^2+B(k_x^2+k_y^2) \end{bmatrix} \begin{bmatrix} a_1 \\ a_2 \\ a_3 \end{bmatrix} = E \begin{bmatrix} a_1 \\ a_2 \\ a_3 \end{bmatrix}, \quad (1)$$

and the wave function is given by

$$\psi = a_1\varphi_1 + a_2\varphi_2 + a_3\varphi_3, \quad (2)$$

φ_1, φ_2, φ_3 being the p-like degenerate functions at the top of the valence band. The essential result of our investigation is that to obtain the level scheme with an external field one need only replace k_x by $(1/i)(\partial/\partial x) - (e/\hbar c)A_x$, etc., where **A** is the vector potential of the field, and regard the a_i as functions of the coordinates. If there is any ambiguity in the order of two non-commuting factors, the symmetrized product is meant. If spin-orbit coupling is taken into account then, *mutatis mutandis*, the identical prescription still applies. Just what matrix replaces that of Eq. (1) depends on which model of the band one chooses. Kittel's model,[4] which seems most reasonable at the present time, would lead to a four-by-four matrix, the elements of which are linear combinations of those of Eq. (1). The resulting system of coupled differential equations is at present being investigated. A more detailed publication is in preparation.

This work was carried out while we were guests of the Bell Telephone Laboratories, and we should like to take this opportunity of thanking the staff for their cooperation and friendliness.

* Permanent address: Carnegie Institute of Technology, Pittsburgh, Pennsylvania.

† Permanent address: University of Michigan, Ann Arbor, Michigan.

[1] The classical theory is due to W. Shockley, Phys. Rev. **79**, 191 (1950).

[2] The theory of the behavior of such bands near a degeneracy point is due to W. Shockley, Phys. Rev. **78**, 173 (1950). Shockley did not take into account the effect of spin-orbit coupling on the degeneracy, and its importance seems first to have been pointed out by R. J. Elliott (unpublished). As far as we know, there is no treatment of the spin-orbit case in print.

[3] Dexter, Zeiger, and Lax, Phys. Rev. **94**, 557 (1954).

[4] Dresselhaus, Kip, and Kittel, Phys. Rev. **95**, 568 (1954).

Redetermination of the Hyperfine Splitting in the Ground State of Atomic Hydrogen*

J. P. Wittke and R. H. Dicke
Palmer Physical Laboratory, Princeton, New Jersey

(Received August 30, 1954)

A REDETERMINATION has been made of the zero-field hyperfine splitting of the ground state of atomic hydrogen. A microwave absorption technique was used employing a resonance line of ~3-kc/sec width at half-maximum absorbed power. This width ($\frac{1}{8}$ of the normal Doppler breadth) was obtained through the mechanism of collision reduction of the Doppler effect.[1] Atomic hydrogen at a partial pressure of about 5×10^{-4} mm was mixed with very clean molecular hydrogen (~0.2 mm pressure), a medium with which the atomic hydrogen can collide without disturbing its spin state. This provided a long diffusion time to the gas container walls where spin relaxation collisions may occur. The primary relaxation mechanism was electron exchange collisions[2] between two hydrogen atoms, the cross section for which is much greater than the geometrical cross section. Because of the paired electron spins in the molecule, electron exchange effects in the atom-molecule collisions are negligible. Furthermore, dipole-dipole and spin-orbit relaxation effects are very weak in such a collision. The production of narrower lines is presently limited by the rather poor noise figure of the detection equipment.

The resonant frequency, as measured, was shifted slightly by the following pressure-dependent mechanism: during an atom-molecule collision, although the molecular electric fields do not appreciably disturb the atom's hyperfine state (quantum numbers F, m_F), they mix some P state into the wave function. As the hyperfine interaction in P states is much weaker than in the $1S$ state, the result is a reduction in the time-averaged interaction energy, causing a small reduction of the measured splitting. The measured shift of about 100 cycles/sec is in agreement with a rough calculation.

The hyperfine transitions were induced in a cylindrical cavity excited in the TE_{112} mode, the hydrogen sample being confined in a glass bottle at the cavity center. The atomic hydrogen was produced in a Wood's discharge external to the cavity, and was pumped and diffused into the bottle. A triode oscillator, phase locked to the sum frequency of a harmonic of a very stable crystal-controlled oscillator and a stable variable-frequency oscillator (~433 kc/sec), supplied the microwave energy. A weak magnetic field of ~0.06 gauss parallel to the rf magnetic field led to the $\Delta M_F=0$ transition. The direction of this weak field was varied from parallel to nearly perpendicular at 30 cycles/sec causing a 30-cycle modulation of the absorbed power. The resultant modulated signal was detected in a balanced barretter mixer, amplified at 30 cycles/sec, and fed into a lock-in amplifier. The locking signal was derived from the 30-cycle magnetic field modulation. A cavity-tuning technique was developed that kept the phase of the signal from the cavity, with respect to the carrier in the barretters, adjusted at all times to to produce a purely absorptive resonance. The line contour was determined experimentally to be Lorentz shaped.

Data were taken by measuring the signal strength at three discrete frequencies on the resonance line and fitting a Lorentz curve through the points. The line center was determined from this fitted curve. About 35 determinations were made at each of three pressures.

TABLE I. Results of the measurement of ν_0.

Pressure, mm Hg	No. of observations	Frequency,[a] Mc/sec
0.14	35	1420.40572±0.00003
0.18	35	1420.40575±0.00003
0.27	33	1420.40569±0.00002
0 (extrapolated)	···	1420.40530±0.00005

[a] A 10-cycle/sec correction to the frequencies caused by the 0.06-gauss field is included.

The results, together with the value obtained by extrapolation to zero pressure, are given in Table I.

These results are not likely to be changed by more than ±20 cycles/sec by the astronomical time correction to the nominal *WWV* frequencies, which, however, will not be available for several months. The listed uncertainties are probable errors. The present determination is in disagreement with the value of the hyperfine splitting using a molecular beam technique,[3] which gave

$$\nu_0 = 1420.4051 \pm 0.0002 \text{ Mc/sec.}$$

Both of the above results are in agreement with theory within the uncertainties introduced by high-order radiative corrections and proton structure effects.

* This research was supported by the Signal Corps.

[1] R. H. Dicke, Phys. Rev. **89**, 472 (1953).

[2] First proposed to E. M. Purcell by N. F. Ramsey and V. F. Weisskopf.

[3] A. G. Prodell and P. Kusch, Phys. Rev. **88**, 184 (1952).

Hall Effect in Positive Column

KAZUO TAKAYAMA, TOMIZO SUZUKI, AND TADAICHI YABUMOTO
Electrical Communication Laboratory, Musashino, Tokyo, Japan

(Received July 29, 1954)

HALL voltage was observed in the positive column of dc gas discharge tubes, and was measured as a function of magnetic field, tube current, distance between probes, and gas pressure by the floating double probe method.

With a Helmholtz coil having a radius of 20 cm, a homogeneous magnetic field was applied perpendicular to the axis and to the line joining two probes which were placed perpendicular to the tube axis.

A hot cathode tube was constructed with a Pyrex cylinder 37 mm in inside diameter and 70 cm in total length, and four probes were inserted in the positive column near the middle part of this tube as shown in Fig. 1. Probes 1 and 2 were used to measure the Hall voltage and variations of the plasma densities at these points, and probes 3 and 4 were used for determining the electric field and density on the axis of the column. Argon and neon were used, with pressures ranging from 0.2 to 15 mm Hg, and the tube current ranged from 0.04 to 4 amperes.

An external magnetic field deflected the column in the same direction as electrons would be bent in vacuum, but the sign of the Hall voltage was opposite to that of an *n*-type semiconductor.

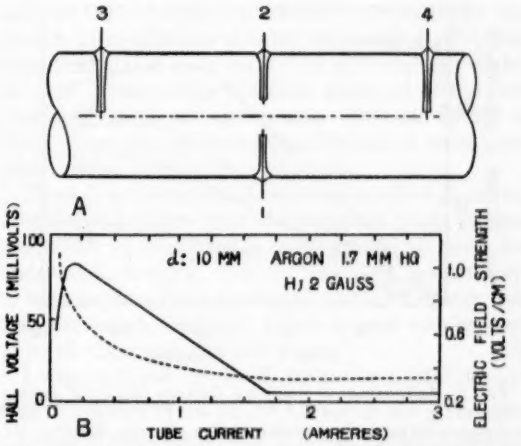

FIG. 1. A: The part of the tube where four probes are inserted. B: The Hall voltage and the electric field in the column *vs* tube current, in a magnetic field of 2 gauss. The tube contains argon at a pressure of 1.7 mm Hg. The solid and dotted lines indicate the Hall voltage and electric field, respectively.

Figure 1 indicates a general relation between the Hall voltage and the tube current at constant magnetic field and pressure. When the tube current was increased, the Hall voltage first increased to a maximum, then decreased, and finally reached a constant value, whereas the electric field in the column decreased monotonically. Therefore three regions were distinguished, corresponding to the character of the Hall voltage.

When the gas pressure was increased, the second region became narrow and the constant value in the third region became larger. It should also be noted that at large tube current and very low pressure the sign of the Hall voltage was reversed.

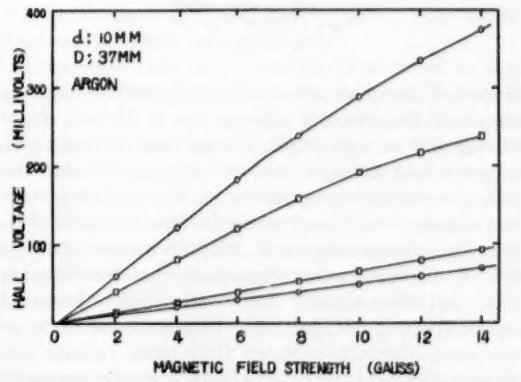

FIG. 2. Hall voltage *vs* magnetic field. The open circles and squares are data taken with the tube containing argon at pressures of 0.7 mm Hg and 1.4 mm Hg, respectively. The upper two lines are taken in the second region (at 1.0 amp) and the lower two lines in the third region (at 2.7 amp).

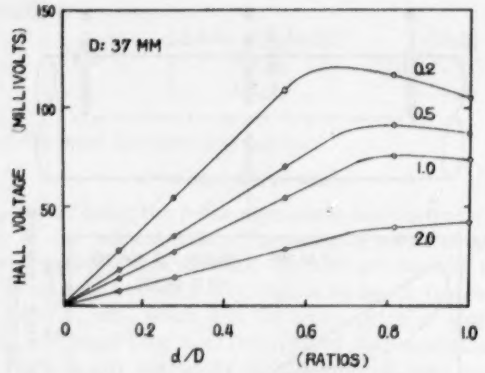

FIG. 3. Hall voltage *vs* fractional distance (d/D) for various values of the tube current (0.2, 0.5, 1.0, and 2.0 amperes), where d is distance between the probes and D is the tube diameter (37 mm). The tube contains argon at a pressure of 2 mm Hg. The magnetic field is 2 gauss.

An experiment with a tube of inside diameter 22 mm indicated that in the second region the Hall voltage was changed through zero to a negative value.

The variation of the Hall voltage with magnetic field strength in the second and third regions is shown in Fig. 2. The Hall voltage is exactly proportional to the magnetic field strength in the third region. However, in the second region deviations appear for magnetic fields greater than several gauss.

Another tube was prepared with five double probes, and the relation between Hall voltage and distance between probes was studied; the results are shown in Fig. 3. The abscissa is the ratio of the distance between probes to the tube diameter, and the parameter is the tube current in amperes. The Hall voltage was nearly proportional to the distance between the probes when these were placed near the tube axis.

To a first approximation, if we neglect the effect of ion current, the observed value of Hall voltage (V_0) is expressed by

$$V_0=\frac{kT}{e}\log\frac{n_2}{n_1}-\frac{vHd}{c},$$

where e, T, and k are electron charge, electron temperature, and Boltzmann's constant; c, v, H, and d are the velocity of light, the electron drift velocity, the magnetic field strength, and the distance between the probes respectively; n_1 and n_2 are the random plasma densities at probe 1 and probe 2. Here, the ratio of n_2 to n_1 depends not only on H, but also on the tube current. V_0 is considered to be composed of the diffusion term[1] and the ordinary Hall term. Under the usual experimental conditions, the diffusion term is large compared with the ordinary Hall term, because the electron temperature is very high and the magnetic field is weak. This was verified by the fact that the value of $(kT/e)\log(n_2/n_1)$ calculated from the characteristic curves[2] of the double probe agreed approximately with the observed voltage. The measurement of Hall voltage seems to be a valuable method for studying the positive column.

The authors wish to express their thanks to Professor S. Kojima for discussions during the course of the investigation.

[1] R. Landauer and J. Swanson, Phys. Rev. **91**, 555 (1953).
[2] S. Kojima and K. Takayama, J. Phys. Soc. (Japan) **5**, 357 (1950).

Alignment of Sodium Atoms*

W. B. HAWKINS† ‡
Palmer Physical Laboratory, Princeton University, Princeton, New Jersey

(Received August 20, 1954)

IN the course of work on the polarization of sodium atoms by the absorption of circularly polarized resonance radiation,[1] observations were also made with the incident light unpolarized. An effect was observed which is interpreted as a partial alignment induced in the sodium by the scattering of the unpolarized photons. Because of the definite direction of incidence, the unpolarized photons possess some order, and the scattering of such photons induces alignment along the axis of the incident light. The alignment of the sodium affects the polarization ratio $(\sigma-\pi)/(\sigma+\pi)$ of the light scattered at 90°. In Fig. 1 the measured shift in this

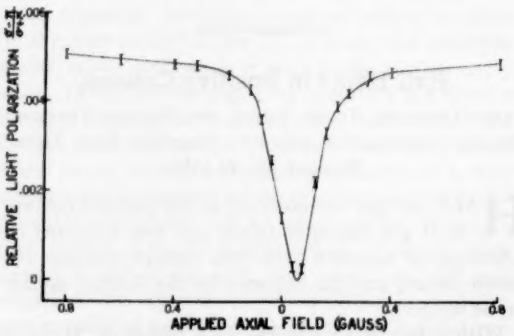

FIG. 1. Polarization ratio of the scattered resonance radiation with incident radiation unpolarized.

polarization ratio is plotted against the magnetic field strength applied along the direction of the incident light. The total magnetic field in the two other directions was made as nearly as possible zero by the use of compensating Helmholtz coils. The corresponding plot with the incident radiation circularly polarized differs mainly in the scale of the ordinate, and its features have been described previously.[1] The asymmetry previously observed has been removed by the use of more nearly homogeneous magnetic fields.

From Fig. 1, the polarization ratio of the scattered light for sodium in thermal equilibrium occurs for an applied field of 0.055 gauss, for which the axial com-

ponent of the earth's field is compensated. The resulting residual transverse magnetic field causes a spin precession after a first scattered photon which serves to destroy essentially all alignment and to restore thermal equilibrium before a second photon can be scattered. At values of the applied axial field far from 0.055 gauss, atoms are not restored to thermal equilibrium after scattering a photon and may scatter a second photon while in this non-equilibrium state. The polarization ratio of this second scattered photon is computed to be larger than that of the first photon scattered, in agreement with the experimental observations. The total observed shift in light polarization ratio should depend on the intensity of the light source, since this determines the number of atoms which scatter more than one photon. As expected, it is found experimentally that for the range of light intensity available, the shift in polarization ratio is in direct proportion to the intensity of the incident light. With the maximum intensity available, a shift of 0.0034 is calculated; the observed value is 0.0048, indicating that the incident light may not be completely unpolarized.

The alignment of sodium by the scattering of unpolarized light may be understood from reference 1, considering the unpolarized light as composed of equal numbers of right and left circularly polarized photons. In Table I of reference 1, it may be noted that the $m_F=0$ populations are reduced by the scattering of a circularly polarized photon independent of the rotational sense. Consequently, the scattering of an unpolarized photon will reduce the $m_F=0$ state populations relative to those with $|m_F|=F$, the condition of alignment. For two scattered photons there are atoms which scatter photons of the same polarization and contribute to the alignment of the ensemble and atoms which scatter oppositely polarized photons and do not contribute significantly. For more than two photons the process does not proceed to complete alignment but reaches an equilibrium partial alignment, for the effect of unpolarized resonance radiation on a completely aligned ensemble is to reduce the alignment.

TABLE I. Occupation numbers of atoms which have scattered n unpolarized photons, $n=\infty$ corresponding to the equilibrium state. P_1 and P_2 are the total numbers of atoms in the two hyperfine states. R_n is the polarization ratio of the nth scattered photon.

	$F=1$			$F=2$				
n $m_F=$	±1	0	±2	±1	0	P_1	P_2	R_n
0	0.125	0.125	0.125	0.125	0.125	0.375	0.625	...
1	0.128	0.119	0.144	0.115	0.106	0.375	0.625	0.0700
2	0.128	0.116	0.154	0.110	0.100	0.372	0.628	0.0905
3	0.126	0.115	0.161	0.108	0.099	0.367	0.637	0.0997
∞	0.125	0.115	0.163	0.106	0.098	0.365	0.636	

Table I gives the probability of an atom being in various states having the quantum numbers F, m_F (total angular momentum, magnetic quantum number) after having scattered one, two, or three photons, as well as the values at equilibrium. Although the approach to equilibrium is fairly rapid, the equilibrium alignment is seen to be small. The difference in populations of corresponding magnetic substates of the two hyperfine levels at equilibrium, although small, is many times that in thermal equilibrium at room temperature due to the energy separation.

There is no reason to believe that the effect should be confined to sodium, since the argument given for the production of alignment is quite general. It must be understood, however, that the argument applies only to light incident from a restricted part of a sphere; for isotropic unpolarized light defines no axis with respect to which alignment can take place.

I wish to thank Dr. R. H. Dicke for helpful discussion and criticism.

* Research supported by the U. S. Atomic Energy Commission and the Higgins Scientific Trust Fund.

† National Science Foundation Predoctoral Fellow.

‡ Now at: Physikalisches Institut der E. T. H., Gloriastrasse 35, Zürich, Switzerland.

[1] W. B. Hawkins and R. H. Dicke, Phys. Rev. **91**, 1008 (1953).

Photovoltaic Effect in Cadmium Sulfide

D. C. REYNOLDS, G. LEIES, L. L. ANTES, AND R. E. MARBURGER

Aeronautical Research Laboratory, Wright Air Development Center, Air Research and Development Command, United States Air Force, Wright-Patterson Air Force Base, Ohio

(Received September 2, 1954)

DURING the course of a recent investigation with the photoconduction and rectification properties of CdS crystals, a pronounced photovoltaic effect was observed. The crystals used for this investigation were grown from the vapor phase by a technique previously reported.[1]

The rectification studies were conducted on crystals using an indium base electrode and such metals as silver, copper, gold, and platinum as counter electrodes. It was in some of these rectifiers that pronounced photovoltaic effects were observed.

The photovoltaic cells that have been tested to date have been made by applying the base electrode and counter electrode on opposite faces of a CdS crystal approximately 3 mm thick. Light more or less parallel to the electrodes was then applied to the open face of the crystal. From this arrangement open-circuit voltages of 0.4 v have been measured in direct sunlight and 0.6 v in focused sunlight. Short-circuit currents of 15 ma cm^{-2} have been measured in direct sunlight and 300 ma cm^{-2} in focused sunlight. The photovoltaic effect has also been observed in pellets of CdS powder (pressed and fired); however, the current obtained from these cells is less than that obtained from a single crystal as expected. Work is currently being carried out to prepare a semitransparent electrode on one face so that crystals can be illuminated perpendicular to the face.

The spectral response of a typical cell is shown in Fig. 1. The peak in the red is interesting in that it is a region of considerable transparency.[2] This peak has been observed on all crystals with various types of electrodes. In some crystals the peak in the red is so pronounced it masks the peak in the green. This observed peak in the red may be explained on the basis of the conduction mechanism proposed by Brosser, Kallmann, and Warminsky.[2] It appears that by proper control of impurities the spectral response can be tailor-made within limits.

In measuring the spectral response it was observed that for some crystals the short-circuit current at a given wavelength grows or decays with time depending on the wavelength of the previous illumination. Under illumination of chopped white light (up to 18 000 interruptions per second), the voltage trace as observed

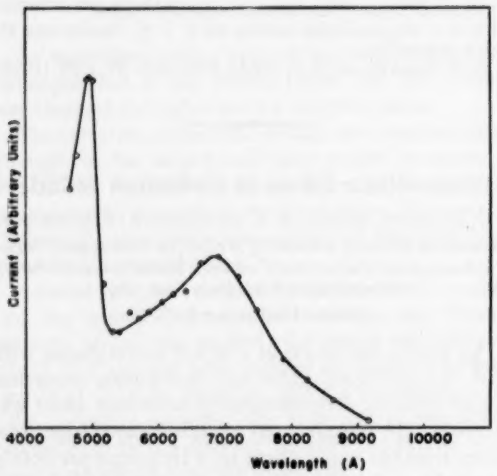

FIG. 1. Spectral photovoltaic response of CdS crystal with silver and indium electrodes.

on an oscilloscope retained the same shape although reduced in amplitude at the higher frequencies. This reduction may have been due to a capacitance effect.

With increasing intensity of illumination, the short-circuit current and the open-circuit voltage increased in such a manner as to give a linear increase of their product. Even up to intensities ten times that of sunlight, there appeared no indication of current or power saturation that could not be attributed to a temperature rise.

The average of all the crystals tested showed that the open-circuit voltage at room temperature dropped to half its value at approximately 150°C; and the closed-circuit current dropped to 80 percent of its room temperature value at approximately 150°C.

[1] Czyzak, Craig, McCain, and Reynolds, J. Appl. Phys. **23**, 932 (1952).
[2] Brosser, Kallmann, and Warminsky, Z. Naturforsch. **4a**, 631 (1949).

Optical and Infrared Absorption of Copper at 4.2°K

MANFRED A. BIONDI
Westinghouse Research Laboratories, East Pittsburgh, Pennsylvania
(Received August 25, 1954)

RECENTLY, a number of theories have been published[1–3] concerning the anomalous skin effect in metals. These theories treat the case in which the electronic mean free path is large compared to the skin depth of penetration of an electromagnetic field, and hence the absorptivity of the metal is not properly described by conventional theory.[4] Under these circumstances, the conduction electrons in the metal no longer make collisions in traversing the skin-depth region but collide only with the surface of the metal. The theories predict a different absorption of energy depending on whether the electrons are specularly or diffusely reflected from the surface of the metal. Holstein[2] has shown that in the high-frequency region (visible and infrared frequencies) if a fraction p of the electrons are specularly and $(1-p)$ are diffusely reflected from the surface, the absorptivity for normal incidence radiation is given by

$$A=A_{\text{spec}}+A_{\text{diff}}=p\frac{2\pi ne^2 v_0^3}{m^*\omega^2 c^3}+(1-p)\frac{3}{4}\frac{v_0}{c}, \qquad (1)$$

where v_0 is the Fermi velocity and m^* and n are the effective mass and density of the electrons, respectively. Ramanathan[5] has measured the absorptivity of an electropolished copper surface at 4°K for room temperature radiation ($\lambda\sim 14\,\mu$) and finds $A=0.0062$, which is in order of magnitude agreement with the theory for $p=0$ (diffuse reflection).

In order to provide a more extensive test of the theory, an experiment was devised to measure the absorptivity as a function of the wavelength of the impinging radiation from $\lambda=0.5\,\mu$ to $\lambda=4\,\mu$. The principle of the measurements is illustrated in Fig. 1. Radiation of the desired wavelength is incident on a copper target which is mounted on a stage carrying a resistance thermometer and a heater winding. The stage is connected through a heat leak to the helium bath. The radiation reflected from the copper target is absorbed by the gold-black absorber stage,[6] which also carries a resistance thermometer and a heater winding.

With the radiation turned on, the target and absorber stages reach an equilibrium temperature somewhat in excess of the bath temperature. The changes in resistance of the thermometers imbedded in the target and the absorber stages are noted. With the radiation off, power is applied to the heater in each stage to produce the resistance change noted with the radiation on. By measuring the heater power applied to each stage, one can determine the absorptivity of the copper target.

The measured absorptivity of copper is shown in Fig. 2. Two samples of high-purity copper were used, one a single crystal, the other polycrystalline (crystal size ~2 mm). The electronic mean free path of these samples at 4.2°K, determined from dc conductivity measurements, was $l_e \geq 10^{-3}$ cm, which greatly exceeds the skin depth ($\sim 2\times 10^{-6}$ cm). The single-crystal target was vacuum annealed at 1040°C for 45 hours and electropolished. The polycrystal target was hydrogen annealed at 1020°C for six hours and then electropolished. The close agreement between the absorptivities of the two samples suggests that the measured values represent an intrinsic property of the copper rather than of the surface preparation. Over the range $\lambda = 2.1\,\mu - 4\,\mu$, we find $A = 0.0039$, independent of λ. The rapid rise in absorptivity at $\lambda \leq 0.55\,\mu$ is ascribed to direct interzonal transitions within the conduction band.[7] The long tail from $\lambda = 0.55\,\mu$ to $2\,\mu$ is either a continuation of this process or may possibly be caused by "indirect" electronic transitions ($\mathbf{k}_{\text{final}} \neq \mathbf{k}_{\text{initial}}$) of the type recently predicted for germanium.[8]

In the present note, we shall discuss in detail only the absorption caused by the "free" electrons near the Fermi level and, therefore, shall consider only data for $\lambda > 2\,\mu$. The observed lack of dependence of A on λ suggests that the electrons are diffusely reflected at the surface. Assuming one conduction electron per atom and $m^* = m$, where m is the free electron mass, Dingle[3] calculates $A = 0.004$ ($p = 0$), in excellent agreement with our observations. However, the assumption that $m^* = m$ for electrons at the Fermi level is open to question. Specific heat measurements, which apply to these electrons, give $m^* = 1.4m$ for copper. With this value of m^*, Eq. (1) gives $A = 0.0028$ ($p = 0$). The observed value is therefore too high if electrons can only make collisions at the surface of the metal. Holstein[9] has recently investigated the two-stage volume process in which a conduction electron absorbs a photon with simultaneous emission of a phonon. At optical and near infrared frequencies, the mean free path for this process is comparable to the skin depth; hence the absorptivity given by Eq. (1) is increased to 0.0046.[9]

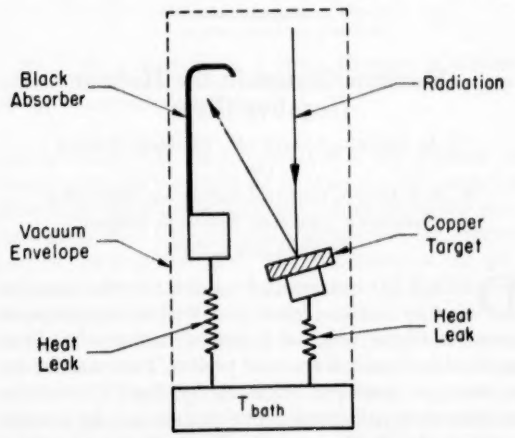

FIG. 1. Schematic diagram of the apparatus. The target and absorber stages each carry a resistance thermometer and a heater winding.

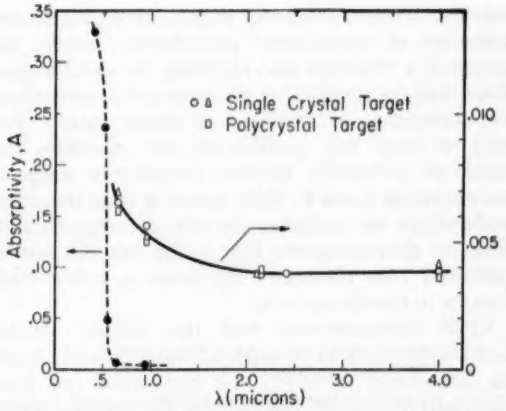

FIG. 2. Absorptivity of copper measured at 15° angle of incidence. Runs taken on the single crystal target on successive days are indicated by the symbols ○ and △. The "free' electron absorption ($\lambda > 2\mu$) is 0.0039 (corrected to normal incidence). The scale for the solid curve is at the right of the figure, that for the dashed curve at the left.

The present experimental results are therefore in fair agreement with the predictions of theory for diffuse electron reflection. In view of the operation of the two-stage volume process in addition to the surface scattering of electrons, the measurements are being extended to other metals (e.g., silver) to provide more adequate tests of the various theories.

The author is indebted to various members of the Low Temperature Group and the Physics Department for their considerable advice and assistance. In particular, he wishes to thank A. Wexler, who contributed greatly to the design of the experiment.

[1] G. E. H. Reuter and E. H. Sondheimer, Proc. Roy. Soc. (London) **A195**, 33 (1948).
[2] T. Holstein, Phys. Rev. **88**, 1427 (1952).
[3] R. B. Dingle, Physica **19**, 311, 348 (1953).
[4] See, for example, A. H. Wilson, *The Theory of Metals* (Cambridge University Press, Cambridge, 1936), Chap. V.
[5] K. G. Ramanathan, Proc. Phys. Soc. (London) **A65**, 532 (1952).
[6] The measured absorptivity of the gold black is $A > 0.99$.
[7] N. F. Mott and H. Jones, *The Theory of the Properties of Metals and Alloys* (Oxford University Press, London, 1936).
[8] Hall, Bardeen, and Blatt, Phys. Rev. **95**, 559 (1954).
[9] T. Holstein, following Letter [Phys. Rev. **96**, 535 (1954)].

Optical and Infrared Volume Absorptivity of Metals

T. HOLSTEIN
Westinghouse Research Laboratories, East Pittsburgh, Pennsylvania
(Received August 25, 1954)

THIS letter gives the results of a quantum-mechanical treatment of the electromagnetic absorptivity of metallic conduction electrons in the optical

and near infrared frequency region. According to the formalism of second-order perturbation theory, the process is a two-stage one, involving the simultaneous absorption (or emission) of electromagnetic energy and the absorption (or emission) of lattice quanta. For each of these four possibilities, one calculates the transition probability between one-electron states of wave numbers $\mathbf{k}$ and $\mathbf{k}'$. With the aid of these transition probabilities one computes the rate of energy transfer from the electromagnetic field to the material system (electrons plus phonons); the latter quantity leads directly to the absorptivity.

Close correspondence with the classical Drude-Lorentz theory is to be expected for sufficiently small $\hbar\omega$ (specifically $\hbar\omega \ll kT$); this expectation has been confirmed by detailed calculations. On the other hand, at sufficiently low temperatures such that $T \ll \Theta$ (the Debye temperature), and for optical and infrared frequencies, where the two conditions $\hbar\omega \gg k\Theta$, $\hbar\omega \gg kT$ are fulfilled, radical deviations from the classical theory are encountered. The origin of these deviations may be described as follows.

According to the classical theory, the absorption is proportional to the rate of momentum-transfer from electrons to lattice vibrations. At low temperatures ($T \ll \Theta$) this process is severely inhibited by the requirements of energy conservation. In particular, the energy available for the generation of an individual phonon is $\sim kT$. Hence, only the low-frequency, i.e., low-momentum, phonons can be emitted.[1]

In this connection, the chief significance of the quantum-mechanical treatment is that, in the two-stage process described above, a quantum of electromagnetic energy $\hbar\omega$ is imparted to the electron, with the result that the energy available for the generation of a phonon is no longer kT but $\hbar\omega \gg kT$. If, in addition $\hbar\omega \gg k\Theta$ as assumed in the treatment, phonons of all frequencies, and, hence, all possible momenta may be generated. It then follows that the momentum-transfer, and, hence, the absorptivity is much larger than that given by the Drude-Lorentz theory.

The specific result obtained for the absorptivity may be written in the form

$$A_v = \left(\frac{m^*}{4\pi n e^2}\right)^{\frac{1}{2}} \frac{2}{\tau_{eff}}, \tag{1}$$

where n and m^* are electron density and effective mass. In the case of the classical theory, τ_{eff} would be the ordinary conductivity-relaxation time; in the quantum-mechanical case, however, τ_{eff} is given by the formula,

$$1/\tau_{eff} = \tfrac{3}{4}(\Theta/T\tau), \tag{2}$$

where τ is the value of the conductivity-relaxation time at some reference temperature T, *large* compared to the Debye Θ.

The connection between τ_{eff} and the high-temperature relaxation time may be explained as follows. As stated above, the scattering responsible for τ_{eff} involves the emission of the whole phonon spectrum. In this respect it is quite similar to the high temperature relaxation process. In fact, the principal difference between the two is that, in the case of τ_{eff}, the zero-point lattice vibrations are alone active whereas, at high temperatures, the thermally excited vibrations are the primary scattering agents. Now, the intensity ratio of the two types of excitation is, apart from numerical factors, Θ/T; hence, the occurrence of the latter factor in (2).

It is of interest to compare (1) with the absorptivity

$$A_s = \tfrac{3}{4} v_0/c \tag{3}$$

arising from the anomalous skin effect.[2] One has

$$\frac{A_v}{A_s} = \frac{16}{15}\frac{\Theta}{T}\frac{\delta_f}{v_0},$$

where $\delta_f = (m^* c^2/4\pi n e^2)^{\frac{1}{2}}$ is the high-frequency skin depth. In the case of copper, for example, with $\Theta = 310°\text{K}$, $m^* = 1.4m$ (specific heat data), n = atomic density[3] $= 8.5\times10^{22}$ cm^{-3}, room temperature (293°K) conductivity $\sigma = 5.92\times10^{5}$ ohm^{-1} cm^{-1}, $\sigma/v_0\tau = 1.54\times10^{11}$ ohm^{-1} cm^{-2} (reference 3, p. 487), one has $\delta_f = 2.14\times10^{-6}$ cm, $v_0\tau = 3.82\times10^{-6}$ cm, and, hence, $A_v/A_s = 0.63$, which, with A_s equal to 0.28 percent,[4] gives a total absorptivity of 0.46 percent, in moderately good agreement with experiment.[4]

[1] Momentum transfer due to phonon absorption is, of course, also limited when $T \ll \Theta$, since only low-momentum phonons are available. This situation, in contrast to phonon emission, is not altered by the quantum-mechanical consideration presented immediately below.

[2] T. Holstein, Phys. Rev. **88**, 1427 (1952), Eq. (10) with $p=0$ (diffuse reflection of electrons at the metallic boundary). In this equation v_0 is the Fermi velocity.

[3] R. G. Chambers, Proc. Roy. Soc. (London) **A215**, 481 (1952).

[4] M. A. Biondi, preceding Letter [Phys. Rev. **96**, 534 (1954)].

Electron Groups in the Helium Negative Glow

D. H. PRINGLE, *Ferranti Ltd., Edinburgh, Scotland*
AND
W. E. J. FARVIS, *Sanderson Engineering Laboratories, University of Edinburgh, Edinburgh, Scotland*

(Received July 6, 1954)

DETAILED examination of the electron energies in the negative glow of a helium discharge at pressures of the order of 1 mm of mercury has been made with the aid of screened probes. These are similar to the type developed originally by Boyd[1,2] but differ in constructional details. The probes can be rotated and moved radially across the discharge.

The screened probe consists basically of a positive collecting electrode in front of which is placed a fine

mesh grid to which a variable retarding potential can be applied. The fundamental advantage of a probe of this type is that it is possible to separate the positive ion component of current from the electron component directly, and thus avoid the uncertain extrapolation of the high energy part of the curve which is necessary in the analysis of the characteristic of an unscreened Langmuir probe. This particular feature of the screened probe has been used to study the "primary" electron component, which can now be measured with considerable accuracy.

By using this improved technique it has been definitely established that in the negative glow region of an abnormal glow discharge in helium there exist three distinct electron groups of differing mean energies, but each having a Maxwellian distribution: this confirms and extends earlier work by Emeléus and his group.[3,4] The axial variation in the concentration and temperature of the three groups taken with the probe grid facing the cathode of the discharge is reproduced in Fig. 1. It

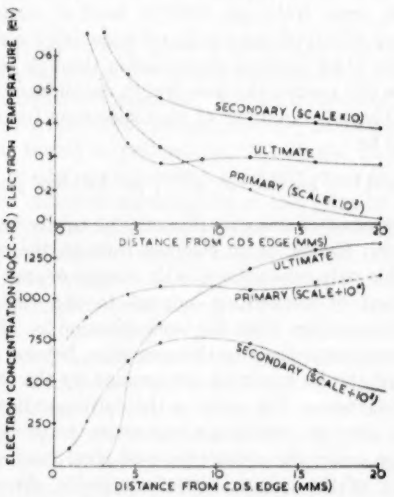

FIG. 1. Electron groups in a 600-μa discharge in 0.58-mm helium. The probe is facing the cathode in the negative glow. (C.D.S. means cathode dark space.)

will be noted that the temperature of the primary or fastest group falls rapidly on moving into the negative glow from the cathode dark space edge while the concentration of this group varies little over the greater part of the negative glow. The directivity of the primary group is established by its failure to be detected when the probe grid is rotated so that it faces the anode: these electrons appear to have originated near the cathode, and to have been accelerated right across the cathode dark space. The "ultimate" or slowest group of electrons, which also has the highest number density, is only detectable after moving some way into the glow. When the probe grid faces the anode, however, the concentration of both this group and the intermediate or "secondary" group is considerable at the cathode dark space (C.D.S.) edge and electrons from these slow groups are detectable even a few millimeters into the dark space. Comparison of the two sets of results thus indicates the presence of a considerable drift of low-energy electrons from the region of maximum concentration, a few millimeters into the flow, towards the cathode dark space. This drift will be maintained by the electron concentration gradient in this region and by the field, for there was found to be a pronounced maximum in the space potential curve near the cathode dark space edge.

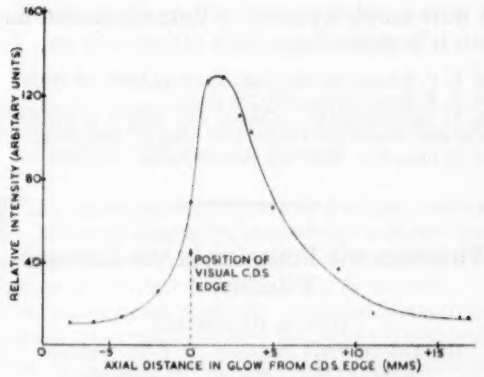

FIG. 2. Relative intensity *vs* axial distance in glow for the line $\lambda = 3888.6$A $(2^3S - 3^3P)$. ×—× Experimental spectroscopic points. ●—● Calculated from screened probe data and excitation probability values.

The physical interpretation of the existence of the two slow electron groups has been the subject of previous discussion. The suggestion advanced by Emeléus and Brown that their existence might be associated with the presence of a minimum in the Ramsauer electron free paths is not valid in the case of helium at this pressure, where no such minimum occurs. A more likely explanation is that the secondary group of electrons are those which have been ejected after collision between the fast primaries and gas atoms, and that they have not had time to reach thermal equilibrium with the slower "ultimate" group which are produced by the degeneration of primary and secondary groups in successive collision to very low energies, before removal by diffusion to the walls. Some support for this picture is provided by the form of the screened probe results.

Agreement has been obtained between spectrophotometric measurements of the relative intensities of the helium spectral lines and the intensities derived from the screened probe data by using Lees'[5] figures for the excitation probabilities. Figure 2 shows a mean curve for the relative intensity of the line 3888.6A $(2^3S - 3^3P)$ as a function of axial position in the negative glow. The two sets of points are seen to be in quite good agreement. No impurity or He II lines were detectable in the helium spectrum observed.

A more complete account of these experiments and results is in preparation.

[1] R. L. F. Boyd, Proc. Roy. Soc. (London) **A201**, 329 (1950).
[2] R. L. F. Boyd, Nature **165**, 228 (1950).
[3] K. G. Emeléus and W. L. Brown, Phil. Mag. **7**, 17 (1929).
[4] Emeléus, Brown, and Cowan, Phil. Mag. **17**, 146 (1934).
[5] J. H. Lees, Proc. Roy. Soc. (London) **A137**, 173 (1932).

Photoelectric Emission in the Extreme Ultraviolet

HANS E. HINTEREGGER
Geophysics Research Directorate, Air Force Cambridge Research Center, Cambridge, Massachusetts

(Received June 1, 1954; revised manuscript received August 2, 1954)

EXPERIMENTAL studies on photoelectric emission from various metals for quantum energies up to 21.2 ev show general features which led the author to the conclusion that the common "free electron"-"surface effect" picture cannot even qualitatively account for the photoelectric phenomena at higher photon energies. These features are:

1. The number of electrons emitted per incident photon (yield Y) starts rising very steeply as soon as the quantum energy increases beyond a certain value (μ) which is appreciably higher than the work function (φ). With further increase of quantum energy, Y reaches a flat maximum followed by a slow decrease. These yields[1] for $h\nu>\mu$ are, by several orders of magnitude, greater than the highest ones known from the many studies at longer wavelengths.

2. The energy distribution curves of emitted electrons practically cut off at $E_1=h\nu-\mu$ and not at the usually much higher maximum $E_s=h\nu-\varphi$ related to the common surface effect.[2]

3. There is a surprising insensitivity to some changes in the surface condition and to exposure to air.

4. Higher temperatures generally seem to reduce the number of electrons of only the lowest energies. This "true" temperature effect appears to cause only a small change in the total emission and should be clearly distinguished from larger, essentially irreversible changes of Y during the first outgassing cycle, and also from possible, closely reproducible types of an "apparent" temperature dependence which may disappear after a sufficient increase in temperature.

The following theoretical model seems to offer a reasonable interpretation of the above phenomena: For sufficiently high photon energies, most of the electron emission originates inside the metal ("volume effect") by removal of an electron from an energy level μ (below vacuum potential). This level is supposed to represent electrons which are much more strongly bound than could be attributed to ordinary conduction electrons, thus offering a high cross section for "photoionization." The same primary process is considered responsible for absorption of the primary radiation. Assuming, as a first approximation, that all the emitted electrons come from one definite level μ, neglecting secondary effects of any kind, and assuming a constant coefficient D for electron transmission through the surface, one can predict the wavelength dependence of the yields. The total number of photoelectrons from level μ should be

$$Y=0.5D\{1-[1+(h\nu-\mu)/\varphi]^{-1}\} \text{ per incident photon.}$$

The derivation of this equation may be briefly outlined as follows: Escape of an electron through the surface is possible only when the kinetic energy related to its component of momentum normal to the surface is equal to or greater than the work function φ. This defines a maximum angle to the normal, α, beyond which no escape can be expected, determined by the relation $(h\nu-\mu)\cos^2\alpha=\varphi$. The ratio of the corresponding solid angle to the total solid angle represents the probability of escape under the assumptions of ideal random distribution of the original directions inside the metal, no absorption along the way to the surface and $D=100$ percent. For $h\nu-\mu\gg\varphi$ and $D=100$ percent the maximum possible yields would be 50 percent, independent of wavelength and nature of metal. The solid curve in Fig. 1 represents the above function for $\mu=9.2$ ev, $\varphi=3.7$ ev and $D=80$ percent and is compared with experimental data for outgassed beryllium.

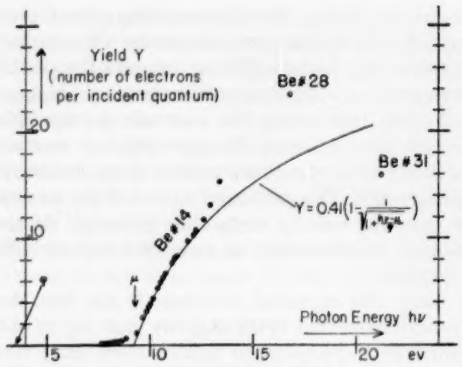

FIG. 1. Photoelectric yields of beryllium.

The energy distribution of emitted electrons, cutting off at $E_1=h\nu-\mu$, is expected to show relatively high numbers of lower energy electrons extending down to $E=0$ because of collisions. There is also an interesting possibility that secondary radiation of maximum quantum energy $h\nu'=\mu-\varphi$ (emitted when a vacancy in level μ is filled by a conduction electron of maximum Fermi-energy) causes a regular photoelectric surface effect whenever $\mu>2\varphi$. This should contribute a subgroup with a maximum energy $E_2=\mu-2\varphi$. For $h\nu-\mu>\varphi$, the primary may cause emission of a secondary

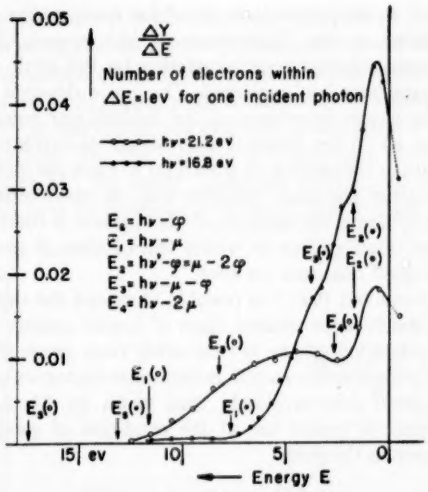

FIG. 2. Differential energy distribution of electrons emitted from beryllium for two different photon energies.

from level φ, adding another group ($E_3=h\nu-\mu-\varphi$). If $h\nu>2\mu$, the primary photoelectron has enough energy for a "secondary ionization" leading to another group having the maximum energy $E_4=h\nu-2\mu$ outside the metal. It should be pointed out that E_1 and E_4 do not depend on the work function explicitly, and E_2 is the same for different wavelengths of the primary radiation. Beryllium has been chosen to illustrate this model, because the simple assumption of only one definite level seems to be a fair approximation. Figure 2 presents experimental energy distribution curves for two different wavelengths ($h\nu=16.8$; 21.2 ev). If one uses $\mu=9.2$ ev as estimated from the experimental spectral yield distribution, and $\varphi=3.7$ ev, then the energies E_1, E_2, E_3, and E_4 derived from this model are those indicated by vertical arrows in Fig. 2. No matter how much of our model will survive further theoretical investigation, the experimental curves of Fig. 2 show clearly that only a negligible number of emitted electrons could have come from levels near the top of the Fermi band, and that a fairly sharp increase of the cross section for photon-electron interactions in a metal occurs at much deeper levels than those which are important for thermal emission, field emission, and the common photoelectric surface effect.[3]

[1] Quantitative indications of extremely high photoelectric yields in the vacuum ultraviolet have been reported by C. Kenty, Phys. Rev. 44, 896 (1933); R. F. Baker, J. Opt. Soc. Am. 28, 60 (1938); H. E. Hinteregger and K. Watanabe, J. Opt. Soc. Am. 43, 604 (1953); Wainfan, Walker, and Weissler, J. Appl. Phys. 24, 1318 (1953).

[2] J. Dickey, Phys. Rev. 81, 612 (1951), found no agreement of photoelectron energy distribution curves for Na and K with the shapes expected from common theories although his highest photon energy was only 6.7 ev.

[3] Some additional publications of interest in connection with this Letter are: I. Tamm and S. Schubin, Z. Physik 68, 97 (1931); M. M. Mann and L. A. Du Bridge, Phys. Rev. 51, 120 (1937); H. Y. Fan, Phys. Rev. 68, 43 (1945).

Nuclear Magnetic Octupole Moments of the Stable Gallium Isotopes*

R. T. DALY, JR., AND J. H. HOLLOWAY
Department of Physics and Research Laboratory of Electronics, Massachusetts Institute of Technology, Cambridge, Massachusetts
(Received July 28, 1954)

THE three zero-field hyperfine structure intervals of the metastable $^2P_{\frac{1}{2}}$ state of Ga^{69} and Ga^{71} have been remeasured[1] to higher precision to establish the existence of a nuclear magnetic octupole moment.

The atomic-beam magnetic resonance method was employed; the transitions were induced by the Ramsey technique[2] of separated oscillating fields. One oscillating field was phase modulated at 93 cps with respect to the other so that the oscillating fields were alternately in phase and 180° out of phase. The alternately in-phase and out-of-phase Ramsey patterns produced were electronically subtracted by a synchronous detector and displayed on an oscilloscope (see Fig. 1).

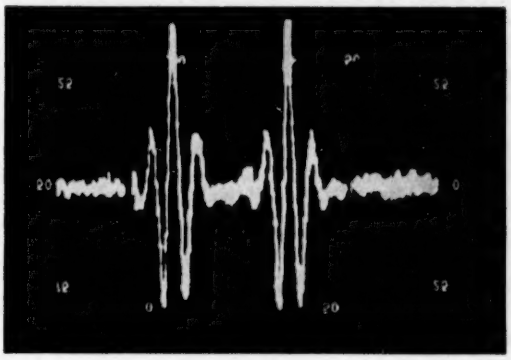

FIG. 1. Typical oscilloscope photograph showing the quadratic Zeeman splitting of the $(F=2, m_F=0)\leftrightarrow(1,0)$ and $(2,1)\leftrightarrow(1,1)$ transitions in an external magnetic field of 0.4 gauss. The Ramsey technique (see reference 2) of separated oscillating fields was used. The two blank portions of the trace calibrate the picture in frequency. The width at half-maximum of each central peak is 500 cps.

The intervals were measured in several external fields ranging from 0.2 gauss to 1 gauss, extrapolated to zero field, and corrected[3] for the perturbing effects of the neighboring $^2P_{\frac{1}{2}}$ ground state as well as the admixture of $(4s)(4p)(5s)$ electronic configuration (see Table I).

The magnetic dipole, electric quadrupole, and magnetic octupole interaction constants,[4] a, b, and c, are calculated from the corrected intervals to be

Ga^{69}

a: 190.794280±0.000150 Mc/sec
b: 62.522470±0.000300 Mc/sec
c: 84±6 cps

Ga^{71}

a: 242.433950±0.000200 Mc/sec
b: 39.399040±0.000400 Mc/sec
c: 115±7 cps,

TABLE I. Measured and corrected hfs intervals of the metastable $^3P_1$ state of Ga^{69} and Ga^{71}.

	Ga^{69} (Mc/sec)	Ga^{71} (Mc/sec)
	Measured	
$F=0\leftrightarrow F=1$	128.27730±0.00020	203.04340±0.00020
$F=1\leftrightarrow F=2$	319.06706±0.00020	445.46960±0.00020
$F=2\leftrightarrow F=3$	634.90183±0.00020	766.69580±0.00020
	Corrected	
$F=0\leftrightarrow F=1$	128.27650±0.00030	203.04133±0.00040
$F=1\leftrightarrow F=2$	319.06373±0.00050	445.46566±0.00060
$F=2\leftrightarrow F=3$	634.90597±0.00060	766.70181±0.00080

where the uncertainty is the root-sum-square of the uncertainties in each of the terms of the equations which yield the interaction constants in terms of the intervals.

The data cannot be explained by the mechanism of off-diagonal terms in the interaction matrix giving rise to octupole-like $(\mathbf{I}\cdot\mathbf{J})^3$ terms, since $(ab)^{69}/(ab)^{71}$ and $(b^{69})^2/(b^{71})^2$ are greater than unity, and c^{69}/c^{71} is less than unity. To within the quoted uncertainty, $a^{69}/a^{71}=c^{69}/c^{71}$.

Schwartz has evaluated the nuclear octupole moment, Ω, and finds

$$\Omega^{69}=(0.107\pm0.02)\times10^{-24} \text{ nuclear magneton cm}^2,$$

and

$$\Omega^{71}=(0.146\pm0.02)\times10^{-24} \text{ nuclear magneton cm}^2.$$

Here, as in the corrected intervals, the quoted uncertainty includes the experimental error and the uncertainty in theoretical evaluation.

The results and experimental procedure will be presented in greater detail in a later paper.

The interest and encouragement of Professor J. R. Zacharias during the investigation are gratefully acknowledged.

* This work was supported in part by the Signal Corps, the Office of Scientific Research, Air Research and Development Command, and the Office of Naval Research.

[1] Previous measurement by P. Kusch and G. E. Becker, Phys. Rev. **73**, 584 (1948).

[2] N. F. Ramsey and H. B. Silsbee, Phys. Rev. **84**, 506 (1951).

[3] We are indebted to C. Schwartz for the calculation of the interval corrections.

[4] For the interaction Hamiltonian, as well as an explicit definition of the constants a, b, and c, see Jaccarino, King, Satten, and Stroke, Phys. Rev. **94**, 1798 (1954). For gallium, the definition of b given should be taken with opposite sign.

Scattering of Gamma Rays by Nucleons*

R. H. CAPPS† AND R. G. SACHS
University of Wisconsin, Madison, Wisconsin
(Received August 23, 1954)

THE cross section for the scattering of photons of energy $\hbar\omega$ by any nonrelativistic, bound system in which the number of particles is conserved has been shown[1] to be proportional to ω^4 for wavelengths large compared to the dimensions of the system if the Thomson scattering and scattering by the static magnetic moment are neglected. The proof depends only on the gauge invariance of the Schrödinger equation, not at all on the detailed distribution of currents and charges in the system. It is natural to raise the question of whether the same theorem may be established for other systems, for example, if the nucleon is treated as a structured system in which the number of pions is not a good quantum number.

It turns out that it is possible to extend the theorem to a much more general class of bound systems, the only condition on the system other than gauge invariance being that its wave function must be normalizable. The proof follows closely that given by Sachs and Austern.[1] It makes use of the condition of gauge invariance in the form

$$e^{g}H_m\{\mathbf{A}\}e^{-g}=H_m\{\mathbf{A}+\text{grad}G\},$$

where $H_m\{\mathbf{A}\}$ is the Hamiltonian of the matter field in the presence of an external electromagnetic field having vector potential $\mathbf{A}$, $G(\mathbf{r})$ is an arbitrary function which in fact may be any electromagnetic field operator that commutes with $\mathbf{A}$, and

$$g=(ie/\hbar c)\int G(\mathbf{r})\rho(\mathbf{r})d^3r,$$

where $\rho(\mathbf{r})$ is the charge density operator of the matter field.

A calculation of the scattering of gamma rays by nucleons by Sachs and Foldy[2] based on nonrelativistic, no-recoil, pseudoscalar meson theory led to a result contrary to the above-stated result. It was found that the scattering amplitude contained a spin-dependent term proportional to the frequency at long wavelength, and that this term was not related to the static magnetic moment.[3] This contradiction has to do with the fact that the unrenormalized nonrelativistic meson theory does not lead to a normalizable state vector as is required to establish the theorem. In fact, the results of SF were finite by virtue of a cancellation between infinite integrals, and in particular, the questionable term resulted from that cancellation. Such cancellations are usually ambiguous and some convergence procedure must be established to eliminate the ambiguity.

The problem has been reconsidered by one of us (RHC) on the basis of a pseudovector interaction containing a finite source. The finite source theory has been made gauge invariant by introducing the necessary line currents. The state vector is then normalizable and all relevant integrals are finite. If the source size is allowed to become small without limit, the scattering amplitude differs from that obtained by SF simply by the elimination of the term that violates the general theorem.

The corrections to SF have been obtained as a function of energy to energies well above pion threshold by this convergence procedure. A further, and important, correction to SF, namely the inclusion of the absorptive part of the scattering, has also been introduced in these calculations. For the purpose of comparison with the results of SF, the newly calculated total scattering of gamma rays by neutrons is shown in Fig. 1 along with

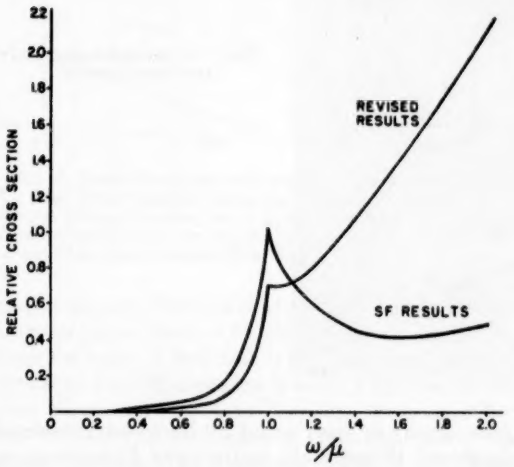

FIG. 1. Total cross section for scattering of gamma rays by neutrons calculated in weak-coupling, no-recoil, pseudoscalar meson theory. Results obtained by SF (see reference 2) are also given for comparison. The energy is given in units of the pion mass, the absolute cross section is proportional to g^4, and the above values are given in units of the Thomson cross section for $g^2/\hbar c = 0.116$.

the old results. The neutron was used for this purpose since the shape of the curve is independent of the choice of coupling constant. That is not the case for the proton because of the interference between Thomson and mesonic scattering. It is to be borne in mind that this is a weak coupling calculation carried only to order g^4 in the meson-nucleon coupling.

The energy dependence of the total cross section of the proton shows an equally important change from the curve obtained by SF, as does the differential cross section. These results will soon be submitted for publication along with a detailed discussion of both the general arguments and the method of calculation.

* This work supported in part by the U. S. Atomic Energy Commission and in part by the University of Wisconsin Research Committee with funds provided by the Wisconsin Alumni Research Foundation.

† National Science Foundation Predoctoral Fellow.

[1] R. G. Sachs and N. Austern, Phys. Rev. **81**, 705 (1951).

[2] R. G. Sachs and L. L. Foldy, Phys. Rev. **80**, 824 (1950). Referred to as SF.

[3] The fact that this term probably should not occur has been pointed out to the authors by Foldy, Kroll, and Goldberger in discussions at Brookhaven National Laboratory.

Nuclear Spin of Np^{239}†

JOHN G. CONWAY AND RALPH D. MCLAUGHLIN
Radiation Laboratory, University of California, Berkeley, California

(Received August 20, 1954)

MICROGRAM quantities of Np^{239}, a 2.3-day beta-gamma activity, were produced by a neutron irradiation of uranium in a high-flux pile. The chemistry used to separate the neptunium from the uranium was an extraction of the Np^{+4} ion into a TTA (thenoyltrifluoroacetone) benzene phase. The intense radiations of the neptunium produced enough peroxide to interfere with the separation, however, sufficient Np^{239} was obtained to conduct the experiment. The Np^{239} was also radiochemically identified and assayed.

The Np^{239} was evaporated on a $\frac{1}{4}$-inch graphite electrode and arced at 15 amperes dc. Neptunium-237, a graphite blank, and an iron arc were photographed for comparison. The spectra were photographed in the second and third order on a 21-foot Paschen-Runge mount with a 30 000-line/inch grating.

The hyperfine pattern of Np^{239} showed two lines and, thus, a spin of $I=\frac{1}{2}(h/2\pi)$ can be assigned to this isotope. The Np^{237} comparison spectrum showed the six-component flag pattern as reported by Tomkins.[1]

The neptunium line at 3999.5A was the best-resolved and widest line observed. The distances from the centers of the first and last components of the line are in the ratio of 1 to 6.9 (± 0.1) for Np^{239} to Np^{237}.

We wish to acknowledge the help of Dr. J. C. Wallmann and Professor B. B. Cunningham, and also the Health Chemistry Department of the Radiation Laboratory, particularly D. Martin, Jr., J. E. Anderson, and T. C. Parsons. We are also indebted to Professor F. A. Jenkins of the Department of Physics of the University of California for the use of the spectrograph and to Dr. G. H. Higgins for the radiochemical assay.

† This work was performed under the auspices of the U. S. Atomic Energy Commission.

[1] F. S. Tomkins, Phys. Rev. **73**, 1214 (1948).

Possible Existence of a New Hyperon*

Y. EISENBERG†
Laboratory of Nuclear Studies, Cornell University, Ithaca, New York

(Received August 26, 1954)

AN unusual event has been found in a stack consisting of 42 Ilford G-5 400-μ stripped emulsions flown for $6\frac{1}{2}$ hours at approximately 100 000 ft from Goodfellow Air Force Base, Texas (41°N geomagnetic latitude). The event is shown in Fig. 1. Particle K_2 comes to rest in the emulsion and gives rise to a star containing 5 visible prongs. Of these 1, 2, and 3 are protons of 1.0, 5.5, and 0.5 Mev, respectively. Track No. 4 is a 29-Mev alpha particle, and the light track L

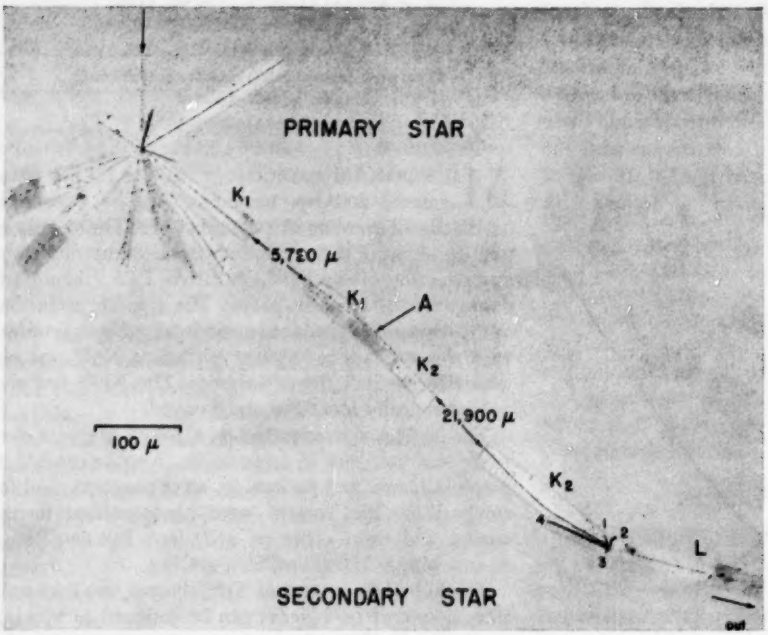

FIG. 1. A microphotograph of the event observed.

has been identified by scattering *vs* ionization measurements as an L (π or μ) meson of kinetic energy 33 ± 4 Mev. Track L leaves the stack after 12 000 μ, therefore the sign of the charge of the particle is unknown. The total visible energy of this sigma star (including the rest mass of the π meson, and not counting binding energies) is 209 ± 4 Mev, therefore it must have been induced by the capture of a heavy meson. Indeed, the mass of K_2 as determined by the scattering *vs* residual range measurements (using the constant sagitta method)[1] from the point A to the sigma star turns out to be $M(K_2)=940\pm200\ m_e$. Also the ionization *vs* residual range curve of K_2 is the expected one for a particle of mass about 1000 m_e (see Fig. 2). We consider, therefore, that the identification of K_2 as a heavy negative meson is established.

In the following K_2 back to its origin it was found that 21 900 μ before the capture star it suffered a 10° deflection (point A in Fig. 1). The part of the track before A is labeled K_1. K_1 originates in a $5+11_p$ star produced by a fast charged particle of energy about 30 Bev (estimated by the angular distribution of the meson shower).

The ionization of K_1 (which crossed 3 different plates from point A to the primary star) is about 10 ± 4 percent above the expected ionization of a K meson having the range of K_2, as determined by extrapolating the ionization-range measurements of K_2 into the region before point A (see Fig. 2). Random nearby background tracks crossing the same emulsions were also grain-counted and failed to show any systematic change in grain density among these plates. This difference in grain density by itself would not have been considered significant. However, the scattering of K_1 turns out to be 3.3 times smaller than the expected scattering of a K meson of the same range. The calculated mean scattering angle of a K meson (mass 965 m_e) between the point A and the primary star is $\bar{\alpha}_{calc}=0.259°/100\ \mu$, whereas the observed value is $\bar{\alpha}_{obs}=0.078\pm0.017°/100\ \mu$. The cell length chosen was 170 μ and the scattering values obtained for the 3 plates were 0.087, 0.067, and $0.081°/100\ \mu$, respectively. The probability of such a difference in the scattering to happen by chance is extremely small.

The three facts mentioned above, namely, (1) the 10° deflection, (2) the ratio of 1.1 ± 0.04 between the grain density of K_1 and K_2, and (3) the difference of $0.181\pm0.017°/100\ \mu$ between the scattering of K_2 and the expected value if $K_2=K_1$, suggest that this is perhaps an example of a decay in flight of a negative hyperon, Y_1^-. The possibility that K_1 and K_2 are both the same particle, a negative hyperon which gives rise to a sigma star (the scattering of K_2 yielding a mass value smaller than that of a hyperon due to the steepness of the tracks and the slight distortion in the emulsions) is excluded since, as mentioned before, the grain-density range measurements of K_2 agree very well with the expected ones for a meson of mass $\sim1000\ m_e$ (see Fig. 2).

There is no particle which is known to decay into a K meson. Therefore, if this is a decay process it must be either an alternate mode of decay of a known particle, or a decay of a new unknown particle. If one assumes that this is a two-body decay, the following

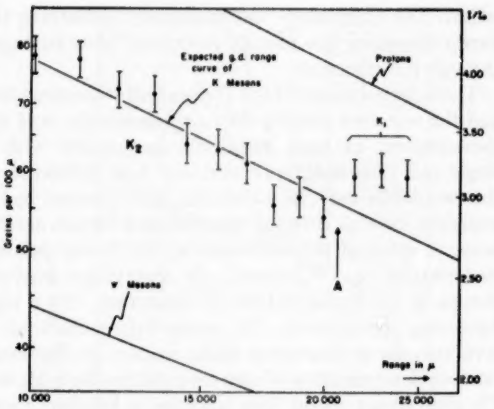

FIG. 2. Grain density *vs* range measurements (log-log scale) of K_2. Solid lines: expected curves for protons, K mesons, and π mesons. (Note: the three points of K_1 are plotted as a function of their distance from the endpoint of K_2. Therefore, it is not the correct grain density-range plot of K_1.)

may be argued. From the relative grain density, the velocity of K_2 is about 1.05 times the velocity of Y_1. Since the angle of deflection is only 10°, the Q value of the decay $Y_1 \rightarrow K_2$+neutral is about 5 Mev no matter what the neutral particle is. Therefore, the mass of Y_1^- will essentially be the mass of K_2 plus the mass of the neutral particle. The known hyperons, Λ^-, Ω^-, have masses equivalent to 1200 and 1320 Mev, respectively. $Y_1^- \rightarrow K_2^- + n$ would require $M(Y_1) = 1440$ Mev, and $Y_1^- \rightarrow K_2^- + K^0$ would require $M(Y_1) = 1000$ Mev. Thus the possibility of an alternate two-body mode of decay of a known hyperon is ruled out.

If it is a three-body decay process, nothing can be said about the Q value. But, even in this case, it seems unlikely to be an alternate three-body decay scheme of a known hyperon because of the following argument. The scheme $Y_1^- \rightarrow K_2^- + n$ (or Λ^0)+neutral+Q can be discarded since it gives for the mass of Y_1^- at least 1440 Mev, which is much over the masses of the known hyperons. If $Y_1^- \rightarrow K_2^- + K^0$ (or π^0)+neutral+Q, by a proper choice of Q and the neutral particle, one can make the mass of Y_1^- agree with the mass of Λ^- or Ω^-. But, by assuming the last decay scheme, we are admitting the possibility that hyperons, which may be regarded as a combination of nucleons and mesons, especially since they are produced at cosmotron energies[2] much below the nucleon production threshold, are capable of disintegrating into mesons only. That would mean annihilation of a nucleon in the decay process, which we do not like to believe possible.

On the assumption that Y_1 is a new particle, we obtain:

if $Y_1^- \rightarrow K_2^- + n + Q$, then $M(Y_1) \approx 2830\ m_e$;
if $Y_1^- \rightarrow K_2^- + \Lambda^0 + Q$, then $M(Y_1) \approx 3160\ m_e$.

A search for a Λ^0 particle in the direction determined by the second of the above schemes failed to yield positive results. The chances of finding the Λ^0, if it existed, were about 25 percent. The direct mass measurements of Y_1 by scattering *vs* ionization gave $M(Y_1) = (3200^{+1200}_{-500})$ electron masses. Either one of the above schemes agrees with the observed mass of Y_1. All errors quoted in the discussion are standard statistical errors.

The author is greatly indebted to Professor G. Cocconi for many helpful discussions and suggestions during the analysis of this event.

* Assisted by the joint program of the U. S. Office of Naval Research and the U. S. Atomic Energy Commission.

† Now at the Weizmann Institute of Science, Physics Department, Rehovoth, Israel.

[1] Biswas, George, and Peters, Proc. Indian Acad. Sci. **38**, 418 (1953).

[2] Fowler, Shutt, Thorndike, and Whittemore, Phys. Rev. **93**, 861 (1954).

Measurement of the Spin and Gyromagnetic Ratio of C^{13} by the Collapse of Spin-Spin Splitting

VIRGINIA ROYDEN
Varian Associates, Palo Alto, California
(Received July 29, 1954)

A PRECISE and interesting measurement of the ratio of the resonance frequency of C^{13} to that of H^1 has been obtained in the course of some experiments on indirect spin-spin interactions between nuclei in molecules.[1-3] The multiplet structure in the nuclear resonance of a given nucleus caused by spin-spin interaction with another nucleus of like or different atomic species can be reduced to a single line by irradiating the second nucleus with an rf magnetic field of its own resonance frequency.[4,5]

The transmitter section of a standard nuclear induction probe was modified so that it tuned to both 30 Mc/sec and 7.5 Mc/sec simultaneously. The proton spectrum of CH_3I enriched with 51 percent C^{13} was observed at 30 Mc/sec under "slow passage" conditions with the high-resolution spectrometer.

The oscilloscope trace showed three peaks, of which the central one was caused by those protons attached to C^{12} (Fig. 1). The two outer proton peaks were separated by 11 milligauss from the central peak as a result of the spin-spin interaction between C^{13} and its companion H^1 nuclei. The number and relative amplitudes

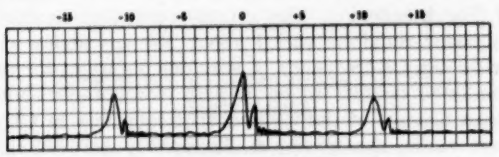

FIG. 1. Proton spectrum at 30 Mc/sec of CH_3I enriched with 51 percent C^{13}. The two outside lines are split by the spin-spin interaction between C^{13} and H^1.

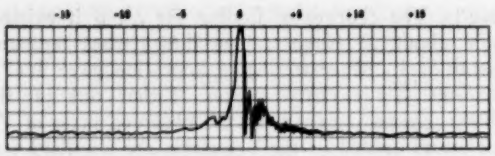

FIG. 2. Proton spectrum at 30 Mc/sec of CH_3I enriched with 51 percent C^{13} with strong 7½ Mc/sec rf-coupled into the transmitter. The side peaks are almost completely collapsed.

of the peaks give a spin of ½ for the C^{13} nucleus, verifying the earlier result obtained by Jenkins from hyperfine structure measurements.[6]

An auxiliary transmitter was link-coupled into the transmitter section of the probe and its frequency varied slightly around 7.544 Mc/sec. At the C^{13} resonance frequency, the two side peaks of the 30-Mc/sec proton spectrum coalesced with the central peak, which doubled in amplitude and became quite sharp (Fig. 2). The frequency of the auxiliary transmitter at which this occurred and the frequency of the 30-Mc/sec transmitter were then counted with a frequency counter.

A comparison of the resonant frequency of C^{13} in CH_3I to that of H^1 in the same molecule gave

$$\nu(C^{13})/\nu(H^1)=0.2514431\pm0.0000005.$$

This result is in excellent agreement with that previously obtained by Poss.[7] The proton resonances in CH_3I and in mineral oil occur, within experimental error, at the same frequency; hence a direct comparison of the above result with that of Poss is justified.

The C^{13} line is a quadruplet, being split into $2I+1$ equally spaced lines, where I refers to the total spin of ½ for the three protons in CH_3I. Since the side peaks of the proton resonance split out symmetrically as a function of frequency as the auxiliary oscillator is tuned above and below the coalition frequency, that frequency was assumed to be at the center of the C^{13} quadruplet.

It is interesting to note that although the 7.5-Mc/sec rf field had a peak-to-peak amplitude of 0.75 gauss, a shift in frequency of 30 to 40 cps was sufficient to broaden the central peak markedly and to decrease its amplitude proportionately. This is more sensitive by a factor of ten than one is led to expect on the basis of rf line broadening. The crystal controlled auxiliary oscillator could be varied about 300 cps above and below the C^{13} frequency, a variation sufficient for the irradiated doublet to be in part reconstituted. Nine measurements of the C^{13} and H^1 frequencies in CH_3I were made, the maximum discrepancy between any two C^{13} measurements being 20 cps.

The magnetic field was swept with a 50-milligauss recurrent sawtooth sweep, and it was suggested that the measurement of the frequency ratio might be in question by the amount by which the position of the proton resonance in the magnetic field was undetermined. The uncertainty was minimized by keeping the sweep frequency low enough to ensure "slow passage" through the resonance.

The incorporation of both the nucleus to be measured and the reference nucleus into a single sample, and the measurement of both resonance frequencies with a single coil gives assurance that any field difference at the two nuclei must be a chemical shift inherent in the molecule since all external experimental factors are the same. A merit of this technique is that it was possible to determine the C^{13} frequency by observing a sensitive change in the strong narrow H^1 resonance with a high resolution spectrometer. No sweep field calibration is involved, the measurement being reduced to the simultaneous determination of two frequencies. Both H_1 and F^{19} give strong sharp lines and make excellent companions for more refractory nuclei.

The author wishes to thank C. Reilly of Shell Development Research Laboratories, Emeryville, California for supplying the sample of $C^{13}H_3I$ used in this experiment.

[1] N. F. Ramsey and E. M. Purcell, Phys. Rev. **85**, 143 (1952).
[2] E. L. Hahn and D. E. Maxwell, Phys. Rev. **84**, 1246 (1951).
[3] Gutowsky, McCall, and Slichter, Phys. Rev. **84**, 589 (1951).
[4] J. Shoolery and M. Packard (to be published).
[5] Bloch, Arnold, and Anderson have reported by private communication the application of this technique to the protons in ethyl alcohol.
[6] F. A. Jenkins, Phys. Rev. **72**, 169 (1947).
[7] H. L. Poss, Phys. Rev. **75**, 600 (1949).

Differential Cross-Section Measurements for 1-Mev Bremsstrahlung*

J. W. MOTZ AND WILLIAM MILLER
Radiation Physics Laboratory, National Bureau of Standards, Washington, D. C.

(Received August 30, 1954)

THE energy and angular distribution of the bremsstrahlung, produced in thin targets of beryllium and gold by electrons with a kinetic energy of one Mev, has been measured with a large NaI(Tl) scintillation spectrometer. The electron beam from the NBS constant-potential accelerator[1] passed through baffle openings into the target chamber, which was electrically insulated from the accelerator tube to serve as a Faraday cup. Target currents from 10^{-10} to 10^{-6} amperes were measured with 2-percent accuracy by a Higinbotham-Rankowitz type current integrator.[2] The targets used were a 0.22-mg/cm² gold foil, a 0.43-mg/cm² gold foil, and a 4.3-mg/cm² beryllium foil. The results obtained with the two gold targets indicated that electron energy loss and scattering in the foils were negligible. The radiation emitted from the target at an angle θ with respect to the direction of the incident electron beam was detected by the spectrometer with an angular resolution of approximately one degree.

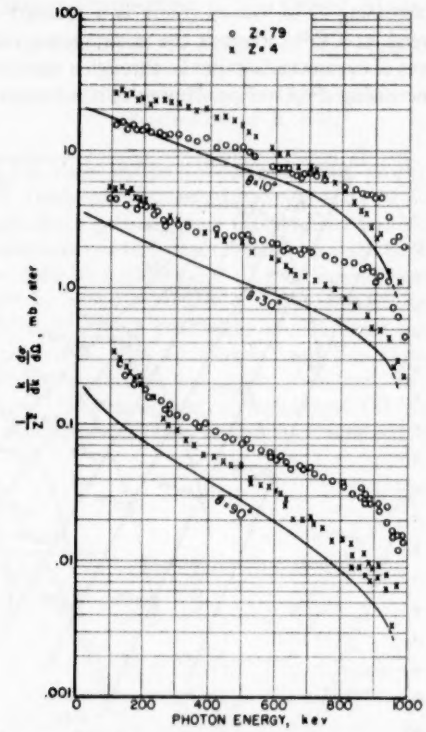

FIG. 1. Differential cross section for 1-Mev bremsstrahlung at photon energies k and angles θ, of 10°, 30°, and 90°. The fractional standard deviations of the experimental points due to counting rate statistics are less than 10 percent for points below 800 kev, less than 20 percent for points below 900 kev, and less than 30 percent for points below 1000 kev. The theoretical cross sections are shown by the solid curves which were obtained from the results of Sauter (see reference 5) and Gluckstern and Hull (see reference 5).

The radiation passed to the spectrometer through a 15-mil Al window in the evacuated target chamber. Electrons traveling in the direction of this window were deflected by an electron trap employing a permanent magnet. To account for the contribution of the radiation arising from normal background and from electron scattering in the chamber, measurements were made with the target foil in and out of the electron beam.

The spectrometer consisted of a $\frac{3}{8}$-inch diameter 12-inch long collimator, a 5-inch diameter 4-inch long NaI(Tl) crystal, a type K1198 Dumont 5-inch diameter photomultiplier tube, and lead shielding extending 12 inches in front, 3 inches on the sides, and $\frac{1}{2}$ inch in the back of the crystal housing. The pulse-height distribution produced by incident radiation was measured with a 12-channel analyzer having approximately 15-kilovolt window widths which were calibrated during runs with a motor-driven sliding pulser. The pulse-height response of this spectrometer to monoenergetic photons appears as a line shape with a low energy tail[3] which replaces the prominent Compton escape peak found with small crystals. This response was characterized by a matrix whose indices corresponded to pulse height and photon energy. Thus, a matrix element specified the counting rate at a given pulse height for photons of a given flux density and of a given energy. These matrix elements were found by interpolation between the response curves measured for the photons from sources of Co^{60}(1.17 Mev, 1.33 Mev),[4] Cs^{137} (0.662 Mev),[4] Hg^{203} (0.279 Mev),[4] and Cd^{109} (0.087 Mev).[4] The matrix determined a set of simultaneous linear equations relating any pulse-height distribution to the corresponding input photon spectrum. In the present case, the bremsstrahlung yielded pulse-height distributions which fell off rapidly with increasing pulse height so that a line-by-line solution of the simultaneous equations was permissible with the aid of a simple perturbation type calculation.

Measurements of the bremsstrahlung spectra were made at angles of 10°, 30°, and 90°, and yielded values of the differential cross section shown in Fig. 1. For comparison, the differential cross section integrated over electron angle, as given by Sauter[5] on the basis of the Born approximation, is shown by the solid lines. It is seen that (a) the prediction of the large intensity variation with angle θ (two orders of magnitude between 10° and 90°) is confirmed, (b) although the measured integrated intensity goes roughly as Z^2, the measured spectral shape is Z dependent, and (c) the theoretical curves appear to underestimate the measured cross sections.[6] Measurements at other angles and materials, and for 500-kev electrons are now in progress.

We thank Dr. H. O. Wyckoff for helpful discussions, and Mr. F. S. Frantz for his help in carrying out the measurements.

* Work supported by the U. S. Atomic Energy Commission.

[1] E. E. Charlton and H. S. Hubbard, Gen. Elec. Rev. **43**, 272 (1940).

[2] W. A. Higinbotham and S. Rankowitz, Rev. Sci. Instr. **22**, 688 (1951).

[3] R. S. Foote and H. W. Koch, Rev. Sci. Instr. (to be published).

[4] *Nuclear Data*, National Bureau of Standards Circular 499 (U. S. Government Printing Office, Washington, D. C., 1950).

[5] F. Sauter, Ann. Physik (5) **20**, 404 (1934). For 1-Mev electrons, the effect of screening will cause slight reductions (up to 10 percent depending on atomic number, and photon energy and angle) in the theoretical curves as determined from the recent calculations by R. L. Gluckstern and M. H. Hull, Jr., Phys. Rev. **90**, 1030 (1953).

[6] Earlier experiments made in this energy range support this observation. See H. Klarmann and W. Bothe, Z. Physik **101**, 489 (1936).

Correlation of Spontaneous Fission Half-Lives

M. H. STUDIER AND J. R. HUIZENGA
Argonne National Laboratory, Lemont, Illinois
(Received August 30, 1954)

EMPIRICAL correlations which can be used in predicting the properties of undiscovered elements and isotopes are of great practical value. Many such

relationships involving alpha-disintegration and spontaneous fission rates have been published.[1–5] Kramish[4] correlated the competition between alpha decay and spontaneous fission with the fissionability parameter Z^2/A. As a measure of the above competition,[6] he used the ratio of the spontaneous fission half-life to the alpha-disintegration half-life, R, and showed a relationship between consecutive alpha-decay products.

Recently, alpha disintegration and spontaneous fission half-lives of a number of newly discovered nuclides have been measured (data and references given in Table I). We have observed that linear lines connecting (on semi-logarithmic paper, see Fig. 1) even-even nuclides differing by two Z units and six A units give better extrapolated values of R than linear lines connecting alpha-decay products. On a particular line ($\Delta Z=2$, $\Delta A=6$; solid lines), the values of R decrease with increasing values of Z^2/A. In general alpha-disintegration half-lives of even-even isotopes of a given element beyond the double closed shell at lead decrease with increasing Z^2/A values (there is a reversal[7,8] of this trend at Cf^{252}), whereas the spontaneous fission half-lives of even-even isotopes go through a maximum[5] with increasing Z^2/A values. However, it is interesting to note that R values increase with increasing Z^2/A values for the even-even isotopes of a given element (dashed lines in Fig. 1).

TABLE I. Alpha-disintegration and spontaneous fission half-lives.

Isotope	$T_{\frac{1}{2}}(\alpha)$ (yr)	Ref.	$T_{\frac{1}{2}}$(s.f.) (yr)	Ref.	$T_{\frac{1}{2}}$(s.f.)/$T_{\frac{1}{2}}(\alpha)$
Th^{230}	8.0×10^{4}	a	$\geq1.5\times10^{17}$	i	$\geq1.9\times10^{12}$
Th^{232}	1.39×10^{10}	a	1.4×10^{18}	i	1.0×10^{8}
Pa^{231}	3.4×10^{4}	a	$\geqslant10^{16}$	i	$\geqslant2.9\times10^{11}$
U^{232}	74	b	$\geqslant8\times10^{12}$	i	$\geqslant1.1\times10^{11}$
U^{233}	1.6×10^{5}	a	$\geqslant3\times10^{17}$	i	$\geqslant1.9\times10^{12}$
U^{234}	2.5×10^{5}	a	1.6×10^{16}	i	6.4×10^{10}
U^{235}	7.1×10^{8}	a	1.8×10^{17}	i	2.5×10^{8}
U^{238}	2.4×10^{7}	a	2×10^{16}	i	8.3×10^{8}
U^{238}	4.5×10^{9}	a	8.0×10^{15}	i	1.8×10^{6}
Np^{237}	2.2×10^{6}	a	$\geq4\times10^{16}$	i	$\geq1.8\times10^{10}$
Pu^{236}	2.7	a	3.5×10^{9}	i	1.3×10^{9}
Pu^{238}	90	a	4.9×10^{10}	i	5.4×10^{8}
Pu^{239}	2.44×10^{4}	a	5.5×10^{15}	i	2.3×10^{11}
Pu^{240}	6.6×10^{3}	a	1.2×10^{11}	i	1.8×10^{7}
Pu^{242}	3.8×10^{5}	a	6.7×10^{10}	i	1.8×10^{5}
Am^{241}	4.7×10^{2}	a	$\geq1.4\times10^{13}$	i	$\geq3.0\times10^{10}$
Cm^{240}	7.3×10^{-3}	a	1.9×10^{6}	i	2.6×10^{7}
Cm^{242}	0.445	a	7.2×10^{6}	i	1.6×10^{7}
Cm^{244}	18.4	d	1.4×10^{7}	i	7.6×10^{6}
Cm^{246}	4×10^{3}	d	...	...	...
Bk^{249}	...	...	$\geq2\times10^{8}$	e	...
Cf^{246}	4.1×10^{-3}	a	2.1×10^{9}	i	5.1×10^{5}
Cf^{248}	0.56	a	7×10^{9}	i	1.3×10^{9}
Cf^{249}	470	e,f	$\geq5\times10^{6}$	e	$\geq1.2\times10^{4}$
Cf^{250}	10	e,f	1.5×10^{4}	e,f,j	1.5×10^{3}
Cf^{252}	2.2	e,f	66	e,f	3.0×10^{1}
99^{253}	5.3×10^{-2}	g,h	$\geq3\times10^{8}$	g	$\geq5.7\times10^{6}$
99^{254}	...	...	≥10	g	...
100^{254}	3.8×10^{-4}	g,h	0.60	g,h	1.6×10^{3}

[a] References given in review by Hollander, Perlman, and Seaborg, Revs. Modern Phys. **25**, 602–612 (1953).
[b] Sellers, Stevens, and Studier, Phys. Rev. **94**, 952 (1954).
[c] J. F. Mech *et al.* (private communication).
[d] Friedman, Harkness, Fields, Studier, and Huizenga, Phys. Rev. **95**, 1501 (1954).
[e] Diamond, Magnusson, Mech, Stevens, Friedman, Studier, Fields, and Huizenga, Phys. Rev. **94**, 1083 (1954); L. B. Magnusson *et al.*, Phys. Rev. (to be published).
[f] Ghiorso, Thompson, Choppin, and Harvey, Phys. Rev. **94**, 1081 (1954).
[g] Fields, Studier, Mech, Diamond, Friedman, Magnusson, and Huizenga, Phys. Rev. **94**, 209 (1954).
[h] Choppin, Thompson, Ghiorso, and Harvey, Phys. Rev. **94**, 1080 (1954).
[i] References given in review by Huizenga, Manning, and Seaborg, *The Actinide Elements* (McGraw-Hill Book Company, Inc., New York, 1954), Chap. 20, National Nuclear Energy Series, Plutonium Project Record, Vol. 14A, Div. IV.
[j] Fields, Studier, Magnusson, and Huizenga, Nature **174**, 265 (1954).

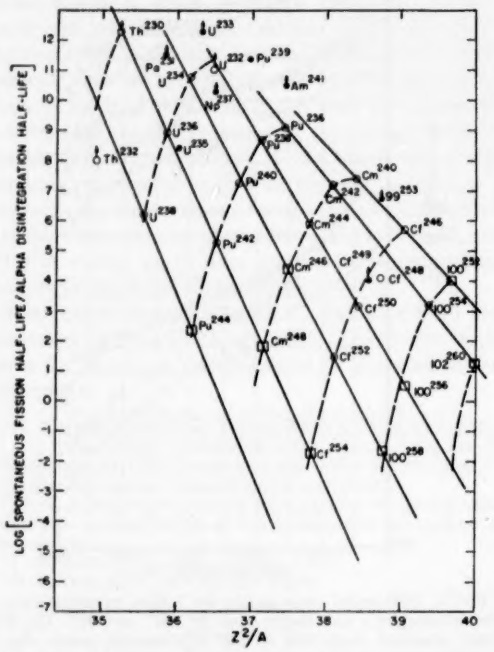

FIG. 1. Plot of the ratios of the spontaneous fission half-lives to the alpha-disintegration half-lives *vs.* the fissionability parameter Z^2/A. The solid lines connect even-even nuclides with $\Delta Z=2$ and $\Delta A=6$. Dashed lines connect even-even isotopes of a given element. Open circles ○, R values of even-even nuclides; solid circles ●, R values of odd nuclides; and squares □, predicted R values.

It can be seen from Fig. 1 that the value of R for Th^{232} appears low indicating that the measured spontaneous fission half-life may be a lower limit. Cf^{252} with an R value of 30 exhibits the largest spontaneous fission decay branching measured to date. The predicted R value for Cf^{254} from Fig. 1 is 0.018, which means that Cf^{254} would decay mainly by spontaneous fission.

[1] Perlman, Ghiorso, and Seaborg, Phys. Rev. **77**, 26 (1950); earlier references to alpha systematics are given in this paper.
[2] W. J. Whitehouse and W. Galbraith, Nature **169**, 494 (1952).
[3] G. T. Seaborg, Phys. Rev. **85**, 157 (1952).
[4] A. Kramish, Phys. Rev. **88**, 1201 (1952).
[5] J. R. Huizenga, Phys. Rev. **94**, 158 (1953).
[6] J. Frenkel, J. Phys. (U.S.S.R.) **10**, 533 (1946).
[7] Ghiorso, Thompson, Higgins, Harvey, and Seaborg, Phys. Rev. **95**, 293 (1954).
[8] Magnusson, Studier, Fields, Stevens, Mech, Friedman, Diamond, and Huizenga, Phys. Rev. (to be published).

Some Properties of Nuclei of Mass 19

G. A. JONES, W. R. PHILLIPS, C. M. P. JOHNSON, AND D. H. WILKINSON
Cavendish Laboratory, Cambridge, England
(Received August 20, 1954)

WE have sought to determine the properties of some of the states of nuclei of mass 19 since this region of the periodic table is of interest in illustrating competition between the $1d_{5/2}$ and $2s_{1/2}$ shells. This we have done by investigating (i) the Coulomb excitation of F^{19} by alpha particles; (ii) the positron decay of Ne^{19}; and (iii) the beta decay of O^{19}. Some results of (i) have been reported already[1] and similar work on Coulomb excitation has been published by other groups.[2,3] The results of investigations (ii) and (iii) are summarized in Fig. 1. Previous work on Ne^{19} has been confined to positron energy and lifetime measurements and to a search for high-energy gamma rays,[4] and on O^{19} to lifetime and beta energy and branching ratio measurements.[5]

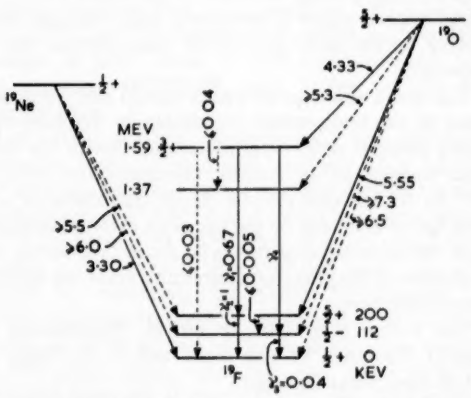

FIG. 1. Properties of Ne^{19}, F^{19}, and O^{19}. The numbers on the beta transitions are their $\log_{10} ft$ values; the numbers on the gamma transitions are their abundances in the decay of O^{19} relative to that of the 200-kev gamma ray as unity. The ground state of F^{19} has been assumed to be $(\frac{1}{2}+)$; the other assignments emerge from the present study. (The limit on the abundance of the transition between the 1.59- and 1.37-Mev states assumes that the decay of the latter is prompt.)

Our observation that the decay of Ne^{19} leads to the ground state of F^{19} shows that no Coulomb cross-over of the F^{19} ground state triplet[6] has been induced and that the ground state of Ne^{19} is unquestionably $(\frac{1}{2}+)$. The limits on the ft values of the decay to the excited states of F^{19} are based on the absence of low-energy gamma rays. The large limit on the ft value for the decay of O^{19} to the 112-kev state of F^{19} makes it very probable that that transition is at least first forbidden as probably also, but with less certainty, is that to the F^{19} ground state. This observation, together with the Coulomb excitation data, the absence of the transition between the 200- and 112-kev states and our observations that the lifetime of the 200 kev state is $(1.0\pm0.2)\times10^{-7}$ sec while that of the 112-kev state is $\ll10^{-8}$ sec demand the spin and parity assignments shown for the first two excited states of F^{19}. These conclusions are identical with those reached by the California Institute of Technology workers[3,7-9] using largely different arguments. The assignment for the 1.59-Mev state we reach from the beta-decay of O^{19}, by a study of γ_4 and by an angular correlation measurement between γ_1 and γ_2 (some $\frac{2}{3}$ of the full correlation remains in Teflon). Our assignment for the ground state of O^{19} accepts the ft value of the ground-state beta transition as evidence against an allowed transition; $(\frac{3}{2}+)$ must remain a possible assignment since this evidence is not conclusive.

We may note that our direct lifetime measurement for the 200-kev state agrees with that determined by the recoil method[8] (0.8×10^{-7} sec with factor of 2 uncertainty) and with the matrix element as determined by Coulomb excitation.[1-3]

Our measurements of the gamma-ray energies are: $\gamma_1=1.366\pm0.008$ Mev; $\gamma_2=199.6\pm1.5$ kev; $\gamma_3=111.5\pm1.5$ kev.

The positions and properties of the even-parity states of the whole mass-19 system, including matrix elements for gamma and beta decay, are remarkably well described by a shell-model computation of Elliott and Flowers.[10]

A full account of this work will be presented shortly.

[1] G. A. Jones and D. H. Wilkinson, Phil. Mag. **45**, 230 (1954).
[2] N. P. Heydenburg and G. M. Temmer, Phys. Rev. **94**, 1252 (1954).
[3] Sherr, Li, and Christy, Phys. Rev. **94**, 1076 (1954).
[4] G. Schrank and J. R. Richardson, Phys. Rev. **86**, 248 (1952).
[5] E. Bleuler and N. Zünti, Helv. Phys. Acta **20**, 195 (1947).
[6] C. Mileikowsky and W. Whaling, Phys. Rev. **88**, 1254 (1952).
[7] Peterson, Barnes, Fowler, and Lauritsen, Phys. Rev. **94**, 1075 (1954).
[8] Thirion, Barnes, and Lauritsen, Phys. Rev. **94**, 1076 (1954).
[9] R. F. Christy, Phys. Rev. **94**, 1077 (1954).
[10] J. P. Elliott and B. H. Flowers (to be published).

Alpha-Gamma Directional Correlation Measurements with Liquid Film Sources

T. B. NOVEY
Chemistry Division, Argonne National Laboratory, Lemont, Illin oi
(Received August 30, 1954)

A SERIES of earlier measurements[1-3] of alpha-gamma directional correlation in Th^{228}, Th^{230}, Ra^{224}, Ra^{226}, Pa^{238}, Am^{241}, and others has yielded anisotropies lower than theoretically predicted. These discrepancies have been explained on the basis of the electric quadrupole interaction due to the presence of large electric field gradients in the solid sources used. That these attenuations are due to external field interactions has been indicated by the experiments of Milton

and Fraser[3] where the anisotropy of Am^{241} was found to be a function of the time delay between the coincident radiations.

The attenuations due to quadrupole interaction can also be reduced or eliminated by the use of thin liquid film sources. This allows the correlations to be studied at more convenient resolving times. The Am^{241} alpha—60-kev gamma correlation has been studied in this way.[4]

The sources were prepared by placing a small drop ($\lesssim 1$ mm^3) of aqueous solution on a rubber hydrochloride film (0.6 mg/cm^2) mounted on an aluminum ring, and covering with a thin glass or mica disk 1 cm^2 in area. Capillary action spreads a liquid film over the defined area. The alpha particles can penetrate the 0.001-in. solution layer and the plastic film and can be detected by a scintillating crystal without serious scattering.

The source was mounted in a vertical plane in the plastic vacuum chamber of the angular correlation apparatus previously described.[5] The chamber was filled with hydrogen bubbled through a solution of the same composition as the source in order to inhibit source evaporation and to reduce alpha absorption in the gas. A coincidence resolving time $2\tau=0.3$ microsecond was used.

Experiments were made with $6N$ H_2SO_4 and $1N$ $HClO_4$ solutions as well as with a dried source of americium nitrate. The results, Table I, show isotropy

TABLE I. Alpha—60-kev gamma anisotropy in Am^{241} solid and liquid sources.

Source	Anisotropy, A
Am^{241} nitrate, dry	0.003 ± 0.007
Am^{241} in $6N$ H_2SO_4	$0.07\ \pm0.02$
Am^{241} in $1N$ $HClO_4$	$0.16\ \pm0.02$

from the polycrystalline source, partial attenuation in the H_2SO_4 source, and a maximum experimental correlation in the $HClO_4$ source in agreement with the value of Milton and Fraser[3] for very short resolving time. It may be noted here that apparently the nuclear recoil does not cause an appreciable attenuation, probably because of its very short duration. The form of the correlation is that expected for a decay involving a dipole gamma transition, $W(\theta)=1+A\cos^2\theta$ or $W(\theta)=1+a_2P_2(\cos\theta)$ with $A=-0.16$ or $a_2=-0.11$.

A typical run is shown in Fig. 1 by plotting $W(\theta)$ *versus* $\cos^2\theta$.

The change in anisotropy with the two acids may indicate an effect due to an asymmetry in the coordination group surrounding the americium ions. Sulfuric acid is a weaker acid than perchloric in the sense that sulfate ions would tend more readily to complex the metal ion and displace one or more water molecules from its coordination sphere. This could produce an asymmetrical grouping and a corresponding electric field gradient at the nucleus that does not vary rapidly

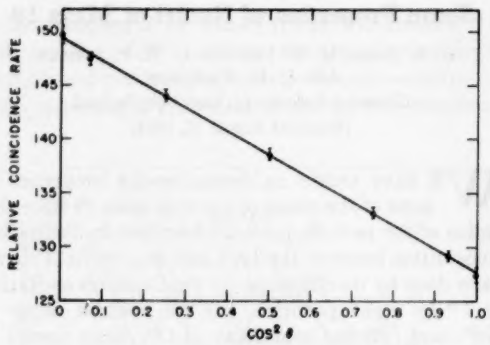

FIG. 1. Alpha-gamma directional correlation, Am^{241} in $1N$ $HClO_4$, $W(\theta)=1+A\cos^2\theta$, $A=-0.15$.

compared to the lifetime of the intermediate state and thus will not average out even in the liquid state. One might expect larger attenuations with stronger complexing agents such as chloride ions, acetate ion, or versene.

The use of this type of source should allow measurement of the undisturbed correlation in the even-even heavy element decays and determination of the magnetic moments of the excited states associated with the 10^{-6} to 10^{-9} second electric dipole transitions in odd-even heavy elements by the use of an external magnetic field. Measurements of this type are in progress as well as studies of the effect of complexing upon the quadrupole interaction.

The author is grateful to Dr. H. Frauenfelder for helpful discussion of this work and to R. Pairs for aid in these measurements.

[1] Beling, Feld, and Halpern, Phys. Rev. **84**, 155 (1951).
[2] G. M. Temmer and J. M. Wyckoff, Phys. Rev. **92**, 913 (1953).
[3] J. C. D. Milton and J. S. Fraser, Phys. Rev. **95**, 628 (1954); **94**, 795 (1954).
[4] A technique using thin metallic gallium liquid films has been used by F. Gimmi and E. Heer to measure the unattenuated conversion electron-gamma correlation in In^{111}: Z. Physik (to be published).
[5] T. B. Novey, Phys. Rev. **89**, 672 (1953).

New Long-Lived Isotopes of Lead

J. R. HUIZENGA AND C. M. STEVENS
Argonne National Laboratory, Lemont, Illinois
(Received August 23, 1954)

MINIMUM half-lives of 500 years were set for Pb^{202} and Pb^{205} on the basis of assumed counting efficiencies and estimated yields of these lead isotopes from a deuteron bombardment of thallium.[1] Duckworth *et al.*[2] set an upper limit of abundance of 0.0004 percent for Pb^{202} in natural lead and concluded that stable Pb^{202} probably does not exist. If the elements are assumed to be 4×10^9 years old and the original cosmic abundance of Pb^{202} equal to that of Pb^{204}, the half-life

of Pb^{202} could be as long as 3×10^8 years and still be undetected in nature (i.e., below the 0.0004 percent abundance limit).

Recently, two short-lived isomers of Pb^{202} were reported,[3,4] and a search for Pb^{205} was described[5] in which the authors concluded that its half-life is longer than 10^6 years by assuming that the counting efficiency of Pb^{205} is equal to that of Pb^{203}.

The possible importance of Pb^{202} and Pb^{205} in cosmological problems led us to search for these isotopes by long deuteron bombardments of thallium. Two samples of thallium were bombarded in the Argonne cyclotron; (1) 0.003-inch thallium foil wrapped in 0.0005-inch aluminum foil was bombarded (cooled with air jet) for eight hours with 25 microamperes of 21-Mev deuteron ions and (2) 2.4 g (10 cm^2 area) of thallium soldered into a depression in a water-cooled copper target was bombarded for eight hours with 100 microamperes of 21-Mev deuteron ions. The reactions $Tl^{203}(d,3n)Pb^{202}$ and $Tl^{205}(d,2n)Pb^{205}$ should produce the unknown lead isotopes in good yields in both bombardments with the expected Pb^{202}/Pb^{205} ratio higher in the first bombardment.

Lead from the first bombardment was chemically separated from thallium and analyzed in a 12-inch, 60° mass spectrometer with a multiple filament surface ionization source.[6] Pb^{202} was detected in approximately 0.07 mole percent. A $(W^{186}O^{16})^+$ ion background, comparable in intensity to the Pb^{202} ion peak, was subtracted by measuring the $(W^{184}O^{16})^+$ intensity (A = 200). The detection of Pb^{205} was much more uncertain in that about 80 percent of the mass 205 peak was due to Tl^{205} ions, which correction was made from the measured intensity of the Tl^{203} ion peak. The isotopic abundance of the Pb^{205} was approximately 0.04 mole percent. The $(d,3n)$ to $(d,2n)$ cross section ratio for 18–21 Mev deuterons on bismuth is about four.[7] Assuming this ratio for the thallium reactions in a 0.003-inch thallium foil and correcting for the normal abundance of the thallium isotopes give a calculated ratio of Pb^{202} to Pb^{205} of 1.7 in agreement with the observed ratio.

The lead from the second thallium bombardment was given a better separation from thallium, but the large natural lead impurity of this sample made a mass spectrometric determination of lead 202 and 205 impractical. This sample was, however, valuable for a study of the nuclear properties of lead 202 and 205. After a growth period sufficiently long to produce Tl^{202} in secular equilibrium with Pb^{202}, a chemical separation of lead and thallium was made. The radiations of these fractions were examined in the L and K x-ray energy regions with a gamma scintillation spectrometer which had a 0.020-inch beryllium window in front of the sodium iodide crystal. The thallium fraction decayed with a 12-day half-life and contained prominent gamma peaks of about 10 and 72 kev. Gamma energy calibration in the K x-ray energy region was made with the K x-rays observed in the decay of Hg^{203} (74 kev). The K x-ray energy and the half-life of the nuclide growing into the lead fraction are characteristic of Tl^{202}, confirming the presence of an electron-capturing Pb^{202}. The lead fraction contained a prominent gamma peak at approximately 10 kev. A limit on the K x-ray activity in the lead fraction was set at less than one-half percent the K x-ray activity of an equilibrium Tl^{202} sample. Pb^{202} decays therefore predominantly by electron-capturing processes other than K capture.

The intensity ratio of the K to L x-rays (uncorrected for fluorescence yields) for the Tl^{202} was 2.6. By assuming fluorescence yields of 0.9 and 0.3, respectively, for K and L electron ionizations in mercury and 0.7 L-electron vacancies per K electron removed and by neglecting the small x-ray contribution[8] from conversion of the 0.43-Mev gamma rays, it appears that Tl^{202} decays about 70 percent by K and 30 percent by L orbital electron capture. A half-life of approximately 3×10^5 years for Pb^{202} was calculated from the equilibrium Tl^{202} activity and an assumed 0.5-barn average cross section for the $Tl^{203}(d,3n)Pb^{202}$ reaction in the second bombardment.

The intensity ratio of the L x-rays in an equilibrium sample of Tl^{202} to the parent lead is 1.6. This is possibly evidence for concluding that about 40 percent of the Pb^{202} decay goes by M orbital electron capture.

It is difficult to set a lower limit on the Pb^{205} half-life since the calculated decay energy[5] of Pb^{205} is in doubt. The neutron binding energy of Pb^{205} calculated

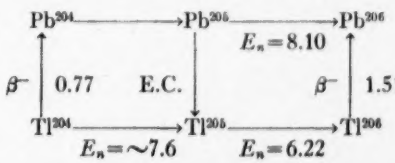

from a closed cycle by using measured beta decay energies and neutron binding energies is 6.46 Mev. One would expect this binding energy to be greater than 6.72 Mev, the neutron binding energy of Pb^{207}. Therefore, one or both of the measured thallium neutron binding energies may be too small. Increasing the value of the neutron binding energy of Tl^{206} would reduce the calculated decay energy of Pb^{205}, possibly below the necessary energy for K electron capture. Since the Pb^{205} yield in the second bombardment was probably comparable to the Pb^{202} yield, the Pb^{205} K-capture half-life is greater than 6×10^7 years. The L-capture half-life of Pb^{205} is certainly as long as that of Pb^{202} and probably much longer since the yield of L x-rays is already insufficient to account for all the Pb^{202} decay.

It is a pleasure to acknowledge the help of J. P. Fitzpatrick for preparing the targets and making the necessary cyclotron bombardments, D. W. Engelkemeir

for the use of his gamma-scintillation spectrometer, and A. L. Harkness for his assistance in some of the mass spectrometer measurements.

[1] Templeton, Howland, and Perlman, Phys. Rev. **72**, 766 (1947).
[2] Duckworth, Black, and Woodcock, Phys. Rev. **75**, 1616 (1949).
[3] N. J. Hopkins, Phys. Rev. **88**, 680 (1952).
[4] D. Maeder and A. H. Wapstra, Phys. Rev. **93**, 1433 (1954).
[5] P. F. D. Shaw and J. R. Prescott, Proc. Phys. Soc. (London) **A67**, 283 (1954).
[6] M. G. Inghram and W. A. Chupka, Rev. Sci. Instr. **24**, 518 (1953).
[7] E. L. Kelly, University of California Radiation Laboratory Report 1044 (unpublished).
[8] G. Wilkinson, Phys. Rev. **79**, 1014 (1950).

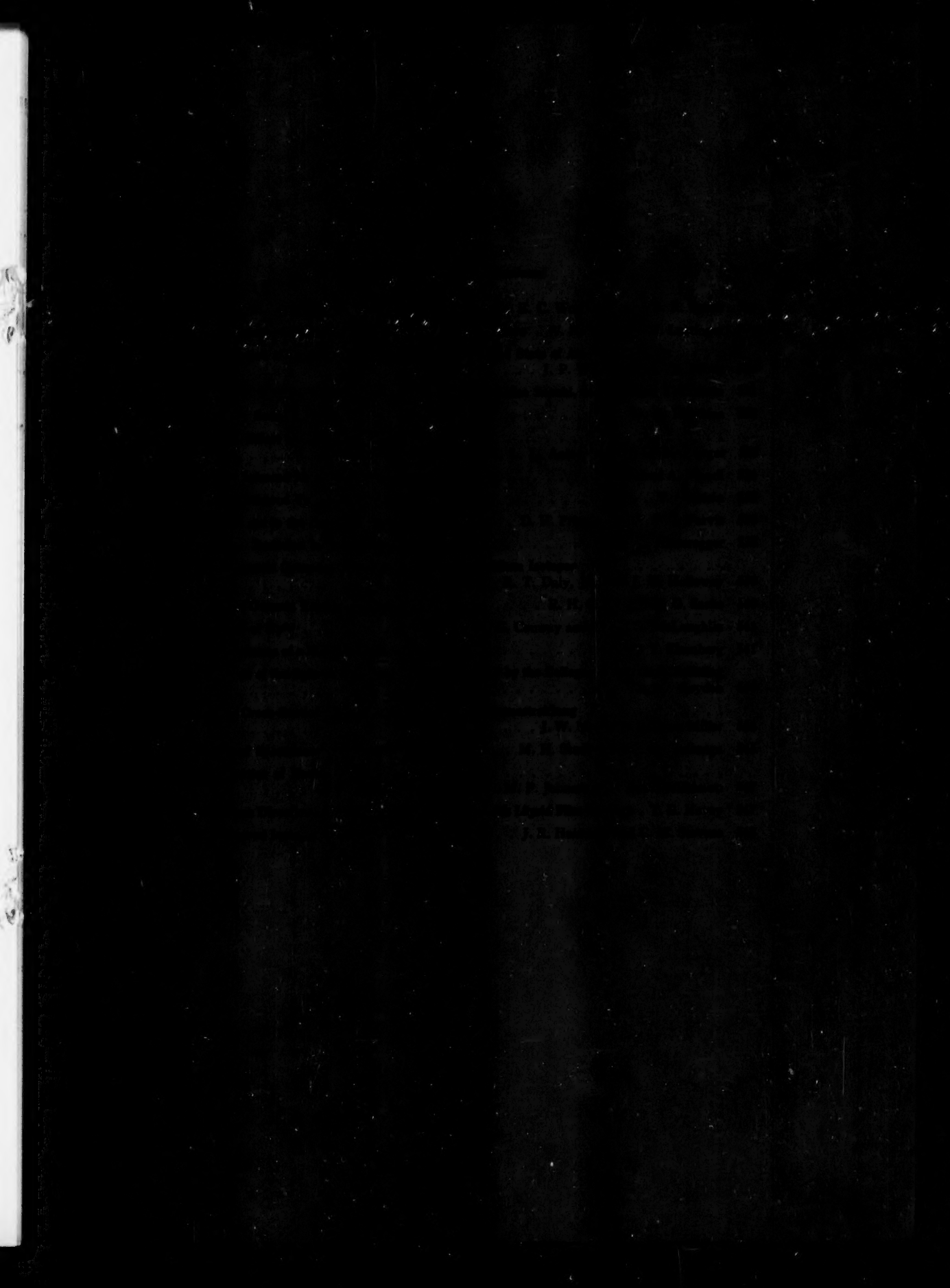

CONTENTS

THE PHYSICAL REVIEW SECOND SERIES, VOLUME 96, NO. 2 OCTOBER 15, 1954

On the Theory of Condensation . . . . . A. J. F. Siegert 243
Principle of Minimum Entropy Production . . . . . Martin J. Klein and Paul H. E. Meijer 250
Flow of Electrons and Holes through the Depletion Barrier Region in Point Contact Rectification . . . . . Melvin Cutler 255
Effect of Oxygen on the Electrical Properties of Lead Telluride Films . . . . . Donald E. Bode and Henry Levinstein 259
Theory of the Effect of Spin-Orbit Coupling on Magnetic Resonance in Some Semiconductors . R. J. Elliott 266
Spin-Orbit Coupling in Band Theory—Character Tables for Some "Double" Space Groups . R. J. Elliott 280
Magnetization of Tin at the Superconducting Transition . . . . . J. C. Thompson and C. F. Squire 287
Light Output of Luminescent Powder . . . . . W. A. Thornton 292
Afterglow of Magnesium Oxide Single Crystals . . . . . Eiso Yamaka 293
Elastic Moduli of Tin at the Superconducting Transition . . . . . Joseph K. Landauer 296
Derivation of Magnetostriction and Anisotropic Energies for Hexagonal, Tetragonal, and Orthorhombic Crystals . . . . . W. P. Mason 302
Magnetostriction and Crystal Anisotropy of Single Crystals of Hexagonal Cobalt . . . . R. M. Bozorth 311
Superconductivity of Vanadium at 24 000 Bits/sec . . . . . C. J. Grebenkemper 316
Analysis of the Three Parameter Ward Function of Hylleraas for the He^1 Ground State in Terms of Central Field Wave Functions . . . . . Louis C. Green, Marjorie M. Mulder, Paul C. Milner, Margaret N. Lewis, John W. Woll, Jr., Eleanor K. Kolchin, and David Mace 319
Auger Ejection of Electrons from Tungsten by Noble Gas Ions . . . . . Homer D. Hagstrum 325
Theory of Auger Ejection of Electrons from Metals by Ions . . . . . Homer D. Hagstrum 336
Statistical Atom with Angular Momentum . . . . . A. M. Sessler and H. M. Foley 366
Gamma Radiation from Deuterons on Beryllium, Lithium, and Boron . . . . . L. C. Thompson 369
Nuclear Forces and β Decay Matrix Elements . . . . . Roland F. Herbst 372
Elastic Scattering of Alpha Particles by Carbon . . . . . J. W. Bittner and R. D. Moffat 374
Energy Levels of the O^{16} Nucleus . . . . . David M. Dennison 378
Inelastic Neutron Scattering in Iron . . . . . D. L. Lafferty, L. A. Rayburn, and T. M. Hahn 381
Some Properties of Nuclear Normal Modes . . . . . Ingram Bloch and Yü-Chang Hsieh 382
Gamma Radiation from Interaction of 2.6-Mev Neutrons with Various Materials . . . . . V. E. Scherrer, B. A. Allison, and W. R. Faust 386
Inelastic Scattering of Alpha Particles by Lithium . . . . . C. W. Li and R. Sherr 389
Range of Nitrogen Ions in Emulsion . . . . . H. L. Reynolds and A. Zucker 393
Beta Spectra of C^{14} and S^{35} . . . . . A. Moljk and S. C. Curran 398
Total Cross Sections of 208-Mev and 310-Mev Protons for Light Elements . . . . . Hervasio G. de Carvalho 398
Gamma Effects in the Chlorine Neutron Cross-Section Resonance in Sodium Chlorate . . . . . Yu Ting, Edward R. Maering, and Dudley Williams 408
Cross-Section Theorem . . . . . Robert A. Mapleton 415
Spatial Distribution of Energy Dissipation by High-Energy X-Rays . . . . . Henry Bryuk 419
Coulomb Excitation Process in the Lighter Odd-Mass Nuclei . . . . . G. M. Temmer and N. P. Heydenburg 426
Pressure Broadening of OCS in Foreign Gas Mixtures . . . . . F. A. Lucima, A. V. Bushkovitch, and A. G. Rouse 434
Pulsing Effects in Coulomb Energies and the Radii of Mirror Nuclei . . . . . B. C. Carlson and I. Talmi 436
Radiations from Ir^{188m} . . . . . J. P. Minn, M. E. Bunker, and J. W. Starner 444
Model for Nuclear Reactions with Neutrons . . . . . H. Feshbach, C. E. Porter, and V. F. Weisskopf 448
Long-Lived Radioactivity of Eu^{152} and Eu^{154} . . . . . R. E. Slattery, D. C. Lu, and M. L. Wiedenbeck 465
Cycle of World-Wide Changes in the Daily Variation of Muon Intensity . . . . . V. Sarabhai, U. D. Desai, and D. Venkatesan 469
Precision Measurement of the Negative Pion Mass from Its Radiative Absorption in Hydrogen . . . . . Kenneth M. Crowe and Robert H. Phillips 470
Indirect Measurement of the π-π Interaction . . . . . Robert H. Phillips and Kenneth M. Crowe 484
Production of Tritons in High-Energy Deuteron-Deuteron Collisions . . . . . C. S. Godfrey 493
Absorption of Positive Pions by Deuterium at 76 and 94 Mev . . . . . Henry L. Stadler 496
Scattering of Polarized Neutrons from Heavy Nuclei . . . . . R. K. Adair, S. E. Darden, and R. E. Fields 503
Nuclear Saturation and Two-Body Forces. II. Tensor Forces . . . . . K. A. Brueckner 508
Space-Time Representation in Wave Mechanics: Illustration of the Method . . . Malcolm K. Brachman 516
Application of Variational Principles to Scattering Problems . . . . . H. E. Moses 519
Radiative Effects in a Constant Field . . . . . Roger G. Newton 524

(continued on cover three)

LANCASTER PRESS, INC., LANCASTER, PA.